GEOMECHANICAL FRAMEWORK FOR SECURE CO_2 STORAGE IN FRACTURED RESERVOIRS AND CAPROCKS FOR SEDIMENTARY BASINS IN THE MIDWEST UNITED STATES

FINAL TECHNICAL REPORT

Reporting Start Date: October 1, 2014
Reporting End Date: September 30, 2017

Principal Author: J.R. Sminchak
sminchak@battelle.org 614-424-7392

September 2017

U.S. Department of Energy National Energy Technology Laboratory
DOE Award No. DE-FE0023330

Submitting Organization: Battelle
505 King Avenue
Columbus, OH 43201-2698
DUNS Number: 00 790 1598

U.S. Department of Energy Disclaimer

This report was prepared as an account of work sponsored by an agency of the United States Government. Neither the United States Government, nor any agency thereof, nor any of their employees, makes any warranty, express or implied, or assumes any liability or responsibility for the accuracy, completeness, or usefulness of any information, apparatus, product, or process disclosed, or represents that its use would not infringe privately owned rights. Reference herein to any specific commercial product, process, or service by trade name, trademark, manufacturer, or otherwise does not necessarily constitute or imply its endorsement, recommendations, or favoring by the United States Government or any agency thereof. The views and the opinions of authors expressed herein do not necessarily state or reflect those of the United States Government or any agency thereof.

Ohio Develoment Services Agency Disclaimer

This report was prepared by Battelle with support in part by a grant from the Ohio Development Services Agency. Neither the State of Ohio nor any of its agencies, nor any person acting on behalf of the State:

1. Make any warranty or representation, express or implied, with respect to the accuracy, completeness, or usefulness of the information contained in this report, or that the use of any information, apparatus, method, or process disclosed in this report may not infringe privately owned rights; or

2. Assume any liabilities with respect to the use of, or for damages resulting from the use of, any information, apparatus, method or process disclosed in this report.

Reference herein to any specific commercial product, process, or service by trade name, trademark, manufacturer, or otherwise, does not necessarily constitute or imply its endorsement, recommendation, or favoring; nor do the views and opinions of authors expressed herein necessarily state or reflect those of the State of Ohio or its agencies.

Notice to Journalists and Publishers: Please feel free to quote and borrow from this report, however, please include a statement noting: “Funding for this project was provided, in part, through the Ohio Development Services Agency.”

Battelle Disclaimer

Battelle does not engage in research for advertising, sales promotion, or endorsement of our clients’ interests including raising investment capital or recommending investments decisions, or other publicity purposes, or for any use in litigation. Battelle endeavors at all times to produce work of the highest quality, consistent with our contract commitments. However, because of the research and/or experimental nature of this work the client undertakes the sole responsibility for the consequence of any use or misuse of, or inability to use, any information, apparatus, process or result obtained from Battelle, and Battelle, its employees, officers, or Trustees have no legal liability for the accuracy, adequacy, or efficacy thereof.

Acknowledgements

Support for this project was provided by the United States Department of Energy National Energy Technology Laboratory under award #DE-FE0023330 and Ohio Coal Development Office of the Ohio Development Services Agency under grant CDO-D-14-16. The project team very much thanks NETL and ODSA for sponsoring this effort, which is an important issue for CO_2 storage projects in the Midwest United States. Project guidance was provided by Bill O'Dowd (NETL) and Mr. Greg Payne (ODSA). NETL and ODSA have continued to support research on carbon storage, building confidence in the technology.

Project results reflect contributions from many people on the Battelle project team. The project lead was Battelle, and J.R. Sminchak was the project manager. Dr. Neeraj Gupta and Mr. Mark Kelley were technical advisors. Initial work on the Basin Scale Paleo Stress-Strain was completed by Mr. Ola Babarinde. Mr. Joel Main and Ms. Amber Conner were leads on the log analysis and integration task. Amber Conner also led the Geomechanical Site Characterization Guidance task. Mr. Ashwin Pasumarti was the lead on the geomechanical simulations. Other contributions were made by Dr. Jit Bhattacharya, Bryan O'Reilly, Isis Fukai, Mark Kelley, Desiree Padgett, Kelly Quigley, Jared Hawkins, and James E. Hicks. Carol Brantley, Mary Allison Comfort, Jess Schmidt, Colin Kegel, Theresa Schaff, and Jackie Gerst assisted with project administration and management. Dr. Samin Raziperchikolaee was an informal technical advisor who provided valuable advice on many geomechanical issues (free of charge).

The project benefited from previous geological research for the Appalachian Basin including: *The Atlas of Major Appalachian Gas Plays* (1996), *Midwest Regional Carbon Sequestration Partnership (2005-2017)*, *A Geologic Play Book for Trenton-Black River Appalachian Basin Exploration* (2006), and *A Geological Play Book for the Utica Shale Appalachian Basin Exploration* (2012). The project also gained from interactions with other researchers in the DOE-NETL FOA1037 program on geomechanical aspects of carbon storage. We'd also like to acknowledge several industrial partners who hosted deep characterization test wells: Duke Energy East Bend Plant, Ohio Department of Natural Resource/Artex Geological Survey Ohio CO2 Test Well, AEP Mountaineer Power Plant, New York State Energy Research and Development Authority JBPU project, and numerous operators in the region.

ABSTRACT

This report presents final technical results for the project *Geomechanical Framework for Secure CO_2 Storage in Fractured Reservoirs and Caprocks for Sedimentary Basins in the Midwest United States* (DE-FE0023330). The project was a three-year effort consisting of seven technical tasks focused on defining geomechanical factors for CO_2 storage applications in deep saline rock formations in the Midwest United States, because geomechancial issues have been identified as a significant risk factor for large-scale CO_2 storage applications.

A basin-scale stress-strain analysis was completed to describe the geomechanical setting for rock formations of Ordovician-Cambrian age in the Midwest United States in relation to geologic CO_2 storage applications. The tectonic setting, stress orientation-magnitude, and geomechanical and petrophysical parameters for CO_2 storage zones and caprocks in the region were cataloged. Ten geophysical image logs were analyzed for natural fractures, borehole breakouts, and drilling-induced fractures. The logs indicated mostly less than 10 fractures per 100 vertical feet in the borehole, with mostly N65E principal stress orientation through the section. Geophysical image logs and other logs were obtained for three wells located near the sites where specific models were developed for geomechanical simulations: Arches site in Boone County, Kentucky; Northern Appalachian Basin site in Chautauqua County, New York; and E-Central Appalachian Basin site in Tuscarawas County, Ohio. For these three wells, 9,700 feet of image logs were processed and interpreted to provide a systematic review of the distribution within each well of natural fractures, wellbore breakouts, faults, and drilling induced fractures. There were many borehole breakouts and drilling-induced tensile fractures but few natural fractures. Concentrated fractures were present at the Rome-basal sandstone and basal sandstone-Precambrian contacts at the Arches and East-Central Appalachian Basin sites. Geophysical logs were utilized to develop local-scale geologic models by determining geomechanical and petrophysical parameters within the geologic formations.

These data were ported to coupled fluid-flow and reservoir geomechanics multi-phase CO_2 injection simulations. The models were developed to emphasize the geomechanical layers within the CO_2 storage zones and caprocks. A series of simulations were completed for each site to evaluate whether commercial-scale CO_2 could be safely injected into each site, given site-specific geologic and geomechanical controls. This involved analyzing the simulation results for the integrity of the caprock, intermediate, and reservoir zones, as well quantifying the areal uplift at the surface. Simulation results were also examined to ensure that the stress-stress perturbations were isolated within the subsurface, and that there was only limited upward migration of the CO_2. Simulations showed capacity to inject more than 10 million metric tons of CO_2 in a single well at the Arches and East Central Appalachian Basin sites without excessive geomechanical risks. Low-permeability rock layers at the Northern Appalachian Basin study area well resulted in very low CO_2 injection capacity. Fracture models developed for the sites suggests that the sites have sparse fracture network in the deeper Cambrian rocks. However, there were indicators in image logs of a moderate fracture matrix in the Rose Run Sandstone at the Northern Appalachian Basin site. Dual permeability fracture matrix simulations suggest the much higher injection rates may be feasible in the fractured interval. Guidance was developed for geomechanical site characterization in the areas of geophysical logging, rock core testing, well testing, and site monitoring. The guidance demonstrates that there is a suitable array of options for addressing geomechanical issues at CO_2 storage sites. Finally, a review of Marcellus and Utica-Point Pleasant shale gas wells and CO_2 storage intervals indicates that these items are vertically separated, except for the Oriskany sandstone and Marcellus wells in southwest Pennsylvania and northern West Virginia. Together, project results present a more realistic portrayal of geomechanical risk factors related to CO_2 storage in a region with many large CO_2 point sources.

Table of Contents

List of Tables

Page

List of Figures

Page

List of Acronyms

2D	two-dimensional
3D	three-dimensional
ACR	artificial corner reflector
AEP	American Electric Power
API	American Petroleum Institute
bbl/min	barrels per minute
Bcf	billion cubic feet
bgs	below ground surface
CBIL™	circumferential borehole imaging log
cm^2	square centimeter
CMG	Computer Modelling Group Ltd.
CO_2	carbon dioxide
CT	computer tomography
DCT	differential capacitance transducer
DFIT™	Diagnostic Fracture Injection Test
DITF	drilling-induced tensile fracture
DOE	U.S. Department of Energy
FBP	formation breakdown pressure
FCP	fracture closure pressure
FIT	Formation Integrity Test
FMI	Formation MicroImager
FOA	Funding Opportunity Announcement
FPP	fracture propagation pressure
ft/s	feet per second
g/cm^3	grams per cubic centimeter
gAPI	gamma radiation measured in API units

GIS	geographic information system
GPa	gigapascal
GPS	global positioning system
HF	hydraulic fracture
HTPF	hydraulic test of pre-existing fractures
IGS	Indiana Geological Survey
InSAR	interferometric synthetic aperture radar
ISIP	instantaneous shut-in pressure
KGS	Kentucky Geological Survey
LOP	leak-off point
LOT	leak-off test
LVDT	linear voltage differential transformer
µm	micrometer
µs/ft	microseconds per foot
m	meter
mD	millidarcy
mD-ft	millidarcy-feet
MFO	mini fall-off
MICP	mercury injection capillary pressure
mm	millimeter
MMbbl	million barrels
MPa	megapascal
Mpsi	megapounds per square inch
MRCSP	Midwest Regional Carbon Sequestration Partnership
ms	millisecond
MT	metric tons (metric tonnes)
NETL	National Energy Technology Laboratory

NCS	net confining stress
NMR	nuclear magnetic resonance
ODNR	Ohio Department of Natural Resources
OGS	Ohio Geological Survey
psi	pounds per square inch
psi/ft	pounds per square inch per foot
PVT	pressure-volume-temperature
RBDMS	Risk Based Data Management System
RMSE	root-mean-squared error
STAR™	Simultaneous Acoustic and Resistivity (imager tool)
S_{Hmax}	maximum horizontal stress
S_{hmin}	minimum horizontal stress
S_v	vertical stress
TC	triple combo
Tcf	trillion cubic feet
TD	total depth
TWT	two-way time
UIC	underground injection control
USGS	U.S. Geological Survey
VSP	vertical seismic profiling
WBO	wellbore breakout
WSM	World Stress Map

Executive Summary

This document presents the final technical report for the project Geomechanical Framework for Secure CO_2 Storage in Fractured Reservoirs and Caprocks for Sedimentary Basins in the Midwest United States. The project was designed to assess the subsurface geomechanical effects of large-scale CO_2 storage applications in the Midwest United States based on site-specific geotechnical parameters and geomechanical conditions for the deep rock formations in the region. Geomechanical processes like fracture development, fracture activation, caprock fracturing, induced seismic activity, and surface deformation have been identified as risk factors for carbon storage applications. The pore pressure increase in response to fluid injection into deep geologic reservoirs may produce stress perturbation in both the target reservoirs and surrounding formations during large-scale CO2 storage. A comprehensive geomechanical assessment of formations integrity is required to study evolution of stress during CO_2 injection and determine whether the stress state compromises the ability of reservoirs to store CO_2 safely and effectively. Consequently, the geomechanical properties of reservoirs and confining layers need to be characterized in order to investigate safe, cost-effective CO_2 storage. The objectives of this project were developed to address these requirements with the following major technical tasks:

- Basin-scale stress-strain analysis of the geomechanical parameters and conditions for deep geologic formations in the Midwest United States,
- Site-specific geomechanical data analysis for three study areas in the Arches Province, East-Central Appalachian Basin, and Northern Appalachian Basin,
- Petrophysical log analysis and integration of data for the three study areas,
- Development of a methodology for geomechanical site characterization,
- Coupled fluid-flow geomechanical simulations to assess the effects of CO_2 injection on reservoirs and caprocks, and
- Assessment of CO_2 storage in areas with hydraulic fracturing for shale gas development.

The research presents an approach for defining geomechanical parameters, potential for subsurface deformation, and CO_2 storage processes based on rock core tests and geophysical logging in the region. Project results present a more realistic portrayal of geomechanical risk factors related to CO_2 storage in a region with many large CO_2 point sources.

The project was a three-year effort and part of the U.S. Department of Energy (DOE)/National Energy Technology Laboratory (NETL) program on monitoring, verification, accounting, simulation, and risk assessment of CO_2 sequestration in geologic formations. The project was supported by U.S. DOE/NETL under agreement DE-FE0023330 and The Ohio Coal Development Office of the Ohio Development Services Agency, Office Energy under agreement CDO/D-14-16.

Basin-Scale Paleo Stress Strain Analysis - In the Midwest United States study area, Precambrian and Paleozoic geologic structures and features reflect regional tectonic and structural evolution of the Basin and Arches. Analysis of 10 wells with geophysical image logs in the Appalachian Basin was completed to define the tendency for natural fractures to occur in Cambrian age rock formations. Wellbore breakouts and drilling induced fractures were also evaluated in the image logs to determine stress orientation and frequency with depth.

Paleo-stress orientation and magnitude analysis indicate that the stress field is a factor controlling the orientation of fractures in the region. Other factors such as basin flank architecture (flexure of

the basin flank) and paleo tectonic stress could also be influencing orientation and spatial distribution of these fractures. Additionally, analysis and interpretation of fracture orientation clusters show the regional fracture systems are highly complex with possibly systematic and non-systematic fractures within the evaluated lithologic units.

The results suggest that none of these fractures are stressed in their original state in normal conditions. At elevated pressure, Mohr's circle analysis suggests that there is increasing likelihood of fractures failing. Image logs had a low fracture intensity, with mostly less than 20 natural fractures per 100 ft vertical log interval (Figure ES-1). There was a dominant northeast – southwest trending fracture orientation as observed in the studied region, and a high percentage of fractures tend to strike sub-parallel to the axis of maximum horizontal stress. Fractures were not stressed in their original state but have the tendency to become critically stressed at elevated pressure. Management of pressure during injection could mitigate the risk of induced seismicity.

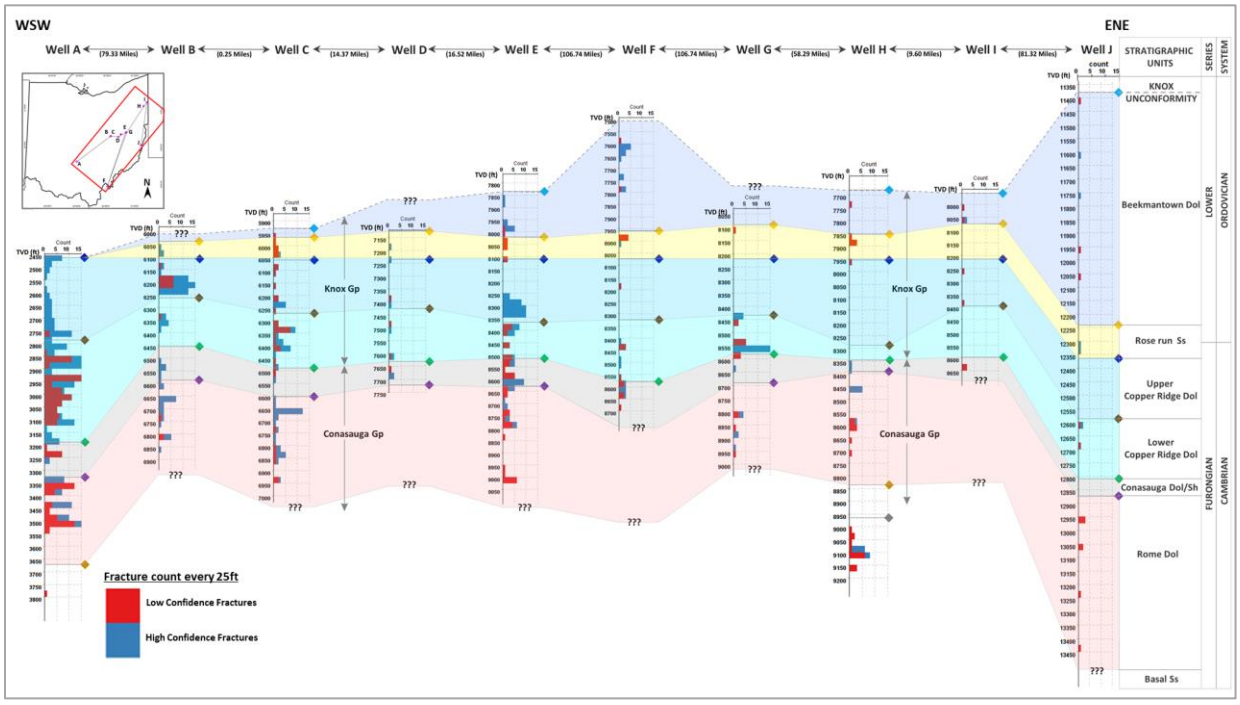

Figure ES-1: Geologic cross section illustrating fracture intensity in Cambrian age rock formations across eastern Ohio based on image log analysis.

Available rock core geomechanical test data were summarized with statistics, histograms, maps, and graphs to better define the distribution of these parameters in the study area. Data from 19 wells were compiled, including eight new test data performed under this project. These samples came from a variety of rock core samples in the region, so they reflect different formations, depths, testing labs, and sample conditions. The samples had average bulk density of 2.60 g/cc. The mean and median values for the parameters were fairly similar, indicating both statistics capture the central tendency of the populations. Compressional velocity averaged 17,302 ft/s and shear velocity averaged 9,791 ft/s. Dynamic Young's modulus averaged 8.69 1E+6 psi. Dynamic Poisson's ratio averaged 0.25. Static Young's modulus averaged 6.23 1E+6 psi. Static Poisson's ratio averaged 0.26.

Site Data Analysis and Log Integration - Based on the basin-scale stress-strain analysis, three sites were identified for more detailed examination: Arches Province, East-Central Appalachian Basin, and Northern Appalachian Basin (Figure ES-2). These sites had a full, modern set of geophysical logs and geomechanical rock core testing to provide control on geomechanical conditions in the subsurface. The sites provide a regional portrayal of the variability of geologic storage settings in the region.

In the study area, three sites were identified for image log processing to determine the horizontal stress orientation and nature of fractures. Geophysical image logs and other logs were obtained for three wells located near the sites where specific models are being developed for geomechanical simulations: Arches Site in Boone County, Kentucky; Northern Appalachian Basin Site in Chautauqua County, New York; and E-Central Appalachian Basin site in Tuscarawas County, Ohio. The Chautauqua log had unprocessed image logs from 3,878 feet (ft) to 7,305 ft from the Ordovician Queenston shale through the Cambrian Potsdam rock formations. The Tuscarawas log had an image log for 6,200 to 8,700 ft from the Ordovician Black River through Mount Simon sandstone. The Boone County log had an unprocessed interval for 900 ft to 3,500 ft from the Knox Group into the Precambrian basement rock. Processing and interpretation of the image log digital files were completed to provide a systematic review of any natural fractures, wellbore breakouts, faults, bedding planes, and drilling induced fractures.

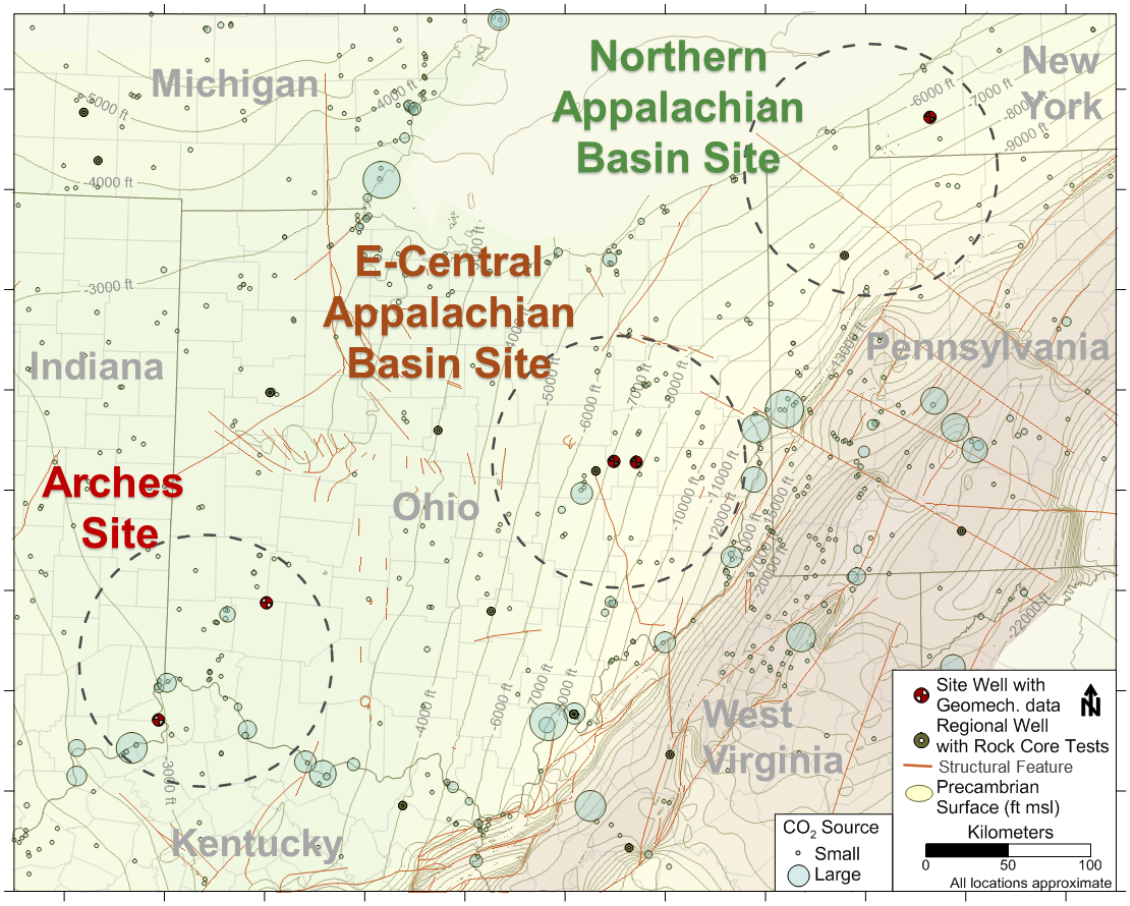

Figure ES-2: Map showing three study areas.

Results indicated that fractures were sparse and faults virtually non-existent (Figure ES-3). The maximum horizontal stress in the wells average approximately N65E orientation and match closely with the world stress map data. The orientation of the maximum horizontal direction trends from NE-SW in the northeast of the Appalachian Basin to ENE-WSW in the Arches site. The southwestern part of the Appalachian Basin appears to be more fractured than the northeastern part and contains a dominant northeast-southwest trend. The Arches site appears to contain very few fractures in comparison to the Appalachian Basin.

Geomechanical parameters were calculated from the sonic logs and used as an input in the isotropic fracture migration prediction model. The Arches and East-Central Appalachian Basin well sites contained high caprock Young's moduli values in comparison to the reservoir rocks, meaning that strong caprocks are present along the Cincinnati Arch and East-Central Appalachian Basin. The Northern Appalachian Basin contained high moduli values throughout the well with the highest values in the Galway dolomites. Most of the reservoir rocks displayed high moduli values showing few weak zones and a low potential for hydraulic fracturing at typical injection pressures.

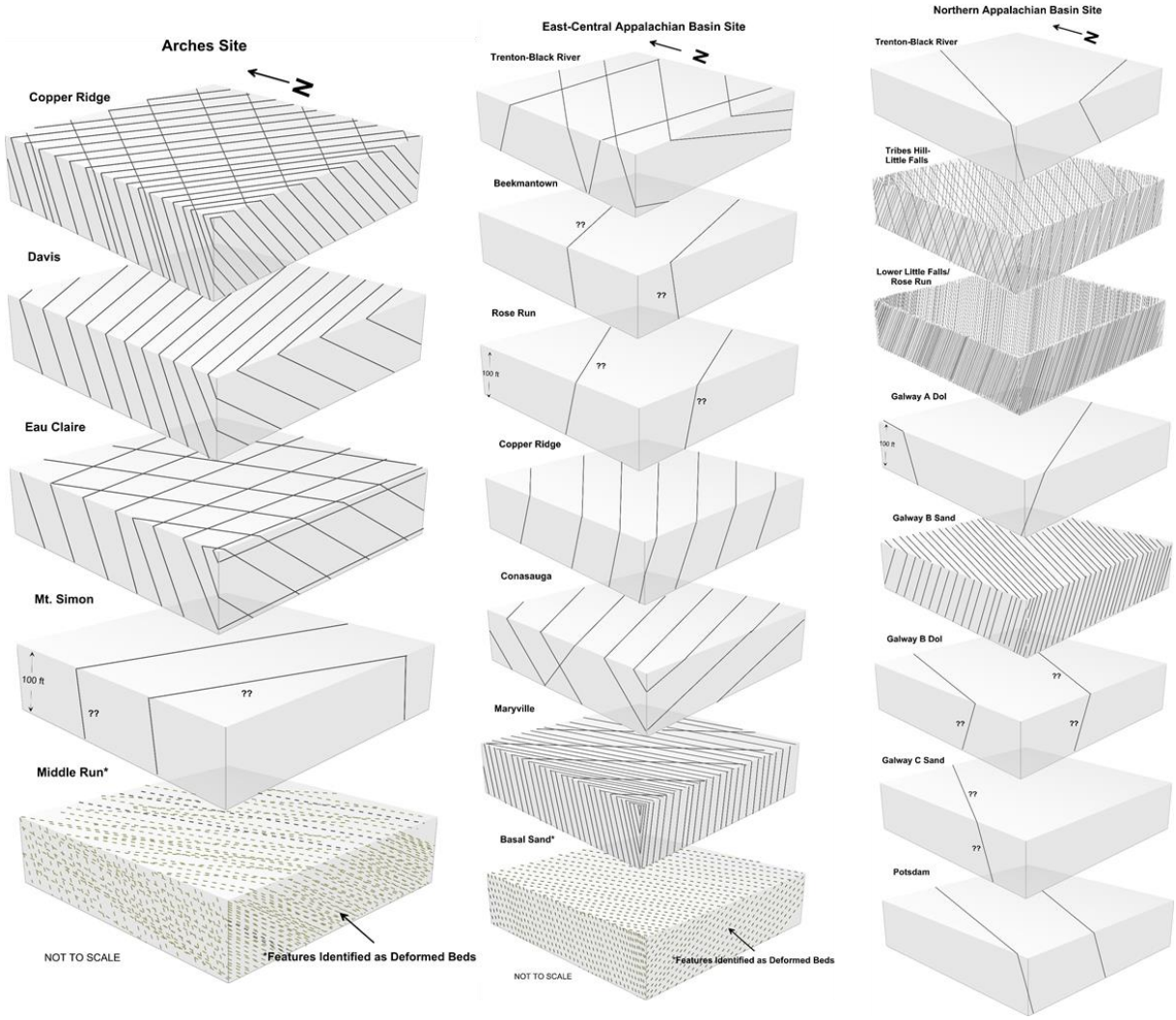

Figure ES-3: Conceptual fracture diagrams for the three study areas.

Coupled Fluid-Flow Geomechanical CO_2 Storage Simulations – A series of coupled fluid flow-geomechanical simulations were completed for the for the Arches, East Central Appalachian Basin, and Northern Appalachian Basin local study areas. Geocellular models were developed for the study areas to depict site-specific variations in subsurface geology and geomechanical parameters based on geophysical logs and rock-core tests. The Arches study area was a relatively shallow site, consisting of the Eau Claire shale overlying the Mount Simon sandstone as a target for CO_2 injection. The East-Central Appalachian study area included several deeper Ordovician-Cambrian age rock formations that were targets evaluated for storage. The Northern Appalachian study area is more influenced by the Appalachian Mountains and associated geologic structures, and image logs suggested a moderate fracture matrix in the Galway-Rose Run formation.

Geocelluar models were used to develop coupled fluid-flow and geomechanics simulations for each site to evaluate site-specific geomechanical constraints on industrial-scale CO_2 storage feasibility. The simulations were analyzed to assess the integrity of the caprock, intermediate and reservoir zones, quantify the areal uplift at the surface, determine if stress-stress perturbations were isolated within the subsurface, and evaluate upward migration of the CO_2. At the Arches study site, simulations suggested the capacity to inject 24-51 million metric tons CO_2 into the Mount Simon Sandstone over 30 years in a single well. No tensile or shear failure was observed in any of the layers in the caprock, intermediate or reservoir zone, despite highly conservative assumptions in the model. Stress-strain perturbations were generally isolated beneath the caprock. Surface uplift was estimated at 26 mm or less in the simulations. The East Central Appalachian Basin simulations also had no tensile or shear failure in any of the layers in the caprock, intermediate or reservoir zone, and stress-strain perturbations were isolated beneath the caprock. Up to 5 mm of uplift may be expected at the surface, which was lower than that predicted for the Arches site, owing to the lower level of pore-pressure increase, the much higher Young's modulus values, and the deeper location of the injection zone. Simulations suggest the 30-year effective capacity of this well is at least 10 million metric tons of CO_2. Results indicate that the East Central Appalachian Basin is an appealing area for stacked, multi-reservoir storage of commercial-scale volumes of CO_2. The Northern Appalachian basin site simulation results suggested that the site could not maintain industrial-scale injection, mainly due to the low permeability of the deep rock layers. Because this site had indications of moderate fracture matrix in the Galway-Rose Run interval, a fracture matrix model was developed for the study site and ported to dual permeability fracture matrix simulations. The fracture matrix simulations suggest the interval may support much higher CO_2 injection rates of more than 500,000 metric tons per year. The fracture matrix parameters were based on single well's geophysical image logs,and additional logs and well tests would reduce uncertainty on fractured zone. At sites with indications of fracture matrix, injection testing and core studies would help constrain the estimates for geomechanical parameters (minimum and maximum horizontal stress gradients, Young's Modulus, Poisson's Ratio, rock cohesion). Together, these three study areas provide a realistic portrayal of the range of geomechanical impacts of CO_2 storage in the Midwest U.S. Acquiring site-specific geomechanical parameters is essential for a wholistic evaluation of CO_2 injection sites. Simulation results generated in this research benefit the establishment of CO_2 storage applications.

Development of Methodology for Geomechanical Site Characterization - Geophysical logging, rock core testing, well testing, and site monitoring provide a wide variety of options for

geomechanical site characterization of CO_2 storage projects. The methods have advantages and disadvantages as well as cost limitations for each technology. The combined technologies can be used to design site-specific programs which will provide detailed evaluations of the potential storage site. There are many different options to address geomechanical concerns, but each site will require a distinct subset of options based on its system specifications, geological setting, and subsurface conditions.

Key geomechanical processes that may affect a CO_2 storage project include hydraulic fracturing of the injection zone and/or caprock, fracture activation, induced seismic activity, wellbore damage, and surface uplift/deformation. The geomechanical site characterization, rock core testing, well testing, and site monitoring methods can be used to provide either indirect parameters that may be used to analyze the effect of CO_2 injection or direct indication of subsurface deformation.

As described in this research, the geologic setting will affect the suite of geomechanical options selected for a site. If the site has competent caprock and reservoir, few natural fractures, no nearby faults, and no history of seismic activity, a low-level program of geomechanical testing and monitoring may suffice for the project. This program may include rock core testing of selected units, basic wireline logging suite, basic step-rate injection testing, and limited geomechanical monitoring. At sites with nearby faults, fractures, and history of low-level seismic activity, a more substantial program may be necessary. In this scenario, the program may include rock core testing of multiple samples from several injection and caprock zones, more advanced wireline logging of storage zone and intermediate zones, mini-fracture well testing, and application of a monitoring network at the site. Sites with active seismic activity may require an extensive characterization, testing, and monitoring system. This system may include continuous monitoring of seismic activity, periodic survey of surface deformation, and development of a mitigation plan for addressing geomechanical effects of injection. Overall, the methods for geomechanical site characterization, testing, and monitoring provide a wide range of options to support safe, effective, and secure CO_2 storage projects.

CO_2 Storage/Shale Gas Risk Factor Assessment - Mapping of unconventional hydrocarbon plays, horizontal Marcellus/Utica-Point Pleasant wells, and CO_2 storage formations was completed to determine potential interactions between shale gas development and CO_2 storage applications in the Midwest. Significant items of this assessment are listed below.

- The geologic framework in the Midwest United States contains many different deep saline formations and depleted oil and gas fields suitable for CO_2 storage. These formations are extensive and dispersed across the region, requiring consideration of the potential interaction with unconventional shale gas development.
- Mapping of 10,719 Marcellus and 2,114 Utica-Point Pleasant unconventional well top-hole and bottom-hole locations and true vertical depths portrays the wells' spatial distribution in the subsurface. Marcellus wells had an average horizontal length of 5,668 feet; Utica Point-Pleasant wells had an average horizontal length of 7,258 feet. These long horizontal legs affect a much greater area in the subsurface than conventional vertical oil and gas wells. Hydraulic fracturing of 20 to 75 stages in horizontal wells results in a large stimulated reservoir volume in the subsurface. This process results in a fractured zone around the horizontal well that may extend 1,000 feet on both sides and 500 feet vertically.

- Both the Marcellus shale and the Utica-Point Pleasant shale cover vast lateral areas, unlike conventional oil and gas pools that have more restricted boundaries. However, both plays have fairways where there is concentrated well density because of favorable conditions for hydrocarbon production.
- The organic shales in the Midwest are not considered primary caprocks for CO_2 storage formations, and unconventional shale gas development does not generally preclude CO_2 storage applications in the region.
- Both the Marcellus shale and the Utica Point-Pleasant shale are vertically separated from most key CO_2 storage rock formations by several caprock layers and/or intermediate layers with a combined thickness of greater than1,000 ft in most areas.
- In terms of CO_2 storage, the Oriskany sandstone is located only a few hundred feet below the Marcellus shale in much of the Appalachian Basin. As such, there may be more potential for interaction between Oriskany CO_2 storage and Marcellus shale operations. The Oriskany has variable thicknesses of 0 to 150 ft, with the best reservoir quality in southwestern Pennsylvania and West Virginia. These areas also have extensive Marcellus development. Oriskany CO_2 storage applications in these areas would need to consider interactions with unconventional Marcellus shale gas wells.
- The organic shale sequences in the Midwest may have a very large capacity to adsorb CO_2. Thus, they may provide additional caprock security for CO_2 storage. Additional studies of CO_2 mobility in fractured organic shales may help understand the potential for CO_2 to migrate through these organic shales.
- Geomechanical simulations suggest that stress changes from CO_2 storage applications are confined to the injection zone and immediate caprock layers. Thus, stress changes are unlikely to affect developed shale gas intervals where they might activate previously hydraulically fractured zones.
- Geomechanical effects on legacy oil and gas wells appear to be limited to areas where legacy oil and gas wells are present near both CO_2 storage zones and shale gas development. Areas with the highest intersection of these conditions are present in northern West Virginia and southwestern Pennsylvania, where there is a high concentration of Marcellus wells.

Overall, the study suggested that the interaction of shale gas development and CO_2 storage applications in the Midwest U.S. requires consideration. While no critical technical issues were identified that may prevent CO_2 storage near shale gas fields in general, the potential interaction of CO_2 storage projects and shale gas wells will require investigation in certain geographic areas. The subsurface footprint of shale gas development in the Midwest has expanded rapidly over the last 10 years and continues to grow. There may be perception issues for any CO_2 storage projects near areas with a dense concentration of unconventional shale gas wells. The description of the geologic framework, the subsurface mapping analysis, and the risk factor analysis presented in this report provide a basis for evaluating CO_2 storage near unconventional shale gas plays.

1.0 Introduction

This final report summarizes the technical work completed for the project titled Geomechanical Framework for Secure CO_2 Storage in Fractured Reservoirs and Caprocks for Sedimentary Basins in the Midwest United States. The overall research scope included an approach for defining geomechanical parameters, potential for subsurface deformation, and CO_2 storage processes based on rock core tests and geophysical logging in the region. The project consisted of nine tasks over three years. Major project tasks included: a basin-scale paleo-stress/strain regime for the region; systematic compilation of geomechanical parameters; analysis of geophysical logs; and reservoir simulations of geomechanical processes. The project was designed to leverage tools and technologies to improve methods for defining geomechanical issues at CO_2 storage sites.

1.1 Project Background

The objectives of this project were to 1) complete a systematic assessment of the stress-strain setting for geologic formations in the Midwest United States, 2) develop a methodology for evaluating potential geomechanical stress at CO_2 storage sites, 3) complete reservoir simulations to evaluate geomechanical deformation in and around the reservoirs and study its effect on the safe storage of CO_2, 4) complete reservoir simulations to assess the effects of activated natural fractures on injectivity enhancement and storage security within reservoirs, and 5) assessment of CO_2 storage in areas with hydraulic fracturing for shale gas development. Project results were focused on presenting a more realistic portrayal of risk factors related to CO_2 storage in a region that is heavily dependent on fossil fuels.

This research project was selected under the U.S. Department of Energy (DOE) National Energy Technology Laboratory (NETL) carbon storage program (Award DE-FE-0023330). Support was also provided by the Ohio Coal Development Office of the Ohio Development Services Agency (Grant CDO/D-14-16). The project was designed to address the research needs listed under DOE Funding Opportunity Announcement (FOA) 1037 Area of Interest 1-Geomechanical Research. Results will improve the understanding of geomechanical processes and impacts critical to CO_2 injection operations to assess the geomechanical behavior and effects of increased reservoir pressure on fractures, faults, and sealing formations. Research output will contribute to an improved geomechanical framework that will form the basis for studying the effects of CO_2 injection on opened and closed fractures and the potential for further slippage of fractures (including hydraulic fracturing in sealing shale layers) at both a basin scale and at individual project scales.

1.2 Geomechanical Processes and CO_2 Storage

During large-scale CO_2 sequestration, pore pressure variation in response to fluid injection into the reservoirs induces stress perturbation in both the target reservoirs and surrounding formations. A comprehensive geomechanical assessment of formation mechanical integrity is required to study the evolution of stress during CO_2 injection and determine whether the stress state compromises the ability of reservoirs to store CO_2 safely and effectively. Consequently, the geomechanical properties of reservoirs and confining layers need to be characterized to investigate safe, cost-effective CO_2 storage.

Gathering the information needed to formally determine the geomechanical characteristics of the reservoirs and confining layers is difficult and expensive. As a result, the lack of information on geomechanical processes introduces uncertainties to the evaluation of stress field changes and large geomechanical deformation of the sealing layers that preserve the integrity of the reservoirs. In addition, areas in the Midwest United States have many formations, including reservoirs and caprocks, which are known to be fractured (Milici, 1980; Roen and Walker, 1996). Such fractures could be formed inside geological formations due to rock rupture associated with the tectonic stress field at the time of fracture formation (Mandl, 2005). Fractures can exhibit various types, sizes, orientation, and arrangement, all of which can affect the pathway of fluid flow in the underground fractured rock mass. Where the permeability of the intact rock is low, fractures having the potential to be activated could even provide the main conduit of the fluid flow (Zoback, 2007). This phenomenon should be investigated to determine its potential for enhancing CO_2 injection capacity and study its role on safe storage of CO_2.

In addition, shale gas development in the overburden formations should be considered as a factor that may affect safe storage of CO_2 in the underground reservoirs. Building a complex network of fractures during hydraulic stimulation of gas shale reservoirs to increase permeability and gas production from stimulated reservoir volume (Mayerhofer et al., 2010) can affect the sealing integrity of large portions of caprock of CO_2 storage reservoirs. The complexity of a fracture network in the shale reservoirs and its associated caprock deformation is a function of the distribution and geological properties of natural fractures, the stress anisotropy in the shale reservoir, and the mechanical properties of heterogeneous shales (Cipolla et al., 2010).

The ability to determine the amount of feasible pressure increase at a site was critical to the research because allowable pressure increase is a key factor for total injection capacity. Changes in mechanical stress and deformation fields in and around the injection reservoirs can induce seismic activity by generating new fractures or activating pre-existing fractures to provide a pathway for CO_2 leakage. CO_2 injection into reservoirs may lead to high pore pressure at the top of the reservoir, which could hydraulically fracture the caprock or trigger slip on reservoir-bounding faults by reducing effective normal stress on the fault surface (Chiaramonte, 2009). A safe injection pressure is one that falls below the least compressive principal stress of the reservoir to avoid hydraulic fracturing. The amount of pressure increase feasible at a site is also a regulated operational parameter. If the amount of pressure increase considered to be safe for injection is lower than initially calculated due to low fracture pressure, this could significantly decrease the total CO_2 storage capacity in the reservoirs.

In addition, in the context of a critically stressed crust, it is thought that much of the intraplate continental crust is likely in frictional equilibrium (Townend and Zoback, 2000); therefore, slip on pre-existing faults could trigger seismicity, providing leakage pathways by fault permeability enhancement (Zoback and Gorelick, 2012). As a result, the investigation of induced seismicity potential due to fault slippage during CO_2 sequestration is important for understanding the risk associated with such an endeavor (Sminchak and Gupta, 2003). Also, the presence of natural fractures and their movement as a function of effective stress changes during CO_2 injection into the fractured reservoirs could affect the geomechanical stability of natural fractures. The slippage of cemented fractures depends not only on the rock-mechanical properties of the formation, but also on the properties of natural fractures. For example, depending on whether the fracture is parallel or perpendicular to the maximum horizontal stress, it experiences different normal and

shear stresses which affect the potential of natural fracture movement and its permeability enhancement. An activated fracture network in a reservoir can increase the practical capacity of the reservoir for storage of CO_2 by creating a high-permeable flow path without endangering seal integrity. Natural-fracture networks can also influence long-term trapping of geologically sequestered CO_2 by affecting the position and shape of the CO_2 plume.

1.3 Project Objectives

This research focused on sedimentary basins and arches in the Midwest United States using available regional and site-specific geomechanical data to determine the stress state and suitability of deep saline formations for CO_2 storage. Selected research (Zoback and Gorelick, 2012) suggests that some potential reservoirs in this part of the world may be in a critically stressed state such that an increase in pore pressure could potentially lead to formation fracture pressure which could concurrently initiate hydraulically activated tensile/shear fractures in the reservoir-caprock system. The research approach was designed to systematically assess the geomechanical state of potential CO_2 storage reservoirs on a basin scale and tie it to local-scale data.

A comprehensive geomechanical evaluation of different formations laid the groundwork for 1) investigation on the in-situ stresses and their changes during CO_2 injection in the various potential basin reservoirs, and 2) analysis of the effect of geomechanical deformation on safe CO_2 storage. Results from the geomechanical analyses were used to evaluate the potential for mechanical failure of pre-existing faults and fracture networks, and assess the type and orientation of expected failure leading to injection-induced seismicity as a function of stress field changes.

The project was organized into seven technical tasks. Table 1-1 summarizes the main task objectives. The information on the basin-scale stress-strain analysis provided regional information on the distribution of rock formations, geomechanical parameters, geomechanical conditions in the subsurface, and variations across the region. Based on this information, three study areas were selected for more detailed analysis based on analysis of geophysical logs, rock core tests, and geologic setting. This information was ported into coupled fluid flow geomechanical simulations to evaluate the CO_2 injection scenarios. In addition, tasks were completed to provide guidance on geomechanical site characterization and potential interaction between CO_2 storage applications and shale gas development in the region.

Table 1-1: Summary of project objectives.

Item	Objectives	Methods
Basin-Scale Stress-Strain Analysis	Collect and analyze geotechnical data for basin scale paleo-stress/strain analysis	Define tectonic setting, paleo stress orientation, stress magnitude, and geomechanical parameters
Site Geomechanical Data Analysis	Acquire and process 3-4 advanced geophysical logs from key wells in the region, complete testing of 10 rock cores for geomechanical parameters	Monitor regional oil and gas drilling activities and contact operators drilling deep oil and gas wells in key areas. Review existing image logs for unprocessed intervals.
Petrophysical Log Analysis and Integration	Integrate petrophysical data from geophysical logs and rock core test data to determine geomechanical properties of key CO_2 storage zones and caprocks in the region	Translate petrophysical log data for derived geomechanical parameters, calibrate data to rock core test data
Development of Methodology for Geomechanical Site Characterization	Complete development of a methodology for geomechanical site characterization for CO_2 storage sites	Compile methods for geophysical well logging, rock core testing, injection testing, and site monitoring
Geomechanical Simulations of CO_2 Storage	Complete geomechanical simulations for CO_2 storage for three study areas based on site specific data, evaluate natural fractures in storage intervals and caprocks	Develop numerical models for three sites across region, complete coupled multi-phase geomechanical simulations for CO_2 injection scenarios, analyze stress changes, potential for subsurface deformation
CO_2 Storage/Shale Gas Risk Factor Assessment	Develop maps and identify risk factors for CO_2 storage/shale gas zones in the region	Depict spatial and vertical arrangement of shale gas plays, unconventional horizontal wells, and CO_2 storage formations, determine geomechanical risk factors for technologies to interact in the subsurface
Reporting and Technology Transfer	Prepare final technical report detailing all test data, analysis, and project results	Describe key findings of research, document project progress, communicate results to stakeholders, research community

2.0 Basin-Scale Stress-Strain Analysis

The Paleo Stress-Strain Analysis task (Task 2) was designed to provide input parameters for subsequent tasks on geomechanical simulations and site-specific analysis. Under Task 2, a methodology for depicting the stress-strain regime for the Midwest United States was developed. The methodology involved defining the tectonic setting, analyzing the paleo-stress orientation and magnitude, and systematically surveying the geomechanical and petrophysical parameters for CO_2 storage zones and caprocks. The task was focused on sedimentary basins and arches in the Midwest United States, especially the Northern Appalachian Basin, using geomechanical data to determine the stress state and suitability of deep saline formations for CO_2 storage. The task involved systematically assessing the geomechanical state of potential CO_2 storage reservoirs on a basin scale as opposed to a site-specific assessment.

2.1 Tectonic Setting Definition

The objective of defining the tectonic setting was to describe the geologic structures and features in the Midwest United States study area. In addition, regional tectonic and structural evolution of the Basin and Arches was summarized to determine trends in stress-strain setting in the various rock formations being considered for CO_2 storage. This section gives a general overview and description of sedimentary basins within the Midwest United states—specifically, the Appalachian Basin, its bordering basins, and the structural arches.

2.1.1 Basins

Appalachian Basin

The Appalachian Basin (Figure 2-1) is a stretched, asymmetric retro-arc foreland basin with a preserved northeast-southwest trending central axis that extends from central Alabama through West Virginia, Pennsylvania, and New York into Canada. The basin is about 1,300 miles north-south and approximately 350 miles wide at its broadest point. The eastern limit of the basin is buried beneath thrust sheets in the Blue Ridge and Valley Province of the Appalachian Mountains; the western limit of the basin reaches to central Ohio and east-central Kentucky. The northern limit of the basin is bounded by the Canadian Shield and the southern limit is transitional into the Black Warrior Basin.

The history of the basin began as early as the Cambrian time when a basement aulacogen formed during the Iapetan Rifting. After the rifting event, the eastern margin of proto-North America was subsequently impacted by multiple collisional events during the Taconic (Upper Ordovician), Acadian (Middle to Upper Devonian), and Allegheny (Upper Carboniferous) orogenies in the Paleozoic era. The multiple orogenic events led to reactivation of structures and molded the present-day shape of the basin.

Figure 2-2 illustrates how the Precambrian basement is overlain by more than 45,000 feet (ft) of sedimentary rocks in the central Pennsylvania portions of the northern part of the basin. Sedimentary rocks of the Appalachian Basin range from Neoproterozoic to Carboniferous-Permian in age.

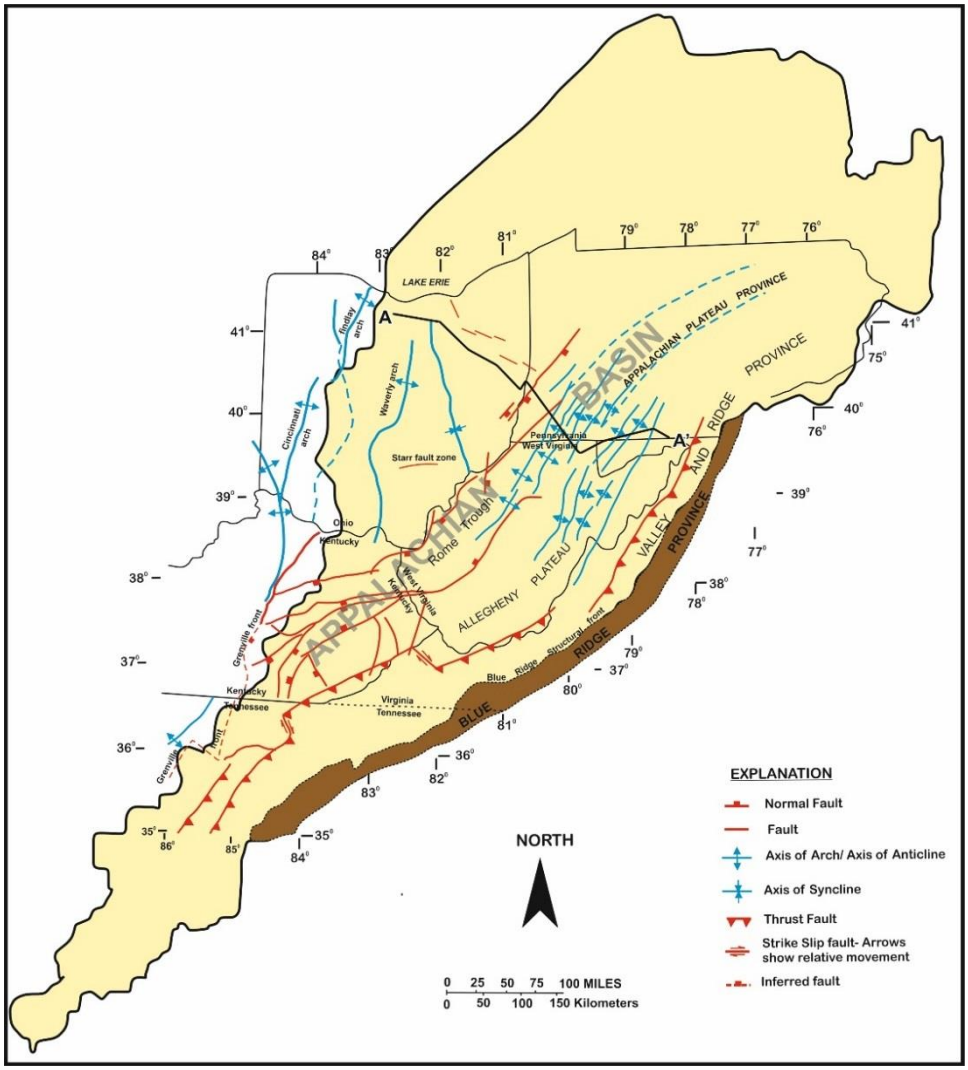

Source: Prepared and modified after Ryder et al., 2012.
Note: Line A-A' shows approximate trend of cross section shown in Figure 2-2.

Figure 2-1: Generalized structural map showing the Appalachian Basin extent and known structural elements with selected features.

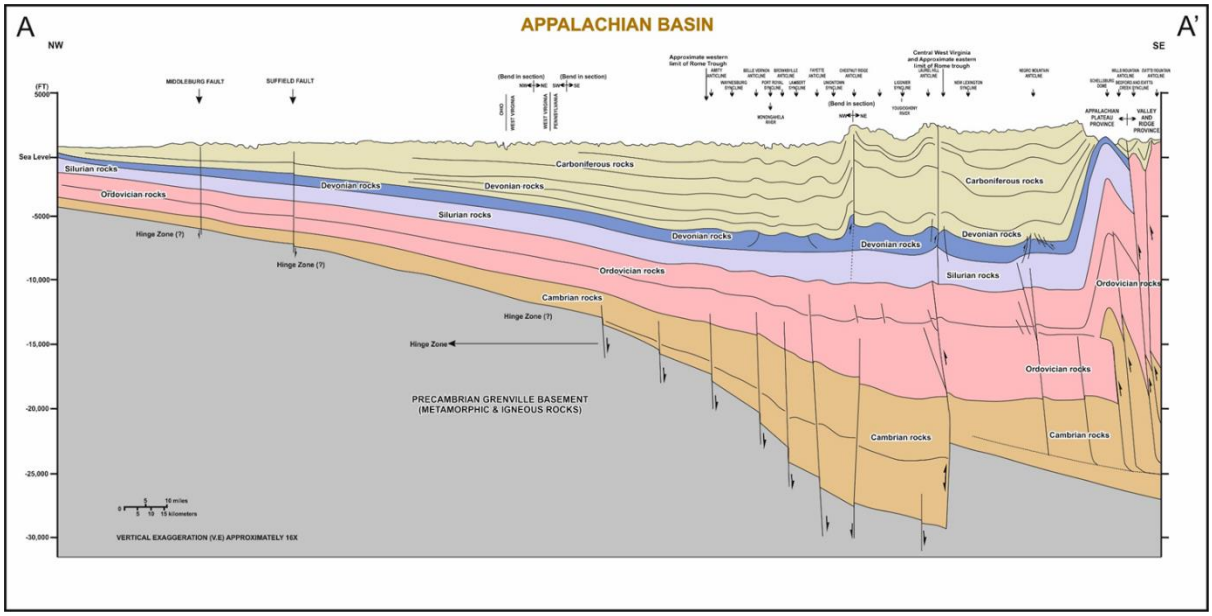

Source: Prepared and modified after Ryder et al., 2012.

Figure 2-2: Generalized geologic cross section across the Appalachian Basin trending northwest to southeast.

Michigan Basin

The Michigan Basin is an intracratonic basin with a nearly circular shape. The bulk of the basin underlies the State of Michigan and locally extends into its neighboring states. The basin (Figure 2-3) is approximately 248 miles in diameter and about three miles deep with only minor structural disruption (Howell and van der Pluijm, 1999). In a clockwise direction starting from northern Michigan, the basin is bordered by the Canadian Shield to the north, the Findlay arch to the southeast, Kankakee arch to the southwest, and the Wisconsin highland to the west. The basin has remained circular throughout its history, with minor shifts in its depo-center. It is covered with approximately 16,000 ft of Paleozoic-age sedimentary strata that were deposited from the Cambrian through the Carboniferous time. A geologic cross section running west to east through the basin center is shown in Figure 2-4.

Illinois Basin

The Illinois Basin appears as a complex intracratonic downwarp characterized by a range of structures that mirrors a long and complex tectonic history (Nelson, 1990). The basin itself is a north-northwest- to south-southeast-trending spoon-shaped synclinal feature (Archer, 1979) that covers a major portion of Illinois and extends into south-western Indiana and western Kentucky. The basin extends over an area of approximately 53,000 square miles (Archer, 1979).

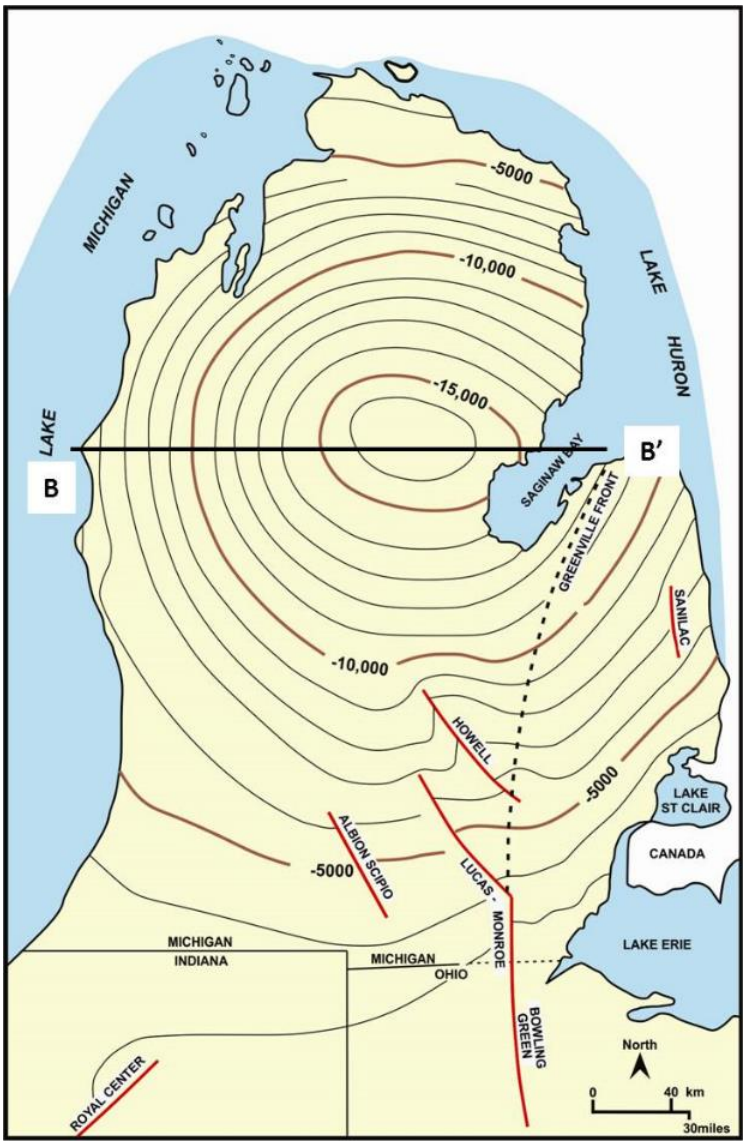

Source: Prepared and modified after Montgomery, 1984.
Note: Line B-B' shows approximate trend of cross section shown in Figure 2-4.

Figure 2-3: Generalized structure map of the Michigan Basin region showing the intracratonic Michigan Basin.

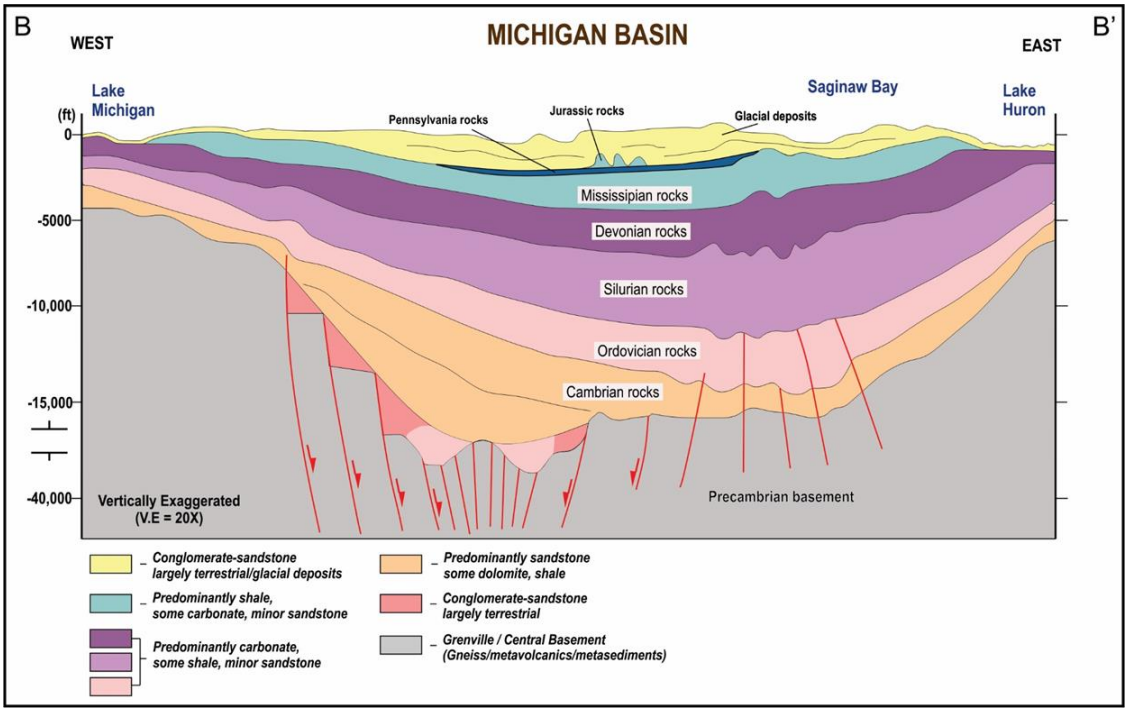

Source: Prepared and modified after Montgomery, 1984.

Figure 2-4: Cross section B-B' (west to east) across the Michigan Basin illustrating the shape and possible failed rift system within the basin's center.

2.1.2 Arches

The Findlay, Kankakee, Cincinnati, and Algonquin structural arches are shown in Figure 2-5. The Findlay arch is a positive anticlinal-shaped feature that might have started developing in the late Ordovician, following the impact from the last phases of Taconic orogeny. The arch is located in northwestern Ohio as a broad shallow platform overlain by a thinner package of Paleozoic sedimentary rocks compared to the thicker package of Paleozoic sedimentary rocks present in the adjacent Michigan and Appalachian Basins.

Another anticlinal-shaped feature, the Kankakee arch, is located southwest of the Michigan Basin, separating the Michigan Basin from the Illinois Basin. The Kankakee arch probably developed in the Ordovician time.

The Cincinnati arch separates parts of the Appalachian Basin located in the western part of Ohio and eastern Kentucky from the Illinois Basin. At the junction where the Cincinnati and the Kankakee arches merge is a broad, relatively flat-lying area known as the Indiana-Ohio platform. Unlike the previously mentioned arches, where Precambrian crystalline rocks (igneous and metamorphic) rise close to the surface, the Cincinnati arch is underlain by the East Continent rift basin, an elongate north-south trending basin filled with a thick sequence of Proterozoic arenaceous rocks (Shrake et al., 1990; Drahovzal et al., 1992; MRCSP, 2005).

2.2 Tectonic and Structural Evolution

In order to develop a complete overview of how sedimentary basins in the Midwest developed over time, it is essential to understand the tectonic events and geologic processes that occurred since deposition of the sediments. These events and processes configured the shape of the basins and influenced the sequences of deposits that filled them up. Tectonic dynamics around

the eastern margin of the North America plate initiated the growth of the Appalachian Basin and consequently produced stresses that instigated the development of geologic structures observed in the basin today.

The evolution of the Appalachian Basin dates as far back as 1 billion years ago, during the Mesoproterozoic era. Since then, the basin has been subjected to different tectonic phases of uplift and erosion; has passed through different longitudes and latitudes and different climatic conditions; and has experienced multiple depositional settings (Ettensohn, 2008) and different tectonic stresses. The complexity of the basin is reflected in its structural architecture, the distribution of trapped hydrocarbon, and the distribution of primary/secondary porosity in sedimentary strata across basins.

The tectonic history of the Appalachian Basin is characterized by multiple orogenic events that resulted in crustal deformation and development of folds, thrust faults, strike-slip faults, and other structures associated with a compressional regime. Analyzing the different structural styles observed in the basin today contributes to our understanding of the tectonic history around the eastern margin of North America and the stress field that developed through time.

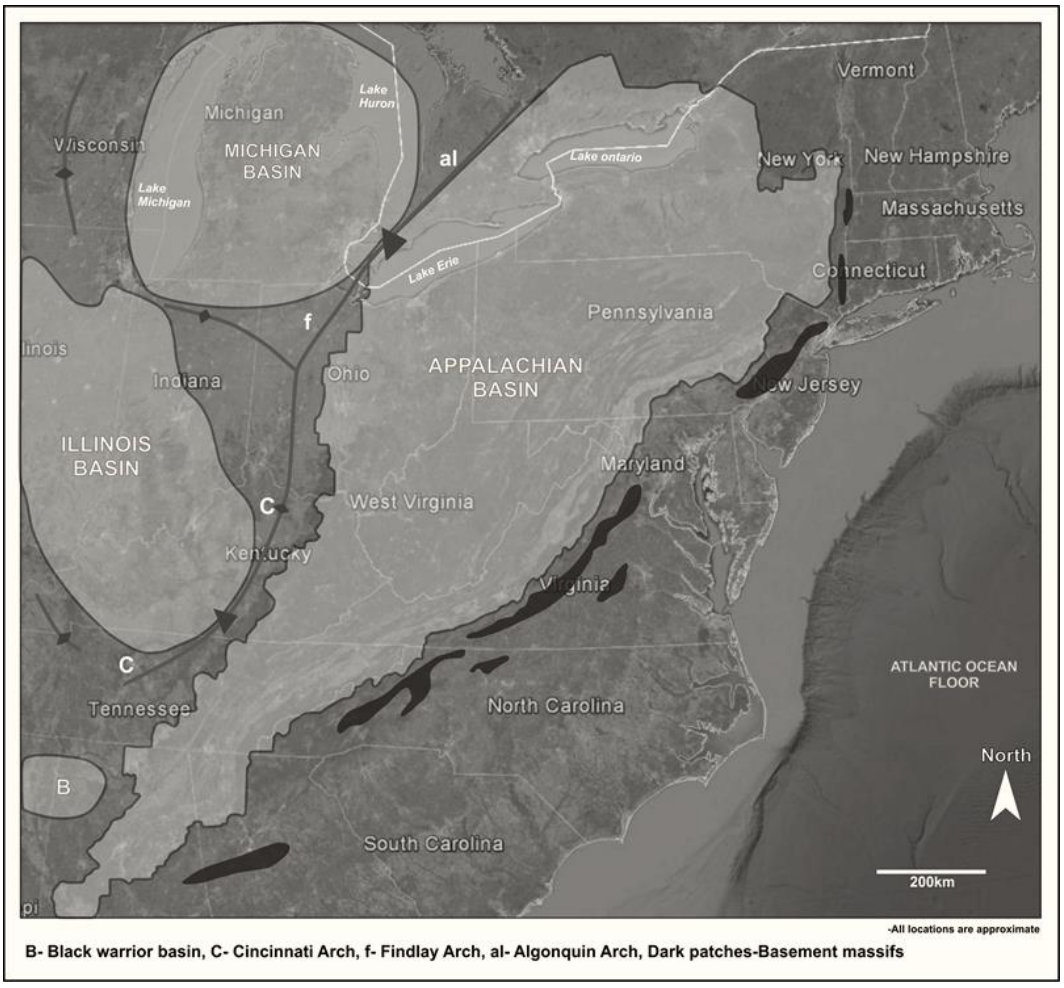

Sources: Prepared from Google Earth and modified after Ettensohn (2008), Sweezey (2002), and Battelle (2014).

Figure 2-5: Extent of the Appalachian, Michigan, and Illinois Basins and structural arches along with overlaid features in the Midwest region of the United States.

Figure 2-6 shows a compilation of charts (lithostratigraphic, sea level, paleoclimate, and ice volume charts) alongside a parallel chart that catalogs the different episodes of tectonic events that could have impacted the Paleozoic-age sedimentary package filling the Appalachian Basin. The regional tectonic and stratigraphic evolution of the basin is explained in more detail in Ettensohn (2008), Colton (1970), and Hansen (1997a, 1997b, 1998).

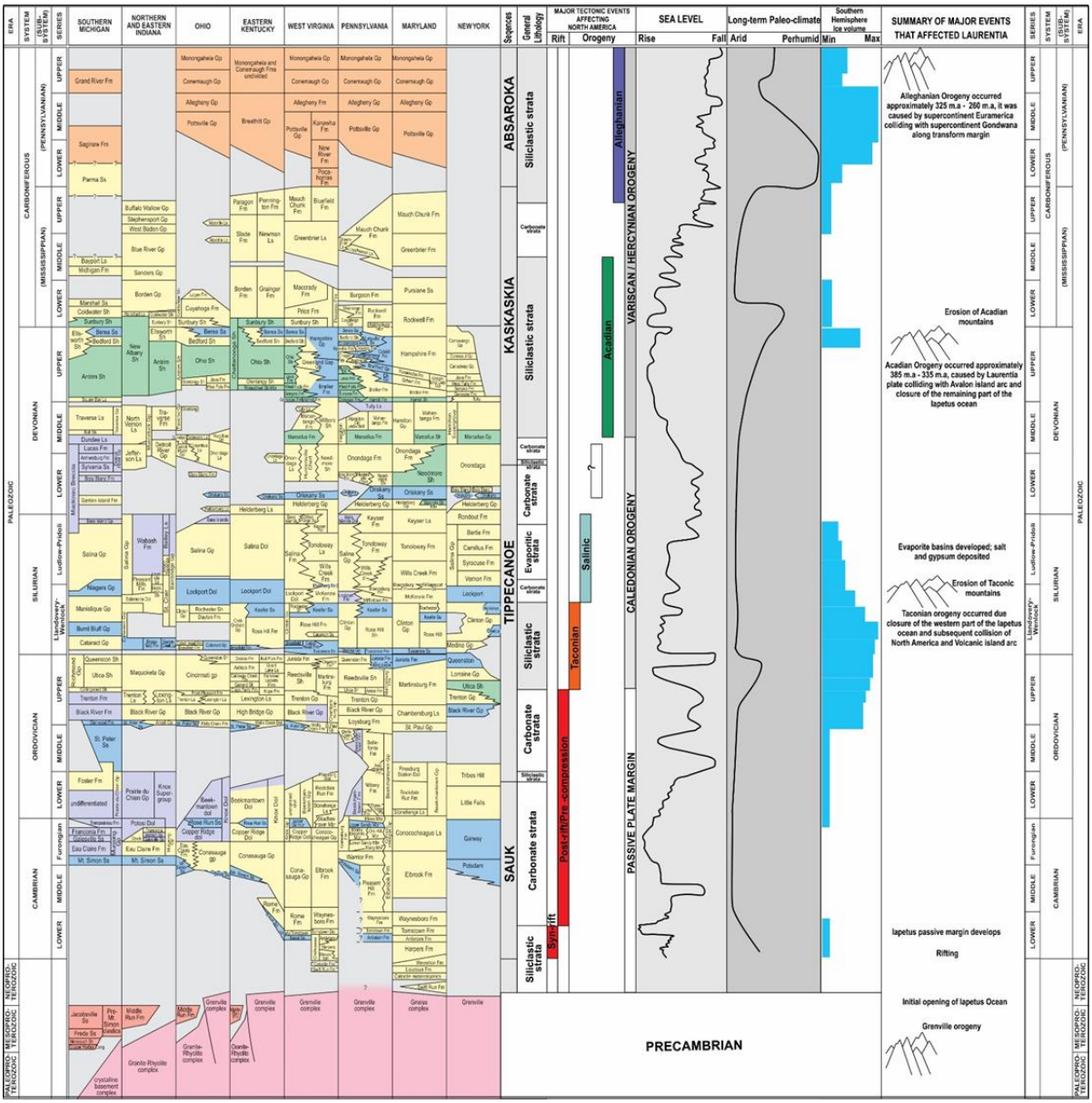

Sources: Compiled and modified after Battelle (2013), MRCSP (2005), and Ettensohn, 2008.

Figure 2-6: Chronostratigraphic chart of the Appalachian Basin region, followed by (left to right) tectonic events affecting North America, sea level chart, paleoclimate chart, and ice volume chart.

The Appalachian Basin continues to be useful ground for work on structural styles and tectonic concepts such as thrust and fold belts, isostasy, deformational mechanisms, and thin-skinned deformation, based on outcrop and subsurface structures in the basin (Rogers and Rogers, 1843; Willis, 1893; Gwin, 1964; Ettensohn, 2008). In addition, the basin is recognized as a global model for mountain borderlands (Schuchert, 1923; Ettensohn, 2008).

2.2.1 Tectonostratigraphic Evolution of the Cambrian-Ordovician Strata

This section provides a general overview of and introduction to the depositional settings and the sequence of deposition during the Cambrian-Ordovician time period in the Appalachian Basin as it relates to tectonism. A more detailed explanation is provided in Ettensohn (2008) and MRCSP (2005).

Cambrian Sandstone

During the Late Precambrian to Early Paleozoic time, the North American plate (known as Laurentia) straddled the equator (MRCSP, 2005). In the Late Precambrian time, Laurentia rifted away from an adjacent plate (Rodinia); this process led to the development of the Iapetus Ocean (Dietz, 1972). At that point, the Iapetus Ocean separated the margin of these two plates, and Laurentia was configured in such a way that its southern margin became a passive continental margin. Around that time, the Grenville basement, which is now buried underneath the Appalachian Basin states, was exposed to erosion. Following the erosional phase that affected the surface of the Precambrian-Grenville basement, the deposition of sand on the Precambrian unconformity surface began late in the Middle Cambrian as the sea level began to rise. This led to the onset of subsidence on the southern margin in response to sediment loading and thermal subsidence (Thomas and Astini, 1999). In addition, around the Lower or Middle Cambrian, the Rome trough was created; it extends from the Mississippi embayment through Kentucky to southwestern Pennsylvania (Thomas, 2006). The development of the Rome trough could have been due to the impact of stresses generated in the course of opening the Iapetus Ocean.

During this time, the Cambrian-age basal sandstone was deposited across Appalachian Basin states and neighboring states as a transgressive sequence of sandstone, shales, and carbonates (MRCSP, 2005) on the regional Precambrian unconformity surface. The basal sandstone interval that was deposited in the Rome trough is separated from the Mount Simon sandstone and the unnamed Conasauga sandstones because it is depositionally younger than the unnamed basal sandstone of the Rome trough (MRCSP, 2005).

The Cambrian-age sandstone is believed to have been deposited in a wide range of environments within the studied region. These environments vary from marginal marine to marine, littoral, fluvial, and estuarine (Janssens, 1973; Driese et al., 1981; Haddox and Dott, 1990; MRCSP, 2005).

Copper Ridge and Rome Dolomite

The depositional setting during the period of deposition of the Rome and Copper Ridge dolomite was configured in such a way that the proto-Appalachian and Michigan Basins (and possibly other basins) were covered by a shallow epicontinental sea. Subsidence above the Rome trough and lesser subsidence in the proto-Michigan and Appalachian Basins influenced depositional facies, as did sea-level fluctuations (MRCSP, 2005). The pervasive dolomitization of the upper part of this interval (Copper Ridge equivalents) throughout the North American continent continues to be enigmatic, although it may be related to the expulsion and migration of fluids

from the Ordovician Sevier or late Paleozoic Alleghenian orogenies (Glumac and Walker, 2002; Montanez, 1994).

Tomstown/Rome/Waynesboro/Lower Conasauga Formations - The Shady-Tomstown dolomite was deposited as a carbonate ramp along the Cambro-Ordovician passive margin of the craton (Read, 1989). The substantial uniformity in the thickness of the dolostone across the southern bounding faults of the Rome trough permitted the interpretation of the package as a pre-rift deposition (Harris et al., 2004). The great thickness of the Rome Formation within the trough documents growth during the rifting event (Harris et al., 2004). Evidence suggests that sediments were transported into the trough from the north and that the deeper parts of trough were occupied by a clastic shelf or ramp (MRCSP, 2005). Along the northwest margin of the trough, delta front and shallow marine shelf deposits dominated a shallower structural platform, with sand supplied by fluvial systems located to the north (MRCSP, 2005). It is presumed that the areas north and west of the trough were probably either starved of sediment due to non-deposition or affected by erosion on the Precambrian surface. During the period of deposition of the upper Rome Formation, the deeper Rome trough was occupied by a carbonate ramp. A deeper-water, intra-shelf basin is interpreted in south-central Kentucky, based on the few wells drilled there (Harris et al., 2004). Lateral facies of the lower Conasauga Formation may represent downslope facies equivalents of Rome clastic wedges building off the northern trough margin into deeper water (Ryder, 1992b; Ryder et al., 1996, 1997).

Eau Claire/Conasauga/Elbrook/Warrior Formations - Marine conditions prevailed in the units capping the trough fill. The marine shales of the Eau Claire Formation in the western part of the Appalachian study area represent the continuation of the Mount Simon transgression (Driese et al., 1981). It is important to note that this transgressive sequence is different in comparison to the transgressive sequence of sand deposits that filled the Rome trough and areas to the east. Across the Appalachian Basin study area, there is a west-to-east transition in this sub-interval from shallow marine siliciclastics of the Eau Claire Formation, to mixed carbonates and clastics deposited in intra-shelf settings in the Conasauga, to peritidal carbonates of the Elbrook and Pleasant Hill Formations (Read, 1989).

Upper Munising/Trempealeau/Potosi/Davis/Copper Ridge/Gatesburg/ Conococheague Formations - At the time of deposition of this sub-interval, regression in sea level caused progradation of peritidal carbonates across the entire Appalachian Basin study area (Read, 1989). The regression, which may have been related to the ending of extensional tectonics on the passive margin, marks the Sauk II/Sauk III boundary (Glumac and Walker, 2000). The Copper Ridge dolomite is interpreted to have been deposited in a variety of peritidal environments. The Conococheague was deposited as platform carbonates transitional to deeper basinal facies to the south and east (Demicco, 1985). Shallowing-upward cycles within the Conococheague record repeated facies successions from storm to subtidal algal reef to subtidal shoal to intertidal flat and, ultimately, to sabkha (Demicco, 1983). Sandstones in the lower part of the Conococheague and lateral equivalents may be related to detrital influx following the Sauk II/Sauk III sea-level fall (Marchefka and Glumac, 2002).

Rose Run

During the late Cambrian period following the failed rifting event, sands including the Rose Run were reworked and deposited across the Appalachian Basin area. The sands were mixed with shelf carbonates that eventually dominated this passive margin (Riley et al., 1993). Provenance studies of the Rose Run sandstone suggest that they are compositionally mature and were derived from the crystalline Precambrian shield complexes and overlying platform rocks (Miall,

1984; Riley et al., 1993). The widespread Knox unconformity developed during the initial collision of the passive margin and the lowering of eustatic sea level in the Middle Ordovician (Mussman et al., 1988; Read, 1989). The widespread Knox unconformity might have been related to the Taconic orogeny period, which might have caused the creation of a western fore-bulge along with basin loading. This event was likely accompanied by a tectonic quiescence that eventually resulted in the widespread Knox unconformity surface.

Deposition of the Rose Run and adjacent Knox units has been attributed to represent a peritidal-to-shallow subtidal marine environment (Mussman and Read, 1986; Anderson, 1991; Gooding, 1992; Ryder, 1992a; Ryder et al., 1992; Riley et al., 1993). The Rose Run is part of a heterogeneous assemblage of interbedded siliciclastic and carbonate facies in the Knox that were deposited on a carbonate shelf referred to by Ginsburg (1982) as the “Great American Bank.” The Rose Run represents low-stand deposits of siliciclastic sediments that were transported onto the peritidal platform and reworked during subsequent sea-level rises (Read, 1989). Many geologists have also interpreted tidal flat deposition for the Rose Run and equivalent strata based on core and outcrop description (Mussman and Read, 1986; Anderson, 1991; Enterline, 1991; Riley et al., 1993).

In summary, the Cambrian-Ordovician succession represents a period of shallow water conditions with deposition of a thick sequence of predominantly shallow carbonates that formed on what Ginsburg (1982) referred to as Great American Bank.

2.2.2 Precambrian Structures

Structural features that impact the Precambrian crystalline rocks within the Grenville terrane are continuously updated from time to time as geologists identify features from newly acquired data. Multiple phases of deformations that occurred in the history of the Appalachian Basin initiated some of these structural features in the Precambrian and subsequently reactivated them. The Grenville basement, which is composed of variety of igneous and metamorphic rock types, is exposed in the complex terrain of southern Ontario and has been subjected to multiple deformations and faulting.

The Precambrian rocks extend north into New York, Pennsylvania, and Ohio, then farther south into Kentucky and possibly Alabama. They also extend south of New York into Pennsylvania, beneath the Appalachian Plateau and Ridge and Valley Province and into Ohio beneath the Paleozoic cover rocks. Figure 2-7 illustrates the approximate western extent of the Appalachian Basin along with related basement structural features. Structural features in Ohio are construed primarily from mapping the bedrock-geology contacts and from interpreting oil and gas drilling data (Baranoski, 2002). In addition, other data, such as two-dimensional (2D) and three-dimensional (3D) seismic data used by oil and companies in exploring for hydrocarbon plays, are effective in providing high-resolution images of the subsurface and therefore can be used to identify structural features. However, the availability of such data is limited due to the high cost associated with acquisition and processing and the proprietary nature of the data.

The basement has been affected by the various orogenies listed in Figure 2-6, and it has subsided in response to accumulating Paleozoic sedimentary cover rocks deposited on the basement unconformity surface. The accommodation of the cover rocks by basin subsidence was further accompanied by minor faults observable around the Appalachian Basin. These faults potentially represent the reactivation of larger Precambrian faults and the localized uplifting of the basement in response to compressive stress transmitted into the interior of the Laurentia plate.

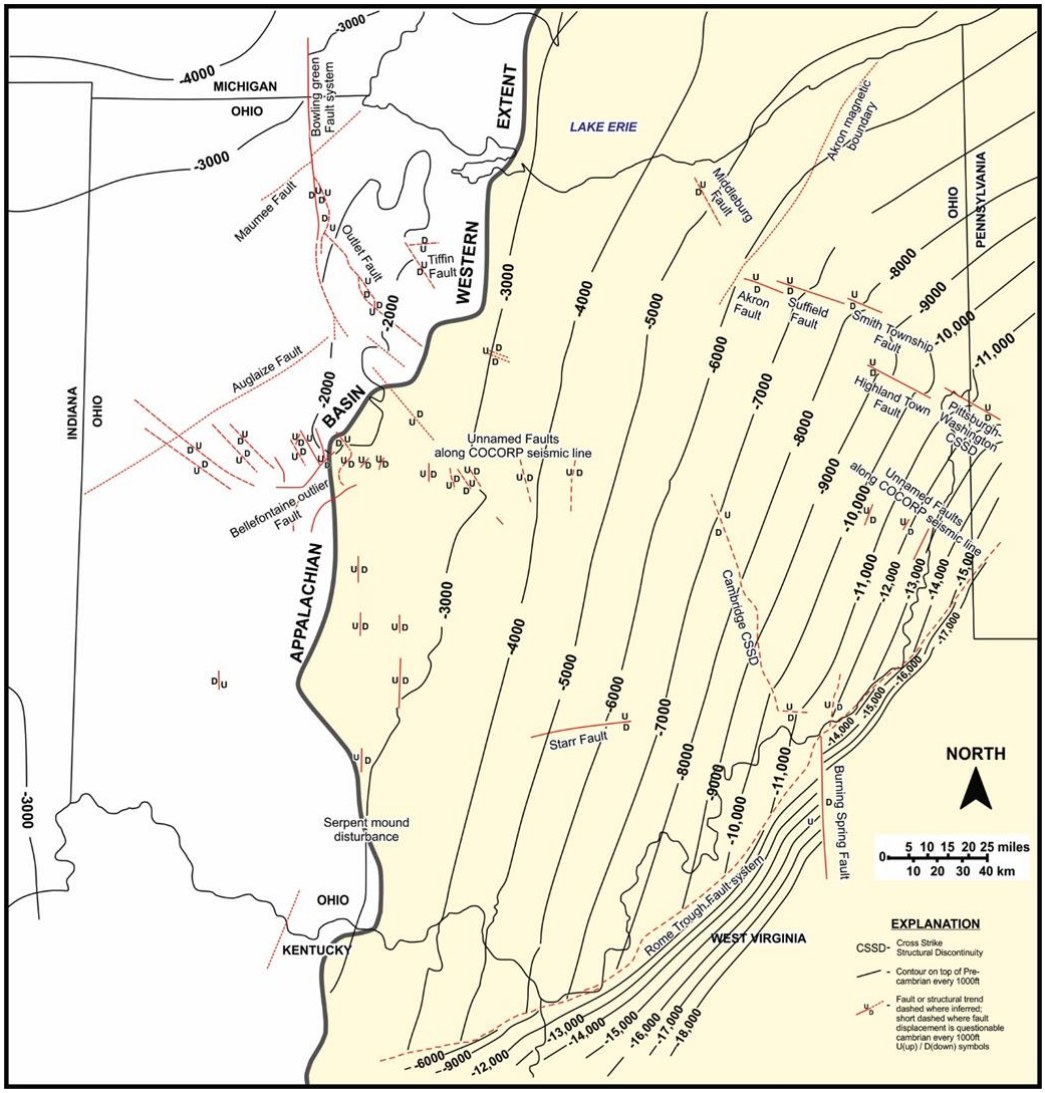

Source: Prepared and modified after Baranoski, 2002.

Figure 2-7: Precambrian unconformity surface map illustrating the western extent of the Appalachian Basin and structural components of the Precambrian surface.

2.2.3 Paleozoic Structures

Paleozoic structures are interpreted by geologists from oil and gas drilling data and available seismic data. They are difficult to discern from basement-related structures because of limited available data and the prolonged tectonic history of the basin. Due to the constraints involved in using drilling data/well data in interpreting faults, the extent and displacement of interpreted faults are often inferred. In other words, the data constraint makes the process of discriminating between structures related to thin- or thick-skinned deformation very challenging.

A generalized map showing known structural features in the Appalachian Basin is shown in Figure 2-8. Most of the interpreted structures are typically folds and thrust faults. These structures are styles of deformation that would normally develop in a collisional zone. Due to the complexity in the styles observed, it is difficult to identify structures related to the Paleozoic sedimentary cover rocks alone; therefore, only the folds (anticlines and synclines) could be interpreted as Paleozoic structures.

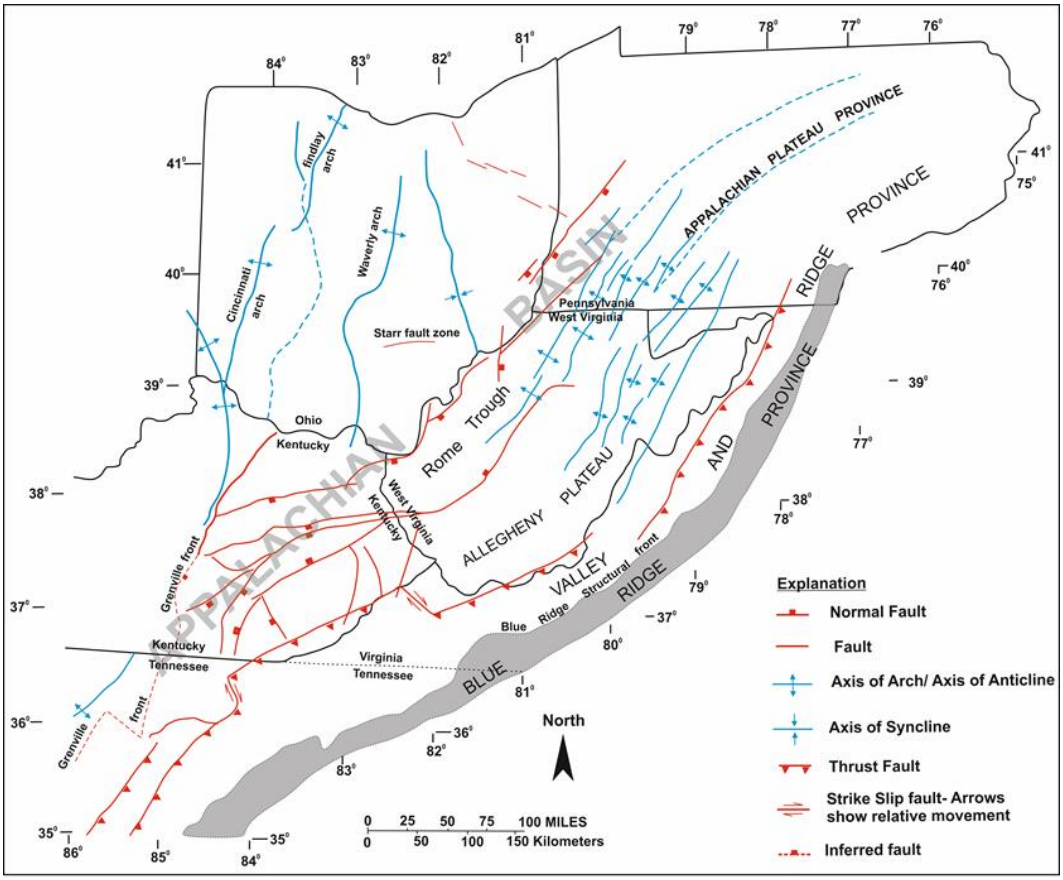

Figure 2-8: Structural elements within the Appalachian Basin.

2.3 Regional Fracture Studies

Fractures and faults are deformations that develop in the lithospheric crust in response to stress. Stresses can vary from reference states as a consequence of either natural or man-made processes (Engelder, 1993). The failure of a geological formation under stress is influenced by its mechanical properties, stress rate, temperature, and pressure conditions. Small-scale structures such as natural fractures that have developed during the tectonic and diagenetic history of the Appalachian Basin could be relevant in understanding and predicting the basin's history. Advances in technology have allowed imaging/logging of this type of structure by using resistivity and acoustic responses around a wellbore profile; this advanced type of log is known as a resistivity and acoustic image log. The logs are occasionally collected from wells drilled within the Appalachian Basin region for multiple purposes related to geologic characterization or geomechanical assessment. The geophysical log data provide valuable subsurface information on the orientation of fractures, bedding, principal horizontal stresses, and partial identification of geologic features such as vugs that could enhance porosity and permeability systems at a specific depth in the subsurface.

Natural fractures are known to enhance permeability and porosity if they are present within a target formation. The presence of natural fractures within a reservoir has the potential of increasing the efficiency of a storage or production reservoir. The intensity of natural fractures at a specific location also influences the likelihood of vertical wells intersecting a fracture as well as enhancing production. Conversely, if natural fractures are intersected by a vertical injection well within the target formation, they could also enhance injectivity of fluid into the formation.

2.3.1 Distribution of Natural Fractures

Using available image log data, a structural analysis study on natural fractures and their distribution within the Cambrian-Ordovician-age carbonate interval was conducted for the data coverage area (i.e., the northern portion of the Appalachian Basin within central to eastern Ohio). Ten image logs were available from ten vertical wellbores. Figure 2-9 shows the study area and the locations of image log data that were available for analysis. All of the image log data analyzed penetrate through the Cambrian-Ordovician section in the subsurface. This uniformity allows for lateral stratigraphic correlation and comparison of natural fracture distribution from one location to another.

Due to the shape of the basin, the portion of the Cambrian-Ordovician wedge that was logged at well locations close to the Rome trough was thicker than the portion logged at well locations closer to the western platform. A representative geologic cross section generated from geophysical log correlation is shown in Figure 2-10. This figure shows how the Cambrian-Ordovician sedimentary wedge thickens towards the east. All the wells used for the natural fracture analysis strike nearly parallel to the cross section shown. In other words, the wells trend from shallower parts of study area (west) to deeper parts of the study area (east), as shown in Figure 2-9.

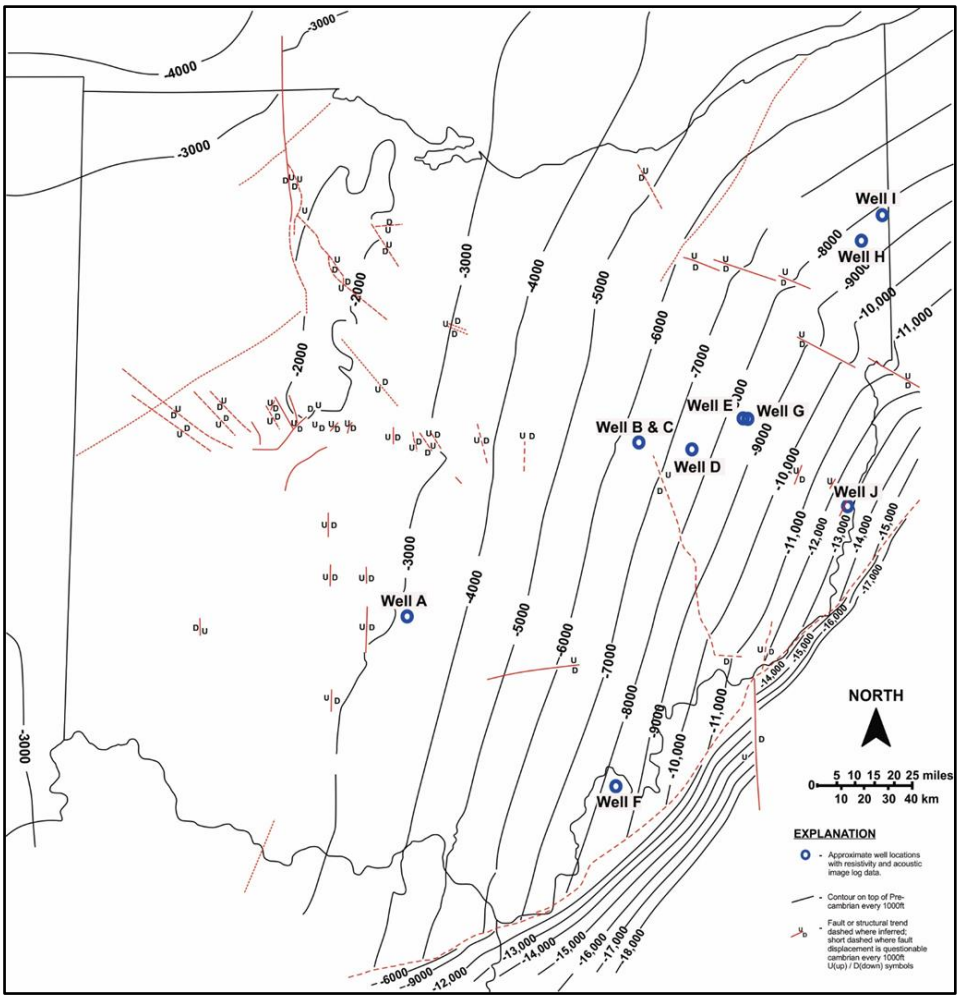

Figure 2-9: Approximate location of image log data overlaid on the Precambrian unconformity surface of Ohio with known structural features.

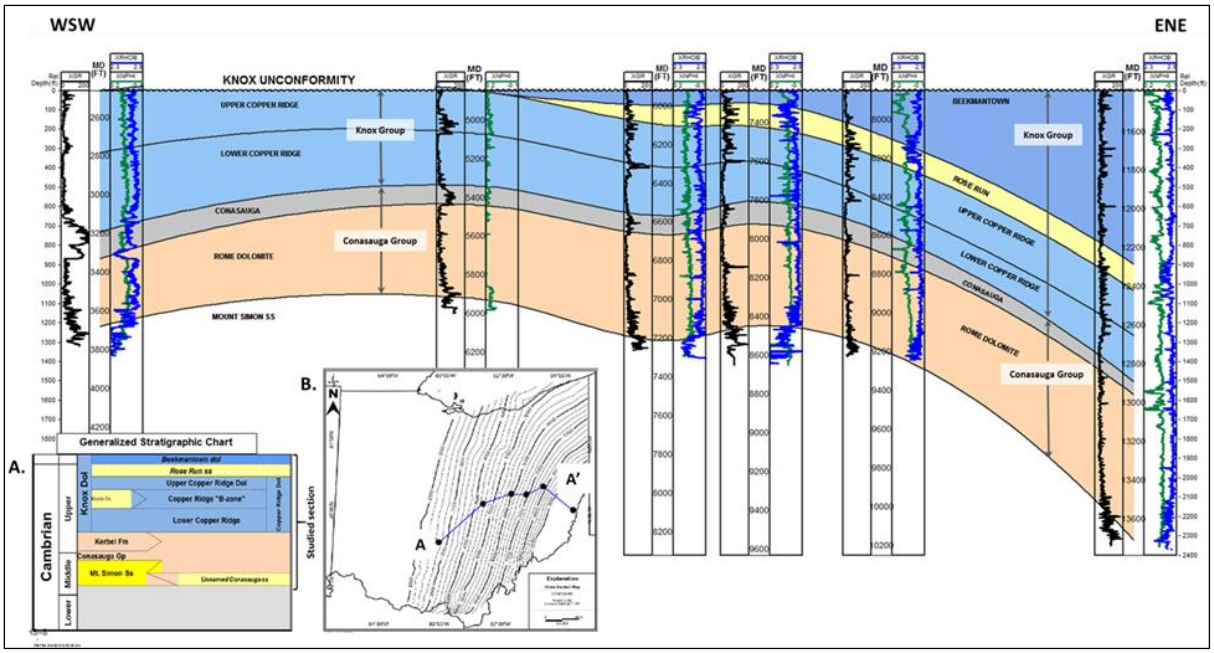

Note: Insert (A) shows a generalized lithostratigraphic chart of the section studied. Insert (B) shows the cross section wells overlaid on a contoured map for the Rome Formation.

Figure 2-10: West-southwest to east-northeast (A-A') cross section of the study area showing the Knox unconformity surface and the change in sediment thickness in an eastward direction.

The main objective of conducting this natural fracture analysis was to develop an understanding of the distribution of natural fractures spatially within the study area and assess any dominant trend in natural fracture orientation within these reservoirs. Fracture intensity variation was studied using information from image logs that were available for the abovementioned wells. The process initially involved interpreting the acoustic and resistivity image logs to identify natural fractures. Figures 2-11 and 2-12 show examples of a pre-existing natural fracture observable and interpretable on acoustic and resistivity image log data. Natural fractures and drilling-induced tensile fractures (DITFs) were interpreted on the 10-image log data that were available. These fractures were subsequently classified based on their nature (drilling-induced or pre-existing natural fracture).

The natural fractures were then assessed by systematically plotting the number of such fractures observed at every 25 ft for each well on a histogram. A histogram cross section was generated in order to analyze how the natural fractures varied from well to well. The result of this approach is shown in Figure 2-13. Figure 2-14 shows the results of a systematic assessment that differentiated the high-confidence natural fractures from the low-confidence ones.

The cross sections show that more fractures were observed around the wellbores of wells drilled in the western part of the study area than wells that were closer to the Rome trough (i.e., Well J), despite the fact that a thicker interval was logged at this location. In summary, the preliminary study on fracture intensity variation shows that formations on the western part of the study area are more fractured and may be more suitable for CO_2 injection and storage if other constraints for CO_2 sequestration are met.

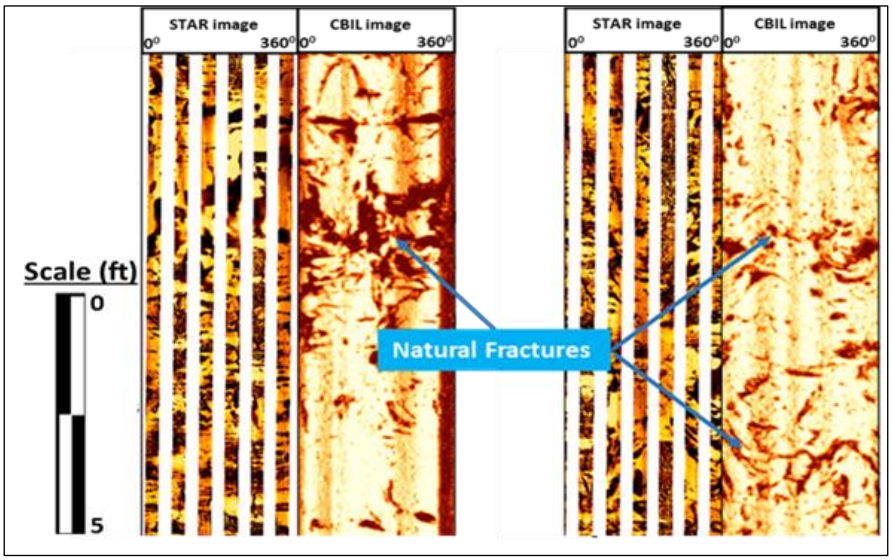

Figure 2-11: Example of observed natural fractures on a resistivity and acoustic image log.

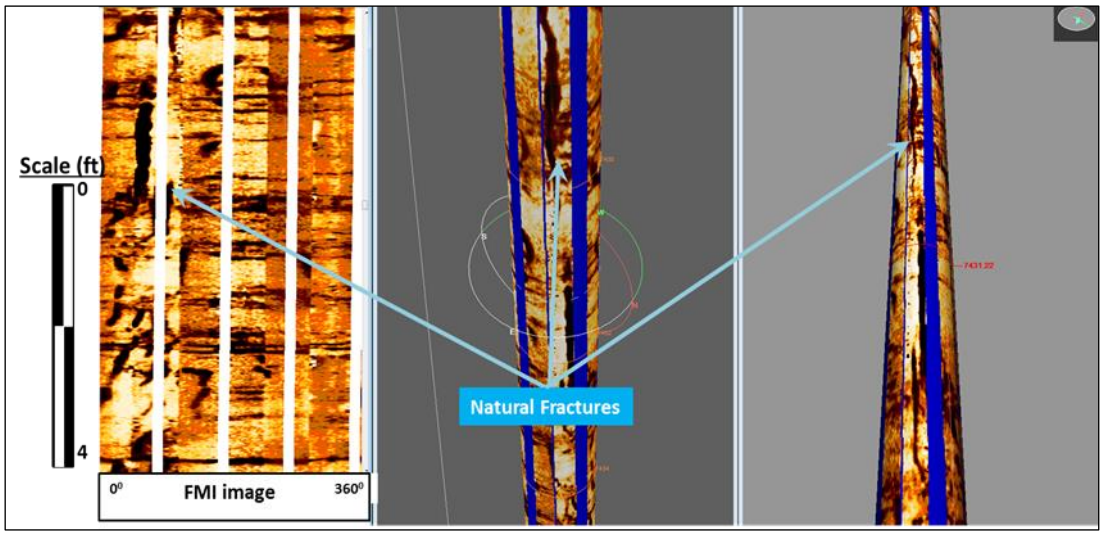

Figure 2-12: Dynamic 2D view of potential natural fracture and 3D view of the fracture striking northeast to southwest (from WellEye™) along a wellbore trajectory within a carbonate unit.

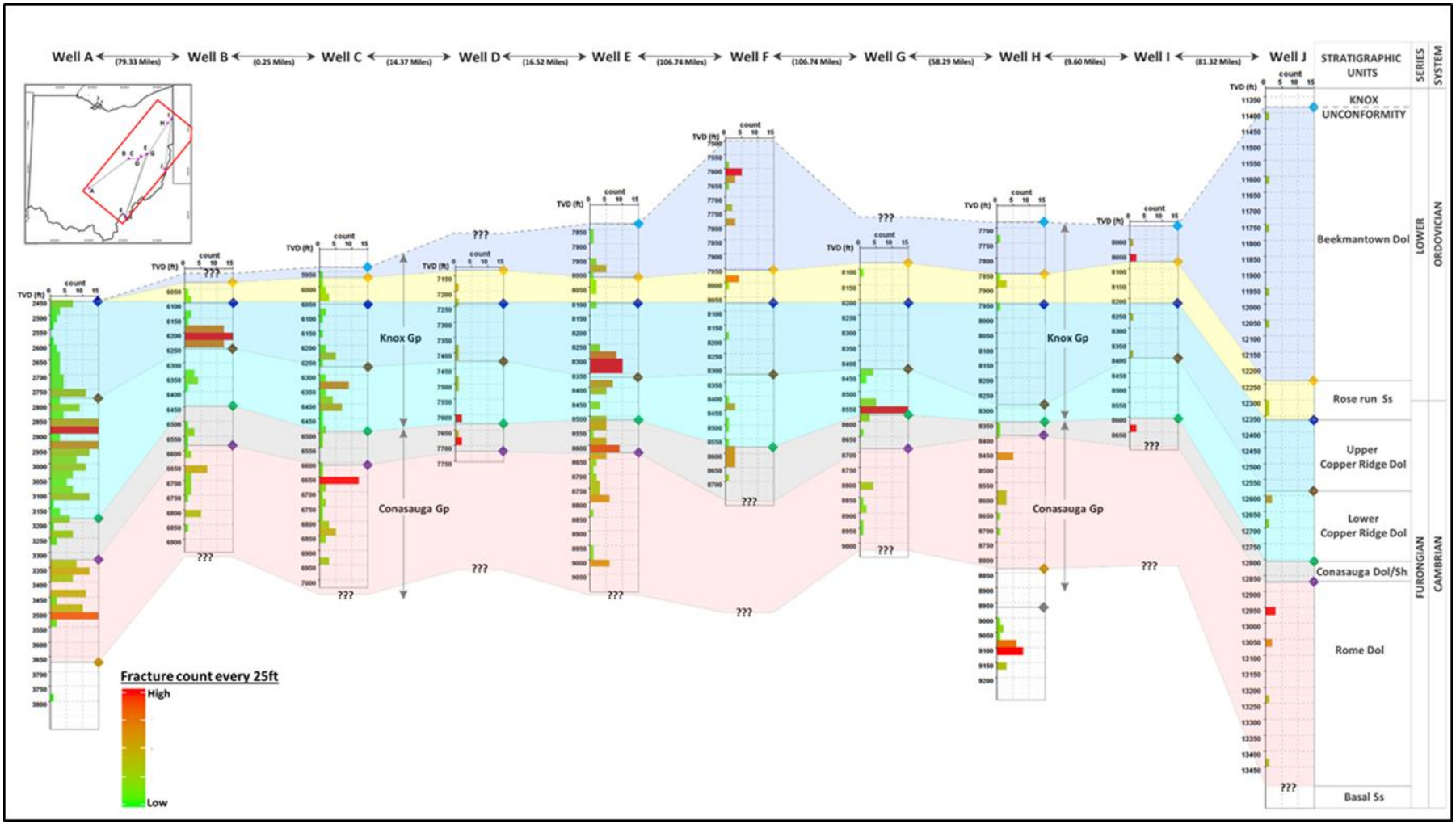

Figure 2-13: Southwest-northeast cross section illustrating frequency of natural fractures identified in image logs.

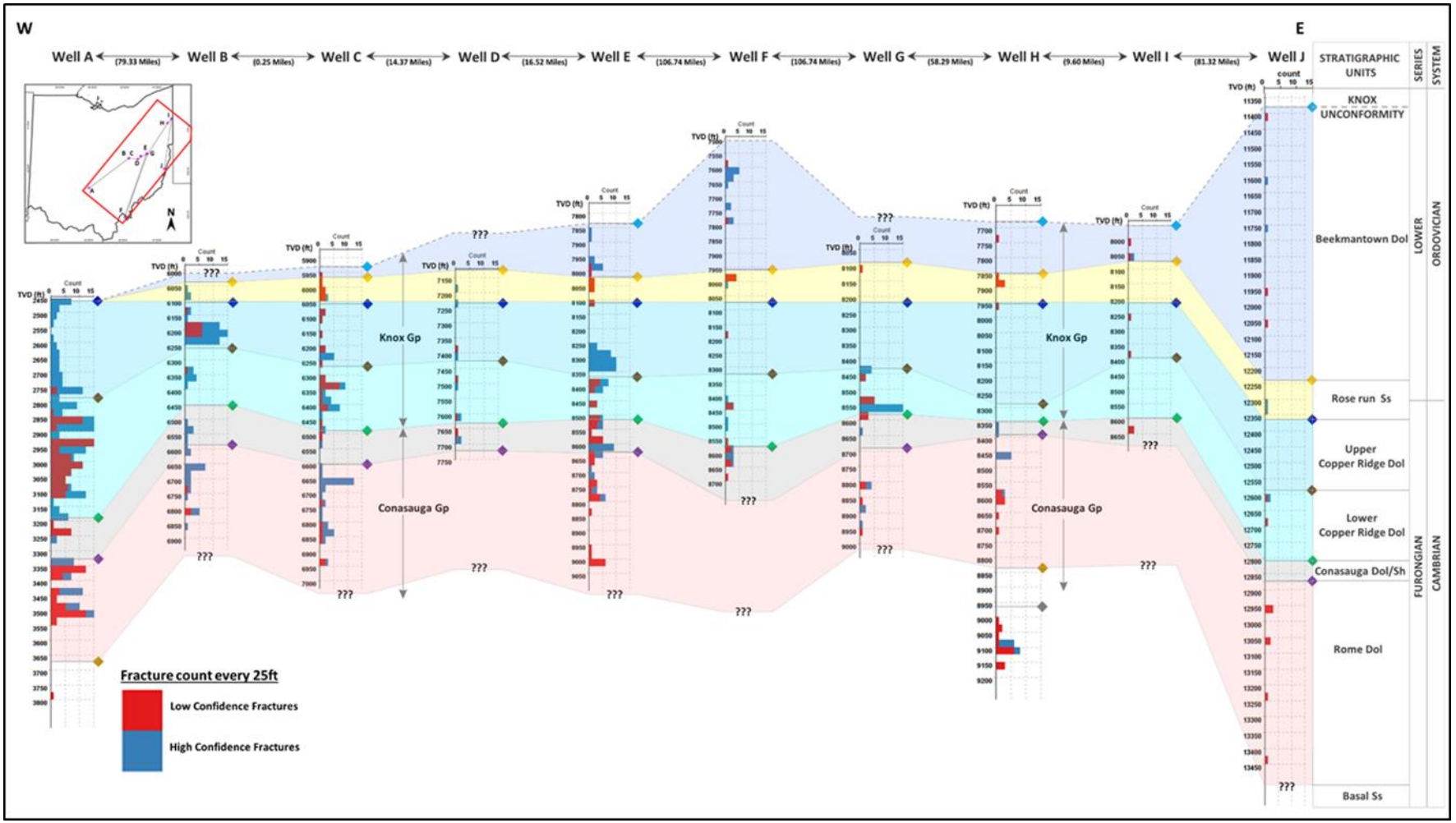

Figure 2-14: Southwest-northeast geologic cross section illustrating frequency of fractures identified in image logs classified by low and high confidence.

2.3.2 Orientation of Natural Fractures

In addition to gaining a basic insight on how the natural fractures were distributed, reservoir models require knowledge of their orientation to assess potential fracture activation. Rose diagram plots were used to study the predominant trend of these natural fractures on a well-by-well and formation-by-formation basis. For simplicity, formations that would have normally been mapped separately were merged. The Copper Ridge dolomite formation of the Knox dolomite group is normally divided into three different zones: Upper Copper Ridge, Copper Ridge B," and Lower Copper Ridge. This unit was evaluated as a single formation. This same approach was used for the Rome dolomite and Conasauga dolomite/shale of the Conasauga Group. The structural parameters (i.e., dip angle and direction) of observed fractures were used to produce a rose diagram plot. The rose diagram plot exhibits fracture orientation clusters on a well-by-well basis. The rose diagram plots for each grouped formation were then overlaid on a structure map of the Precambrian unconformity surface.

Fracture orientation clusters in the Copper Ridge dolomite formation (Knox Group) and the Conasauga and Rome dolomite formation (Conasauga Group) are shown on Figures 2-15 and 2-16, respectively. On the rose diagram plots for each well, careful observation shows that most of the clusters tend to strike in a northeast-southwest orientation, implying that if fracture networks are present in the vicinity, there is a high likelihood that fractures would be striking in this orientation. These natural fractures tend to trend in a similar orientation as the J1 joint set of the Devonian Marcellus black shales of the Appalachian Basin. The J1 joint set trend observed in the black shales is similar to the orientation of the contemporary tectonic stress field (S_{Hmax}), leading many authors to conclude that all east-northeast striking joints were de facto neotectonic (Engelder, 2009). Finally, it was understood that a pre- or early Alleghenian joint set, the J1 set, occupies nearly the same orientation as Appalachian neotectonic joints and S_{Hmax} of the contemporary tectonic stress field (Pashin and Hinkle, 1997; Engelder, 2004; Engelder and Whitaker, 2006; Lash and Engelder, 2009).

It is important to note that the fracture analysis does not imply that the fractures are connected from well to well. This study also does not imply anything about the spacing of these fractures laterally or the extent of the observed fractures. It only shows the dominant orientation of the fractures that were observed on image logs used for this study.

Unlike the J1 set, which is understood to consist of fluid-driven joints that propagated as a result of burial-related maturation of organic matter, the Cambrian-Ordovician intervals within the study area are known to be under hydrostatic conditions and have not been subjected to pore pressure elevation from hydrocarbon accumulation. Therefore, the challenge was to discern whether these natural fractures were formed in response to paleotectonic stresses or neotectonic stresses. The puzzle arose from the complex history of the basin during the early to late Paleozoic time, when the modern eastern edge of North America (Laurentia) was oriented approximately more than 45 degrees clockwise from its present-day position such that this same edge of Laurentia was facing south of modern-day coordinates.

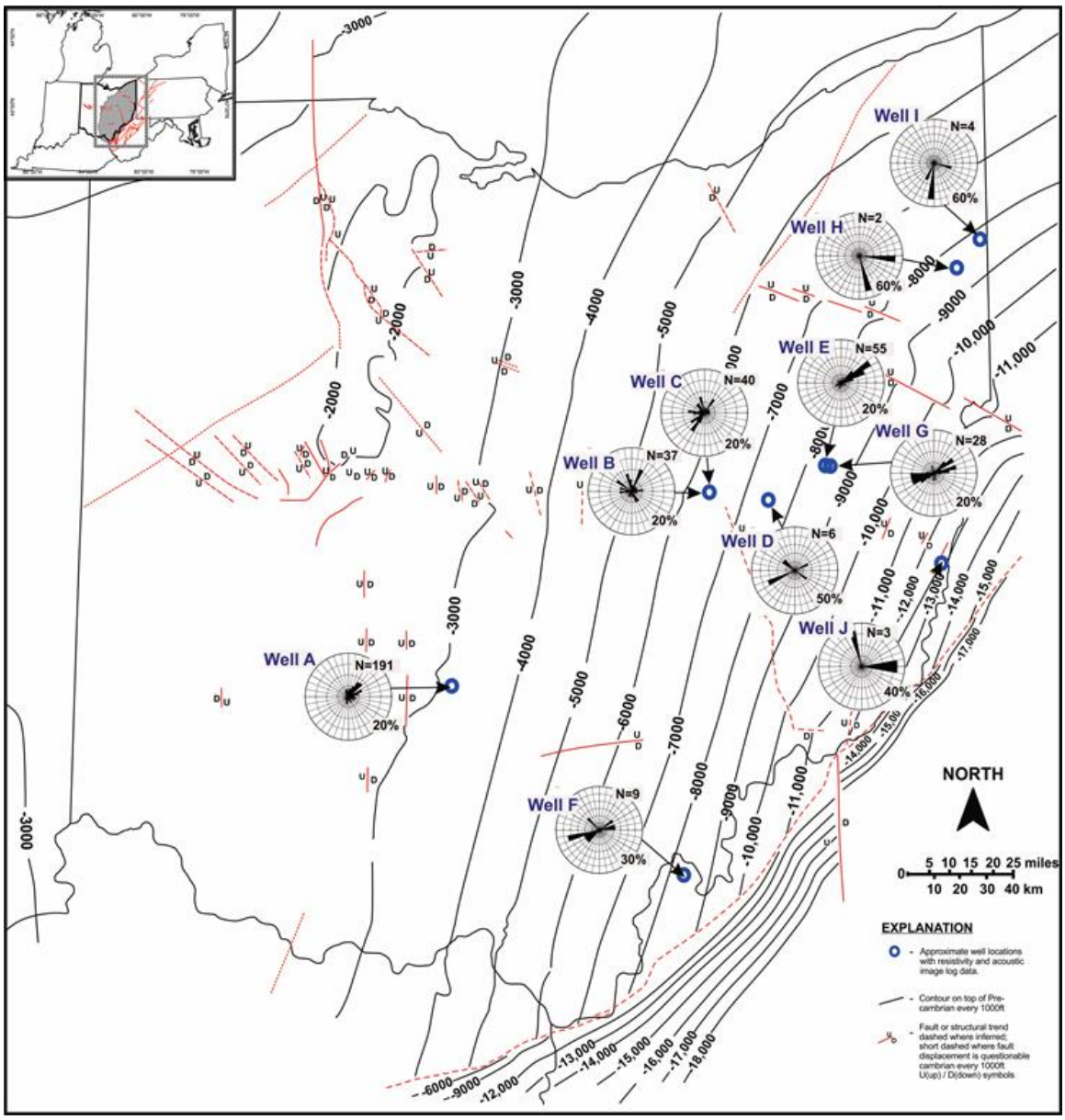

Figure 2-15: Rose diagrams of natural fractures observed within the Knox dolomite group overlaid on a structure map of the Precambrian basement.

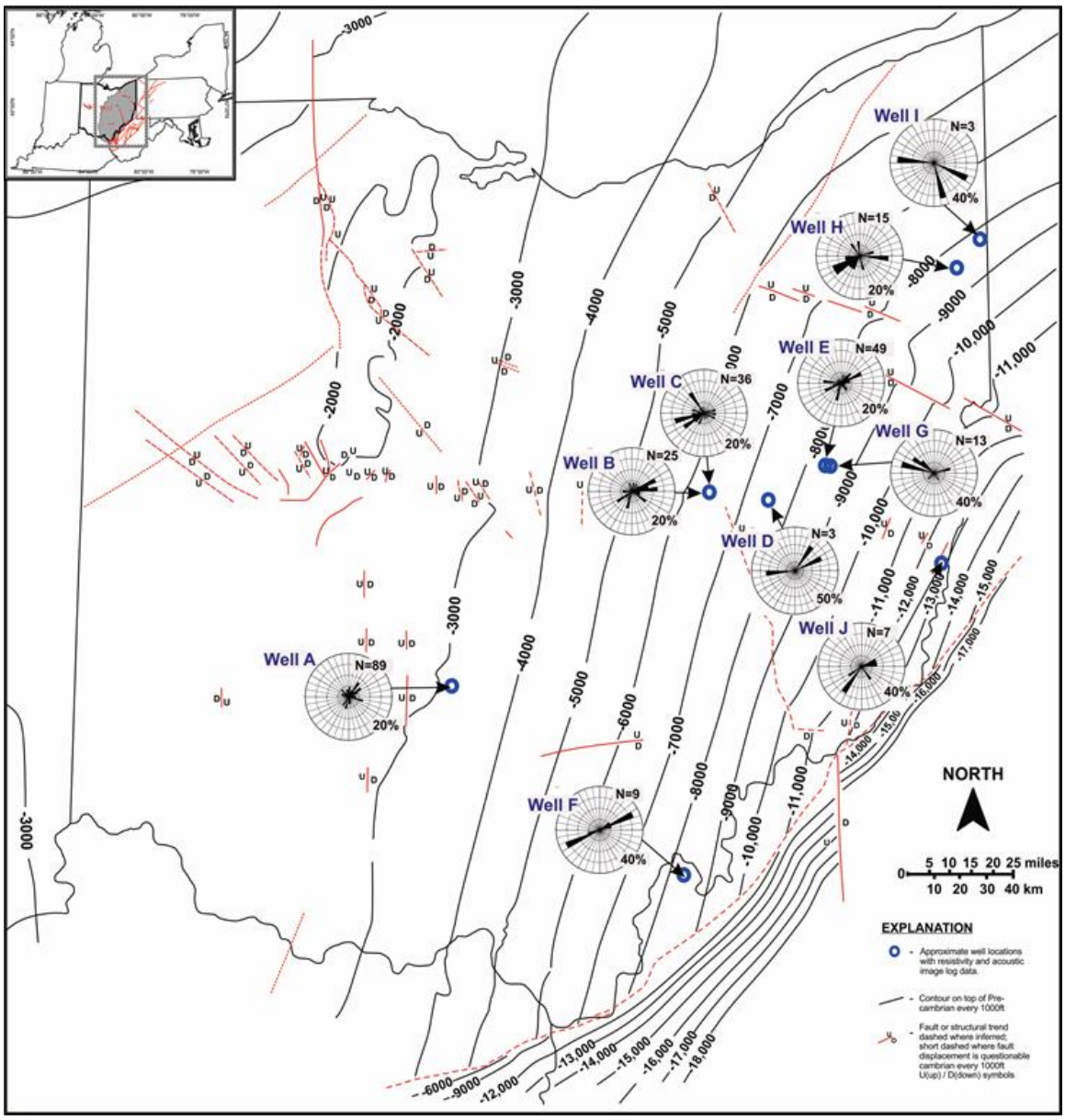

Figure 2-16: Rose diagrams of natural fractures observed within the Conasauga dolomite group overlaid on a structure map of the Precambrian basement.

Finally, analysis was completed on the type of fracture network that could be present and whether it was systematic or non-systematic by inferring trends on the plot. These trends were also related to the axis of maximum horizontal stress to understand whether the stress field played a role in the dominant fracture trend observed. Figures 2-17 and 2-18 lead one to conclude that some correlation exists between the orientation of the stress field and the dominant fracture trend.

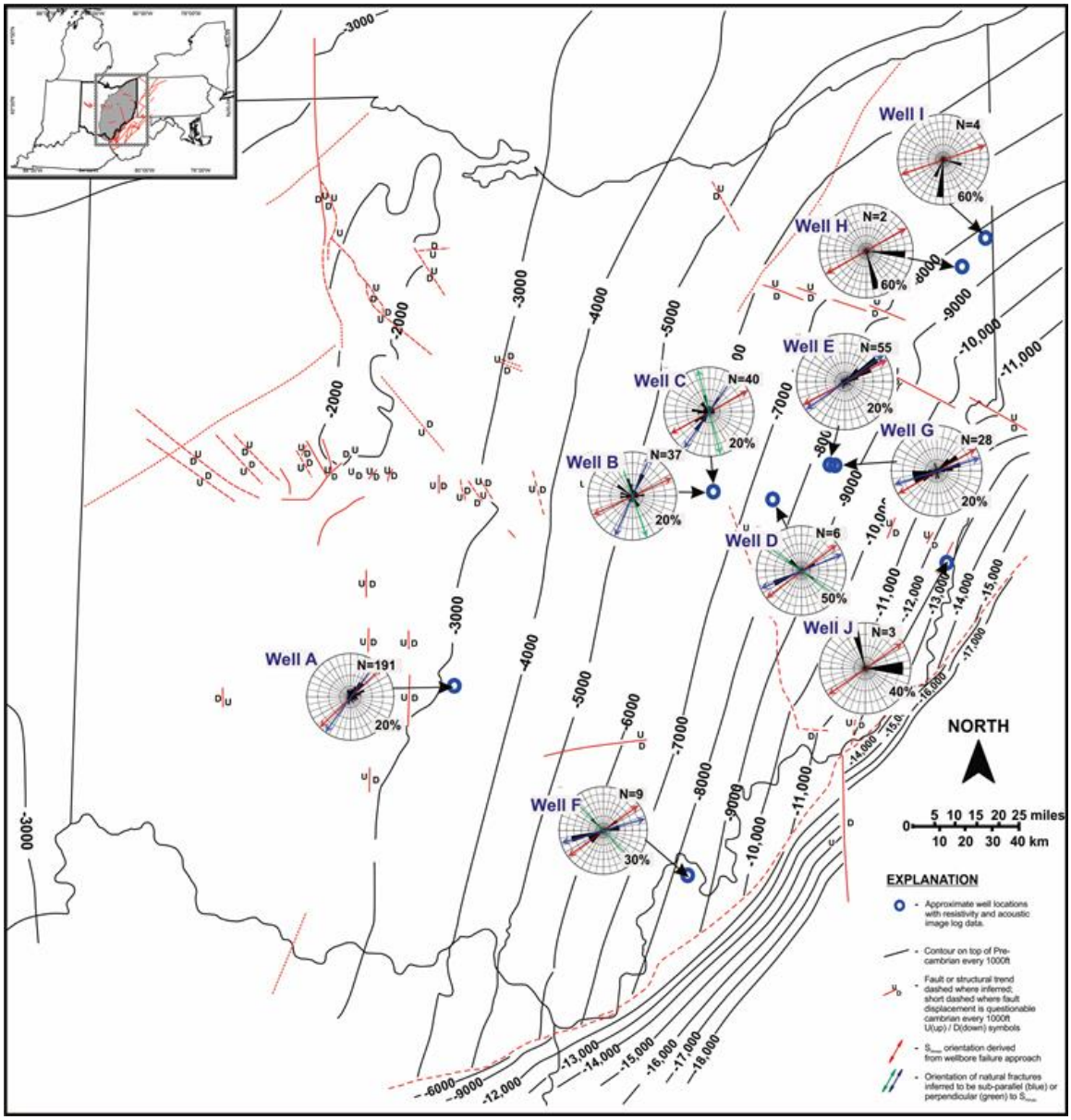

Figure 2-17: Rose diagrams with predetermined S_{Hmax} orientation along with inferred orientation of natural fractures observed within the Knox dolomite group overlaid on a structure map of the Precambrian basement.

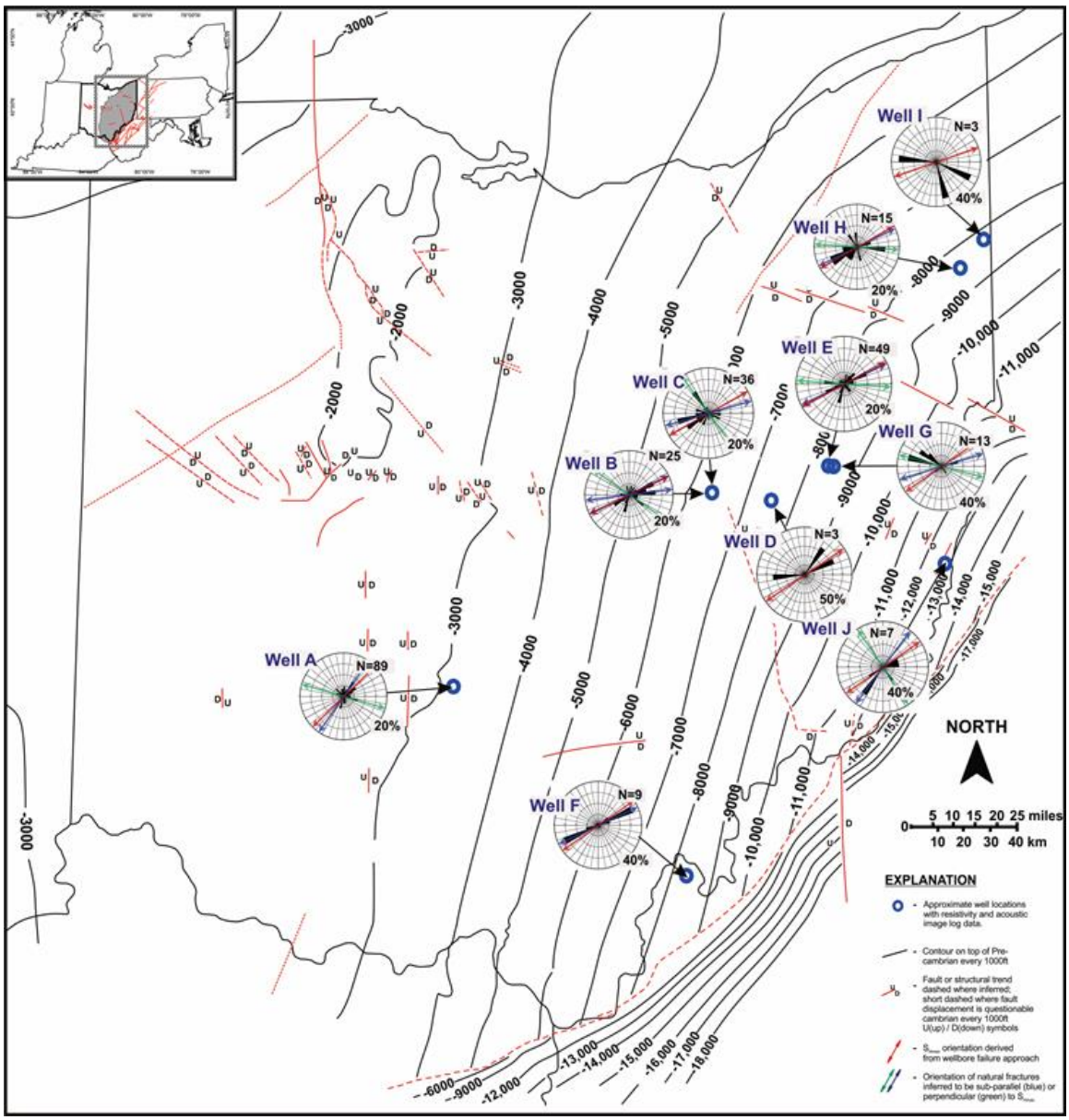

Figure 2-18: Rose diagrams with predetermined S_{Hmax} orientation along with inferred orientation of natural fractures observed within the Conasauga dolomite group overlaid on a structure map of the Precambrian basement.

A high percentage of the natural fractures are observed to strike sub-parallel to the axis of the maximum horizontal stress, indicating that the present-day stress field could have played an important role in the development of the pre-existing natural fractures observed on the image log. Some of the fractures are also inferred to strike perpendicular to fractures striking in a northeast orientation.

The analysis indicated that during different times in the evolution of the basin, the stress field could have controlled the orientation of natural fractures in the region. Other factors such as basin flank architecture (flexure of the basin flank) and paleotectonic stress could also be influencing orientation and spatial distribution of these natural fractures (Jadoon et al., 2007). In addition, analysis and interpretation of fracture orientation clusters show that the regional fracture systems are highly complex, with possibly systematic and non-systematic fractures within the evaluated lithologic units.

More rigorous analysis was conducted to support the inferred dominant orientation of fractures. This was done by plotting combined structural parameters of fractures observed in a single formation at all well locations on a 3D stereo-net and histogram. Figure 2-19 shows an example of this plot. In this example, a denser amount of the poles (colored dots) plotted on the lower hemisphere stereo-net falls in the northwest quadrant, which indicates that a denser amount of these fractures strike perpendicular to this quadrant and dips to the southeast quadrant. Additionally, the kernel density plot on the histogram chart in Figure 2-19 indicates that the peak is around ±45 degrees, suggesting that most of the natural fractures strike ±45 degrees northeast.

The kernel density plot histogram was repeated for all of the formations under study; the results are shown in Figure 2-20. This figure shows that the highest peaks on all the plots occur at angles less than 90 degrees, which further supports our inference that a denser portion of the fractures observed strike in a northeast direction. Other types of analyses performed to interpret the number of fracture trends observed are provided in Appendix A of this report.

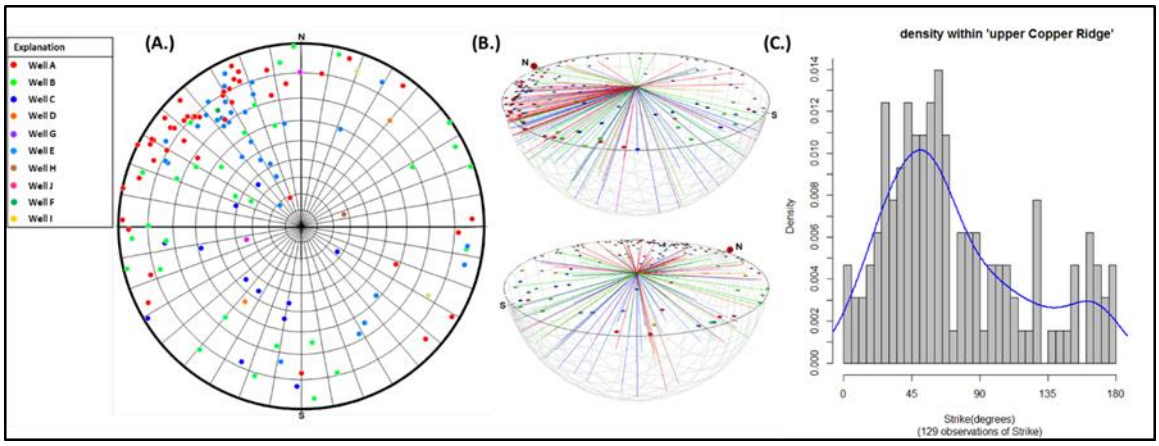

Note: Wells are plotted on a lower hemisphere stereo-net as poles to plane. Figure (A) shows a 2D projection of the lower hemisphere, (B) shows a 3D projection of the lower hemisphere, and (C) shows a histogram plot and kernel density of fracture strike (degrees).

Figure 2-19: Fractures observed within the upper Copper Ridge dolomite in all wells.

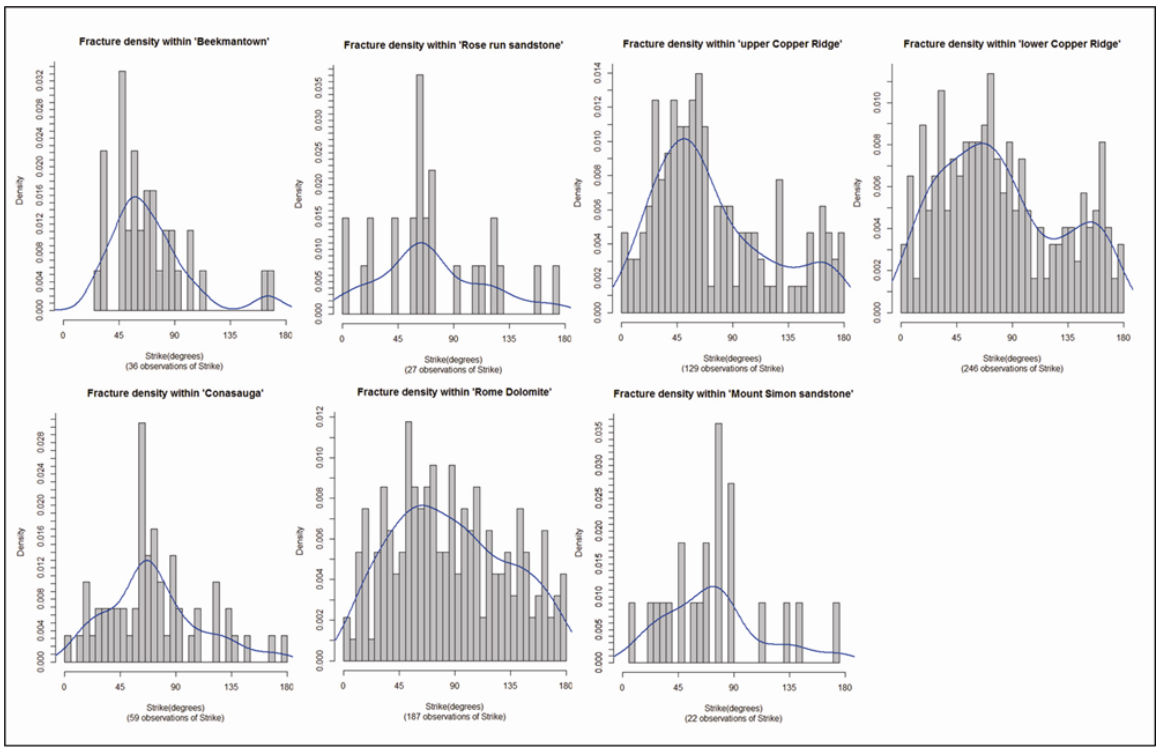

Figure 2-20: Histogram and kernel density plot of fracture strike observed within the different formations.

2.4 Paleo Stress-Strain Analysis

The Appalachian Basin is largely dominated by northeast-southwest trending structures that have been formed by compressional events (orogenies) along the eastern plate boundary. Figure 2-21 shows the continental configuration at the end of the Precambrian before the onset of the mountain-building events. The compressional events produced stresses that were transmitted into the interior of the plate, producing dominant structures such as thrust faults, anticlines, and strike-slip faults. The Appalachian Basin has gone through multiple periods of extension and compression. Evidence for reactivation and multiple movements on fault planes includes the inversion structures (harpoon structures) seen in Figure 2-22, indicating alternating periods of extension and compression.
A transition from an extensional regime into a compressional regime is a major indicator of fault reactivation, which can concurrently initiate new faults. While the timing of the faults observed in the present day is difficult to tell from field observations, it can often be inferred from a structural analysis of the geophysical data.

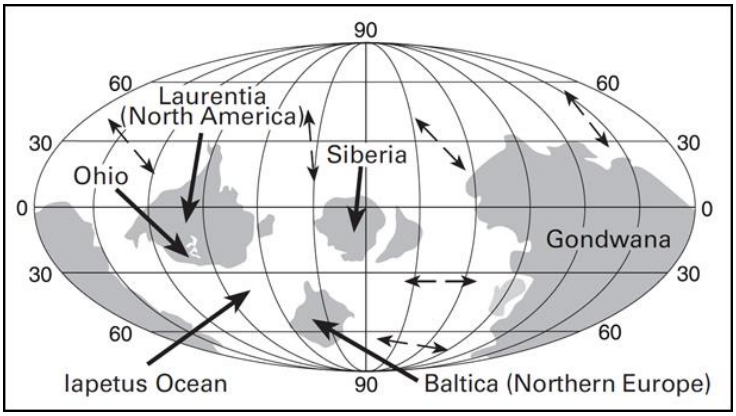

Figure 2-21: Continental configuration at the end of the Precambrian (Hansen, 1998b).

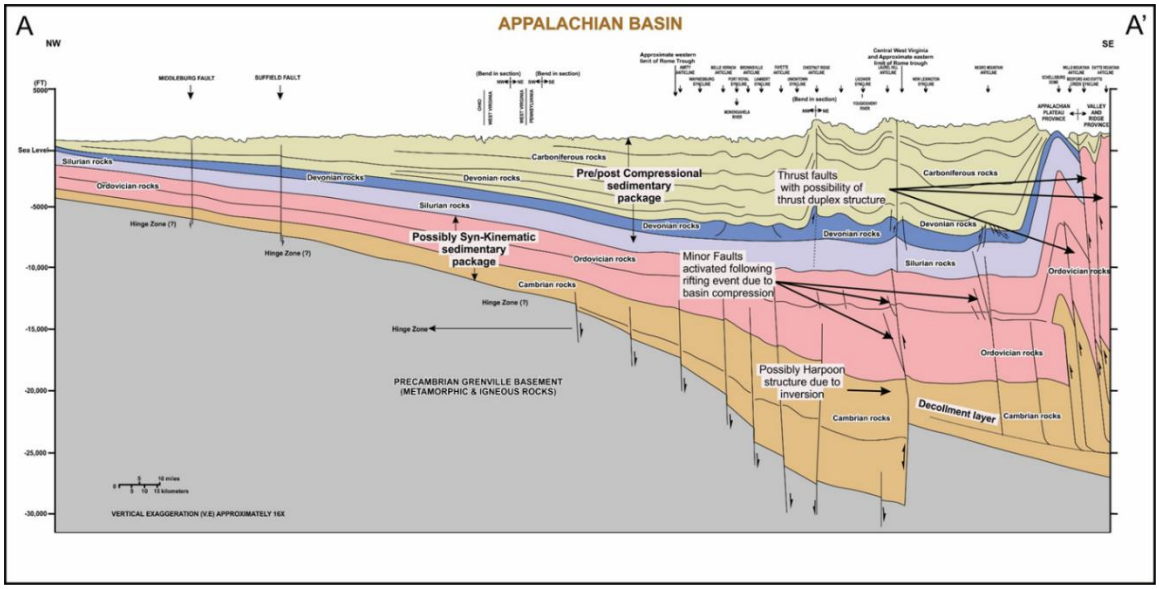

Figure 2-22: Structural analysis of the Appalachian Basin geologic cross section (after Ryder, 2012).

Evaluation of large volumes of seismic data is prohibitively expensive. However, E.M. Anderson's (1905) fault classification scheme can be used to perform an initial characterization of the state of stress acting during the development of the Appalachian Basin by analyzing the principal stresses in the lithospheric crust that could lead to initiation or movement of a pre-existing regional fault. Most, if not all, of the large-scale faults within the Appalachian Basin area are very old and have been reactivated multiple times. This could make it nearly impossible to use these geologic structures to predict the state of stress in the basin today because of rotation of the stress regime. Nevertheless, the fact that the basin still shows relatively dense northeast-to-southwest trending structures implies that the stress state has been fairly uniform during the more recent developmental stages of the basin.

Furthermore, stresses are known to have acted within the basin during the period when the observable structures were formed (referred to herein as paleo-stresses). These paleo-stresses can also be mapped and characterized based on the fault classification scheme described by Anderson (1905). The three principal stresses—vertical stress (S_v), maximum horizontal stress (S_{Hmax}), and minimum horizontal stress (S_{hmin})—are discussed in more detail in Section 2.5, Regional Analysis if Present-Day Stress Orientation and Magnitude. This section discusses how structures seen in the present-day Appalachian Basin may be used to map out stress trajectories during the basin dynamics.

Applying this knowledge on a basin scale, stress trajectories can be systematically mapped during the tectonic dynamics of the Appalachian Basin. Stress trajectory, in this instance, refers to the orientation of the apparent principal maximum and minimum horizontal stresses during the development of any structure. Though this does not yield an exact orientation of the stresses in the past or in the present, it does yield a fair amount of information that can be used to determine the most dominant direction of movement.

The transmission of stresses within the interior of the basin can be inferred by characterizing each geological structure seen on the Appalachian Basin structural map (Figure 2-23). For example, both the literature and geophysical data suggest how different phases of collision occurred along the eastern margin of the North American plate. Evidence of such collisions can be seen in the structures formed in a compressional regime in the eastern part of the basin. Using the orientation of these structures, the orientation of the principal stresses acting to form the observed structures can be inferred (Figure 2-23). Most of the anticlinal structures, thrust faults, and strike-slip faults present within the basin were formed when the principal S_{Hmax} was oriented at a normal angle to the axis of the structure and perpendicular to the orientation of the S_{hmin}. Conversely, the extensional structures, which are mostly normal faults in this instance, have the S_{Hmax} acting parallel to the axis of the structures and the S_{hmin} acting perpendicular to the structure. It is important to understand that these were the stresses acting during the movement of these major faults/structures; present-day stresses may be different.

Lucier et al. (2006) used borehole breakouts and DITFs interpreted from image logs to determine the orientation of the principal horizontal stresses in the eastern United States. A similar approach is also discussed in Section 2.5. The results validate the fact that paleo-stresses acting in the interior of the basin within northern Kentucky and northern Ohio are still prevailing, while areas closer to the eastern plate boundary, such as the West Virginia and Virginia areas, have changed. These findings are contrary to what one would have expected for the changes in principal horizontal stresses due to past orogenic events along the eastern margin of the Laurentia plate. This change confirms that the Laurentian eastern plate boundary is now in a period of relative tectonic stability and that stresses acting in the present day are in a northeast-southwest orientation, possibly from the opening of the mid-Atlantic ridge. While Lucier's stress analysis gives us the current stress state, one limitation of that study is that most of the analyses from observation of borehole breakouts and DITFs were done at a specific depth of study. At shallower or deeper depths, stress orientation could be different.

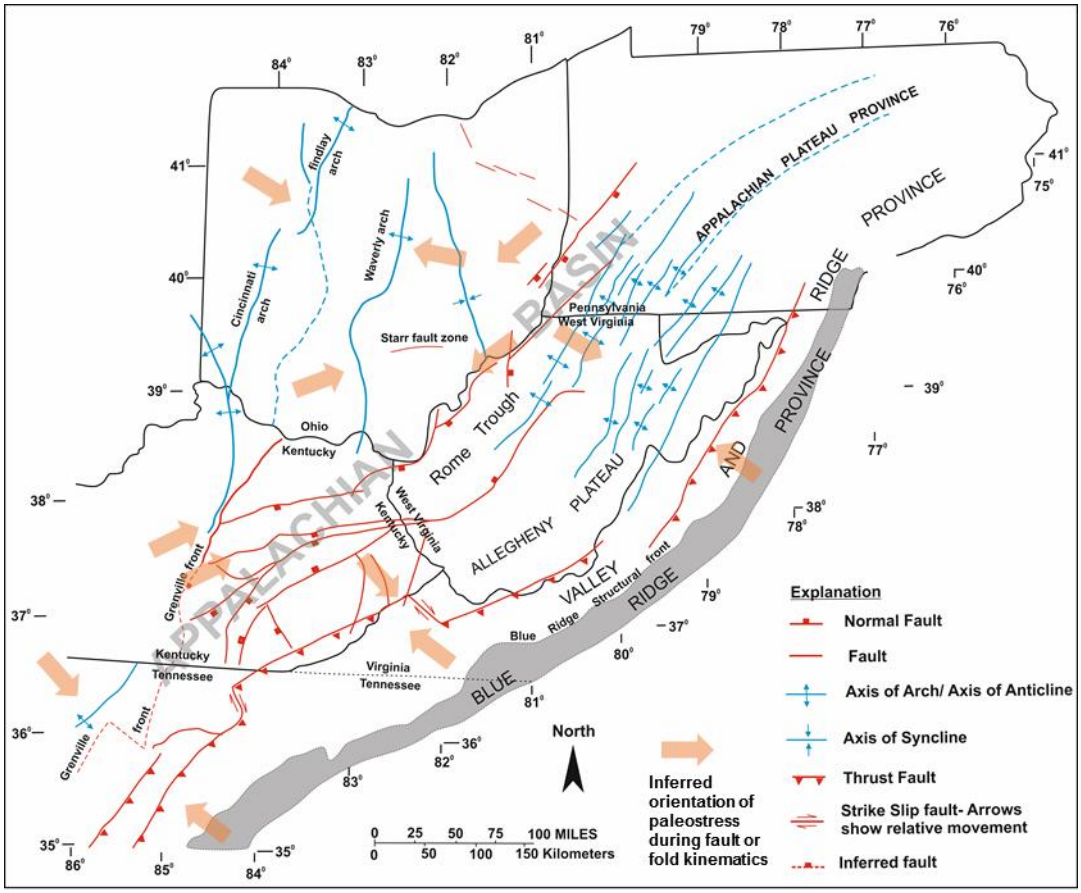

Figure 2-23: Hypothetical approach for analysis of paleo-stress during the development of structures in the Appalachian Basin.

2.5 Regional Analysis of Present-day Stress Orientation and Magnitude

In a geomechanical-related study, the knowledge of the current state of stress in the lithosphere is extremely crucial in building any geomechanical model. Many studies have been carried out in the literature to determine stress orientations and magnitudes in the crust. The most common stress indicators known include a well-constrained earthquake focal mechanism, stress-induced wellbore breakouts (WBOs), DITFs, and open-hole hydraulic fracturing stress measurements (Zoback, 2007). Other methods, such as using surface features indicating radial dike patterns of volcanoes (Nakamura, 1977) and using fault slip data by inverting sets of slickensides on fault scarp, are also known to be helpful in determining stress orientation. In addition, fast shear polarization that also coincides with the azimuth of the maximum stress axis can also be helpful in determining maximum stress orientation using cross-dipole acoustic logging (Tang and Cheng, 2004).

While these various methods of studying stress are all unique, the availability of the required dataset for analysis could be limited and proprietary. Stress orientation is widely determined using one of the following methods:

1) Observation of wellbore failure (DITFs and WBOs on acoustic and resistivity image logs) (Figure 2-24)

2) Azimuth of fast shear wave from cross-dipole sonic log.

Ten wells with acoustic and resistivity image log data were available for this analysis. The wells were spatially distributed from west to east within the study area and ranged in depth from 2,300 ft to 13,600 ft. Figure 2-25(A) shows the locations of the wells that were used for this analysis; results are shown in the histograms in Figure 2-25(B). The histograms show frequencies of wellbore failures observed that indicate S_{Hmax} azimuth (degrees) in the 10 wells. Table 2-1 shows a statistical summary of the derived azimuth.

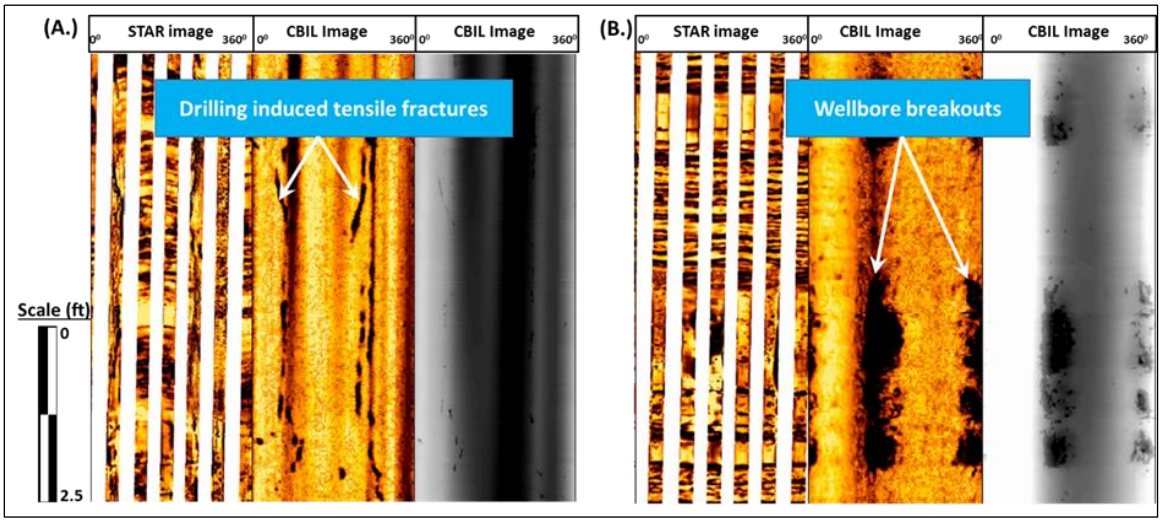

Note: Figure (A) shows DITFs and (B) shows WBOs. STAR™ = Simultaneous Acoustic and Resistivity imager tool.

Figure 2-24: Example of wellbore failures observed on resistivity imaging (STAR™) and acoustic circumferential borehole imaging log (CBIL™).

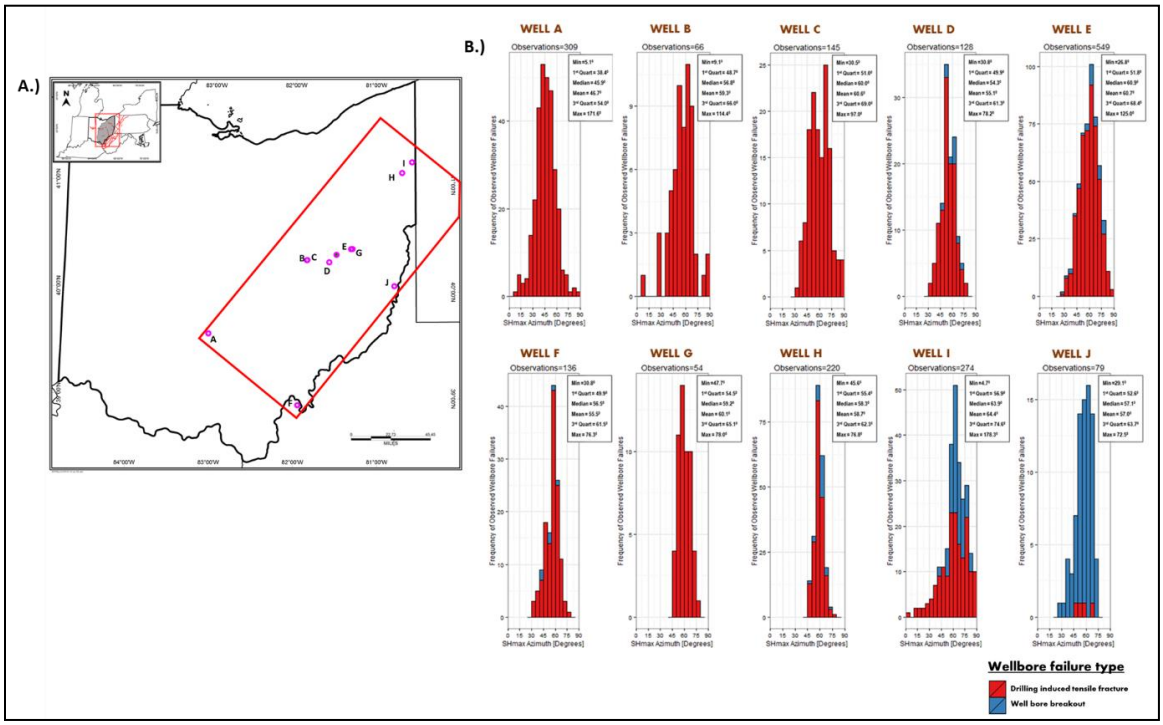

Note: Statistical results are provided in Table 2-1.

Figure 2-25: Locations of 10 wells (A-J) (Figure (A)) with acoustic and resistivity images and histograms (Figure (B)) with statistical results of wellbore failures that indicate S_{Hmax} azimuth observed in the wells.

Table 2-1: Statistical results of S_{Hmax} azimuth from wellbore failure observations.

Wells	Min (degrees)	Mean (degrees)	Median (degrees)	Max. (degrees)	No. of observations
A	2.1	46.7	45.9	>90	309
B	9.1	59.3	56.8	>90	66
C	30.5	60.6	60	>90	145
D	30.8	55.1	54.3	78.2	128
E	26.8	60.7	60.9	>90	549
F	30.8	55.5	56.5	76.3	136
G	47.7	60.1	59.2	78	54
H	45.6	58.7	58.3	76.8	220
I	4.7	64.4	63.9	>90	274
J	29.1	57	57.1	72.5	79

2.5.1 Stress Field

The World Stress Map (WSM) is a global synthesis of data on the present-day stress field of the lithospheric crust. The current WSM database was released in 2008 and contains 21,750 stress data records (Heidbach et al., 2008). These data were compiled to create the WSM shown in Figure 2-26. Figure 2-26 also shows the approximate location of our study area. Using the quality ranking system table recommended by Zoback (2007), we created a table to rank observations made from individual wells. Results of this effort are provided in Table 2-2. This information was subsequently used to fill gaps on the stress maps where stress orientation is unknown.

Figure 2-27 shows that the axis of the maximum horizontal stress is approximately in an east-northeast to west-southwest orientation (between 46 degrees and 71 degrees). This result is consistent with past stress records in the area.

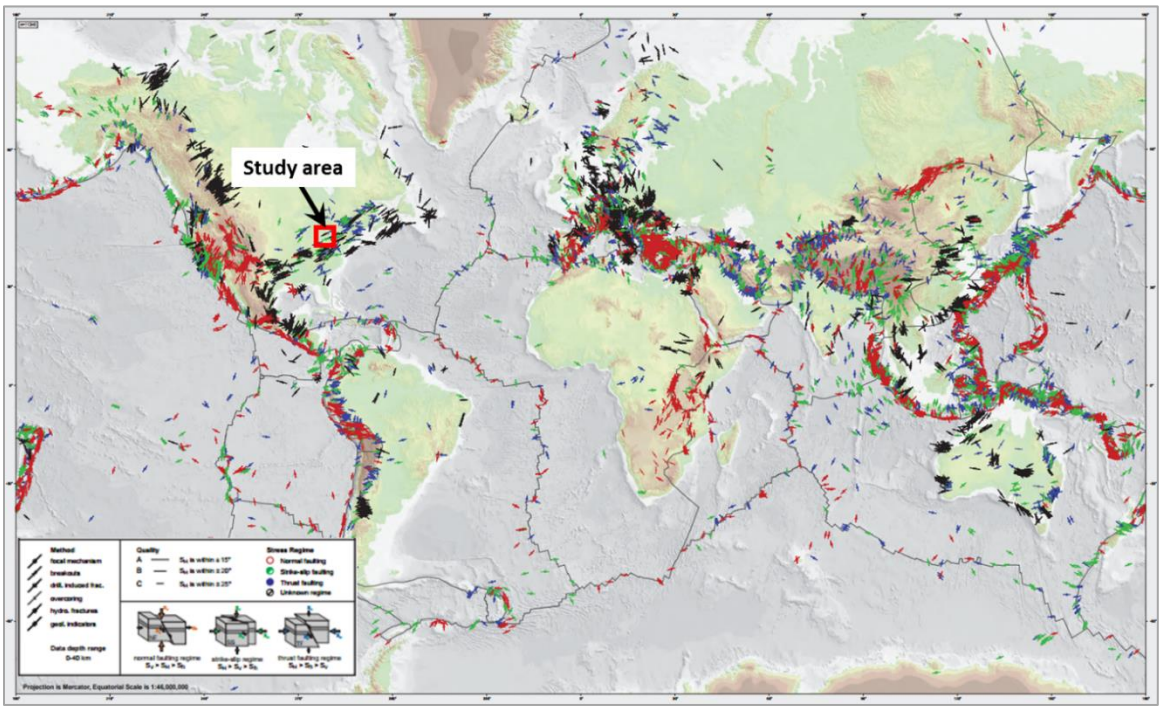

Source: Heidbach et al., 2008.

Figure 2-26: WSM showing the study area for this geomechanical framework study.

Table 2-2: Mean azimuth of the different failure types used to rank observations from individual wells.

Wells	Wellbore failure azimuth (degrees)	Failure type	S_{Hmax} azimuth (degrees)	Quality rank
A	46	DITF	46	C
B	65	DITF	65	B
C	61	DITF	61	B
D	53	DITF	53	C
E	62	DITF	62	C
F	52.7	DITF	52.7	B
G	60	DITF	60	C
H	60	DITF	60	C
I	71	DITF	71	C
J	55	DITF	55	D
D	151	WBO	61	D
E	152	WBO	62	C
F	147	WBO	57	D
H	145	WBO	55	C
I	151	WBO	61	C
J	149	WBO	59	C

Note: Results were used to update the stress map for the study area shown in Figure 2-27.

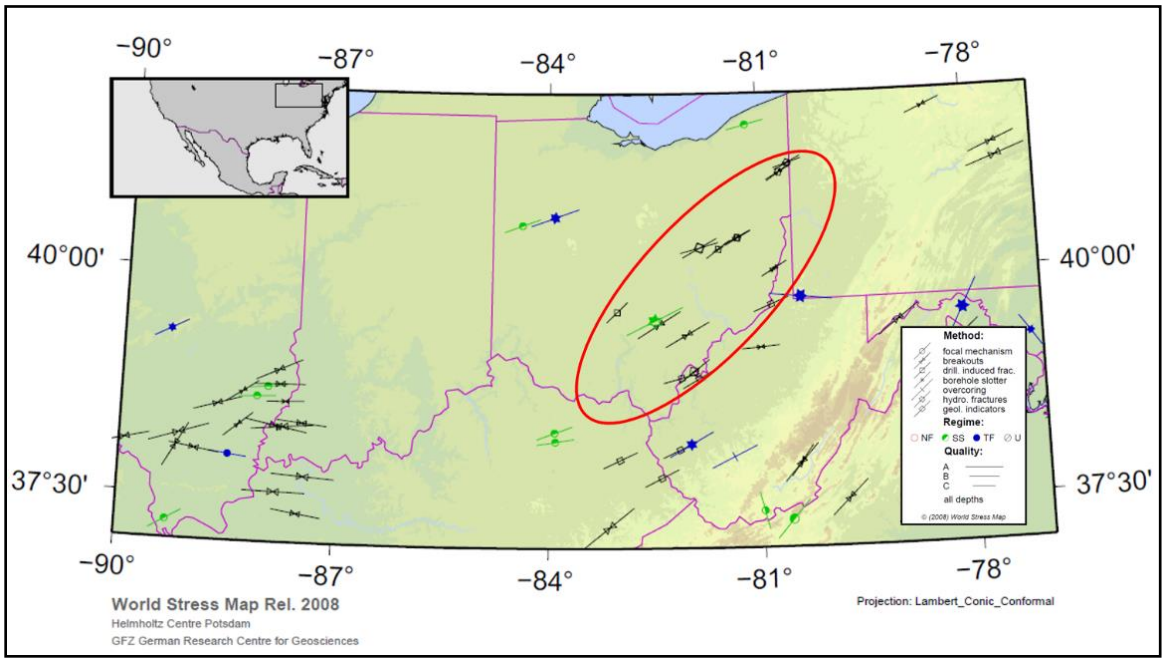

Note: Oval red circle shows approximate coverage area of wells used to synthesize data.

Figure 2-27: Updated stress map for the study area.

2.5.2 Stress Regime and Magnitudes

Stress is a tensor which describes the pressure acting on all surfaces passing through a given reference point. In an arbitrary Cartesian coordinate system, there are nine components and nine magnitudes of stresses; however, due to this complexity, it is unrealistic to characterize the stresses acting in the earth crust this way. Generally, the state of stress at depth is known by defining six stress magnitudes or three stress magnitudes and associated angles that define the orientation of the stress with respect to a reference coordinate system (mostly geographic).

The magnitudes of the greatest, intermediate, and least principal stress at depth in terms of the vertical stress (S_v) correspond to the weight of the overburden, the maximum horizontal stress (S_{Hmax}), and the minimum horizontal stress (S_{hmin}) in the manner originally proposed by Anderson (Zoback, 2007) as shown in Figure 2-28. These three principal stresses (S_v, S_{Hmax}, and S_{hmin}) act at depth during the movement of any fault or structure and can be rewritten as S1, S2, and S3, depending on the type of fault/structure and the magnitude of the principal stresses. One of the principal stresses (i.e., S_v) would generally act normal to the earth's surface (gravity driven) and to the two horizontal principal stresses S_{Hmax} and S_{hmin} acting in an approximate horizontal plane. The Anderson scheme classifies an area in the earth's crust as being characterized by normal, strike-slip, or reverse faulting, depending on the movement of the hanging wall with respect to the footwall (Figure 2-28).

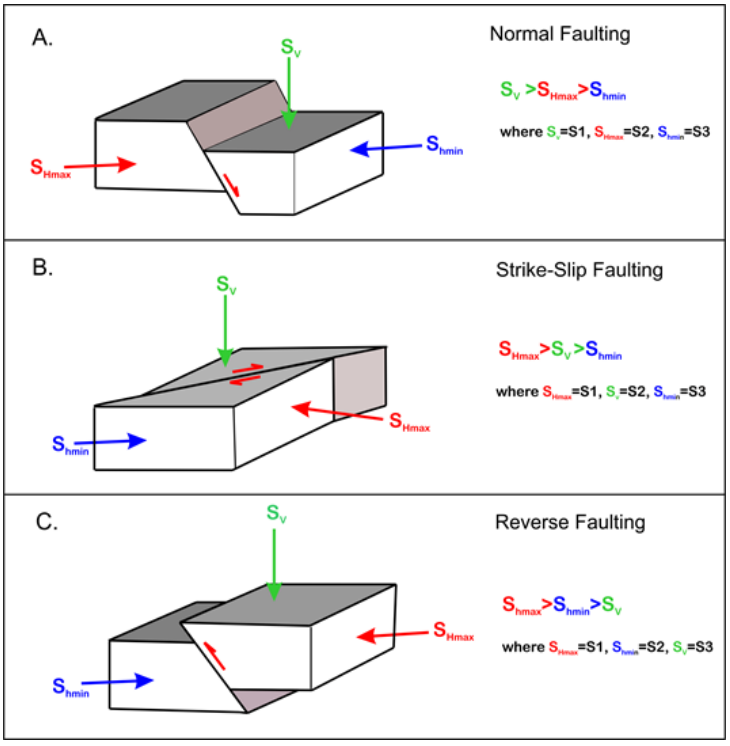

Figure 2-28: Different types of fault system (Anderson [1905] classification scheme).

In this study, the analysis focused on defining five major parameters that would help in describing the state of stress at depth. These five parameters are the three principal stress magnitudes (S_v, S_{Hmax}, S_{hmin}); the azimuth of S_{Hmax}; and the pore pressure. The azimuth for maximum horizontal stress was derived using the wellbore failure approach discussed above.

The magnitude of vertical stress, S_v, is derived simply by integrating rock density data from the surface to the depth of interest. It is given by:

$$S_v = \int_0^z \rho(z) g dz \qquad \text{Eq. 2.1}$$

where ρ is the bulk density at the depth of interest, g is acceleration due to gravity and z is the depth of interest. Figure 2-29 shows how a density log from a well was integrated in estimating overburden stress gradient. S_v is also used as one of the parameters in estimating the magnitude of the minimum horizontal stress.

The most accurate method for determining the magnitude of S_{hmin} is to perform a leak-off test (LOT) or a mini-frac test. The leak-off point (LOP) and the fracture propagation pressure (FPP) observed from an extended test usually provide reliable estimates about the magnitude of S_{hmin}. Because this test has been carried out previously on one of the wells (well F) and results were reported for different formations that was tested at depth in the study by Lucier et al. (2006), we assumed that the S_{hmin} magnitudes at the different well locations would be similar to those reported. The range of magnitudes derived for S_{hmin} is shown in Table 2-3.

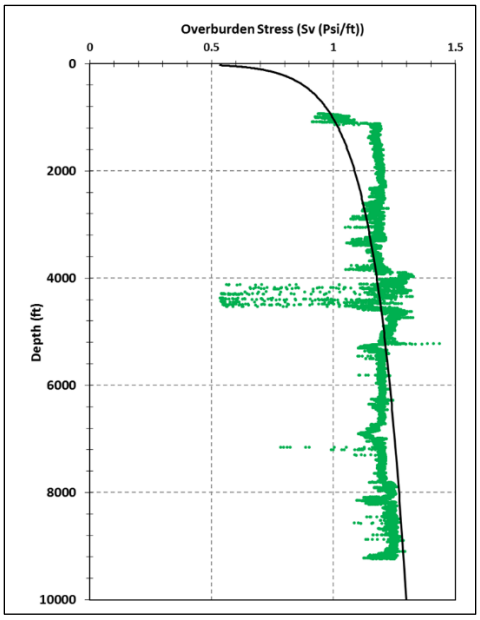

Figure 2-29: Overburden stress gradient in the study area.

Table 2-3: Range of derived stress magnitudes.

Lithologic unit	Depth (ft)	Pore pressure (psi/ft)	S_v	S_{hmin} range	S_{Hmax} range
			(psi/ft)		
Rose Run sandstone (top)	7,727	0.49	1.16	0.583-0.602	0.79-1.185
Rose Run sandstone (middle)	7,760	0.49	1.16	0.637-0.674	0.786-1.180
Rose Run sandstone (bottom)	7,835	0.49	1.16	0.649-0.686	0.779-1.168
Copper Ridge dolomite	8,088	0.49	1.16	0.826-0.898	1.311-1.707
Copper Ridge dolomite	8,209	0.49	1.16	0.832-0.903	1.292-1.681
Nolichucky shale	8,613	0.49	1.16	0.827-0.894	1.366-1.687

Note: Stress magnitudes derived in Lucier et al., 2006.
psi/ft = pounds per square inch per foot.

S_{hmin} magnitude is also widely estimated using the equation proposed by Eaton (Zoback, 2007). Due to bilateral constraints associated with this equation, it is necessary to use an empirically determined effective Poisson's ratio that is obtained from calibration against least principal stress measurements obtained from LOTs. The equation assumes that the only source of horizontal stress is the overburden; other factors are neglected.

$$\sigma_h = \left(\frac{\upsilon}{1-\upsilon}\right)(\sigma_v - P_p) + P_p \qquad \text{Eq. 2.2}$$

where υ is Poisson's ratio, σ_v (S_v) is the vertical stress, σ_h is minimum horizontal stress, and P_p is pore pressure.

Once we have an estimate of the magnitude of S_{hmin}, we can then constrain the magnitude of the maximum horizontal stress using a stress polygon (Figure 2-30) and observed wellbore failure. By constraining the magnitude of S_{Hmax}, we could then tell the prevailing faulting regime at depth. The work by Lucier et al. (2006) and Hurd and Zoback (2012) has shown that the study area is in a normal faulting/strike-slip faulting regime whereby S3 = S_{hmin}.

The determination of pore pressure was straightforward as it was available from pressure data. Pore pressure data were available for three wells in the study area. A plot of the pore pressure gradient is shown in Figure 2-31. Overall, the ranges of the pore pressure gradient observed were between 0.45 pounds per square inch per foot (psi/ft) to 0.48 psi/ft in the three wells, which is close to pore pressure estimates in Lucier et al., 2006. The gradient is very close to the hydrostatic gradient (0.44 psi/ft), as expected, because these formations are water-bearing.

The derived stress magnitudes (S_v, S_{Hmax}, S_{hmin}, and pore pressure) in Lucier et al. (2006) are shown in Table 2-3 above. The presented values are for formations that were tested. These estimated parameters are used to analyze critically stressed fractures.

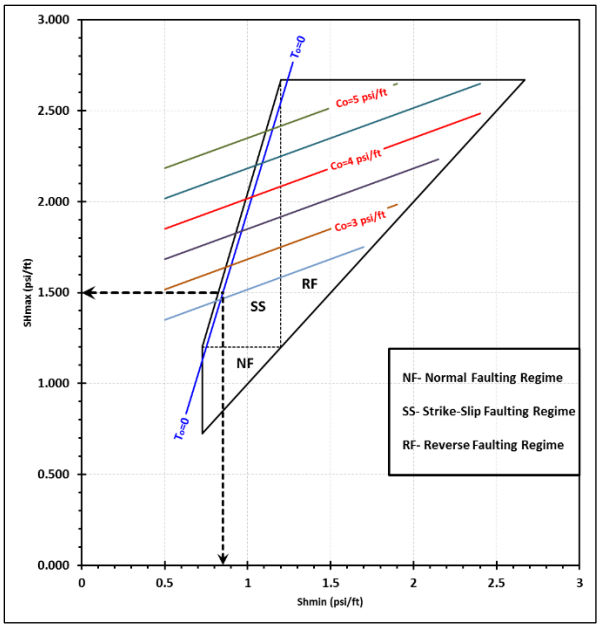

Figure 2-30: Stress polygon.

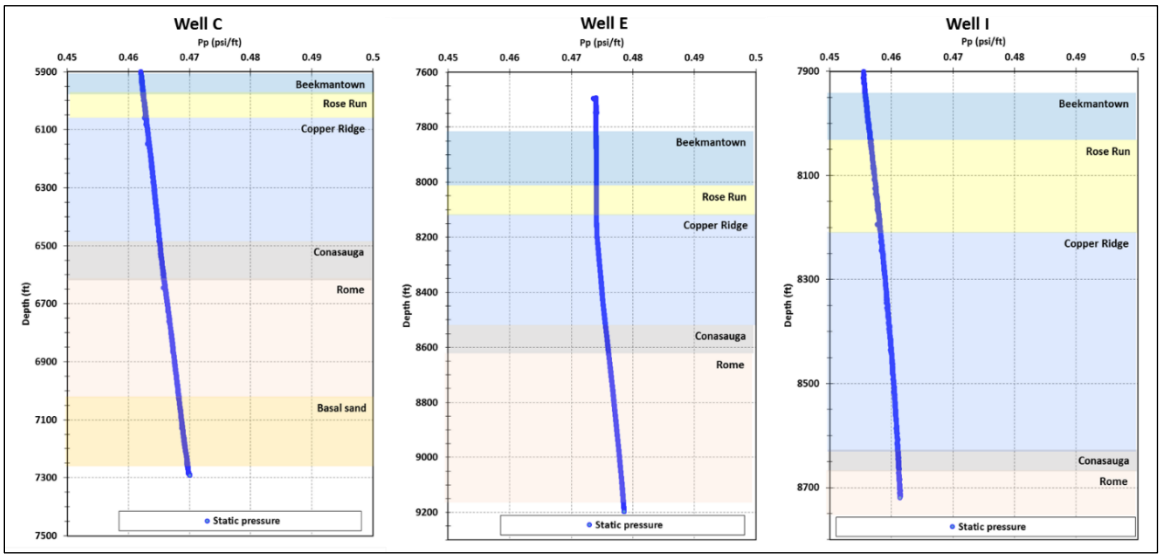

Note: Wells are shown in Figure 2-25.

Figure 2-31: Static pore pressure data from wells C, E, and I.

2.5.3 Critically Stressed Fracture Analysis

After studying the distribution and orientation of the natural fractures and the parameters that define the state of stress at depth, we used a 3D Mohr diagram to analyze the current state of the fractures at depth (i.e., whether they are critically stressed) and their likelihood of slipping at increasing pore pressures. For this analysis, using the stress magnitudes shown in Table 2-3, two scenarios served to illustrate the state of these fractures at depth: Scenario A used the lower bound of the magnitudes, and Scenario B used the upper bound.

Figure 2-32 shows an example of this analysis on well A under both scenarios; the related parameters used are presented in the tables below the 3D Mohr diagrams. For this example, it is important to note that we used structural parameters only for pre-existing natural fractures observed; other geologic features such as bedding, DITFs, or WBOs were eliminated.

The results show that for both scenarios, none of these fractures are stressed in their original state; however, at elevated pressure, we start observing the diagrams shifting to the left, indicating an increased likelihood of the fractures failing under pressure (Figure 2-33). While the failure of these fractures has been related to induced seismicity (Lucier et al., 2006), detailed management of elevated pressure could mitigate slippage on the fracture plane.

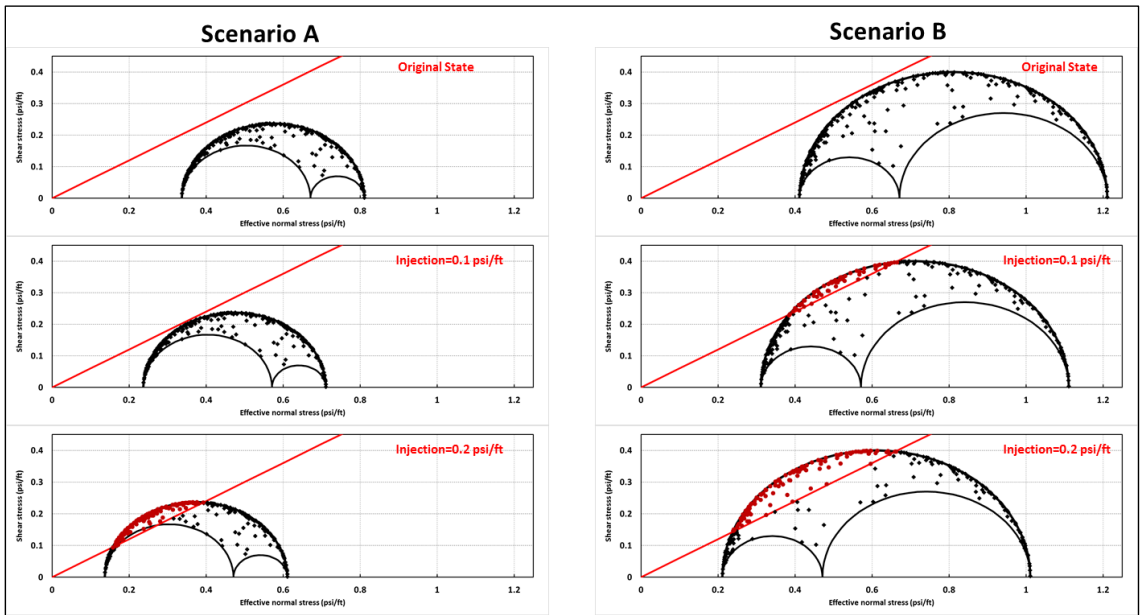

Parameters	Magnitude (Psi/ft)
S1=SHmax	1.3
S2=Sv	1.16
S3=Shmin	0.826
SHmax azimuth	46^0
Pore pressure	0.489
Coefficient of friction (μ)	0.6 (unitless)
Cohesion	0

Parameters	Magnitude (Psi/ft)
S1=SHmax	1.7
S2=Sv	1.16
S3=Shmin	0.9
SHmax azimuth	46^0
Pore pressure	0.489
Coefficient of friction (μ)	0.6 (unitless)
Cohesion	0

Figure 2-32: Analysis of critically stressed natural fractures observed in well A.

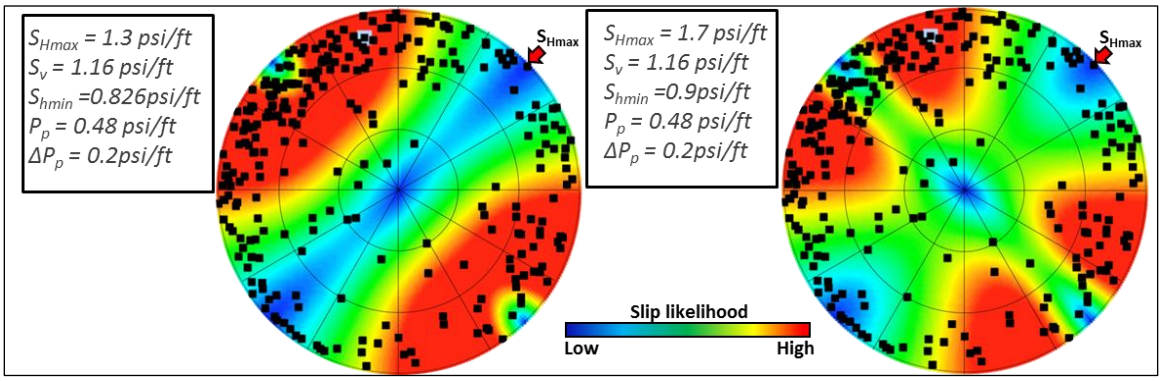

Note: Points on stereo-net represent poles to natural fracture planes.

Figure 2-33: Slip likelihood of observed natural fractures.

2.5.4 Structural and Seismic Analysis

Regional 2D seismic data available within the study area are the Evans 2D seismic lines and the COCORP 2D seismic lines. Some of the 2D seismic lines were examined to evaluate structures that present within the study area. The lines are generally dip-oriented into the basin and are of good quality for local and regional interpretation. Synthetic seismograms (an example is shown in Figure 2-34) were generated from offset wells to correlate formation tops to seismic horizons.

Some sections on the lines in southeastern Ohio show faulting that can be observed throughout the entire sedimentary section. Previously known interpreted structures that have been mentioned in Baranoski's (2002) work were confirmed on some of the seismic lines. Some of the structures impacted deeper sedimentary layers without much effect on shallower layers, thereby confirming impacts of the tectonic history. Figure 2-35 shows the Precambrian unconformity surface map with locations of confidential seismic lines that are available for evaluation with respect to the known structures that affected the Precambrian surface.

In general, the seismic lines examined show east-dipping sedimentary layers with some evidence of fault reactivation.

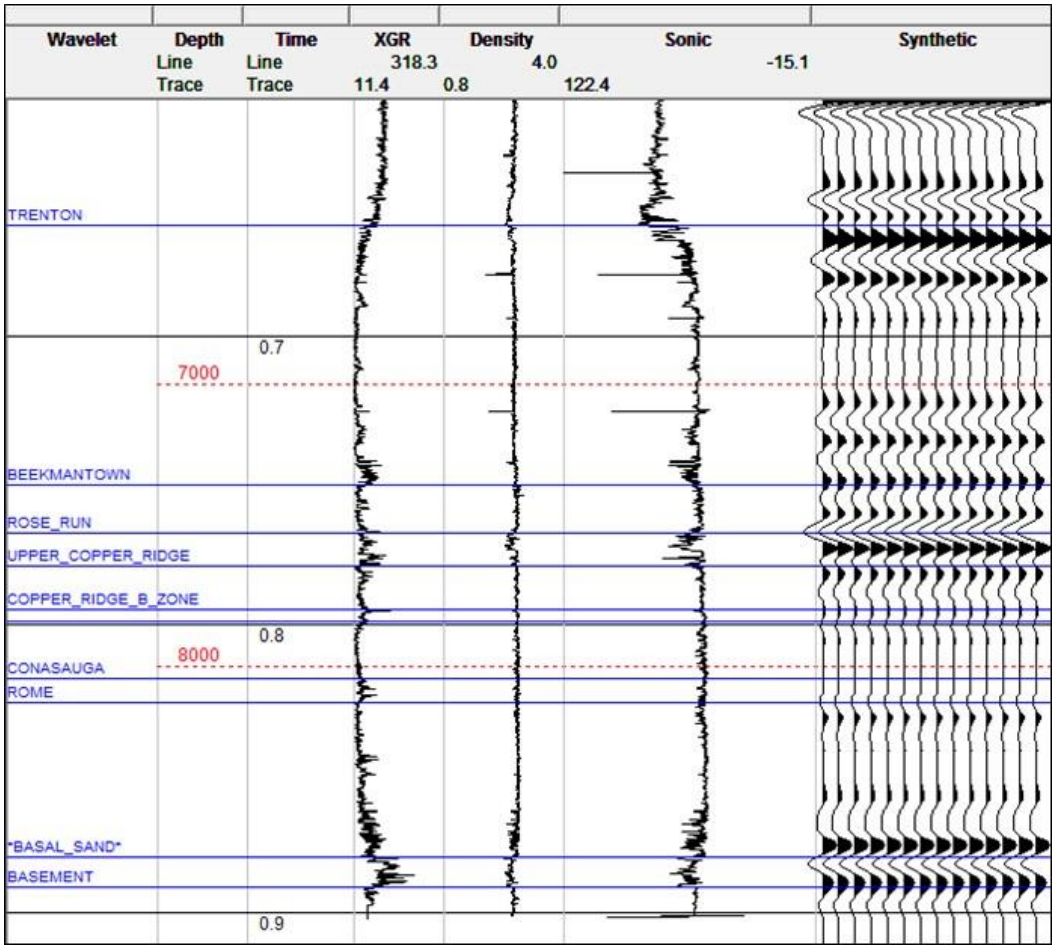

Figure 2-34: Example of synthetic seismogram.

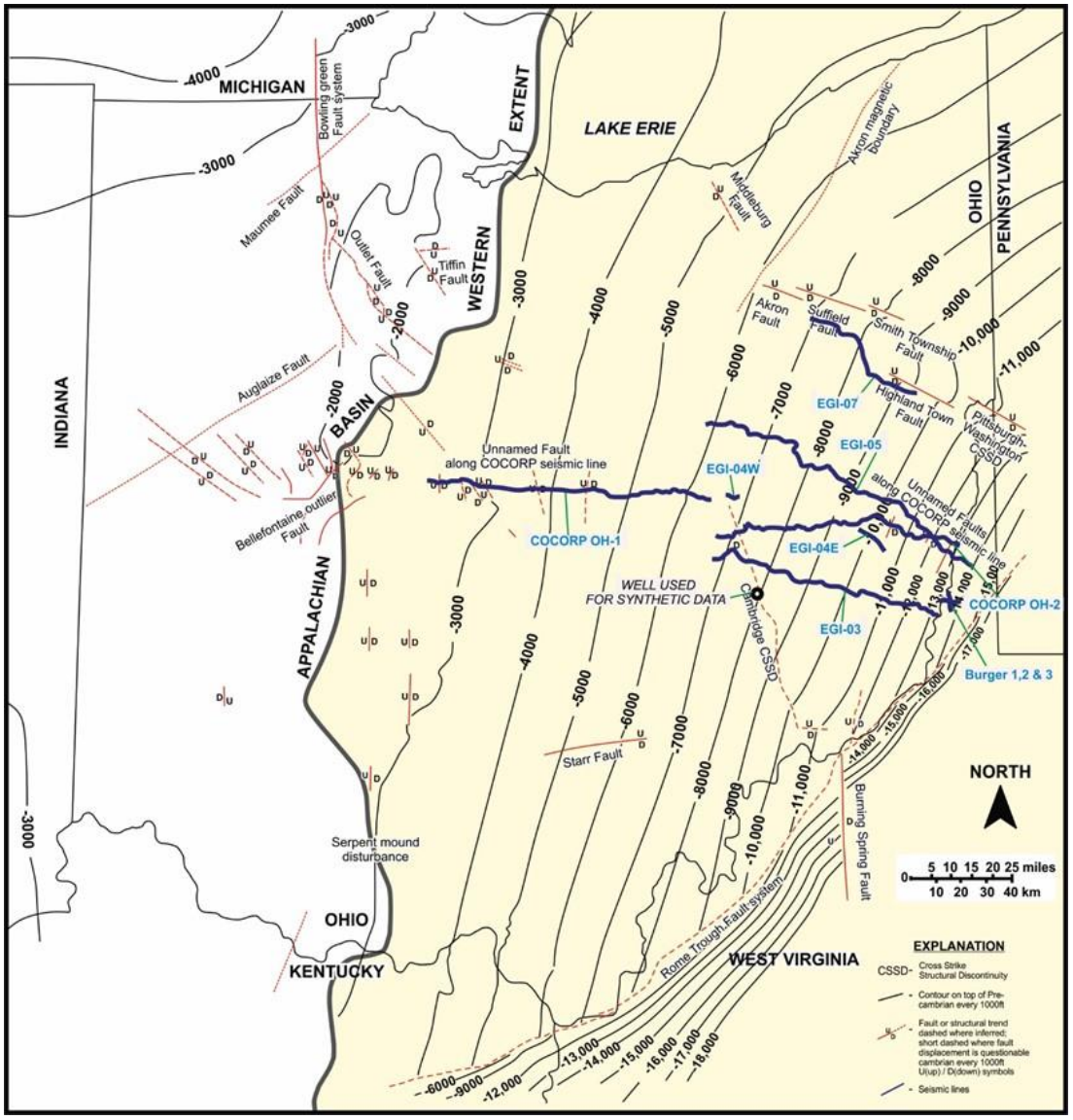

Figure 2-35: Precambrian unconformity surface with locations of available seismic lines.

2.6 Systematic Survey of Geomechanical and Petrophysical Parameters

The survey of geomechanical and petrophysical parameters was designed to obtain, review, and interpret available data (including available well logs and rock core test data) in order to analyze trends related to location, depth, formation, and test methods. The goal was to better understand the regional distribution of geomechanical parameters and reservoir conditions from the standpoint of CO_2 storage zones and caprocks in the Basin and Arches area of the Midwest.

2.6.1 Well Log Review

Advanced log mapping of the Appalachian Basin region was conducted to acquire a better understanding of the availability of advanced logs (sonic and image log) for geologic interpretation. Advanced log data locations were gathered from a Battelle in-house log database, from the Risk Based Data Management System (RBDMS) (ODNR, 2015) and through personal correspondence with the Ohio Geological Survey (OGS), the Kentucky Geological Survey (KGS), and the Indiana Geological Survey (IGS), which have mapped sonic logs in the Midwest Regional Carbon Sequestration Partnership (MRCSP) region. Oil and gas databases from geologic surveys for the states of Michigan, Pennsylvania, West Virginia, and Indiana were not accessible; therefore, we were unable to obtain data for those states. The only available source of image log data was the RBDMS database for Ohio; the other states' information consisted of sonic log data. Information collected was imported into ArcGIS 10.2 and mapped according to log type. Figures 2-36 through 2-38 show log locations for the Appalachian and Michigan Basin regions.

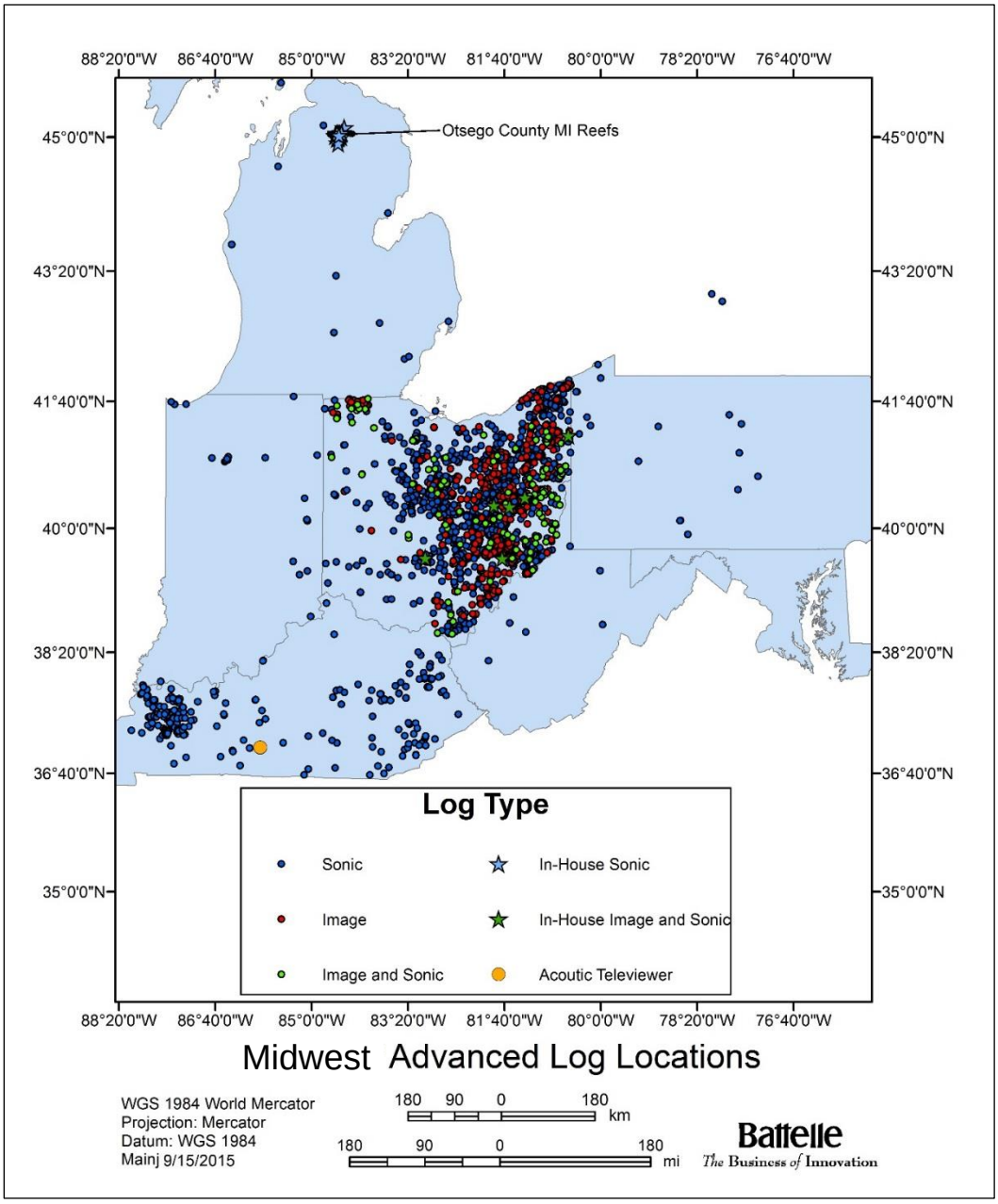

Figure 2-36: Advanced log locations for the Appalachian Basin region.

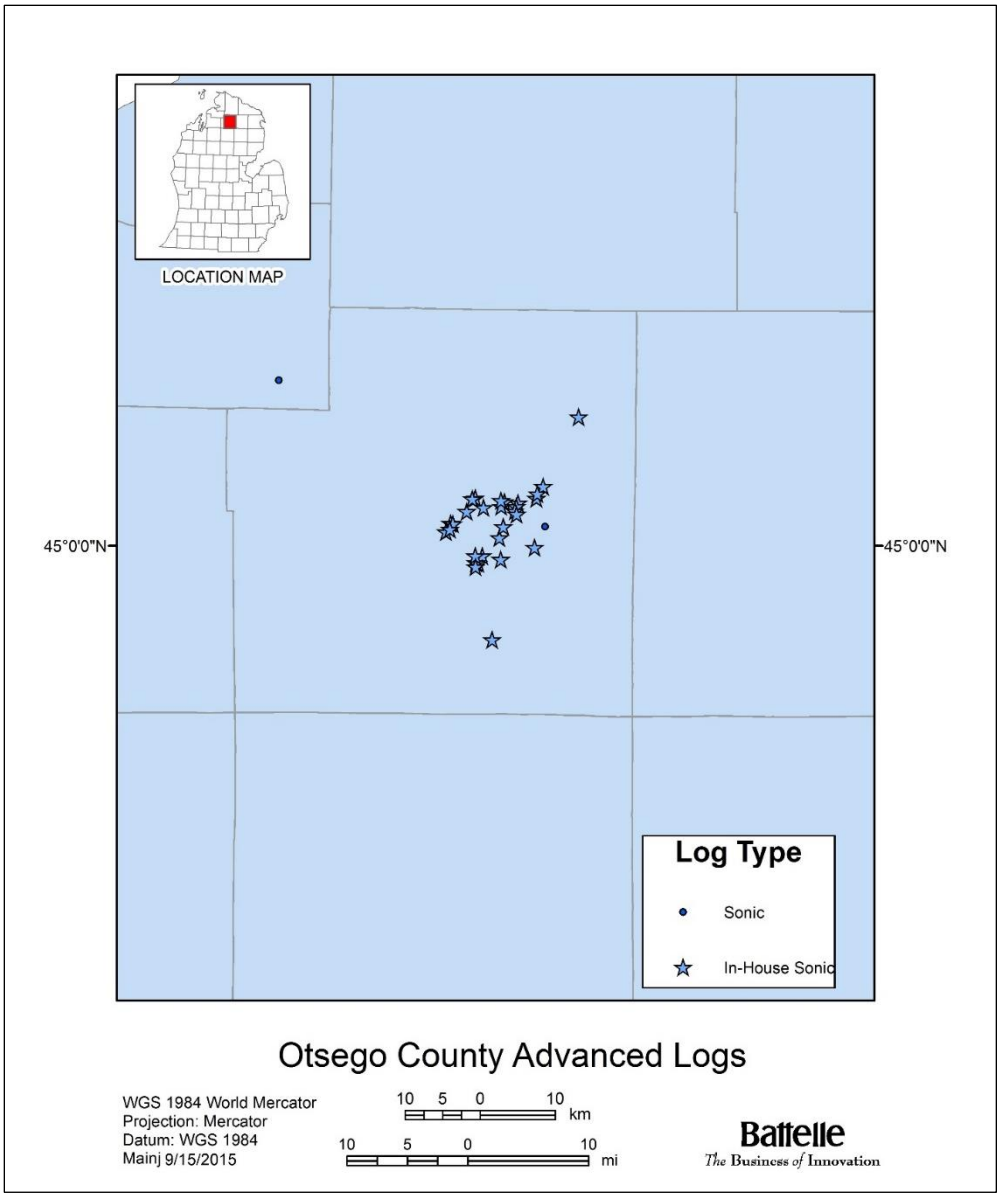

Figure 2-37: Advanced log locations for Otsego County, Michigan.

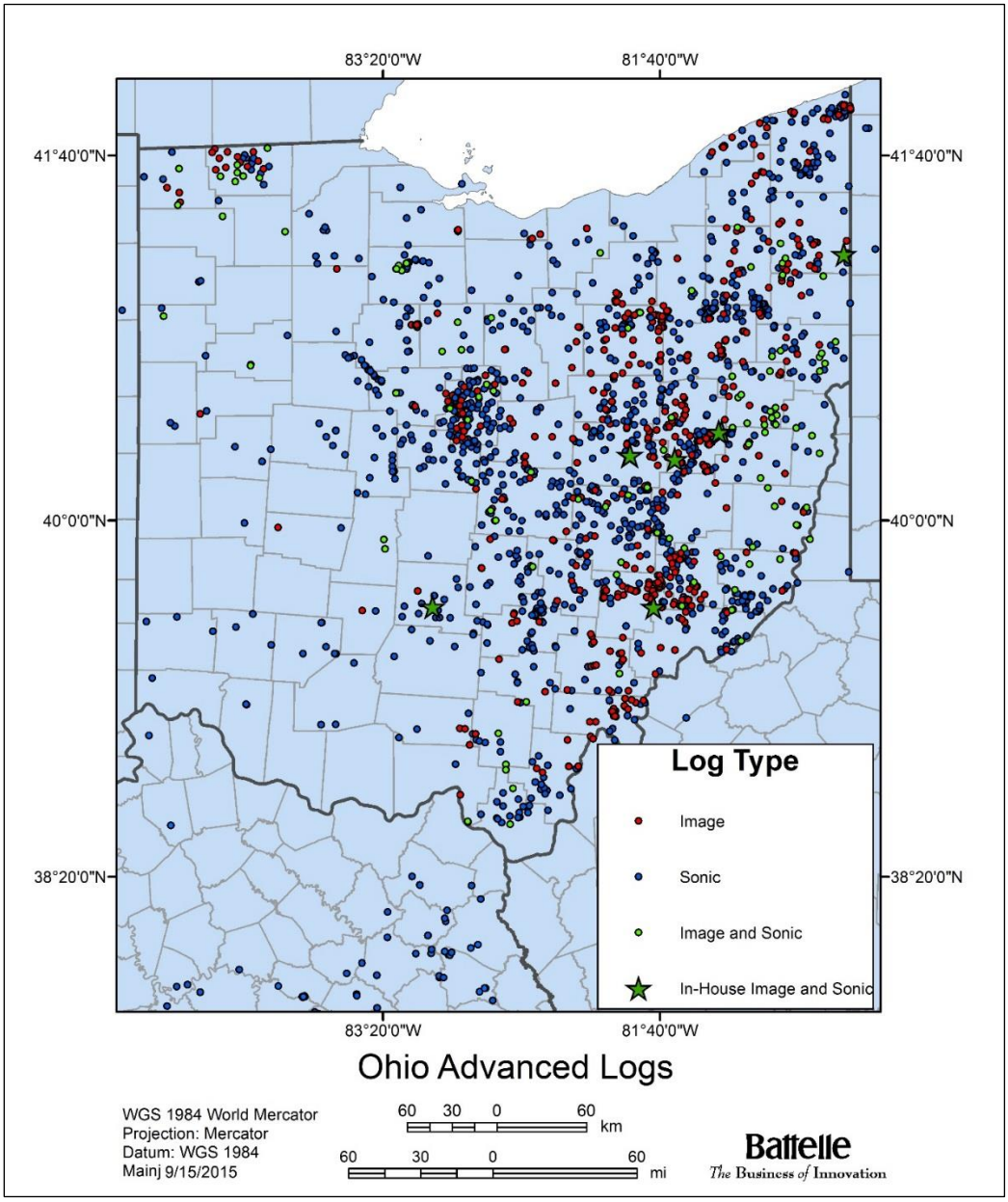

Figure 2-38: Advanced log locations for Ohio.

2.6.2 Geomechanical Data Review

This section presents a review of available geomechanical data for the study area. Available data are presented in tabular format along with summary statistics. Histograms, maps, and graphs of the data are also presented, along with relevant discussions.

2.6.2.1 Available data and summary statistics

Available geomechanical data for the study area are presented in Table 2-4. These data were compiled from state databases, other CO_2 storage research, and geologic research projects. The data were supplemented with additional rock core tests performed as part of this project. In general, for many of the deep saline rock formations being considered for CO_2 storage, the availability of geomechanical core test data is limited for three reasons: the formations do not contain hydrocarbons; it is fairly expensive to obtain rock cores while drilling; and geomechanical testing has only recently become more common. However, a more rigorous examination of these data may provide better depiction of the population distribution for use in assessing geomechanical processes associated with CO_2 storage projects.

A total of 50 data points are available from 19 wells. For these wells, data are available from a minimum of 1 to a maximum of 10 cores at varying depths. Depths range from about 1,400 ft to about 9,000 ft. Data are available from 22 geologic formations, with a minimum of 1 data point in a number of formations and a maximum of 11 data points in the Mount Simon Formation. Summary statistics are presented in Table 2-5.

2.6.2.2 Data distribution

The distributions of the various geomechanical parameters are presented in histograms (Figures 2-39 through 2-48). The histograms of bulk density, compressional velocity, shear velocity, dynamic Young's modulus, and shear modulus are approximately symmetric. The histogram of dynamic Poisson's ratio is skewed left. The histograms of bulk modulus and static Young's modulus are bimodal. Finally, the histograms of compressive strength and static Poisson's ratio are skewed right.

Table 2-4: Geomechanical data for the study area.

Well Name	API Number	Longitude	Latitude	Formation	Depth (ft)	Confining pressure (psi)	Confining pressure gradient (psi/ft)	Bulk density (g/cc)	Ultrasonic wave velocity				Dynamic elastic parameters				Static parameters			Source
									Compressional		Shear		Young's modulus (1e+6 psi)	Poisson's ratio	Bulk modulus (1e+6 psi)	Shear modulus (1e+6 psi)	Compressive strength (psi)	Static Young's modulus (1e+6 psi)	Static Poisson's ratio	
									ft/sec	µsec/ft	ft/sec	µsec/ft								
AEP#1	4705300423	-81.9379750	38.9761030	Black River	6825	1200	0.18	2.71	18885	52.95	9560	104.60	8.85	0.33	8.56	3.33	NA	NA	NA	Battelle, AEP#1
AEP#1	4705300423	-81.9379750	38.9761030	Gull River	7025	1200	0.17	2.69	17721	56.43	9147	109.32	8.00	0.32	7.34	3.03	NA	NA	NA	Battelle, AEP#2
AEP#1	4705300423	-81.9379750	38.9761030	Wells Ck	7166.1	1300	0.18	2.82	19640	50.92	9519	105.06	9.26	0.35	10.06	3.44	50972	9.48	0.28	
AEP#1	4705300423	-81.9379750	38.9761030	Beekmantown	7700	1400	0.18	2.80	18788	53.23	9785	102.19	9.51	0.31	8.51	3.62	NA	NA	NA	Battelle, AEP#3
AEP#1	4705300423	-81.9379750	38.9761030	Beekmantown	7745	1400	0.18	2.79	20301	49.26	9797	102.07	9.75	0.35	10.70	3.62	51600	10.51	0.30	
AEP#1	4705300423	-81.9379750	38.9761030	Rose Run	7763	1400	0.18	2.53	16606	60.22	9526	104.98	7.76	0.25	5.27	3.09	34484	7.65	0.23	
AEP#1	4705300423	-81.9379750	38.9761030	Rose Run	7818.6	1400	0.18	2.49	14786	67.63	8953	111.70	6.50	0.21	3.74	2.69	32753	6.09	0.20	
AEP#1	4705300423	-81.9379750	38.9761030	Copper Ridge	8219	1500	0.18	2.83	19950	50.13	10315	96.95	10.68	0.32	9.75	4.05	NA	NA	NA	Battelle, AEP#4
AEP#1	4705300423	-81.9379750	38.9761030	Nolichucky	8575	1500	0.17	2.79	19227	52.01	10074	99.27	10.00	0.31	8.81	3.81	NA	NA	NA	Battelle, AEP#5
AEP#1	4705300423	-81.9379750	38.9761030	Maryville	9004	1600	0.18	2.61	17284	57.86	8957	111.65	7.44	0.32	6.76	2.83	NA	NA	NA	Battelle, AEP#6
American Aggregates DS-2	3416560005	-84.116055	39.565829	Black River	1388	460	0.33	2.719	17833	56.08	10045	99.55	9.37	0.27	6.72	3.70	17119	5.76	0.26	
American Aggregates DS-2	3416560005	-84.116055	39.565829	Black River	1544	510	0.33	2.699	18610	53.73	10529	94.97	10.20	0.26	7.22	4.03	28895	6.91	0.27	
American Aggregates DS-2	3416560005	-84.116055	39.565829	Knox	2488	820	0.33	2.782	21364	46.81	11613	86.11	13.04	0.29	10.37	5.05	22333	8.35	0.38	
American Aggregates DS-2	3416560005	-84.116055	39.565829	Knox	2537	840	0.33	2.782	22629	44.19	13199	75.76	16.22	0.24	10.49	6.53	27863	10.84	0.23	
Berkey Gas Unit 4	3711120087	-79.1744329	39.9425731	Medina	8885.65	3160	0.36	2.59	16778	59.60	9949	100.51	8.48	0.23	5.21	3.45	43004	7.09	0.28	Battelle, RPSEA
E I Dupont de Nemours #2	4703902571	-81.5551170	38.2429940	Newburg	5155.76	1720	0.33	2.56	14150	70.67	8867	112.77	6.39	0.18	3.29	2.71	39265	6.63	0.16	Battelle, RPSEA
Goldsberry Russel 12004	3407321968	-82.5239335	39.5381216	Clinton	2543	850	0.33	2.25	12500	80.00	7966	125.54	4.44	0.16	2.17	1.92	18882	3.65	0.23	Battelle, RPSEA
Hanson Agg 1	1604300105	-83.1325970	38.4695520	Rose Run	3312.81	1100	0.33	2.41	16075	62.21	8295	120.56	5.89	0.32	5.41	2.23	24111	5.43	0.19	Battelle, RPSEA
Hanson Agg 1	1604300105	-83.1325970	38.4695520	Copper Ridge	3790.3	1350	0.36	2.71	21770	45.93	11010	90.82	11.74	0.33	11.38	4.42	24544	8.33	0.19	Battelle, RPSEA
Hanson Agg 1	1604300105	-83.1325970	38.4695520	Mount Simon	4686.35	1560	0.33	2.35	14209	70.38	8961	111.60	5.96	0.17	3.01	2.55	23254	4.56	0.30	Battelle, RPSEA
Kalamazoo	21077003277000	-85.5504576	42.2157630	Mount Simon	4970.65	1650	0.33	2.65	NA	NA	NA	NA	NA	NA	NA	NA	36729	6.451	0.288	Battelle, Arches
Kalamazoo	21077003277000	-85.5504576	42.2157630	Mount Simon	4978.9	1650	0.33	2.44	NA	NA	NA	NA	NA	NA	NA	NA	31557	5.546	0.208	Battelle, Arches
Kaufman 7	4708700963	-81.2654780	38.7519750	Big Injun	2186.87	730	0.33	2.65	16544	60.44	10630	94.07	9.28	0.15	4.40	4.04	30749	5.53	0.15	Battelle, RPSEA
Lloyd Cupp #1-11	21149313350000	-85.4311615	41.9548646	Mount Simon	5022	1650	0.33	2.59	NA	NA	NA	NA	NA	NA	NA	NA	17259	2.334	0.308	Battelle, Arches
Midwest#2	IN159092	-87.1707280	41.6295411	Eau Claire	2817	1000	0.35	2.38	NA	NA	NA	NA	NA	NA	NA	NA	15161	3.634	0.282	Battelle, Arches
Midwest#2	IN159092	-87.1707280	41.6295411	Eau Claire	3911.9	1300	0.33	2.41	NA	NA	NA	NA	NA	NA	NA	NA	24259	4.148	0.169	Battelle, Arches
Miller #2	310132573700	-79.3089980	42.2112010	Black River	6272.09	1950	0.31	2.68	16527	60.51	9253	108.08	7.86	0.27	5.74	3.09	24786	5.59	0.42	JBPU
Miller #2	310132573700	-79.3089980	42.2112010	Little Falls	6344.14	1950	0.31	2.72	20064	49.84	10730	93.20	10.96	0.30	9.12	4.22	42509	9.28	0.31	JBPU
Miller #2	310132573700	-79.3089980	42.2112010	Rose Run	6367.56	1950	0.31	2.68	18880	52.97	11510	86.88	11.54	0.20	6.50	4.79	60443	11.45	0.27	JBPU
Miller #2	310132573700	-79.3089980	42.2112010	Rose Run	6370.08	1950	0.31	2.59	17577	56.89	11550	86.58	10.43	0.12	4.58	4.66	74276	10.78	0.18	JBPU
Miller #2	310132573700	-79.3089980	42.2112010	Galway caprock	7069.45	1950	0.28	2.80	21637	46.22	11477	87.13	12.97	0.30	11.04	4.97	44327	10.45	0.31	JBPU
Miller #2	310132573700	-79.3089980	42.2112010	Galway c-sand	7076.31	1950	0.28	2.57	17094	58.50	10948	91.34	9.57	0.15	4.59	4.15	89225	10.00	0.24	JBPU
Montague#1	21121000000000	-86.4038274	43.3954557	Mount Simon	5730.25	1850	0.32	2.71	NA	NA	NA	NA	NA	NA	NA	NA	41184	7.862	0.253	Battelle, Arches
Montague#1	21121000000000	-86.4038274	43.3954557	Mount Simon	5731.5	1850	0.32	2.44	NA	NA	NA	NA	NA	NA	NA	NA	30082	4.647	0.3	Battelle, Arches
Oakleif Waldo 1	3403124092	-81.650407	40.358834	Beekmantown	6804.4	2250	0.33	2.702	20510	48.76	10780	92.76	11.08	0.31	9.67	4.23	37083	7.33	0.41	
Oakleif Waldo 1	3403124092	-81.650407	40.358834	Knox	6904	2280	0.33	2.67	16528	60.51	10120	98.82	8.84	0.20	4.92	3.68	25753	7.09	0.30	
Oakleif Waldo 1	3403124092	-81.650407	40.358834	Knox	6916	2280	0.33	2.665	15306	65.34	9568	104.52	7.75	0.18	4.03	3.29	29958	6.90	0.32	
Oakleif Waldo 1	3403124092	-81.6504071	40.3588344	Rose Run	6926.7	2310	0.33	2.58	17417	57.42	10050	99.50	8.78	0.25	5.86	3.51	32949	5.78	0.16	Battelle, RPSEA
ODGS CO_2 No. 1	3415725334	-81.4901229	40.3536373	Rose Run	7441	2600	0.35	2.50	15282	65.44	9261	107.98	7.00	0.21	4.02	2.89	41110	4.818	0.384	Battelle, ODGS
ODGS CO_2 No. 1	3415725334	-81.4901229	40.3536373	Mount Simon	8561	2950	0.34	2.45	14839	67.39	9176	108.98	6.62	0.19	3.56	2.78	45360	5.649	0.252	Battelle, ODGS
Ottawa	21139000707000	-86.1305371	42.7945592	Mount Simon	5334.1	1850	0.35	2.42	NA	NA	NA	NA	NA	NA	NA	NA	28477	4.54	0.173	Battelle, Arches
Ottawa	21139000707000	-86.1305371	42.7945592	Mount Simon	5528.55	1850	0.33	2.44	NA	NA	NA	NA	NA	NA	NA	NA	32376	4.957	0.347	Battelle, Arches
Redman-Barth #3	3403122838	-81.7798985	40.3062666	Utica	5661.5	2500	0.44	2.56	13418	74.53	7636	130.96	5.06	0.26	3.52	2.01	19493	1.87	0.23	ODGS
Redman-Barth #3	3403122838	-81.7798985	40.3062666	Utica	5680.5	2500	0.44	2.55	13789	72.52	8172	122.37	5.64	0.23	3.47	2.29	19921	2.15	0.23	ODGS
Redman-Barth #3	3403122838	-81.7798985	40.3062666	Utica	5683.5	2500	0.44	2.59	15272	65.48	8801	113.62	6.78	0.25	4.54	2.71	25790	3.11	0.25	ODGS
Redman-Barth #3	3403122838	-81.7798985	40.3062666	Trenton	5790	2500	0.43	2.61	14293	69.96	8074	123.85	5.79	0.27	4.12	2.29	19397	1.93	0.25	ODGS
Roma Sellars A3	3411721478	-82.9134819	40.5256051	Trempealeau	2950.5	1050	0.36	2.65	16788	59.57	8655	115.54	7.04	0.32	6.49	2.67	17473	5.43	0.16	Battelle, RPSEA
Vistron #1	34003200670000	-84.1278278	40.7161536	Mount Simon	2967.55	1000	0.34	2.24	NA	NA	NA	NA	NA	NA	NA	NA	15202	3.027	0.362	Battelle, Arches
Vistron #1	34003200670000	-84.1278278	40.7161536	Mount Simon	3066.4	1000	0.33	2.36	NA	NA	NA	NA	NA	NA	NA	NA	15729	3.338	0.32	Battelle, Arches
Wuchevich 1	3712136455	-79.9628370	41.4681750	Oriskany	5292	1760	0.33	2.55	13945	71.71	9391	106.48	6.59	0.09	2.65	3.03	50279	7.13	0.16	Battelle, RPSEA

NA = Data not available for this well at this depth.

Table 2-5: Summary statistics for geomechanical data.

Parameter	Confining pressure (psi)	Bulk density (g/cc)	Compressional velocity (ft/s)	Shear velocity (ft/s)	Dynamic Young's modulus (1e+6 psi)	Dynamic Poisson's ratio	Bulk modulus (1e+6 psi)	Shear modulus (1e+6 psi)	Compressive strength (psi)	Static Young's modulus (1e+6 psi)	Static Poisson's ratio
Count	50	50	39	39	39	39	39	39	44	44	44
Minimum	460	2.24	12500	7636	4.44	0.085	2.17	1.92	15,161	1.87	0.151
Maximum	3160	2.83	22629	13199	16.22	0.350	11.38	6.53	89,225	11.45	0.417
Range	2700	0.59	10129	5563	11.78	0.27	9.22	4.61	74,064	9.57	0.266
Median	1650	2.60	17094	9568	8.78	0.26	5.74	3.44	30,020	5.77	0.26
Mean	1656.60	2.60	17302.97	9791	8.69	0.25	6.35	3.47	33,136	6.23	0.26
Sample Standard Deviation	615.94	0.15	2592.66	1182.57	2.48	0.07	2.71	0.96	15,529	2.59	0.07

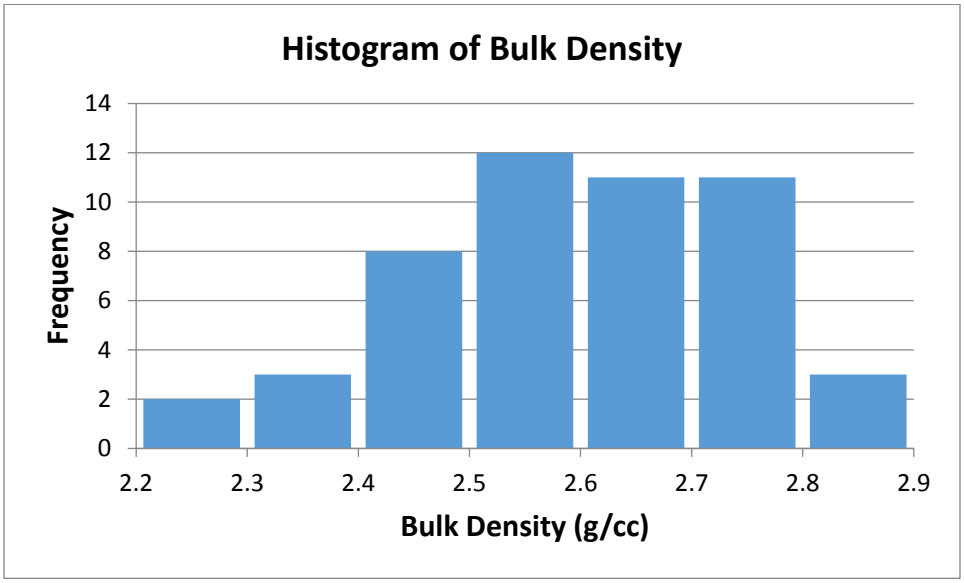

Figure 2-39: Histogram of bulk density.

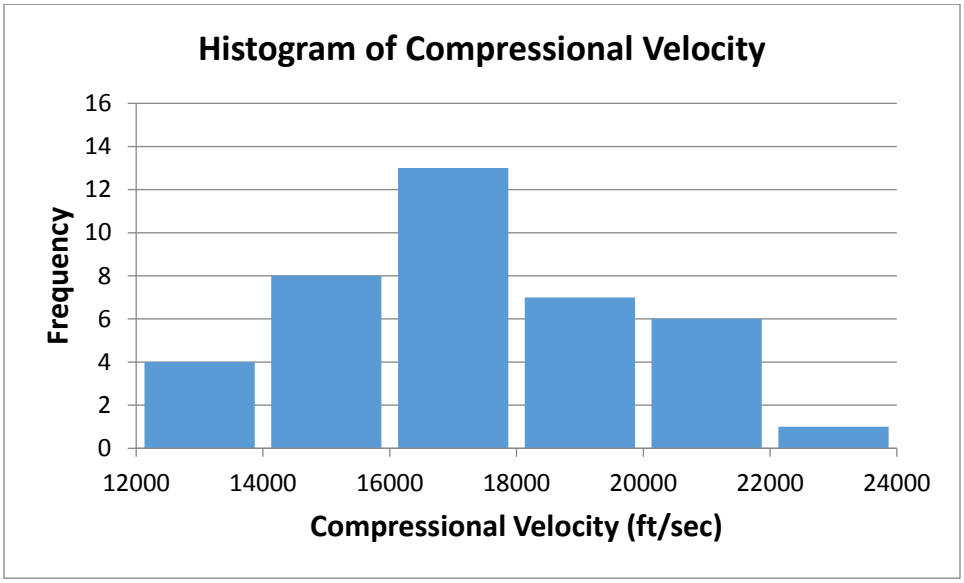

Figure 2-40: Histogram of compressional velocity.

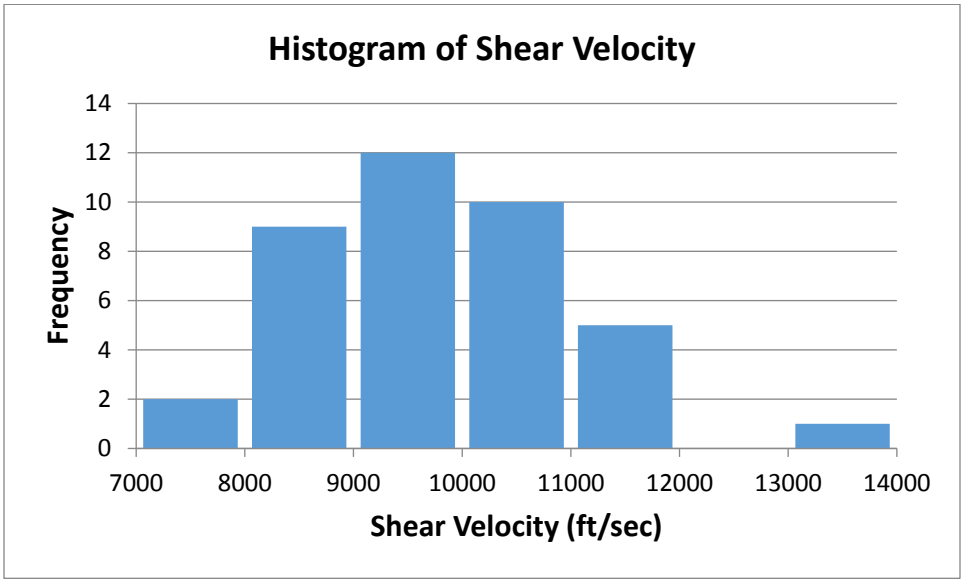

Figure 2-41: Histogram of shear velocity.

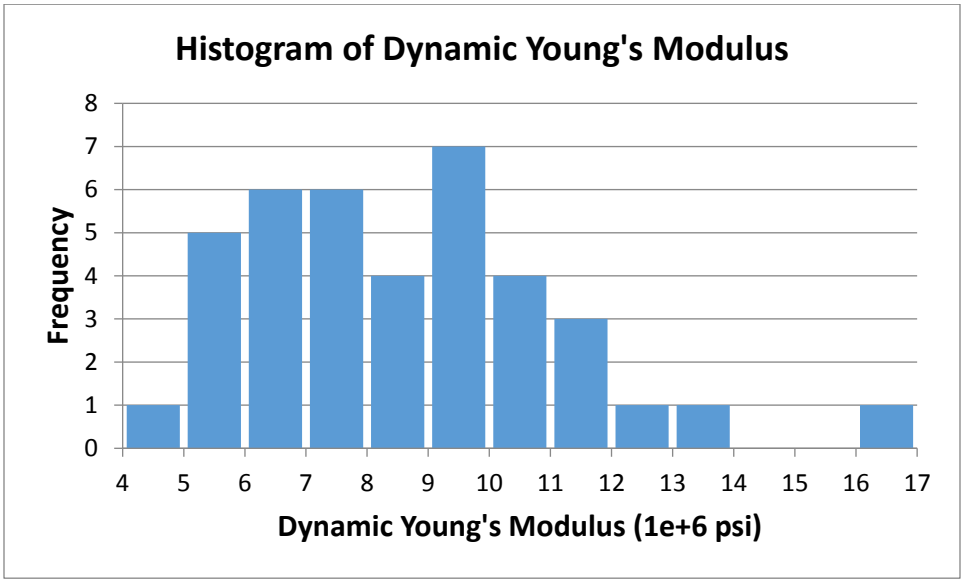

Figure 2-42: Histogram of dynamic Young's modulus.

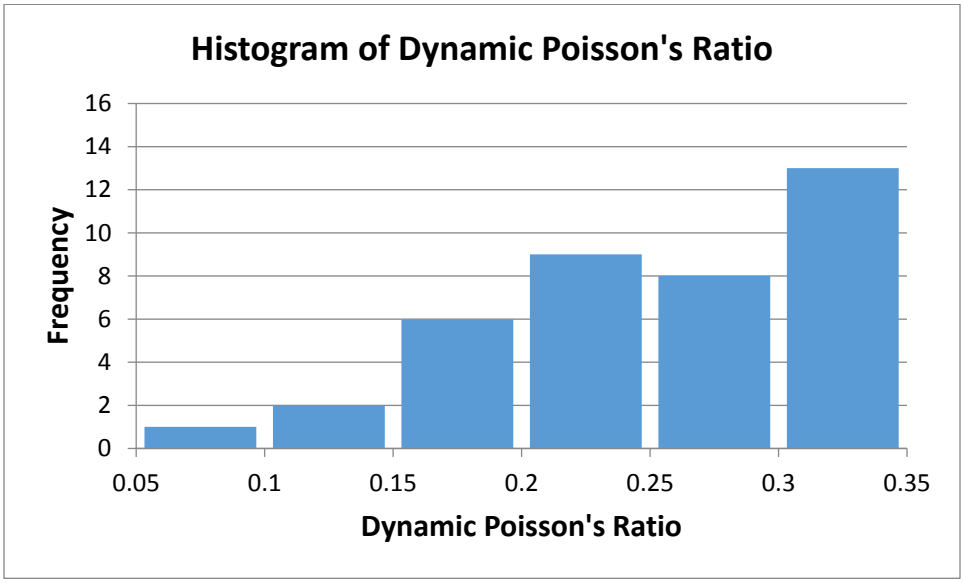

Figure 2-43: Histogram of dynamic Poisson's ratio.

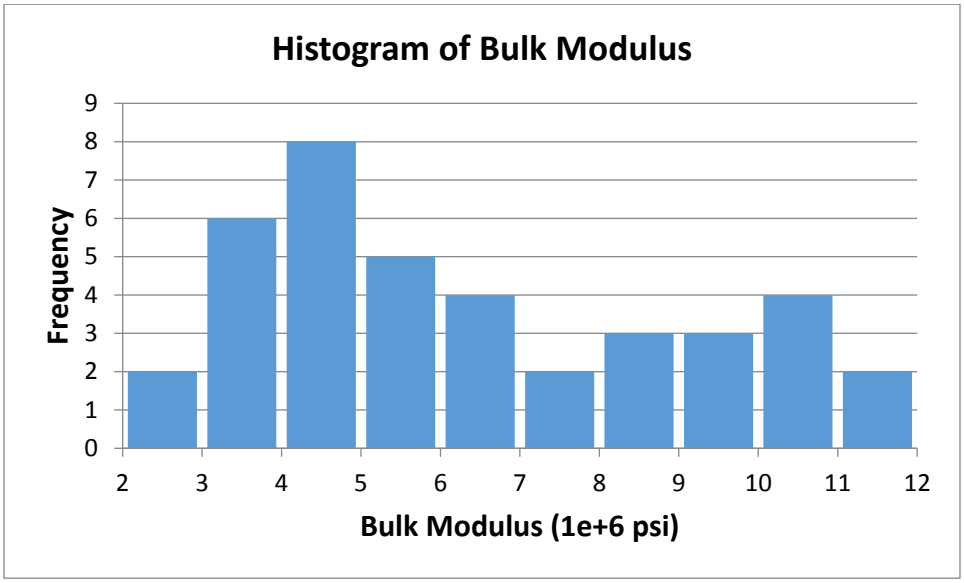

Figure 2-44: Histogram of bulk modulus.

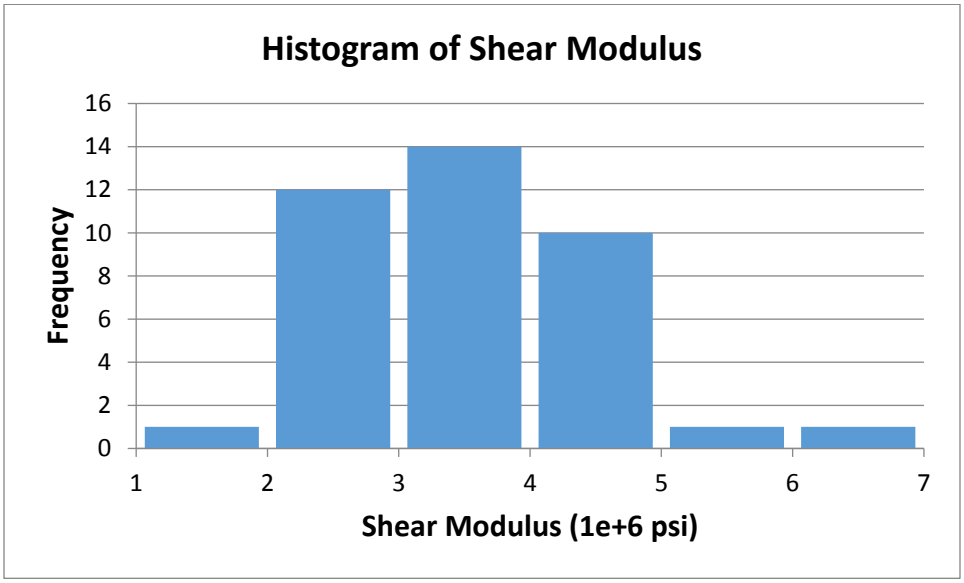

Figure 2-45: Histogram of shear modulus.

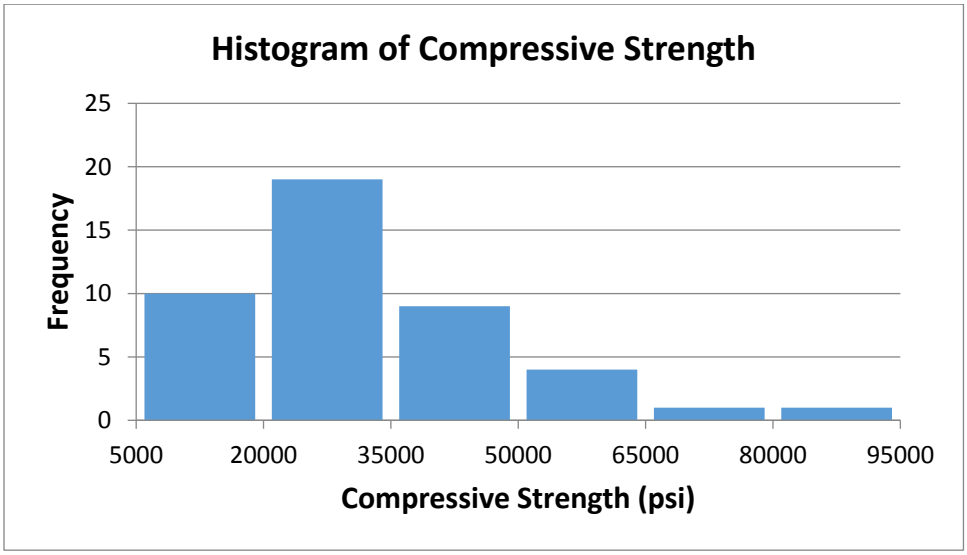

Figure 2-46: Histogram of compressive strength.

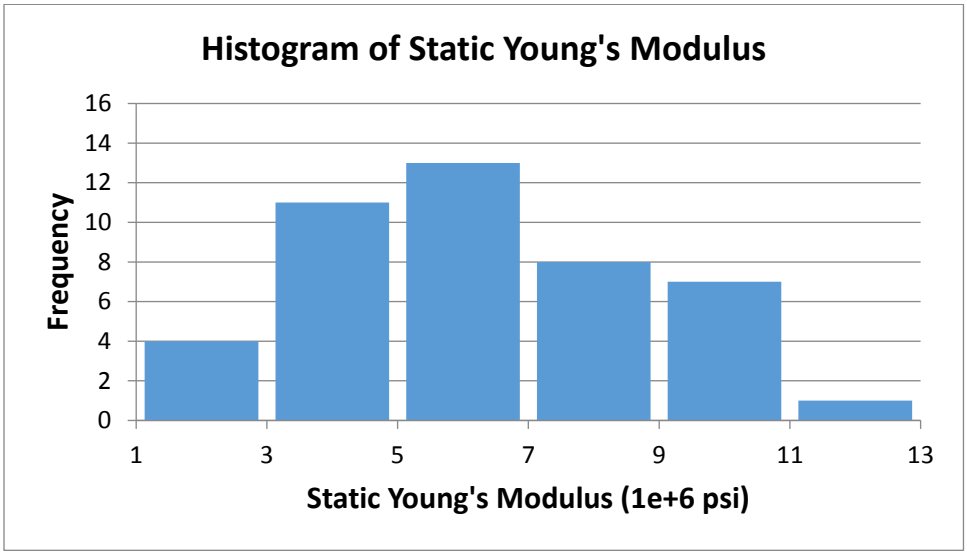

Figure 2-47: Histogram of static Young's modulus.

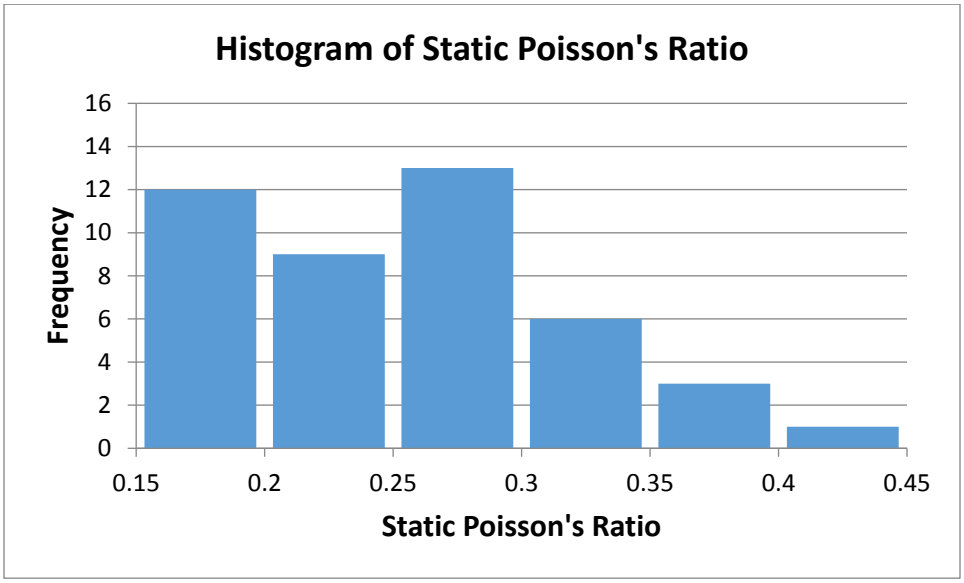

Figure 2-48: Histogram of static Poisson's ratio.

2.6.3 Spatial Data Distribution

The spatial distributions of the various geomechanical parameters are presented on maps in Figures 4-49 through 4-57. Because the overall data are relatively sparse (50 data points over an area of approximately 100,000 square miles) and derive from 22 different geologic formations over a depth range of about 7,600 ft, the data were not contoured in two or three dimensions. Instead, data locations and values are simply posted on the figures. Higher data values are represented by larger, warmer-colored symbols, while lower data values are represented by smaller, cooler-colored symbols. Symbols are posted in an order such that smaller symbols are not concealed by larger symbols at a given well. At each well location, available data values are posted along with the associated depth below ground surface. Posted data values for a given well are ordered from top to bottom by increasing depth, which is included in parentheses for each posting.

Some individual wells show increasing hardness and velocity with depth, potentially due to greater compression with depth. However, more often, the hardness and velocity are not directly related to depth at individual wells, as the core samples at individual wells typically originate from multiple different formations. At a well in Mason County, West Virginia, for example, the 10 core samples originate from nine different geologic formations. This likely accounts for the variability in compressional velocity, for example, with depth at this well.

2.6.4 Parameter Correlations

Potential correlations between geomechanical parameters and depth below ground surface of the associated core were explored via plots of geomechanical parameter versus depth. Most parameters showed weak correlation with depth. Graphs for those parameters with a coefficient of determination (R^2) for linear regression of greater than 0.1 are presented here. Those parameters are compressive strength and static Young's modulus versus depth (Figures 2-58 and 2-59, respectively). Depth is plotted on the vertical axis and increases down the axis, to mimic depth in the field.

In addition, potential correlations were explored between bulk density and both dynamic Poisson's ratio and dynamic Young's modulus. Stronger correlations were evident in both cases than with geomechanical parameters versus depth. Dynamic Poisson's ratio versus bulk density is presented in Figure 4-60, while dynamic Young's modulus versus bulk density is presented in Figure 2-61. The stronger correlations likely occur because bulk density is tied to formation.

Finally, potential correlations between geomechanical parameters and depth below ground surface were explored for the various geologic formations. Of these, only the Mount Simon Formation had sufficient data to support investigating correlations. For the Mount Simon, compressive strength, static Young's modulus, and static Poisson's ratio all yielded a coefficient of determination (R^2) for linear regression of greater than 0.1 when compared to depth below ground surface. Graphs of these three parameters in the Mount Simon versus depth are presented in Figures 4-62 through 4-64. For the remaining geomechanical parameters in the Mount Simon, insufficient data were available (two data points) to explore correlations to depth.

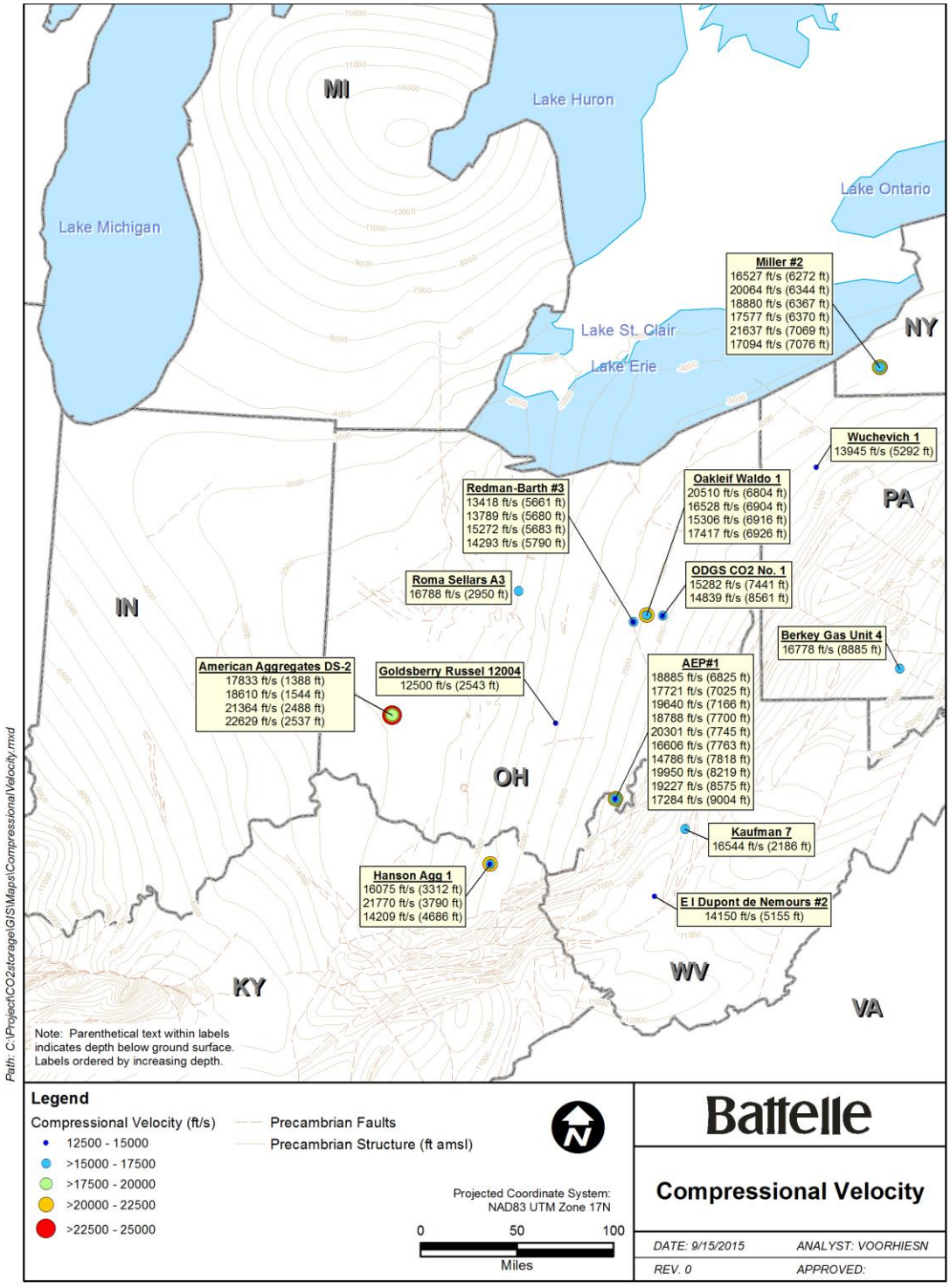

Figure 2-49: Spatial distribution of compressional velocity.

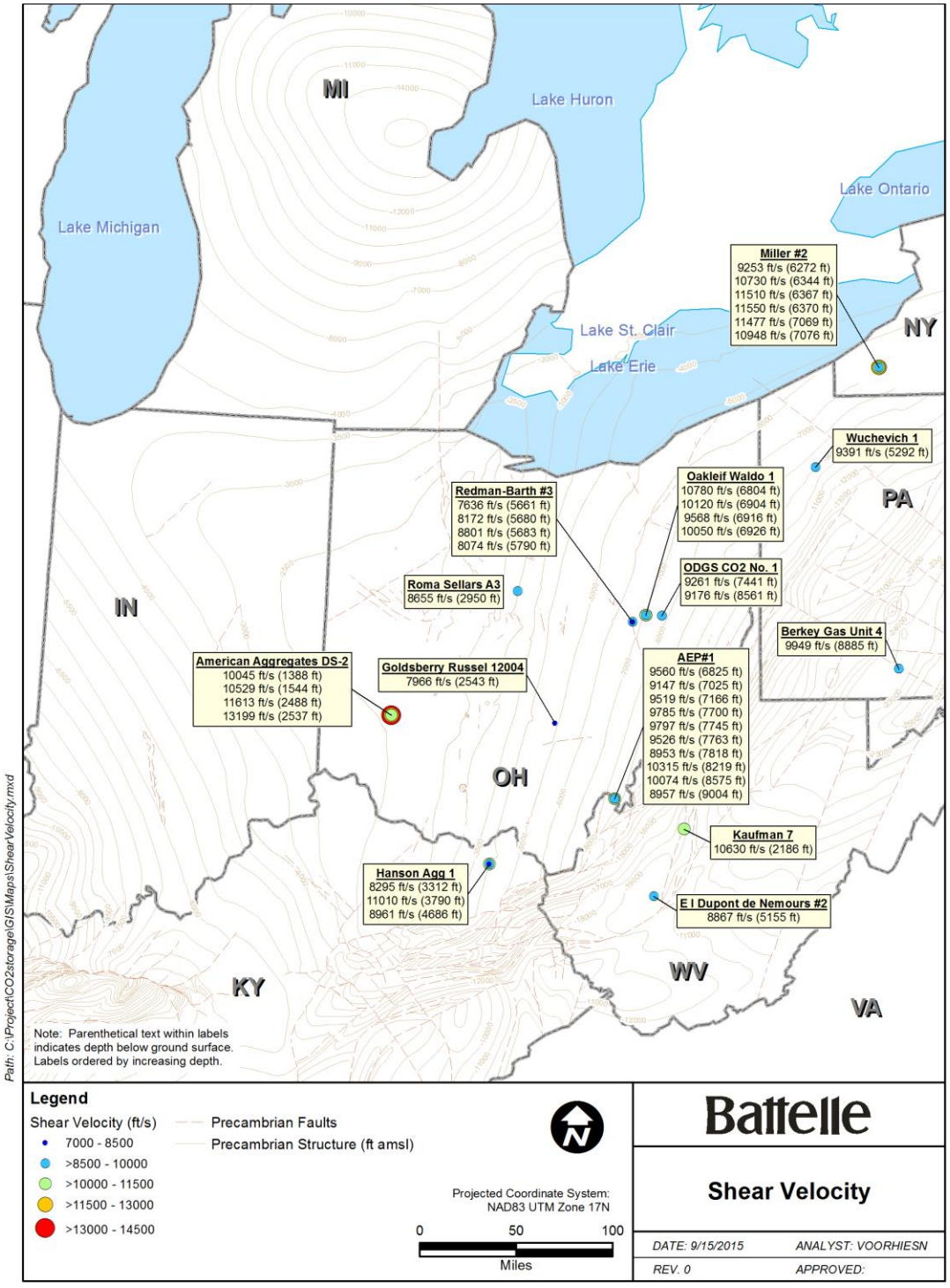

Figure 2-50: Spatial distribution of shear velocity.

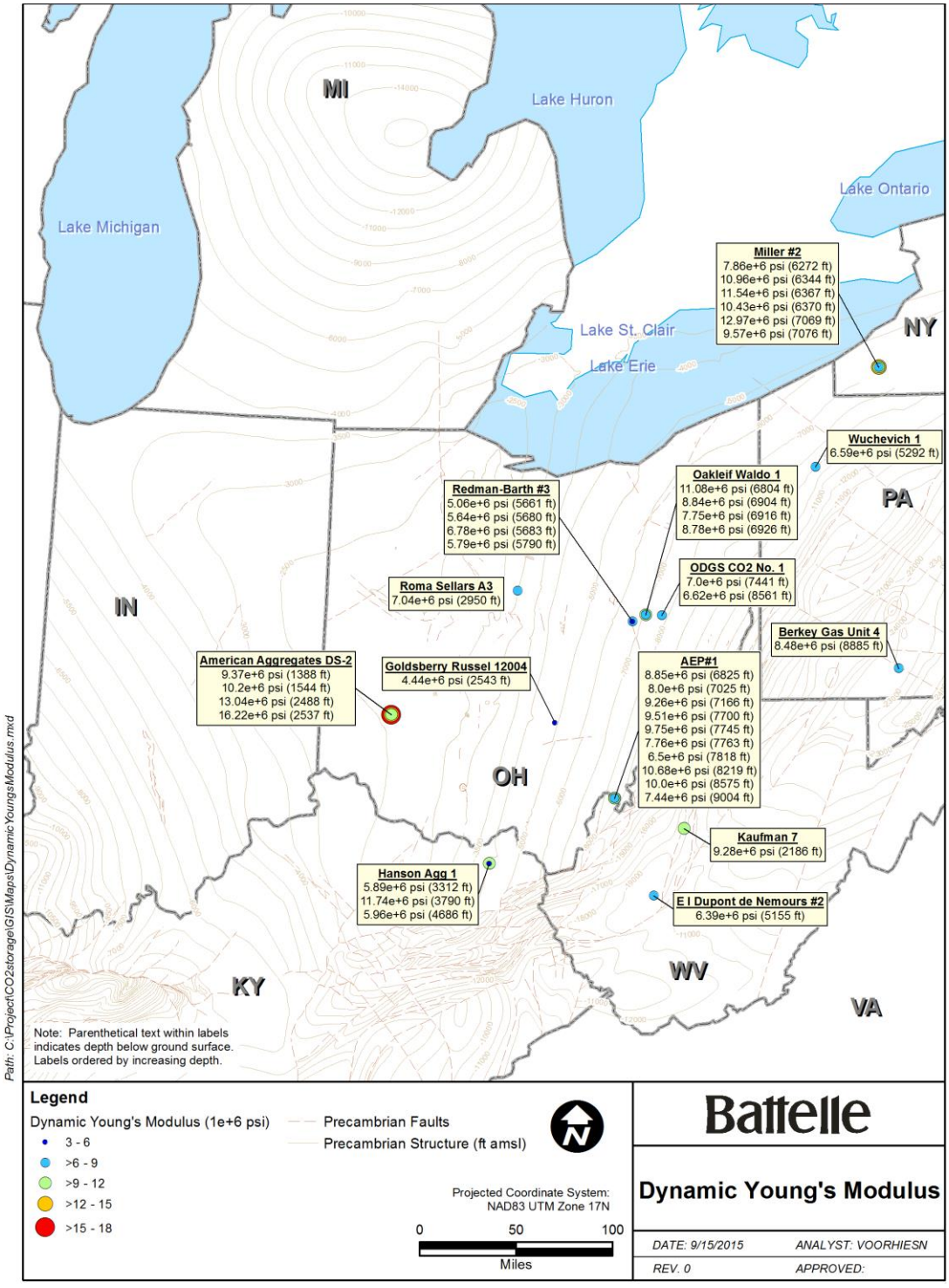

Figure 2-51: Spatial distribution of dynamic Young's modulus.

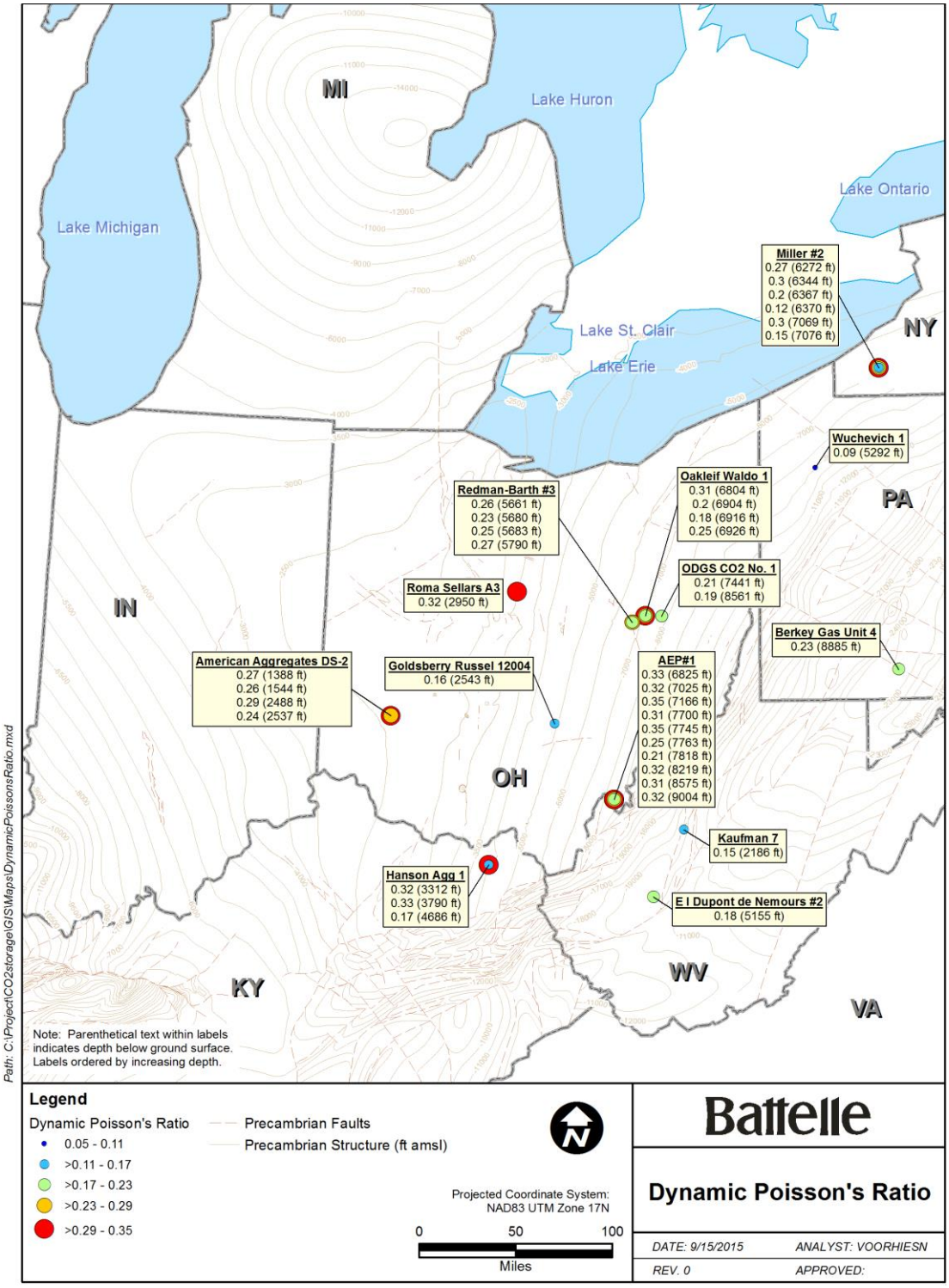

Figure 2-52: Spatial distribution of dynamic Poisson's ratio.

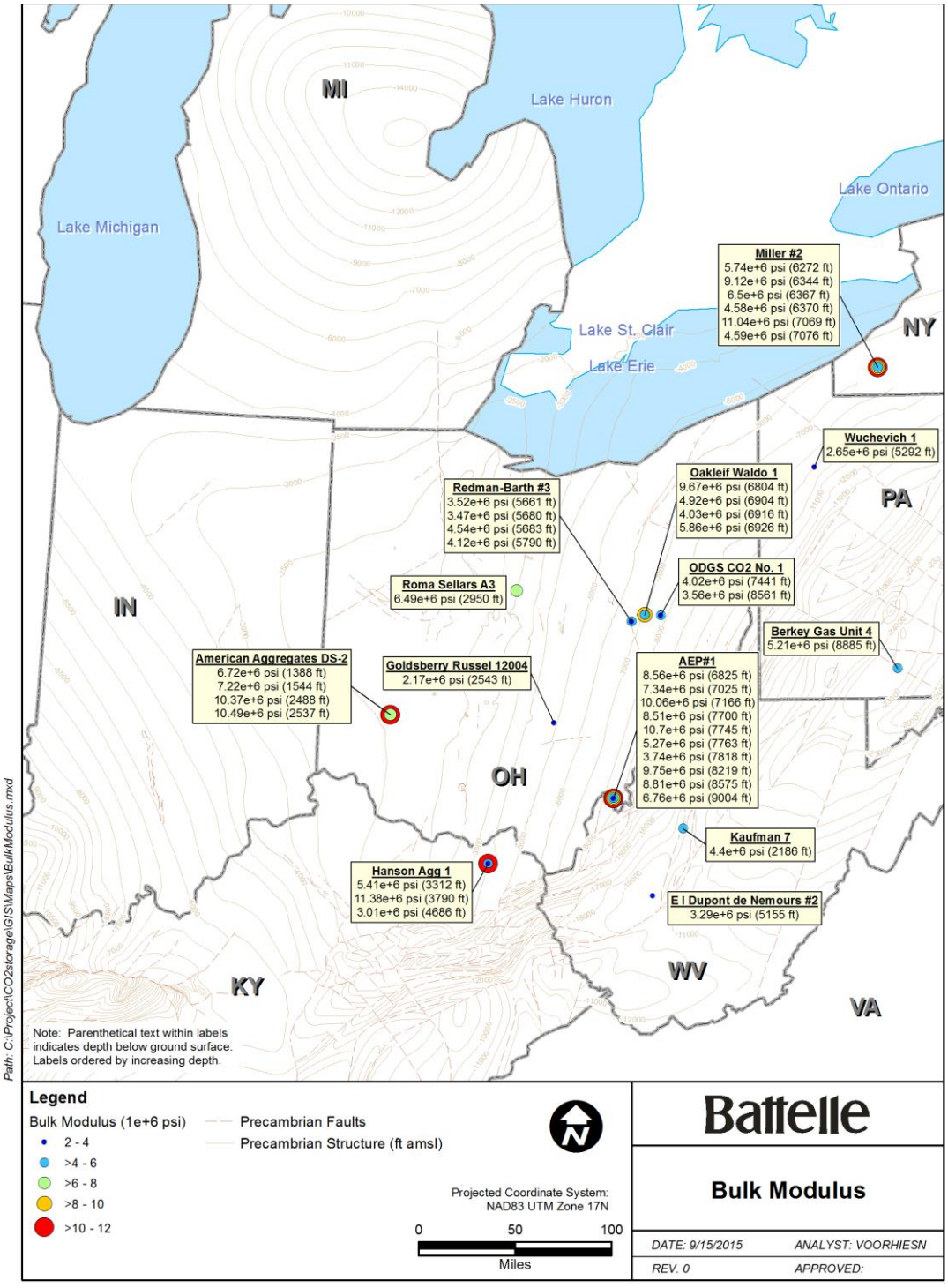

Figure 2-53: Spatial distribution of bulk modulus.

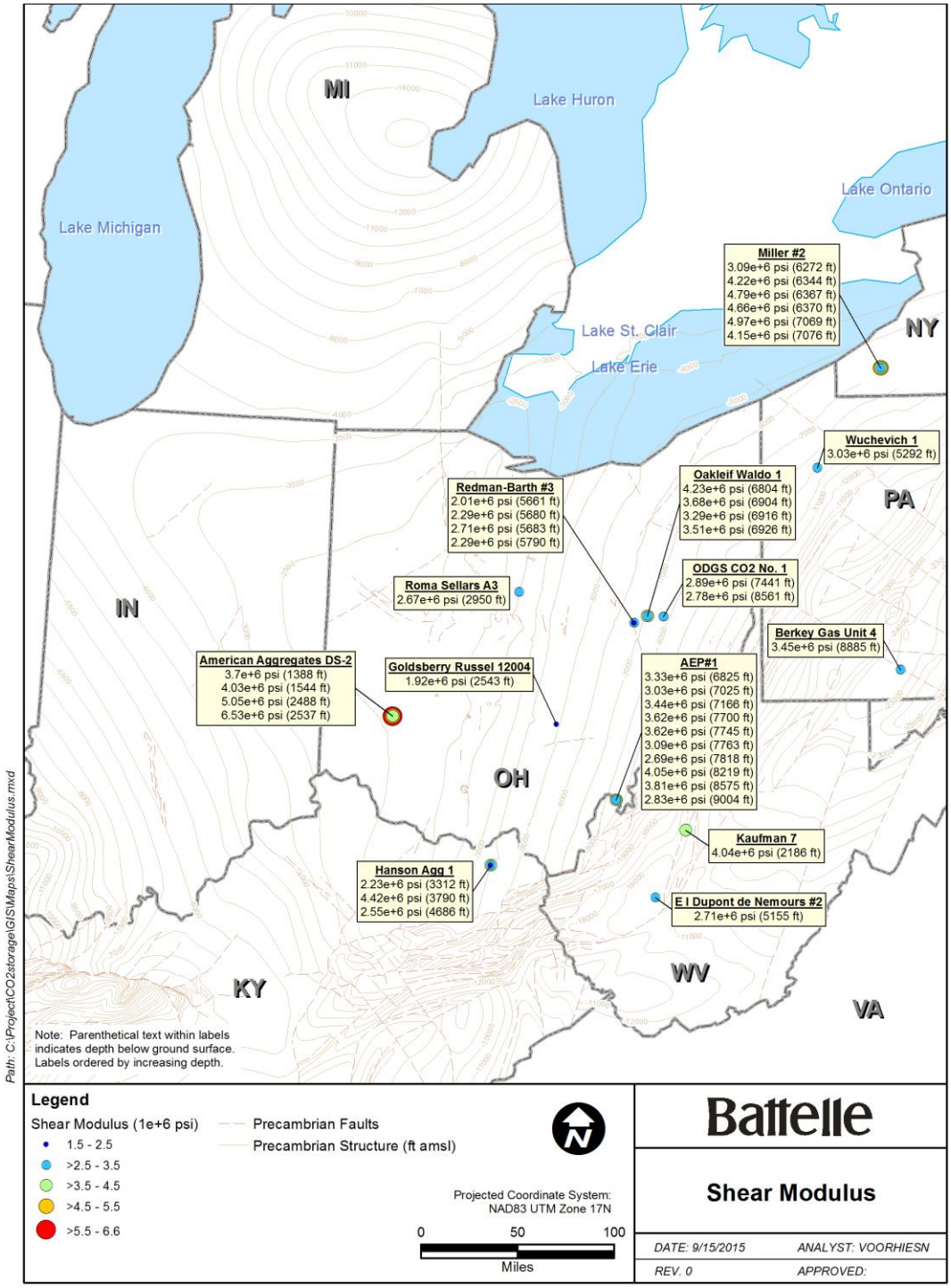

Figure 2-54: Spatial distribution of shear modulus.

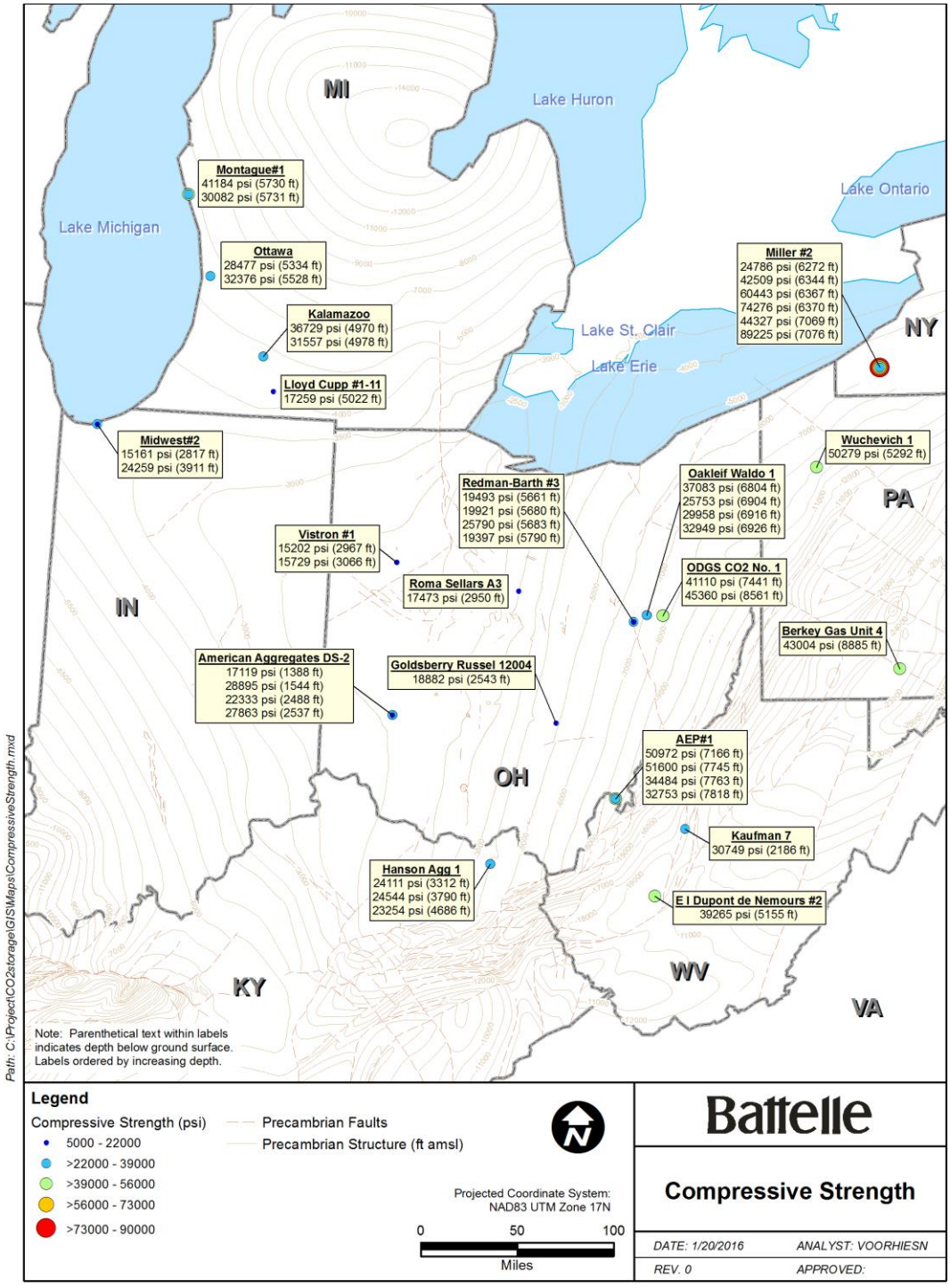

Figure 2-55: Spatial distribution of compressive strength.

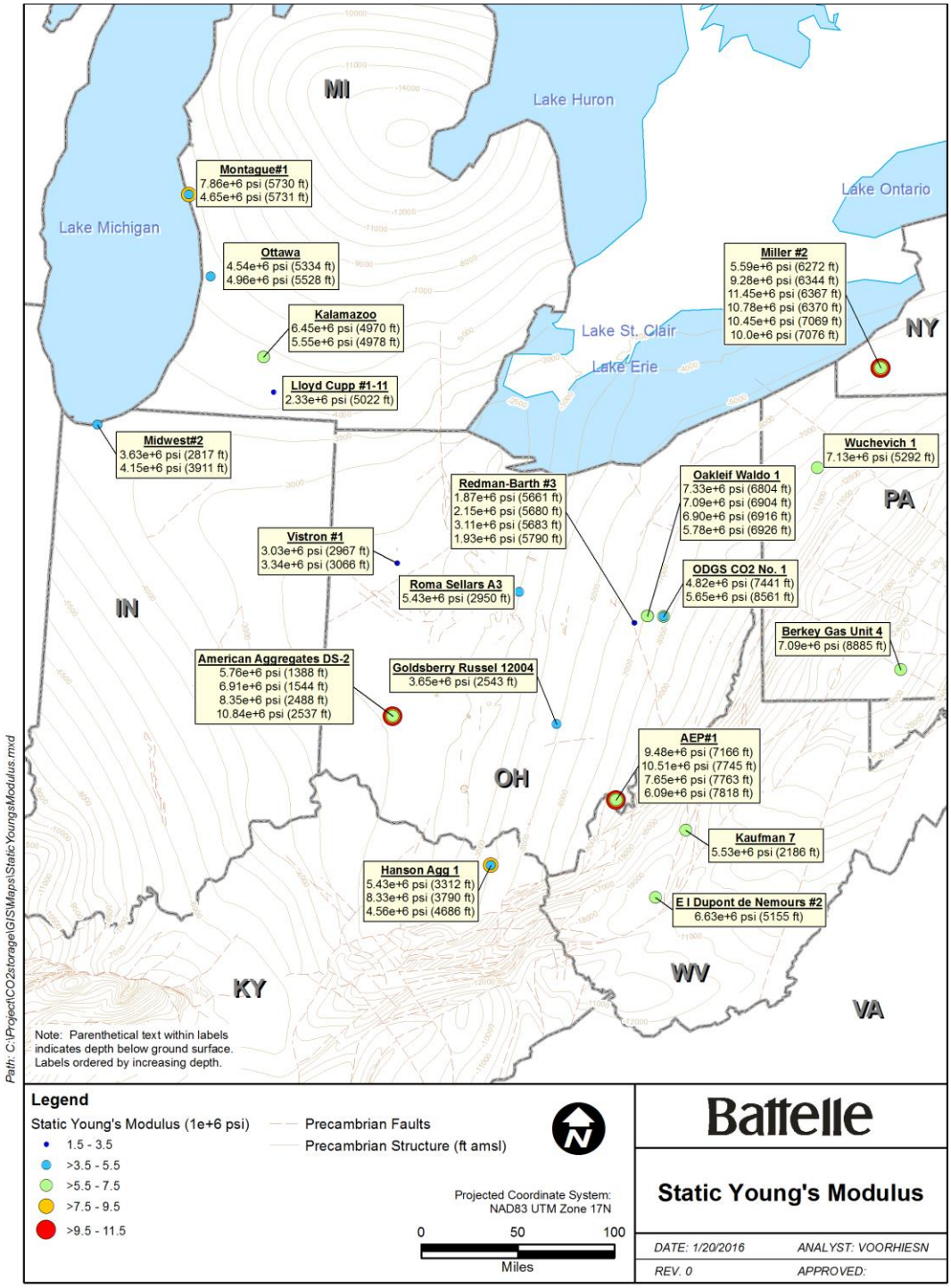

Figure 2-56: Spatial distribution of static Young's modulus.

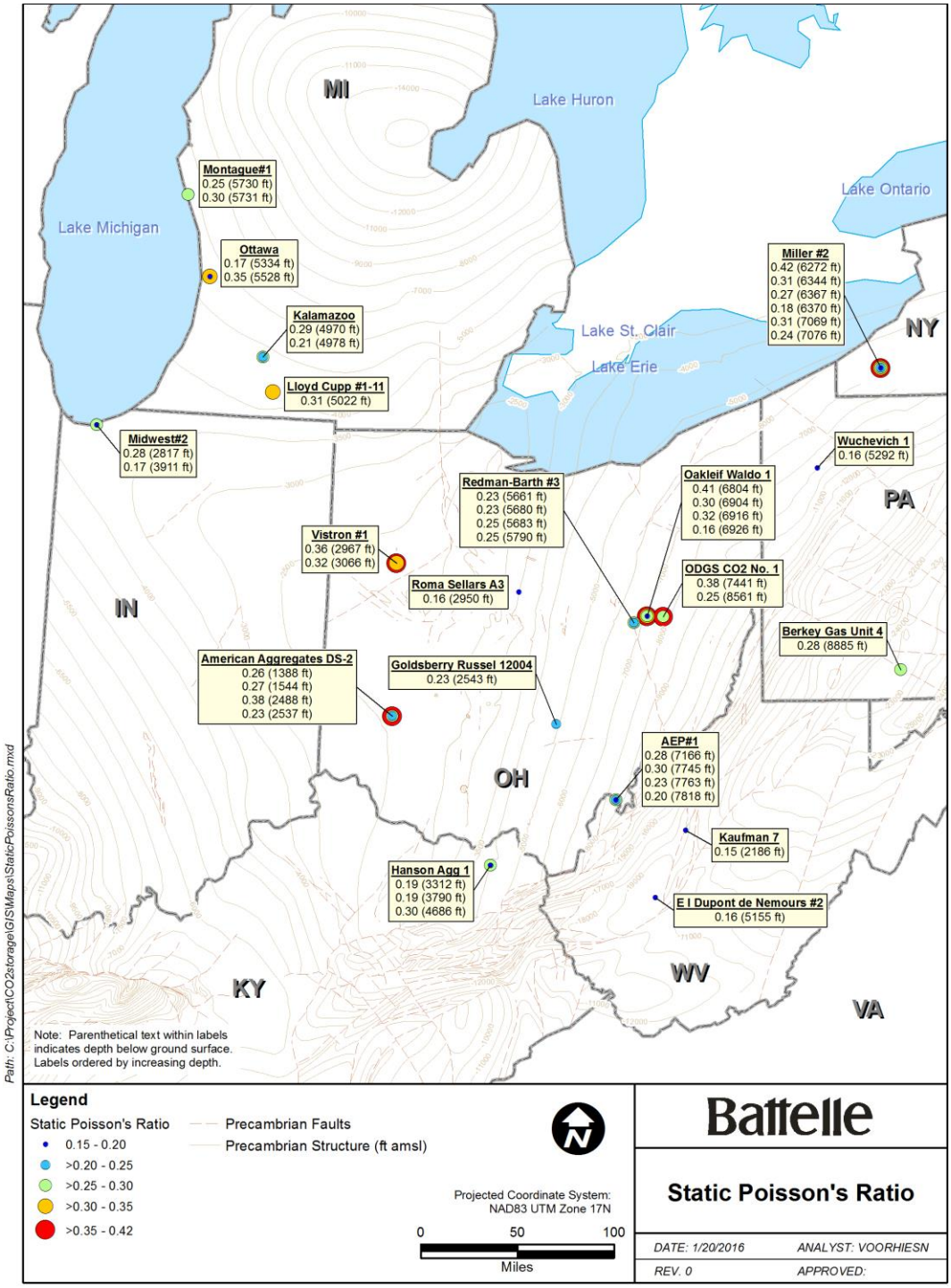

Figure 2-57: Spatial distribution of static Poisson's ratio.

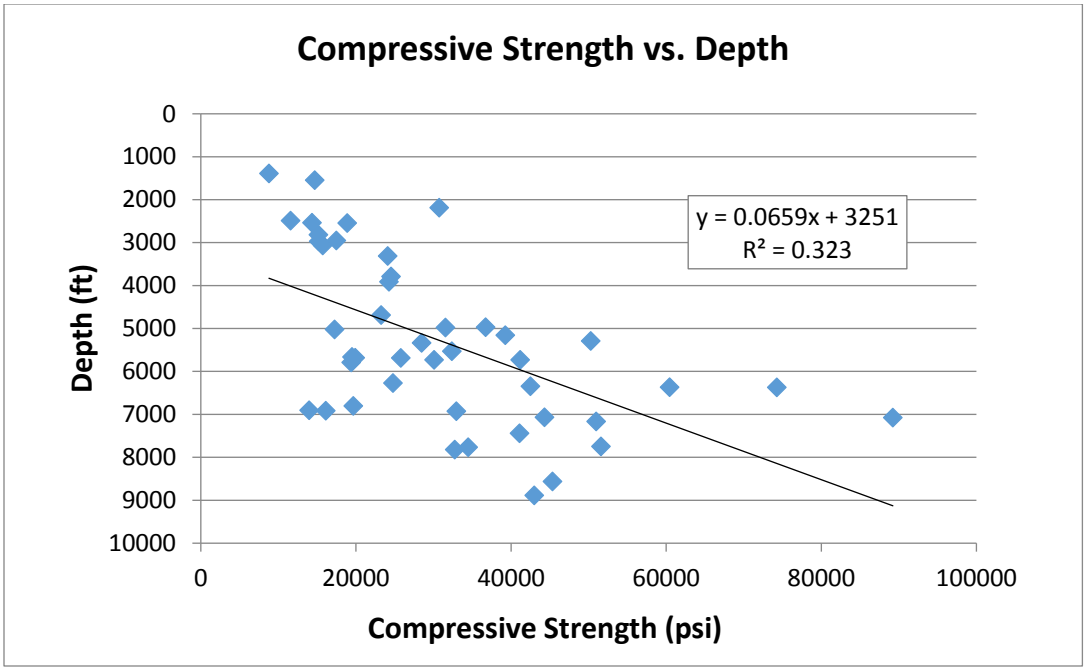

Figure 2-58: Compressive strength versus depth.

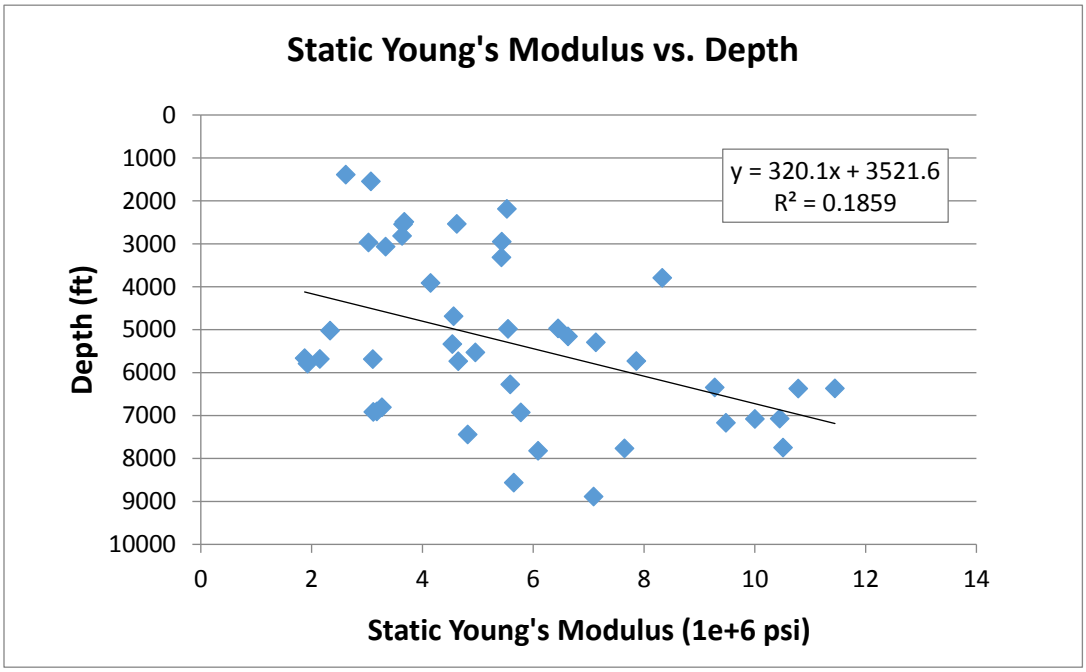

Figure 2-59: Static Young's modulus versus depth.

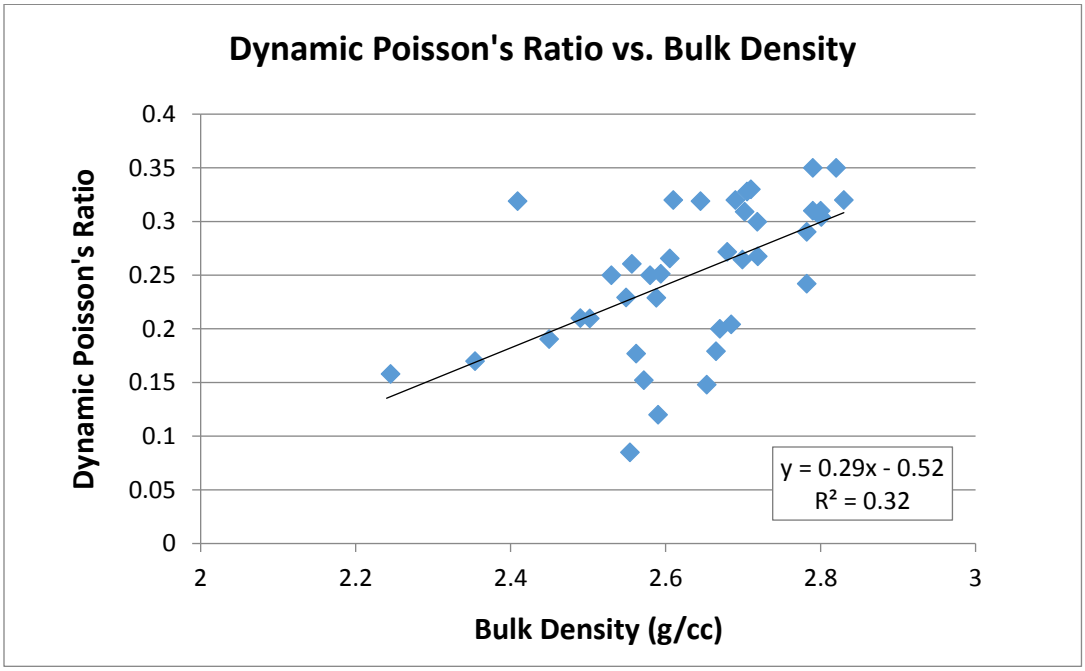

Figure 2-60: Dynamic Poisson's ratio versus bulk density.

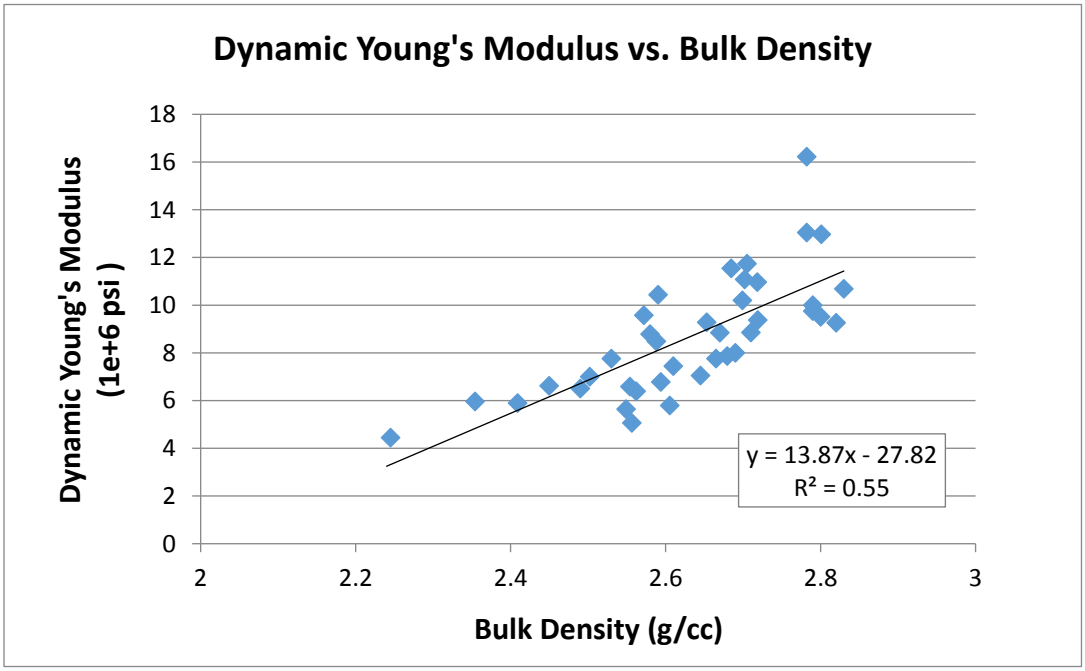

Figure 2-61: Dynamic Young's modulus versus bulk density.

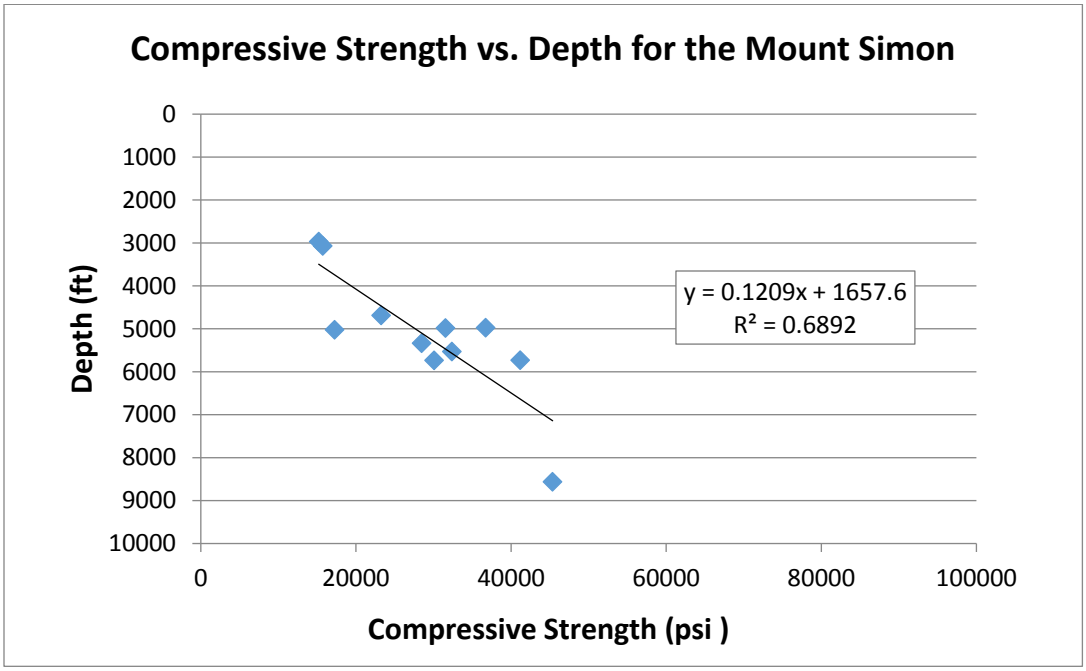

Figure 2-62: Compressive strength versus depth for the Mount Simon Formation.

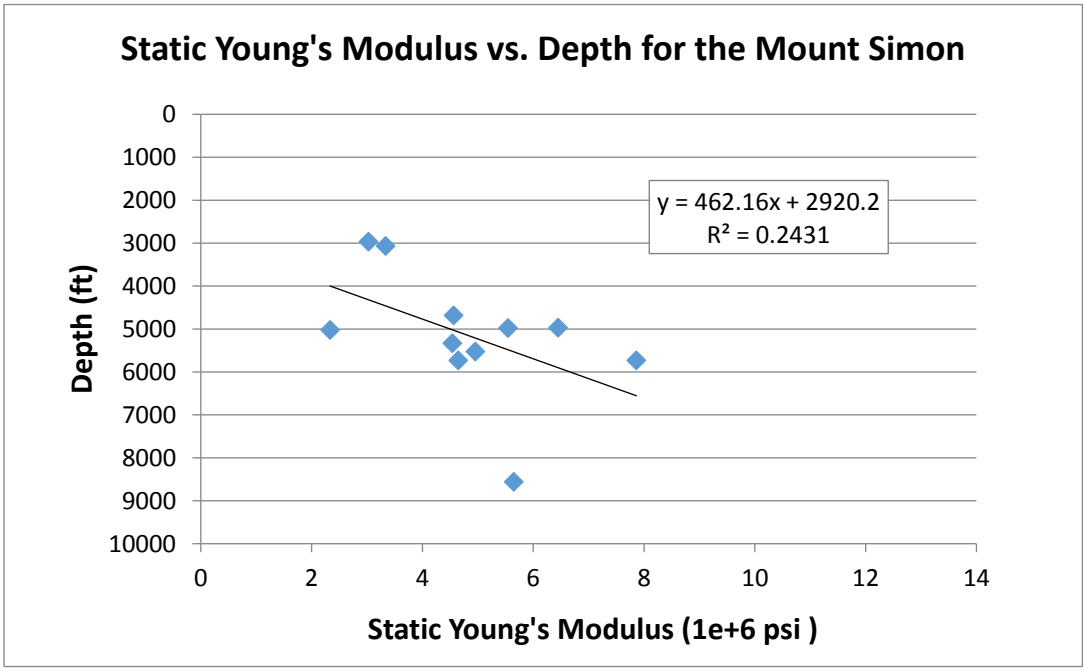

Figure 2-63: Static Young's modulus versus depth for the Mount Simon Formation.

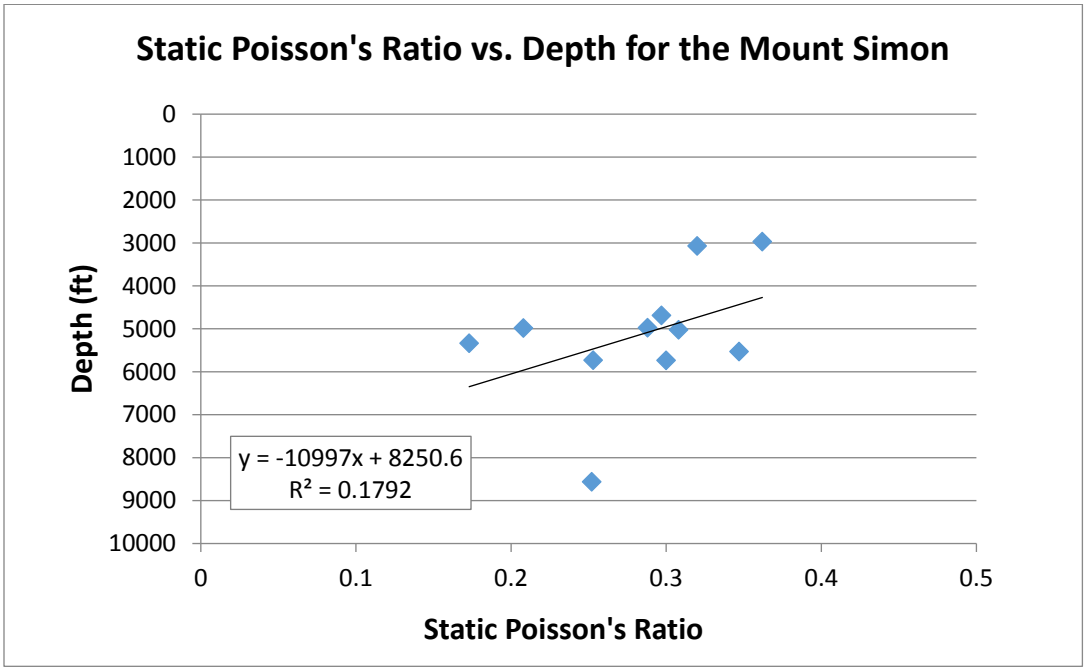

Figure 2-64: Static Poisson's ratio versus depth for the Mount Simon Formation.

3.0 Site Geomechanical Data Analysis

The objective of this task was to interpret geophysical image logs to determine stress orientation/magnitude and fracture/fault density and network. The sonic and image log data were then integrated into the Isotropic Fracture Migration Analysis log (HSTRESS) and used to calculate geomechanical parameters needed for geomechanical modeling in later tasks. The Young's modulus and Poisson's ratio of these wells were then calibrated to core data from wells nearby or within the well itself. Three sites were selected for this analysis: Arches site, E-Central Appalachian Basin site, and Northern Appalachian Basin sites (Figure 3-1). Geomechanical modeling at the Arches site will occur at the Duke Energy #1 well (Boone County, Kentucky), the E-Central Appalachian Basin site at the OGS CO_2 #1 well (Tuscarawas County, Ohio), and the Northern Appalachian Basin site well (Chautauqua County, New York). Logging intervals are presented in Table 3-1.

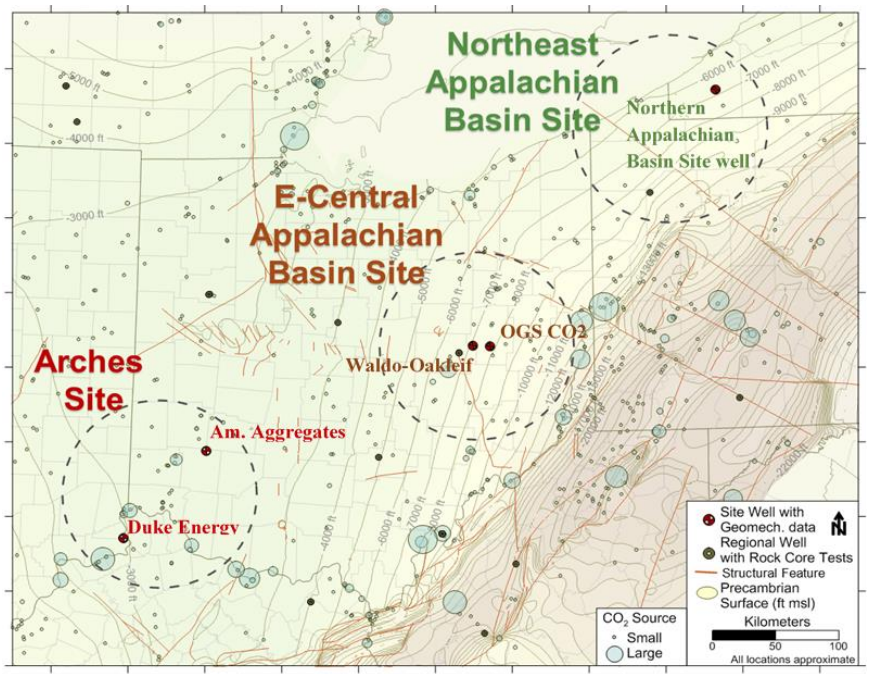

Figure 3-1: Map of study areas and associated wells with geomechanical and core data overlain on the Precambrian structural contour map and structural features.

Table 3-1: Footages of processed and interpreted logs for the three sites of interest.

Well site	Image log intervals (ft)	HSTRESS log intervals (ft)
Northern Appalachian Basin	3,870-7,305	3,880-7,282
East-Central Appalachian Basin	5,024-8,709	3,090-8,660
Arches	906-3,700	170-3,704
Total Footage Interpreted	**9,914**	**12,506**

The wireline suite needed for this analysis include the triple combo (TC) log suite, sonic log, and image log. The basic dataset produced from each of the wireline logs is presented in Table 3-2. Basic open-hole logs included: gamma ray, calipers, litho-density, density porosity, neutron porosity, photoelectric effect, variable density/sonic, resistivity, and caliper log. Typically, these logs are combined into one or two tool strings and are operated in the well at the same time. In addition to basic open-hole logs, the Formation MicroImager (FMI) logging tool (image logs) was performed in each well. Image logs provide visual 360-degree portrayal of the borehole based on high-resolution resistivity measurements, showing sedimentary features, natural fractures, faults, and borehole damage intersected by the boring (Veltman et al., 2012; Barton et al., 2009; Luthi et al., 1990).

Table 3-2: Applications of the specific wireline tools.

Test name	Application
Gamma ray log	Rough definition of lithologic boundaries, correlation, rough indicator of shale and zonation of sand and shale.
Neutron log; density log	Evaluation of formation density, porosity, and lithology identification, direct indication of gas in the formation. Density log also is required to calculate a synthetic seismogram using the sonic log.
High resolution resistivity log	The resistivity tools are run to get information about the fluid content of the pore space of the formation and the resistivity of the fluids.
Sonic log	Porosity indication, mechanical properties.
Caliper	Calipers are used to calculate hole volume, determine hole diameter to be used in the interpretation of other wireline logs and determine cement volumes.
Formation MicroImager (FMI*)	Determination of structural (tectonic) and sedimentary dip. Facies indicators. Open and healed fracture identification. Also a high-resolution resistivity tool.
HSTRESS interpreted log	Quantitative in-situ stress and fracture migration analysis.

*Schlumberger trade name.

3.1 Arches Well Site Analysis

3.1.1 Site Geology

The Arches site was located in Boone County, Kentucky, where a CO_2 injection test well was drilled by the MRCSP in 2009 (Kelley et al., 2011). The regional geology near the test site (southeastern Indiana, north-central Kentucky, and southwestern Ohio) consists of layered sedimentary rocks of Precambrian through Ordovician age. On a local scale, these layers are relatively flat-lying, but two geologic features affect the structure of these rock layers on a regional scale: the Cincinnati arch and the East Continental Rift Basin (Figure 3-2). Of the geologic formations present in this region, the Mount Simon sandstone and the Eau Claire Formation are important from a CO_2 sequestration perspective. The Mount Simon sandstone was the injection reservoir that was the focus of the East Bend project; the Eau Claire Formation, which overlies the Mount Simon sandstone, provides a seal to prevent upward movement of the CO_2 stored in the Mount Simon sandstone. Much of the information provided in this section was obtained from two documents: *Preliminary Assessment of Potential CO_2 Storage Reservoirs and Caprocks at the Cincinnati Arch Site* (Solano-Acosta et al., 2006) and *Characterization of Geologic Sequestration Opportunities in the MRCSP Region* (Wickstrom et al., 2006).

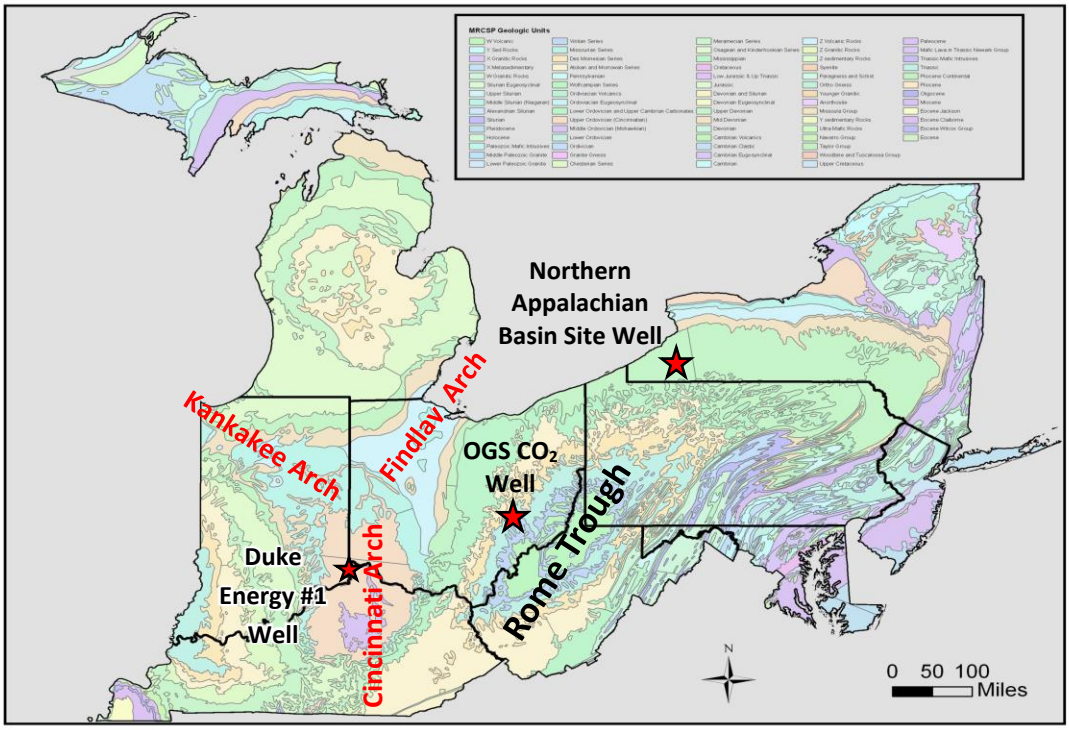

Figure 3-2: Major geologic structures in the region of the MRCSP (after Wickstrom et al., 2006).

The East Bend site lies just west of the axis of the Cincinnati arch, a broad, north-south trending geologic structural feature (anticline) that separates the Illinois and Appalachian basins (Figure 3-2). The geologic layers generally dip to the east into the Appalachian Basin on the eastern side of the arch, and to the west into the Illinois Basin on the western side of the arch. Figure 3-3 shows an east-west cross section of the Cincinnati arch near the test site. The structure of the arch is more pronounced in the Upper Cambrian and Ordovician formations (Knox Group through Black River Group). On this cross section, the center of the arch is in the proximity of Well 66.

The East Continental Rift Basin is a north-south trending feature aligned approximately parallel to, but slightly east of the crest of the Cincinnati arch (see Figure 3-2). This structural feature is older than the Cincinnati arch and therefore unaffected by it. The rift basin is bordered on the east by the Grenville Front and on the west by the Eastern Granite-Rhyolite Province. The East Continental Rift Basin is characterized by a series of small basins or depositional centers created by faults. Such faults, if present, could have implications on the safe storage of CO_2 in the deepest geologic deposits within the East Continental Rift Basin. These faults are generally limited to formations below the Precambrian unconformity (Figure 3-4). However, in some locations, seismic data suggest faulting extending above the Precambrian. For example, seismic data from Shelby County, Kentucky (approximately 45 miles southwest of the test site) indicate that faulting may extend above the Precambrian unconformity and into the Ordovician formations. Seismic data from the test site show no indication of faulting or fractures in the vicinity of the site.

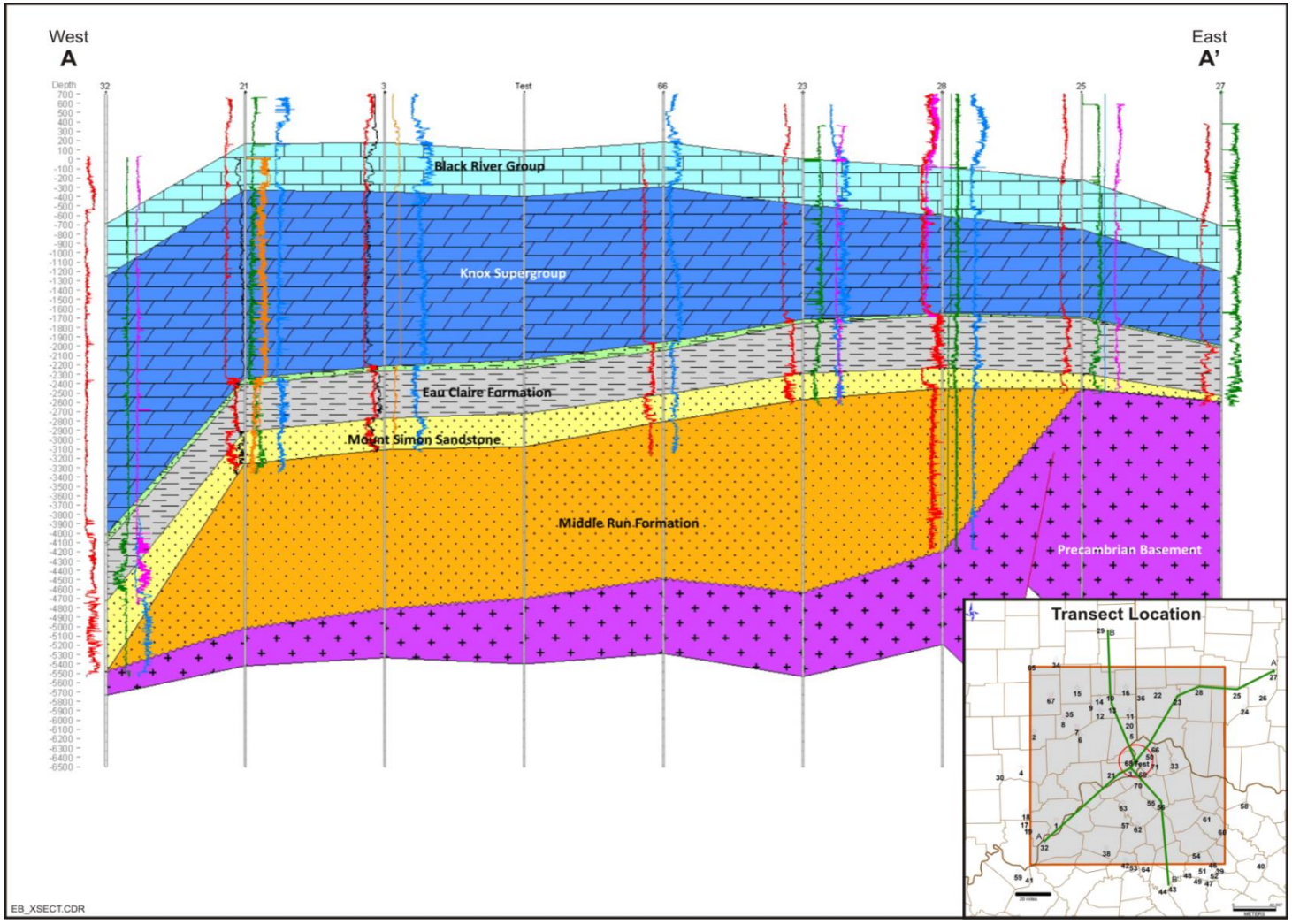

Figure 3-3: East-west geologic cross section of the region. Line marked “Test” indicates the approximate location of the East Bend site (Solano-Acosta et al., 2006).

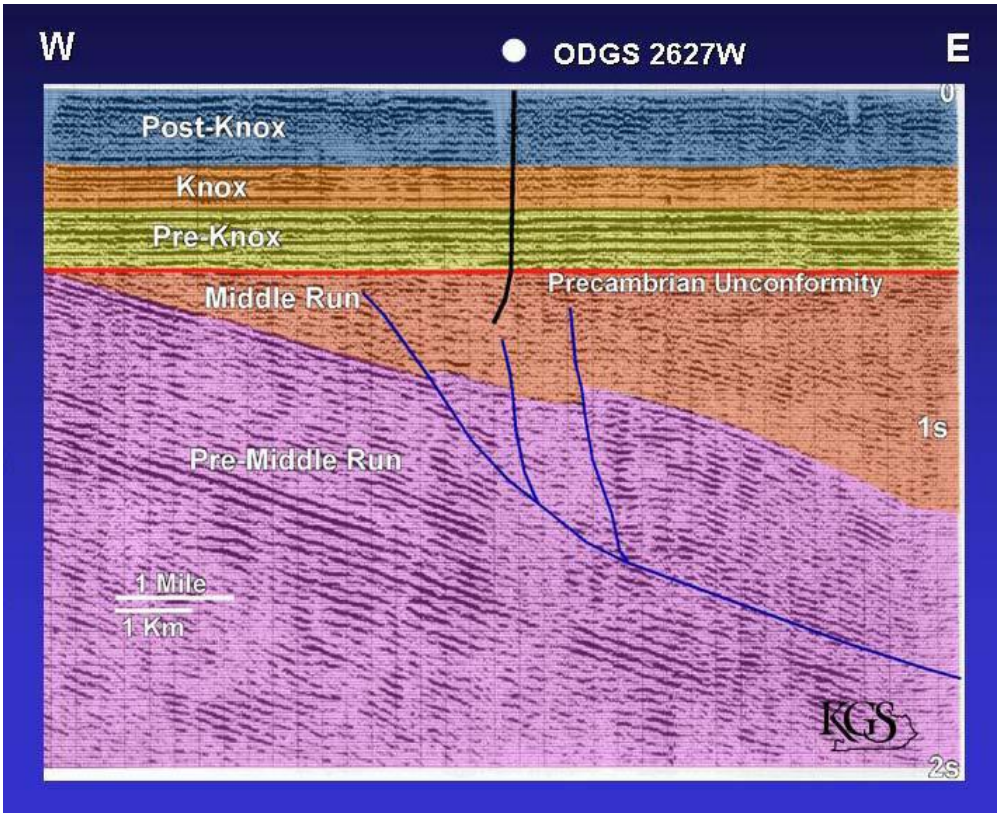

Figure 3-4: Interpretation of seismic data in Warren County, Ohio (approximately 45 miles northeast of the East Bend site; pre-Knox includes Mount Simon and Eau Claire formations). (The ODGS 2627 borehole [near-vertical black line] is a core that penetrates 1,922 ft of the Middle Run. Blue lines represent thrust faults.) (Solano-Acosta et al., 2006).

The generalized stratigraphy for the region, including the site, is shown in Figure 3-5. A well schematic and general lithology of the site can be seen in Figure 3-6. In north-central Kentucky, west of the axis of the Cincinnati arch, the subsurface stratigraphy consists of the Lexington (Trenton) limestone, High Bridge (Black River) Group, Wells Creek dolomite (where it can be delineated), St. Peter sandstone (where it occurs), Knox Group (Beekmantown, Rose Run sandstone [where it occurs], and Copper Ridge dolomite), Eau Claire Group, and Mount Simon sandstone. In the western portion of the study area, the Middle Run Formation overlies Precambrian igneous and metamorphic basement and there are no deeper possibilities for CO_2 injection. The Mount Simon sandstone represents the target injection reservoir at the East Bend site. Sedimentary rock of the Middle Run Formation is found within the East Continent Rift Basin beneath the Mount Simon sandstone, so there are speculative possibilities for deeper reservoirs.

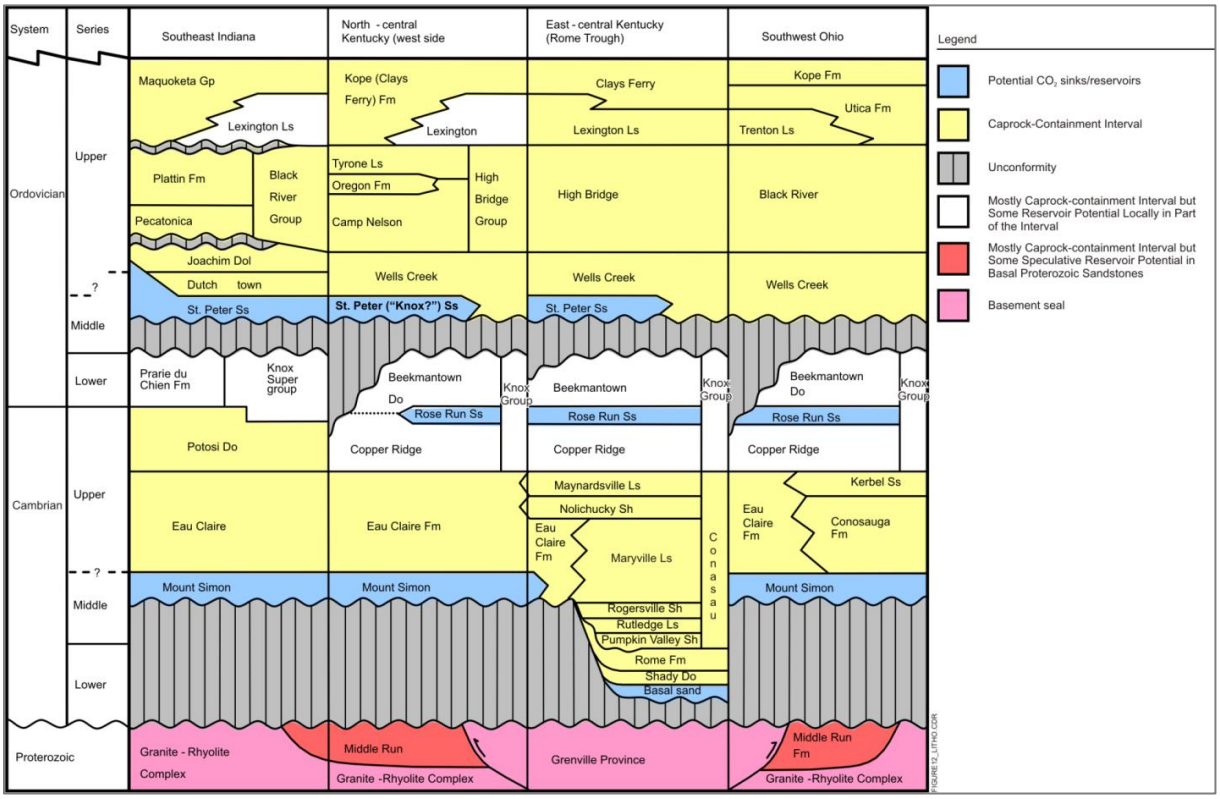

Figure 3-5: Generalized regional stratigraphy (Solano-Acosta et al., 2006).

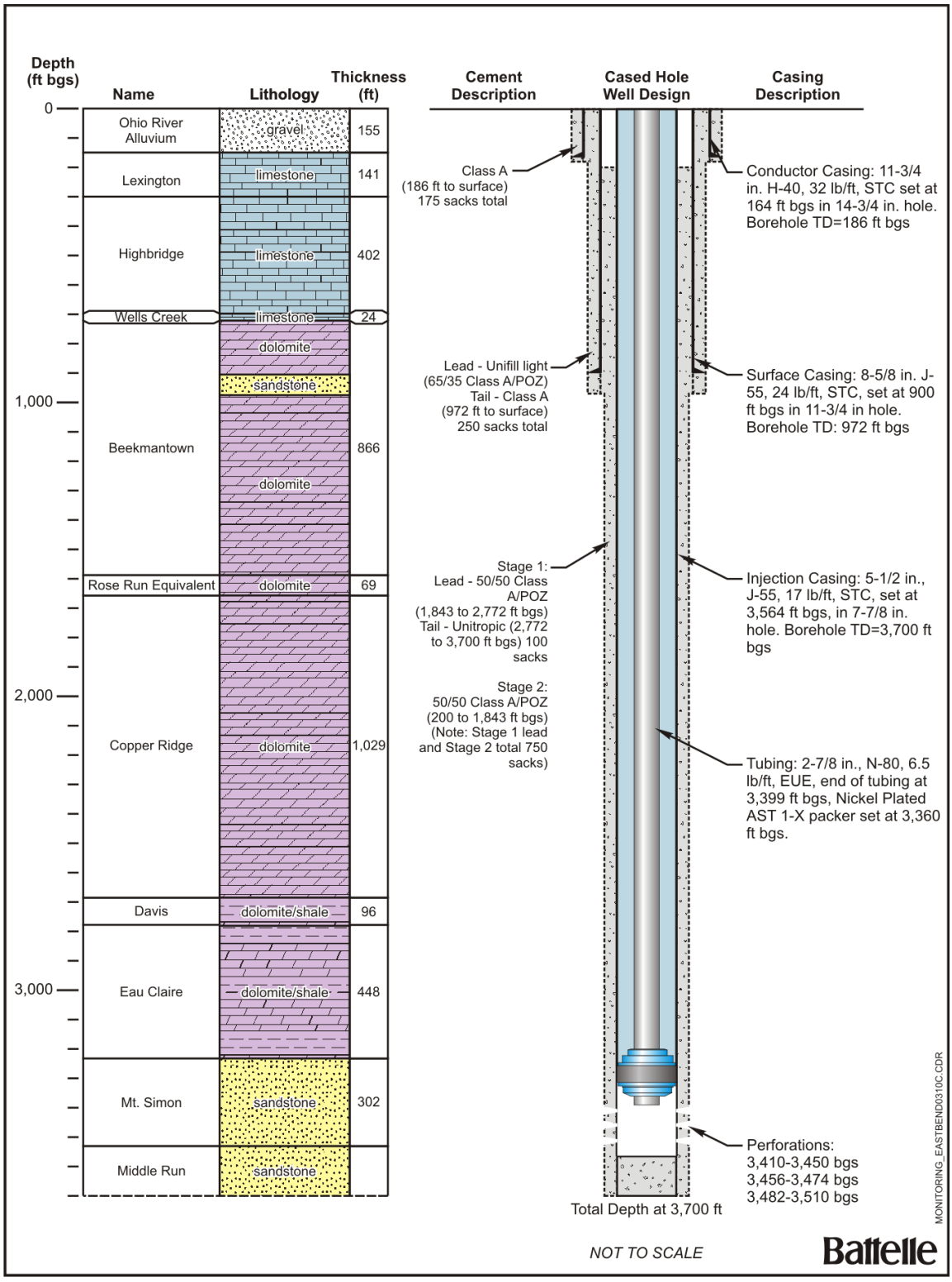

Figure 3-6: Completion diagram for the East Bend well.

3.1.2 Geophysical Well Log and Core Summary

A suite of wireline logs was performed on the East Bend well. The TC suite, image logs, and sonic logs were used for geomechanical analysis and are therefore the logs mentioned in this report. Table 3-3 shows the footage intervals used for this analysis and the interpreted log footage from integrating the logs mentioned above. The TC and sonic data were logged from the Lexington limestone to the Middle Run Formation in the interval 164 ft to 3,700 ft measured depth (MD). The image was logged from the Beekmantown dolomite to the Middle Run Formation in the interval 906 ft to 3,700 ft MD.

Core was acquired from the East Bend well but not analyzed for geomechanic parameters. Therefore, approximately 60 miles northeast at the American Aggregates DS-2 well (34-165-60005), the closest Cambro-Ordovician core available (see Figure 3-1) was taken for geomechanical analysis. Four sidewall cores were analyzed: two in the Black River Group (Cambro-Ordovician reservoir caprock), and two in the Lower Copper Ridge Formation (Table 3-4). Cores were sent to Weatherford Laboratories for triaxial compressive tests and Brazilian indirect tensile tests to obtain key calibration parameters such as the static Young's modulus and static Poisson's ratio.

3.1.3 Image Log Description and Analysis

Image log analysis for the Arches site was conducted from 906 ft to 3,700 ft with the structural interpretation conducted by Baker Hughes. The Beekmantown showed numerous low angled beds (Figure 3-7) that dip in all directions in the formation. Micro-faults at 973 ft, 982 ft, and 1,104 ft tend to occur with varying orientated laminations, bedding, and some fractures (Figure 3-8). Borehole breakouts occur toward the bottom of the formation at 1,474 ft and 1,475 ft (Figure 3-9). There has been known vugular development at the base of the Beekmantown which potentially present these borehole breakouts as a result of vugs. These features merit additional analysis as they may potentially be vugs at these intervals.

Table 3-3: Wireline logs performed on the Duke Energy #1 well.

Type	Logs run	Depth interval (ft MD)
Injection borehole (open-hole logs)	Gamma ray, caliper, spontaneous potential, resistivity, litho-density, density porosity, neutron porosity, directional survey	164 – 3,700
	Formation MicroImage (FMI*)	906 – 3,700
	Sonic Log	164 – 3,700
Interpreted logs	HSTRESS	170 – 3,700

*Schlumberger trade name.

Table 3-4: Core samples collected from the American Aggregates #1 well.

Formation	Core interval (ft MD)	Young's modulus (x10^6 psi)	Poisson's ratio
Sidewall cores			
Black River	1,388 and 1,544	5.76 and 6.91	0.26 and 0.27
Lower Copper Ridge	2,488 and 2,537	8.35 and 10.84	0.38 and 0.23

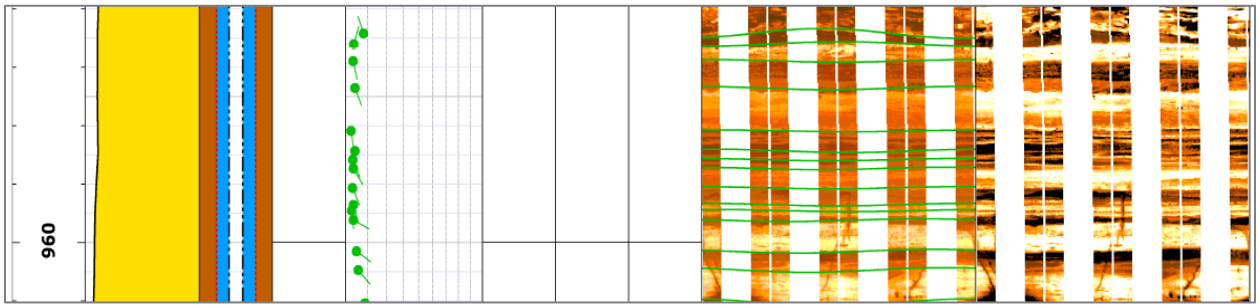

Figure 3-7: Low-angled bedding at 957 ft to 961 ft, Arches site.

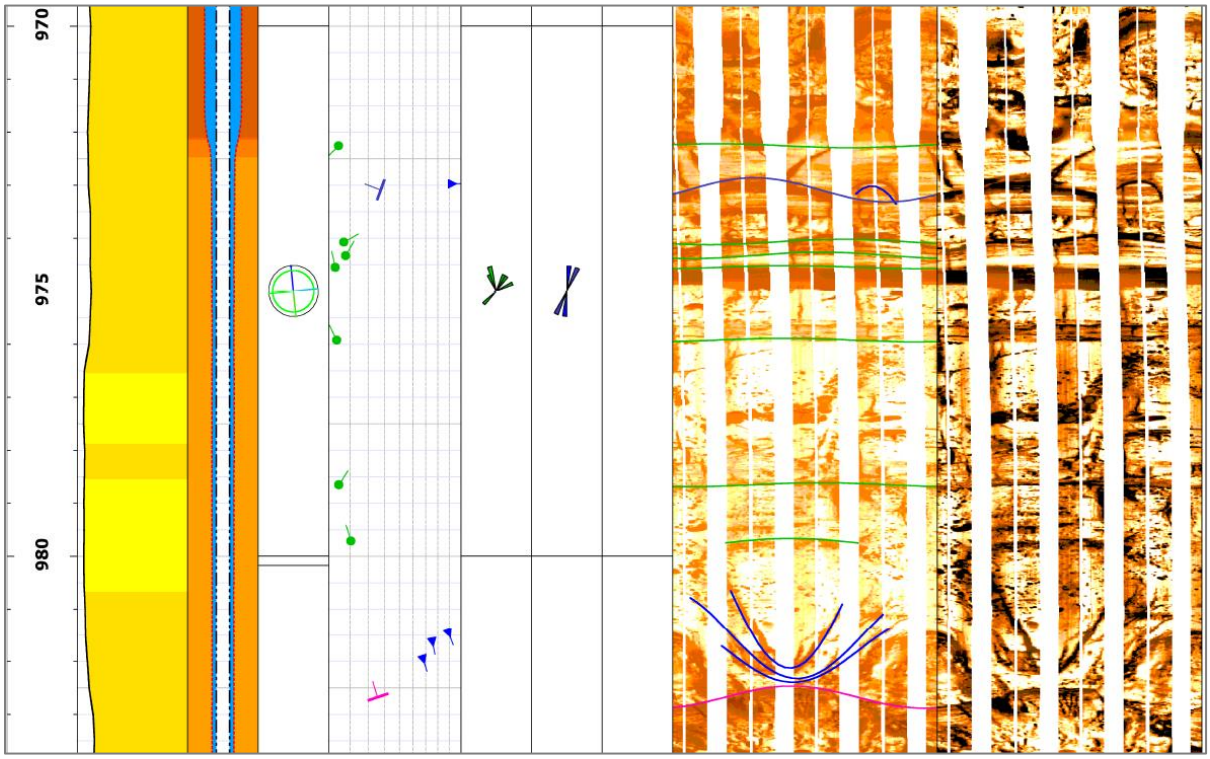

Figure 3-8: Micro-faults at 976 ft and 982 ft with low-angled bedding and fractures at each occurrence, Arches site.

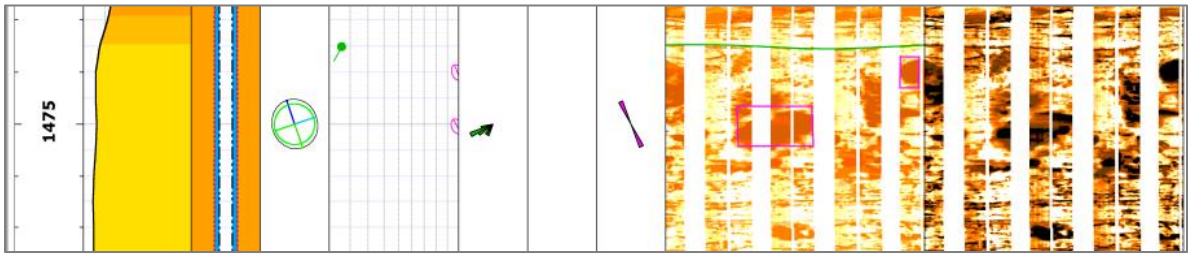

Figure 3-9: Listed as borehole breakouts at 1,474 ft and 1,475 ft, Arches site. These features may be due to potential vugs.

The Rose Run shows many low-angle beds with strikes in all directions and very few fractures at the Rose Run/Copper Ridge contact. The beds have low conductivity and could have potential porosity. There are three fractures and four induced fractures which occur predominantly at the Rose Run/Copper Ridge contact. The Upper Copper Ridge exhibits scattered low-angled bedding in the upper 100 ft of the formation, in the middle of the formation at 2,095 ft to 7,173 ft, and at the Copper Ridge/Davis contact at 2,672 ft. DITFs are found throughout the formation. A number of fractures (Figure 3-10) occur from 2,244 ft to 2,247 ft. These fractures range from medium to high angle. There are borehole breakouts indicated at 2,441 ft., 2,496 ft, and 2,546 ft. These features may be due to potential vugs at these intervals.

The gamma ray signatures in the Eau Claire Formation slightly decrease below 150 gAPI (gamma radiation measured in American Petroleum Institute units). There are numerous low-angled laminations and a few beds throughout the formation. The laminations and beds are less resistive than the overlying Davis shale laminations and beds. High gamma ray signatures and low resistivity suggest potential argillaceous sands in the formation. Additionally, there is one microfault at 2,799 ft between several variously dipping laminations (Figure 3-11). Figure 3-12 illustrates a convoluted lamination feature at 2,832 ft. At the base of the Eau Claire Formation are several beds that have high conductive and gamma ray signatures, which suggest potential shale or clay layers at the Eau Claire/Mount Simon contact.

The image log analysis for the Mount Simon does not show fractures, breakouts, or microfaults in this formation. The gamma ray signature significantly decreases, from 150 gAPI to less than 75 gAPI. There are numerous laminations and beds throughout the interval. Burrows (Figure 3-13) were observed at 3,265 ft. These features suggest potential sand or clay sedimentary structures in the Mount Simon. Gamma ray is relatively high at 3,415 ft, around 150 gAPI, and the interval at the base of the formation shows high conductivity.

The Middle Run to total depth (TD) shows laminations and bedding throughout the interval. One fracture was noted at 3,562 ft in the formation. Several deformation structures were seen at 3,570 ft, 3,611 ft, 3,616 ft, 3,639 ft, 3,647 ft, and 3,680 ft (Figure 3-14). Log quality of the image data ends at 3,697 ft.

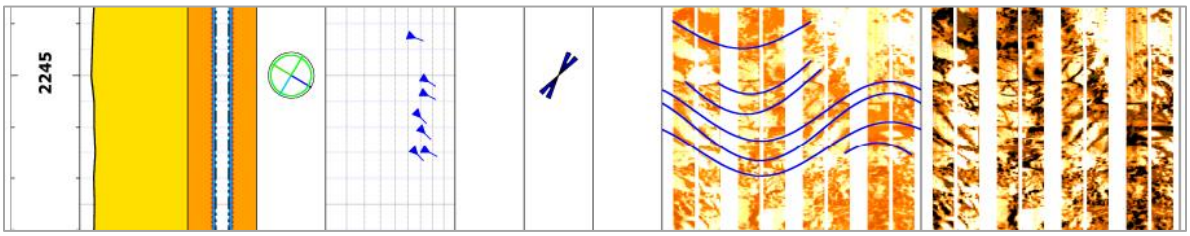

Figure 3-10: Induced fracture at 2,244 to 2,247 ft, Arches site.

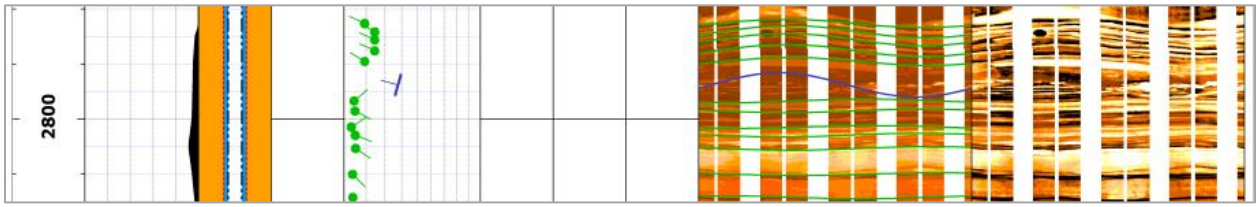

Figure 3-11: Microfault at 2,799 ft between several beds, Arches site.

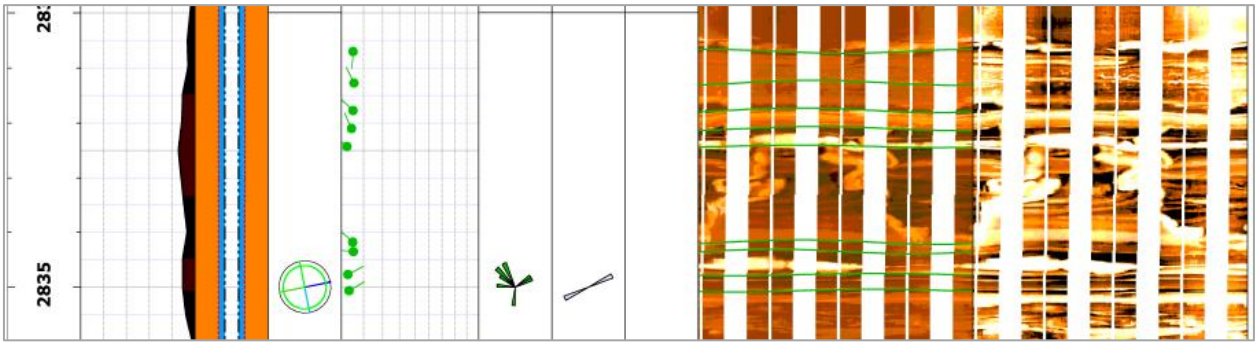

Figure 3-12: Convoluted lamination at 2,832 ft, Arches site.

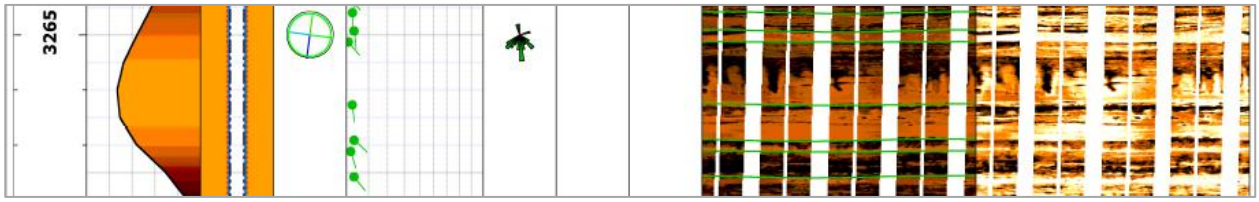

Figure 3-13: Burrows at 3,265 ft, Arches site.

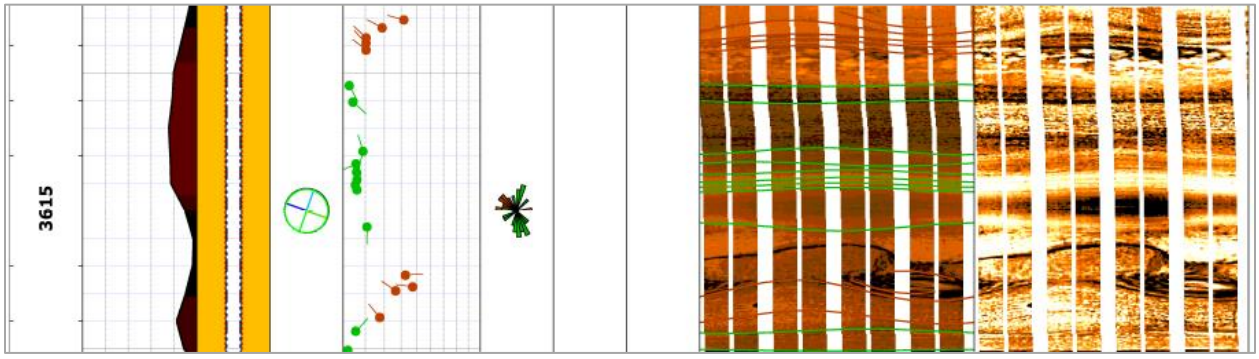

Figure 3-14: Deformed beds at 3,611 ft and 3,616 ft, Arches site.

3.1.4 Summary of Arches

Table 3-5 summarizes the analysis of the image log information given above. The Beekmantown, with several borehole breakouts and potential vugular development, represents a mixture of textures consistent in an unconformity zone. The microfaults in this interval merit further investigation but could potentially be representative of the unconformity. The Rose Run, Copper Ridge, and Davis shale formations show minor to no structural features. There is potential vugular development in the Copper Ridge which may present porosity in this interval. The Middle Run Formation merits additional investigation of the deformed beds and laminations starting at 3,570 ft. These structures could be due to features below the logged interval.

Table 3-5: Notable features from image log analysis for the formations of interest, Arches site.

Formation of interest	Zones / depth intervals of interest (ft)	Notable features or log signatures	Interpretation and implication
Beekmantown	906-1,588	Microfaults, borehole breakouts, and potential vugular development	Structural features including microfaults potentially due to multiple textures, merits further analysis
Rose Run	1,588-1,657	Some fractures, low conductivity beds	Potential porosity in this formation, merits further analysis, fractures predominantly at the Rose Run/Copper Ridge contact
Copper Ridge	1,657-2,686	Induced fractures, potential vugs	Induced fractures due to multiple laminations and beds, potential vugs merit additional analysis of potential porosity
Davis Shale	2,686-2,782	Induced fractures	Due to several beds and laminations
Eau Claire	2,782-3,230	Microfault	Merits further investigation
Mount Simon	3,230-3,532	Laminations and beds	Potential porosity in this formation, merits further analysis
Middle Run	3,532-TD (3,700)	Deformed laminations and beds	Potentially due to texture changes, merits further analysis

Figure 3-15 shows a histogram of structures for the well binned at 100-ft intervals, a plot of the orientation of wellbore failures, and rose diagrams for induced fractures and borehole breakouts for the Arches site well. There are four faults interpreted in the well: three are microfaults and one is a minor fault. Here we define a minor fault as a fracture surface that exhibits bedding offset but no lithologic change. The majority of the structures in the well occur in the Copper Ridge Formation and taper out toward the base of the Eau Claire Formation. The wellbore failures are sparse but show a preliminary maximum horizontal stress orientation of ~070 degrees. This is seen through the long-axis orientation of the borehole breakouts and drilling-induced fractures. Borehole breakouts form perpendicular to the maximum horizontal stress, whereas drilling-induced fractures form parallel to it (Plumb and Hickman, 1985; Aadnoy, 1990).

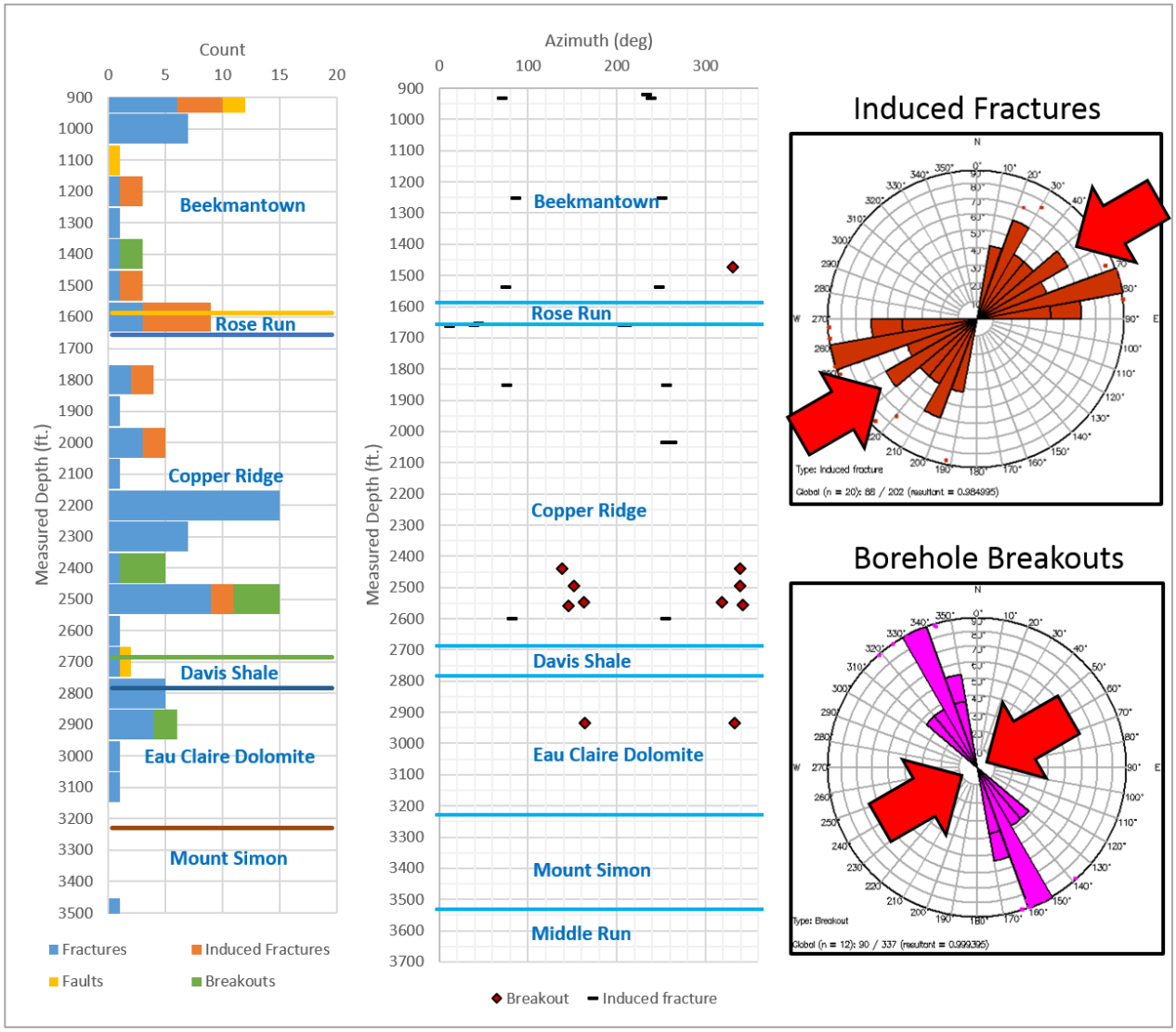

Figure 3-15: Histogram of structures for the Arches site well binned at 100-ft intervals, plot of the orientation of wellbore failures, and rose diagrams for induced fractures and borehole breakouts. Red arrows represent the maximum horizontal stress direction.

3.2 East-Central Appalachian Basin Site

3.2.1 Site Geology

The OGS CO_2 test well was drilled in Tuscarawas County, Ohio, in 2007 to characterize deep saline formations CO_2 storage potential. The regional geology near central and eastern Ohio consists of layered sedimentary rocks of Precambrian through Pennsylvanian age. These layers are relatively flat-lying on a local scale, but on a regional scale are affected by two structures: The Cincinnati arch and the Appalachian Basin (see Figure 3-2). Stratigraphic analysis (Wickstrom et al., 2011) indicated six potential deep injection zones: the Cambrian basal sandstone, the Lower and Upper Copper Ridge dolomite (both of which contain vuggy carbonate zones), the Copper Ridge “B-zone” dolomite (which is a clastic interval within the Copper Ridge), the Rose Run sandstone, and the Beekmantown dolomite.

The OGS CO_2 site lies at the east-central flank of the Appalachian Basin, a regional sedimentary basin that stretches from eastern Kentucky, eastern Ohio, West Virgnina, Pennsylvania, and New York (see Figure 3-2). The Appalachian Basin is a northeast-southwest trending feature aligned approximately parallel to and northwest of the Allegheny structural front (Figure 3-16). This basin is bordered on the west by the Cincinnati and Findlay arches and on the east by the Allegheny structural front. The Appalachian Basin contains significant faulting in the Rome trough but northwest of the trough contains few major faults. The closest structural feature to the OGS CO_2 No. 1 well is the Cambridge cross-strike structural discontinuity 25 miles to the east. Figure 3-17 is a west-east cross section of the western flank of the Appalachian Basin near the well site. The cross section represents the pinching out of the Beekmantown dolomite and Rose Run along the Knox unconformity and the eastward thickening of the Cambro-Ordovician rock units.

The generalized stratigraphy for the region is shown in Figure 3-18. Janssen’s 1973 stratigraphic nomenclature was used for the E-Central Appalachian Basin site. A well schematic and general lithology of the site can be seen in Figure 3-19. On the eastern flank of the Appalachian Basin, the subsurface stratigraphy consists of the Trenton limestone, Black River Group, Wells Creek Formation, Beekmantown dolomite, Rose Run sands, Copper Ridge dolomites, Conasauga Group, Rome dolomite, and basal sand. In the western portion of the study area, the Beekmantown dolomite then the Rose Run sandstone pinch out along the Knox Unconformity. The basal sandstone pinches out as it approaches the Cincinnati arch to the west. Overlap of the basal sand in the east of Ohio and the Mount Simon sandstone in the west of Ohio occurs just east of the Cincinnati arch. No deeper formations exist above the Precambrian basement rock.

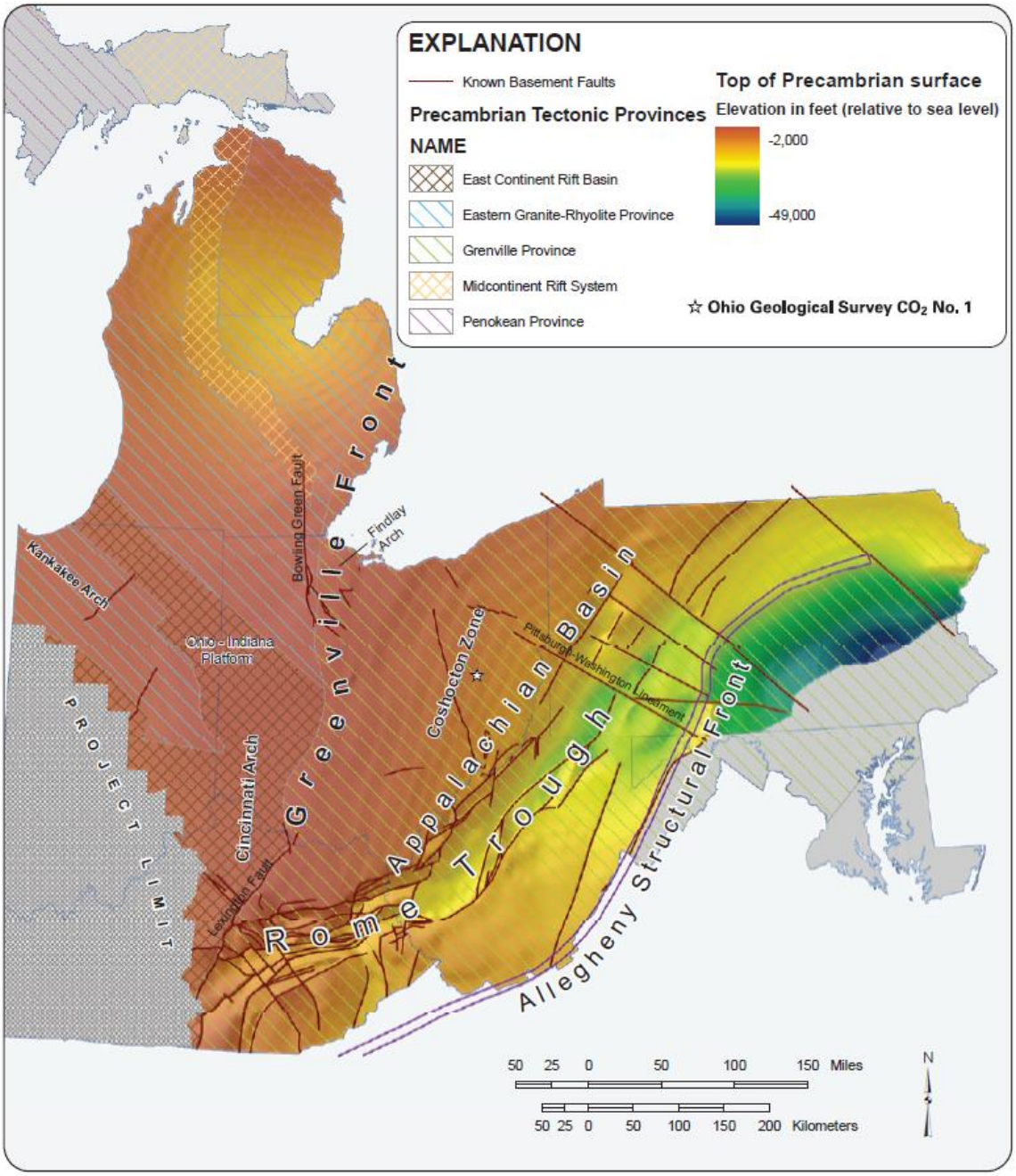

Figure 3-16: Structural map of the Precambrian unconformity with major known basement faults and Precambrian tectonic provinces. From Wickstrom et al. (2006).

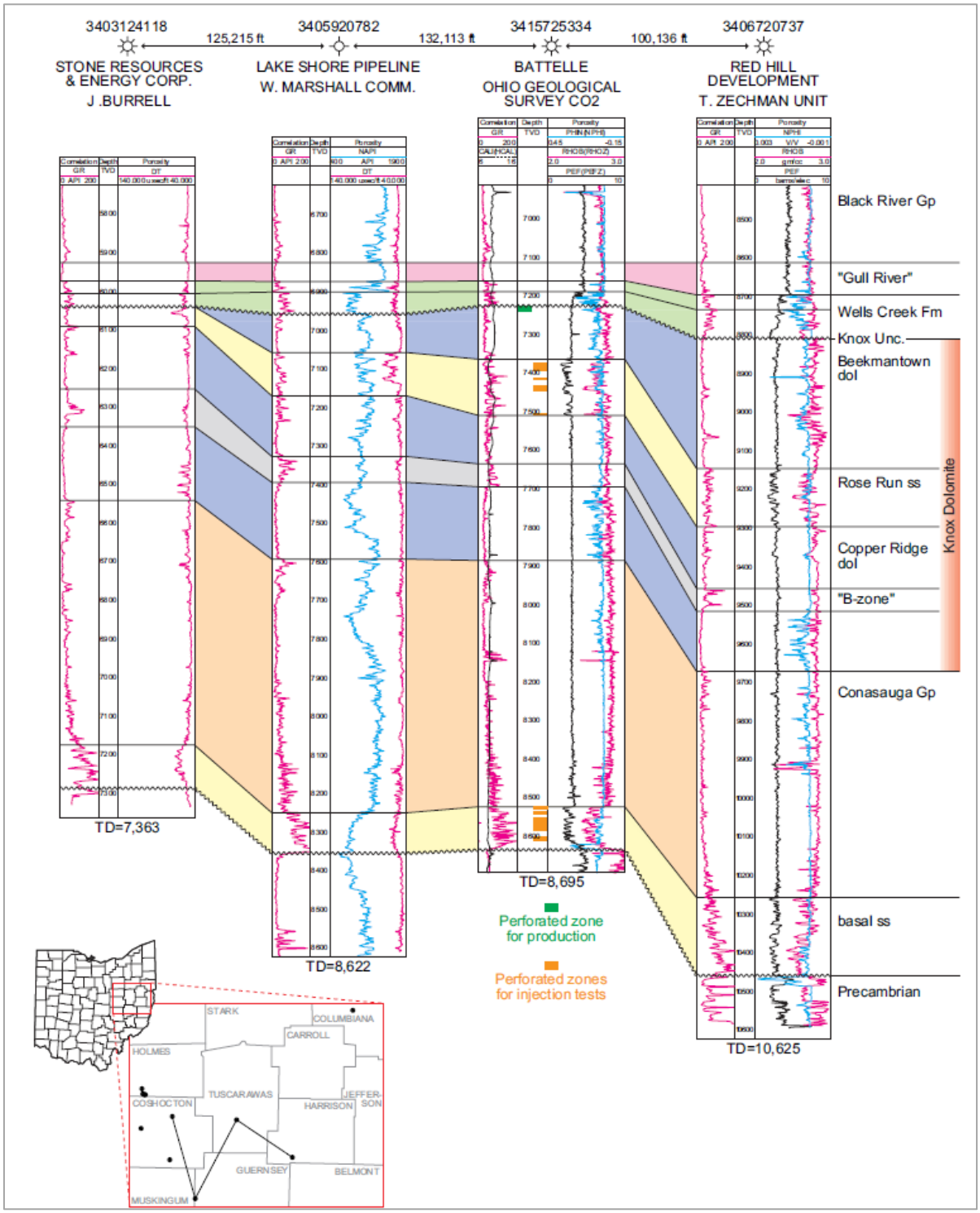

Figure 3-17: Stratigraphic cross section through the OGS CO_2 No. 1 well in Tuscarawas County representing the pinching out of the Beekmantown dolomite and Rose Run along the Knox unconformity and the eastward thickening of the Cambro-Ordovician rock units. From Wickstrom et al. (2011).

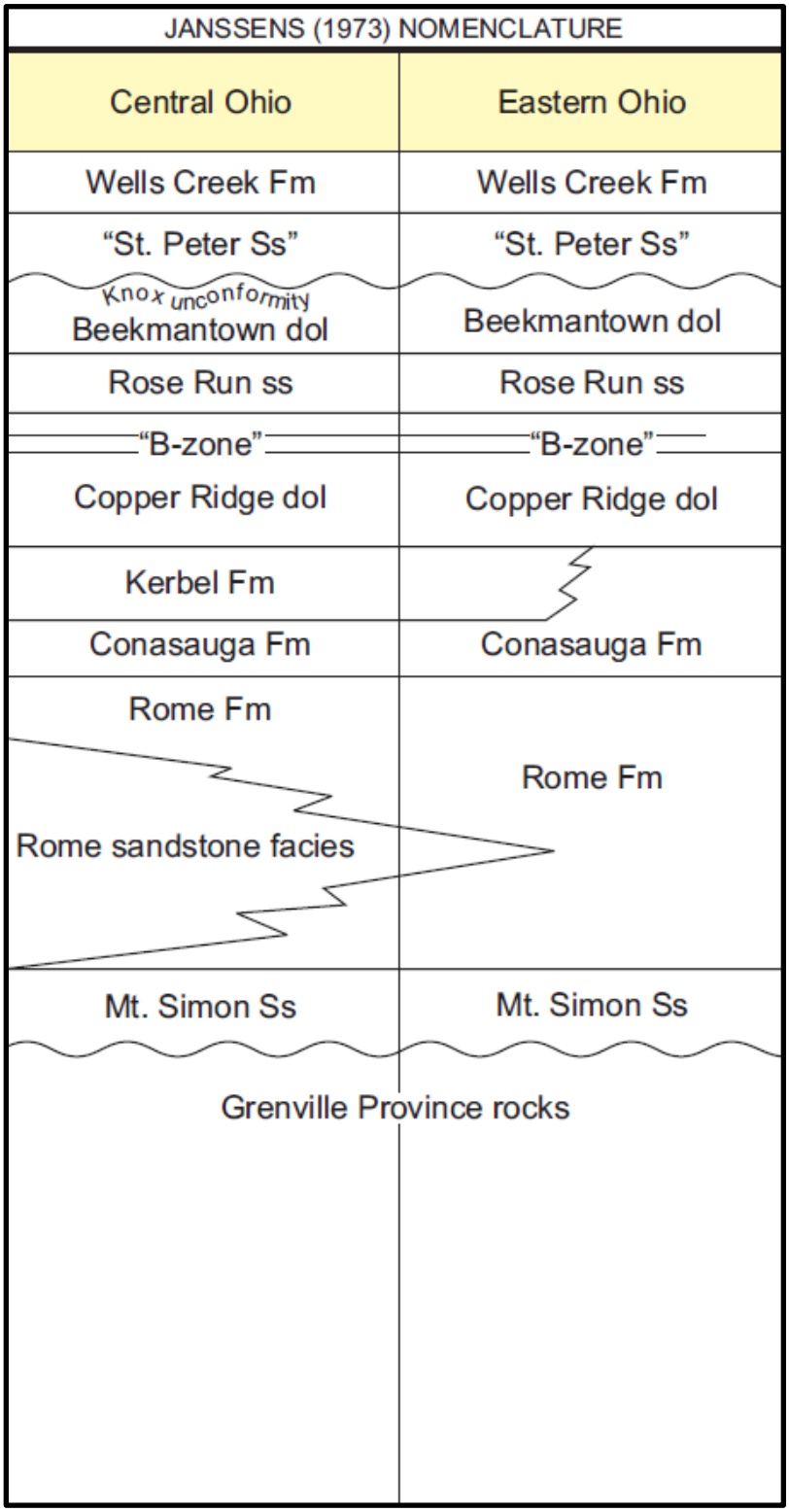

Figure 3-18: Stratigraphic correlation chart showing Janssens (1973) Ohio nomenclature. The Eastern Ohio nomenclature is used for the E-Central Appalachian Basin site.

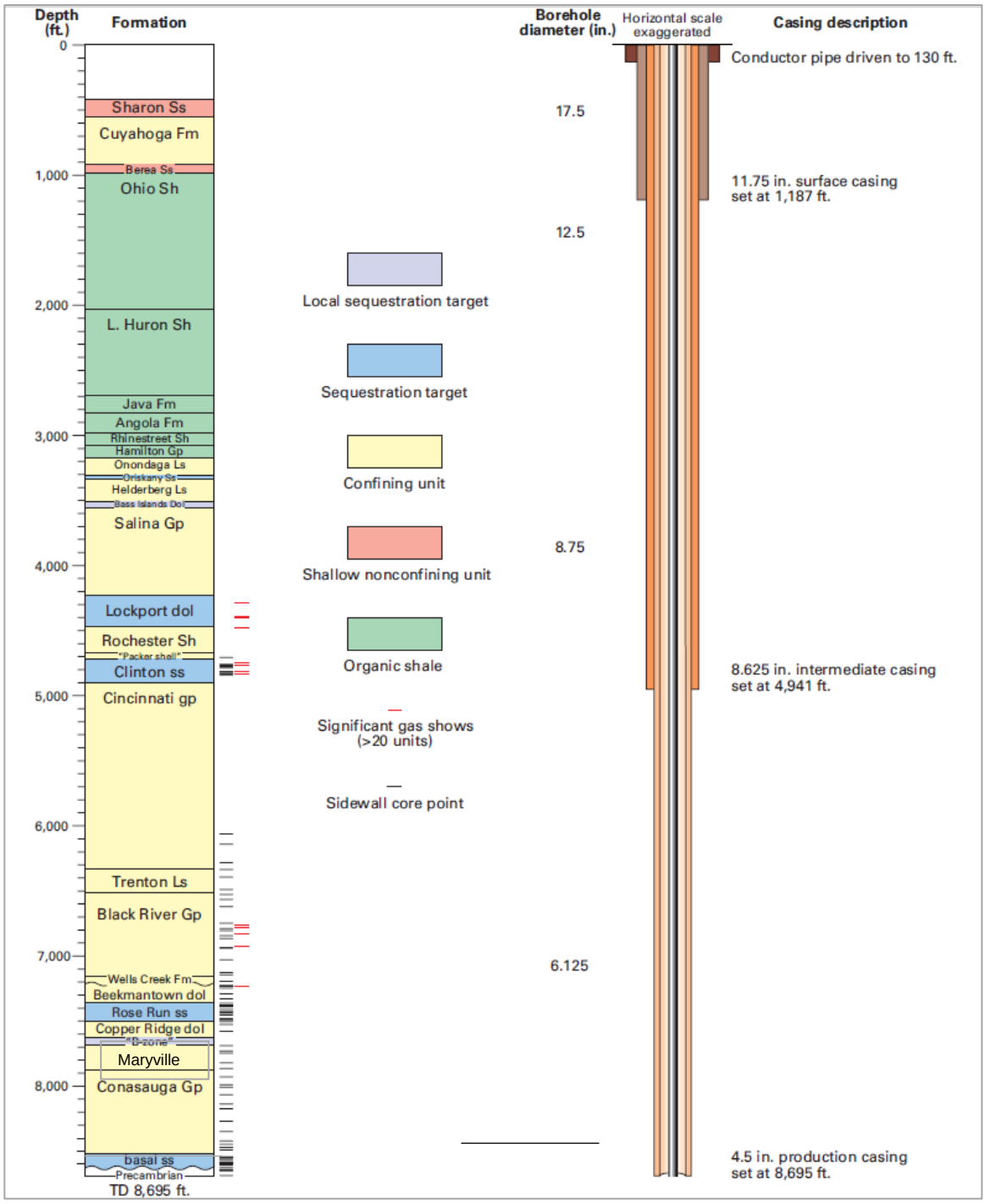

Figure 3-19: OGS CO_2 No. 1 well schematic showing the well construction and primary stratigraphic units with respect to depth. Edited from Wickstrom et al., 2011.

3.2.2 Geophysical Well Log and Core Summary

A suite of wireline logs was performed at the OGS CO_2 well. The TC suite, image logs, and sonic logs were used for geomechanical analysis and are therefore the logs mentioned in this report. Table 3-6 shows the footage intervals used for this analysis and the interpreted log footage from integrating the logs mentioned above. The TC data were logged from the Sharon sandstone to the basal sandstone. The sonic data were logged from the Rhinestreet shale to the basal sandstone. The image data were logged from the Cincinnati Group to the basal sandstone.

Two sidewall cores were analyzed for geomechanics in the OGS CO_2 No. 1 well. More data were needed to calibrate the geomechanical logs; therefore, four extra sidewall cores from the Oakleif Waldo #1 well (3403124092) were sent to Weatherford Laboratories and analyzed using the same techniques mentioned in Section 2.6 of this report. The Oakleif-Waldo #1 Well in Coshocton County is ~10 miles west of the OGS CO_2 No. 1 well.

A total of six sidewall cores were analyzed: one in the Black River Group (Cambro-Ordovician reservoir caprock), one in the Beekmantown dolomite, three in the Rose Run sandstone, and one in the basal sandstone (Table 3-7). Cores were sent to Weatherford Laboratories for triaxial compressive tests and Brazilian indirect tensile tests to obtain key calibration parameters such as the static Young's modulus and static Poisson's ratio.

Table 3-6: Wireline logs performed on the OGS CO_2 No. 1 well.

Type	Logs run	Depth interval (ft MD)
Injection borehole (open-hole logs)	Gamma ray, caliper, spontaneous potential, resistivity, litho-density, density porosity, neutron porosity, directional survey	878 – 8,718
	Formation MicroImager (FMI*)	5,024 – 8,709
	Sonic log	3,088 – 8,709
Interpreted logs	HSTRESS	3,090 – 8,660

*Schlumberger trade name.

Table 3-7: Core samples collected from the American Aggregates #1 well.

Formation	Core interval (ft MD)	Young's modulus ($x10^6$ psi)	Poisson's ratio
OGS CO_2 No.1 sidewall cores			
Rose Run	7,441	4.818	0.384
Basal sandstone	8,561	5.649	0.252
Oakleif-Waldo #1 sidewall cores			
Black River	6,804.4	7.33	0.41
Beekmantown	6,904	7.09	0.30
Rose Run	6,916 and 6,926.7	6.9 and 5.78	0.32 and 0.16

3.2.3 Image Log Description and Analysis

Image analysis for the East Central Appalachian basin was conducted from 5,024 ft to 8,709 ft. From 5,024 ft to 5,487 ft, there are several borehole breakouts. At 5,300 ft to 5,421 ft, laminations are abundant and the interval has several induced fractures. One microfault occurs within this interval, which may be caused by the numerous laminations in this interval (Figure 3-20). A large conductive fracture, approximately 10 ft, occurs at 5,632 ft.

The Utica shale shows a few induced fractures in the upper 7 ft of the formation containing low conductivity. There are minimal to no fractures, faults, or borehole breakouts until 6,684 ft in the Trenton/Black River Group. Several induced fractures occur in the upper and middle interval of the group. The Upper Chazy, Gull River, Lower Chazy, and Wells Creek have very few fractures, faults, or borehole breakouts in the formations. There are numerous laminations and beds with a mix of low, medium, and high conductivity signatures. At 7,224 ft, fractures occur at the Wells Creek and Beekmantown contact. The image logs show a mottled texture with some regions of potential vugular development (Figure 3-21).

The Rose Run has several laminations and beds with low to moderate conductivity. At 7,375 ft, there is an approximately 44-ft interval with several induced fractures (Figure 3-22). The conductivity is high from 7,433 ft to 7,442 ft, and there are several deformed beds at the base of this interval (Figure 3-23).

The Copper Ridge interval has rare and scattered clusters of laminations and bedding. Where these clusters occur, the image log shows several occurrences of induced fracturing in these intervals (Figure 3-24). Intervals that do not have laminations or bedding show a mottled texture with various-sized vug development (Figure 3-25). The differing vug concentrations may be due to the vug development being controlled by the different sequences of sediment packages. At 7,898 ft, there is a microfault between several beds and fractures (Figure 3-26). This microfault occurs at the base of the Copper Ridge and Conasauga contact, which could be caused by a texture change between the two formations. The Conasauga has multiple low-angle, low-conductivity laminations and beds. Induced fractures occur from the top of the formation at 7,513 ft to 7,963 ft.

The Rome Formation has similar mottled textures as the Copper Ridge Formation. Potential vugular development is shown in the upper interval, approximately 100 ft, of the image log. At 8,094 ft, bedding and laminations occur with multiple induced fractures, which continues to the basal sand formation. At the base of the basal sand, 8,613 ft, there is an increase of fractures and deformed bedding. These features and a significant decrease in gamma ray at 8,631 ft suggests an unconformity at the basal sand/Precambrian contact (Figure 3-27). The Precambrian does not show any significant structural features for the logged interval.

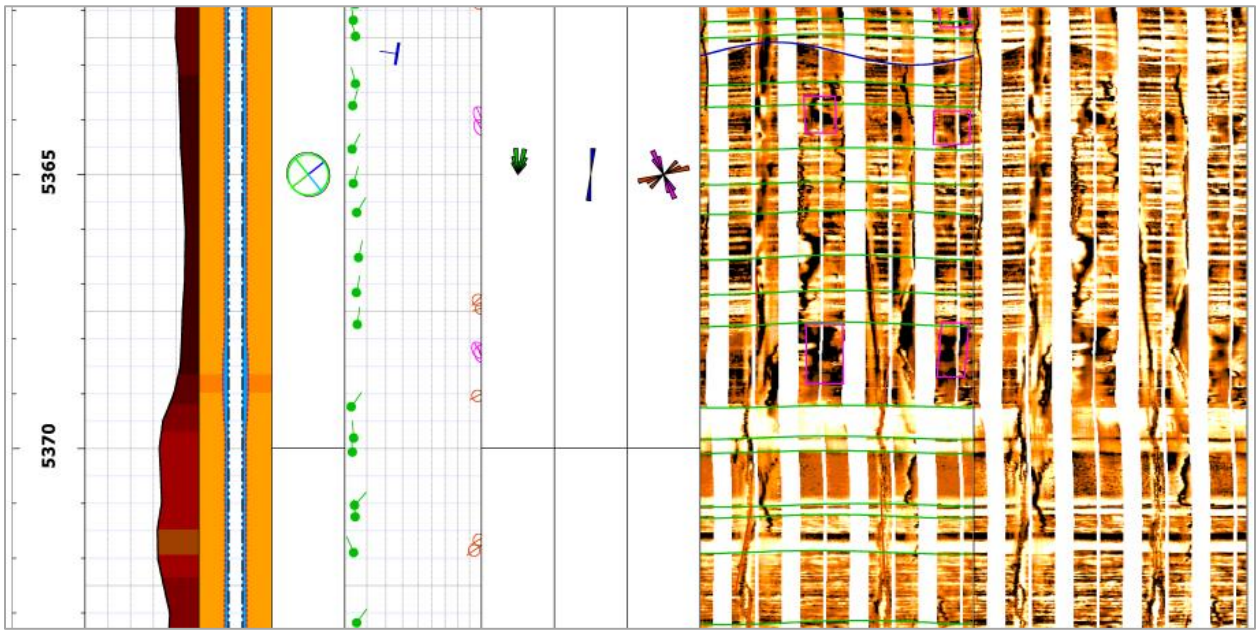

Figure 3-20: Laminations and beds in the interval with one microfault at 5,362 ft. Induced fractures and borehole breakouts occur at 5,367 ft, East-Central Appalachian Basin site.

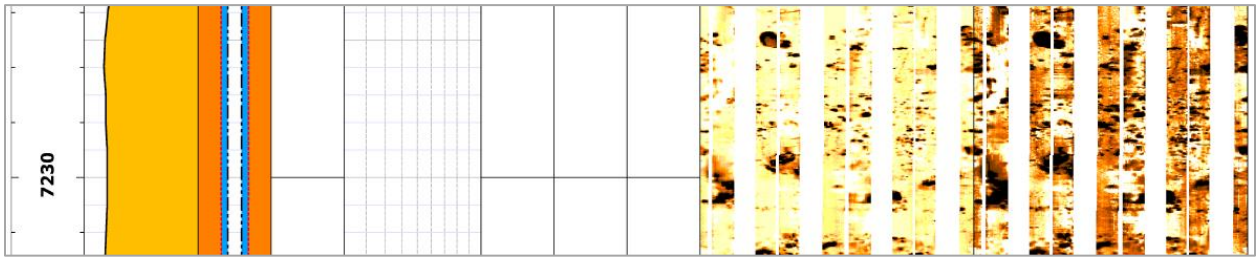

Figure 3-21: Potential vugular development, East-Central Appalachian Basin site.

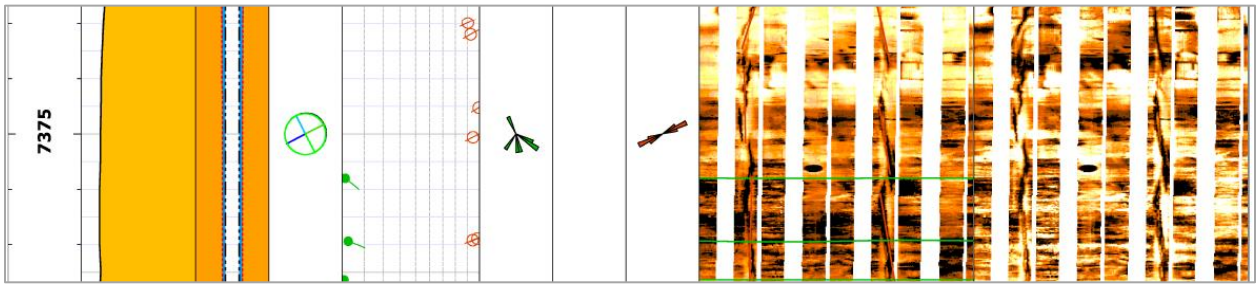

Figure 3-22: Several induced fractures above laminations, East-Central Appalachian Basin site.

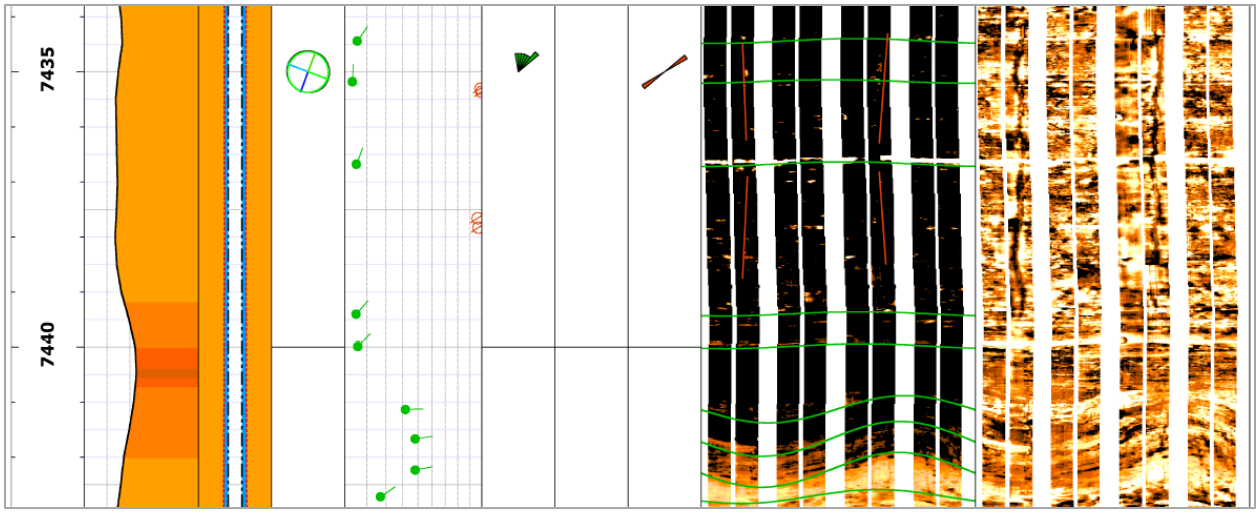

Figure 3-23: High-conductivity interval with deformed beds at the base of the interval, East-Central Appalachian Basin site.

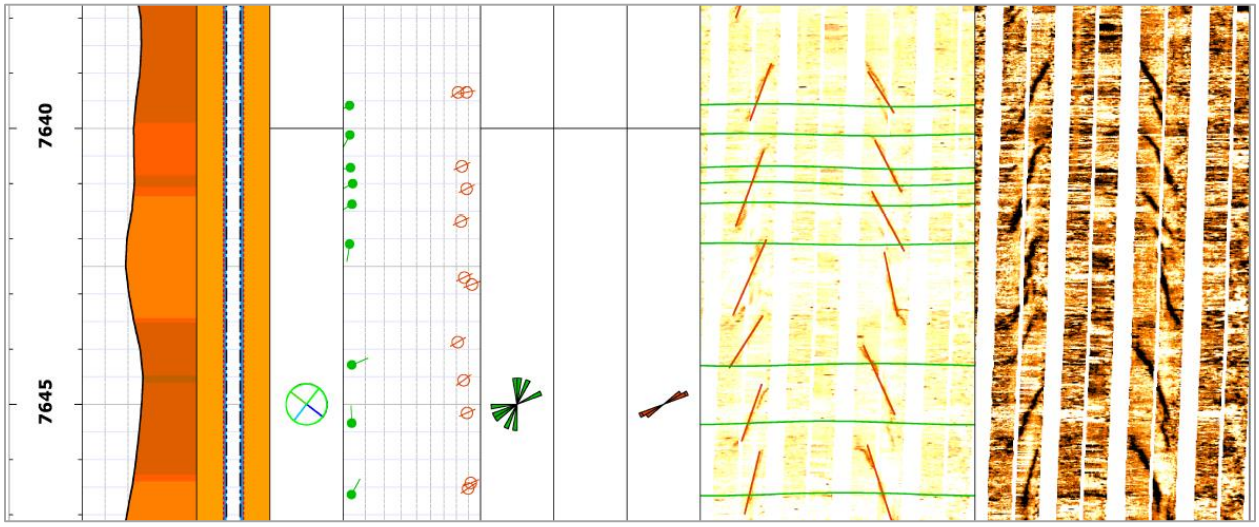

Figure 3-24: Induced fractures in a cluster of beds, East-Central Appalachian Basin site.

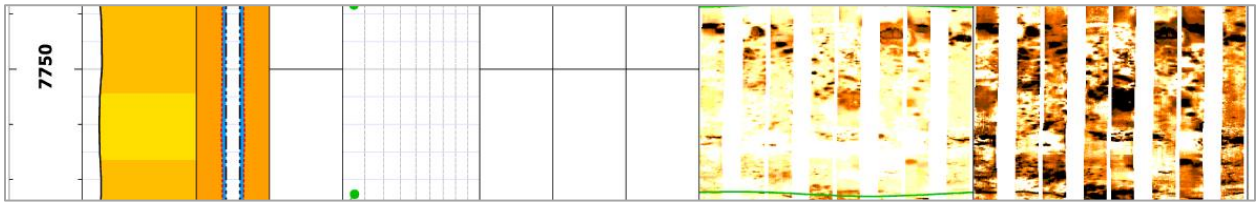

Figure 3-25: Potential vugular development in the Copper Ridge intervals, East-Central Appalachian Basin site.

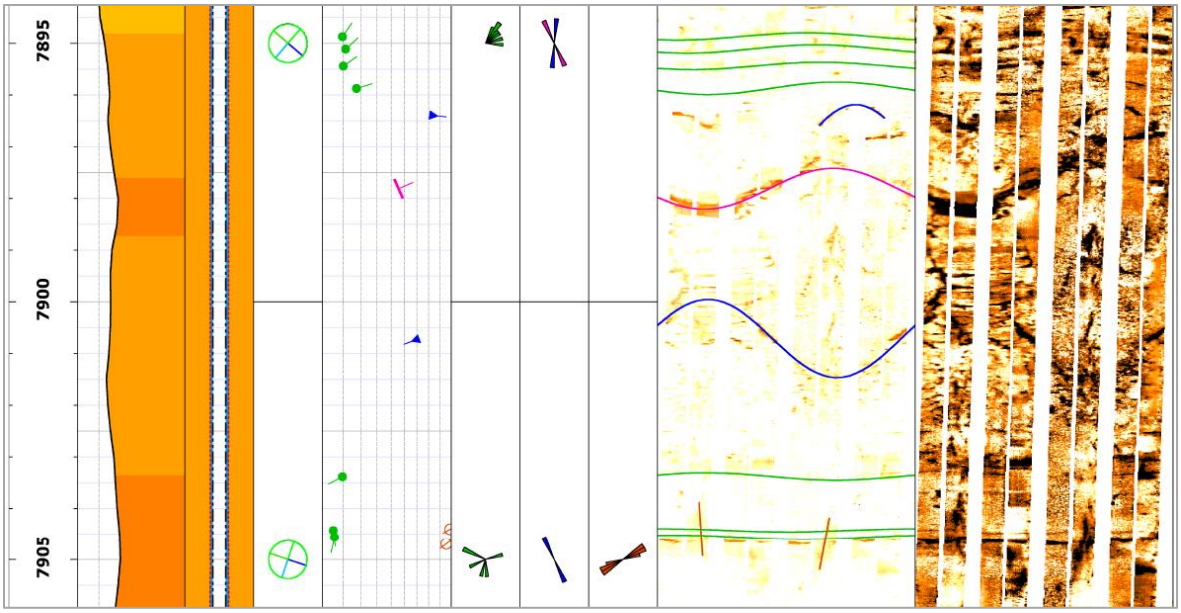

Figure 3-26: Microfault at the base of laminations, East-Central Appalachian Basin site.

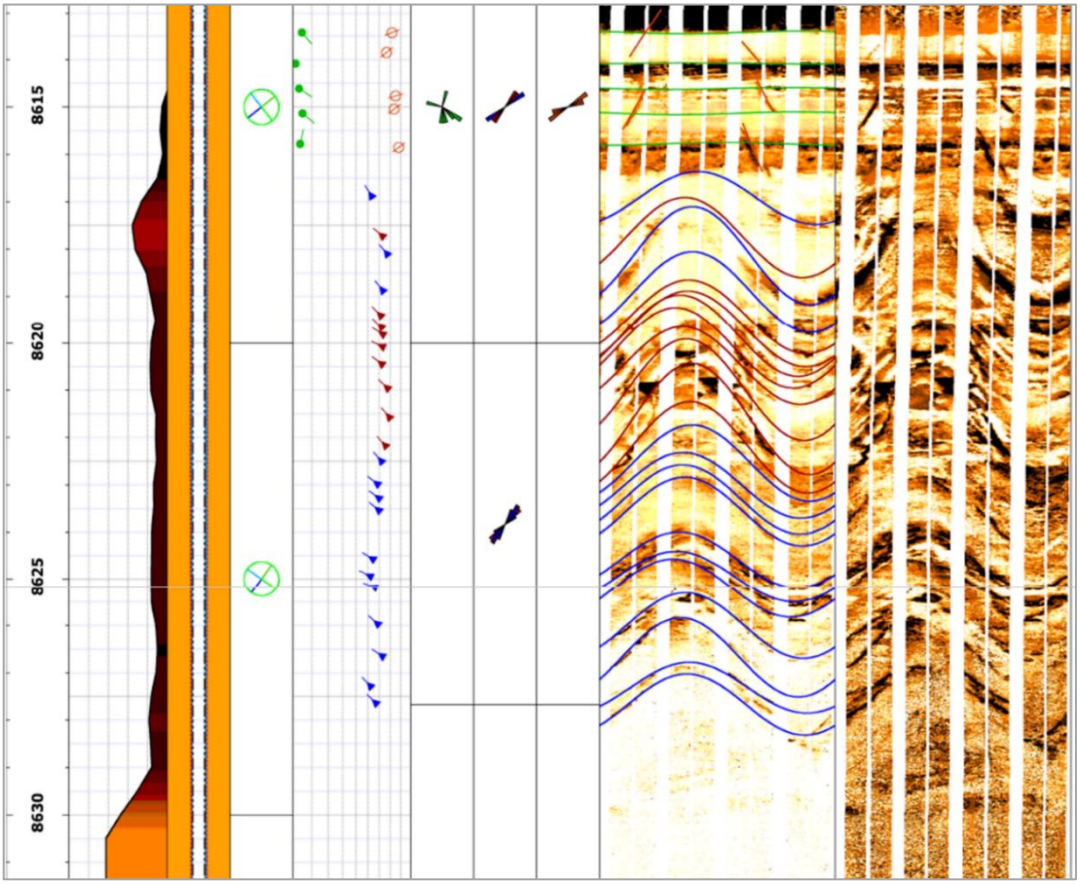

Figure 3-27: Several deformed beds at the basal sand and Precambrian contact, East-Central Appalachian Basin site.

3.2.4 Summary of East-Central Appalachian Basin

Table 3-8 summarizes the analysis of the image log information given above. The majority of the structural occurrences in the East Central Appalachian Basin site well appear to be induced fractures caused by drilling and borehole breakouts due to potential vugular development and washout intervals. Several deformed bed and high-conductivity changes at 7,433 ft to 7,442 ft are representative of texture changes in formations and between formation contacts. The Copper Ridge has several textural changes in the formation, noted by scattered bedding and laminations and potential vugular development. The microfault and the bed clusters around the 7,898-ft interval merit additional analysis. The Conasauga and Rome Formation have minor structural features that include induced fractures, potentially due to multiple laminations and beds, and potential vugular development. Deformed beds at the basal sand/Precambrian contact are indicative of depositional features at the Precambrian contact. Thelogged interval of the Precambrian was limited and did not present any notable structural features.

Table 3-8: Notable features from image log analysis for the formations of interest, East-Central Appalachian Basis site.

Formation of interest	Zones / depth intervals of interest (ft.)	Notable features or log signatures	Interpretation and implication
Above Utica shale	5,024-6,136	Numerous borehole breakouts	High min-max stress contrast, under balanced drilling fluids
Beekmantown	7,227-7,372	Fractures and potential vugs	Unconformity contact at the Wells Creek and Beekmantown contact
Rose Run	7,372-7,513	Several induced fractures	Fracturing due to numerous laminations and beds
Copper Ridge	7,513-7,900	Induced fractures, potential vugs and microfaults	Induced fractures due to multiple laminations and beds, potential vugs merits additional analysis of potential porosity, microfaults occur at texture changes
Conasauga	7,900-7,995	Induced fractures	Due to several beds and laminations
Rome	7,995-8,526	Potential vugs and induced fractures	Potential porosity, merits additional analysis, induced fractures potentially due to beds and laminations
Basal sand	8,526-8,633	Induced fractures, deformed beds	Potentially due to beds and laminations, deformed bed due to major texture change due to Precambrian formation

Figure 3-28 shows a histogram of geomechanical features for the well binned at 100-ft intervals, a plot of the orientation of wellbore failures, and rose diagrams for induced fractures and borehole breakouts for the East-Central Appalachian Basin Site well. There are two faults interpreted in the well: one is a microfault and the other is a minor fault. A minor fault is a fracture surface that shows bedding offset but no lithologic change. Many of the structures in the well occur in the Queenston and Rome formations with the majority of the structures in the reservoir formations. The wellbore failures are abundant and show a relatively consistent preliminary maximum horizontal stress orientation of approximately 65 degrees.

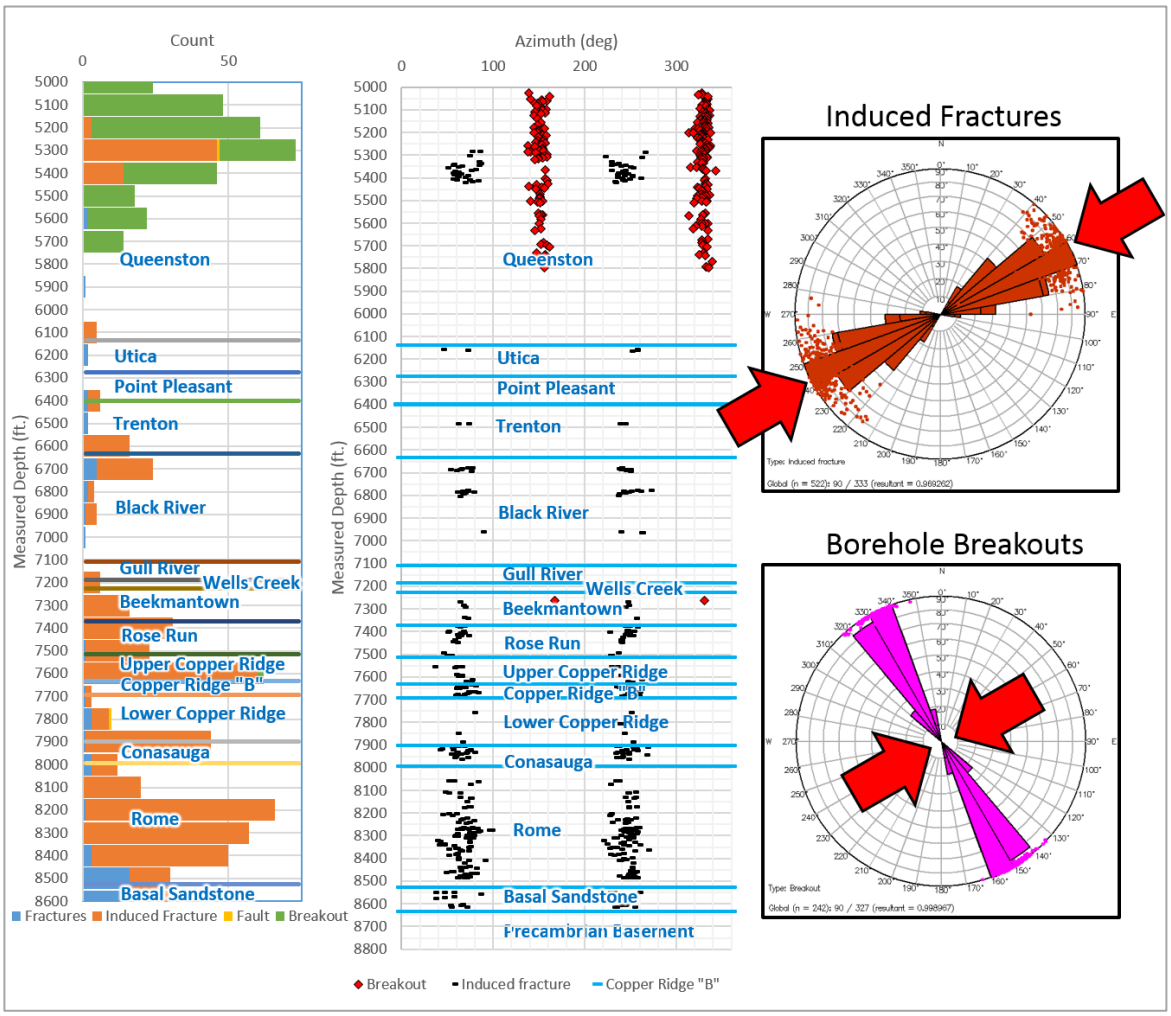

Figure 3-28: Histogram of structures for the well binned at 100-ft intervals, plot of the orientation of wellbore failures, and rose diagrams for induced fractures and borehole breakouts for the East-Central Appalachian Basin site well. Red arrows represent the maximum horizontal stress direction.

3.3 Northern Appalachian Basin Site

3.3.1 Site Geology

The Northern Appalachian Basin site is located in Chautauqua County in southwestern New York (Figure 3-29), where a test well was drilled to a depth of approximately 7,300 ft in the Potsdam sandstone formation. The area is situated along the northwestern flank of the Appalachian Basin. Structurally, the strata have regional dip 40 to 50 ft per mile (0.4 to 0.5 degrees) to the south-southeast and an east-northeast strike (Richardson, 1941). A full program of mud logging, wireline logging, rock core collection, and geotechnical testing of rock cores was completed in the test well.

The main targets of the test well were the Cambrian-age Rose Run sandstone and the Potsdam sandstone. Figure 3-30 summarizes the well construction, the stratigraphic section penetrated, whole core and sidewall core interval, gas and water shows, Trenton oil and gas production, and fracture and vug analysis.

The lithology of the Rose Run sandstone and Potsdam Formation (Figure 3-30) was mostly a dolomitic quartz sandstone. There were only minor amounts of clay and iron-oxide minerals that might result in CO_2 dissolution/precipitations reactions. The Galway sand zones were mostly dolomite with minor detrital quartz. The Rose Run sandstone was 181 ft thick and the Potsdam sandstone appeared to be at least 108 ft thick. Both formations were slightly thicker than predicted in the well prognosis. Both the Galway B-sand and the Galway C-sand were identified in the test well, but the formations were present as thin, sandy intervals.

According to Riley and Baranoski (2006), the Tribes Hill is equivalent to the Beekmantown dolomite, the Little Falls Formation is equivalent to the Rose Run sandstone, and the Galway Formation is partly correlative to the Copper Ridge dolomite and the Conasauga Formation of eastern Ohio (Figure 3-31). Key caprocks penetrated in the test well included the Queenston shale, Utica shale, Black River Group, and Little Falls Formation (Figure 3-30). Together, these formations represent over 2,500 ft of containment layers. Log and core test data demonstrate that the formations have low permeability and porosity.

Figure 3-29: Location of the Northern Appalachian Basin study area site.

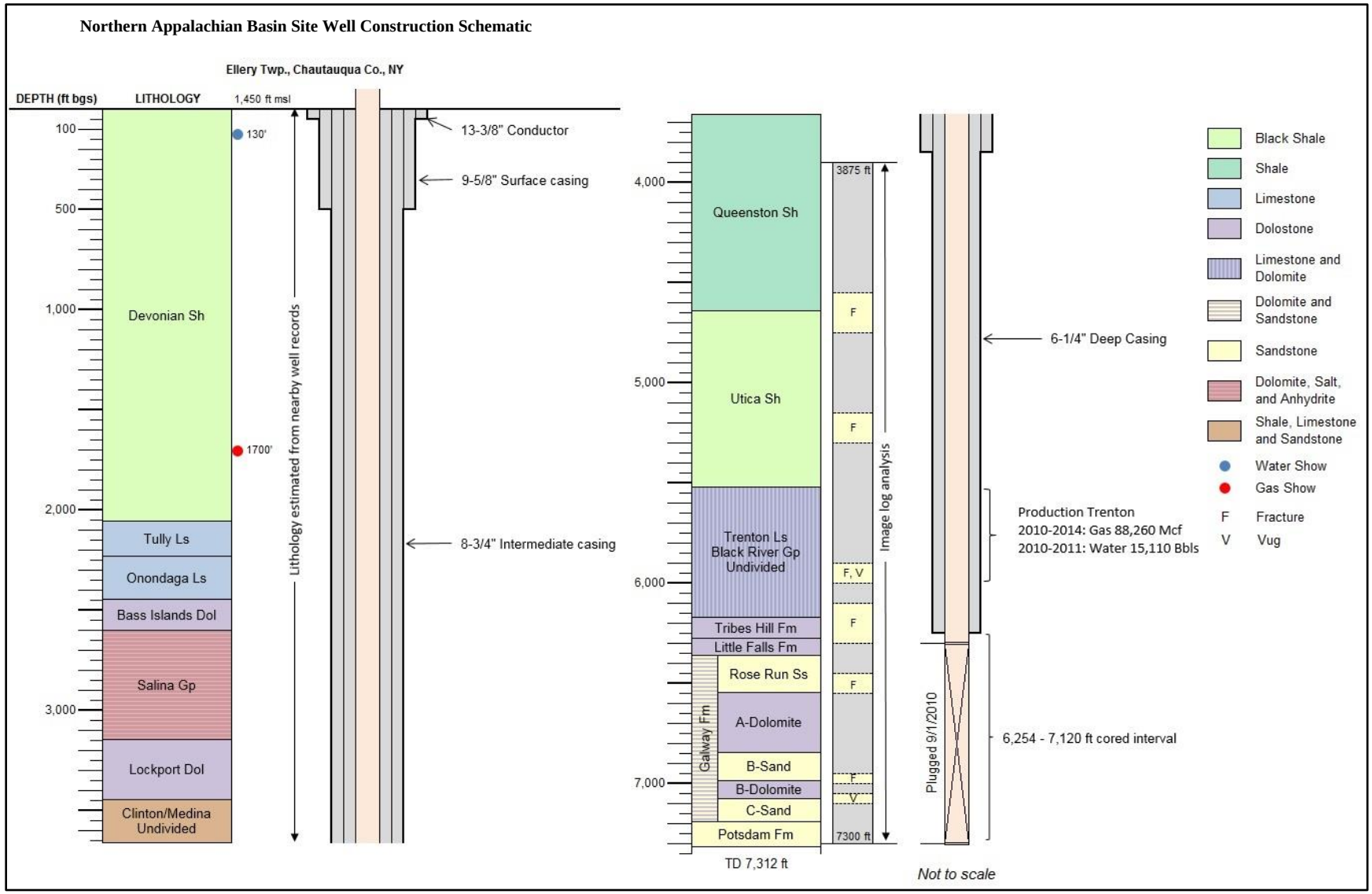

Figure 3-30: Well construction and stratigraphic section for the Northern Appalachian Basin site well, Chautauqua County, New York.

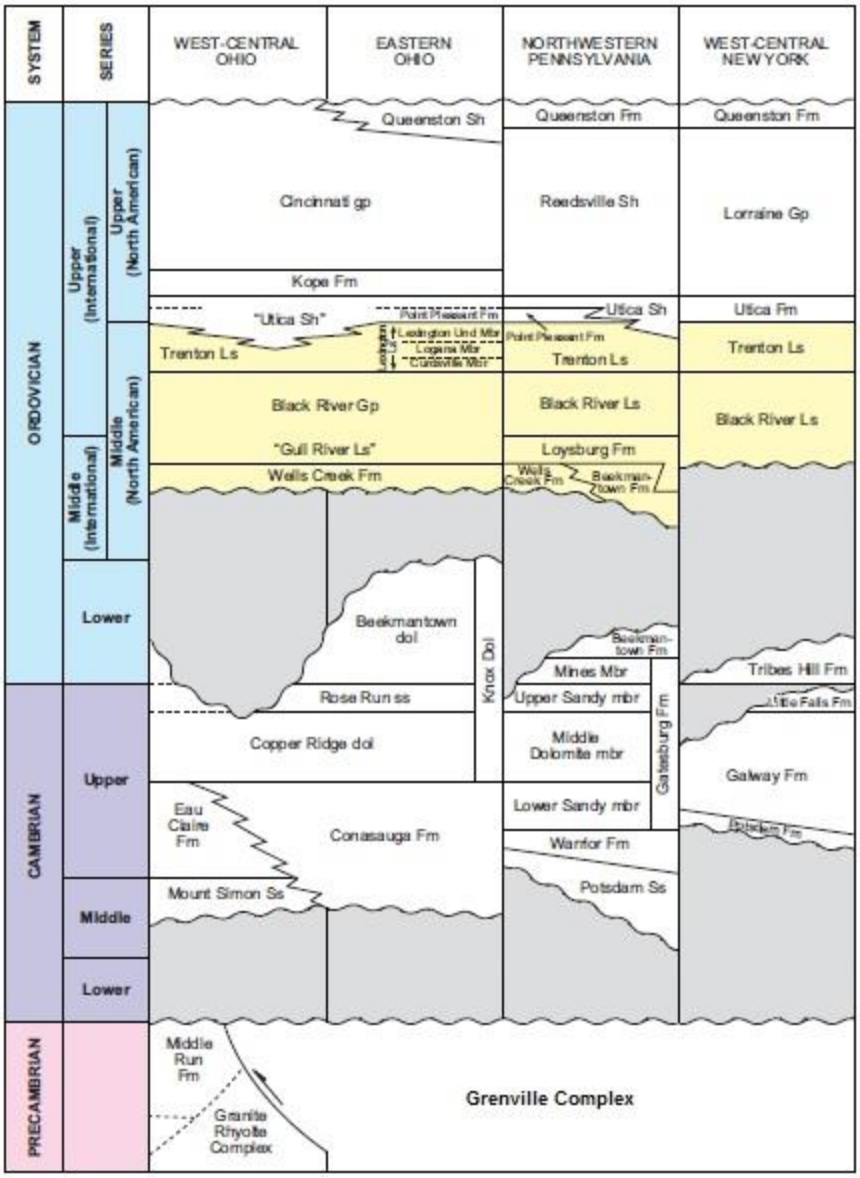

Figure 3-31: Correlation chart of Cambrian and Ordovician formations in Ohio, northwestern Pennsylvania, and west-central New York (modified from Riley and Baranoski, 2006).

.

3.3.2 Geophysical Well Log and Core Summary

A suite of wireline logs was performed on the Northern Appalachian Basin Site well. The TC suite, image logs, and sonic logs were used for geomechanical analysis and are therefore the logs mentioned in this report. Table 3-9 shows the footage intervals used for this analysis and the interpreted log footage from integrating the logs mentioned above. The TC, sonic, and image data were logged from above the Utica shale to the Potsdam Formation.

A total of 150 ft of full core was collected in the test well from the deeper Ordovician and Cambrian Formations. Six sidewall cores were analyzed for geomechanical parameters: two in the Little Falls Formation, two in the Rose Run sandstone, and two in the Galway "B" dolomite (Table 3-10). Cores were tested to obtain key calibration parameters such as the static Young's modulus and static Poisson's ratio.

Table 3-9: Wireline logs performed on the Northern Appalachian Basin well.

Type	Logs run	Depth interval (ft MD)
Injection borehole (open-hole logs)	Gamma ray, caliper, spontaneous potential, resistivity, litho-density, density porosity, neutron porosity, directional survey	3,269-7,322.5
	Formation MicroImager (FMI*)	3,870-7,305
	Sonic Log	3,269-7,325
Interpreted logs	HSTRESS	3,880-7,282

*Schlumberger trade name

Table 3-10: Core samples collected from the Northern Appalachian Basin well.

Formation	Core interval (ft MD)	Young's modulus (x10^6 psi)	Poisson's ratio
Northern Appalachian Basin site well core plugs			
Little Falls	6,272.09	5.59	0.42
Little Falls	6,344.14	9.28	0.31
Rose Run	6,367.56	11.45	0.27
Rose Run	6,370.08	10.78	0.18
Galway B Dol	7,069.45	10.45	0.31
Galway B Dol	7,076.31	10	0.24

3.3.3 Image Log Description and Analysis

Image analysis for the Northern Appalachian Basin was conducted from 3,870 ft to 7,302 ft. The first 220 ft, from 3,870 ft to 4,088 ft, there are several borehole breakouts. The rest of the formations from 4,088 ft to the Utica shale show very little to no additional structural features. This interval has numerous laminations and beds with a range of conductivity signatures from low to high. The Utica shows numerous low-angle laminations and bedding that strike in all directions. There are several fractures and borehole breakouts in the middle and lower interval of the formation. One microfault (Figure 3-32) was observed at 4,819 ft, where numerous bedding and less-conductive beds occur. The Tribes Hill and Little Falls Formations show very few structural features in the upper intervals. At 6,174 ft (Figure 3-33), the conductivity signatures increase and there are two microfault occurrences with various dipping laminations and beds.

The Rose Run Formation has high conductivity combined with high gamma ray signatures, suggesting potential shale or clay occurrences at the top of the formation. Gamma ray decreases with low conductivity signatures at 6,359 ft suggest potential sand beds. Several fractures that intersect the borehole could be indicative of higher-than-expected porosity at a depth near 6,377 ft (Figure 3-34). It is difficult to quantitatively describe this type of porosity without further investigation, such as hydraulic testing, into the condition.

The A-dolomite has low gamma ray signatures with low conductivity for the majority of this interval. There are beds and laminations in this interval with no additional structural features. The B-sand has slightly high gamma ray signatures and laminations with high conductivity throughout the formation. There are a few fractures at the B-sand and B-dolomite contact. Fractures occurred only in the upper zone of the B-dolomite formation. Additionally, indications of vugular porosity exist on a small interval, approximately 5 ft, in the B-dolomite. Over an interval of approximately 28 ft in the B-dolomite, at 7,042 ft, there are dark, electrically conducive circles on the borehole wall (Figure 3-35). Sometimes, this is an effect caused by vugs, small gaps in the formation created by dissolution. However, the net total thickness of these potentially vuggy intervals is approximately 5 ft over the 28-ft section. The C-sand formation has one structural feature, a fracture, at 7,223 ft. The rest of the formation shows low to moderate conductivity with some moderately high conductive beds.

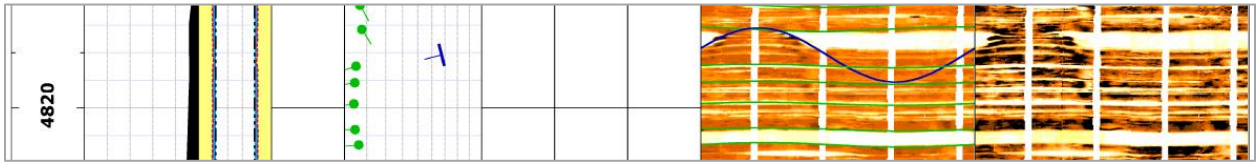

Figure 3-32: Microfault at 4,819 ft, Northern Appalachian Basin site.

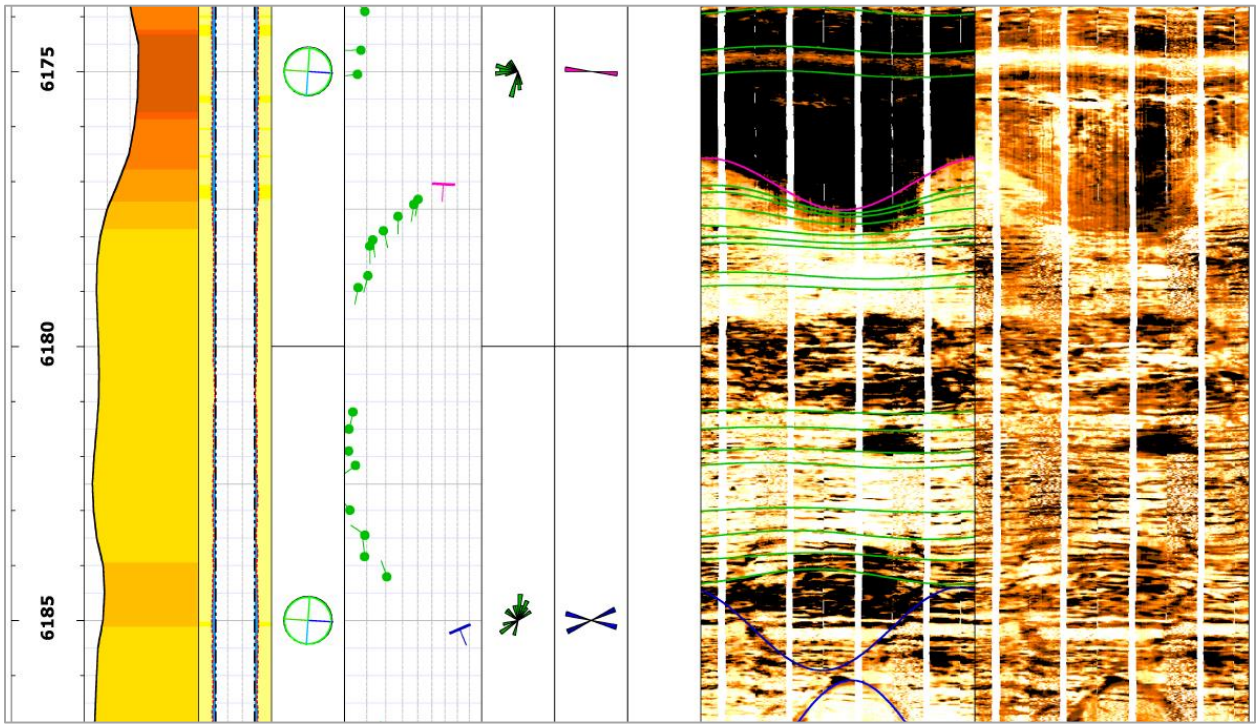

Figure 3-33: Microfaults at the top and the base of several dipping beds, Northern Appalachian Basin site.

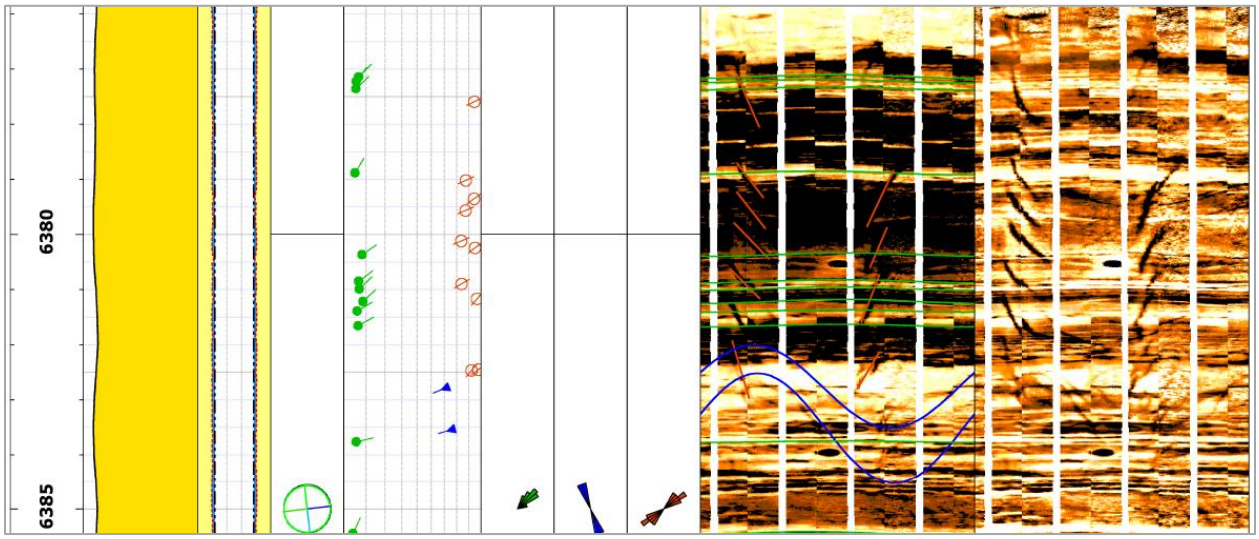

Figure 3-34: High-conductivity interval with several induced and conductive fractures, Northern Appalachian Basin site.

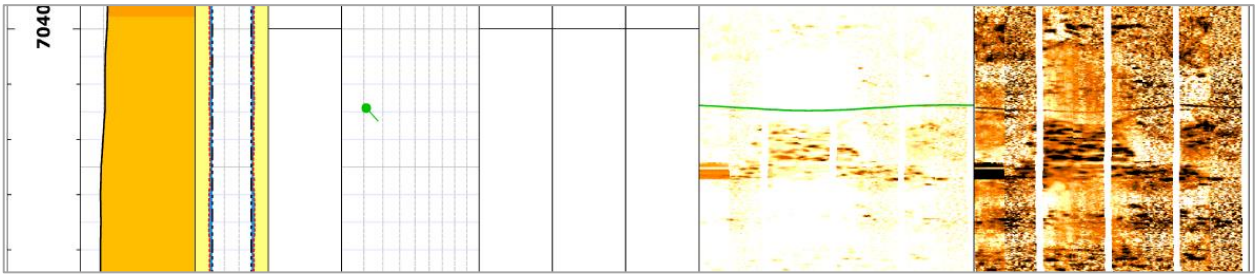

Figure 3-35: High-conductive spots as potential vugular cluster, Northern Appalachian Basin site.

3.3.4 Summary of Northern Appalachian Basin

Table 3-11 summarizes the analysis of the image log information given above. The majority of the structural occurrences in the Northern Appalachian Basin site well appear to be induced fractures caused by drilling and borehole breakouts due to potential vugular development and washout intervals. The dipping beds and microfaults, 6,177 ft to 6,186 ft, that occur at the top and base of this interval merit additional analysis in order to characterize this structural feature. Additionally, potential vugular development occurs in the dolomite interval, which suggests porosity in this interval. Supplemental analysis is needed to determine porosity potential.

Table 3-11: Notable features from image log analysis for the formations of interest, Northern Appalachian Basin site.

Formation of interest	Zones / depth intervals of interest (ft)	Notable features or log signatures	Interpretation and implication
Above Utica shale	3,870-4,640	Numerous borehole breakouts in the upper 220 ft	High stress contrast
Utica	4,640-5,518	Fractures and borehole breakouts, one microfault	Shale beds and sandy beds are prone to breakouts and induced fractures
Trenton/Black River Group/Little Falls	5,518-6,359	High conductivity interval with two microfaults and various dipping beds	Merits additional analysis of this region
Rose Run	6,359-6,546	Fractures and borehole breakouts	High occurrences of laminations and beds present possible cause for fractures and breakouts
B sand	6,848-6,985	Fractures	Occur at the B-sand and B-dolomite contact, suggesting texture change
B dolomite	6,985-7,132	Fractures and vugs	Potential porosity, merits additional analysis
C sand	7,132-TD (7,302)	One fracture where there are bedded features	Minor structural feature

Figure 3-36 shows a histogram of structures for the well binned at 100-ft intervals, a plot of the orientation of wellbore failures, and rose diagrams for induced fractures and borehole breakouts for the East-Central Appalachian Basin site well. There are five faults interpreted in the well: four are microfaults and the other is a minor fault. A minor fault is defined as a fracture surface that shows bedding offset but no lithologic change. The wellbore failures mainly occur above the Utica Formation, in the Utica Formation, and in the Rose Run Formation. The majority of the natural structures such as microfaults, minor faults, and natural fractures occur at the base of the Tribes Hill to the base of the Rose Run. Wellbore failures are abundant and show a relatively consistent preliminary maximum horizontal stress orientation of approximately 55 degrees.

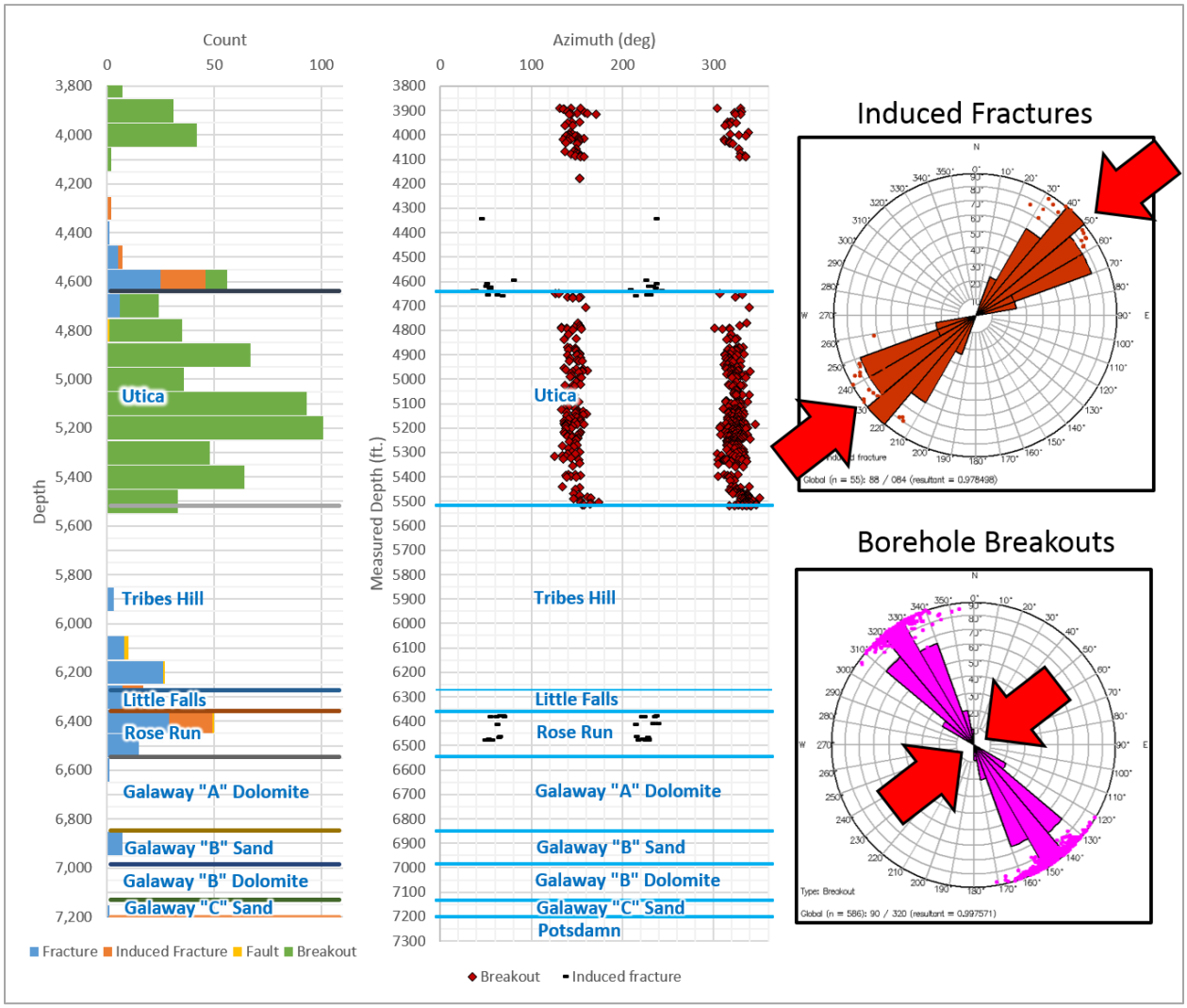

Figure 3-36: Histogram of structures for the well binned at 100-ft intervals, plot of the orientation of wellbore failures, and rose diagrams for induced fractures and borehole breakouts for the Northern Appalachian Basin Site well. Red arrows represent the maximum horizontal stress direction

4.0 Petrophysical Log Analysis and Integration

The objective of the petrophysical log analysis and integration task was to derive a continuous estimate of geomechanical parameters based on geophysical log data for the three study sites to support evaluation of CO_2 storage in fractured reservoirs. Estimation of the stress properties of rock formations determined from geophysical logs will aid in depiction of stress conditions and variations in geomechanical properties in the different parts of the Midwest United States.

4.1 Geomechanical Parameter Derivation

A suite of logs was given to Baker Hughes to determine the stress magnitudes and change in pressure needed for fracture migration at all three wells sites. Baker Hughes used Franquet and Rodriguez (2012) methodology to derive static elastic moduli, Poisson's ratio, compressive strength, stiffness tensor, in-situ stress, and stress gradient profiles. Inputs used to create the model included gamma, sonic log, bulk density, and pore pressure data. Pore pressure gradient was assumed to be 0.43 psi/ft for all wells. The general workflow used to analyze the log data is provided in Figure 4-1.

4.1.1 Arches Site

The Duke Energy #1 well showed the caprocks with a high average Young's modulus, Poisson's ratio, and bulk modulus as compared to the reservoirs. The Young's modulus ranged from 3 to 15 megapounds per square inch (Mpsi), Poisson's ratio from 0.2 to 0.35, and bulk modulus from 3.5 to 13 Mpsi. The transition between Wells Creek to Beekmantown shows that the average Young's modulus decreased from 12 to 8 Mpsi, the average Poisson's ratio decreased from 0.35 to 0.25, and the average bulk modulus decreased from 10 Mpsi to 6 Mpsi (Figure 4-2). In the formations with the lowest average moduli, the Mount Simon and Middle Run, Young's modulus decreased to an average of 6 Mpsi and bulk modulus decreased to an average of 3 Mpsi (Figure 4-3).

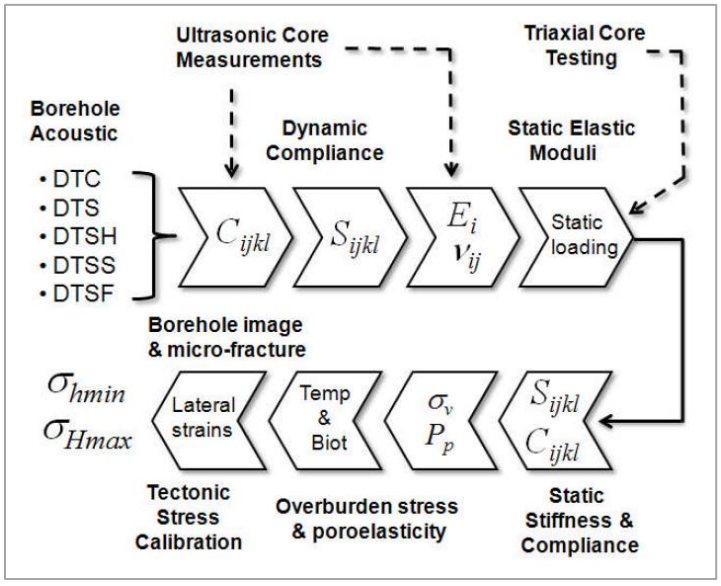

Figure 4-1: Isotropic stress profiling general workflow (from Franquet and Rodriguez, 2012).

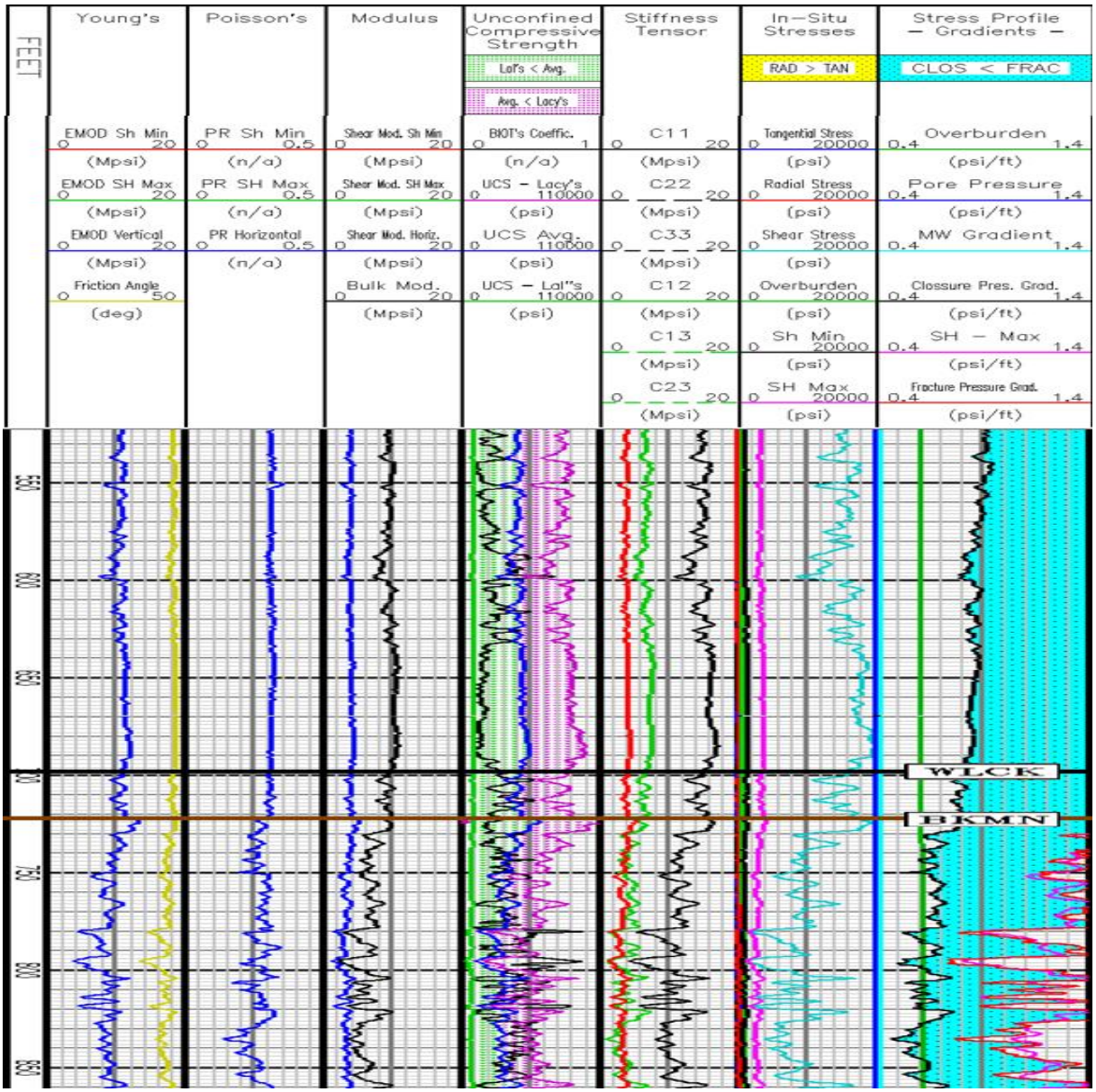

Figure 4-2: Geomechanical log analysis for Duke Energy #1 Beekmantown interval showing the boundary between the caprocks and reservoirs.

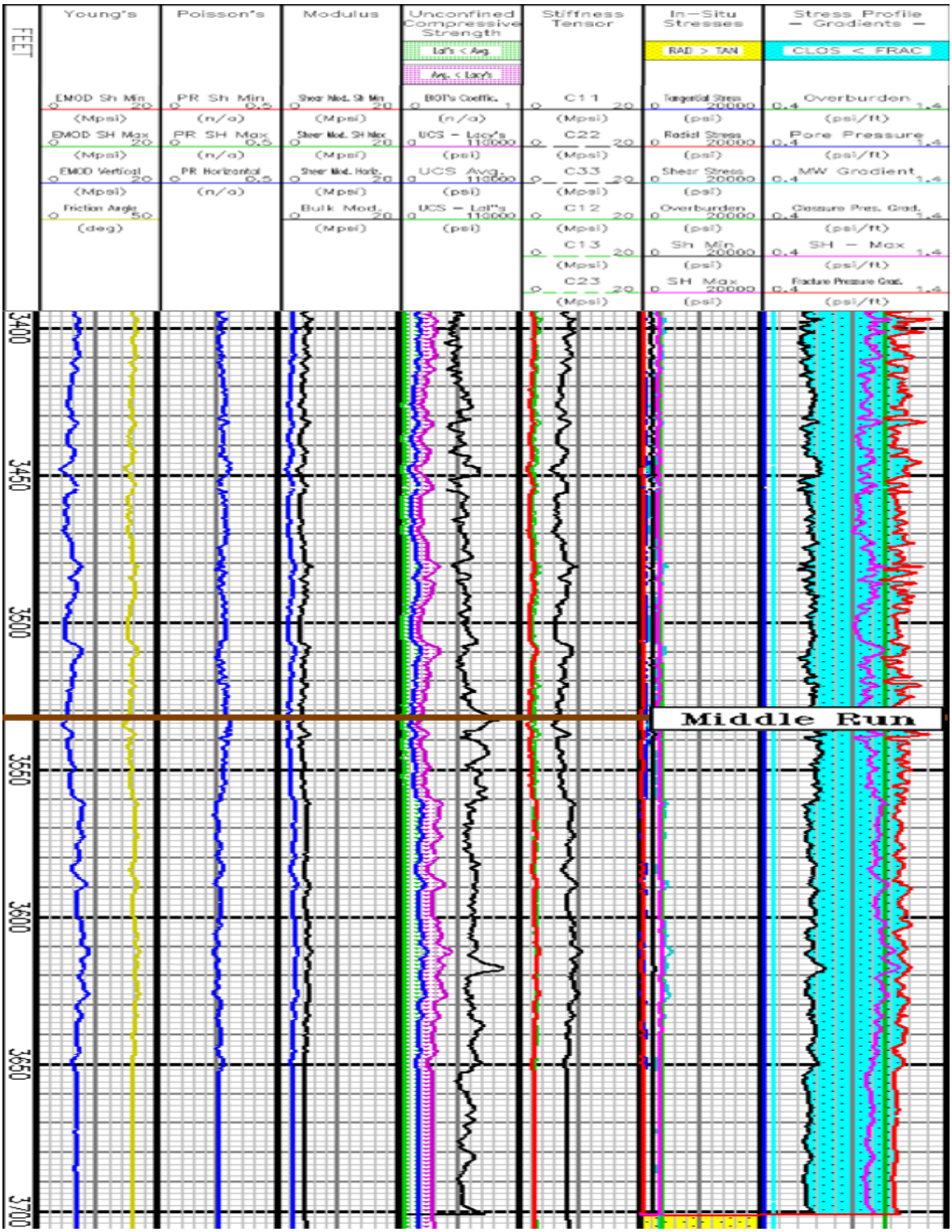

Figure 4-3: Geomechanical log analysis for Duke Energy #1 showing the Mount Simon and Middle Run sandstone formations.

4.1.2 East-Central Appalachian Basin Site

The OGS CO_2 well showed a slight decrease in the Young's modulus, Poisson's ratio, and bulk modulus starting at the Rose Run Formation and down in depth (Figure 4-4). The Young's modulus ranged from 4 to 14 Mpsi, Poisson's ratio from 0.175 to 0.35, and bulk modulus from 2.5 to 12 Mpsi. In the formations with the lowest average moduli, the Rose Run Formation and basal sandstone, the Young's modulus, Poisson's ratio, and bulk modulus decreased to average values of 10 Mpsi, 0.25, and 4 Mpsi, respectively (Figure 4-4).

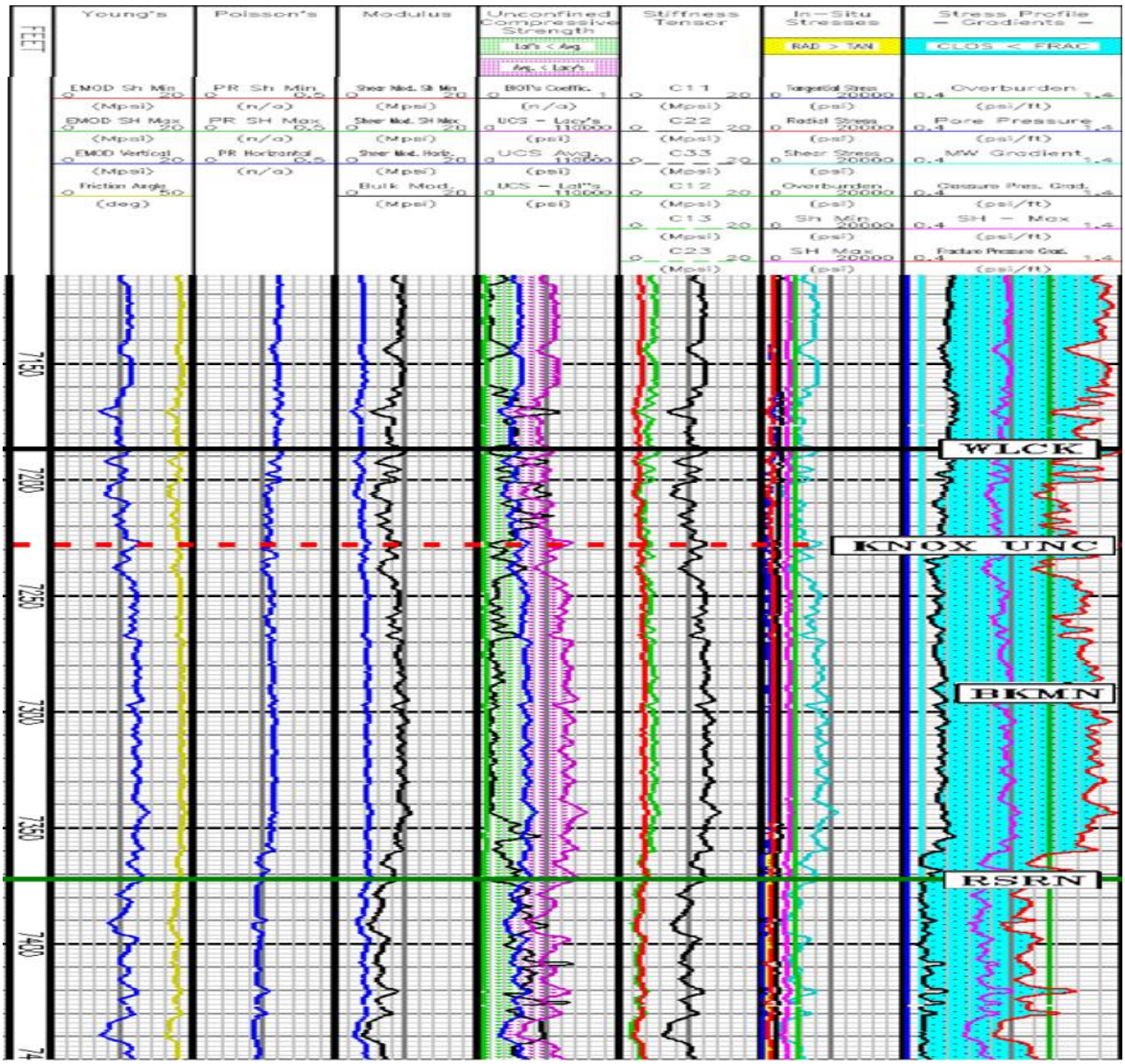

Figure 4-4: Geomechanical log analysis for East-Central Appalachian site showing the Wells Creek to Rose Run interval.

4.1.3 Northern Appalachian Basin Site

The Northern Appalachian Basin site well showed caprocks with high average Young's modulus, Poisson's ratio, and bulk modulus values, but even higher values in some of the reservoir rock. The Young's modulus ranged from 5 to 21 Mpsi, Poisson's ratio from 0.225 to 0.375, and bulk modulus from 2 to 8 Mpsi. The formations with the highest average moduli, the Galway "A" and "B" dolomites, had an average Young's modulus of 20 Mpsi, Poisson's ratio of 0.3, and bulk modulus of 8 Mpsi. The formations with the most varying moduli values were the Tribes Hill, Little Falls, Rose Run, and Galway sands (Figures 4-5 and 4-6) and had similar values as the caprock. The Galway dolomites had very high moduli values, indicating that they are highly resistant to fracturing under increased hydraulic pressure. In general, the high Young's moduli values suggest that these data require calibration to rock core test data.

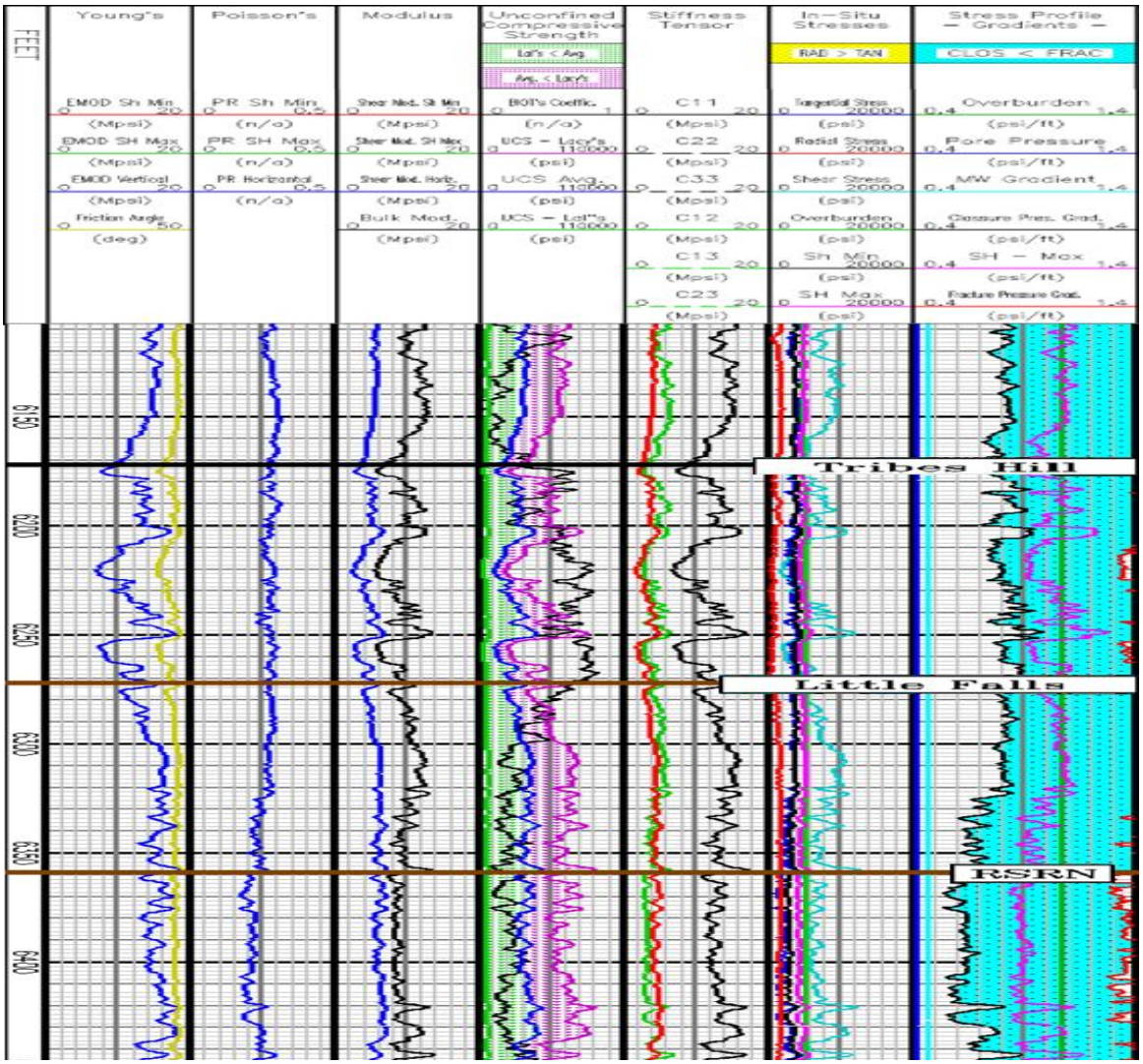

Figure 4-5: Geomechanical log analysis for the Northern Appalachian Basin site showing the Tribes Hill-Rose Run interval.

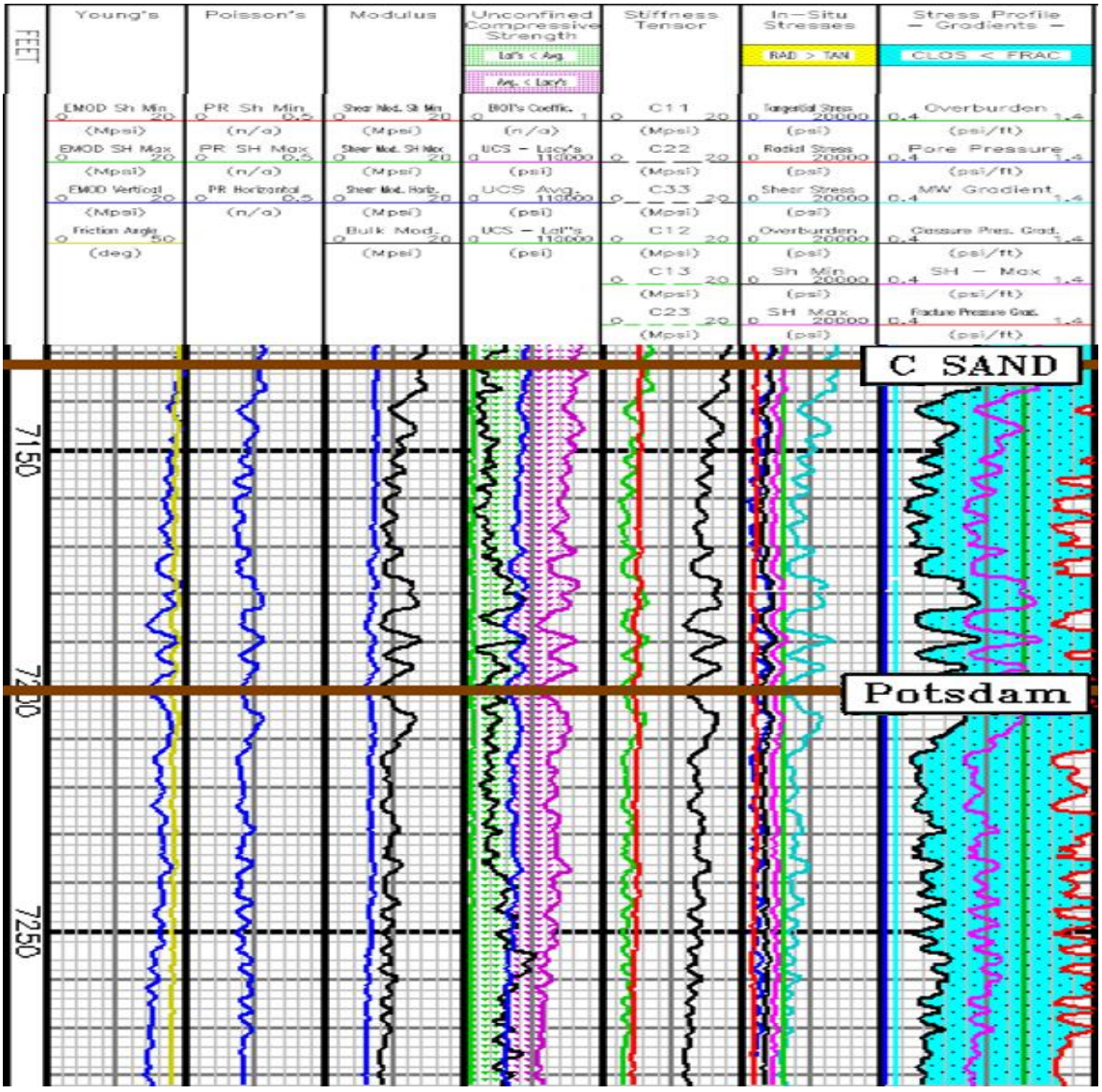

Figure 4-6: Geomechanical log analysis for the Northern Appalachian Basin site showing the Galway “C” sand and Potsdam Formation.

5.0 Development of Methodology for Geomechanical Site Characterization

The objectives of Task 5 were to develop a methodology for geomechanical site characterization, well testing, and monitoring for CO_2 storage applications. The task provides guidance for operators considering drilling CO_2 injection wells, preparing Class VI underground injection control (UIC) permits, and monitoring CO_2 storage sites. Methods were also evaluated for different sedimentary basins in the United States to provide operators with perspective on the suitability of technologies in different geologic settings. Results were compiled into easy-to-use tables and figures. Costs were described in terms of low ($0 to $100s), medium ($1,000 to $10,000s), and high ($100,000 to $1,000,000s). Guidance was divided into the following categories:

Geophysical Logging Options for Evaluating CO_2 Storage Sites. Geophysical logging practices are used to define physical rock characteristics such as lithology, mineralogy, water saturations, porosity, and permeability measurements. Logged data are incorporated into the petrophysical evaluation and identification of potential reservoirs and seal zones. The different geophysical logging technologies available to determine geomechanical parameters at depth were reviewed, including a discussion of methods used in terms of borehole requirements, field application, results, processing, approximate costs, and limitations.

Geomechanical Rock Core Testing Options for Evaluating CO_2 Storage Sites. Rock core testing provides a direct measurement of data from collected rock samples. Routine core analyses provide lithology, mineralogy, porosity, permeability, and fluid saturation measurements. Advanced rock mechanics methods are used to analyze elasticity, failure and fracture mechanics, and stress propagation. These advanced tests are used to calibrate geomechanical data derived from geophysical logs. The different geotechnical rock core testing methods available to determine geomechanical parameters at depth were reviewed. Methods were described in terms of borehole requirements, laboratory methods, results, processing, approximation of costs, and limitations. Results are compiled into easy-to-use tables and figures.

Injection Testing Options for Evaluating CO_2 Storage Sites. Injection testing methods such as step-rate tests, pressure fall-off tests, and interference tests were reviewed in terms of their ability to determine geomechanical parameters at depth in the subsurface. These tests analyze in-situ stresses and the hydraulic properties of the formation. Measurements are used to determine the upper and lower bounds for the minimum horizontal stress and estimate the maximum horizontal stress. These results are used to determine reservoir parameters and to assess the risks associated with CO_2 injection and storage. These methods are described in terms of borehole requirements, field application, results, processing, approximation of costs, and limitations.

Geomechanical Monitoring Options for Evaluating CO_2 Storage Sites. Monitoring options for CO_2 storage related to geomechanical parameters were reviewed. These methods can be used to spatially track injected subsurface CO_2 and the proximity and remote spatial deformation of CO_2 in a storage site. These options include microseismic monitoring, vertical seismic surveys, crosswell seismic monitoring, remote sensing of surface deformation, near-surface seismic activity monitoring, reservoir pressure monitoring, borehole deformation sensors, and other

technologies. Methods are described in terms of borehole requirements, field application, results, processing, approximation costs, and limitations.

5.1 Geophysical Logging

Borehole geophysical logs are the most common tools to characterize the subsurface and assess the risks associated with drilling, injection, and fluid storage. Various common and advanced logging tools can be used to evaluate different petrophysical and geomechanical properties of subsurface formations in terms of lithology, porosity, anisotropy, rock strength, in-situ stresses, faults, and fractures. Such tools include gamma ray log, resistivity, neutron, bulk density, multi-component sonic, multi-component induction, pulsed neutron spectroscopy, and image logging tools (Table 5-1). These tools can be utilized for CO_2 injection and storage related to geomechanical site characterization.

Generic petrophysical logs can be acquired for a comprehensive geomechanical evaluation of CO_2 storage sites. Each tool has limitations in terms of resolution, time, cost, and manufacturer support (Table 5-1). Manufacturers should be consulted when choosing logging tools because their operational standards and procedures vary significantly. Examples of manufacturer differences include, but are not limited to, borehole size, borehole environment (high-pressure and/or high-temperature), type of drilling fluid, and presence of casing. In addition, most of the advanced tools require petrophysicists or formation evaluation engineers for proper borehole geophysical data processing and interpretation. Costs associated with logging include logging crew, equipment, transportation, cranes (if needed), wireline, and processing fees.

5.1.1 Basic Well Logs

Basic well-logging tools (such as quad-combo logging package) are typically run to obtain a general understanding of lithology, mineralogy, porosity, and density. Gamma ray measures natural gamma radiation from the formation, which is used to interpret general lithology. After characterizing lithology, all porosity tools (neutron porosity, bulk density, and sonic) should be used to characterize primary intergranular porosity. Secondary porosity is the porosity attributed to the possible presence of fractures and faults or vugs. Porosity measurements can be used to determine the quality of targeted reservoirs and estimate their fluid storage capacity. Sonic porosity can also be useful to calculate subsurface pore pressure, which is important for designing a safe mud weight window and attaining wellbore stability. In combination, these basic measurements are critical components for subsurface studies. However, advanced well logs are necessary to gain an adequate understanding of subsurface geomechanics for long-term storage and monitoring of a CO_2 injection well.

5.1.2 Advanced Well Logs

Multi-component Sonic: This logging tool can measure compressional P-waves (V_P) and S-waves (V_S) oriented on both the fast and slow azimuth, and Stoneley waves (Stoneley wave capability is limited to certain vendor tool capabilities). Both V_P and V_S logs are important to characterize elastic moduli (such as Young's modulus, Poisson's ratio, bulk modulus, and shear modulus, etc.). Elastic moduli analysis is significantly important to estimate rock strength and in-situ stresses, and can be used to determine the fracture intensity distribution.

Table 5-1: Descriptions of basic and advanced logs for CO_2 storage.

Logging tools	General functions	General limitations	Estimated relative total cost per 2,000-ft interval[a]
Gamma ray	Measures natural gamma radiation from formations that can be used to interpret lithology, and control depth information	Resolution: ~12” (vertical), ~24” (horizontal); logging speed: 3,600 ft/hr (open-hole), 180-450 ft/hr (LWD).	Medium
Neutron porosity	Measures hydrogen index in formations as a porosity indicator	Resolution: 12”-22” (vertical), ~9” (horizontal); logging speed: 1,800 ft/hr (open-hole), 90-180 ft/hr (LWD). Bad borehole conditions, e.g., washout, and high clay volume can affect neutron measurements.	Medium
Bulk density	Measures formation density through gamma ray scattering. Formation porosity can be derived from density logs, if matrix lithology is known.	Resolution: ~10” (vertical), < 6” (horizontal); logging speed: 1,800 ft/hr (open-hole), 450 ft/hr (LWD). Density logs can be affected by bad borehole conditions (e.g., washout) and type of drilling mud used (e.g., barite).	Medium
Sonic	Measures compressional sonic velocity that can be used to distinguish lithology, fractures, and generate synthetic seismogram for well-seismic tie	Resolution: ~24” (vertical), ~3” (horizontal); logging speed: 4,500 ft/hr (open-hole), 1,800 ft/hr (LWD). Borehole rugosity and gas-bearing unconsolidated, and/or fractured formations can affect sonic measurements.	Included in multi-component sonic
Multi-component sonic	Measures Vp, Vs, and potentially Stoneley waves that can be used to derive elastic moduli and anisotropy	Resolution: 2”-24” (vertical), 24”-36” (horizontal); logging speed: ~3,600 ft/hr (open-hole), 1,800 ft/hr (LWD).	Medium
Multi-component induction	Measures azimuthal resistivity in different directions that can be used for fracture analysis	Resolution: ~4’ (vertical), 6’- 9’ (horizontal); logging speed: 1,800 ft/hr (open-hole).	High
Elemental spectroscopy	Measures individual elemental composition to evaluate formation mineralogy	Resolution: 18” (vertical), 6”-9” (horizontal); logging speed: 1,800 ft/hr (open-hole).	Medium
Image logging	Produces 3D borehole view of resistivity and/or acoustic reflectance	Resolution: 2”-24” (vertical), 1”-12” (horizontal); logging speed: 600-1,800 ft/hr (open-hole), 150 ft/hr (LWD). Data acquisition and analysis are time-intensive and expensive.	High

Note: LWD = logging while drilling.

a. Estimated costs include logging and processing a 2,000-ft interval, excluding crane, transportation costs, discounts, and additional miscellaneous charges. Costs are described in terms of low ($0-$100s), medium ($1,000-$10,000s), and high ($100,000-$1,000,000s).

Multi-component sonic tools can also be used to identify the presence of acoustic anisotropy in a rock, because shear waves propagate with different velocities (V_S_fast and V_S_slow) in different directions in a homogeneous anisotropic and heterogeneous anisotropic medium (Veltman et al., 2012). The study of acoustic anisotropy is valuable in borehole stress analysis, fractured reservoir characterization, and tectonic studies, all of which are necessary for safe containment of CO_2 in the subsurface. Stoneley waveform should also be analyzed because its attenuation and reflection coefficients can indicate, among other things, open, permeable fractures (Bammi et al., 2015; Endo et al., 1998).

Multi-component Induction: This tool is sensitive to changes in azimuthal resistivity. It includes multi-directional coil-based magnetic field measurements (one vertical and two co-axial horizontal resistivity components) that can detect azimuthal resistivity variations caused by vertical, sub-vertical natural or drilling-induced fractures. Such tools can be used to estimate fracture length, orientation, and aperture. They can also be used to better analyze deviated boreholes, tilted formations, and sedimentary structures, because electric current flow pattern changes with different directions. Multi-component induction tools can be combined with multi-component sonic logs for fracture characterization (Kriegshauser et al., 2005).

Elemental Spectroscopy: These logs can be used to derive multi-mineral solutions. Evaluation of multi-mineral solutions can give a better understanding of formation mineralogy and porosity that can be used to analyze which formations and facies are relatively ductile and brittle, and more fracture-prone. Thus, a “pseudo” geomechanical log can be constructed in certain cases (Bemer et al., 2004). Delineation of brittle and ductile units can be useful to characterize fracture intensity and its extent in the reservoir and seal components of CO_2 storage sites. Conventional or quad-combo well logged-based data can be calibrated to local elemental spectroscopy data to derive deterministic and/or statistical multi-mineral solutions, which can later be applied to all wells without elemental spectroscopy logs for a regional-scale study.

Image Logging: Image logs are essentially high-resolution wellbore (360-degree) views of resistivity and/or acoustic reflectivity measurements. They can provide important structural and sedimentological information, which can be used for geomechanical evaluation. Interpretation of a fully processed image log contains detailed information about different bedding and fracture styles, fault/fracture orientation, aperture and length, and stress regimes (Shahinpour, 2013). The present day in-situ stress field can be evaluated using borehole breakouts and DITFs. Analysis of these parameters allows a better understanding of the subsurface fracture network, wellbore stability, seal integrity, and their potential effects on fluid injection and storage. This logging approach can help to delineate low-risk to high-risk segments of the subsurface reservoir and seal formations for CO_2 storage.

5.2 Rock Core Testing

Rock core tests are often the most definitive method for determining geomechanical properties of rocks, because they provide a direct measurement on a rock sample. Methods are described in terms of borehole requirements, laboratory methods, results, processing, costs, and limitations. Rock core testing requires physical samples of a rock, usually obtained from a well at depth (Figure 5-1).

Figure 5-1: Conventional whole core, sidewall core, and drill cutting rock samples.

Conventional or whole core is obtained by advancing a corebit and core barrel attached to the drill string. Whole core is usually 1.75 to 5.00 inches in diameter and collected in 30-ft increments up to 330-ft sections. Various core barrel options are available, depending on downhole conditions and preservation requirements. Wireline tools are available to collect smaller-diameter full core in shorter lengths. Sidewall cores are obtained with a wireline tool that drills the core in the side of the borehole. Sidewall cores are usually 1 inch in diameter by 1.75 inches in length. Drill cuttings and surface outcrop samples can also be used for testing, but these samples may be too broken up to reflect downhole rock fabric. Most geomechanical testing is best performed on cylindrical plugs cut from whole conventional core that is intact, undamaged by drilling, and at least 6 to 12 inches long to allow collection of a core plug. The plugs are drilled through the side of the core and the ends of the plug are ground flat for testing. For static tests at confined conditions, the plug is placed in a pressure vessel filled with hydraulic oil and pressurized to the assigned confining pressure.

Core Description. Core description involves visual inspection of a rock sample and general description of lithology, rock grains, texture, depositional features, fossils, minerals, cement, porosity, diagenesis, and other geologic features. Natural fractures, mineralization, healed faults, and mineral deformation are of special interest to geomechanical characterization. Core description is a fundamental portion of rock core examination, best completed by an experienced geologist familiar with the rocks in the region. A thorough rock core description requires little equipment other than a petrographic microscope and/or hand lens.

Bulk Density. Bulk density of a rock sample is a basic measurement performed on plug or full core samples. Bulk density can be determined by several methods (such as caliper, water displacement, or wax immersion) at a fairly low cost. The water displacement and wax immersion methods can be less accurate with high- or very low-porosity samples. Fluid can get trapped in the pore spaces or the sample may not dry completely, causing erroneous data to be collected. Rock density is often a useful indicator of many geomechanical parameters.

Ultrasonic Compressional Wave Velocity / Slowness. Ultrasonic compressional wave velocity/ slowness is a measurement of compressional, or P-wave, sonic velocity through a rock sample in the direction of propagation under confining pressure. The wave velocity is typically measured with a sonic instrument applied to the core sample. The sonic P-wave velocity can be used to determine other geomechanical parameters and calibrate geophysical logs where borehole fluids or conditions have affected logging results. This method will destroy the samples.

Ultrasonic Shear Wave Velocity / Slowness. Ultrasonic shear wave velocity/slowness is a measurement of perpendicular, or S-wave, sonic velocity through a rock sample. The S-wave velocity is typically measured with a sonic instrument applied to the core sample under confining pressure. The sonic S-wave velocity can be used to determine other geomechanical parameters and calibrate geophysical logs where borehole fluids or conditions have affected logging results. This method will destroy the samples.

Triaxial Compressive Test. The triaxial compressive test is a basic geomechanical core test in which a core plug is subjected to pressure load at both ends at a specified confining pressure until failure. The test provides static compressive strength, static Young's modulus, and Poisson's ratio. Figure 5-2 shows the stress-strain curve from a triaxial core test. The red slope reflects radial strain and the blue curve shows axial strain. The steeper the blue axial curve, the higher the static Young's modulus, and more resistant the rock is to axial deformation. In this case, the modulus was 7.09 × 10^6 pounds per square inch (psi). The ratio of the radial and axial strain curves is the static Poisson's ratio; the closer the curves are to each other, the higher the Poisson's ratio. Compressive strength was measured at 25,753 psi, because the rock could withstand that pressure before fracturing.

Static Compressive Strength. Static compressive strength is a measure of rock failure strength, which is determined from stress-strain curve testing of a core plug. Compressive strength is a basic geomechanical parameter included with triaxial rock core testing under confined conditions. Like many tests, it is inaccurate if performed with damaged or unconsolidated cores, which may provide inconclusive test curves.

Static Young's modulus. Static Young's modulus is a measurement of axial strain-slope under confining conditions. Confining conditions are specified for the test based on sample depth. It is a fundamental measurement of rock strength necessary for geomechanical analysis. Damaged or unconsolidated cores may limit the test results.

Static Poisson's ratio. Static Poisson's ratio is a measure of the axial-to-radial strain under confined conditions. The ratio is another fundamental measurement of rock deformation potential used for many types of geomechanical analysis (Gercek, 2007). Static Poisson's ratio is a typical measurement of the triaxial compressive test.

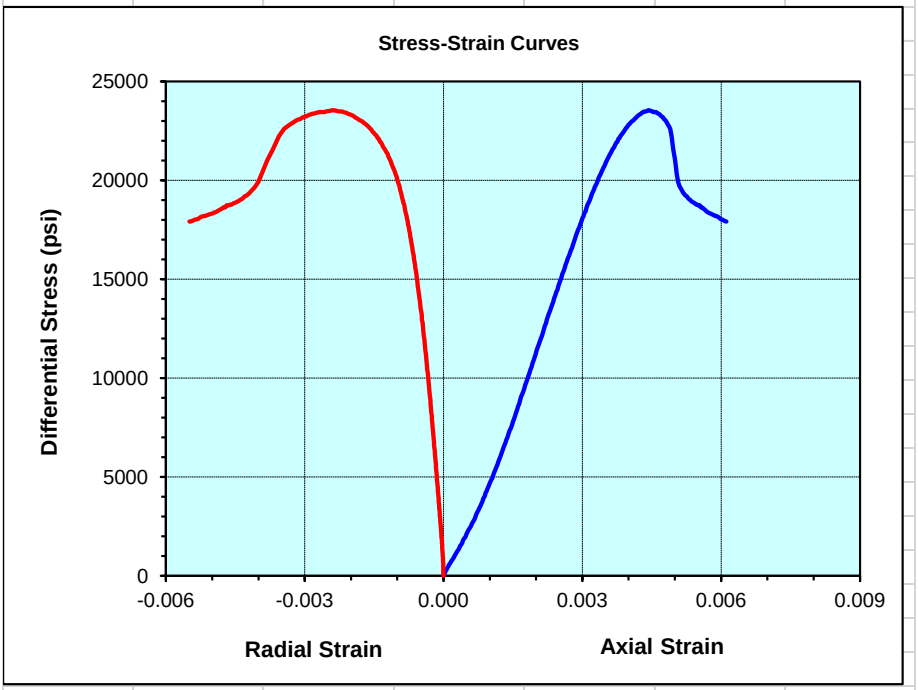

Company	Battelle Memorial Institute		Project	DOE-FE0023330	
Sample No.	3-1RMV		Depth (ft)	6904.00	
Confining Pressure (psi)	2200		Bulk Density (g/cc)	2.67	
Compressive Strength (psi)	25753		Young's Modulus (10^6 psi)	7.09	
Saturation State	As Is		Poisson's Ratio	0.30	

Figure 5-2: Example triaxial compressive test.

Unconfined Compressive Strength. Unconfined compressive strength is a measure of rock failure strength, which is determined by applying constant axial load to the core plug under zero confining pressure until the rock fractures. Unconfined compressive strength is not as indicative of rock properties at depth because it is measured under unconfined conditions.

Dynamic Young's modulus. Dynamic Young's modulus is a measurement of axial strain-slope under unconfined conditions. It is similar to static Young's modulus, but the results are usually higher because the rock is not subject to confining pressure (Figure 5-3). Dynamic modulus may be derived from acoustic geophysical logs; a rock core test is a useful calibration point for checking on geophysical logs.

Dynamic Poisson's ratio. Dynamic Poisson's ratio is a measure of the axial-to-radial strain under unconfined conditions. It is similar to static Poisson's ratio, but it is measured without confining pressure. In general, dynamic rock properties are more relevant to applications occurring in shallow conditions where there is not as much confining pressure.

Dynamic bulk modulus. Dynamic bulk modulus is a measure of the change in overall rock volume under pressure under unconfined conditions. It is a function of the rock's total elastic deformation potential under pressure.

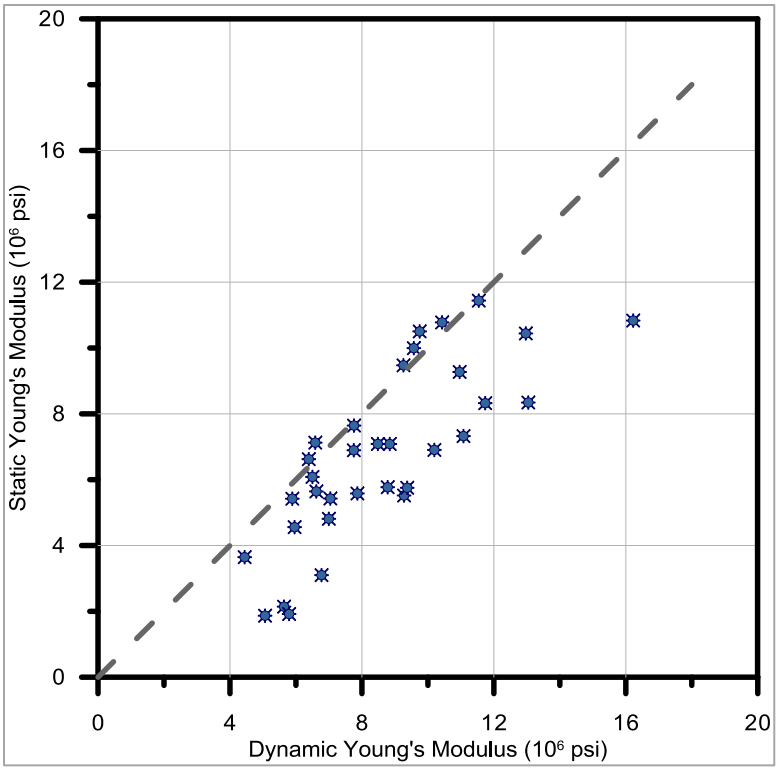

Figure 5-3: Plot of dynamic Young's modulus versus static Young's modulus from rock core test data collected under this project. The plot illustrates how dynamic Young's modulus is usually higher than the static modulus.

Dynamic shear modulus. Shear modulus is measured on a sample under a shear pressure testing setup, where the sample is subject to cross/shear stress under unconfined conditions. The shear modulus is not typically used for geomechanical analysis.

Brazilian Tensile Strength. The Brazil test measures sample resistance to tensile stress. The test differs from a triaxial test in that the load is applied along the length of a core plug until failure. The test provides a measure of the tensile failure point of the rock, which is usually much lower than the compressive strength.

Fracture Toughness. For samples with pre-existing fracture, a fracture toughness test provides a measurement of the sample's resistance to fracturing. The sample is loaded with pressure until it breaks along the fracture, and the pressure at fracturing is the test result. The test requires a competent sample with a pre-existing natural fracture. Consequently, it is not very commonly measured.

Permeability. Permeability is a measure of fluid/gas flow potential in a rock sample. Permeability is typically measured with a gas permeameter on a core plug from a rock core. Permeability is an indirect parameter for geomechanical characterization.

Porosity. Porosity is a measure of the fraction of pore space in the overall sample volume. Several methods are available for determining porosity from rock cores, including, but not limited to,

sampling saturation/drying, Dean-Stark analysis, Boyle's law, and thin-section image analysis. Porosity is an indirect parameter for geomechanical characterization.

Mercury Injection Capillary Pressure (MICP). Mercury injection capillary pressure (MICP) tests are used to determine properties of very low-permeability rocks, such as caprocks. The test provides measurement of permeability, pore throat diameter, and pore space tortuosity. The test is more of an indirect measurement that helps to describe caprock properties.

Thin-Section Mineralogy. A thin section is a 30-micrometer (µm)-thick slice of rock sample prepared for analysis under a petrographic microscope. Thin sections provide an understanding of minerals, grain size distribution, porosity, cementation, and sedimentary features at small scales (25X to 200X magnification). Thin sections show small-scale features such as fractures and cements that lend insight into geomechanical rock parameters.

Computed Tomography (CT) Scan. Computer tomography (CT) scan refers to a computerized X-ray scan through a rock sample. The CT scan can be performed at various orientations and resolutions to visualize pore space geometry, fractures, and other features. CT scans do not provide a direct quantitative measurement, but image processing can be used to estimate porosity, tortuosity, and other parameters.

X-ray Diffraction. X-ray diffraction provides an estimate of mineral abundance in a small, crushed or powdered rock sample. The machine provides a diffractogram curve reflecting fractions of elements in the sample. The results can be used to understand rock mechanics based on mineralogy. Since X-ray diffraction requires very small amounts of rock (5 to 10 grams), the method can be used with chips or cuttings.

Scanning Electron Microscopy (SEM). Scanning electron microscopy (SEM) uses a high-power electron microscope to provide images of samples at 100X to 5,000X magnification. The method can be used to illustrate crystalline structures, cement, and porosity. It can be used on chips, cuttings, or small rock fragments.

Overall, the results of rock core testing provide information on many essential geomechanical rock properties (Table 5-2). The testing allows a conclusive, direct measurement of a rock sample. For CO_2 storage applications, static rock properties (static Young's modulus and static Poisson's ratio) are important factors, because they have a large effect on the development of fractures in reservoir or caprocks (Nygaard, 2010). The static properties are also more appropriate for analyzing geomechanical properties in deeper zones (deeper than 3,000 ft), which are the most likely zones for CO_2 storage projects. These parameters help demonstrate the potential for subsurface fracture development caused by CO_2 injection in terms of fracture breakdown pressure, fracture geometry, fracture width, and fracture extent (Barree and Miskimins, 2015). Core tests are limited to a spot test of a small portion of the rock. In addition, core collection and testing can be expensive and time consuming. Consequently, core tests are often used to calibrate geomechanical data derived from geophysical logs. Other core tests such as bulk density, porosity, mineralogy, permeability, CT scan, X-ray diffraction, and SEM can be used to further characterize trends in rock properties.

Table 5-2: Core description and results.

Method	Description	Sample	Lab method	Results	Cost[a]	CO_2 application	Limitations
Core description	General description of rock grains, fabric, color, and physical features	Core or chip	Sample examination with petrographic microscope	Sample description, general abundance of minerals	Low	Provides basic understanding of rock, features, facies, grains	Results may be somewhat subjective, requires larger sample
Bulk density	Lab test of sample mass over bulk volume	Full core or plug	Caliper, water displacement method, wax immersion	Bulk density of sample	Low	Indicator of rock porosity, strength, used for overburden calculation	Non- continuous, high/low porosity samples may have erroneous results
CT scan	Computed axial tomography scan through rock sample	Full core or core plug	Computerized X-ray scan to generate cross-sectional views through core sample	Image of slices through rock	Low	Shows nature of porosity, fractures, variations within rock	Resolution limited to larger features, spot sample
Ultrasonic compressional wave velocity /slowness	Sonic velocity in direction of wave propagation	Core plug	Ultrasonic instrument applied to core plug	Sonic velocity (ft/s) /slowness (µs/ft)	Low	Used to estimate Young's modulus of elasticity, Poisson's ratio, and calibrate geophysical logs	Destructive method
Ultrasonic shear wave velocity /slowness	Sonic velocity perpendicular to wave propagation direction	Core plug	Ultrasonic instrument applied to core plug	Sonic velocity (ft/s) /slowness (µs/ft)	Low	Used to estimate Young's modulus of elasticity, Poisson's ratio, and calibrate geophysical logs	Destructive method
Static compressive strength	Measure of rock capacity to resist deformation at load under confining conditions	Core plug	Apply axial load to core in pressure vessel under constant confining pressure while measuring axial and radial strain until failure	Compressive strength value based on stress-strain curve (psi or MPa)	Medium	Measure of rock failure strength	Measured at user input confining pressure, destructive method
Static Young's modulus	Slope of axial strain under differential stress under confining conditions	Core plug		Pressure value illustrating axial strain slope (psi or GPa) under confined conditions	Medium	Key parameter for analyzing geomechanical deformation potential under injection pressures	Measured at user input confining pressure, destructive method
Static Poisson's ratio	Ratio of axial to radial stress/strain slope measured confined conditions	Core plug		Axial/radial strain ratio under confined conditions	Medium	Key parameter used to estimate fracture development	Measured at user input confining pressure, destructive method, sometimes curves are not clear
Dynamic Young's modulus	Slope of axial strain under differential stress under unconfined conditions	Core plug	Apply axial load to core under unconfined conditions while measuring axial and radial strain	Pressure value illustrating axial strain slope (psi or GPa) under unconfined conditions	Low	'Soft' rock modulus for elastic deformation	Destructive method
Dynamic Poisson's ratio	Ratio of axial to radial strain under unconfined conditions	Core plug		Axial/radial strain ratio under unconfined conditions	Low	'Soft' rock parameter used to analyze fracture development	Destructive method
Dynamic bulk modulus	Measure of change in overall rock volume at pressure under unconfined conditions	Core plug		Pressure ratio (psi or MPa)	Low	Indicator of overall elastic deformation potential for rock sample	Destructive method
Dynamic shear modulus	Ratio of shearing stress to shearing strain unconfined conditions	Core plug		Pressure ration (psi or MPa)	Low	Indicator of shear failure potential in rock	Destructive method
Brazil tensile strength	Measure of strain due to tensile stress	Core plug	Apply tensile load to core while measuring axial strain	Tensile strength (psi or MPa) and max load	Low	Tensile strength for	Destructive method
Permeability	Measure of fluid/gas flow potential in rock sample	Core plug	Measure flow rate and pressure differential at different pressure gradients in permeameter	Permeability to air and est. Klinkenberg permeability (mD or cm^2)	Low	Used to analyze fluid/gas movement in rocks	Difficult in damaged or fractured samples, best for moderate-high permeability (>0.001 mD)
Porosity	Measure of pore space in rock	Core plug	Sample drying and saturation, Dean Stark, Boyles, or similar	% pore volume / bulk volume	Low	Indicator of rock properties, fluid saturation	Difficult in shales
MICP	Mercury injection capillary pressure test for low permeability rocks	Core plug	Mercury flow cell	Pore throat diameter, porosity, saturation, permeability, J function	Medium	Used to analyze capillary entry pressure for caprocks	Best for low permeability caprocks

Table 5-2: Core description and results (continued).

Method	Description	Sample	Lab method	Results	Cost	CO_2 application	Limitations
Mineralogy thin section	Description of minerals, grains, pore spaces in rock sample	Thin section from core sample	Thin-section examination with petrology microscope	Mineral abundance, visual image of pore space	Low	Used to determine rock grains, porosity distribution	Qualitative, spot sample, doesn't capture larger features
X-ray diffraction	X-ray diffraction on powdered sample	Chip or core sample	Rock sample powdered and analyzed with XRD machine to develop curve showing elemental percentages	Bulk mineral composition	Low	Used to provide quantitative elemental breakdown of minerals in rock sample	May require clay analysis
SEM	Scanning electron microscopy on sample	Chip or core sample	Rock sample examined under SEM device to produce image of rock surface at 10- to 100-µm scale	Images of texture, morphology, cements, and particles	Low	Provides high resolution morphology of minerals, cement, porosity	Susceptible to sample contamination, spot sample

Note: CT = computed tomography; ft/s = feet per second; µs/ft = microseconds per foot; psi = pounds per square inch; GPa = gigapascal; MPa = megapascal; mD = millidarcy; cm^2 = square centimeter; MICP = mercury injection capillary pressure.

a. Costs are described in terms of low ($0-$100s), medium ($1,000-$10,000s), and high ($100,000-$1,000,000s).

5.3 Well Testing for Determination of Geomechanical Properties

For the purposes of measuring geomechanical properties, well tests are continuous pressure measurements taken at the well (either downhole or at the wellhead) as a small volume of fluid is injected into an interval of the formation and then allowed to stabilize. These fluid injection tests are performed mainly to extract the magnitude and the orientation of each of the two principal horizontal stresses within the formation, referred to as the maximum (S_{Hmax}) and minimum (S_{hmin}) horizontal stresses. These quantities are useful for calculating risks associated with injecting into a formation (e.g., risks of creating/activating tensile or shear fractures, identifying stable well trajectories), and for running coupled fluid flow-geomechanical simulations that model the poro-elastic effects of CO_2 injection. Costs for well testing are medium to high, because testing requires a large amount of equipment, well preparation, rig time, and analysis. Some of the more specialized testing methods for geomechanical aspects can be especially expensive because they are not typical procedures for oil and gas service companies.

5.3.1 Common Hydraulic Fracture Tests

There are essentially two types of hydraulic tests associated with fracture testing: the hydraulic fracture (HF) test and the hydraulic test of pre-existing fractures (HTPF). The HF tests are also often referred to as “DFIT™” (Diagnostic Fracture Injection Test), “mini fall-off” (MFO), “mini-frac”, and “micro-frac” tests. Similarly, “step-rate” tests and “hydraulic jacking” tests refer to HTPFs. Both HF tests and HTPFs are very similar in terms of equipment needed, costs, and the nature of the measurements made; they are often performed in succession. They differ in terms of three factors: 1) the number of tests required, 2) the type of result obtained (and hence the methodology applied to analyze the measured data), and 3) near-wellbore conditions required to be applicable. HF tests are performed in intervals where there are no fractures, while HTPFs are performed with the intent of activating existing fractures.

Typically, multiple HF tests and HTPFs are performed to adequately characterize the uncertainty in the derived parameters. Generally, while HF tests only enable the determination of S_{hmin} (magnitude and direction), an HTPF is usually performed after a HF test in order to constrain the estimates of S_{hmin} and S_{Hmax}. While the procedure for determining S_{Hmax} is fairly complex (an inversion of the test results from both HF tests and HTPFs to determine the full stress tensor), the procedure for S_{hmin} is relatively straightforward. Graphical manipulations are sufficient to determine the upper and lower bounds for the magnitude of S_{hmin}. Finally, the wellbore imaging that is performed at the end of each test allows a very precise measurement of the orientations of the minimum and maximum horizontal stresses. Well testing options are summarized in Table 5-3.

5.3.2 Test Procedures

Both HF and HTPF tests involve the injection of a small volume of fluid, such that the inflection points of the pressure profile shown in Figure 5-4 can be measured. While the HF test is carried out at a constant rate, the HTPF test involves a systematic and gradual step-wise increase in the injection flow rates until peak pressure is obtained.

The idealized pressure response during a HF test is described below and is essential to understanding the terminology associated with the procedure for interpreting well tests.

Table 5-3: Essential differences between the two categories of well tests.

Relevant comparisons	HF test	HTPF test
Near-wellbore conditions	No fractures	Fractured
Pre-test requirements	None	A few HF tests must have been performed
Number of tests	1-3 are sufficient	> 2, but as many as possible, total number of tests including HF tests must be >5. This ensures that there is sufficient information to perform the stress tensor inversion.
Type of analysis	Graphical manipulations to determine magnitude. Visual examination to determine orientations.	Inversion of at least 5 equations to solve for the full stress tensor.
Magnitude of S_{hmin}	√	√
Orientation of S_{hmin}	√ (if fracture imaging is possible)	√
Magnitude of S_{Hmax}	Generally, no (qualitative estimates in some cases)	√
Orientation of S_{Hmax}	√ (if fracture imaging is possible)	√

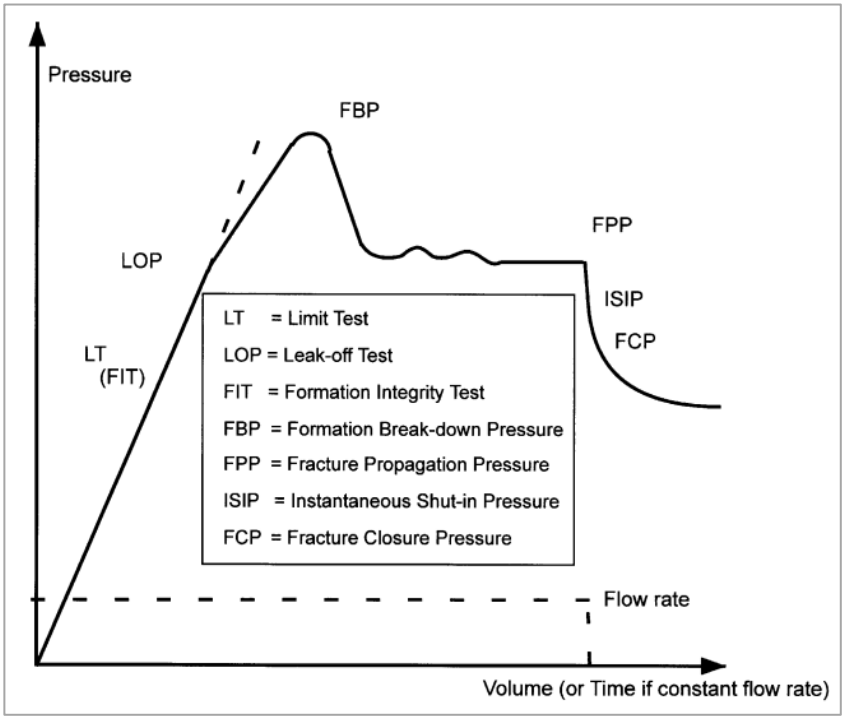

Figure 5-4: An idealized pressure profile during a HF test with constant injection rate (after Zoback et al. [2003]).

Test Terminology

Leak-off Point (LOP). As injection commences, the downhole pressure rises linearly up to the LOP. During this period, no fractures have formed and the pore pressure rises due to the viscoelasticity of the rock. If the test is stopped before the LOP is reached, then this test is called the Formation Integrity Test (FIT) and the data can be used to glean information about the injectivity and other near-wellbore effects of the formation. The LOP represents the highest pressure beyond which tensile fractures will be created.

Formation Breakdown Pressure (FBP). With further injection beyond the LOP, pressure continues to rise, although not as steeply. A climax is reached at formation breakdown pressures (FBPs). This pressure measurement is important to determine the pressure threshold that, when breached, will result in fractures that will propagate into the formation.

Fracture Propagation Pressure (FPP). With still further injection beyond the FBP, pressure falls toward the pressure at which the tensile fractures (created when formation pressure has crossed the FBP) begin to extend and grow into the formation from the wellbore. The FPP is a pressure greater than the minimum in-situ horizontal stress at which fractures are extended.

Instantaneous Shut-In Pressure (ISIP). After pressure has fallen toward the FPP (because of continued injection), if the injection is stopped abruptly, the pressure also immediately falls to the ISIP as there are no longer frictional pressure losses. The ISIP is generally tough to discern but is viewed as being a more accurate estimate of the pressure required to propagate the fracture, or a better constraint on the minimum in-situ horizontal stress.

Fracture Closure Pressure (FCP). Continued measurement of the pressure decay beyond the ISIP after injection has stopped will also include a record of FCP, which is said to be the closest estimate of minimum in-situ horizontal stress (Nelson et al., 2007). Like the ISIP, this quantity is also often difficult to ascertain precisely from the curve. The FCP is also the last pressure point beyond which the data no longer carry geomechanical information, but are influenced by reservoir properties instead.

Test Procedure

The procedure for conducting HF tests is summarized below. Figure 5-5 provides an illustrative example of the procedure.

After the target zone has been drilled and the well has been circulated clean, straddle-packers are run through the tubing to seal the test interval by pumping water down the tubing. Time and cost permitting, a packer integrity test and a short slug test are recommended before commencing the actual test.

Next, fluid is injected at a constant flowrate into the interval, allowing the pressure to rise to beyond the FBP and creating a hydraulic fracture. After a short period of sustaining the pressure, the injection is stopped and the well is shut in to record two events: 1) a decay and 2) a subsequent 50% recovery (approximately) in the interval pressure. Venting the well of the remaining injected fluid and pressure by opening the wellhead valve completes the procedure for the chosen interval. This process is typically repeated two to three times with the same flowrate for redundancy and reproducibility of results before moving to the next interval. An image log is run at the end for a record of the fractures created.

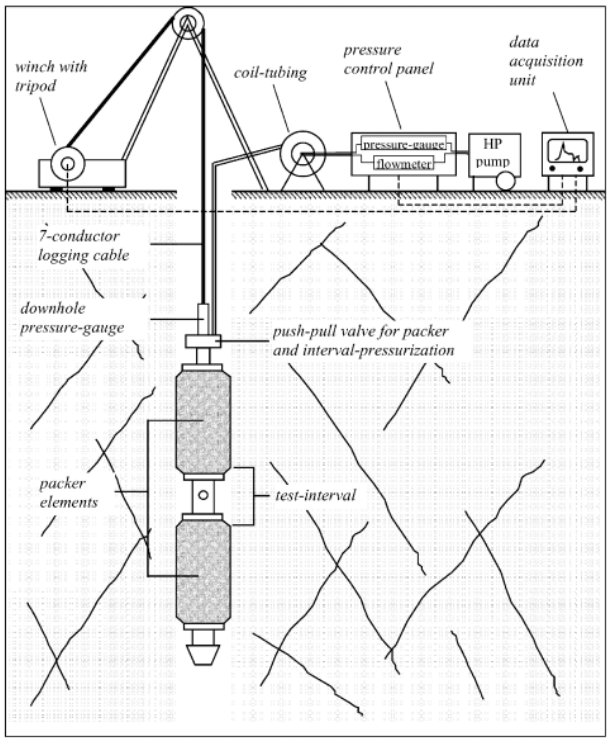

Figure 5-5: Schematic of equipment for a HF test (from Ljunggren et al. [2003]).

The procedure for the HTPF test is essentially identical to that of the HF test, except injection is performed over a series of increasing rates (a “step-rate” manner). HTPF tests are typically performed right after HF tests have been performed on the interval. Beginning with a low injection rate, injection is performed at a constant rate until pressure rises and obtains equilibrium. The injection rate is then raised incrementally until the pressure stabilizes, around five times. With the highest injection rate (pressure does not reach equilibrium and peak pressure is obtained), injection is ceased without venting the fluid, and sufficient time is allotted for recording the pressure decay. This entire cycle is repeated at least three times. Note that a similar step-rate *depressurization* cycle can be employed at the end of each cycle to obtain data (measurements) used to extract the shut-in pressure.

Figures 5-6 and 5-7 illustrate the procedure described above in terms of recorded pressures and rates.

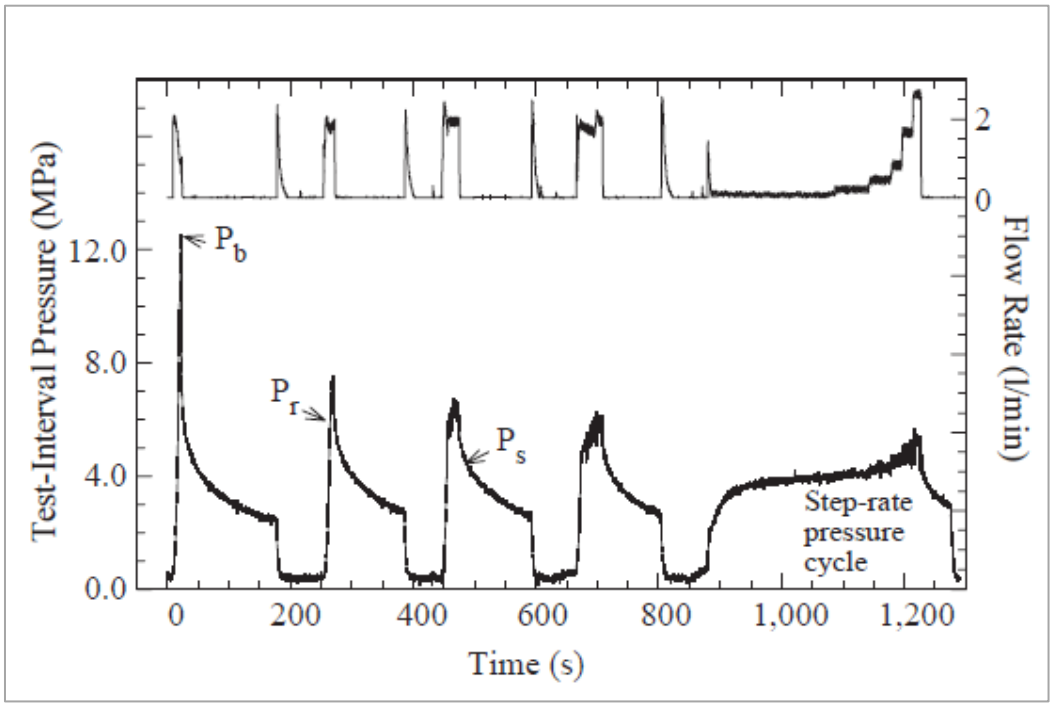

Figure 5-6: Series of HF tests followed by a HTPF test (P_b, P_r, and P_s refer to the breakdown pressure, fracture reopening pressure, and shut-in pressure, respectively. These data are then further analyzed to extract P_r and P_s more accurately (from Haimson and Cornet [2003]).

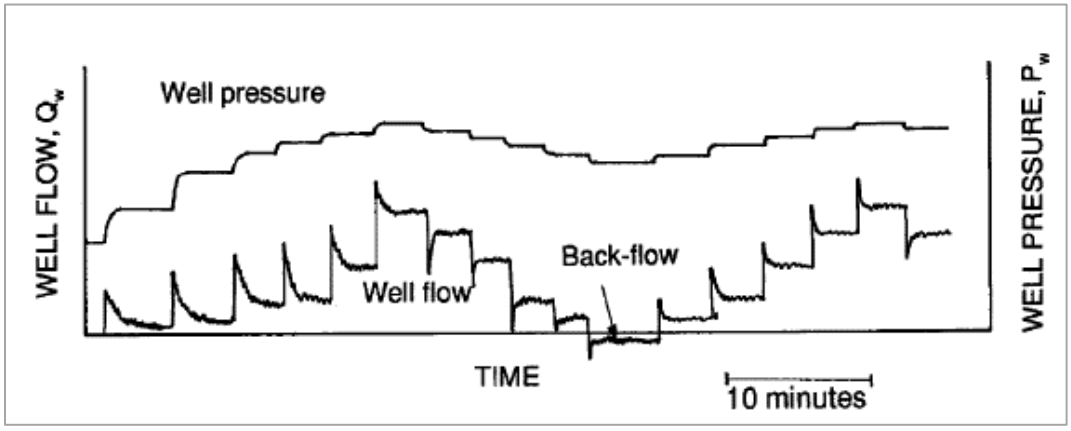

Figure 5-7: Depressurization step-rate cycle test in between two pressurizing step-rate cycle tests. Three sets of data have been obtained from these HTPF tests to determine the shut-in pressure (from Haimson and Cornet et al. [2003] and Rutqvist and Stephansson [1996]).

5.3.3 Analyzing Results

For vertical wells, analyzing the image log data (Figure 5-8) to determine the orientation of the maximum and minimum horizontal stresses is straightforward. The hydraulic fractures created are generally in the direction of the maximum horizontal stress (opening perpendicular to the direction of minimum horizontal stress), and are parallel to the wellbore.

Constraining the magnitude of S_{hmin} involves determining upper and lower bounds to the shut-in pressure. The lower bound is typically obtained by the method developed by Aamodt and Kuriyagawa (1981), which involves an empirical description for the pressure decay *after* the fracture has *closed*. The lower bound for the shut-in pressure is extracted from the late-time portion of the pressure data, the highest value of wellbore pressure for which the recorded decay follows the empirical description. On a semi-log plot, this pressure is described as the highest value of P_{wb} for which a linear relationship may be fit (Figure 5-9).

The method recommended by Cornet et al. (2003) is employed to determine the upper bounds of this shut-in pressure. They recommend fitting a parabola to the pressure data. A parabola is fit to this curve using an increasing number of points from the pressure data, and the corresponding root-mean-squared error (RMSE) is calculated for each (Figure 5-10). Generally, as the number of points included in the parabola calculation is increased, the RMSE is expected to increase, stabilize and then decrease. At the point where the pressure decay does not follow the expected behavior, the RMSE begins to increase again, and this inflection point defines the upper-bound estimate.

These quantities for the upper and lower bounds define the 99% confidence interval for the shut-in pressure. An illustration of these graphical techniques is shown (Figure 5-11) using the results from an HF test performed in the Mount Simon Formation (Cornet, 2004).

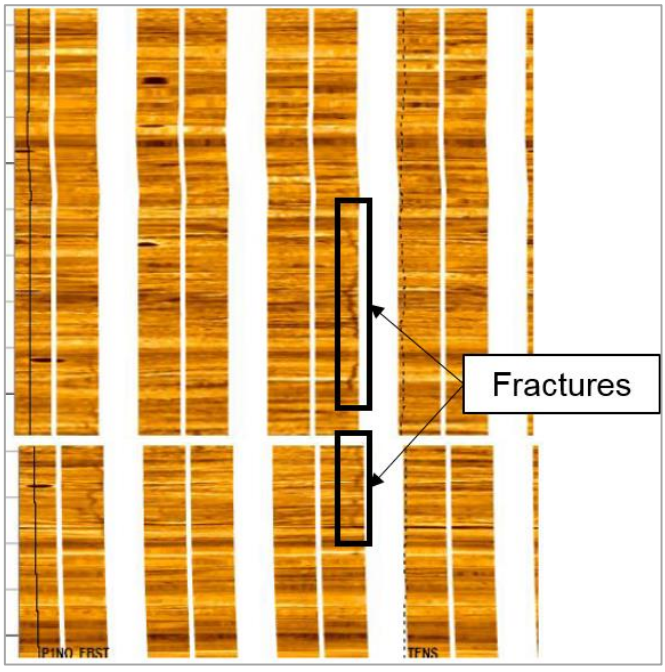

Figure 5-8: Image log of the wellbore after HF testing (Cornet, 2004).

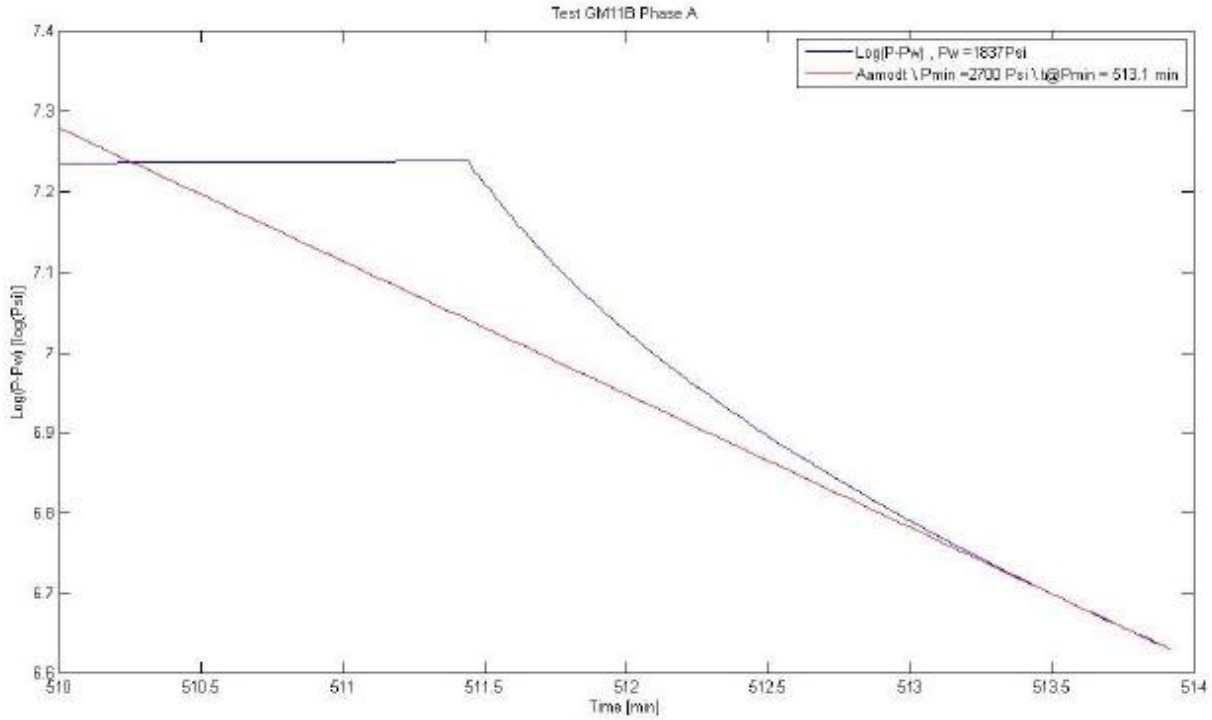

Figure 5-9: Semi-log plot of the pressure decay data obtained from a HF test. A straight line has been fit to late-time portion to determine the lower bound of the shut-in pressure.

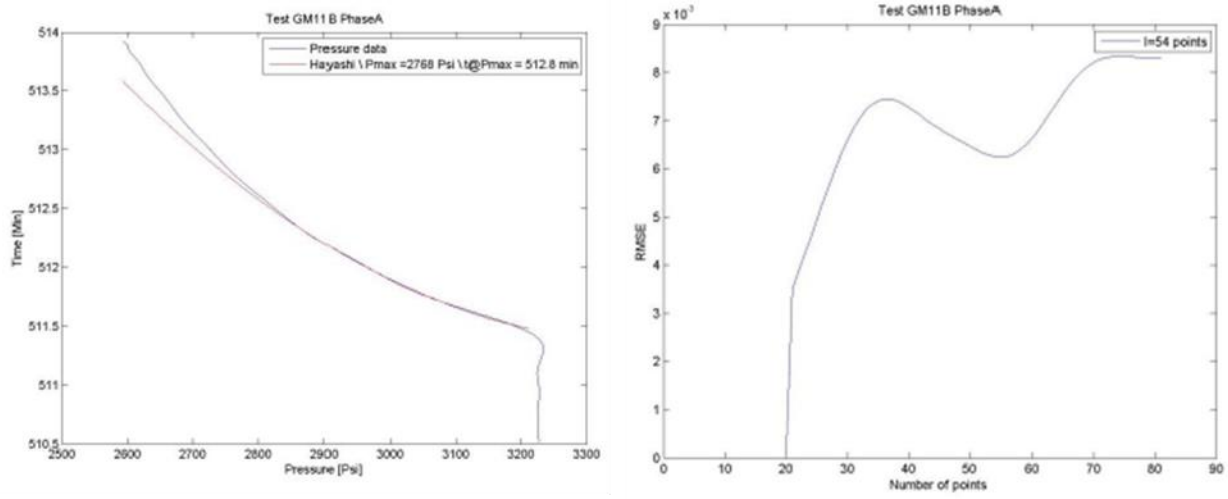

Figure 5-10: Left: Behavior of the RMSE as an increasing number of points are fit to the parabola. Right: Once the correct number of points has been determined, the left panel displays the resulting curve fit to the pressure decay data from the first HF test used to determine the upper bound of the shut-in pressure (Cornet, 2004).

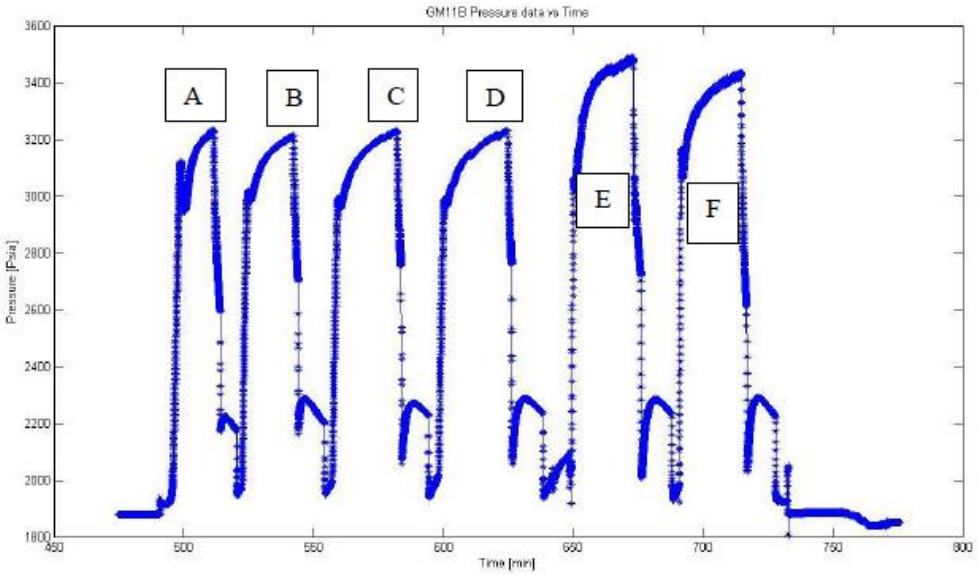

Figure 5-11: Results of six HF tests performed on an interval of the Mount Simon (Cornet, 2004).

5.4 Monitoring Options

Effective monitoring requires data collection, analyses, and modeling techniques for storage site characterization and integrity evaluation during pre-, active-, and post-injection processes. Several monitoring methods are available and can facilitate a diverse and extensive analysis of the immediate storage site and the affected surrounding storage area. Geomechanical monitoring technologies related to CO_2 storage were reviewed and divided into three categories: remote sensing and near-surface; subsurface; and data integration and analysis technologies. Technologies for each category applicable to this study were evaluated and described in terms of borehole requirements, field application, input and output of data analysis, effective costs, and limitations. Monitoring tools analyzed include interferometric synthetic aperture radar (InSAR), tilt meters, global positioning systems (GPSs), downhole pressure gauges, operational monitoring, crosswell seismic, vertical seismic profiling (VSP) surveys, and microseismic technologies (Figure 5-12). A summary of CO_2 storage technologies is provided in Table 5-4.

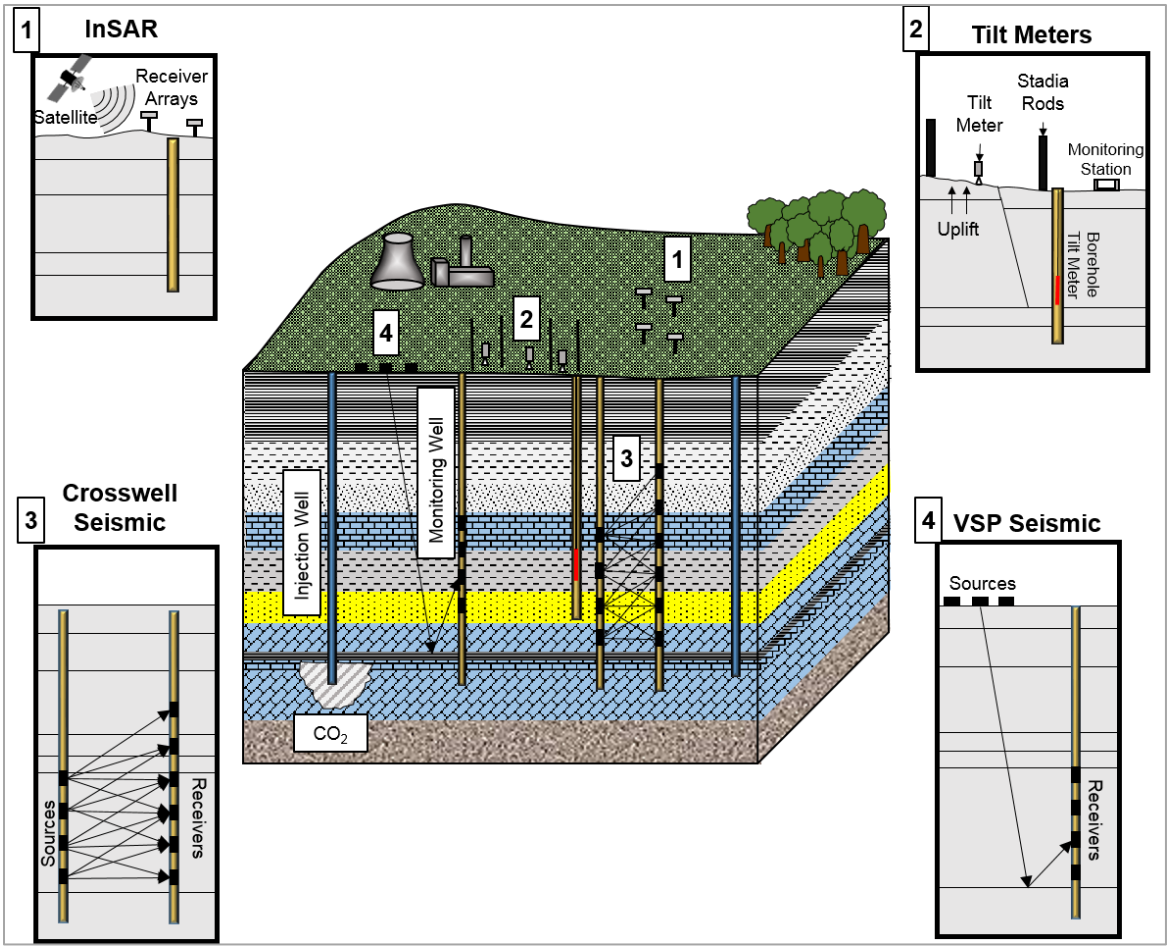

Figure 5-12: Monitoring technologies: 1) InSAR with receiver arrays for monitoring ground deformation; 2) tilt meters – aboveground and borehole tilt meters; 3) crosswell seismic with sources and receivers in wellbores; 4) VSP seismic with sources and receivers.

Table 5-4: Summary of CO_2 monitoring technologies.

Method	Description	Equipment	Other	Resolution	Costs	CO_2 application	Limitations
InSAR	Satellite-based technique that provides topographic images of site surface area	Satellite, Reflectors	May need additional reflectors or a GPS station	mm-scale	High	Monitoring injection of CO_2 in the subsurface at carbon sequestration test sites.	Level terrain, minimal land use, atmospheric effects, and satellite orbit coverage
Tilt meters	Inclinometer technology which measures deviation from horizontal and vertical plane	Tilt meter and Monitoring Station	Use of sand for installation in borehole	microradian	Low to Medium	Measure surface deformation in proximity to injection sites	Land access, data collection, spurious changes due to temperature and rainfall
Global positioning system	Satellite technique that provides epochs with displacement measurements	Receiver, GPS antenna, power supply, pseudolites, pressure gauges, and satellite system	Pressure gauges set up in the borehole	mm-scale	Medium	Measures displacement in proximity or area of CO_2 reservoir	Temporal sampling may be limited, land use and access, atmospheric effects, satellite orbit coverage
Crosswell seismic	Source and receivers set in close proximity wells	Wireline vendor, service rig, source and receiver arrays	Data will need modeling and processing pre and post logging	1 – 5 m	High	Subsurface monitoring of injection of CO_2 plumes. Estimate rock and fluid properties. Identification of potential fractures and faults in the subsurface.	Source strength is limited by the distance between wellbores. Presence of gas in the well can reduce detection of CO_2. Geologic complexity and noise interferences can degrade seismic data. The maximum distance between wells is dependent on casing.
Vertical seismic profile	Surface source with wellbore receivers	Wireline vendor, service rig, source and receiver arrays	Permits for use of explosives, data will need modeling and processing pre and post logging	10 – 30 m	High	Site characterization prior to injection and time-lapse monitoring to survey migration of CO_2 plumes. Identification of potential fractures and faults in the subsurface.	Presence of hydrocarbons or high salinity. Must verify that potential historical sites are not damaged during logging. 450 m distance limitation.
Microseismic/ seismic activity monitoring	Passive technique for monitoring and identifying downhole fractures and microseismic events	Borehole geophones, monitoring station, solar charge panels, strong-motion-sensor (for injection activity)	Data will need modeling and processing is required	500 m	High	Can monitor fracture properties from downhole, surface to subsurface. Time-lapse monitoring to survey migration of CO_2 plumes. Identification of potential fractures and faults in the subsurface.	Moderate changes in dip perturbation or velocity changes can cause errors in velocity models. Low and high frequency signals can affect mechanism inversion.
Operational monitoring	Injection rates and pressure monitoring	Gauges and flowmeters	Continuous monitoring application	PSI bbl/min	Medium to High	Monitor injection performance for pressure drops and flow variations	Limited to injection well

Note: mm = millimeter; m = meter; bbl/min = barrels per minute.

a. Costs are described in terms of low ($0-$100s), medium ($1,000-$10,000s), and high ($100,000-$1,000,000s).

5.4.1 Remote Sensing and Near-Surface Technologies

Changes in CO_2 pressure and/or geomechanical impacts can cause small uplift and subsidence surface displacements. Geodetic monitoring tools provide paramount detection and measurements of proximity and remote spatial deformation that can be associated with CO_2 injection sites. Instrumentation used for geodetic monitoring include satellite-based systems, tilt meters and GPS.

Interferometric Synthetic Aperture Radar. InSAR technology (Figure 5-13) is a satellite-based system that obtains high-precision information on the position of the ground surface in areas with high radar coherence to provide millimeter-scale measurements of ground displacement (Burgmann et al., 2000). This technology is effective in environments with minimal elevation changes, vegetation coverage, and land usage. At high-vegetation and high-population sites, and at sites with complex surface topography, reflectors such as artificial corner reflectors (ACRs) can be employed to minimize noise and complications with complex surfaces.

The main data provided by this technology include three main sets: 1) geographic information system (GIS) spatial data (which includes displacement rates, cumulative displacements, standard deviations, etc.); 2) time-series graphs of measured points (which are used to calculate displacement rates using linear regressions); and 3) database of shapefiles used to create the maps. These data sets can provide cumulative displacement data over time for a study site. Figure 5-13 shows long-term CO_2 injection monitoring data from several installed ACRs in a study field (Gerst et al., 2014). The reflector network decreases noise- and topography-related errors. To determine the number of reflectors needed and the general configuration of the InSAR plan, site and monitoring steps must be implemented prior to implementing field monitoring. The technical preparation for this method includes three steps: 1) performing a historical deformation study of the area of interest, 2) assessing the topography, vegetation, and population of the area to determine whether reflectors are needed (and if so, how many), and 3) determining monitoring rates needed to effectively produce meaningful data of the monitored CO_2 and surface deformation.

Tilt Meters. Tilt meters (see Figure 5-12) are implemented in the field to measure surface deformation in proximity to injection sites within microradians (Wright et al., 1999). Operation mechanisms vary depending on surface and subsurface installation. Surface tilt meters have a simple liquid level measuring system that utilizes a liquid-filled concave quartz cylinder with an air bubble (similar to a carpenter's level) to detect deviations from the horizontal and vertical plane. Additionally, linear voltage differential transformers (LVDTs) are used to detect the position of the apparent height changes between multiple surface tilt meters. Subsurface tilt meters installed in a borehole, combined with differential capacitance transducers (DCTs), measure ground tilting and apparent height changes based on a simple pendulum method. Data are transmitted to a logging computer or a monitoring location for future data processing. Tilt meters are highly sensitive and respond to changes in the ground due to excessive rainfall and extreme temperatures which can create spurious deformation changes. Land access and permission to install tilt meters on private land is paramount to the utilization of the instrumentation.

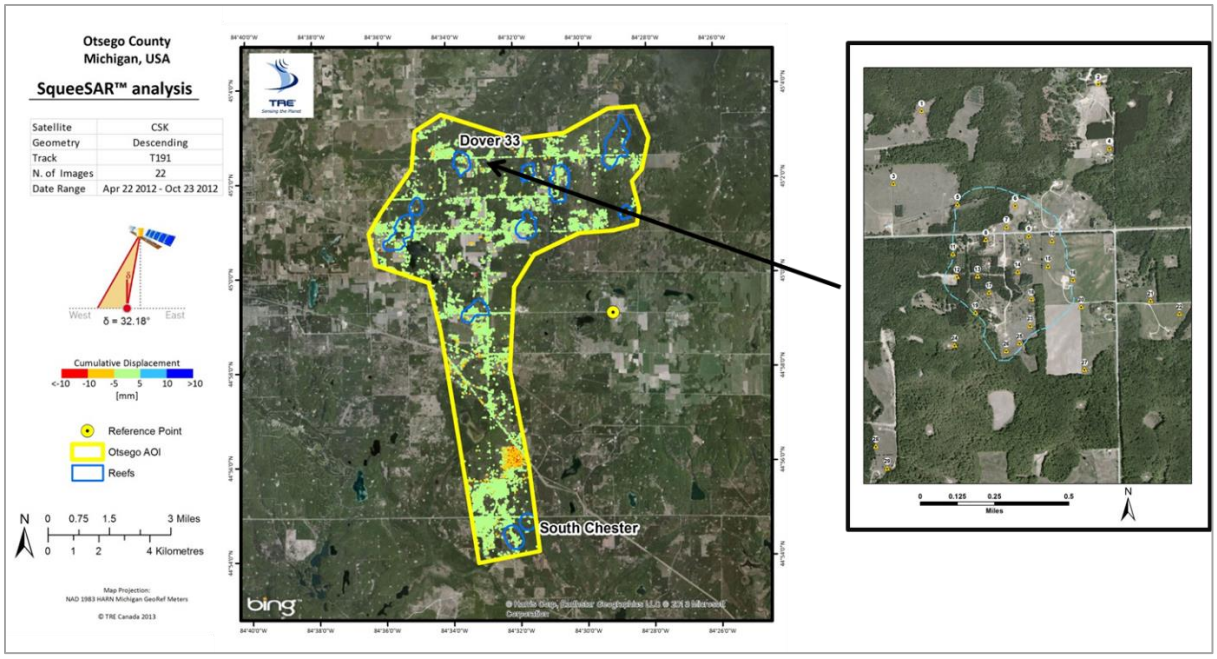

Figure 5-13: Results of baseline analysis for (center) 80-km^2 area of interest; (right) locations of the ACRs installed over an oil field with all measurement points identified from the baseline analysis (Gerst et al., 2014).

Global Positioning System. A GPS provides relatively low-cost 3D positioning data for site deformation monitoring (Dixon, 1991) data. Utilizing several GPS stations, satellite radio frequencies can be used to triangulate and determine displacement of a zone of interest (Zumberge et al., 1997). These GPS stations have the capability of measuring deformation with millimeter accuracy. Data transmission is dependent on satellite orbit and frequency of time sample rates. Equipment includes satellites (with maximum coverage, pressure gauges in the borehole used for vertical calibration in the well), pseudolite arrays (to enhance satellite geometry), power supplies, and GPS antenna (to enhance signal quality). This technology is sensitive to atmospheric interference and large solar flares.

5.4.2 Seismic Surface and Subsurface Monitoring

Seismic surface and subsurface monitoring technologies include a variety of instruments that can provide tracking of CO_2 plumes, pressure and temperature changes caused by injection, and surface and subsurface deformation. Resolution of seismic data depends on the form of seismic technology implemented in the field, nature of the geologic structure, and the spacing between wells. Field assessment, cost analysis, and well and land restrictions should be evaluated to determine the appropriate type of seismic survey that will fit the project scope and data analysis.

Crosswell Seismic Monitoring. Crosswell seismic monitoring provides velocity and anisotropy information which is used to estimate saturation levels and geologic properties between wells. A seismic source transmits high-bandwidth waves, while moving up the wellbore, which are collected at receiver arrays in adjacent wells (see Figure 5-12). Depending on the configuration, crosswell seismic monitoring can provide higher vertical resolution of the interval of interest than surface seismic monitoring. Collected data provide structural and physical characteristics. Multiple crosswell

seismic runs, also known as time-lapse, produce high-resolution images, which increases monitoring accuracy, provides better identification of fine-scale structures, and has the potential to show changes throughout time.

High resolution of the crosswell seismic technology is achieved by close-proximity spacing between wells of approximately less than 450 meters (m). However, the 3-ft to 20-ft accuracy of this technique grants higher frequency propagation between short distance wells (Harris et al., 1995). Application of this technique requires geometry design of equipment and wireline source and receiver array equipment. Prior to implementing this method, a feasibility test should be conducted to determine the efficacy of a crosswell approach to assess the location of the injected CO_2, and the potential movement between wellbores. The study area should be analyzed and well spacing should be factored into the configuration of the crosswell layout. Once data collection and equipment setup have been completed, baseline crosswell seismic monitoring can be conducted. Repeat logging can be conducted to assess injected CO_2, detect potential fluid movement between wellbores, and analyze structural features (deformation and/or fractures). These data can be correlated, as seen in Figure 5-14, with other sources of data, including core measurements (Harris and Langan, 1991).

Vertical Seismic Profiling. VSP is a borehole seismic method where receivers are placed in a wellbore and the seismic source is located on the ground surface (Gerst et al., 2014). The advantage of VSP is the high-resolution velocity and reflection images of the subsurface that can be acquired while providing more freedom in imaging direction (versus crosswell seismic monitoring). This technology facilitates monitoring and distribution of injected CO_2 to better characterize the geology of the injection region and to determine any changes to the reservoir due to the addition of CO_2 (see Figure 5-12).

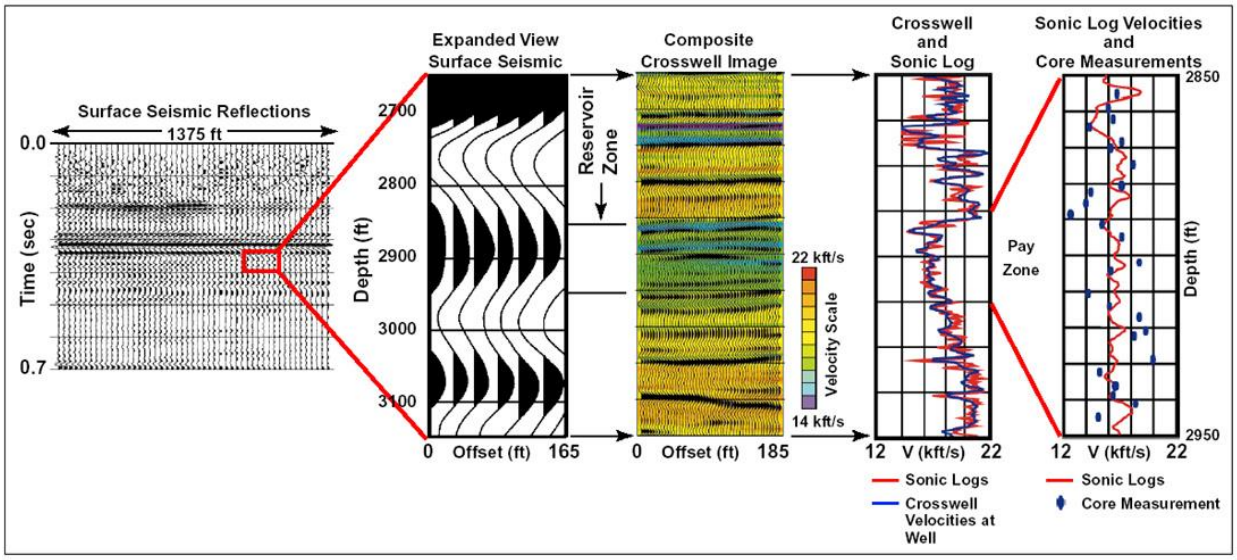

Figure 5-14: Example of crosswell seismic data and correlation process (Harris and Langan, 1991).

There are many types of VSP approaches available to determine subsurface geologic properties. VSP approach examples include offset, walkaway, and zero-offset VSP. Offset VSP has a source positioned a predetermined distance away from one or more receivers in the wellbore. A walkaway uses multiple sensors emplaced in a borehole to measure the seismic response to known sources at ground surface. The zero-offset VSP method provides close-proximity data to the wellbore, approximately 60 ft to 160 ft. The maximum distance the source can be to a receiver is approximately 1,400 ft. This technology can range in cost, totaling over $1 million. Zero-offset configurations are the least expensive of the VSP methods but provide the least amount of coverage.

Depending on the study area and the CO_2 injection volume, preparation for VSP monitoring should include three initial steps: 1) conduct a feasibility study to determine if VSP can be conducted in the region of interest, 2) build a velocity model to predict the effectiveness of the study design, and 3) determine the type of VSP monitoring that will accommodate the field of study. Once the initial design has been completed and the VSP method has been set up, baseline VSP studies should be conducted so that changes in signal response time between the baseline VSP and a post-injection VSP can be evaluated. These changes can be analyzed to determine if there are changes within the formations (Figure 5-15).

Microseismic Monitoring. Microseismic monitoring is a well-established passive technique where sensitive receivers are placed downhole to record microseismic events (Verdon et al., 2013). Microseisms, generally below a magnitude 0.0, are minute magnitude releases of mechanical energy that can occur for many reasons, including the pressure change caused by injection and natural microseismic events. Downhole sensitive receivers continuously record seismic signals that occur in the region around the borehole. The output of these receivers is recorded at the surface and analyzed (Maxwell, 2010). The analysis typically provides both magnitude and location (in three dimensions) of each detected event.

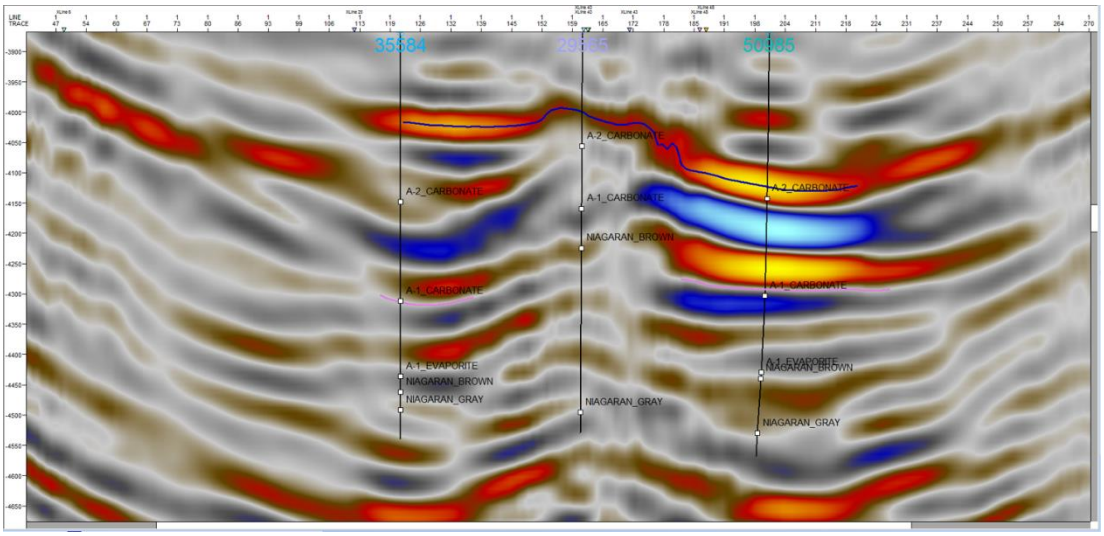

Figure 5-15: VSP data in carbonate rocks (Gerst et al., 2014).

Microseismic technology facilitates the monitoring of potential deformation for CO_2 injection sites. Activity during injection into depleted formations can occur as part of natural seismic events or as the result of activities related to drilling, such as fracturing of a penetrated formation due to pressure change caused by injection of well fluids. Costs generated by this method depend on the monitored coverage area. Small regions in close proximity to one injection well are less costly than several wells with multiple array setups. Configuration and implementation of this technology includes six steps: 1) determining the monitored coverage area, 2) analyzing the locations of monitoring arrays, 3) assessing the signal-to-noise ratio of the region, 4) determining the velocity structure of the study area, 5) calculating discovery pressures to injection and monitoring, and 6) analyzing the well to determine array deployment (is it a near-vertical well or is there a horizontal portion?). Prior to microseismic monitoring, a walk-away VSP survey can be run in the injection well to produce and estimate velocities in the study region. Additionally, once configuration of this technology is complete, baseline monitoring should be conducted during and after injection tests to determine data quality.

5.4.3 Basin and Case Studies Overview

The geologic setting for CO_2 storage sites will determine the most appropriate methodology for geomechanical evaluation. According to the Catalog of Sedimentary Basins of the United States (Colman and Cahan, 2012) there are 144 sedimentary basins (onshore and offshore) in the United States. Of these, 112 basins are in the lower 48 states, several of which may have the geomechanical properties of reservoirs and confining layers needed for CO_2 storage (size, shape, seals and reservoirs, etc.). To determine their storage potential, these basins should be fully characterized and understood, and their regional tectonic/structural evolution should be defined and studied. A high-level geologic overview of the CO_2 storage site should be conducted to define these properties. In order to develop a complete overview of how sedimentary basins developed over time, it is essential to understand the tectonic events and geologic processes that occurred since deposition of the sediments. These events and processes configured the shape of the basins and influenced the sequences of deposits. Understanding the tectonic history of the basin divulges information on structural features such as development of faults, fractures, and other deformation features. Analyzing the different structural settings observed in the basin today contributes to our understanding of the tectonic history and the stress field that developed through time. These results are key to developing an appropriate geomechanical characterization, testing, and monitoring program.

Historic and geomechanical properties and current tectonic seismicity settings play an important role in classifying the characterization, testing, and monitoring program that is needed for a potential site. Using the sedimentary basin classification scheme defined in Colman and Cahan (2012) provides examples of plate tectonic settings which are subdivided by the basin structural type. In the lower 48 states, basin types are associated with four different tectonic settings (Table 5-5). Plate tectonic settings provide essential information about historic tectonic activity. For example, intracratonic basins have no recent tectonic activity since the Permian age (approximately 200 million years ago). These results, combined with review of active fault systems in the United States (Figure 5-16), will further define what type of characterization, testing, and monitoring program is developed for the storage site.

Table 5-5: Sedimentary basin classification of the lower 48 states of the United States.

Plate tectonic setting	Basin type	Number of basins	Example
Intracratonic	Rift and transtensional	24	Rome trough
	Sag	35	Illinois Basin, Michigan Basin
Pericratonic	Passive margin	3	Gulf of Mexico
	Foreland and thrust	38	Appalachian Basin
	Borderland	5	San Joaquin Basin
	Transtensional / transpressional	1	Great Smoky Mountains Rift Basin
Intercratonic	Accreted back-arc	2	Havallah Basin
	Accreted fore-arc	3	Great Valley Basin

As defined by Colman and Cahan, 2012.

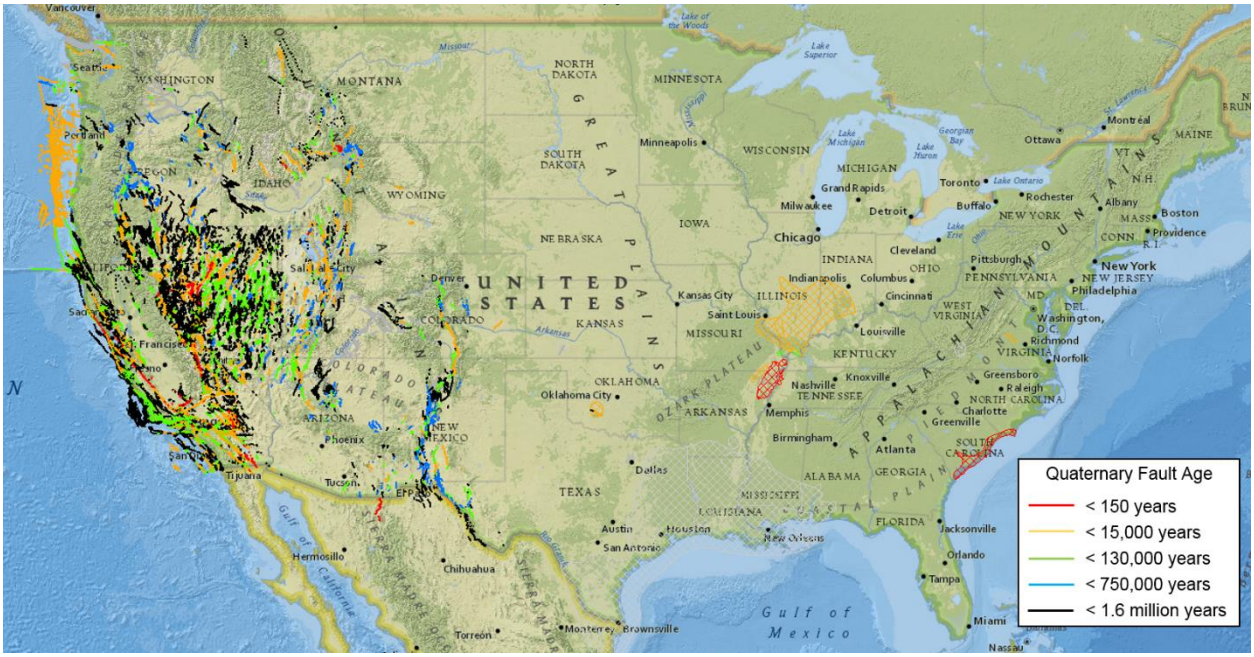

Figure 5-16: Map of major earthquake faults in the United States.
(Map modified from the USGS website https://earthquake.usgs.gov/hazards/qfaults/map/#qfaults).

Selection of a basin and development of each storage program should include the following evaluation steps:

- Literary review of the regional geology of potential storage sites to determine stratigraphy and structural features of basins.
- Geophysical logging to define rock characteristics such as lithology, mineralogy, water saturations, porosity, and permeability measurements.
- Geomechanical rock core testing to define direct measurements of lithology, mineralogy, porosity, permeability, and fluid saturation measurements. Advanced rock mechanics methods should be used to analyze the elasticity, failure and fracture mechanics, and stress propagation.
- Injection testing to analyze in-situ stresses and the hydraulic properties of the formation. Measurements should be used to determine the upper and lower bounds for the minimum horizontal stress and an estimate of the maximum horizontal stress. These results should then be used to build advanced fracture mechanics models and to assess the risks associated with CO_2 injection and storage.
- Geomechanical monitoring to define and spatially track injected subsurface CO_2 and the proximity and remote spatial deformation of CO_2 in a storage site.

Practical applications of these steps have been employed in recent reservoir testing studies conducted by Battelle along with the MRCSP, working with brine disposal companies. From 2003 to 2007, Battelle, in conjunction with American Electric Power (AEP), investigated the feasibility of CO_2 storage in the Rose Run sandstone and Copper Ridge dolomite, Appalachian Basin, at the Mountaineer Power Plant in New Haven, West Virginia (Battelle, 2011; Gupta et al., 2013; McNeil et al., 2014).

Geophysical analyses and wireline tool applications were completed to determine stress orientation/ magnitude and fracture/fault density networks. Multi-component sonic logs (Figure 5-17) and image logging tools were run to calculate Young's modulus and Poisson's ratio, identify sections of borehole breakouts and DITFs, and determine the average directional stress mechanical parameter for the region. This approach was used to better understand and monitor how the additional stress of CO_2 sequestration can affect the safety of the study area (Figure 5-18).

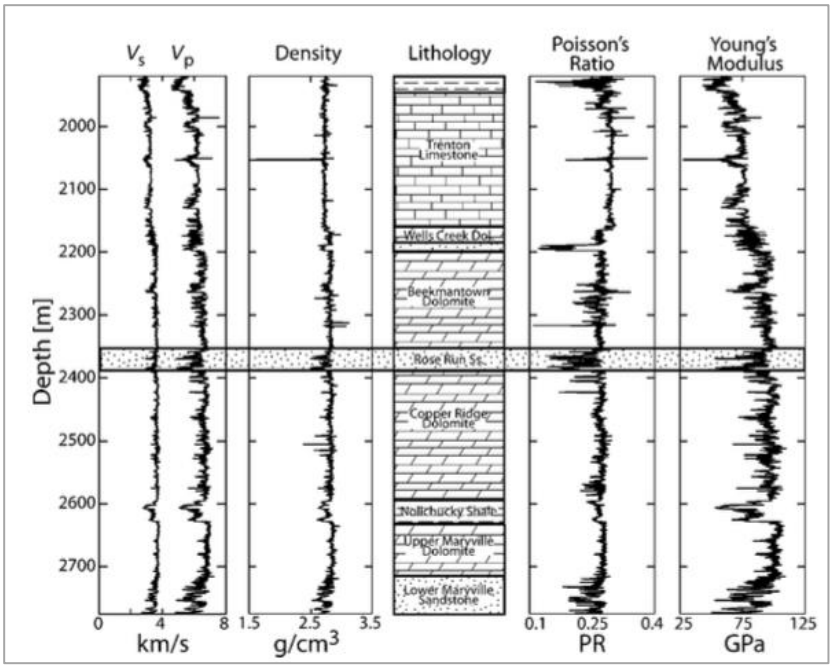

Figure 5-17: Velocity and density logs from AEP 1 well and the calculated Poisson's ratio and Young's modulus (Lucier et al., 2006).

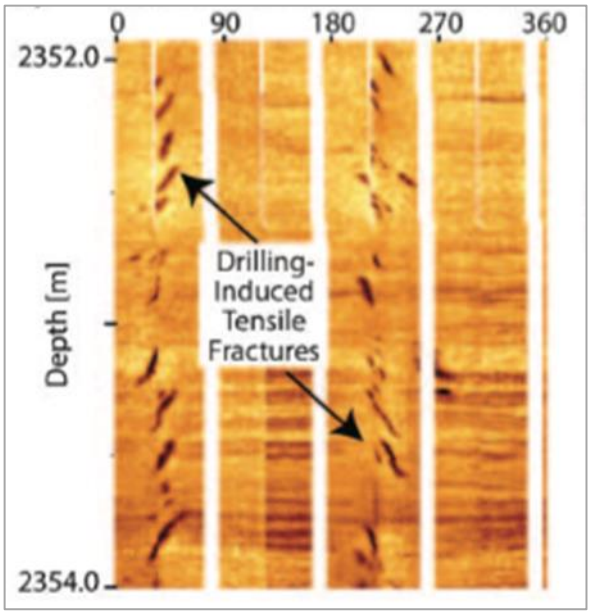

Figure 5-18: Horizontal stress orientation from DITFs from the image logging tool (Lucier et al., 2006).

Injection tests and monitoring of the geomechanical effects of commercial-scale long-term CO_2 storage in reef reservoirs were conducted in the Michigan Basin as part of MRCSP. Monitoring tools used under that research included InSAR, tilt meters, GPS, downhole pressure gauges, operational monitoring, crosswell seismic, VSP surveys, and microseismic technologies (Gerst et al., 2014). Microseismic monitoring was completed during the injection operations to observe whether there were injection-related events. A comparison of the injection operations and recorded microseismic events was evaluated; the evaluation determined that there was no relationship between the events and operations (Figure 5-19).

These examples of the Michigan and Appalachian Basins demonstrate some of the key comprehensive geomechanical assessment steps that should be conducted to determine geomechanical properties and processes that may affect reservoirs and confining layers of a CO_2 site. Each technology and method was designed to capture the complex lithological and structural features of the basins. Additionally, monitoring programs were developed to evaluate potential seismic events that may occur during injection operations.

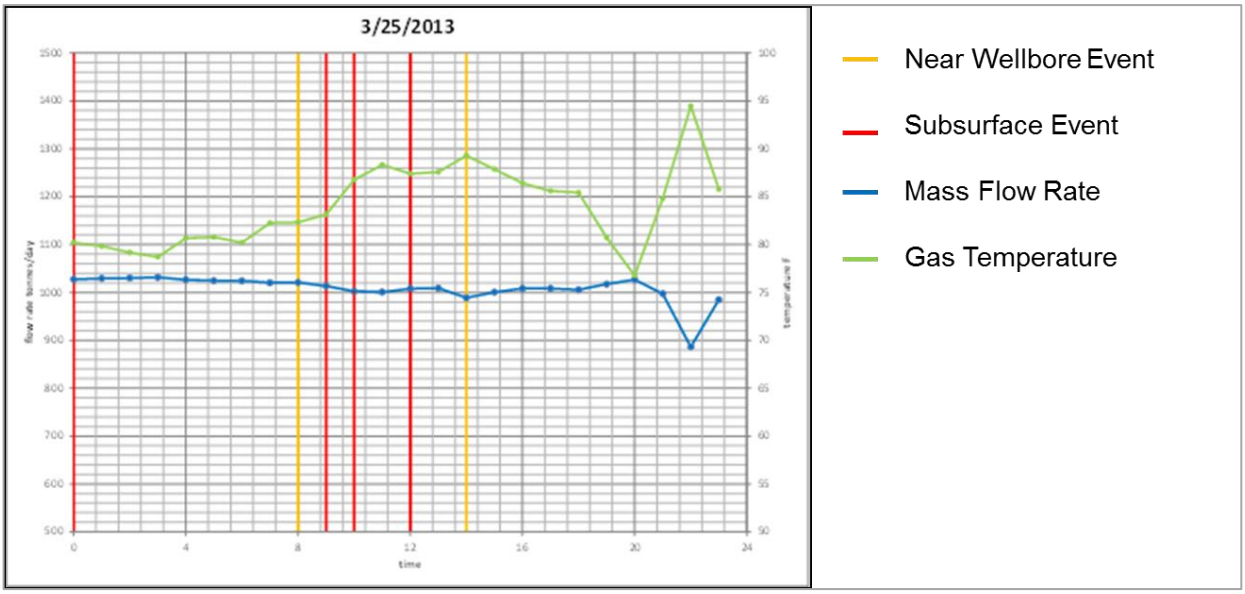

Figure 5-19: Comparison of injection operations with recorded microseismic events (Gerst et al., 2014).

6.0 Geomechanical Simulations for CO_2 Storage

The objective of the geomechanical simulations task was to complete reservoir simulations of CO_2 storage for several different geologic settings in the Midwest United States and assess the effects of CO_2 storage in the subsurface. The task included development of multiple-phase CO_2 injection simulations coupled with geomechanical deformation modules. The models were based on existing wells to depict realistic CO_2 injection rates for the region. Results of the simulations were analyzed to assess the impact of supercritical CO_2 on storage reservoirs at storage locations within a broad regional stress framework. Simulations were run to evaluate both storage reservoir intervals and containment layers to evaluate storage security. Models were developed for three sites in the Midwest United States to investigate variations in geomechanical settings and properties in the region. Site-specific data for the three study areas were translated into a numerical Computer Modelling Group Ltd. (CMG) GEM model. A series of CO_2 injection scenarios was completed to evaluate the stress changes introduced into the subsurface by CO_2 storage applications. Results were analyzed for both reservoir zones and containment layers with maps, graphs, 3D diagrams, and tables.

Models are generally simplified versions of real conditions, and the models described in this report represent averaged conditions to a large extent. Input data were compiled from a variety of sources that collect information from operators, drillers, and service companies. Efforts were made to review the quality of the data, but the accuracy of much of the information relies on external databases. Maps, geologic cross sections, geophysical log analysis, and figures presented in this report are general in nature. None of the simulations were based on existing CO_2 injection wells or proposed projects, and the input should not be considered specific to an existing well. Many of the injection intervals being examined under this project have relatively limited geotechnical data because they are not oil and gas reservoirs. Therefore, it was necessary to estimate some input parameters based on similar rock formations. Site-specific projects would require field work such as seismic surveys, drilling, geophysical logging, reservoir tests, detailed reservoir modeling, and system design. The results of this report shall not be viewed or interpreted as a definitive assessment of the suitability of candidate geologic injection formations, the presence of suitable caprocks, or sufficient injectivity to allow CO_2 injection to be carried out cost effectively.

6.1 Coupled Fluid-Flow – Geomechanics Simulators Survey

The objective of this task was to select the most suitable simulation tool for this project, after a comparison of available options for capturing the physics of CO_2 storage in the subsurface. The survey included a description of available coupled fluid-flow and reservoir geomechanics simulators to place the categories of comparison into context. Simulators were assessed based on technical parameters (e.g., type of coupling, constitutive laws and models available), applicability (previous publications on CO_2-storage oriented problems), and accessibility (user-friendliness, compatibility, technical support availability). The simulators were considered in terms of their ability to evaluate the geomechanical effects of a CO_2 injection program for three sites in the Midwest United States being investigated in this project: Arches Province, East-Central Appalachian Basin, and the Northern Appalachian Basin. A brief description of the workflow that the simulator was expected to execute for each study area is presented in Figure 6-1.

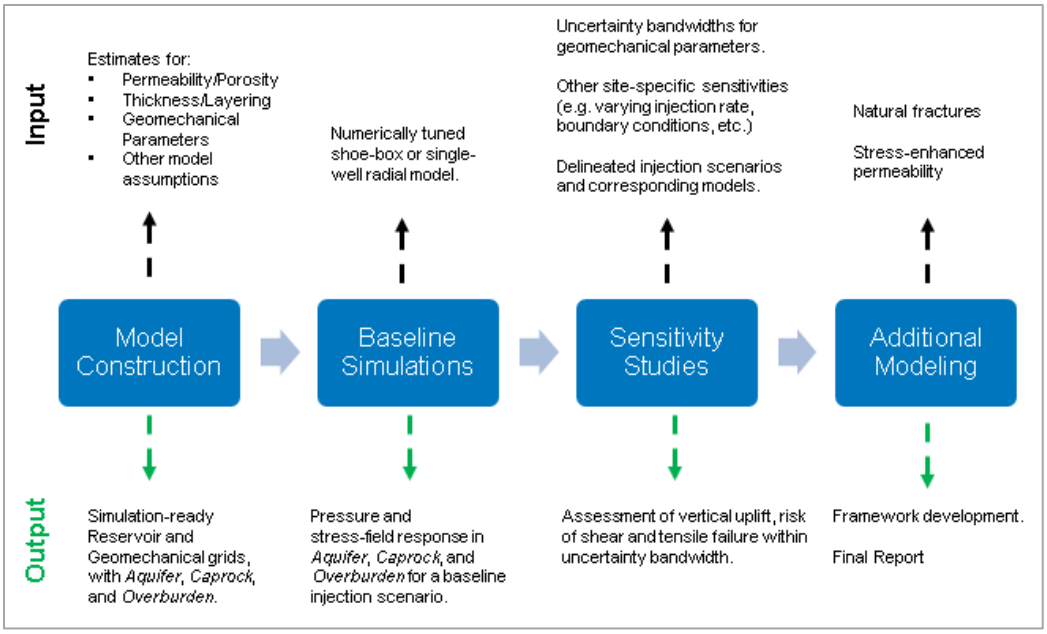

Figure 6-1: Subset of activities involved in each phase of the workflow for the geomechanical risks assessment.

Geomechanical effects has been identified as a significant risk factor for large-scale geologic storage of CO_2. Reservoir modeling of the fate of CO_2 upon injection into the site is part of a rigorous assessment of the risks of CO_2 migration beyond the injection zone. While injection sites are always carefully selected such that the target zone is overlain by an impermeable caprock that will halt any upward migration of the CO_2, the risk of CO_2 migration through fractures induced by the injection of CO_2 remains a tangible one. Such geomechanical aspects of CO_2 injection into geologic media can be examined by coupled thermal-hydraulic-mechanical-chemical simulators, and several such software packages exist.

6.1.1 Geomechanical Simulations Overview

Upon injection into pre-saturated geologic media, the CO_2 is hydraulically transported both laterally (as a result of pressure differentials created by the injection) and vertically (being less dense than the saturating fluid originally in the reservoir). In addition to hydraulic transport through the pores, CO_2 may also partially dissolve into and/or react with the fluid it contacts. Injection of CO_2 into an aquifer for storage can result in a net pressure increase throughout the reservoir. This rise in pressure impacts the distribution of stresses in the reservoir—often in a complex and recursive manner—which can potentially create new fractures or widen existing ones.

Reservoir simulators perform fluid-flow simulations designed to predict the response of the reservoir both spatially and temporally. Spatial resolution is obtained by discretizing the reservoir into gridblocks, and the temporal solutions are obtained by dividing time into a series of successive time-steps. Typically, the engineer must choose the size of the gridblocks and time-steps by balancing the tradeoffs of speed and accuracy. Low-resolution reservoir models with larger gridblocks can provide quick solutions with decreased accuracy, while higher-resolution models using smaller gridblocks provide increased accuracy, but at the cost of time-consuming simulations. The user may typically build the discretized geocellular reservoir model with a gridding program, calculate fluid

properties in another (if necessary), perform the simulation with a numerical solver to obtain the parameters characterizing reservoir response, and then proceed to view results, either using a graphing program or tracking the dynamic changes in the reservoir with a 3D rendering program. As a result, commercial reservoir simulators often come in packages, consisting of a collection of platforms each tailored for these specific tasks. Many academic reservoir simulators refer to only the numerical solver. Their focus is concentrated on the details of the code that performs the numerical solution, which is usually designed to solve a unique suite of problems in a computationally efficient manner. The user is free to opt for the gridding and post-processing software of choice.

Where the goal is solely to analyze how pressure and saturation (mole-fraction) distributions in the reservoir change with time, CO_2 injection is usually modeled via compositional simulation packages. In such simulations, solutions for each time-step may be efficiently obtained in a sequentially implicit manner, rather than a fully implicit one. An “implicit” solution refers to one where two or more unknowns are mutually dependent on each other. These unknowns are coupled parameters and must be solved via numerical schemes designed to iteratively converge pressure and saturation in the present and future time-step. “Explicit” solutions, on the other hand, are straightforward, only requiring previously solved variables to be plugged into an equation to obtain the unknown. In a compositional fluid-flow simulator, “sequentially implicit” refers to a series of implicit solutions where pressure, then saturations, and then compositions (spatial distribution of molar constituents of all fluids) for each successive time-step are obtained.

With geomechanical simulations, an additional type of coupling is introduced. Fluid-flow simulations assume that injection-production activities impact pore-pressure much more significantly than pore volumes; the latter effect is usually assumed to be negligible. With geomechanical simulations, however, the latter assumption is done away with, and pore pressures and pore volumes are now both coupled effects. Changing pore pressures affect the stresses in the reservoir, which control the displacement of the grains in the medium (altering the pore shapes and generally deforming the reservoir). This modifies the distribution of strain in the reservoir. These effects—beyond certain thresholds—can widen fractures (increase fracture permeability) and/or create new ones. In these form of simulations, the output parameters are implicit both in time and between themselves.

The simplified flowchart in Figure 6-2 illustrates the fluid-flow and geomechanical coupling process as performed in most simulators. Coupled geomechanical and fluid-flow simulations may be performed both one-way and two-way; the choice is typically made based on the nature of the geologic medium. For instance, where it is known that the reservoir is consolidated and permeable, one-way coupling may be sufficient. This means that stress-regime changes would serve only to alter the permeability of the reservoir, and deformation is a secondary process. However, where the rock grains are easily deformed, and pore pressure changes result in instantaneous grain deformation, two-way coupling between fluid and geomechanical simulation is required to determine the equilibrium stress and pore pressure state. Naturally, two-way coupled simulations provide greater accuracy than one-way coupled simulations, but at the cost of time.

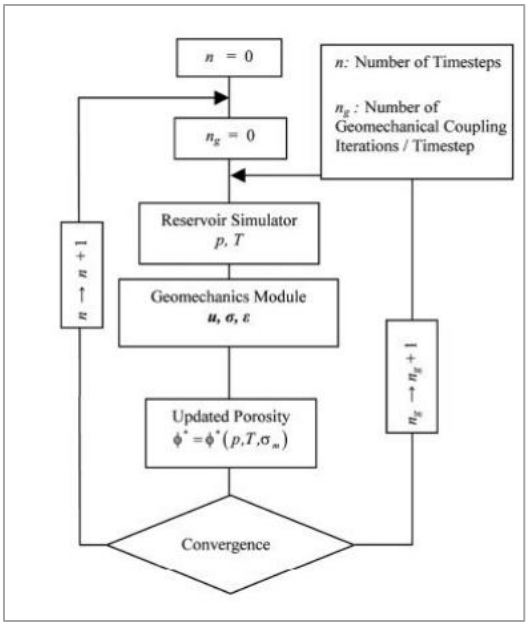

Figure 6-2: Diagram showing how, for each time-step, outputs from the fluid-flow module are passed into the geomechanical module and back in an iterative manner until convergence is obtained in both sets of unknowns for two-way coupling (modified from Tran et al., 2005).

6.1.2 Inputs for Geomechanical Simulation

Reservoir simulation places high demands on data. For the purposes of the simulations conducted for this study, three groups of data were required to construct the base reservoir model for each site. First, geologic data describing the architecture and basic rock properties of the aquifer and the overlying strata were needed. Typically, data from several length scales (e.g., core data, well logs, and seismic data) were used to quantify thicknesses, layering, continuity, porosity, permeability, any natural fracture networks present, pressure, and temperature. These data were used to build and initialize a geocellular model of the aquifer and the strata all the way up to the surface. The second group was fluid and rock-fluid properties of the injected fluid and the reservoir fluid(s). These are the properties of CO_2 and formation brine that may vary a function of pressure (solubility, salinity, density, compressibility, etc.) and relative permeability. Third was the set of geomechanical rock and reservoir properties. These properties included the aquifer and overlying strata: Young's modulus, Poisson's ratio, bulk modulus, rock compressibility, and the principal effective stresses and direction.

Since the objective of this simulation study was to delineate scenarios where rock failure can occur, it was important to select the appropriate type of yield function that determined how stress relates to strain and the yield-point at which failure occurs. The Mohr-Coulomb model was appropriate for the purposes of this study. Modeling fracture propagation was beyond the scope of this project; detecting regions where the stresses cross the failure threshold were considered satisfactory. Finally, to model the scenarios of stress-enhanced fractures conducting CO_2 above the injection zone, the Barton-Brandis fracture model was necessary. The data required are shown in Table 6-1.

Table 6-1: Input data required to run a coupled fluid-flow and geomechanical simulation.

Category	Input	Options	Definition / Units	Notes
Reservoir description	Type of grid	Single porosity	Matrix only	Default
		Dual porosity	Matrix + secondary porosity network	Data in the form of a discrete-fracture-network (DFN) network, or similar (fracture lengths, spacing, aperture, distribution, etc.)
	Layers and thickness			Layering is representative of variations in rock type down to aquifer
	Overburden gradient			May vary per rock type
	Porosity (single and/or dual)	Map or constant		
	Matrix permeability	Map or constant		
	Fracture permeability	Map or constant		If not available, may simply make fractured zones as higher matrix permeability zones
	Pressure dependence of porosity & permeability	Constant		For both matrix and fracture permeability. Specific to rock type
Rock-fluid interactions	Standard properties of CO_2 and brine	Look-up table / correlations	Standard pressure-volume-temperature [PVT] properties viscosity, density, solubility etc.	If unavailable, correlations used.
	Relative permeability	Look-up table		
Initial conditions	Pressure gradient, reservoir pressure	Constant	psi/ft	Through all layers
	Temperature gradient, reservoir temperature	Constant	°F /ft	Through all layers
Geomechanical parameters	Initial stress distribution / total overburden stress	Map or constant		Regional values sufficient
	Principal effective stresses	Constant, dependent on rock-type		Regional values sufficient

Table 6-1 (continued): Input data required to run a coupled fluid-flow and geomechanical simulation.

Category	Input	Options	Definition / Units	Notes
Geomechanical parameters (cont)	Young's modulus	Constant, dependent on rock-type	Ratio of tension/extension (stress / strain)	If lab data not available, empirical correlations based on rock type from literature used
	Poisson's ratio	Constant, dependent on rock-type	Ratio of lateral contraction / longitudinal expansion (displacement)	
	Bulk modulus	Constant, dependent on rock-type	Measure of incompressibility	
	Angle of internal friction	Constant, dependent on rock-type	Measure of the rock ability to withstand shear stress.	
	Thermo-elastic constant	Constant, dependent on rock-type	Temperature-dependent elasticity	Processes are isothermal
	Volumetric thermal expansion constant	Constant, dependent on rock-type	Volume dependence on Temperature	
	Biot's number	Constant, dependent on rock-type	Property of rock expansion under stress	If lab data not available, empirical correlations based on rock type from literature used
	Cohesion	Constant, dependent on rock-type	Property of rock binding to itself	
	Solid rock compressibility	Constant, dependent on rock-type	Lab data	
	Bulk compressibility	Constant, dependent on rock-type	Lab data	
	Stress-dependent matrix permeability model	Look-up table	Lab data	
		Li and Chalaturnyk	Empirical formula	
	Stress-dependent fracture permeability model	Barton-Brandis		Simulates the opening of a conductive fracture through tensile failure, as pore pressure increases
				Applicable only where a natural fracture network has been defined
	Type of constitutive law	Pseudo dilation	A simplification of geomechanical effects	Choice dependent on rock type
		Linear elastic	Simplest model	Most applicable for CO_2 sequestration-type problems
		Elasto-plastic	Drucker-Prager model	Choice dependent on rock type Applicable for CO_2 sequestration-type problems
			Mohr-Coulomb model	

6.1.3 Comparison of Geomechanical Simulators

Table 6-2 summarizes the technical features of the geomechanical simulators reviewed. As shown, many simulators featured different coupling methods, yield functions and constitutive laws, numerical controls, and gridding control. Table 6-3 summarizes the compositional flow and stress-field modelling options for the geomechanical simulators identified in this investigation. Table 6-4 lists simulator accessibility features that could affect suitability of the models to address multiple sites and CO_2 injection scenarios.

Table 6-2: Geomechanical simulator comparison of technical features.

Simulator	Type of coupling	Constitutive laws available	Numerical controls	Gridding control
CMG-GEM	One-way, two-way sequential coupling available. No fully coupled option.	**Linear elastic** **Elasto-plasticity**: Mohr-Coulomb, Drucker-Prager, plastic cap, single surface, generalized plasticity **Nonlinear elasticity:** Hypo-elastic and hyper-elastic **Elasto-viscoplasticity:** Drucker-Prager model **Pseudo-dilation**	Simple controls available (e.g., convergence tolerance, number of iterations, minimum time-step size etc.). Advanced numerical controls available.	Dual porosity grid available for fluid-flow simulations. Grid refinement possible. Grids of various geometries available. Separate grid for geomechanical simulation possible with remapping onto fluid-flow grid.
TOUGH-FLAC	Two-way sequential coupling only.	**Linear elastic** **Elasto-plasticity**: Mohr-Coulomb, Drucker-Prager **Elasto-viscoplasticity:** Drucker-Prager model	Limited control.	Limited by choice of gridding package. Code ability to handle complex grid structures unknown.
TOUGH-ROCMECH	One-way, two-way sequential coupling available.	**Linear elastic** **Elasto-plasticity**: Mohr-Coulomb, Drucker-Prager	Limited control.	Limited by choice of gridding package. Code ability to handle complex grid structures unknown.
TOUGH-RDCA	One-way sequential coupling.	**Linear elastic**	Limited control.	Limited by choice of gridding package. Code ability to handle complex grid structures unknown.

Table 6-2 (continued): Geomechanical simulator comparison of technical features.

Simulator	Type of coupling	Constitutive laws available	Numerical controls	Gridding control
TOUGH-CSN	One-way sequential coupling.	**Linear elastic** **Elasto-plasticity**: Mohr-Coulomb, Drucker-Prager **Elasto-viscoplasticity:** Drucker-Prager model	Limited control.	Limited by choice of gridding package. Code ability to handle complex grid structures unknown.
TOUGH-RBSN	One-way sequential coupling.	**Linear elastic**	Limited control.	Limited by choice of gridding package. Code ability to handle complex grid structures unknown.
TOUGH2-EGS	One-way sequential coupling.	**Linear elastic**	Limited control.	Limited by choice of gridding package. Code ability to handle complex grid structures unknown.
ECLIPSE-VISAGE	One-way, two-way sequential coupling available. Fully-coupled option available.	**Linear elastic** **Elasto-plasticity**: Mohr-Coulomb, Drucker-Prager, plastic cap, single surface, generalized plasticity **Nonlinear elasticity:** Hypo-elastic and hyper-elastic **Elasto-viscoplasticity:** Drucker-Prager model	Simple controls available (e.g., convergence tolerance, number of iterations, minimum time-step size etc.). Advanced numerical controls available.	Dual porosity grid available for fluid-flow. Grid refinement possible. Separate grid for geomechanical simulation possible with remapping onto fluid-flow grid.

Table 6-3: Summary of geomechanical simulator options for compositional flow and fracture-related stress-field calculations.

Simulator	Compositional fluid-flow simulation	Stress-rotation / fracture propagation	Barton-Brandis stress-fracture model	Code/software package
CMG-GEM	Yes, industry-standard compositional fluid-flow software.	No	Yes	Software package: each requires separate license. BUILDER – Gridding package w/ built-in geomechanics options. WinProp – Fluid property modeling GEM – Compositional simulator Results – graphing program Results3D – spatial results viewer
TOUGH-FLAC	Yes, but specific functionalities and/or numerical controls for fluid-flow simulation in TOUGH may be not be readily accessible.	No	Yes	Code only
TOUGH-ROCMECH	Yes, but specific functionalities and/or numerical controls for fluid-flow simulation in TOUGH may be not be readily accessible.	Yes, limited to fracture propagation in plane strain.	Yes	Code only
TOUGH-RDCA	Yes, but specific functionalities and/or numerical controls for fluid-flow simulation in TOUGH may be not be readily accessible.	No	No	Code only
TOUGH-CSN	Yes, but specific functionalities and/or numerical controls for fluid-flow simulation in TOUGH may be not be readily accessible.	No	No	Code only

Table 6-3 (continued): Summary of geomechanical simulator options for compositional flow and fracture-related stress-field calculations.

Simulator	Compositional fluid-flow simulation	Stress-rotation / fracture propagation	Barton-Brandis stress-fracture model	Code/software package
TOUGH-RBSN	Yes, but specific functionalities and/or numerical controls for fluid-flow simulation in TOUGH may be not be readily accessible.	No	No	Code only
TOUGH2-EGS	Yes, but specific functionalities and/or numerical controls for fluid-flow simulation in TOUGH may be not be readily accessible.	No	No	Code only
ECLIPSE-VISAGE	Yes, industry-standard compositional fluid-flow software.	Yes, limited.	Yes	Software package: VISAGE requires separate license from ECLIPSE. VISAGE sets up the geomechanical inputs and gridding that is then passed on to be solved with ECLIPSE. ECLIPSE Compositional Simulator suite with gridding and viewing ability. PVTi – Fluid property modeling

Table 6-4: Summary of geomechanical simulator accessibility.

Simulator	Pre- and post-processing ease	Troubleshooting support availability	Tutorials accessibility	Commercial / academic	Published studies for CO_2 sequestration
CMG-GEM	Fluid properties, pre- and 3D post-processing may be modelled within different modules of the software package. Only number of licenses of each individual module the issue.	CMG engineers may be contacted for help as part of licensing benefit.	Standardized tutorials, classroom sessions and guidance documents available	Commercial	Considerable studies in a broad range of topics.
TOUGH-FLAC	**Code is only efficient matrix solver.** Fluid properties independently modelled. Grid generation packages necessary. Post-processor required.	Possible, but need to contact code writers directly or change code directly.	Guidance document available but no tutorials	Commercial and academic	Available, but studies were performed for specific purposes that geomechanics module was tailored for.
TOUGH-ROCMECH	**Code is only efficient matrix solver.** Fluid properties independently modelled. Grid generation packages necessary. Post-processor required.	Possible, but need to contact code writers directly or change code directly.	Not available	Academic	Available, but studies were performed for specific purposes that geomechanics module was tailored for.
TOUGH-RDCA	**Code is only efficient matrix solver.** Fluid properties independently modelled. Grid generation packages necessary. Post-processor required.	Possible, but need to contact code writers directly or change code directly.	Not available	Academic	Available, but studies were performed for specific purposes that geomechanics module was tailored for.

Table 6-4 (continued): Summary of geomechanical simulator accessibility.

Simulator	Pre- and post-processing ease	Troubleshooting support availability	Tutorials accessibility	Commercial / academic	Published studies for CO_2 sequestration
TOUGH-CSN	**Code is only efficient matrix solver.** Fluid properties independently modelled. Grid generation packages necessary. Post-processor required.	Possible, but need to contact code writers directly or change code directly.	Not available	Academic	Available, but studies were performed for specific purposes that geomechanics module was tailored for.
TOUGH-RBSN	**Code is only efficient matrix solver.** Fluid properties independently modelled. Grid generation packages necessary. Post-processor required.	Possible, but need to contact code writers directly or change code directly.	Not available	Academic	Available, but studies were performed for specific purposes that geomechanics module was tailored for.
TOUGH2-EGS	**Code is only efficient matrix solver.** Fluid properties independently modelled. Grid generation packages necessary. Post-processor required.	Possible, but need to contact code-writers directly or change code directly.	Not available	Commercial and academic	Available, but studies were performed for specific purposes that geomechanics module was tailored for.
ECLIPSE-VISAGE	Fluid properties, pre- and 3D post-processing may be modelled within different modules of the software package. Only number of licenses of Visage the issue.	Schlumberger engineers may be contacted for help as part of licensing benefit.	Standardized tutorials, classroom sessions and guidance documents available	Commercial	Available.

6.1.4 Geomechanical Simulator Survey Conclusions

Geomechanical simulators were compared to determine the best option for modeling a series of CO_2 storage scenarios for three study areas in the Midwest United States. There are a variety of options for modeling CO_2 storage. A review of model inputs, compositional flow and stress options, and accessibility features helps to distinguish the various simulators. Overall, the CMG-GEM, ECLIPSE-VISAGE and TOUGH-FLAC simulators were identified as the most appropriate options for this project. These simulators have been previously applied to CO_2-storage problems and have robust numerical solution methods. Since the project involves simulating various scenarios for multiple study areas, the pre- and post-processing features were considered a key feature in selecting the right tool for this project. Consequently, CMG-GEM was selected to perform the geomechanical simulations for this project.

6.2 Geological Model Development

Geological models were developed to outline the geological layers, hydraulic parameters, geomechanical properties, and fracture networks for the three study areas. This information was used as basis for the numerical fluid-flow geomechanical simulations.

6.2.1 Arches Study Area

The Arches study area is in northern Kentucky, southeastern Indiana, and southwest Ohio. This study area is representative of the region between the major sedimentary basins in the Midwest United States. The main rock formation suitable for CO_2 storage in the Arches study areas is the Mount Simon sandstone. Sedimentary rock formations form broad arch and basin structures in the Midwest United States. Sedimentary strata thicken to over 5,000 m in the Appalachian Basin, Illinois Basin, and Michigan Basin. In between these basins, rocks are arranged in gentle arches and platforms. The ‘Arches Province’ is an informal term referring to the geographical area in northern Illinois, northern Indiana, northern Kentucky, southern Michigan, western Ohio, Ontario, and Wisconsin along several regional geologic structures: the Cincinnati arch, Indiana-Ohio platform, Kankakee arch, and the Findlay arch (Figure 6-3).

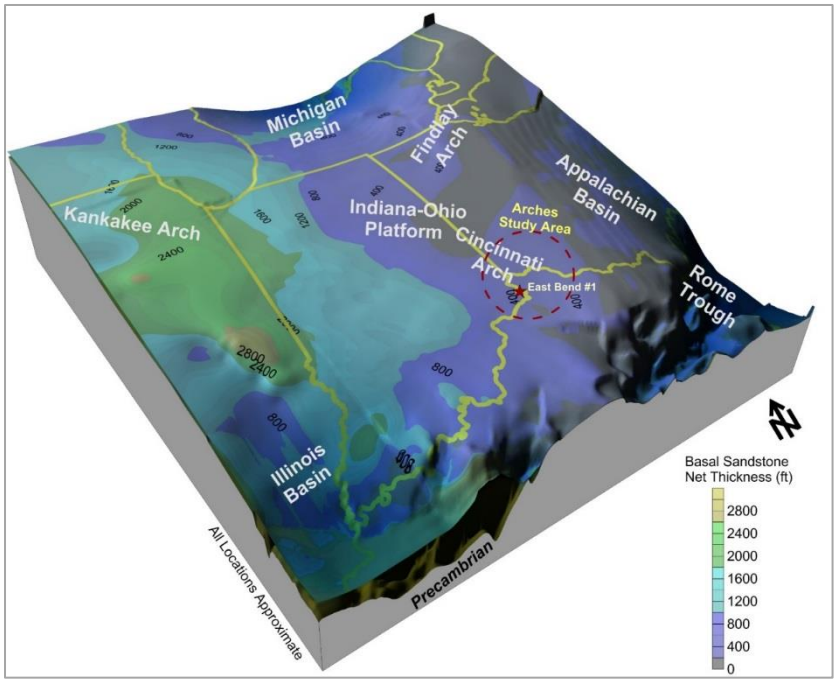

Figure 6-3: 3D geologic diagram illustrating Arches study area and other regional geologic structures.

In the Arches Province, the Lower Cambrian-age rocks have the most suitable pressure and temperature conditions for CO_2 storage in supercritical fluid or liquid state. Specifically, the Mount Simon sandstone is considered the most appealing zone for CO_2 storage in the Arches Province. The Mount Simon is mainly a coarse sandstone ranging from 30 m to 800 m in thickness in the Arches Province. Over 20 billion gallons of wastewater have been injected into the Mount Simon Formation over the last 40+ years (Sminchak, 2015), providing evidence for its injection capacity. The Eau Claire-Conasauga Formations are the main containment unit above the Mount Simon. Younger formations in the Knox Group overlie the Eau Claire-Conasauga, providing additional containment. Precambrian rocks underlie the Mount Simon and are generally considered impermeable.

There are many CO_2 sources along the Ohio River Valley and Great Lakes adjacent to the Arches Province, making it an important CO_2 storage unit. Few oil and gas wells have been drilled into the formation, so there is little information on geotechnical rock properties and even less geomechanical data. However, the location provides contrast to the sedimentary basin in the Midwest. The location was selected for analysis because a CO_2 test well was drilled at a site in the Arches Province. The well had a full suite of geophysical logs, core tests, and CO_2 injection testing.

The basis for the Arches geocellular model was the East Bend #1 well in Boone County, Kentucky (Figure 6-4). The East Bend #1 well was drilled in 2009 as part of the MRCSP (Battelle, 2010). The well was drilled to a total depth of 3,532 ft through the full column of Paleozoic sedimentary rocks and into a portion of Precambrian Middle Run Formation. The well was used for a CO_2 injection test in the Mount Simon sandstone of approximately 1,000 metric tons over two days, achieving injection rates of approximately 5 barrels per minute.

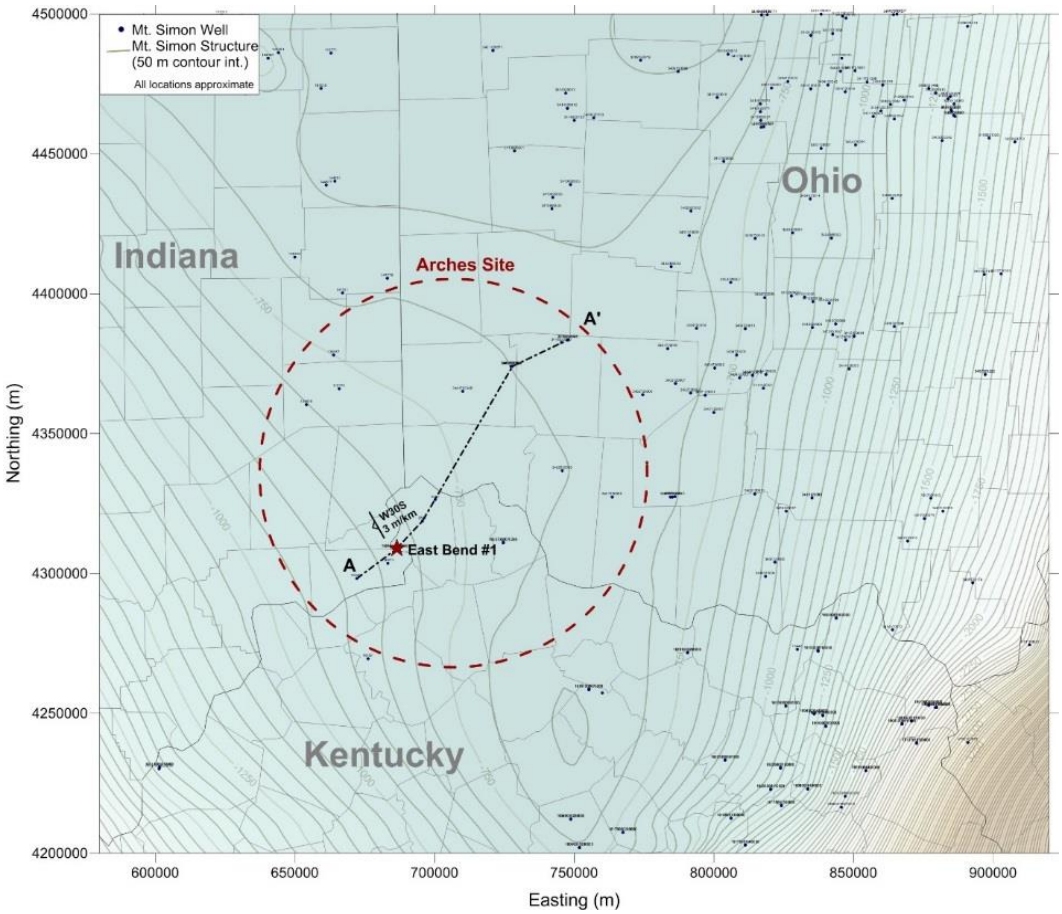

Figure 6-4: Local map showing East Bend #1 well in relation to Mount Simon sandstone structure map.

Figure 6-5 shows a southwest-northeast geologic cross section through the East Bend site. The figure illustrates the continuous, flat-lying nature of the deeper Ordovician-Cambrian age rocks in the region. The Mount Simon sandstone is the main option for CO_2 storage, because other rock formations are not deep enough to maintain supercritical conditions. The primary containment layer is the Eau Claire shale, with additional containment provided in the Davis-Copper Ridge Formations of the Knox Group. Overall, the members of the Knox Group are less distinct than other areas of the Midwest, such that many geologists denote the Knox as one unit. Intermediate layers include the Wells Creek, Highbridge, and Lexington Formations. At the East Bend #1 site, there is also a section of alluvium of the Ohio River Valley.

The Arches area is located on the western flank of the Cincinnati arch, where rocks dip toward the Illinois Basin. On a local scale, the rocks are fairly flat, with a negligible dip of 3 meters per kilometer to the east-southeast (Figure 6-6). The Mount Simon sandstone thickens toward the east into the Illinois Basin and is continuous toward the west and the axis of the Cincinnati arch. Geologic structure is fairly uniform toward the north, but the geologic setting is more complex south of the East Bend site toward the Lexington River fault system.

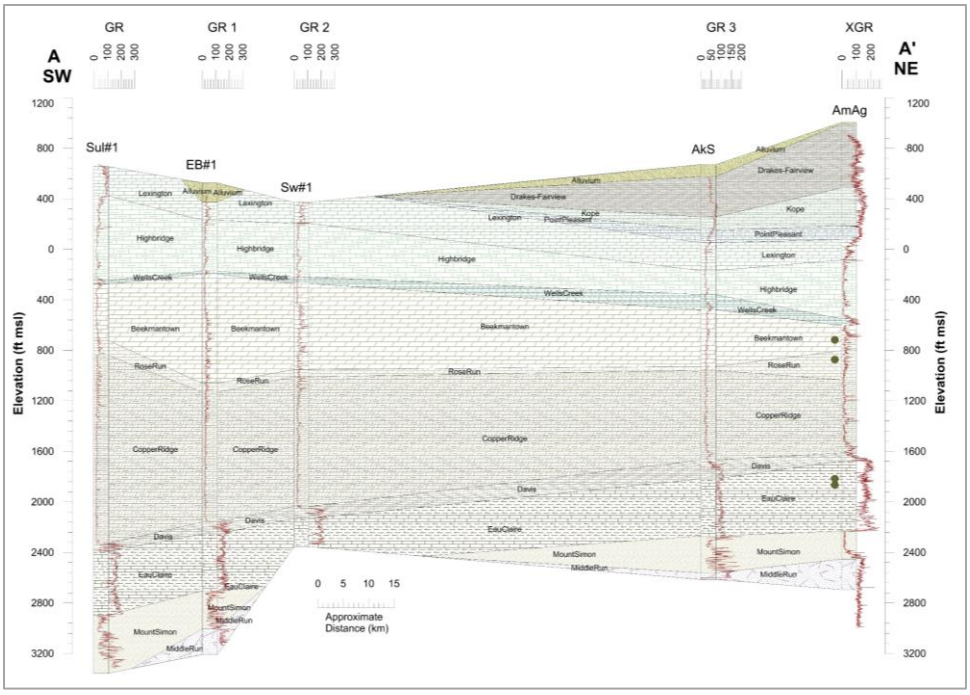

Figure 6-5: Regional A-A’ geologic cross section through East Bend #1 well.

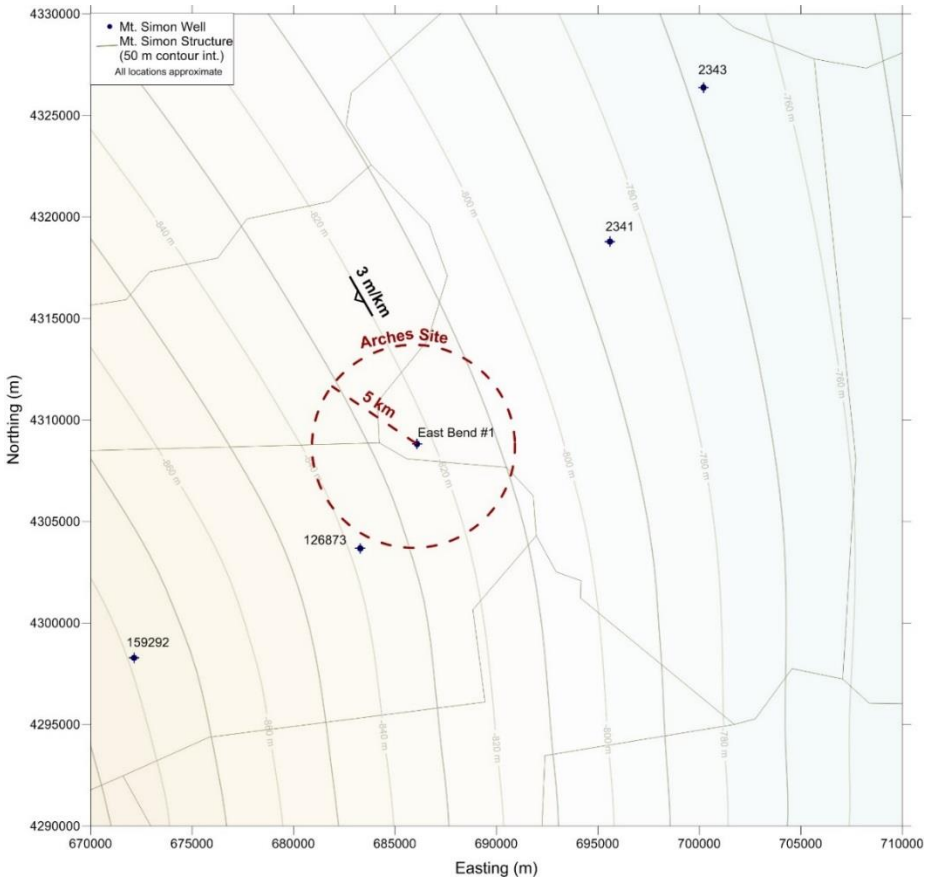

Figure 6-6: Local Mount Simon sandstone structure map.

The Arches model was built using a single well for distribution of hydraulic parameters along with several surrounding wells to build a homogenous, layered model. Stratigraphy at the site was determined with a combination of wireline logs, mud logs, rock core sampling, and examination of drill cuttings (Battelle, 2010).

Figure 6-7 shows geophysical log analysis from the East Bend #1 well. The Lexington limestone is the first bedrock unit, extending to a depth of 296 ft below ground surface (bgs). Beneath the Lexington limestone is the Highbridge limestone (296 to 698 ft bgs), a light-colored limestone with some dolomitization. The Wells Creek limestone, a slightly argillaceous and slightly dolomitized limestone, is present from 698 to 722 ft bgs. The Knox Group was noted from 722 to 2,686 ft bgs. The Knox exhibited a generally consistent log response with subtle indication of the Beekmantown dolomite, subtle Rose Run sandstone, and the Copper Ridge dolomite. The Knox Group is made up of dolomites with sandy layers, clay lenses, and accessory minerals. The Davis limestone/shale was present at 2,686 to 2,782 ft bgs. The Davis was described as an interbedded limestone and shale deposit. The Eau Claire Formation is the main caprock in the East Bend #1 well at 2,782 to 3,230 ft bgs, grading between dolomite and shale. The Mount Simon sandstone was logged as a relatively well sorted fine- to coarse-grained sandstone from 3,320 to 3,532 ft bgs. Below the Mount Simon was the Precambrian Middle Run sandstone, a dense arkose sandstone.

Key hydrostratigraphic layers were classified based on the nuclear magnetic resonance (NMR) permeability log (Figure 6-7). The Knox units follow a consistent low-permeability trend of 0.1 to 1.0 millidarcy (mD). The Davis Formation has indications of high-permeability streaks. The Eau Claire has a very low trend with permeability mostly less than 0.001 mD. The majority of the Mount Simon sandstone has reservoir quality permeability on the order of 10 to 1,000 mD. Well tests in the East Bend well indicated that reservoir transmissivity was 9,100 millidarcy-feet (mD-ft) across a test interval of 3,410 ft to 3,510 ft. Because injection tests are a more reliable measurement of overall transmissivity of the reservoir, the NMR permeability results were scaled to the transmissivity of 9,100 mD-ft in the model input parameters.

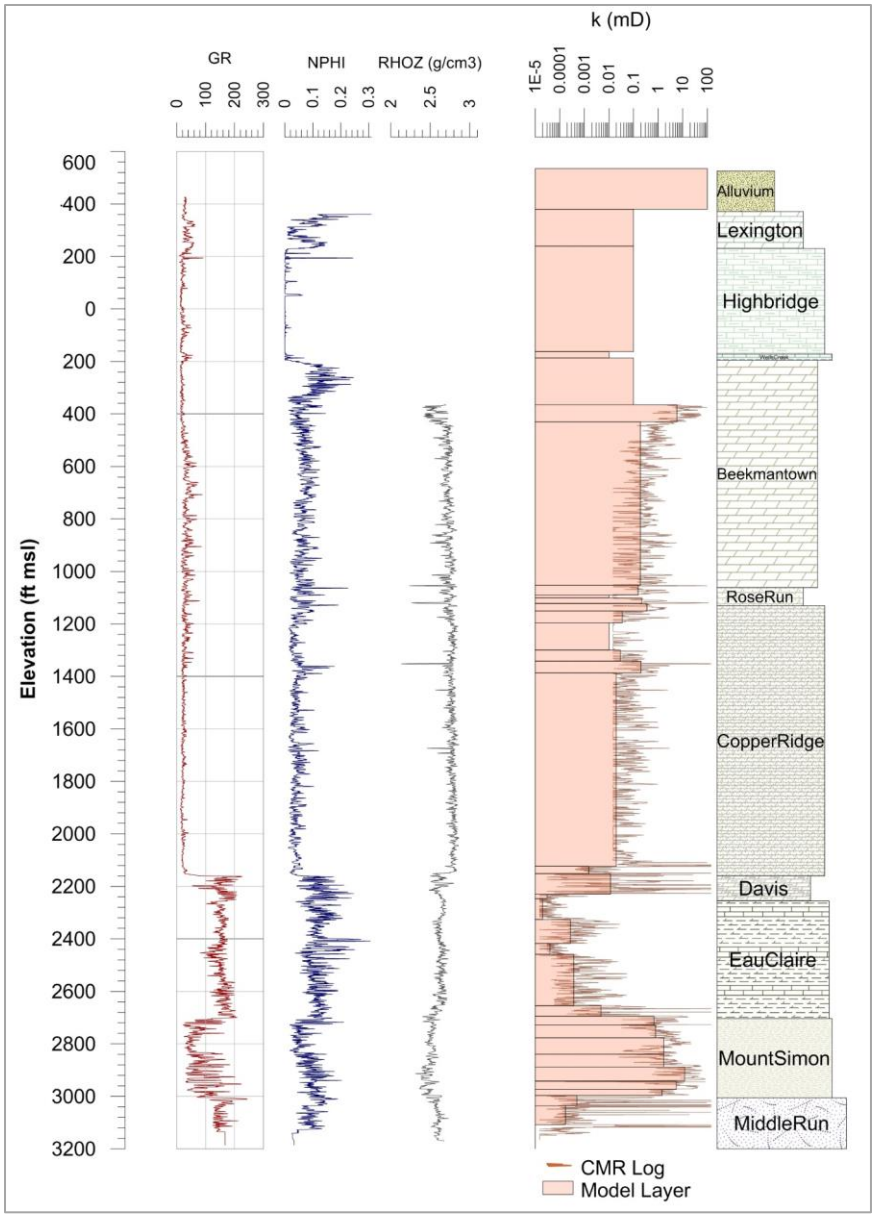

Figure 6-7: East Bend #1 geophysical well log suite with injection interval noted.

Geomechanical Input Parameters

The main objective of this work was to investigate the variations in poro-elastic properties in potential CO_2 storage and caprock layers, which were used as input to the coupled reservoir-geomechanical simulator. Detailed characterization of sedimentary formations, in terms of poro-elastic properties, is critical to delineate suitable CO_2 injection units, then use these units as a guide to geologically meaningful reservoir simulation. Analysis results provide a better understanding of the integrity of subsurface storage reservoirs, in terms of interplay among poro-elastic properties, CO_2 injection rate, and potential subsurface deformation.

Various core samples, basic triple combo logs, and advanced well logs (such as pulsed neutron spectroscopy, multi-component sonic, resistivity image, and NMR) were used to analyze Young's modulus, Poisson's ratio, principal stresses (maximum horizontal stress, minimum horizontal stress, and vertical stress), porosity, and permeability. All these parameters were integrated to subdivide the whole subsurface into different geomechanical units, which are comparable and scalable to certain flow-zone units. These are called "poro-elastic units." Each unit has certain geomechanical and reservoir characteristics that are visible from well log data patterns (Figure 6-8 and Figure 6-9).

In the Midwest United States, the Mount Simon sandstone formation is considered a favorable reservoir for CO_2 injection, where it has a combination of suitable geomechanical properties, porosity, permeability, and required overburden (Figure 6-10). All of the overlying formations are considered as a seal for this reservoir system. The whole alluvium-Eau Claire stratigraphic column contains multiple thick and tight shale and carbonate layers that can work as effective seals. In addition, the Mount Simon sandstone formation has argillaceous units in certain parts (based on gamma ray and mineralogy logs), which have an impact on geomechanical responses. They may act as intraformational seals.

At the Arches study area, the Mount Simon sandstone formation consists of seven poro-elastic units, four of which have higher rigidity compared to the other three. P1, P2, P3, and P4 units have Young's modulus higher than 6.5 MPa, whereas P5, P6, and P7 units have Young's modulus less than 6.5 MPa. In terms of porosity and permeability, P3, P4, P5, and P6 units have porosity and permeability ranging between 7 and 12% and 17 and 119 mD (Table 6-5).

Next, the poro-elastic units were chosen for reservoir gridding inside the full geomechanical system for the Arches site. Average values of geomechanical and reservoir parameters for each poro-elastic unit were chosen as input to coupled flow-geomechanical simulations at the commercial rate of CO_2 injection to analyze corresponding stress-field response in the reservoir and caprock.

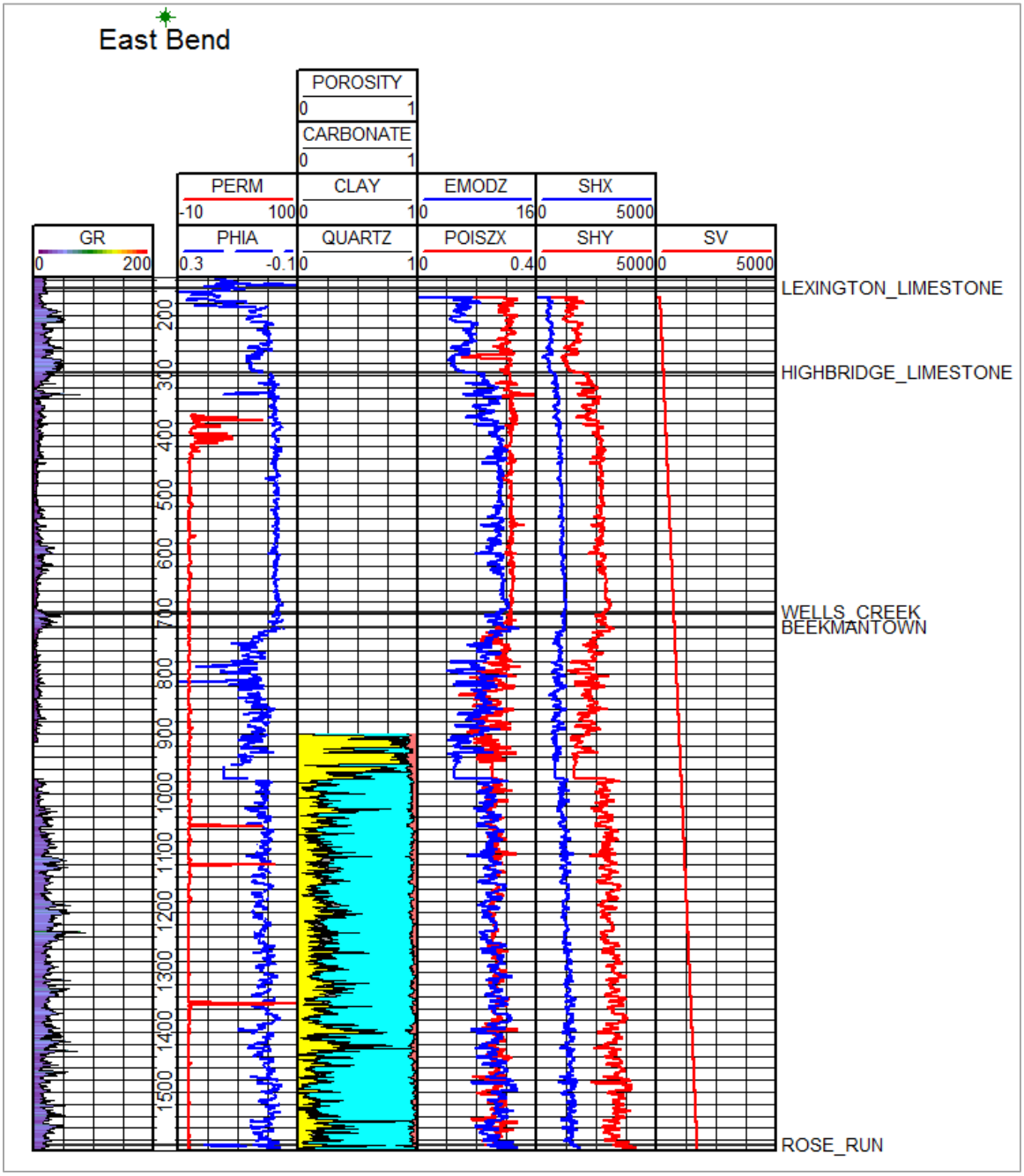

Figure 6-8: Display of well logs showing various geomechanical and reservoir parameters from the Lexington Formation to top of the Rose Run Formation. First, second, third tracks show gamma ray (GR), average permeability (PERM), average porosity (PHIA), mineralogy, whereas fourth, fifth, and sixth tracks show Young's modulus (EMODZ), Poisson's ratio (POISZX), maximum horizontal stress (SHX), minimum horizontal stress (SHY), and vertical stress (SV).

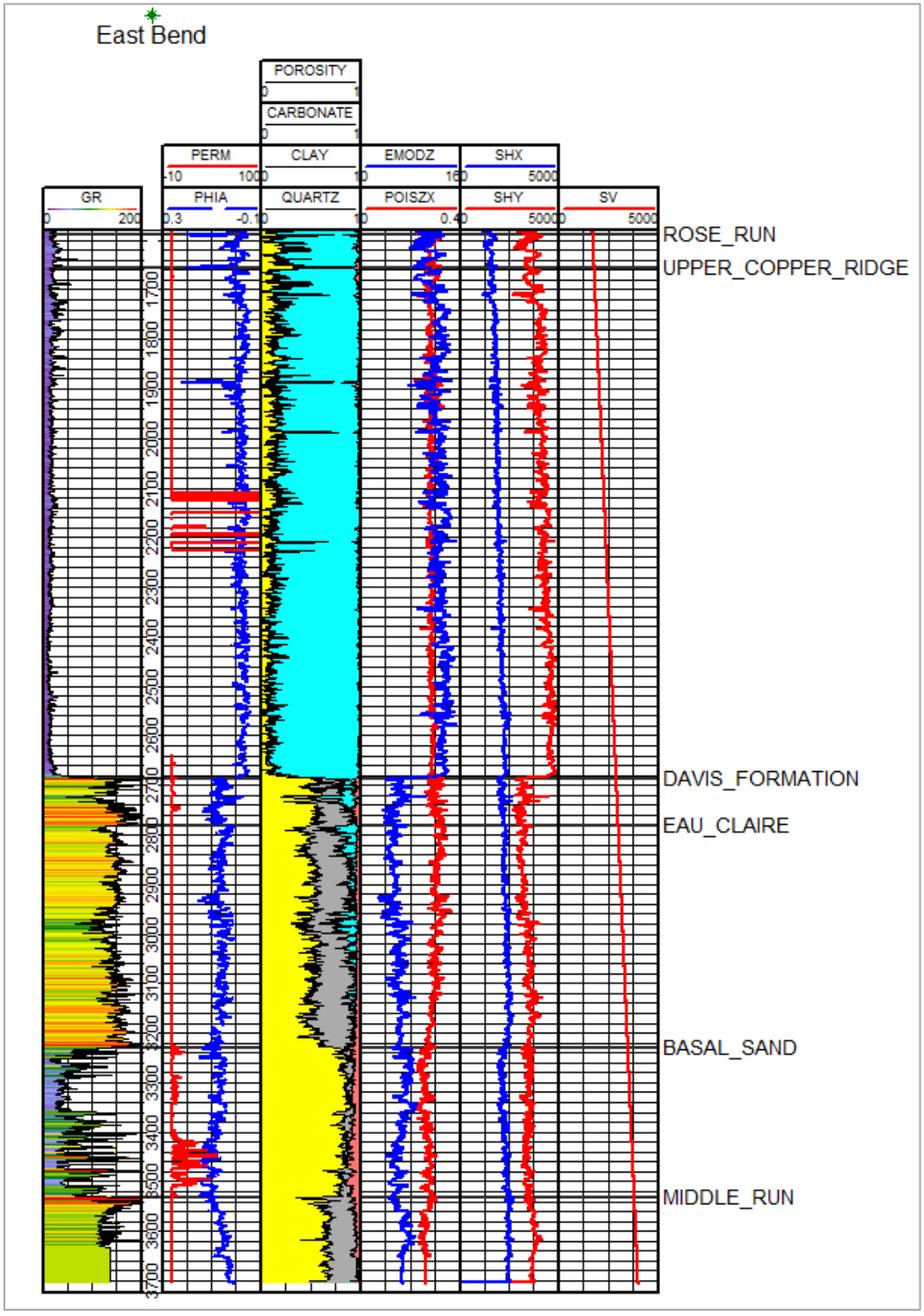

Figure 6-9: Display of well logs showing various geomechanical and reservoir parameters from the Rose Run Formation to the bottom of the Middle Run Formation. The Mount Simon/basal sandstone reservoir has higher poro-perm, and sandy lithology compared to other geologic formations.

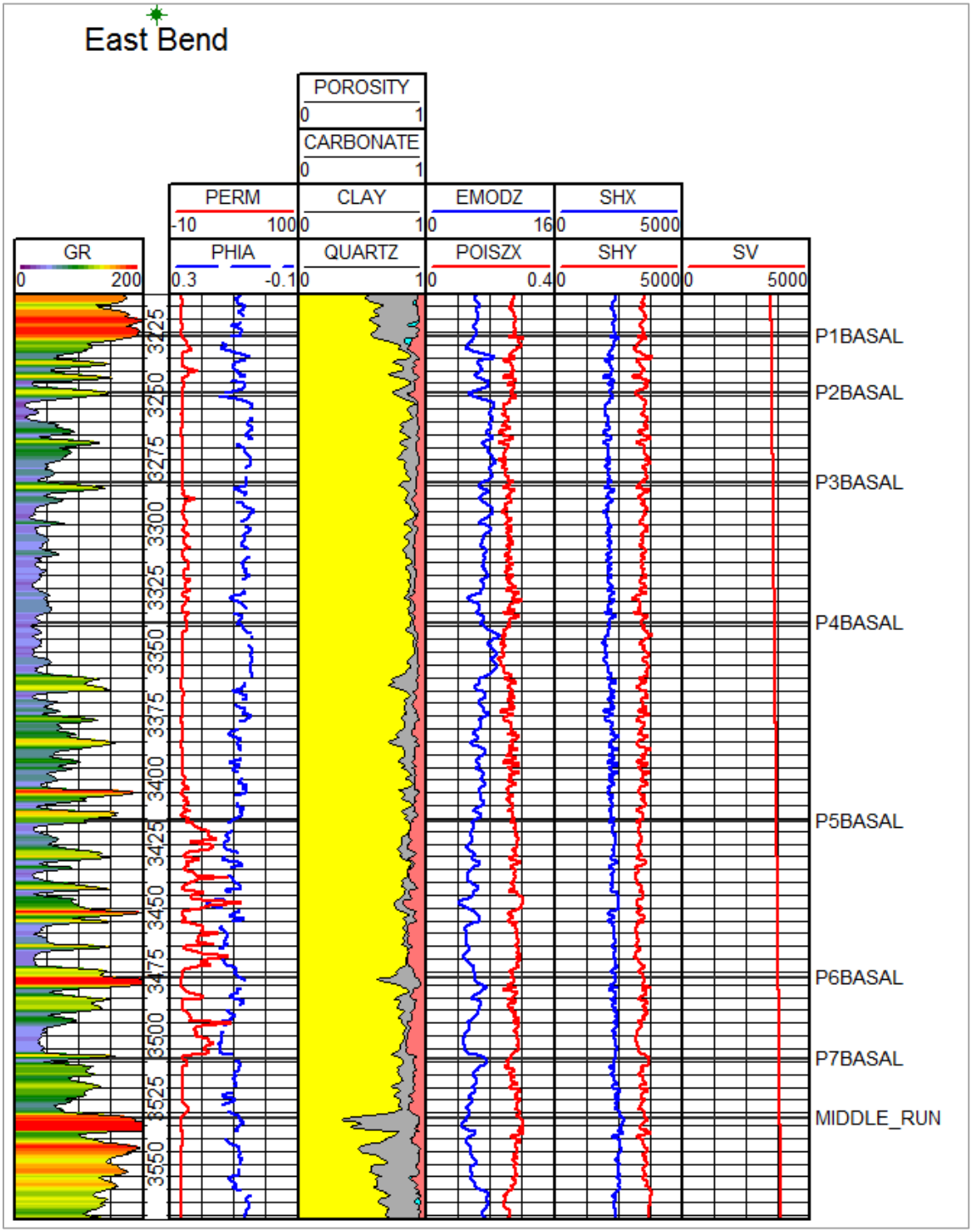

Figure 6-10: Well logs showing various geomechanical and reservoir parameters from the Rose Run Formation to bottom of the Middle Run Formation. The Mount Simon/basal sandstone reservoir consists of seven poro-elastic units. All seven units have certain geomechanical and reservoir characteristics that are comparable and scalable.

Table 6-5: Average values of geomechanical and reservoir properties of different poro-elastic units considered as seal and reservoir at the Arches study area.

	Poro-elastic Units	Bottom Depth (feet)	Young's Modulus	Poisson's ratio	Sh_{min}/ feet	Sh_{max}/ feet	Porosity	Perm.
Seal	Alluvium-Eau Claire	3,227	8.68	0.29	1.31	3.08	0.02	0.52
Reservoir	P1 Basal Sand	3,249	6.52	0.27	0.68	1.05	0.1	7
	P2 Basal Sand	3,284	7.79	0.25	0.64	1.08	0.06	8
	P3 Basal Sand	3,339	7.08	0.26	0.65	1.03	0.07	17
	P4 Basal Sand	3,416	7.09	0.26	0.64	1.02	0.07	17
	P5 Basal Sand	3,477	5.53	0.28	0.67	0.96	0.12	119
	P6 Basal Sand	3,509	5.85	0.27	0.68	0.98	0.11	55
	P7 Basal Sand	3,643	5.97	0.27	0.68	0.98	0.11	14

Note: The gradient values represented here are only a preliminary estimate; those used in reservoir simulation are described in the next section.

6.2.2 E-Central Appalachian Basin Study Site

The East-Central Appalachian Basin study area is in eastern Ohio along the east-central portion of the Appalachian Basin. In this area are thick sequences of Ordovician-Cambrian-age rock formations that provide a suitable framework for CO_2 storage. Brine injection wells provide operational evidence for these rocks to accept large volumes of fluids over long time periods. The region also has many large CO_2 point sources located along the Ohio River Valley.

The East-Central Appalachian Basin site is located on the east-central flank of the Appalachian Basin (Figure 6-11). In this area, Paleozoic rocks dip and thicken toward the east-southeast into the Rome trough and the center of the basin. The site is representative of the Knox-basal sandstone rock interval that includes several key CO_2 storage formations in the region. These Cambrian-age zones are deep, overlain by thick caprocks, relatively continuous, saturated with dense brine, and mostly free of oil and gas reservoirs. There are many Class I and Class II injection wells completed in these zones with a long history of high injection rates, which substantiates the potential for CO_2 injection.

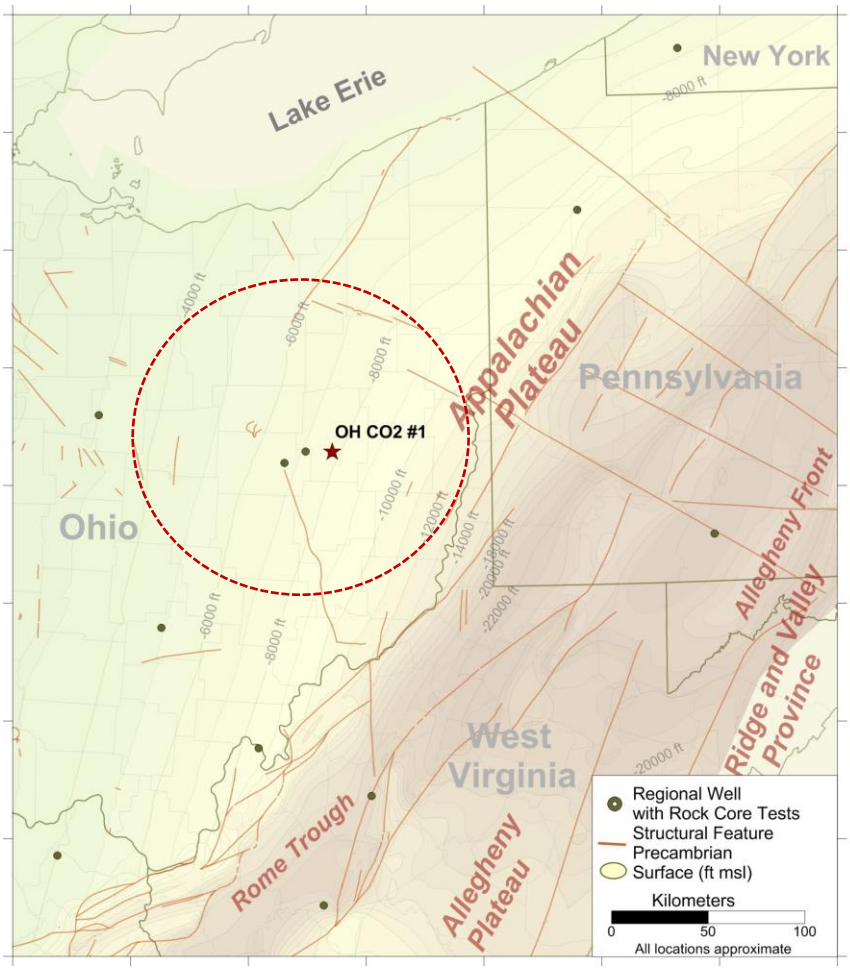

Figure 6-11: East-Central Appalachian Basin study area map.

The East-Central Appalachian Basin geological model was set up to simulate injection scenarios into thick (>500-ft) intervals of the Ordovician and Cambrian section. Many Class I and Class II injection wells in the East-Central Appalachian Basin are cased off through the Beekmantown and Rose Run sandstones and inject into the Upper Copper Ridge to the top of the basal Cambrian sandstone (Figure 6-12). There is oil and gas production from the Beekmantown and Rose Run zones near some of these injection wells, so the zones are cased off to protect offset production. The potential for induced seismicity from injection into the Precambrian has also precluded drilling into the Precambrian basement in the newer wells.

The Upper Copper Ridge to basal Cambrian sandstone model was based on characterization data collected in the OGS CO_2 #1 well (API 3415725334) located in Tuscarawas County, Ohio. This well was drilled in 2007 as part of the regional characterization efforts for CO_2 storage (Wickstrom et al., 2011). An extensive geophysical log suite was completed in the well, along with sidewall rock core collection and well testing. The research was focused on the deeper Ordovician-Cambrian-age rock formations.

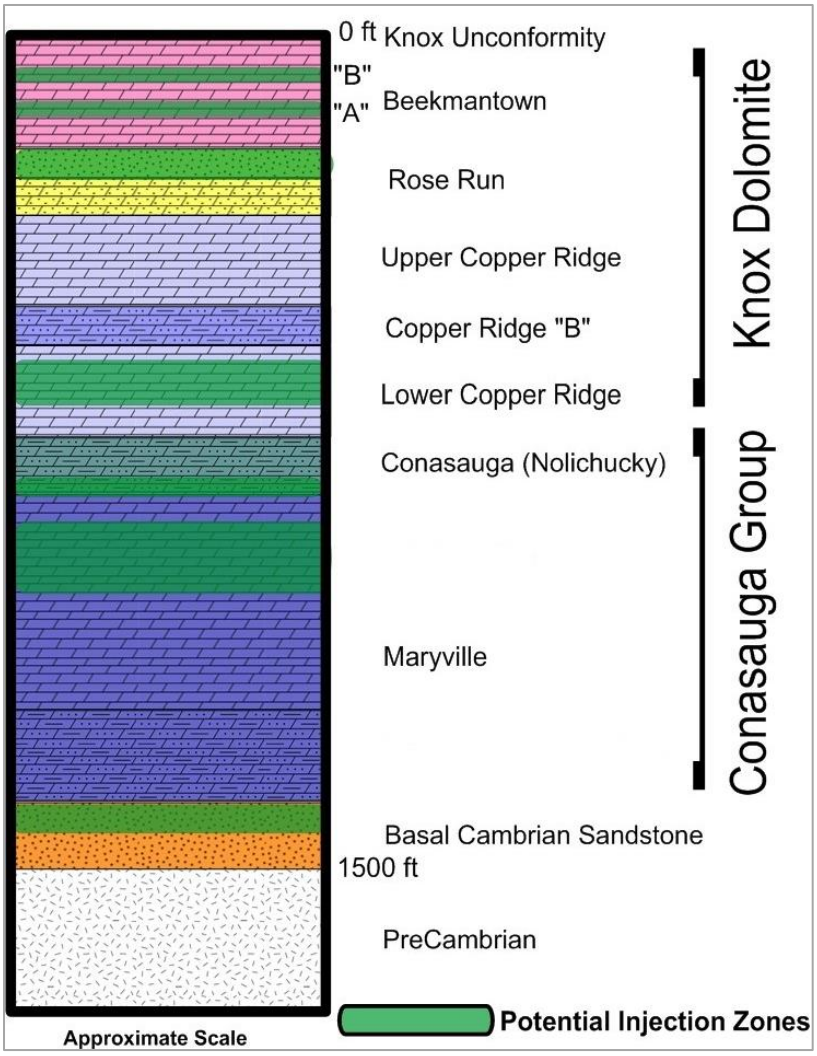

Figure 6-12: Diagram illustrating lithology in the Knox Group for the East-Central Appalachian Basin site.

The main zones of interest for injection in the well were the Lower Copper Ridge dolomite, Maryville Formation, and basal Cambrian sandstone (Figure 6-13). The Rose Run and basal Cambrian sandstone units are regionally thick, stratigraphically continuous zones, but the permeability in these units is lower than the thin, high-permeability reservoir zones in the carbonate units. These permeability trends have a significant impact on reservoir analysis and on efforts to identify the most promising injection zones over several thousand feet of open-hole logs.

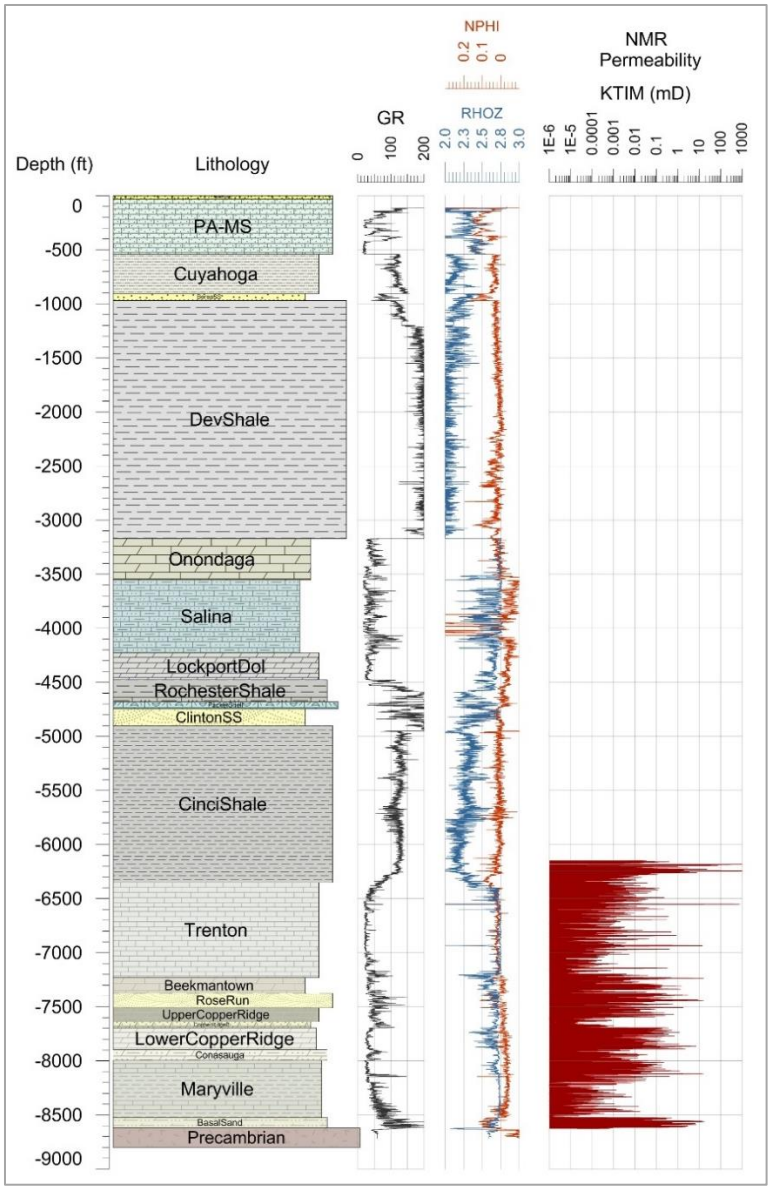

Figure 6-13: Log curves and lithology for the East-Central Appalachian Basin site.

The geologic model was designed to accommodate open-hole single well reservoir simulations. The model includes both clastic and carbonate lithologies to assess the overall performance and differences in geomechanical response to CO_2 storage in the different units. The model layers were assigned based on the gamma, neutron, and bulk density logs. The NMR-derived permeability was used to designate permeability (see Figure 6-13). The NMR-derived permeability for the Rose Run and basal sandstone was compared to the sidewall core-derived and reservoir injection permeability values by Wickstrom et al. (2011). While the permeability values have wide ranges between the methods, the NMR values were comparable to core and injection permeability values. The geological model layers were created in an effort to include both thick moderate-permeability zones along with thin high-permeability zones.

Integrated analysis of geomechanical and reservoir properties for the OGS CO_2 well was completed. Detailed geomechanical and petrophysical characterization of sedimentary formations is important to delineate suitable CO_2-injection units, and to use these units as a guide in the geologically meaningful simulation process. The information helps to better understand the interplay among different poro-elastic properties on fracture initiation and its growth in the reservoir and caprocks upon fluid injection.

Next, all geomechanical and petrophysical logs were analyzed to delineate the reservoir-caprock system. The basal sandstone formation may be considered as a favorable reservoir for CO_2 injection, where it has a combination of suitable geomechanical properties, porosity, permeability, and required overburden (Figure 6-14). All of the overlying formations are considered a seal for this reservoir system (Figure 6-15). The lower portion of the Rome Formation contains two layers with very low porosity and permeability, which can work as effective caprocks. The basal sandstone formation consists of two poro-elastic units: P1 and P2. The P1 unit has a higher permeability and Young's modulus than the P2 unit. The P2 unit has a higher Poisson's ratio than the P1 unit. Next, the poro-elastic units were chosen for reservoir gridding inside the full geomechanical system for the OGS CO_2 well. Average values of different geomechanical and reservoir parameters for each poro-elastic unit were used as input to coupled flow-geomechanical simulations at a commercial rate of CO_2 injection to analyze corresponding stress-field response in the reservoir and caprock.

6.2.3 Northern Appalachian Basin Study Area

The Northern Appalachian Basin study area is located in western New York, northeast Ohio, and northwest Pennsylvania. This study area is closer to the Appalachian Mountains, where the sedimentary rocks are more affected by geologic structures than the other two study areas discussed in this report.

The Northern Appalachian Basin study area is situated along the northern portion of the Appalachian Basin near the New York, Ohio, and Pennsylvania border. Figure 6-16 illustrates the nature of the regional geologic structures in relation to the study area. While the deeper Paleozoic rocks at this site are similar in overall stratigraphy, they reflect a different depositional setting and structural history compared to the other two sites. In general, the site is located in an area where the rocks are more influenced by the Appalachian Mountains compared to the other two sites included in this research. Shumaker (1998) explains that the region includes "low-amplitude plateau folds extending westward to undeformed rocks in northwest New York, Eastern Ohio, and eastern Kentucky." These areas are more characterized by the presence of moderate (>700 ft) anticlines in Paleozoic rocks. Structurally, the strata have a regional dip 40 to 50 ft per mile (0.4 to 0.5 degrees) to the south-southeast and an east-northeast strike (Richardson, 1941).

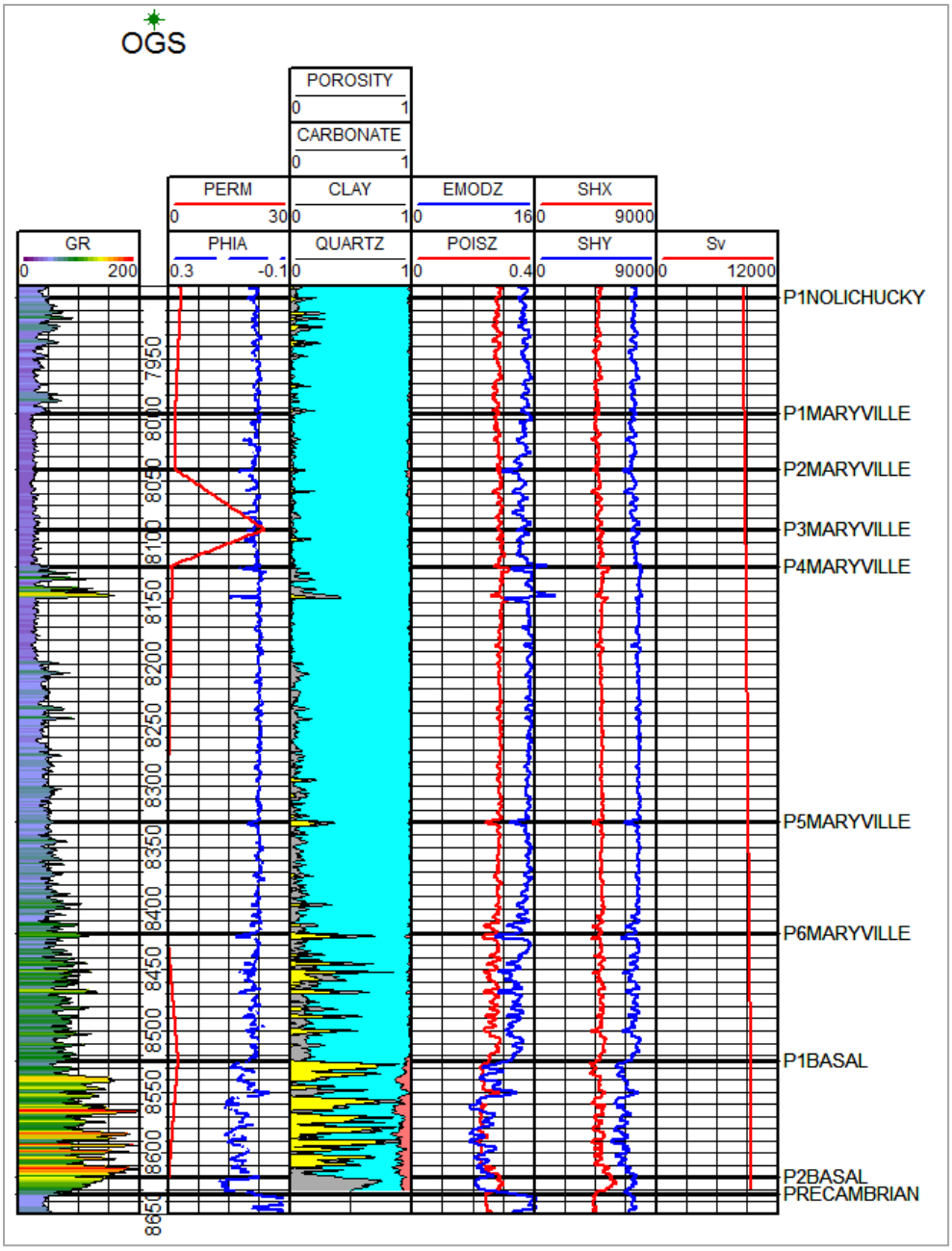

Figure 6-14: Display of well logs showing various geomechanical and reservoir parameters from the Conasauga Formation to top of the Precambrian basement. First, second, third tracks show gamma ray (GR), average permeability (PERM), average porosity (PHIA), mineralogy, whereas fourth, fifth, and sixth tracks show Young's modulus (EMODZ), Poisson's ratio (POISZ), maximum horizontal stress (SHX), minimum horizontal stress (SHY), and vertical stress (Sv).

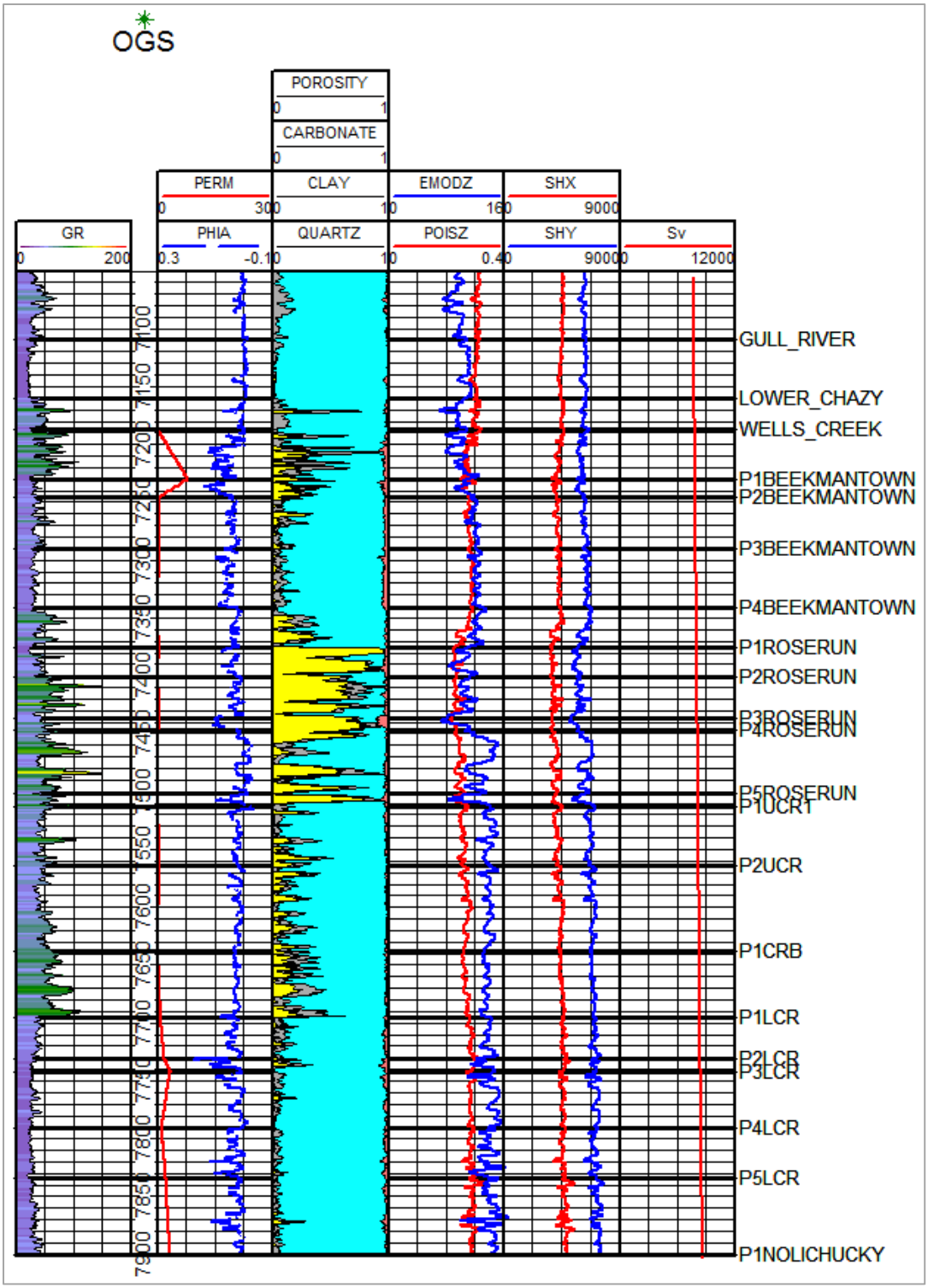

Figure 6-15: Display of well logs showing various geomechanical and reservoir parameters from the Upper Chazy to Copper Ridge formations.

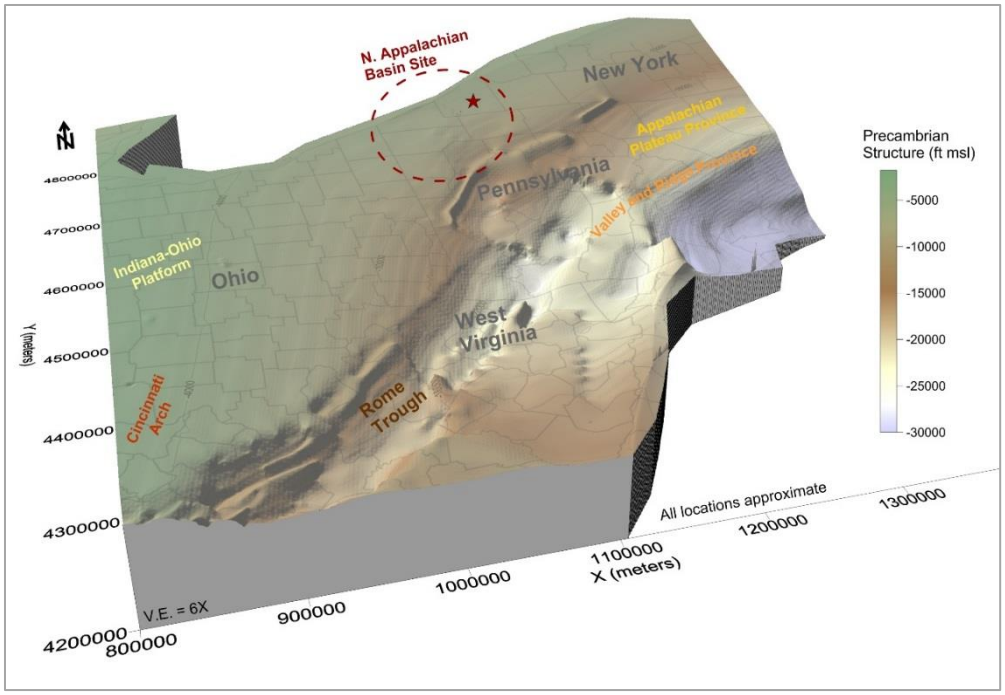

Figure 6-16: Diagram Illustrating regional geologic features for the Northern Appalachian Basin site.

Rock formations at the Northern Appalachian Basin site include Devonian shale through Cambrian Potsdam sandstone. The Paleozoic sedimentary rocks overlie Precambrian age igneous/metamorphic rocks. The Silurian Bass Islands structural play is present south of the study area site. In addition, there is active production from the Silurian Medina/Grimsby-Whirlpool Formation throughout Chautauqua County. Minor hydrocarbon production has also occurred in the Trenton-Black River. Consequently, the deeper Ordovician-Cambrian-age rock formations are the primary option for CO_2 storage. These rock formations include the Galway and Potsdam Formations (Figure 6-17). The Galway (also termed the Theresa Formation in this area) is roughly equivalent to the Knox Group present in other portions of the Appalachian Basin, including the Rose Run sandstone and Copper Ridge dolomite members. Containment intervals above these intervals include the Little Falls, Tribes Hill, Black River, Trenton, Utica-Lorraine shale, and Queenston shale.

The Northern Appalachian Basin study was based on a well in Chautauqua County, New York. At this site, a 7,300-ft test well was drilled into the Potsdam sandstone formation. The characterization in the test well was focused on the deeper Cambrian-age Galway Group and the Potsdam sandstone and the overlying caprocks. Shallower formations like the 'Clinton'-Medina are oil and gas plays with active production, so they were not assessed for CO_2 storage. A full program of mud logging, wireline logging, rock core collection, and geotechnical testing of rock cores was completed in the test well. Figure 6-18 summarizes the well construction, the stratigraphic section penetrated, whole core and sidewall core interval, gas and water shows, Trenton oil and gas production, and geophysical logging runs.

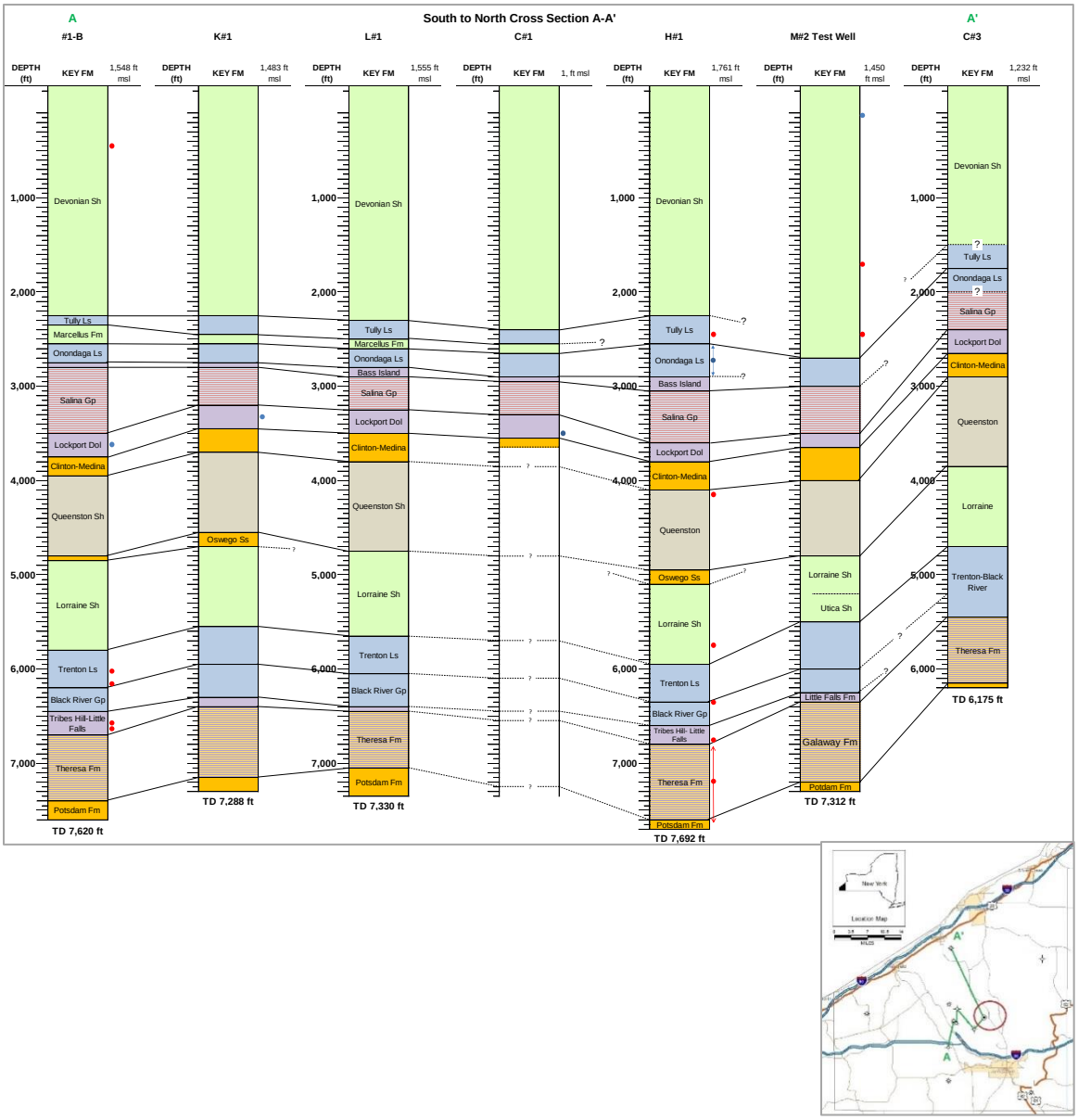

Figure 6-17: Geological cross-section through Northern Appalachian Basin site.

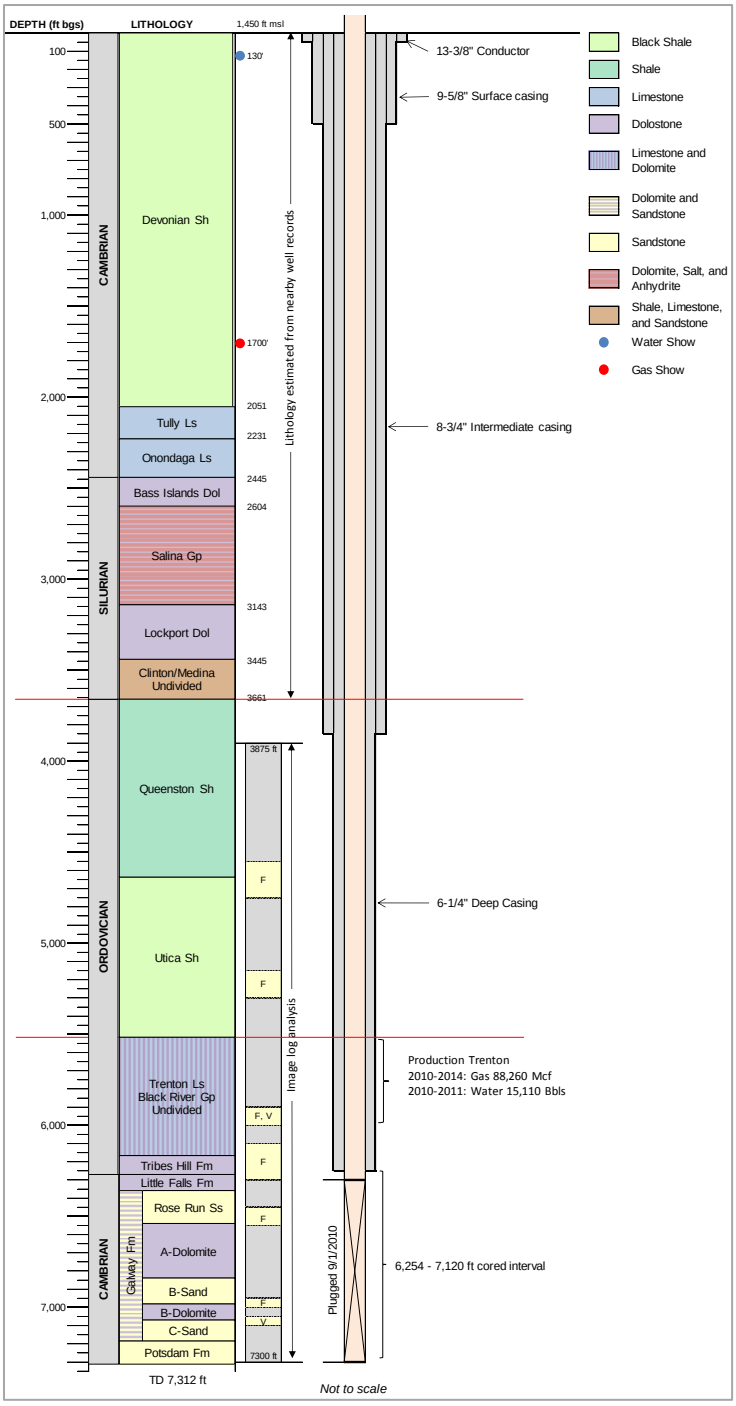

Figure 6-18: Well diagram for Northern Appalachian Basin site.

In the basis well, the Galway Group was 850 ft thick, mainly dolomitic quartz sandstone with minor amounts of clay and iron-oxide minerals. Within the Galway Group, potential injection zones were identified in the Lower Little Falls/Rose Run sandstone, Galway B-sand, and Galway C-sand. However, geophysical log results and core tests showed that these formations were present as thin, sandy intervals. The well penetrated 108 ft of the Potsdam sandstone, which was described as a dolomitic quartz sandstone. Key caprocks penetrated in the test well included the Queenston shale, Utica shale, Black River Group, and Little Falls Formation. Together, these formations represent over 2,500 ft of containment layers. Log and core test data demonstrate that the formations have low permeability and porosity. According to Riley and Baranoski (2006), the Tribes Hill is equivalent to the Beekmantown dolomite, the Little Falls Formation is equivalent to the Rose Run sandstone, and the Galway Formation is partly correlative to the Copper Ridge dolomite and the Conasauga Formation of eastern Ohio.

The geologic model layers were assigned based on geophysical logs, rock core samples, and mud logs. The depths of the shallower Devonian-Silurian layers were based on nearby wells because shallow wireline logs were not available for the basis well. Figure 6-19 shows geologic layers along with geophysical logs. The main injection intervals are present in the Lower Little Falls/Rose Run through Potsdam interval. Containment layers include the Queenston shale through the Little Falls dolomite, which have a combined thickness of over 2,600 ft. The logs generally indicate porosity less than 5% through the caprock intervals. Some reservoir zones have porosity of 5% to 10%, but much of the interval has less than 5% porosity. Permeability measurements from rock cores were generally less than 0.1 mD (Table 6-6). Log-derived permeability was similarly less than 0.1 mD, with some thin streaks in the 1- to 10-mD range. Overall, the Northern Appalachian Basin site has low-permeability storage zones, suggesting that only low CO_2 injection rates may be feasible at the site.

Integrated analysis of geomechanical and reservoir properties for the Northern Appalachian Basin well was completed. All geomechanical and petrophysical logs were analyzed to delineate the reservoir-caprock system. Queenston and Utica shale formations may be considered as caprocks (Figure 6-20). Based on geomechanical and petrophysical logs, the Queenston and Utica Formations were divided into four poro-elastic units. Poro-elastic units in the Utica Formation have higher clay content, higher Poisson’s ratio, and lower Young’s modulus than that of the Queenston Formation, which indicates that the Utica is more ductile than the Queenston.

The Potsdam Formation is the geological equivalent of the basal sandstone reservoir here (Figure 6-21). Most of the formations were divided into two to three poro-elastic units based on well log data. However, most of them (except a few intervals in the Tribes Hill and Potsdam Formations) have very low porosity and permeability (less than 5% porosity), which may not be suitable for CO_2 injection at commercial rate (Figure 6-21).

Next, the poro-elastic units were chosen for reservoir gridding inside the full geomechanical system for the Northern Appalachian Basin study area well. Average values of different geomechanical and reservoir parameters for each poro-elastic unit were used as input to coupled flow-geomechanical simulations at commercial rate of CO_2 injection to analyze corresponding stress-field changes in the reservoir and caprock.

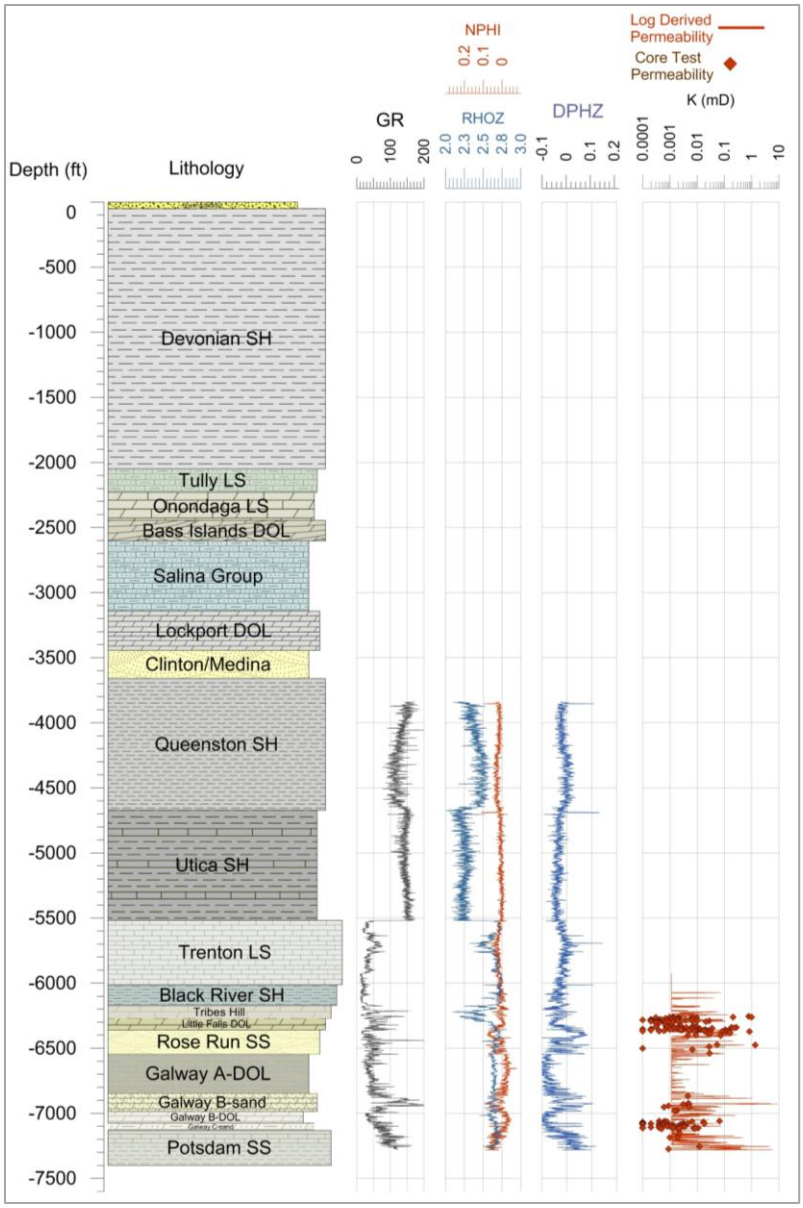

Figure 6-19: Log curves and lithology for the Northern Appalachian Basin site.

Table 6-6: Statistics for rock core test for Northern Appalachian Basin test well.

Rock core test	Count	Mean	Geometric mean	Median	Standard deviation	Range	Minimum	Maximum	Formation
Permeability (mD), to air	26	0.104	0.0076	0.0051	0.302	1.23	0.0007	1.23	Black River sh
Permeability (mD), Klnbrg	26	0.077	0.0023	0.0015	0.240	0.976	0.0001	0.976	
Porosity %, ambient	32	6.4	6.00	6.54	2.12	9.4	2.4	11.8	
Porosity %, NCS	28	5.9	5.59	6.24	2.04	9.4	2.3	11.7	
Grain density, g/cm^3	32	2.8	2.82	2.81	0.027	0.1	2.8	2.9	
Permeability (mD), to air	65	0.035	0.0086	0.0068	0.078	0.397	0.0003	0.40	Little Falls dol
Permeability (mD), Klnbrg	67	0.02	0.0025	0.0021	0.053	0.277	0.00005[a]	0.277	
Porosity %, ambient	68	3.30	2.870	3.03	1.67	8.47	0.49	8.963	
Porosity %, NCS	67	3.20	2.74	2.96	1.68		0.41	8.8462	
Grain density, g/cm^3	68	2.75	2.75	2.76	0.059	0.227	2.62	2.8468	
Permeability (mD), to air	29	0.15	0.0288	0.041	0.380	1.84	0.0004	1.84	Rose Run ss
Permeability (mD), Klnbrg	29	0.11	0.012	0.02	0.289	1.38	0.00005[a]	1.38	
Porosity %, ambient	29	3.43	2.83	3.45	1.81	5.92	0.72	6.64	
Porosity %, NCS	29	3.32	2.67	3.35	1.81	5.96	0.58	6.54	
Grain density, g/cm^3	29	2.67	2.67	2.64	0.053	0.23	2.58	2.81	
Permeability (mD), to air	12	0.01	0.0035	0.0055	0.0051	0.0127	0.0003	0.013	Galway B-sand
Permeability (mD), Klnbrg	12	0.0023	0.0009	0.0017	0.0021	0.005	0.00005[a]	0.0051	
Porosity %, ambient	12	3.38	2.83	3.26	1.69	5.81	0.43	6.24	
Porosity %, NCS	12	3.27	2.69	3.15	1.68	6.10	0.035	6.14	
Grain density, g/cm^3	12	2.65	2.65	2.63	0.071	0.213	2.59	2.8	
Permeability (mD), to air	13	0.014	0.0025	0.0021	0.031	0.11	0.0002	0.111	Galway B-dolomite
Permeability (mD), Klnbrg	13	0.0071	0.0006	0.0005	0.0183	0.066	0.00005[a]	0.066	
Porosity %, ambient	15	1.38	1.22	1.36	0.636	1.87	0.48	2.35	
Porosity %, NCS	15	1.26	1.08	1.26	0.635	1.9	0.35	2.25	
Grain density, g/cm^3	15	2.79	2.79	2.83	0.078	0.23	2.62	2.85	
Permeability (mD), to air	42	0.0067	0.0039	0.0042	0.0075	0.037	0.0004	0.037	Galway C-sand
Permeability (mD), Klnbrg	42	0.0024	0.0011	0.0012	0.0035	0.018	0.0001	0.018	
Porosity %, ambient	46	1.62	1.47	1.53	0.778	3.51	0.63	4.133	
Porosity %, NCS	45	1.52	1.35	1.44	0.783	3.54	0.497	4.03	
Grain density, g/cm^3	46	2.75	2.75	2.80	0.09	0.266	2.59	2.85	
Permeability (mD), to air	2	0.015	0.0097	0.0153	0.0166	0.0235	0.0035	0.027	Potsdam
Permeability (mD), Klnbrg	2	0.0065	0.0033	0.0065	0.0078	0.011	0.0009	0.012	
Porosity %, ambient	3	3.68	3.61	4.18	0.087	1.50	2.68	4.18	
Porosity %, NCS	2	4.08	4.08	4.08	0.012	0.017	4.07	4.09	
Grain density, g/cm^3	3	2.64	2.64	2.63	0.034	0.067	2.61	2.68	

Note: mD = millidarcy; NCS = net confining stress; g/cm^3 = grams per cubic centimeter.

a. Several permeability measurements were below instrument's lower detection limit. In this case, one half of the lower detection limit was used as an approximation.

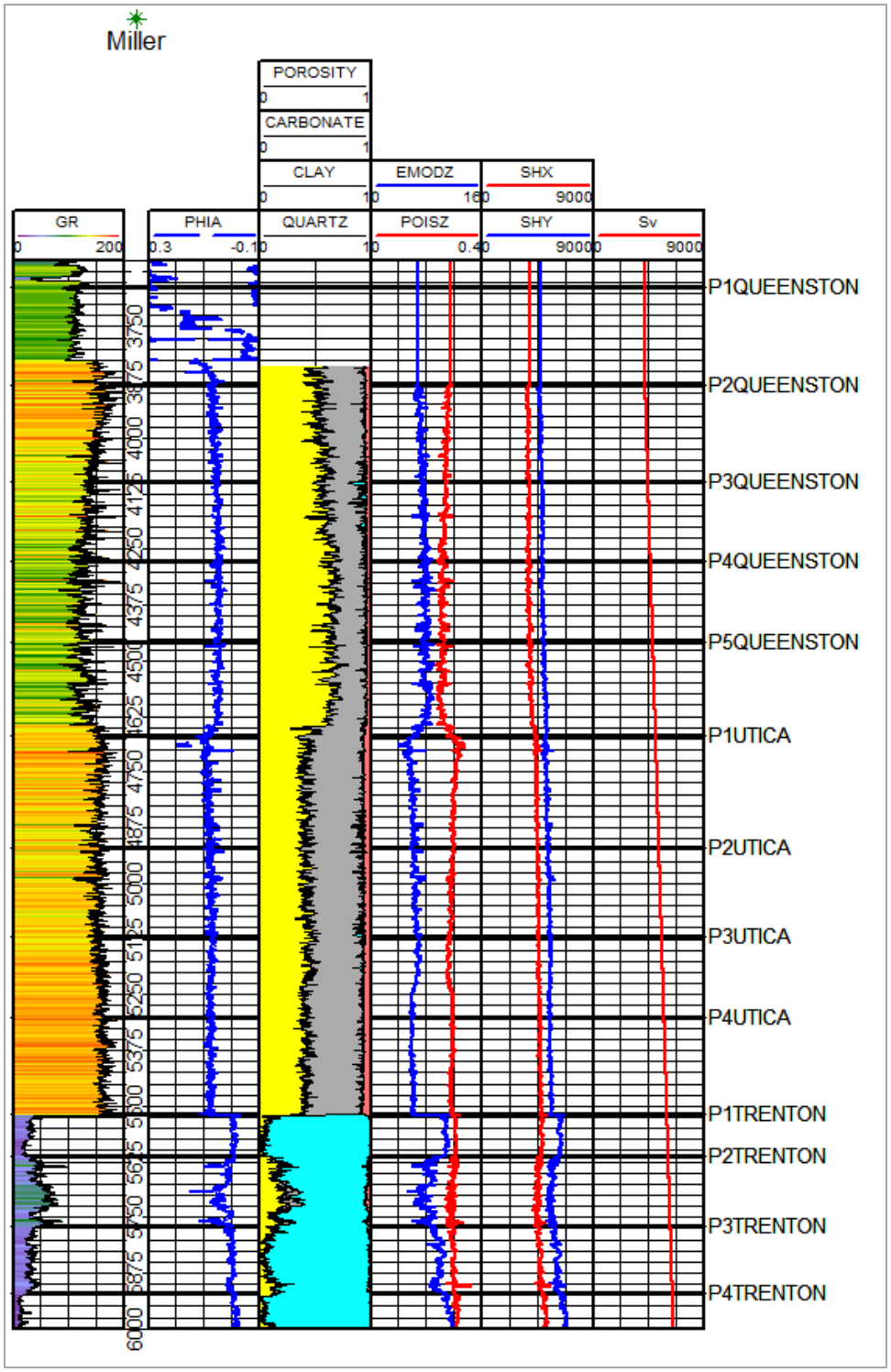

Figure 6-20: Display of well logs showing various geomechanical and reservoir parameters from the Queenston Formation to top of the Trenton Formation. First, second, third tracks show gamma ray (GR), average porosity (PHIA), mineralogy, whereas fourth, fifth, and sixth tracks show Young's modulus (EMODZ), Poisson's ratio (POISZ), maximum horizontal stress (SHY), minimum horizontal stress (SHX), and vertical stress (Sv).

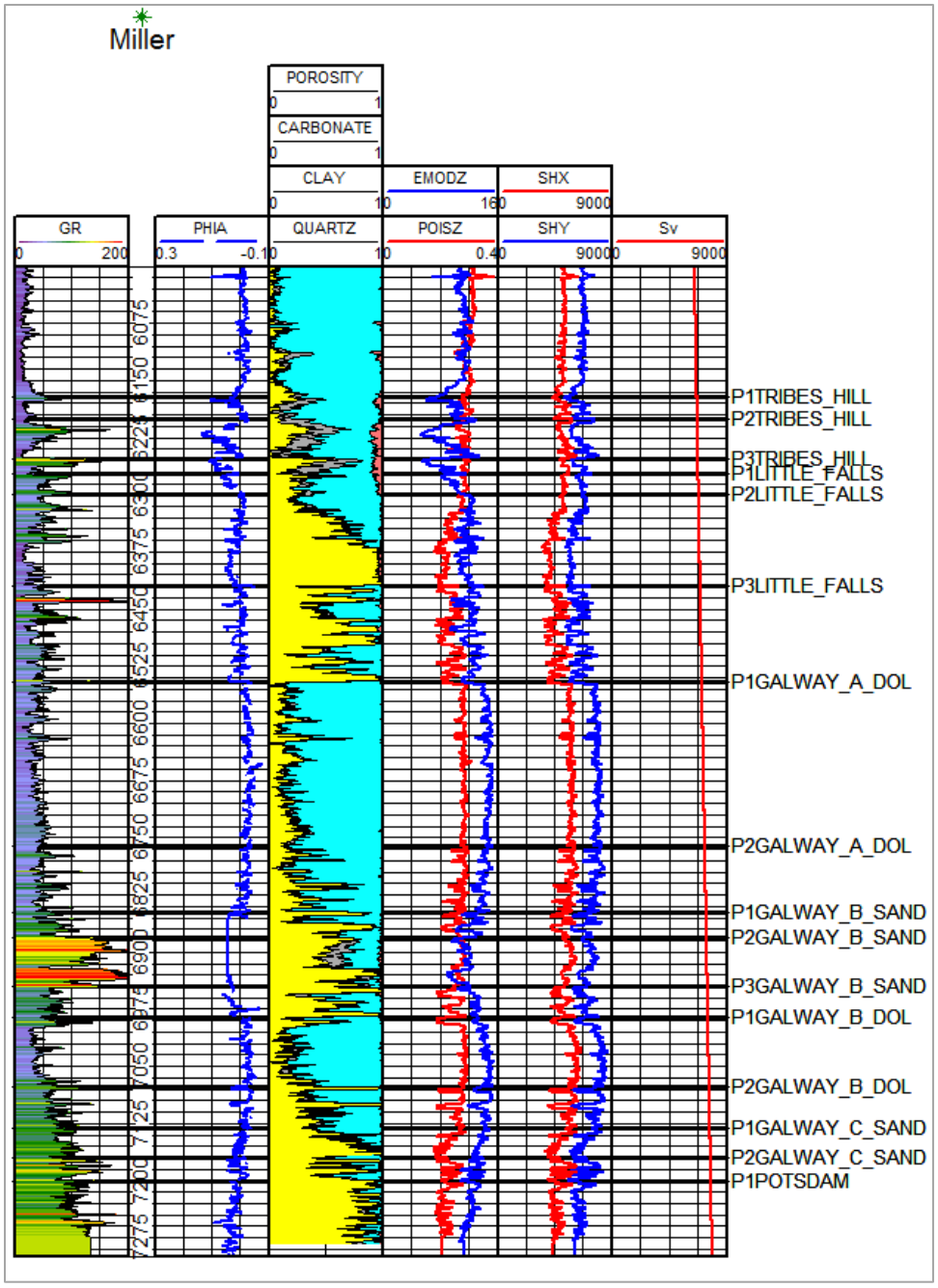

Figure 6-21: Well log curves showing various geomechanical and reservoir parameters from the Tribes Hill Formation to the Potsdam Formation for the Northern Appalachian Basin site.

6.2.4 Fracture Models

The objective of developing fracture models was to depict the nature, frequency/intensity, spacing, orientation, length, and properties of fracture systems in CO_2 storage rock formations and containment intervals for the Northern Appalachian Basin (southwestern New York), East-Central Appalachian Basin (east-central Ohio), and the southern Arches Province (northern Kentucky/southwestern Ohio/southeastern Indiana). These three sites provide a representation of variations in subsurface geomechanical conditions across the region. Figure 6-22 shows the rock layers evaluated for the three sites. The analysis focused on the most suitable storage intervals, which are present in the Ordovician-Cambrian-age rock formations at all three sites. Both the overlying and underlying containment layers were also examined, because they may be affected by CO_2 injection.

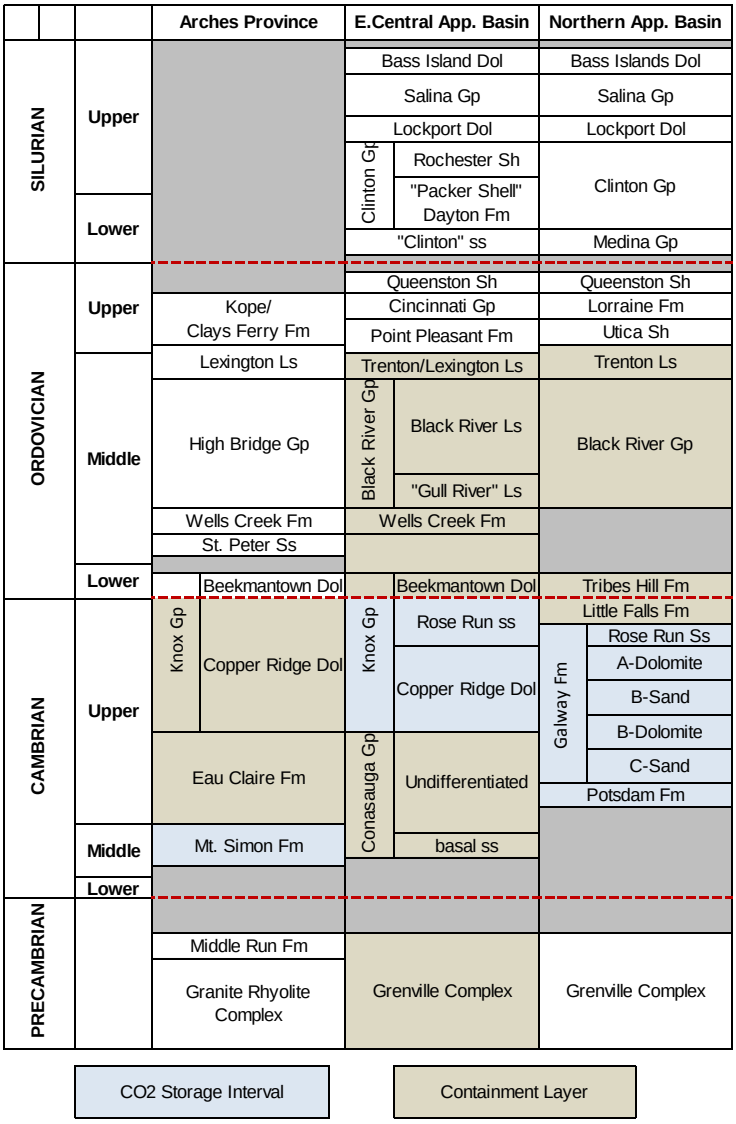

Figure 6-22: Stratigraphic correlation chart for study areas.

6.2.4.1 Arches study area fracture model

The Arches Province is an informal term referring to the geographic area containing broad arch and platform structures in between the regional basin structures in the Midwest United States, with several regional geologic structures: the Cincinnati arch, Indiana-Ohio platform, Kankakee arch, and the Findlay arch (see Figure 6-3). In the Arches Province, the Mount Simon sandstone is the major CO_2 storage rock formation because many other rock formations are not deep enough to sustain supercritical pressure/temperature conditions. The Mount Simon sandstone is also called the informal basal sandstone, because it is found at the base of the Paleozoic rocks in the region. Deposition of the basal sandstone unit is thought to have occurred during the late stages of a Precambrian failed rift system and continued during subsequent sea level rise when sediments were rapidly eroded off Precambrian highlands, resulting in coarse sand rock formations. Research on rock core features suggests that the basal sandstone depositional system included braided fluvial channels with localized alluvial fans that merged into a tidally dominated nearshore environments (Leetaru, 2009; MGSC, 2005; Medina and Rupp, 2010; Ochoa, 2011; Saeed, 2002; Bowen, 2010). Facies trends for basal sandstone show that the unit transitions from the Mount Simon sandstone in eastern Indiana and western Ohio to more dolomitic Conasauga sandstones in eastern Ohio and eastern Kentucky (Battelle, 2017; Wickstrom et al., 2005). In the Arches Province, the Mount Simon is approximately 100 ft to 2,000 ft thick, with the thickest portion in northern Illinois (Figure 6-23).

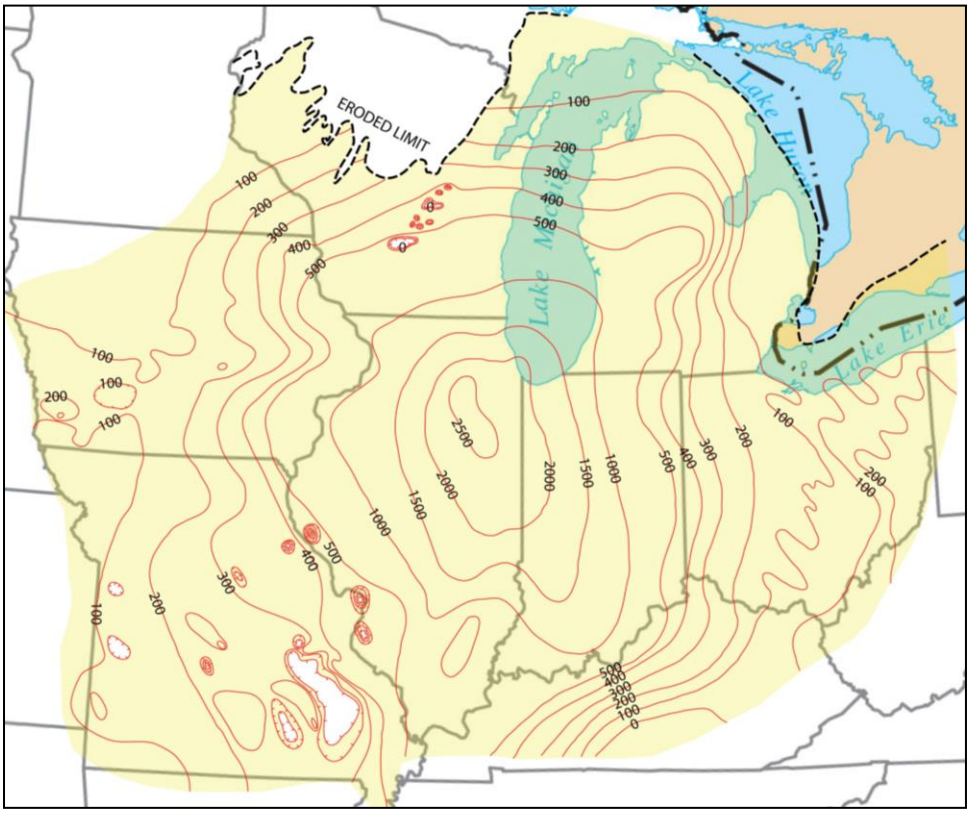

Note: All locations approximate.

Figure 6-23. Isopach map (feet) of Cambrian basal sandstones in the Midwestern United States hydrologic features (from Battelle, 2011).

The Eau Claire shale is the primary caprock with additional containment from the Knox Group. The Eau Claire consists of a mixture of shale, dolostone, and siltstone. In many areas, the lower Eau Claire contains sandstone intervals, indicating a gradational transition from the Mount Simon. The Mount Simon overlies Precambrian bedrock of the Grenville Province. The Precambrian rock formations are an important consideration in the region, because the hypocenters of most seismic activity in the region are located in the deeper Precambrian interval.

Regional Fracture Trends - The broad structures in the Arches Province are considered to have formed during major Paleozoic tectonic orogenies. Structural relief along the arches developed as a result of differential subsidence with the surrounding basins rather than tectonic arching (Wickstrom et al., 1992). Consequently, pervasive faulting and fracturing are not present along the arch structures, as might be found in more localized rock folds. The Rome trough, Kentucky River fault system, Rough Creek fault system, Wabash Valley fault system, and Cottage Grove fault system are present on the periphery of the Arches Province. Faults that have been identified in the Arches Province are more isolated features, which appear to be associated with basement displacement along the Precambrian rocks. Several faults have been proposed in northwestern Ohio (Bowling Green fault system, Maumee fault, Auglaize fault, Anna-Champaign fault), northern Indiana (Royal Center fault, Fortville fault, and the Mt. Carmel fault), and northeastern Illinois (Sandwich fault zone). These faults appear to have limited displacement and extent such that they do not affect the flow of fluids in the subsurface formations being addressed. Structural features in the Arches Province are notable from a regional perspective where they can be traced across large areas. However, rock layers are nearly flat with very little dip on a local basis. Structural dip is very low, on the order of 10 ft to 20 ft per mile or less, with many areas being essentially flat. In the Arches Province, there are few deep boreholes that penetrate the deeper Cambrian age rock formations because not many oil and gas wells were drilled in the region. Consequently, it is challenging to outline regional trends in fracture systems for the study area. A review of well information in the Arches Province indicated that no image logs were available from wells penetrating the Mount Simon within a 50-mile radius of the East Bend site. Consequently, it is difficult to draw many conclusions regarding the regional trends on fracture systems in the Mount Simon for the Arches study area.

Local Fracture Model - The local fracture model for the Arches study area was based on the East Bend #1 test well in Boone County, Kentucky. In this well, an image log was run at a depth interval from 906 ft to 3,700 ft, from the Upper Knox and into the Precambrian basement rock. As described in the *Log Analysis and Integration Summary Report* (Battelle, 2016), the image log was processed and interpreted to determine the presence of any natural fractures (Figure 6-24). The image log showed no natural fractures in the Mount Simon interval. The Eau Claire shale contained some sparse fractures, mostly in the upper portion of the formation. The Knox Group rock formations had more frequent natural fractures. The Beekmantown, with several borehole breakouts and potential vugular development, represents a mixture of textures consistent in an unconformity zone. Microfaults were also identified in this interval. The Rose Run, Copper Ridge, and Davis shale formations showed minor to no structural features. The Middle Run Formation had several deformed beds and laminations starting at 3,570 ft.

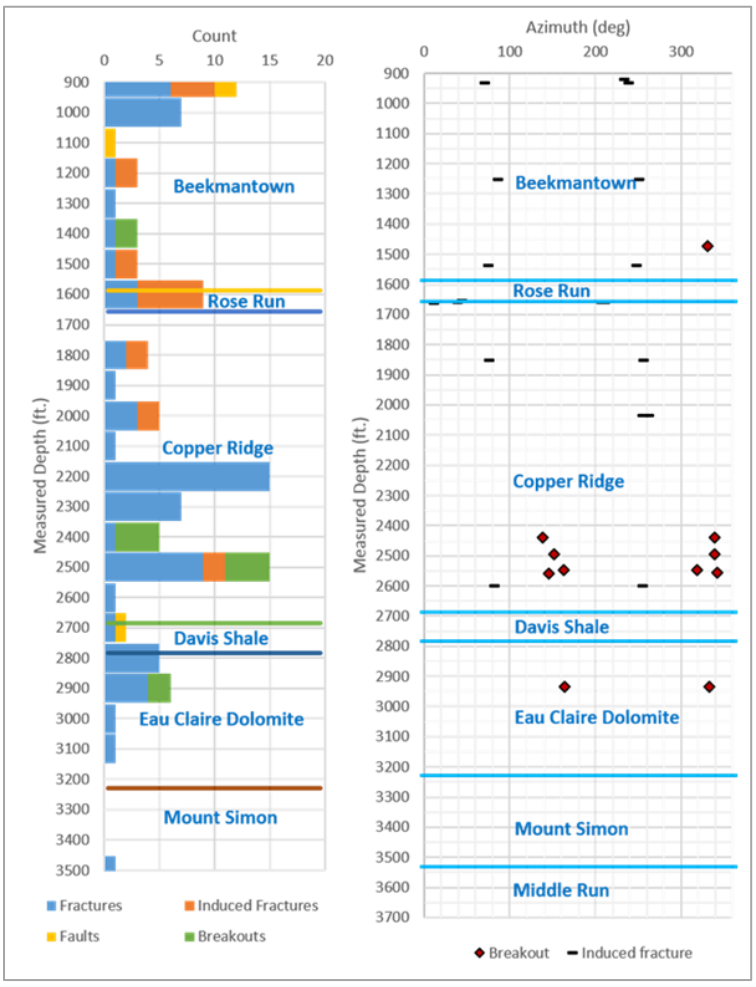

Figure 6-24: Diagram illustrating natural fractures, faults, induced fractures, and breakouts identified in the East Bend #1 well image log.

In the East Bend well, 32.5 ft of conventional core was collected from the Eau Claire Formation from 2,825 ft to 2,857.5 ft. Another 54.2 ft of core was collected from the Mount Simon sandstone from 3,300 ft to 3,330.5 ft and from 3,435 ft to 3,458.7 ft. Detailed descriptions of these core samples did not note any natural fractured zones. The cores did exhibit many bedding planes, laminations, cross bedding, and rip-up clasts. There were many breaks along bedding planes associated with core collection. However, no fractures were evident (Figure 6-25). Thin sections did not show evidence of fractures, and only one sample from the Eau Claire, at 2,128 ft, showed indication of fracture development (Figure 6-26).

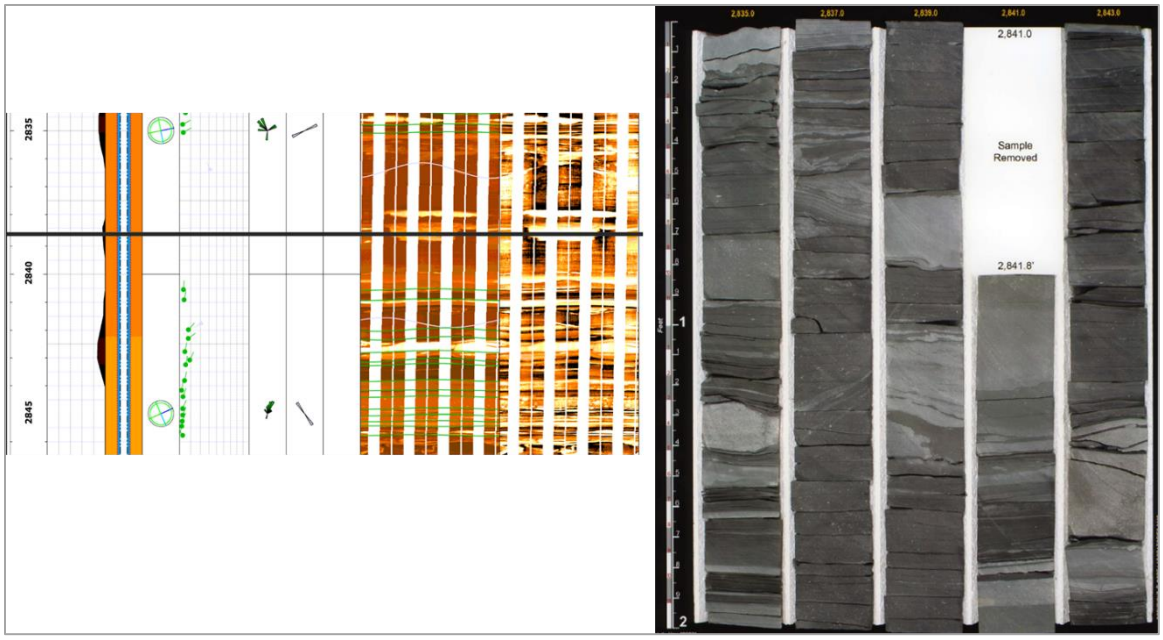

Figure 6-25: Image log (left) and rock core (right) from East Bend #1 well from Eau Claire Formation at depth interval of 2,835 ft to 2,845 ft.

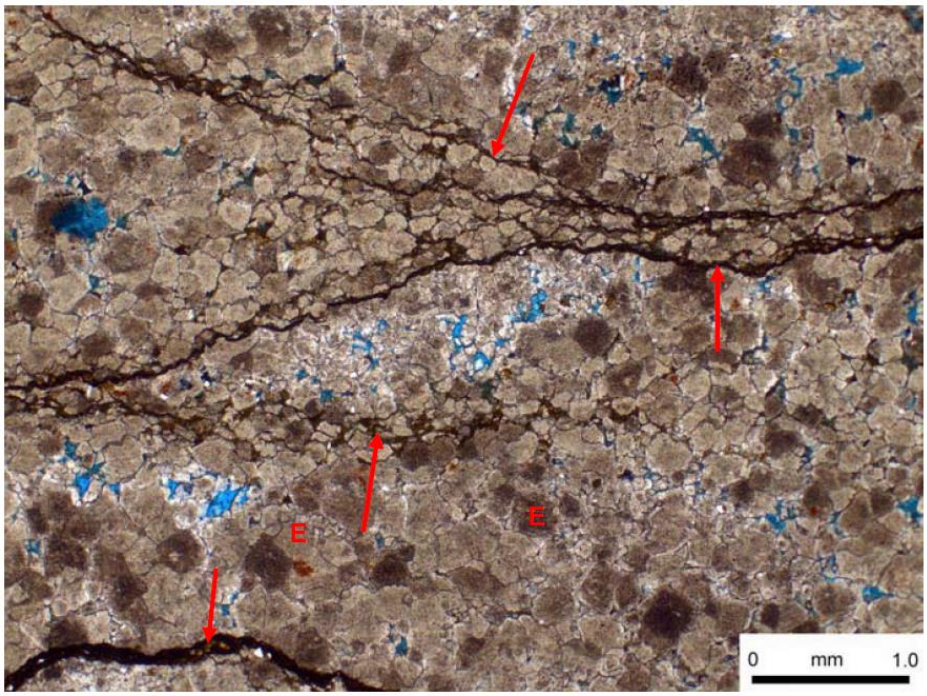

Figure 6-26: Thin-section image for Eau Claire sample at depth of 2,128 ft.

A 2D seismic survey line through the East Bend site was examined for indications of fracture zones (Figure 6-27). Approximately 6.5 miles in length, the line trends from Indiana, across the Ohio River, through East Bend, Kentucky, and runs along Beaver Road. The seismic line shows a gap in the seismic response associated with data loss as the survey traverses the Ohio River. This particular 2D seismic line has a number of bends in it, and this geometry can produce a loss of fidelity in the seismic expression. Still, the lower Cambrian-Ordovician section appears relatively well resolved.

At this location on the Cincinnati arch, the sedimentary section is half as thick as that seen for the other two sites in this study. The Precambrian basement rock is located below 480 milliseconds (ms) two-way time (TWT). The sedimentary, Paleozoic section lies above 480 ms and consists of Ordovician and Cambrian strata. The upper portion of the Mount Simon generally consists of thin, alternating sandstone and shale units resulting in a subtle seismic response. The lower portion of the Mount Simon shows many strong reflectors, which could possibly be the result of seismic interbed multiples—a seismic artifact associated with the overlying units. The top of the Knox Group is a regional unconformity; above this interval, the seismic reflectors are not as pronounced or continuous as those seen for deeper stratum.

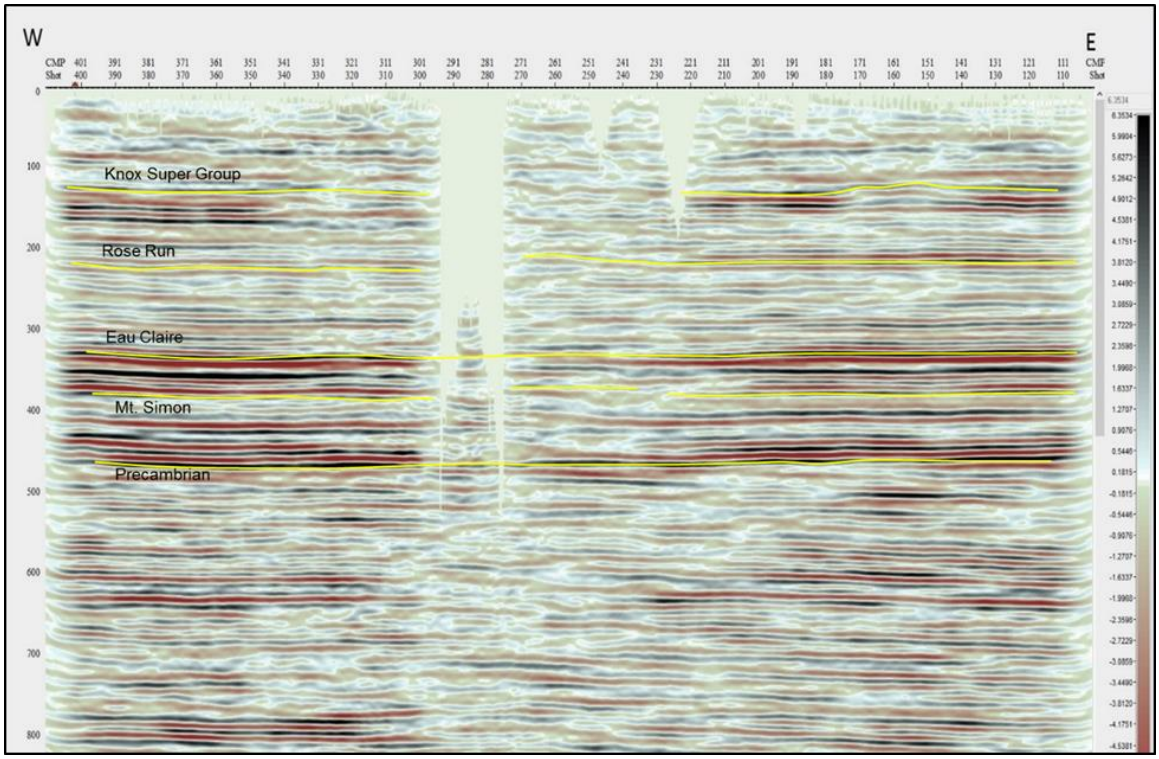

Figure 6-27: 2D seismic line from the East Bend site.

Based on the East Bend #1 well image log analysis, a conceptual fracture diagram was developed for the Arches study area. Ideally, a fracture model would integrate fracture analysis across multiple scales into a 'power law' relationship or discrete fracture network (Wilson et al., 2014). Development of a power law relationship requires analysis of fracture patterns in thin sections, rock core samples, geophysical logs, outcrops, seismic survey data, and surface drainage patterns (Bogdonov, 1947; Heffer and Breven, 1990; Gillespie et al., 1993; Marrett et al., 1999; Ortega et al., 2006). The fracture diagram lists the orientation and dip of the fractures after the method presented by Boswell (1995). This method illustrates general fracture characteristics but cannot determine fracture length, interconnectedness, and pattern.

Figure 6-28 shows a conceptual fracture model for the Arches study area. In general, the Arches conceptual fracture model suggests that there are limited fractures in the Mount Simon and Lower Eau Claire shale. As shown, no natural fractures were identified in the Mount Simon. Fractures were noted at the contact of the Mount Simon and Precambrian Middle Run Formation. Some fractures were noted in the Upper Eau Claire, but the formation is 448 ft thick with roughly three fractures per 100 ft on average. Overall, these units are not likely to result in fracture flow conditions. As mentioned earlier, there are very few wells in the Arches Province with fracture information on the Mount Simon and Eau Claire formations that may substantiate the description of fractures in these units. The East Bend #1 well had very few natural fractures indicated in its image log. Consequently, it is difficult to depict fracture systems in these deeper Cambrian-age rocks. In fact, the conceptual fracture diagram does not appear to capture the nature of the fractures because there are so few features present in the East Bend #1 well borehole.

6.2.4.2 East-Central Appalachian Basin fracture model

The East-Central Appalachian Basin study area is located on the east-central flank of the sedimentary basin where rock layers dip and thicken into the Rome trough. In this area, sedimentary rocks are 8,000 ft to 10,000 ft in total thickness with many different shale, carbonate, salt, and sandstone formations. In this area, 5 to 10 Class II disposal wells inject into multiple Cambrian-age rock formations. The area is also adjacent to many large CO_2 point sources along the Ohio River.

The main injection zones in the East-Central Appalachian Basin are the Knox Group (Beekmantown, Rose Run, Copper Ridge), Conasauga Group (Conasauga-Nolichucky Maryville), and basal Cambrian sandstone (Figure 6-29). These rock formations have low to moderate permeability. However, vugular porosity development in thin carbonate intervals has shown ability to support high injection rates (Battelle, 2016). Most of the shallower rock formations like the Lower Silurian Medina-"Clinton" Group contain hydrocarbons and would be more suitable for enhanced oil recovery than CO_2 storage. Caprock zones above the Knox include the Wells Creek, Trenton-Black River, and Queenston shales. These shale and carbonate formations have a combined thickness of over 2,000 ft in the East-Central Appalachian Basin study area.

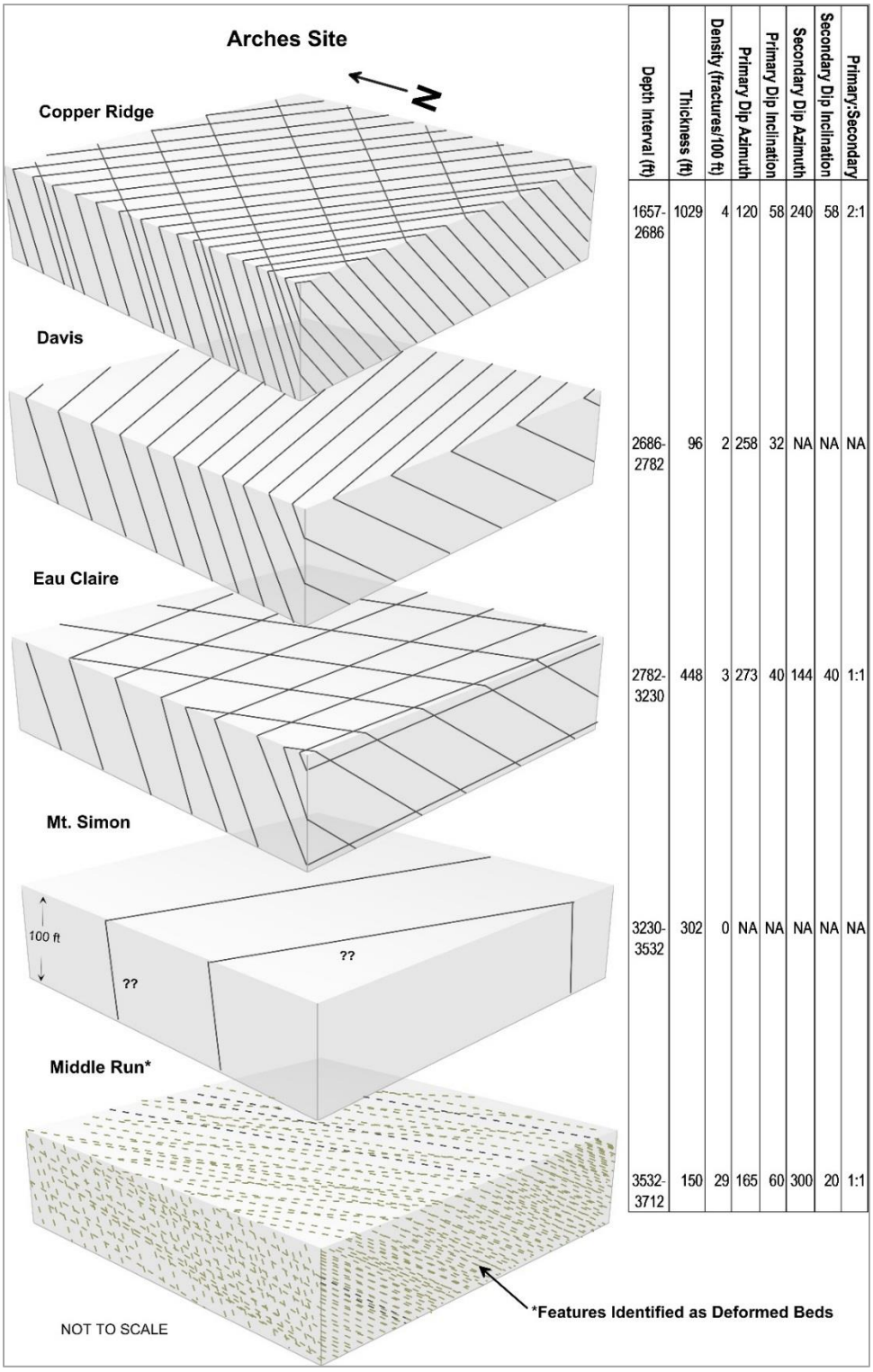

Depth Interval (ft)	Thickness (ft)	Density (fractures/100 ft)	Primary Dip Azimuth	Primary Dip Inclination	Secondary Dip Azimuth	Secondary Dip Inclination	Primary:Secondary
1657-2686	1029	4	120	58	240	58	2:1
2686-2782	96	2	258	32	NA	NA	NA
2782-3230	448	3	273	40	144	40	1:1
3230-3532	302	0	NA	NA	NA	NA	NA
3532-3712	150	29	165	60	300	20	1:1

Figure 6-28: Arches Province conceptual fracture diagram.

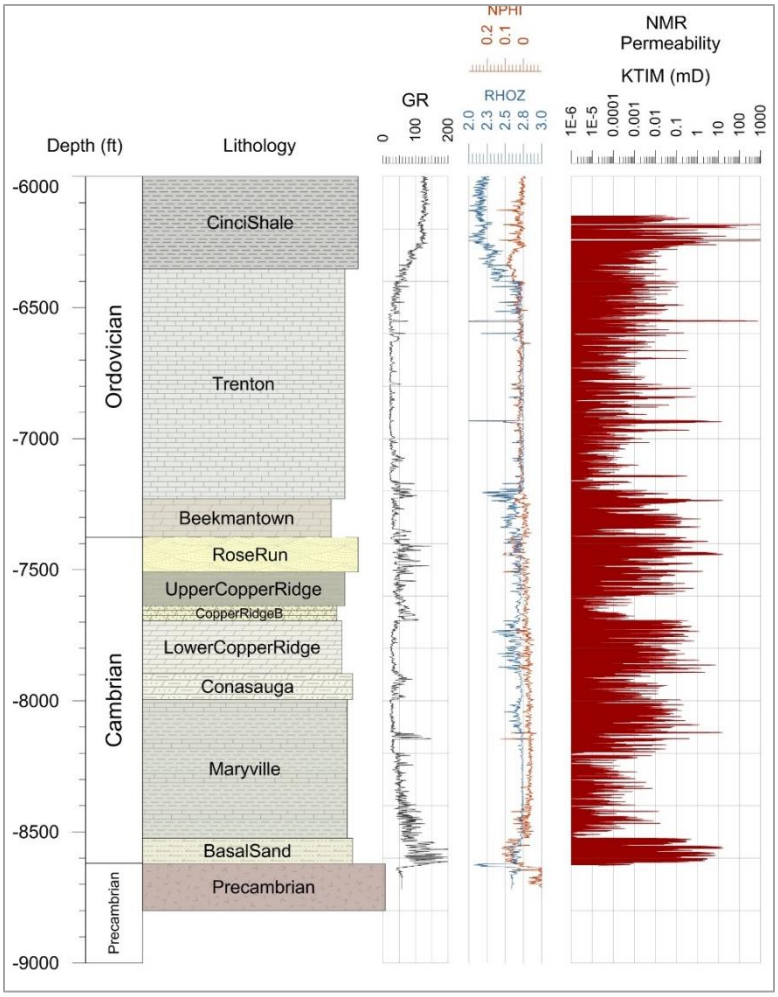

Figure 6-29: Geologic column illustrating deeper Ordovician-Cambrian rock layers.

The Ordovician-Cambrian-age rock formations are continuous rock layers in the East-Central Appalachian Basin. However, the rocks exhibit regional facies changes eastward into the Appalachian Basin and westward toward the broad arch structures (Cincinnati arch, Findlay arch, Indiana-Ohio platform). The basal sandstone thins into the basin and transitions into the Mount Simon sandstone to the west. The Maryville and Conasauga formations thicken into the basin. The Copper Ridge is most prominent in eastern Ohio. The Rose Run sandstone thins in east-central Ohio, where there is notable hydrocarbon production along the subcrop. The Beekmantown and Trenton-Black River are thick continuous formations across the region.

In terms of fracture system development, none of the Ordovician-Cambrian formations are considered extensively fractured rock formations. Much of the hydrocarbon production in these formations relies on hydraulic fracturing to enhance production. This suggests that these formations are amenable to fracturing but are not necessarily naturally fractured. Riley et al. (1993) note that Rose Run “fracture porosity is the least common porosity type observed in cores, but it may be locally significant in areas adjacent to major fault systems.” Fractures in the Beekmantown and Copper Ridge formations may be associated with local vugular porosity, karst zones, and/or brecciated zones. The Trenton-Black River is known to contain local fracture intervals that produce

gas. There are few borings in the deeper Cambrian age Conasauga, Maryville, and basal sandstone, so fracture systems are difficult to discern in these units.

In the *Basin-Scale Paleo Stress-Strain Analysis Report* completed for this project (Battelle, 2016), fracture trends in Ordovician-Cambrian rock units were investigated. The study analyzed image logs available from 10 vertical wellbores that penetrate through the Cambrian-Ordovician section in the subsurface. Data were evaluated for lateral stratigraphic correlation and comparison of natural fracture distribution from one location to another.

Figure 6-30 shows a cross section through eastern Ohio denoting the frequency of low- and high-confidence natural fractures identified in the image logs. Most of the deeper zones contain few or occasional fractures. The cross sections indicate that more fractures were observed in wellbores in the western part of the study area than wells that were closer to the Rome trough (i.e., Well J). General trends suggest somewhat more frequent natural fracturing in the Rose Run and Copper Ridge Formations. In general, regional logs in the Ordovician-Cambrian section in east-central Ohio appear to show limited fracturing at certain depth intervals. These fractures do not appear to form extensive, interconnected fracture networks. However, even a few, discrete, conductive fractures may have a large effect on deep flow systems in the subsurface.

The local fracture model for the East-Central Appalachian Basin study area was based on the Ohio CO_2 #1 test well in Tuscarawas County, Ohio. In this well, a deep image log run was completed at a depth interval of 5,024 ft to 8,709 ft, from the Queenston/Cincinnati shale into the Precambrian basement rock. As described in the *Log Analysis and Integration Summary Report* (Battelle, 2016), the image log was processed and interpreted to determine the presence of any natural fractures. The majority of the structural features noted in the East Central Appalachian Basin borehole appeared to be induced fractures related to drilling and borehole breakouts due to potential vugular development and washout intervals (Figure 6-31). The Copper Ridge had several textural changes in the formation, noted by the scattered bedding and laminations and the potential vugular development. A microfault and bed clusters were observed at a depth of around 7,898 ft. The Conasauga and Maryville Formation had some minor structural features that included induced fractures, potentially due to multiple laminations and beds, and potential vugular development. Deformed beds at the basal sand/Precambrian contact are indicative of depositional features at the Precambrian contact. The logged interval of the Precambrian was short and did not present any notable structural features.

In the OH CO_2 #1 well, 82 sidewall cores were collected from the Cincinnati shale-Precambrian interval. Most cores exhibited massive texture with depositional features such as minor laminations and bedding planes. Detailed thin-section modal analysis of the cores did not note any fractures or calcite fracture fill in three Trenton-Black River samples, three Beekmantown samples, and one Copper Ridge sample. Some potential fractures were present in Black River Formation samples (Figure 6-32). Indications of vugular porosity were present in some Copper Ridge Formation samples (Figure 6-33).

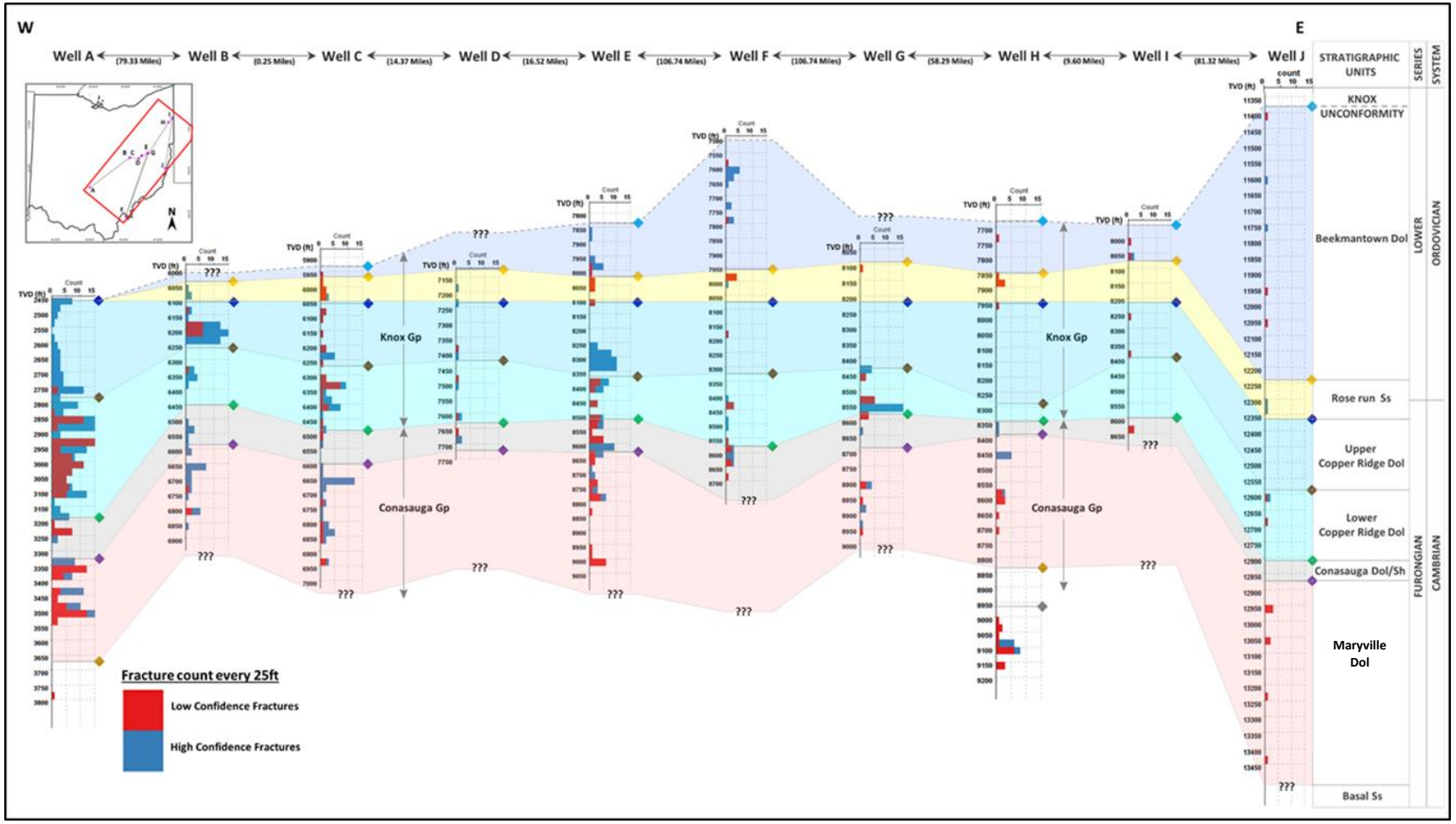

Figure 6-30: Southwest-northeast geologic cross section illustrating frequency of fractures identified in image logs classified by low and high confidence.

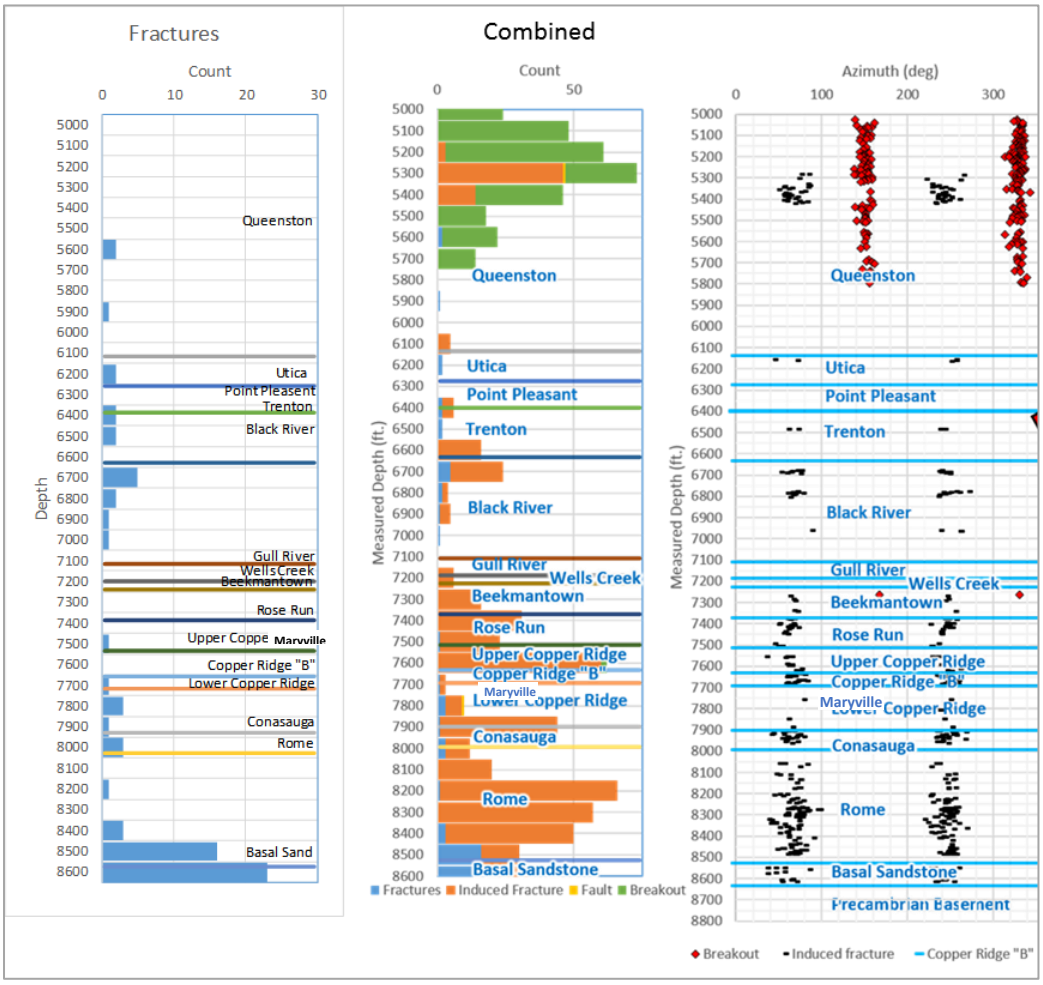

Figure 6-31: Diagram illustrating natural fractures, faults, induced fractures, and breakouts identified in the OH CO_2 #1 well image log.

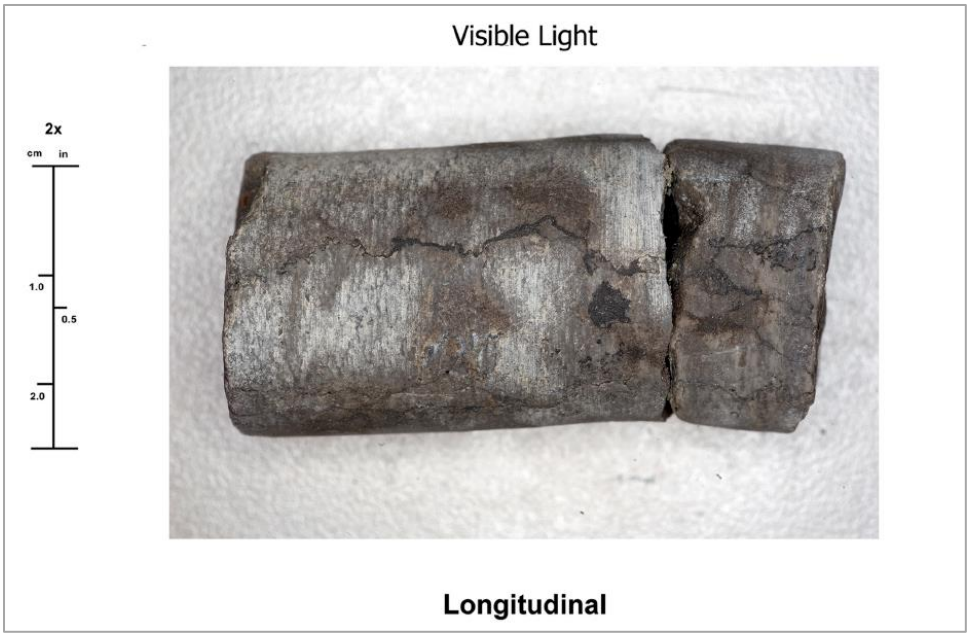

Figure 6-32: Black River sidewall core from OH CO_2 #1 well at depth of 6,808 ft. The sample shows potential thin laminations or fractures.

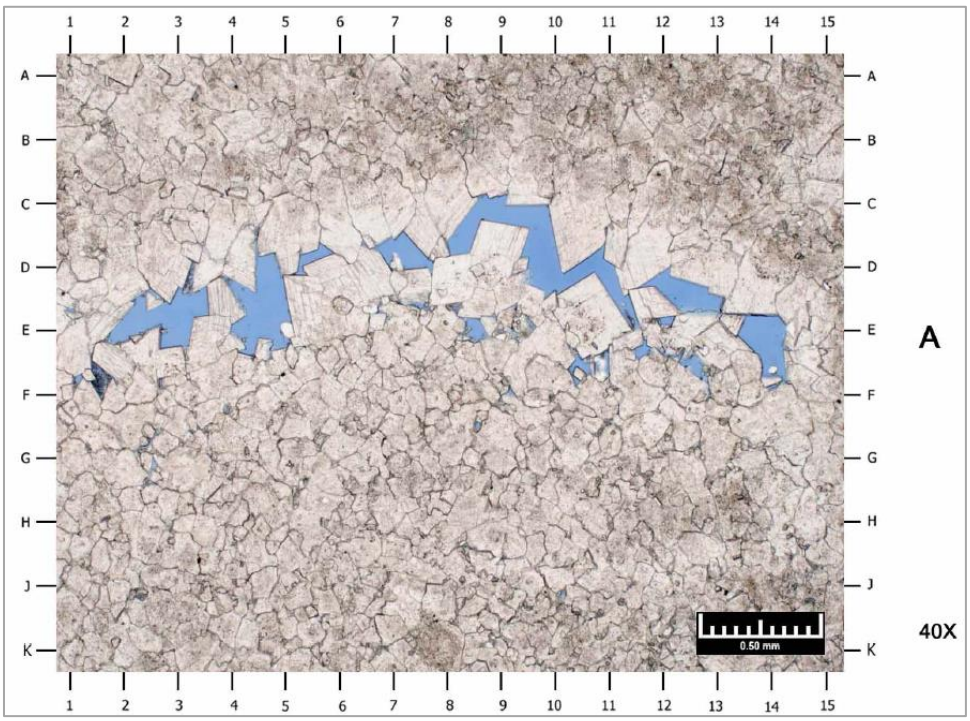

Figure 6-33. Copper Ridge dolomite thin-section image from OH CO_2 #1 well at depth of 7,033 ft. Copper Ridge sample showing potential vugular porosity (blue) in a dolomite matrix.

A 2D seismic line shown from Tuscarawas County, Ohio, was examined for indications of fracture networks or geologic structures in the study area (Figure 6-34). While its length is not known, it trends to the east and has a subtle dip in that direction. The seismic response is remarkably clean, suggesting that the survey's geometry is relatively straight. The top of the Precambrian is at approximately 1,180 ms. This relatively flat contact with the basement rock shows very little relief in the basement topography. This line does not appear to intercept any faults, either in the basement or in the sedimentary section. Reflectors for all major formations are strong and continuous. Some of the strong series of reflectors may be a seismic interbed-multiple effect.

Based on the Ohio CO_2 #1 image log analysis, a conceptual fracture diagram was developed for the East-Central Appalachian Basin study area (Figure 6-35). Similar to the Arches study area, this model was based on geophysical image log information to illustrate general fracture frequency and orientation. Most fractures identified were high angle (45° to 90°) with a northeast orientation. Natural fractures and deformed beds were mainly identified in the Maryville and basal sandstone. These features had a more northerly orientation. The Maryville and basal sandstone are not injection zones at this location, because they exhibited low permeability and porosity. They would be considered more of an underlying caprock for the CO_2 storage zone. The conceptual model suggests that there are limited, discrete fractures in certain depth intervals, rather than extensive fracture systems in these Ordovician-Cambrian rock layers. Limited numbers of conductive fractures can have significant effects on subsurface flow systems. However, they can be difficult to detect or evaluate. The OhioCO_2 #1 well exhibited deformed beds at the Precambrian-Cambrian contact, similar to the East Bend #1 well.

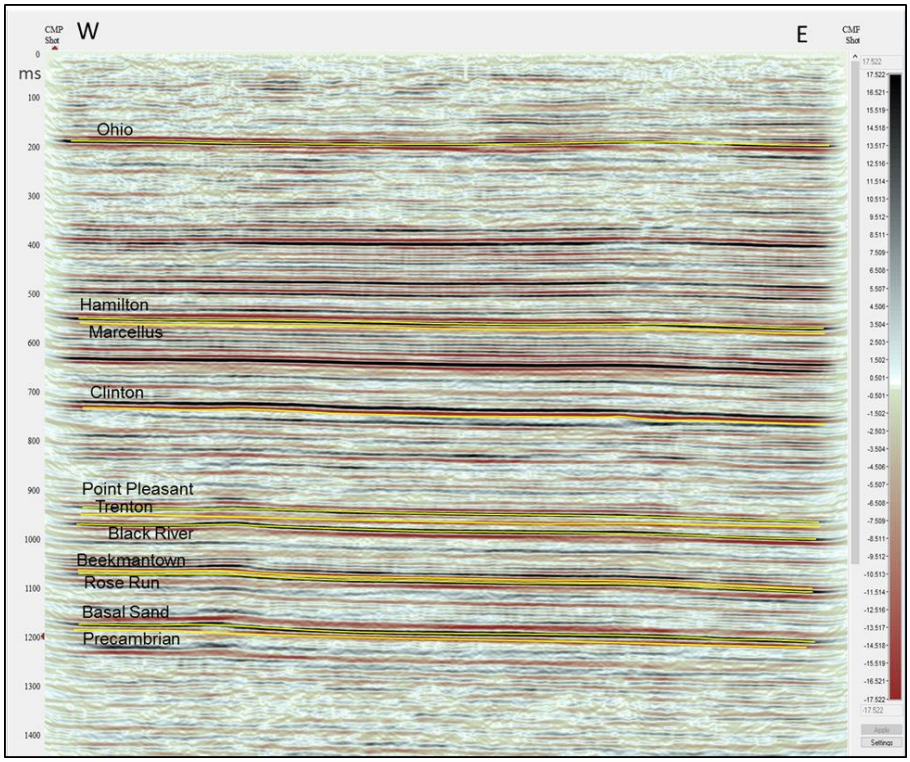

Figure 6-34: Example 2D seismic survey line from East-Central Appalachian Basin study area.

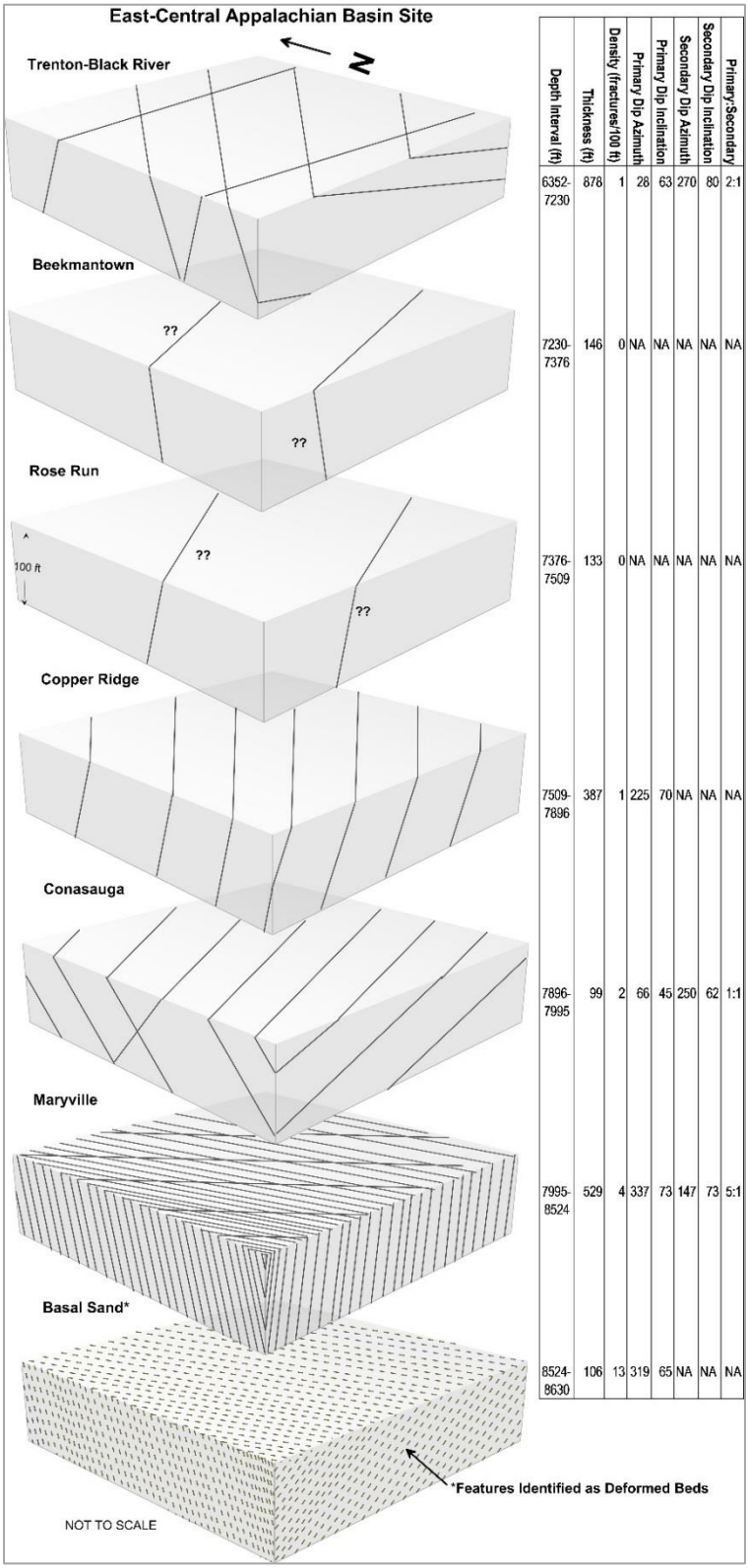

Depth Interval (ft)	Thickness (ft)	Density (fractures/100 ft)	Primary Dip Azimuth	Primary Dip Inclination	Secondary Dip Azimuth	Secondary Dip Inclination	Primary:Secondary
6352-7230	878	1	28	63	270	80	2:1
7230-7376	146	0	NA	NA	NA	NA	NA
7376-7509	133	0	NA	NA	NA	NA	NA
7509-7896	387	1	225	70	NA	NA	NA
7896-7995	99	2	66	45	250	62	1:1
7995-8524	529	4	337	73	147	73	5:1
8524-8630	106	13	319	65	NA	NA	NA

Figure 6-35: East-Central Appalachian Basin study area conceptual fracture diagram.

6.2.4.3 Northern Appalachian Basin fracture model

The Northern Appalachian Basin study area is located in the northern flank of the sedimentary basin adjacent to the Appalachian structural front. Devonian- to Cambrian-age sedimentary rocks have a total thickness of approximately 6,000 ft to 8,000 ft in the area (Figure 6-36). The sedimentary rocks dip gently to the southeast and exhibit low-amplitude folding and faulting, which intensifies into the Valley and Ridge Province.

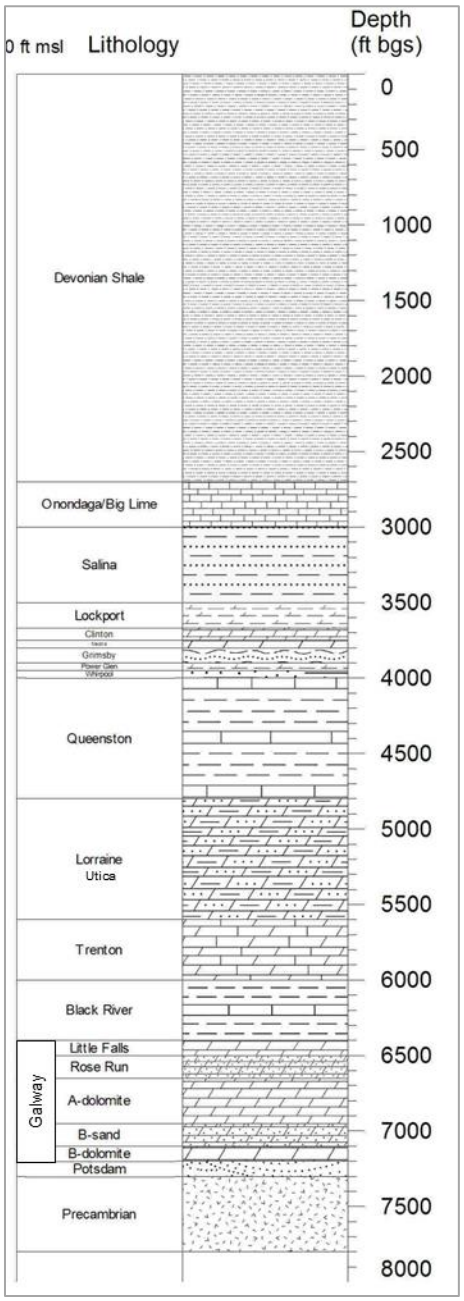

Figure 6-36: General lithology for the Northern Appalachian Basin study area.

The main injection zones in the Northern Appalachian Basin study area are the Cambrian-age Galway and Potsdam rock formations (Figure 6-37). The Galway is also referred to as the informal Theresa Formation. The Galway may be subdivided into the Rose Run sandstone, A-dolomite, B-sand, B-dolomite, and C-sand. Other shallower formations are either too shallow for supercritical-phase CO_2 storage (like the Lockport and Bass Islands/Akron dolomite formations), mainly low-permeability shale (like the Queenston shale), or existing hydrocarbon fields (like the Clinton-Medina sandstone). Thick shale and carbonate layers like the Tribes Hill-Little Falls, Trenton-Black River, Lorraine shale, and Queenston shale are caprocks in the study area.

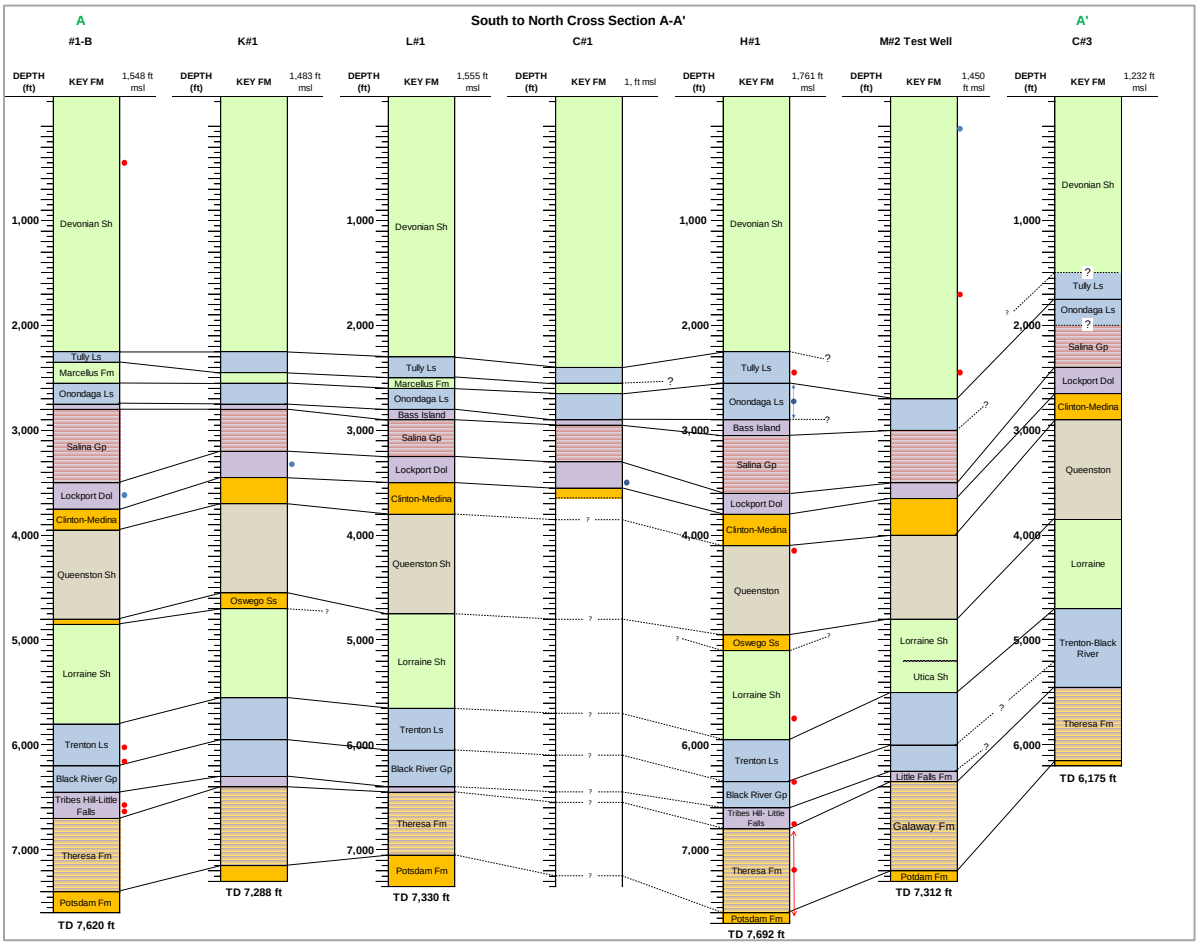

Figure 6-37: Geologic cross section for the Northern Appalachian Basin study area.

Few deep wells penetrate the deeper Ordovician-Cambrian formations in the Northern Appalachian Basin study area. Even fewer wells have modern geophysical logs that may detect fractures. Consequently, little is known about natural fracture systems in these rocks. In addition, there are no Class II injection wells nearby that may provide understanding of subsurface flow regime in the deeper rock units. In general, the Potsdam and Galway are not considered extensively fractured rock formations. As found in equivalent Knox Group rocks in the Appalachian Basin, fractures in the Galway may be associated with local vugular porosity, karst zones, and/or brecciated zones. Like other parts of the Appalachian Basin, the Trenton-Black River is known to contain local fracture intervals that produce gas. Copley et al. (1983) described a series of thrust faults that penetrate the Bass Islands/Akron dolomite oil field in Chautauqua County, New York. Other researchers have interpreted seismic survey data in the region to suggest these faults may extend to deeper Trenton-Black River through Precambrian basement. These faults have been associated with hydrothermal dolomite features.

The local fracture model for the Northern Appalachian Basin study area was based on a test well drilled in Chautauqua County, New York. In this well, a deep image log run was completed at a depth interval of 3,870 ft to 7,325 ft from the Queenston shale into the Upper Potsdam sandstone (Figure 6-38). As described in the *Log Analysis and Integration Summary Report* (Battelle, 2016), the image log was processed and interpreted to determine the presence of any natural fractures, faults, borehole breakouts, and drilling-induced fractures. The majority of the image log features noted in the Northern Appalachian Basin borehole were induced fractures and borehole breakouts related to drilling, mainly in the Utica-Lorraine shale and Queenston shale.

Natural fractures were frequently observed in the Tribes Hill Formation, the Rose Run sandstone, and to a lesser extent the Galway B-sand. Fracture density in the Rose Run was approximately 26 natural fractures per 100 ft. The fractures had a primary dip azimuth of 207° and primary dip inclination of 74°. There was no distinct secondary fracture pattern. Fracture density in the Tribes Hill-Upper Little Falls was approximately 17 natural fractures per 100 ft. The fractures had a dip azimuth of 225° and primary dip inclination of 68°. There was some evidence of a secondary fracture pattern with orientation of 26° and dip of 63°.

In the Northern Appalachian Basin well, 156 ft of full core and 32 sidewall cores were collected from the deeper Ordovician-Cambrian interval. Full core was collected from the Black River, Little Falls, and Galway B-dolomite and C-sand intervals. Most of the core was massive with bedding planes and laminations. Some conductive fractures noted in the image log of the Little Falls Formation were difficult to discern from bedding planes in the full core (Figure 6-39). Isolated calcite-filled vugs were present in portions of the Lower Little Falls core (Figure 6-40).

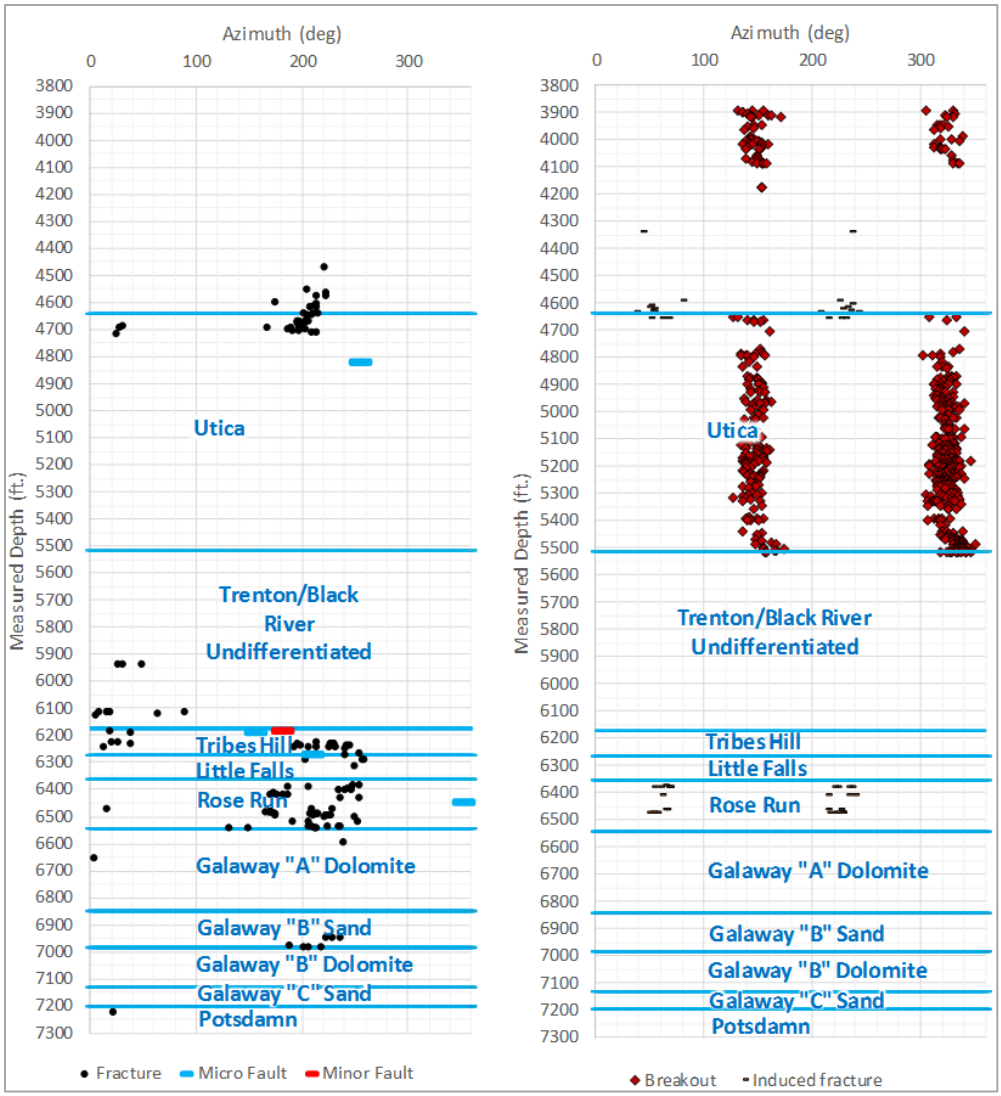

Figure 6-38: Diagram illustrating natural fractures, faults, induced fractures, and breakouts identified in the Northern Appalachian Basin image log.

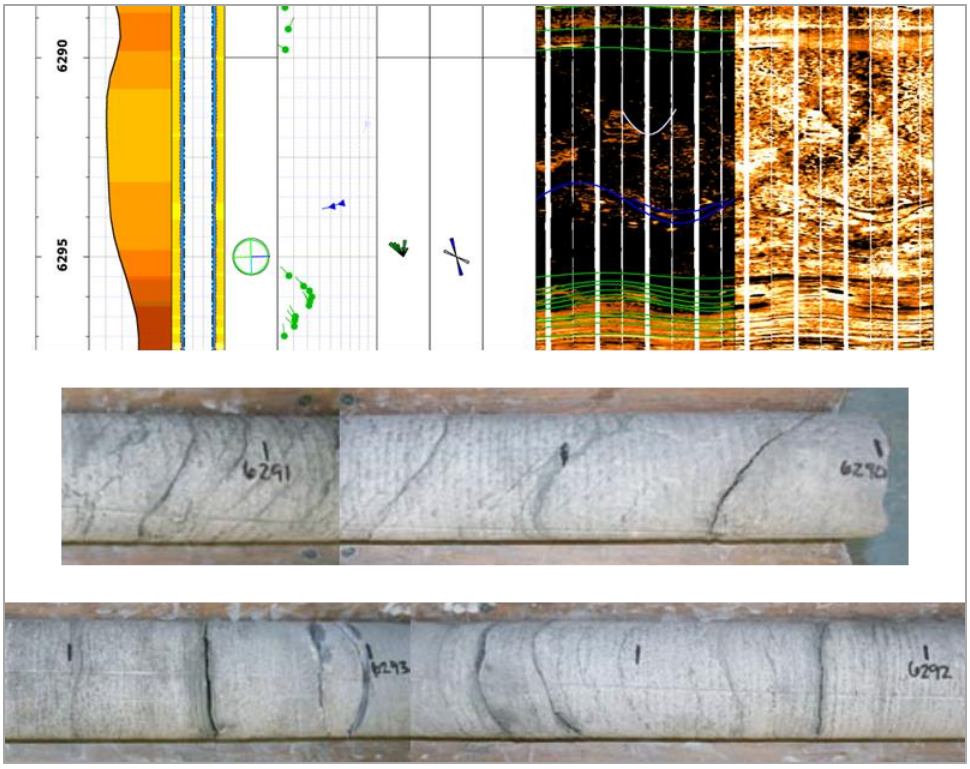

Note: There was a small difference in measured depths for coring runs versus logging runs.

Figure 6-39: Whole rock core sample and image log from Little Falls Formation at ~6,290 ft in the Northern Appalachian Basin test well where conductive fractures were noted.

Figure 6-40: Full core plug sample from lower Little Falls Formation at depth of 6,355 ft showing saddle-shaped dolomite-lined vug.

Twenty thin sections were examined from the core samples for indications of natural fractures and stress conditions in the subsurface. The thin sections were selected from a depth range of 6,254 ft to 7,276 ft in the Black River to the Potsdam sandstone. Sample mineralogy generally consists of dolomite (15% to 90%) in the dolostone intervals and quartz/feldspar (35% to 95%) in the sandstone intervals. Trace minerals include calcite, clays, glauconite, opaques (possible oxides/sulfides), and possible organic matter. Detrital grains of quartz and feldspar (0.20 to 0.40 mm) occur as well-rounded, sub-rounded, and moderately sorted grains in most samples. Dissolution cavities occur in the centers of clastic grains that appear to be altered by carbonate in a few samples (e.g., 6,542 ft).

Euhedral planar dolomite (≤0.20 mm) and anhedral granular dolomite (<0.05 mm) occur as matrix grains at the boundaries of well-rounded to sub-rounded grains of quartz and/or feldspar (0.35 to 0.40 mm) (e.g., 6,542 ft). The bimodal occurrence of anhedral granular (primary) and euhedral planar (secondary) grains suggests that two generations of dolomite are present in some samples (e.g., 6,272 ft). Sandstone samples appear to be primarily matrix-supported, and thin-section porosities are generally less than 7%. Quartz cement fills intergranular pore space and occurs as authigenic overgrowths in sandstones (e.g., 6,388 ft). Secondary calcite (red-stained) cement occurs in trace amounts along grain boundaries and in pore spaces in both quartz-rich (e.g., 6,356 ft) and dolomite-rich samples (e.g., 7,070 ft). Echinoderm and crinoid allochems are visible in samples with greater than 90% dolomite (7,070 ft, 7,082 ft, 7,112 ft). Stylolite dissolution seams are visible in several samples (6,367 ft, 6,958 ft, 7,223 ft, and 7,255 ft), occurring as clay- and opaque-rich veins along bedding planes and at interfaces between clastic detritus and dolomite.

Thin-section samples generally appear tight (low porosity), well compacted, and cemented. The layer of potential authigenic feldspar in the sample at 6,269 ft may represent vein or fracture-filling, although the possibility that the silicate layer represents a depositional feature cannot be ruled out. In either case, feldspar-rich zones, particularly authigenic potassium-feldspar, can be associated with higher occurrences of natural fractures in rocks due to their brittleness. Dolomite rhombs in sample at 6,952 ft bear some resemblance to non-planar baroque (saddle-shaped) dolomite; a feature characteristic of exposure to hydrothermal fluids greater than 122°F (e.g., Flügel, 2006; Al-Awadi et al., 2009). Hydrothermal fluid flow may indicate the presence of nearby fractures. Stylolite dissolution seams indicate that moderate to high compaction has occurred in some samples (e.g., 6,958 ft). These samples tend to have lower thin-section porosities. The tendency of stylolites to occur near mineralogical/compositional boundaries (e.g., sandstone-dolomite interface) suggests these may have been zones of weakness (e.g., high porosity, bedding planes, possible fractures) where stress was localized during compression. The presence of transverse stylolites could not be confirmed in thin sections (image only, non-oriented) to support development along pre-existing fractures.

A 2D seismic line (NYSERDA, 2011) was examined for indications of fracture zones and geologic structures in the Northern Appalachian Basin study area (Figure 6-41). The line was 5.1 miles in length located in southwest Chautauqua County, New York. A synthetic seismogram was used to pick horizons, including the Precambrian basement up to the Devonian Tully Formation. Uncertainty in the seismic interpretation is attributed to the 10-mile distance between the seismic line and the basis well. The top of the Precambrian basement is at approximately 1,200 ms and is defined by discontinuous, low-amplitude reflectors with localized topography. The overlying sedimentary strata appear to dip to the east. This line does not intercept any faults. Most reflectors here have a strong lateral continuity, with variability in reflection frequency and amplitude among formations. The most apparent, locally discontinuous reflectors occur immediately above the Precambrian basement, indicated by the ovals. These reflection geometries suggest possible sedimentary channel-fill and pinch-outs and might occur in the Potsdam Formation.

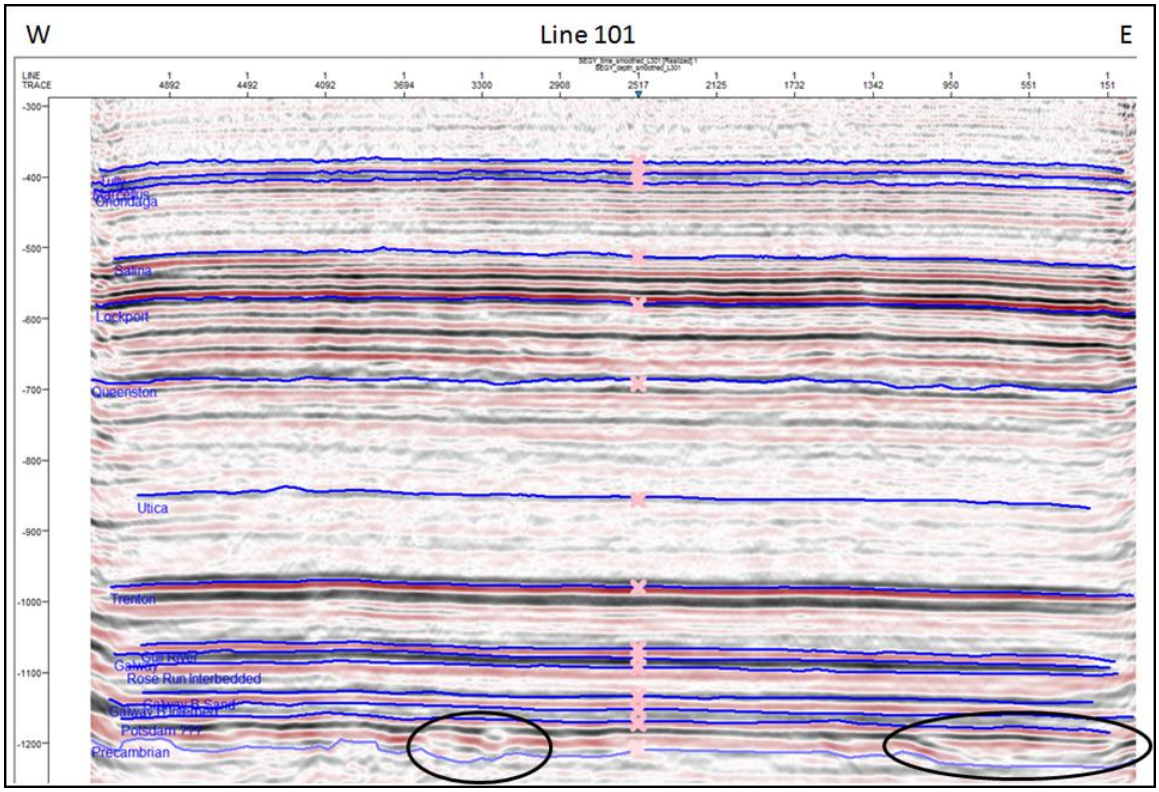

Figure 6-41: 2D seismic line from Chautauqua County, New York.

Based on the Northern Appalachian Basin image log analysis, a conceptual fracture diagram was developed for the study area (Figure 6-42). This model was based on geophysical image log information to illustrate general fracture frequency and orientation. As with the other two study areas, most natural fractures identified were high angle (45° to 90°). The fractures had a more north-northeast orientation, whereas the orientation at the other two study areas was more due northeast. Otherwise, the borehole exhibited many breakouts in the Utica Formation. Overall, the indicators on fractures for the Northern Appalachian Basin site suggests that a sparse fracture system is possible in the Tribes Hill to Rose Run sandstone interval. These rocks had very low primary porosity and permeability. The fractures may contribute to injectivity and CO_2 storage capacity.

6.2.4.4 Fracture model parameters

Image log analysis and core review suggest that the Arches study area and the East Central Appalachian Basin study area have very few natural fractures. The Arches well image log had no natural fractures observed in the Mount Simon sandstone storage zone and few fractures in the lower Eau Claire caprock. Overlying Knox Group formations had indications of more fractures, but these are not likely to contribute to fluid flow. Some deformed beds were noted at the contact of the Mount Simon sandstone and Precambrian bedrock.

Similarly, the East Central Appalachian Basin well had less than two natural fractures per 100 ft in the Rose Run and Copper Ridge storage formations. The Maryville, Beekmantown, and Trenton-Black River caprock formations also had less than two natural fractures per 100 ft observed in the image logs. In the basal sandstone formation, approximately 13 features per 100 ft were identified as deformed beds. For perspective, most fracture models generally have 5 to 10+ fractures per *meter* observed in image logs to be considered fractured zones.

The Northern Appalachian Basin basis well image log exhibited a moderate number of fractures in the Rose Run and Little Falls formations. Consequently, this site was selected to investigate CO_2 storage aspects in fracture flow systems. The Rose Run sandstone exhibited 26 natural fractures per 100 vertical feet at an orientation of 207° and dip inclination of 74°. The Little Falls Formation showed 17 natural fractures per 100 vertical feet at an orientation of 225° and dip inclination of 68° with secondary fracture orientation of 26° and dip of 63°. The image log suggested a 5:1 primary to secondary fracture ratio.

Overall, information on natural fractures for the Northern Appalachian Basin site indicates a sparsely fractured interval in the Rose Run and Little Falls Formations. There were no fractures noted on a millimeter scale in thin sections. A moderate fracture density was noted in image logs and rock core samples. The fractures appear to be distributed throughout the thickness of the formations. Seismic survey data from the general study area suggest that some high-angle normal faults may be present, and more fracture development may be associated with these faults. Consequently, this site was selected to investigate CO_2 storage aspects in fracture flow systems. Because the data on fractures in the deep rocks are limited, the fracture model is not especially precise, but the model does reflect a realistic portrayal of the fractures based on available data.

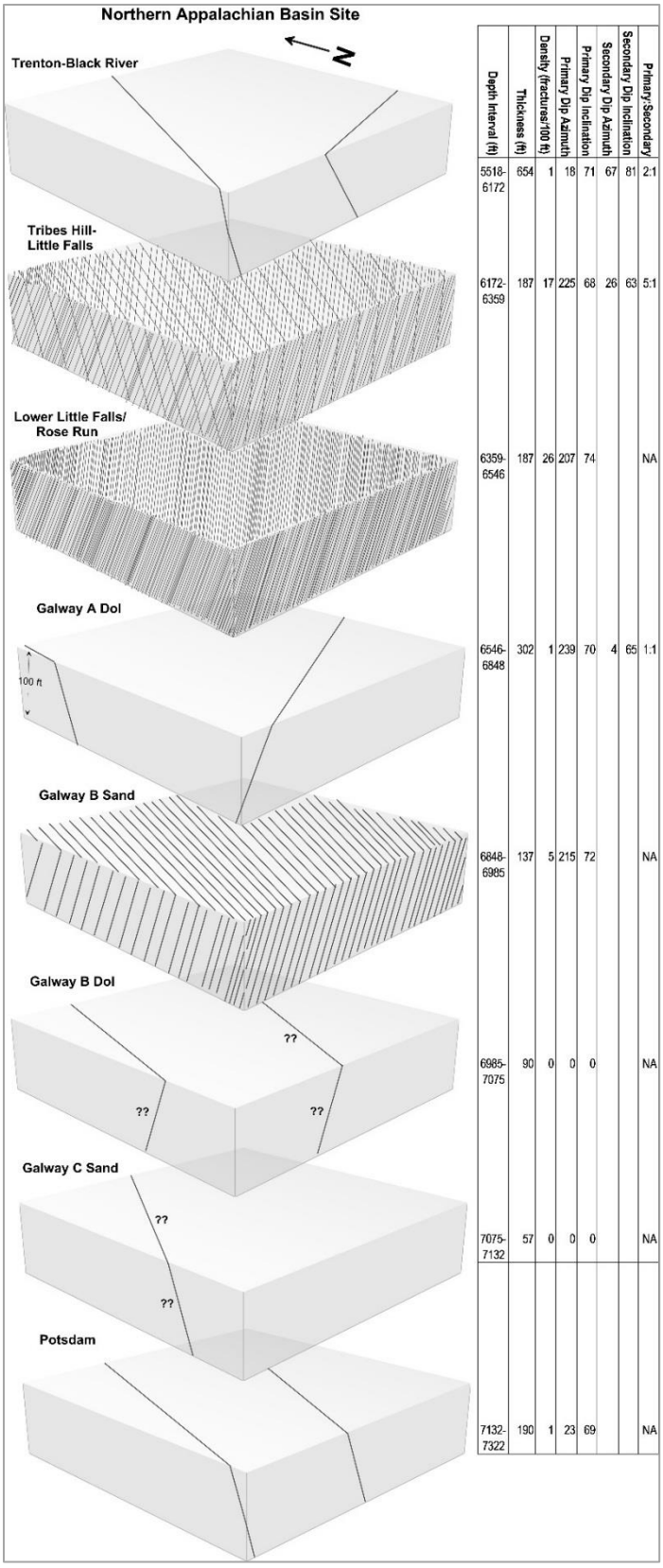

Depth Interval (ft)	Thickness (ft)	Density (fractures/100 ft)	Primary Dip Azimuth	Primary Dip Inclination	Secondary Dip Azimuth	Secondary Dip Inclination	Primary:Secondary
5518-6172	654	1	18	71	67	81	2:1
6172-6359	187	17	225	68	26	63	5:1
6359-6546	187	26	207	74			NA
6546-6848	302	1	239	70	4	65	1:1
6848-6985	137	5	215	72			NA
6985-7075	90	0	0	0			NA
7075-7132	57	0	0	0			NA
7132-7322	190	1	23	69			NA

Figure 6-42: Northern Appalachian Basin study area conceptual fracture diagram.

Table 6-7 summarizes fracture model input parameters for the numerical simulation. Given the few indications of natural fractures, it was necessary to consult other research for some of the parameters. Fracture density, orientation, and dip inclination were based on image log interpretation. Fracture length was based on central tendency for Knox Group data on fracture patterns presented by Gale (2004). Fracture porosity was based on maximum fracture porosity listed for the Knox Group by Gale (2004). Fracture shape factor, a parameter for dual-porosity models of fractured reservoirs, was estimated for a long 2D slab as suggested by Zimmerman et al., 1993):

$$\sigma = \frac{2\pi^2}{L^2} \qquad \text{Eq. 6.1}$$

where σ is the shape factor and L is the primary fracture length.

Fracture aperture was based on image log analysis of natural fractures noted in the Northern Appalachian Basin study area basis well. Within this well, natural fracture occurrence was restricted to relatively short geologic intervals, most likely as a function of lithological competency. Most fractures were designated as conductive and distinct; however, some intervals showed less distinct or resistive fractures present, suggesting that some degree of healing occurred. Natural fractures ranged in dip degree from roughly 50^0 to 90^0. Fracture aperture (width) was measured to determine an approximated porosity within the fracture. Fracture aperture was measured in the Northern Appalachian Basin image log. The size of a feature on a physical image log was converted to relative image tool measured size by measuring the width of the track and establishing a conversion. A total of 33 fractures were measured within the interval of interest. Some fractures were excluded from analysis due to non-distinct onset and termination of the fracture's boundary. Measured fracture aperture values ranged from less than 1 mm to 3 mm, had a mean value of 1.6 mm, with a standard deviation of 0.72 mm. Fracture aperture agrees with research by Gale (2004) for the Knox Group. which suggests fracture aperture of approximately 1.5 mm.

Fracture permeability was derived as a function of aperture width after Witherspoon et al. (1979) cubic law:

$$k = \frac{\alpha^2}{12} = \frac{(1.6\ mm)^2}{12} = 0.213\ mm^2 \cong 213\ mD \qquad \text{Eq. 6.2}$$

where α is the fracture aperture and L is the primary fracture length.

While many researchers have proposed methods to estimate fracture permeability, there is little information available on aperture roughness, mineral precipitation in the fracture, or other data on the nature of the fractures. Therefore, a simple fracture permeability estimate was retained.

Table 6-7: Fracture model parameters for Northern Appalachian Basin study area.

Parameter	Trenton-Black River	Tribes Hill-Little Falls	Rose Run	Galway A dolomite	Galway B sand	Galway B dolomite	Galway C sand	Potsdam	Basis
Depth interval (ft)	5,518-6,172	6,172-6,359	6,359-6,546	6,546-6,848	6,848-6,985	6,985-7,075	7,075-7,132	7,132-7,322	Log analysis
Thickness (ft)	654	187	187	302	137	90	57	190	Log analysis
Features	Natural fractures	N fractures, faults	Natural fractures	Natural fractures	Natural fractures	Natural fractures	Natural fractures	Natural fractures	Image logs
Density (fractures/100 ft)	1	17	26	1	5	0	0.0	1	Image logs
Shape factor (1/cm^2)	NA	6.6	6.6	NA	NA	NA	NA	NA	Derived 2pi2/l2 for long 2D slab (Zimmerman, 1993)
Primary dip azimuth (°)	18	225	207	239	215	NA	NA	23	Image log interpretation
Primary dip inclination (°)	71	68	74	70	72	NA	NA	69	Image log interpretation
Primary length (m)	NA	3	3	NA	NA	NA	NA	NA	Literature estimate (Gale, 2004; Bowersox, 2014)
Primary height (m)	NA	1	1	NA	NA	NA	NA	NA	Assume 1:3 ratio
Primary aperture (mm)	NA	1.5	1.5	NA	NA	NA	NA	NA	Literature estimate (Huck, 2013; Gale, 2004)
Secondary dip azimuth (°)	67	26	NA	4	NA	NA	NA	NA	Image log interpretation
Secondary dip inclination (°)	81	63	NA	65	NA	NA	NA	NA	Image log interpretation
Secondary length (m)	NA	3	3	NA	NA	NA	NA	NA	Literature estimate (Gale, 2004; Bowersox, 2014)
Secondary aperture (mm)	NA	1.4	1.4	NA	NA	NA	NA	1.4	Literature estimate (Huck, 2013; Gale, 2004)
Primary:secondary	2:1	5:1	NA	1:1	NA	NA	NA	NA	Image log interp, primary to secondary frequency
Fracture porosity	NA	0.15	0.15	NA	NA	NA	NA	NA	Based on max Knox porosity (Bowersox, 2013)
Fracture permeability (mD)	NA	281	281	NA	NA	NA	NA	NA	Calculated = α^2/12 (Witherspoon cubic law)
Hydraulic fracture permeability (mD)	NA	500	500	NA	NA	NA	NA	NA	Literature estimate (Zimmerman et al, 1993)

6.3 Coupled Fluid-Flow – Geomechanics Simulations

It is important to consider both geologic and geomechanical factors for safe and secure CO_2 storage applications. Geologic risks are typically minimized by detailed characterization efforts to ensure that the target formation (aquifer) is overlain by layers of impermeable rocks acting as a stratigraphic trap to prevent CO_2 from migrating upward after injection. During injection, the increase in pore pressures decrease effective stresses, which may potentially activate natural fractures (shear failure) or create new tensile fractures in the reservoir/caprock, compromising the effectiveness of the geologic storage system. This section describes the details of a coupled fluid-flow and reservoir geomechanics simulation study designed to assess the geomechanical risks of injection into three wells located at the following basins: Arches, East-Central Appalachian Basin and North-East Appalachian Basin.

6.3.1 Introduction: Review of Basic Concepts and Terminology

Some of the basic geomechanical concepts applied in the analysis performed in this work are described here by means of an introduction and for completeness. Readers familiar with reservoir geomechanics however, may skip this section and proceed to the modelling approach in Section 6.3.2 instead.

A force applied on an element sets up normal and shear stresses (same units as pressure) that have both magnitude and direction. The stress on this element is thus described as a 3 × 3 tensor with six independent components, with normal stresses on the diagonal and shear stresses off-diagonal. The stress in the element may also be described via three principal normal stresses (in decreasing order of magnitude, S1, S2 and S3). These principal normal stresses are so named because they represent the directions in which there are no shearing stresses.

Figure 6-43 describes stress as a tensor and the concept of principle normal stresses. When a force is exerted on an arbitrarily rotated cuboidal element, it results in normal and shearing stresses on the faces of the element as shown. These stresses are symmetrical, and are described mathematically in the form of the tensor described below. If, subject to the same external force, an element with different rotation angle was selected, the normal and shearing stresses set up on each face would be different. At one specific angle, however, there would be no shearing stress at all, and only normal stresses – these are the principal normal stresses.

Essentially, since the orientation of the element is arbitrary, this particular angle – where there are only normal stresses and no shear stresses – is chosen as the best way to describe the state of stress in the system. In the context of stresses in rock layers, these three principal stresses are typically the vertical stress (σ_v), and the two stresses in the horizontal plane: maximum horizontal stress ($\sigma_{H,max}$) and minimum horizontal stress ($\sigma_{h,min}$). It is important to point out that σ_v need not always correspond to the greatest principle stress S1 (least being S3). The relative magnitudes of these three directional stresses will depend on the faulting regime of the strata (Anderson, 1951). In a normal faulting regime, S1 and S3 are σ_v and $\sigma_{h,min}$ respectively. In a strike-slip regime, these are $\sigma_{H,max}$ and $\sigma_{h,min}$ respectively. In a reverse regime, these are $\sigma_{H,max}$ and σ_v respectively.

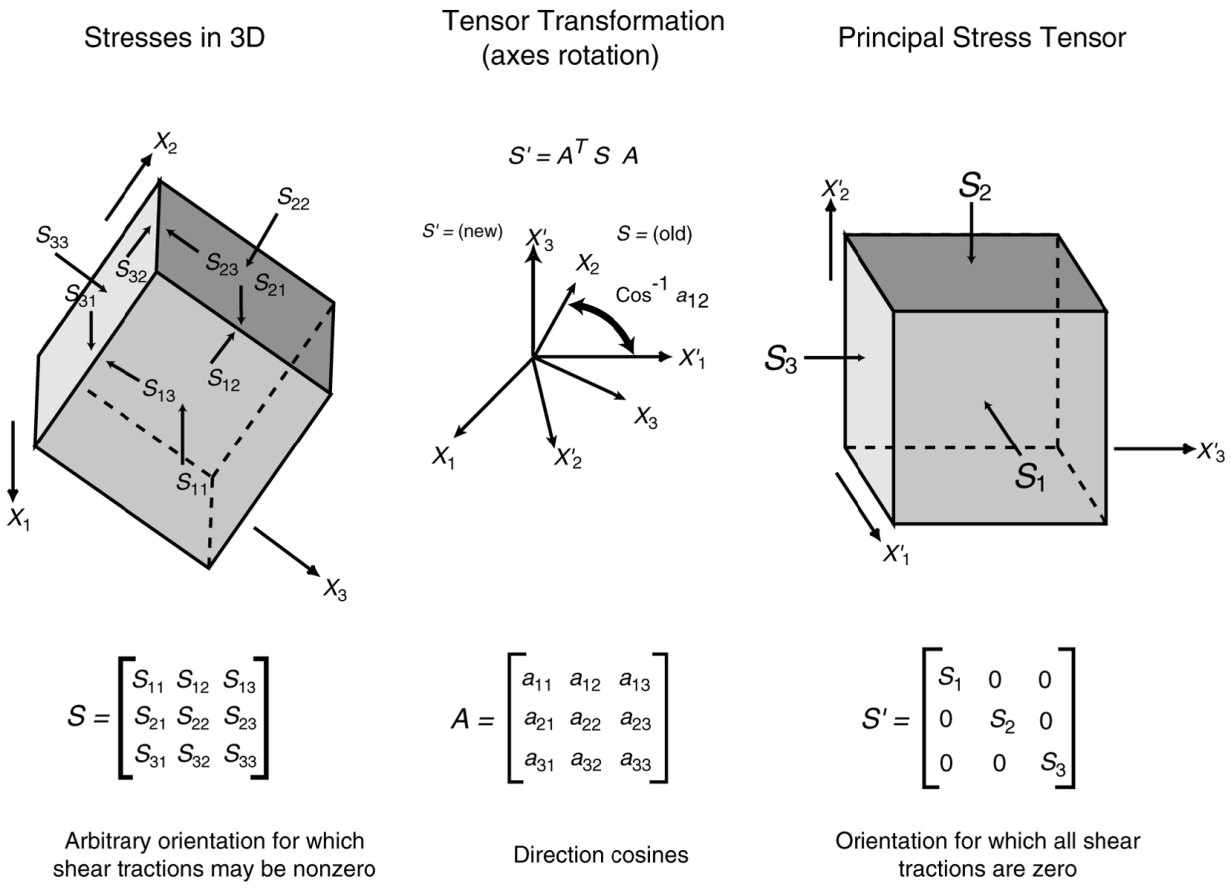

Figure 6-43: The stresses in an element are described as a tensor. When rotated through a particular angle, the shear stresses disappear, and only normal or principle stresses act on the element. Graphic courtesy of GeoMechanics International Inc.

Figure 6-44 shows how the stresses in an element may be presented in the form of a Mohr's circle. The coordinates of any point located on the circumference of the circle represent the stresses set up on the element rotated at all angles 0 to 360 about an axis. The Mohr's circle plots shear stress on the Y-axis versus normal stress on the X-axis (for a two-dimensional [2D] plane through the element). The principle stresses occur on opposite ends of the diameter of the Mohr's circle on the x-axis, and dictates which 2D plane through the element is being represented. For a rock with $\sigma_v > \sigma_{H,max} > \sigma_{h,min}$ for instance, a circle plotted with σ_v and $\sigma_{h,min}$ as the principle stresses would display the stresses occurring through a vertical cross-section of the element, while that plotted with $\sigma_{H,max}$ and $\sigma_{h,min}$ would represent stresses occurring through a horizontal cross-section of the element.

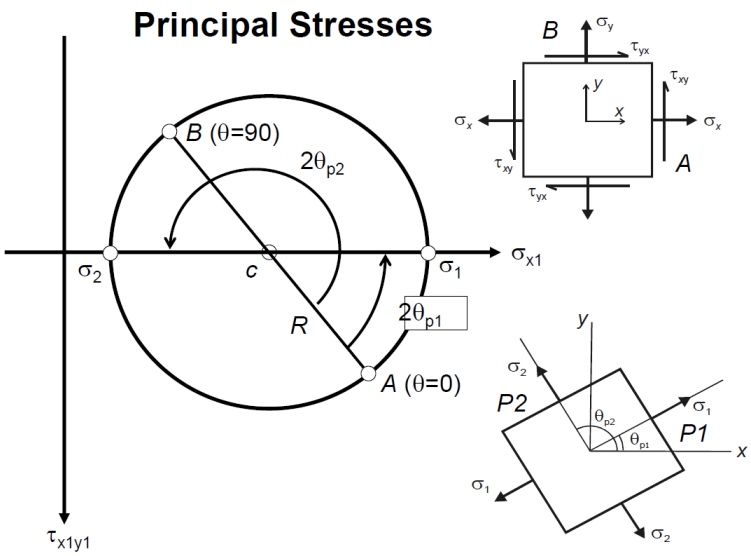

Figure 6-44: Mohr's circle representation of normal and shear stresses on an element. Graphic courtesy of Dr. A.B. Zavatsky's (University of Oxford) supplementary lecture handouts on Mohr's circle for plane stress.

Subsurface rock is saturated with fluid in its pores, which exerts pressure uniformly and outwardly in all directions, on the grains of the rock. This pore pressure is typically described with respect to hydrostatic pressure, or the pressure of an equivalent column of water (0.433 psi/ft) at that given depth. Conceptually, where pore pressure is hydrostatic, it suggests a completely connected pore network from the surface to the reference depth. Such continuity may not always be the case and, as a result, pore pressure may be found to be different from the hydrostatic pressure in some formations, although it can never be greater than vertical stress. In an overpressured regime for instance, pore pressures are significantly greater than hydrostatic pressure and close to lithostatic pressure, or the pressure exerted as a result of the weight of the overburden rock. Finally, note that since pore pressure acts in the opposite direction of the total (or external) stress the rock strata is subject to, it is useful to define effective stresses representing the net stresses in the rock, as shown in Equation 6.3 below. This equation may be written for each direction:

$$\sigma_j' = \sigma_j - \alpha * p_p \qquad \text{Eq. 6.3}$$

where:

σ_j' = Effective Principle Normal Stress in direction j, psi

σ_j = External or Total Principle Normal Stress in direction j, psi

α = Biot's coefficient, dimensionless, between 0 and 1.

p_p = Pore Pressure , psi

j = Principle stress direction 1,2 or 3

This equation suggests that during injection, as the pore pressure rises, the effective normal stress in the rock decreases by a proportion controlled by the Biot's coefficient. When poro-elastic effects are important and the pore spaces are deformed significantly during injection, the external (or total) stresses acting upon the rock are also affected and counter the effect of pore pressure increasing.

Ultimately, normal and shear stresses on the rock serve to bend and deform the rock in the direction that the stresses are acting and set up strains in the rock. The amount and type of deformation that a rock can undergo before failure is quantifiable in lab tests and is captured by four intrinsic rock properties: Young's modulus, Poisson's ratio, shear modulus and bulk modulus. These properties are described in Figure 6-45. The three moduli refer to proportionality constants that control the quantity of strain experienced by the rock per unit of stress. The Young's modulus controls the amount of strain that occurs in the direction of the normal stress (axial) while the shear modulus controls the deformation in the direction of shearing stresses. The bulk modulus represents the total summation of the deformation in the rock in all three directions per unit of resultant stress. The Poisson's ratio is a quantity that relates the deformation of the rock along the direction of the normal stress to the deformation occurring perpendicular to it – the ratio of axial strain to lateral expansion.

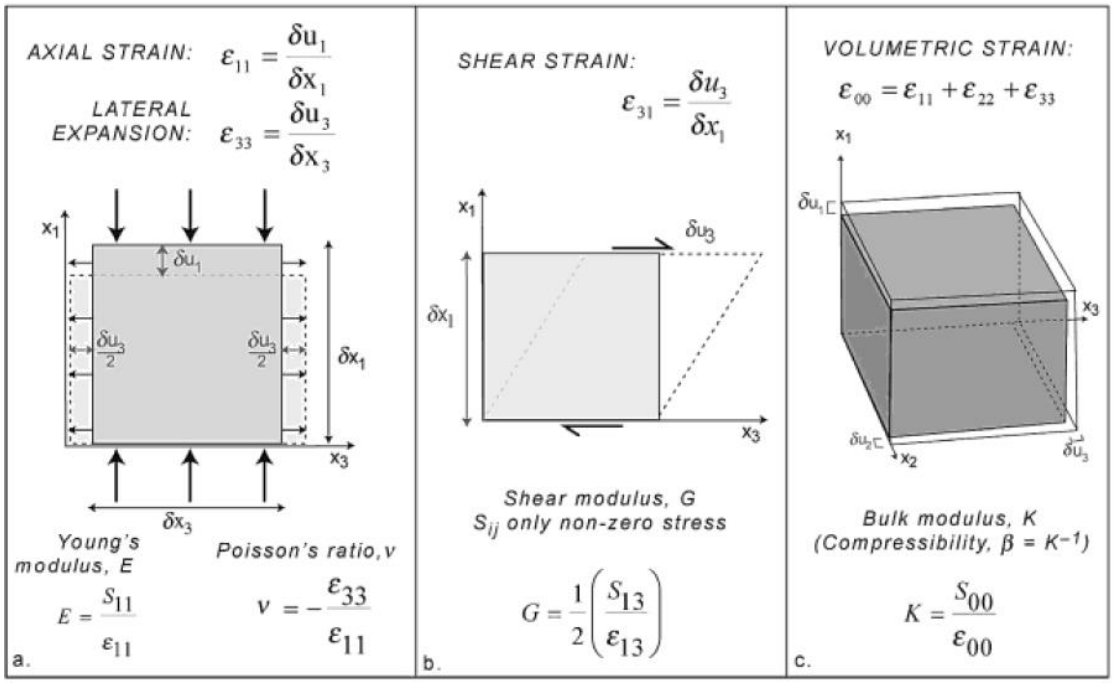

Figure 6-45: Graphic illustrating the concept behind the four intrinsic rock property ratios (Zoback, 2010).

Figure 6-45 illustrates three rock strength properties on a Mohr diagram. The uniaxial tensile strength and compressive strength of a rock represent the maximum tensional (negative) and compressive (positive) stresses the rock can withstand before permanent damage. Failure here represents the rock breaking apart in tensile failure or being crushed by compressive (shearing) stresses. Both are lab-measured properties obtained via uniaxial destructive core testing - with increasing stress on the rock sample applied in one direction only. Given that the tensile strength of a rock is usually small, and that in-situ stresses at depth are always compressive, this particular rock property is generally considered unimportant. The two Mohr's circles drawn based on these properties may be connected by a tangent line that represents the criteria for shear failure or the shear strength of the rock.

Figure 6-46 shows how the failure envelope is determined with Mohr diagrams using data from triaxial compression tests. In these tests, the maximum compressive stress to failure (σ_1 or S1) is determined at various confining pressures (σ_3 or S3). Together, these two quantities represent the opposite ends on the diameter (principle stresses plotted on the x-axis) of the Mohr circle. The shear strength of the rock is found by tracing the common tangent to all circles plotted from several experiments. The intersection of this tangent with the y-axis represents the cohesion of the rock or the minimum amount of shearing stress required for fracture generation via shear failure. Where shearing stresses in the rock grow large enough to reach any value on this line (envelope), the rock will tend to fracture alone a plane whose orientation may be determined from the angle of the tangent with the Mohr circle. Both figures also suggest that the shear strength of the rock is a function of normal stress, and is approximately linear when stresses are compressive. This proportional increase in the shear strength of the rock, or the slope of this failure line, is a property of intact rock and is referred to as the coefficient of internal friction.

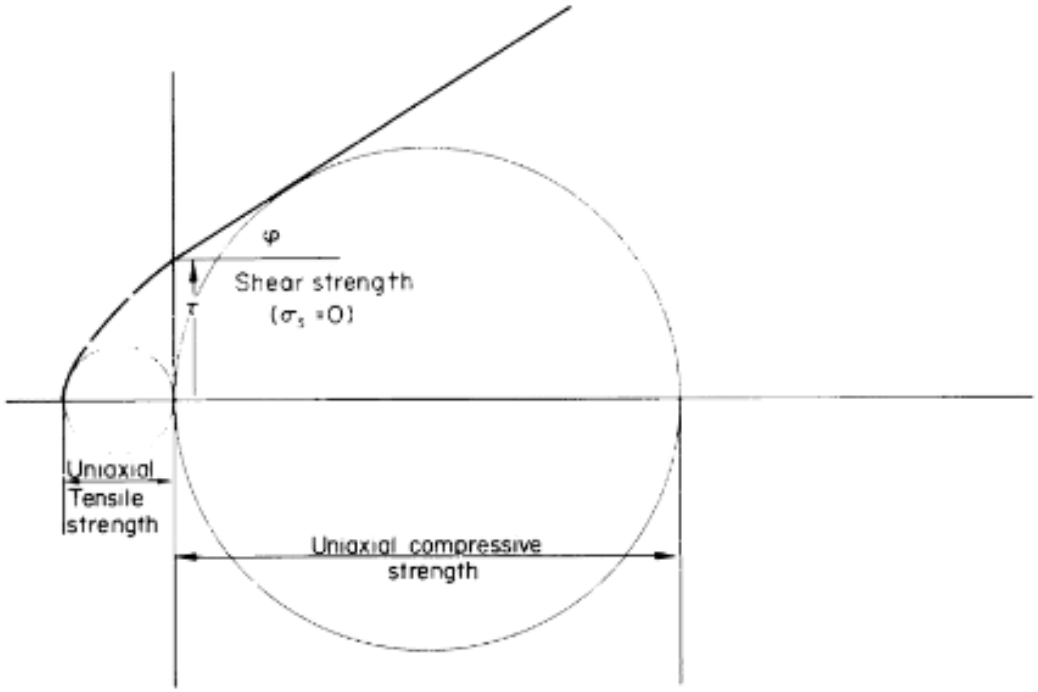

Figure 6-46: Coulomb-Naiver failure criterion for a rock material (Roberts, 2014).

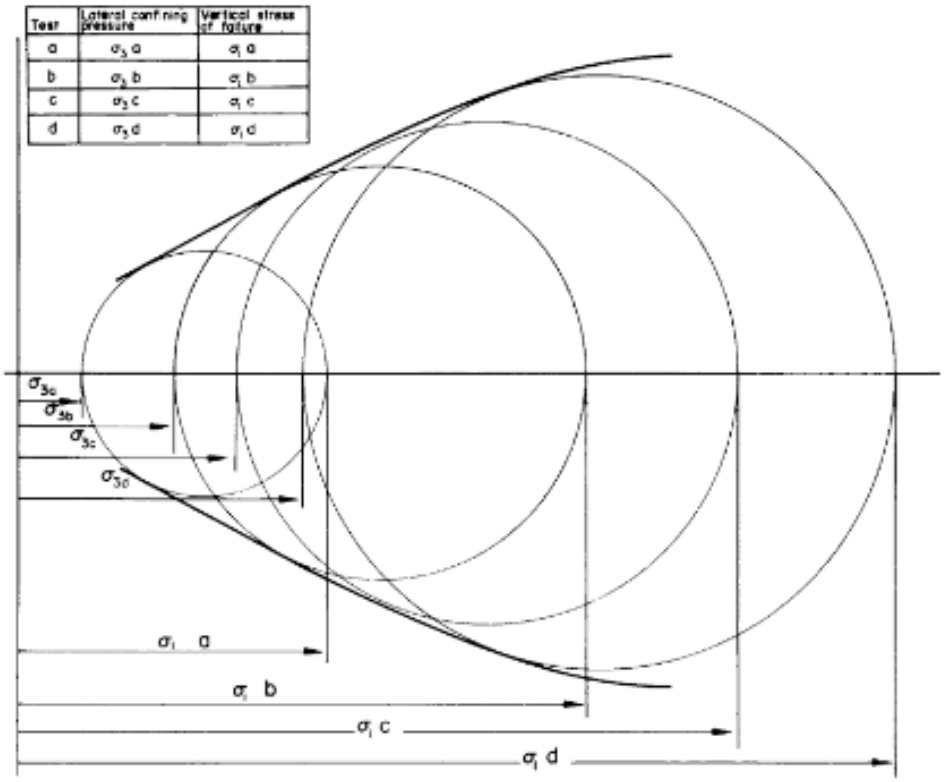

Figure 6-47: Shows how the failure envelope may be traced using triaxial compression tests (Roberts, 2014).

This work is most interested with fault activation and shear failure induced during injection. The Coulomb failure function (CFF) for slip on a pre-existing fault plane is defined as shown in Equation 6.4 below (Coulomb, 1773).

$$CFF = \tau - \mu * \sigma_n \qquad \text{Eq. 6.4}$$

where:
τ = shear stress on the sliding plane
μ= coefficient of fault friction
σ_n= effective normal stress on the sliding plane

This function is typically negative, and the fault remains stable. When injection occurs and the effective normal stress is reduced however, slippage will occur when the CFF approaches zero. Numerous rock mechanic tests have confirmed Byerlee's law (Byerlee, 1978), which dictates the coefficient of friction in this equation to be constrained between 0.6 and 1. Similarly, a value of 0.6 has been recommended as a standard and reasonable value applicable for most cases, based on numerous field and lab evaluations (Zoback and Townend, 2001). The coefficient of friction referred to here controls the maximum shear strength of a correspondingly oriented fracture (within the rock), while the coefficient of internal friction dictates the shear strength of an intact (or relatively unfractured) rock.

This coefficient of friction is important for two reasons. Firstly, studies performed by various authors have all consistently determined that the crust is generally in a state of incipient frictional failure (Healy et al., 1968; Stein et al., 1992; Townend & Zoback, 2000). Essentially, they suggest that rocks at depth rarely unfractured, and more importantly, appear to always on the verge of shear or failure along numerous planes of fractures of widely distributed lengths and orientations embedded throughout the strata (Zoback, 2010). Secondly, based on numerous in-situ stress measurements, it appears that these stresses in a rock and the magnitudes they take on are controlled by this coefficient of fault friction (Zoback and Townend, 2001). This is shown in Figure 6-48.

Figure 6-49 is a schematic of a hypothetical rock with an array of fractures of various orientations distributed within, shown in three different shades of grey, subject to an external stress S1. The subset of fractures in black and bold (Figure 6-49b) indicate those that are critically oriented - at an angle corresponding to the coefficient of friction or an angle of β to the direction of maximum compressional stress S1. The external stress has set up shearing stresses great enough to cause failure along these pre-existing lines of slippage only for fractures (sets) with peculiar orientations, and others are not activated. Essentially, the only “activatable” faults are those that correspond to coefficients of friction ranging between 0.6 and 1. Fractures of all other orientations may never be activated.

Figure 6-50 integrates the concepts discussed in this section by comparing the Mohr’s circles of rocks before and after CO_2 injection. The blue line represents initial conditions, while the red line represents the stress in the rock post-injection. As pore pressure rises during injection, the effective stress in the rock is reduced and the Mohr circle moves toward the Mohr-Coulomb failure envelope. In the case of an intact rock or a rock with sparsely scattered fractures, (non-zero cohesion) with minimal poro-elastic effects with injection, no shear failure is induced as the effective stresses have not been reduced far enough to touch the failure line. The shear stresses are not great enough to induce a fracture. For a fractured rock (zero cohesion) with poro-elastic effects, injection has reduced the effective stresses such that the resultant Mohr’s circle is enlarged and is now tangent to the failure envelope – critically oriented fractures in the rock will have slipped. Assuming rock at depth has negligible tensile strength, tensile failure is said to occur when effective stresses have been reduced to zero. No tensile failure occurs in both cases as the effective stress has not been reduced to zero.

Finally, while the amount of vertical uplift experienced at the surface does scale with the volume of injection into the subsurface, the relationship between the two is complex and depends on a combination of many factors. These factors include: the quantity of effective stress reduction in the subsurface – which is itself a function of the amount of pore-pressure increase and the level of poro-elasticity in the rocks –, the stiffness or geomechanical rock properties of the subsurface, as well as the thickness and geomechanical rock properties of the overburden. Generally, a greater amount of perturbation of the effective stress field translates to a greater level of deformation of the subsurface. All things kept equal, a stiffer rock with a greater Young’s modulus will tend to deform less. The overburden acts as a cushion, and dampens the quantity of deformation occurring at the subsurface that is communicated to the surface.

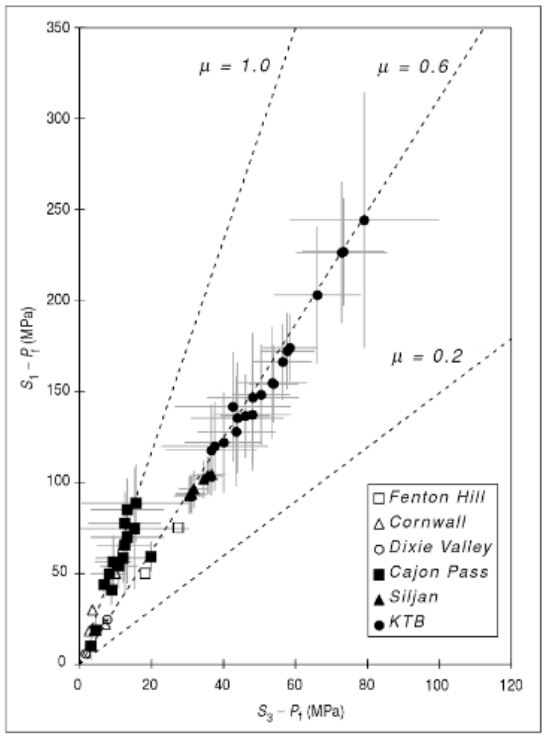

Figure 6-48: Various field measurements indicate that magnitudes of stress in a rock at depth are controlled by the coefficient of fault friction of pre-existing fractures. This quantity typically lies between 0.6 and 1 (Zoback and Townend, 2001).

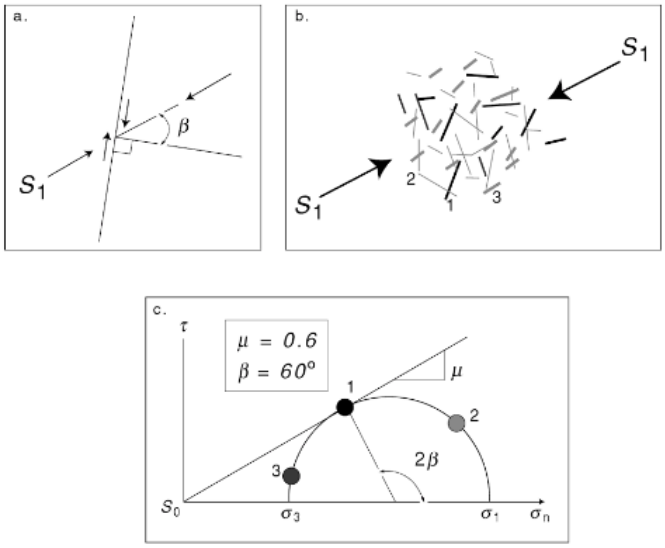

Figure 6-49: Shows that of the various array of pre-existing fractures in a rock, upon external stress, only critically-oriented fractures on the shear-failure line will fail (Zoback, 2010).

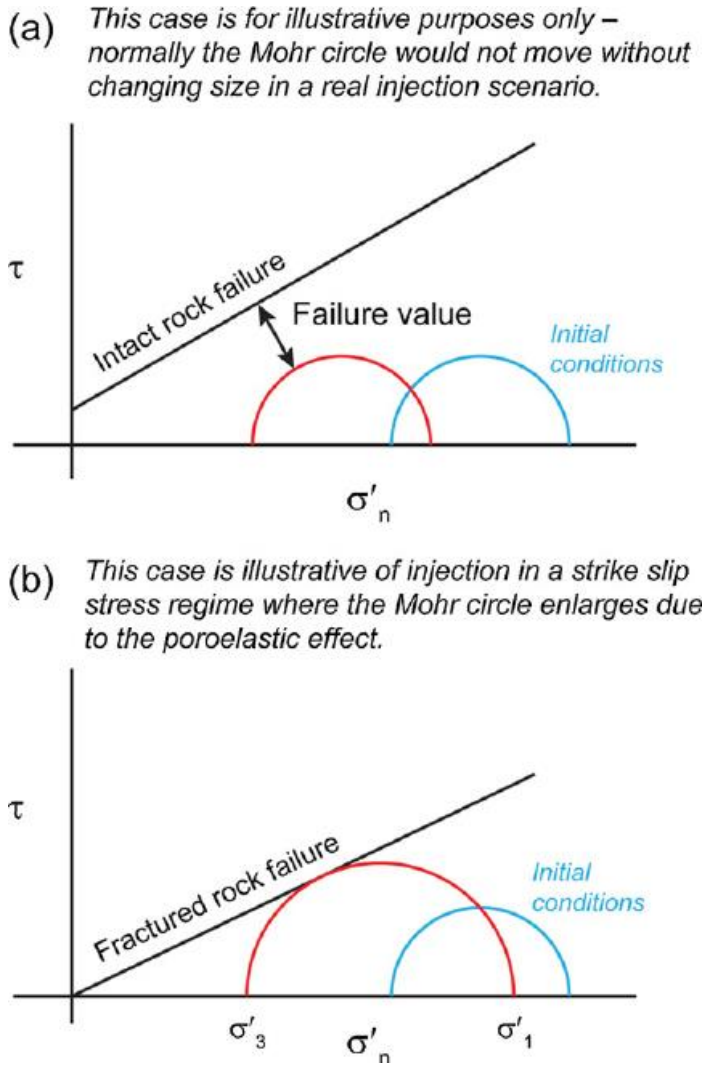

Figure 6-50: Illustrates how failure in the rock is analyzed using Mohr's Circles with effective stress (Olden et al., 2012).

The blue semi-circles in Figure 6-50 represent initial conditions, while the red semi-circles represent the stress in the rock post-injection. In the top graphic, there are no poro-elastic effects changes with injection, and the rock is assumed to be an intact rock with a non-zero cohesion (intercept of the failure line with the y-axis). The injection activity reduces the effective stress in the rock, but no shear failure occurs as the Mohr circle does not hit the failure envelope. i.e.: The shear stresses are not great enough to induce a fracture. In the bottom graphic, the rock is assumed to have pre-existing faults and a high degree of poro-elasticity. Since the Mohr circle hits the failure envelope, the injection has activated shear fractures in the rock oriented at an angle dictated by the coefficient of internal friction. No tensile failure occurs in both cases as the minimum effective stress has not been reduced to zero.

6.3.2 Modelling Approach

6.3.2.1 Scope

This section outlines the scope of the simulation study described in this report and presents the details of the modelling approach, including the underlying assumptions. The three sites selected for modelling were the East Bend #1 well in Boone County, Kentucky in the Arches Basin, OGS CO_2 #1 well in Tuscarawas County, Ohio in the East-Central Appalachian Basin and a deep test well in Chautauqua County, New York in the Northern Appalachian Basin.

The primary objectives behind the numerical modelling for each site was to evaluate the following three parameters, upon injection of commercial-scale volumes of CO_2 (several millions of metric tons):

- Caprock's geomechanical integrity (shear and tensile failure)
- Reservoir and intermediate layers' geomechanical integrity
- Expected areal uplift at the surface

The secondary objectives were to demonstrate/quantify the:

- Isolation of stress-strain perturbations within the subsurface
- CO_2 plume migration upward from the injected zone and the effectiveness of caprock in containing the injected CO_2.
- Effective CO_2 storage capacity on a per-well basis

The paucity of geomechanical characterization data – both in terms of number of wells/well logs available at each site and availability of quality leak-off test data – implies considerable uncertainty inherent in the input parameters of the model. The prudent approach to modelling under such circumstances is to create a conservative base-case model composed of modest estimates for (most of) the input parameters. Upon identifying an appropriate range of values for a selection of critical parameters, a sensitivity analysis can then be performed to quantify a range of predictions from the coupled fluid-flow geomechanical simulations.

6.3.2.2 Model Construction: Overview

Considering the limited volume of available characterization data and the objectives listed above, an isothermal, pseudo-3D fluid-flow model coupled with the geomechanical module in CMG-GEM (CMG, 2012) was deemed to be adequate. The model grid was constructed using the workflow described in Figure 6-51. The geomechanics module in CMG-GEM requires defining a separate geomechanics grid on which stress and porosity changes are computed. Within each time-step, pressures and saturations are first calculated on the fluid-flow grid and then passed onto the geomechanics module, which uses this as an input to perform its calculations (stress-strain field, porosity changes, displacement, etc.). The porosity changes calculated from the geomechanics module are mapped back onto the fluid-flow grid where the calculations are repeated. Since the two-way coupling option in the geomechanics module was employed for all models, these two pairs of calculations are performed recursively in a loop until the output from both grids are stable, before moving to the next time step. Figure 6-51 outlines the workflow and data inputs required to build the fluid-flow model grid.

Figure 6-52 provides an example of the geologic-reservoir caprock system as modeled in this work, showing both the fluid-flow grid and the geomechanical grid constructed for the OGS CO_2#1 well. While the fluid-flow grid has been limited to only the depths where the CO_2 plume will penetrate/migrate into (the target aquifer, intermediate layers and the caprock itself), the geomechanical grid captures the layers from the basement rocks below the injection to the surface, and also extends beyond the fluid-flow grid laterally. The geomechanics module calculates the vertical displacement occurring in each gridblock because of injection, and thus enables a prediction of the uplift all the way at the surface. The geomechanical grid envelopes the fluid-flow grid to minimize boundary-related effects of the stress-strain calculations mapped into the fluid-flow grid.

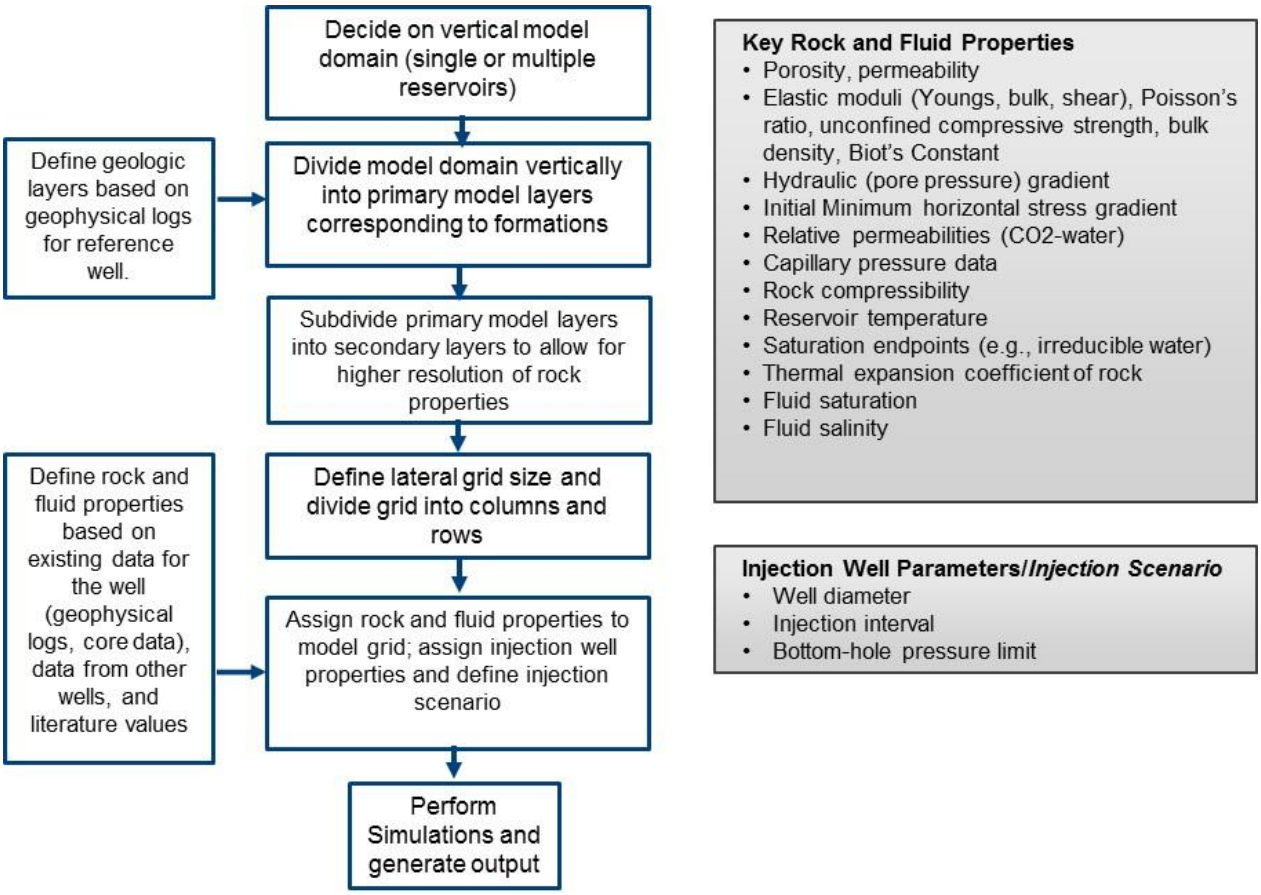

Figure 6-51: Workflow employed in constructing the model grid for fluid-flow simulation.

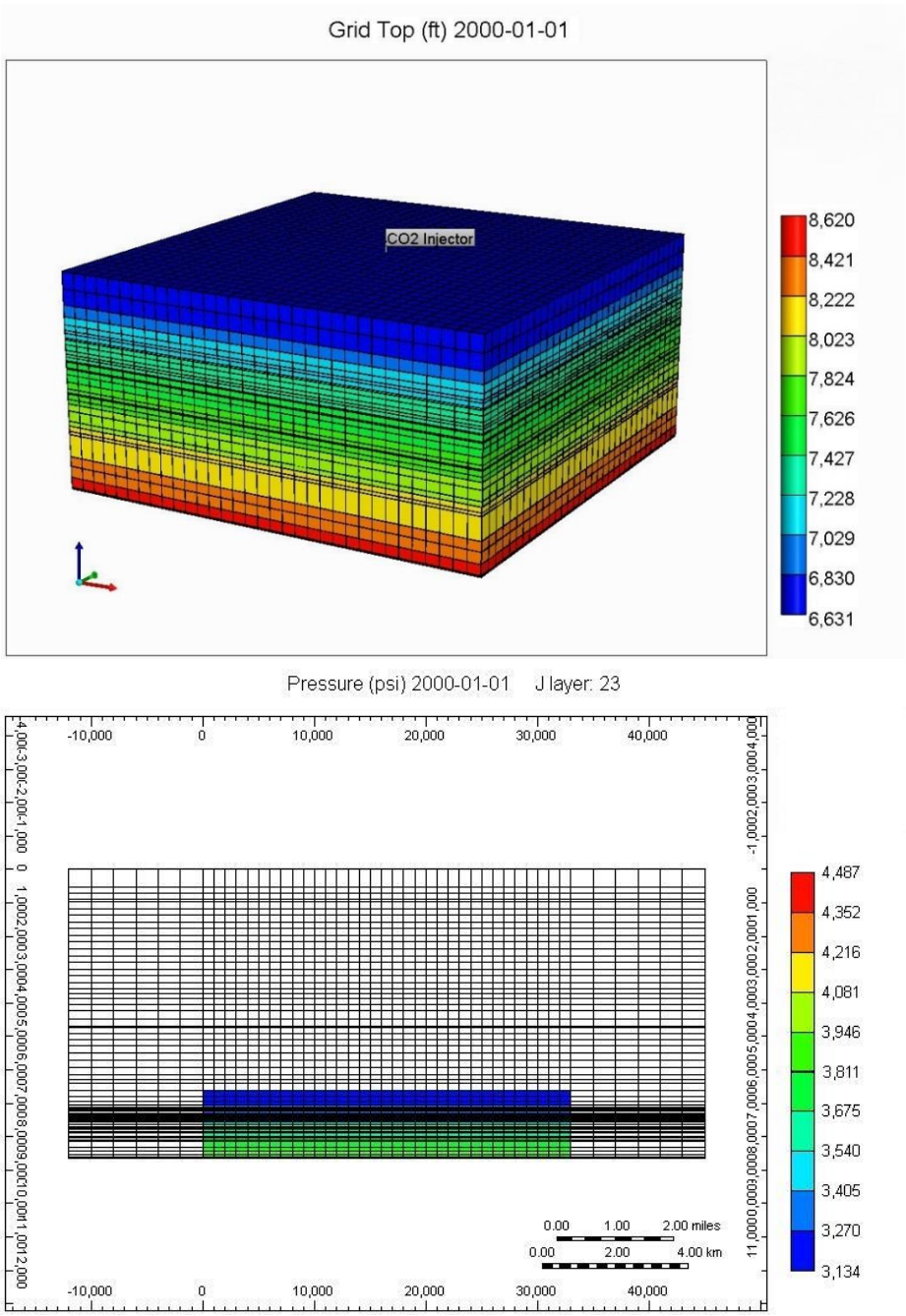

Figure 6-52: The top image shows the fluid-flow simulation grid constructed using the workflow outlined in Figure 6-51. The bottom image shows the fluid-flow grid embedded within the grid used for geomechanical calculations.

The OGS CO_2#1 well is shown at the center of the modelled domain, spanning an approximately 2000 ft interval containing the caprock, intermediate layers, and the injection zone. The geomechanical grid on the other hand – a cross-section of which is shown in the bottom image – has been constructed to model layers from the basement rocks underneath the injection zone all the way up to the surface. The highlighted region shows how geomechanical grid envelopes the fluid-flow grid (by design) both in lateral extent and in depth.

6.3.2.3 Model Construction: Assumptions

As shown in Figure 6-52, the subsurface has been modelled using a regular rectangular, cartesian grid with four boundaries with a single injector well in the center. The fluid-flow grid represents an area of 25,000 acres (~100 km^2), while the geomechanical grid extends further out and captures an area of 74,586 acres (~300 km^2). Both grids use an areal grid-dimension of 1000 ft x 1000 ft within the fluid-flow zone with the vertical thickness of each layer not exceeding 100 ft. The gridblocks near the injection well-bore up to 3000 ft away, are locally refined both areally (to a minimum of 100 ft x 100 ft) and vertically (to a minimum of 20 ft) reflecting the fact that this region is likely to have the highest pressure and saturation changes within each time-step during injecton. The amount of refinement is intentionally limited, as increasing the total number of gridblocks exponentially increases the total simulation time.

The model is constructed with each layer having uniform depths and thickness, as well as porosity, isotropic permeability and rock compressibility values that are homogeneous throughout each horizontal layer but vary between vertical layers (vertical heterogeneity). The selection of formation tops and layering in each site model has been chosen to also represent the series of geologically and geomechanically similar units with depth. There was little formation dip observed and as such, was not modelled in the strata within the fluid-flow grid. The values for each layer have been chosen based on a combination of well-log, lab-measured core data, and well-test data where available. All formations captured in the fluid-flow grid are assumed to be normally-pressured with a pore-pressure gradient of 0.433 psi/ft. Formation temperature has been modelled with a gradient of 1 °F /100 ft assuming 50 °F at the surface. In all the three sites of interest, the reservoir pressure and temperature target zones ensure that the injected CO_2 would be in a supercritical state. Capillary pressure effects have not been considered in this work. Default empirical relative permeability curves have been used in each model to retain the emphasis on modeling the stress-field impact of injection. The CO_2-brine relative permeability curves used in this work are shown in Figure 6-53.

The input parameters input for the geomechanical grid are the three principle stresses (vertical, minimum horizontal and maximum horizontal stresses), Biot's coefficient, static Young's modulus and the Poisson's ratio. The I-direction corresponds to the minimum horizontal stress, the J-direction to maximum horizontal stress and the K-direction to the vertical stress in the model. To maintain the conservative nature of the model, the Biot's coefficient was assumed to be equal to unity for all layers, ensuring the maximum possible reduction of effective stress with injection. All other properties were assumed to be laterally homogeneous (across each layer) but vertically heterogeneous. The static Young's modulus was obtained by applying a correction factor to a log-based dynamic Young's modulus estimate. For the OGS CO_2#1 well, several laboratory measurements were performed on cores collected from wells drilled around Ohio, and the correlation shown in Figure 6-54 was available. For the East Bend #1 well in Kentucky and Northern Appalachian Basin basin well however, no such data were available. The static Young's modulus for these models was thus assumed to be a conservative 70% of the log-based estimate of dynamic Young's modulus. The Poisson's ratio was also derived from a sonic log-based analysis for all layers in each well. The vertical stress gradient was obtained based on data from the density log (typically between 1.08 to 1.15 psi/ft). Since no mini-frac or leak-off tests were conducted in any of the three wells, literature on the Appalachian region was consulted to estimate the horizontal stress gradients, especially for the formations within the fluid-flow model (Evans, 1989). Where there were no literature sources available, log-derived estimates were used instead and compared. Equation 6.3 was used to calculate the effective stresses in each formation.

For purposes of interpretation, the effective stresses computed at a gridblock near the wellbore (where the stress changes are the most) and from a layer in the middle of the target formation, is chosen to be representative of the perturbations of the stress field for the entire formation. Most of the formations encountered in all wells show little evidence of being naturally fractured; they may be considered “intact” rock for all practical purposes. Some formations, however, such as the Rose Runsandstone, have some limited evidence indicating sparsely scattered vertical fractures. As a result, a value of 1000 psi has been selected as a sufficiently conservative and balanced value for cohesion, when performing the Mohr’s circle analysis for shear failure for all formations.

“Caprock” zones refers to rock layers that contain at least one layer with a permeability of 0.001 mD or less. “Intermediate” zones refer to rock layers in between the injection zone (reservoir) and the caprock, and refer to the layers that the injected CO_2 may be expected to migrate through upon injection. The “reservoir” or “injection zone” was identified as the Mount Simon for the East Bend #1 well, the formations from the Maryville to the Copper Ridge – consisting of Upper Maryville, Nolichucky, Lower Copper Ridge, Copper Ridge B and Upper Copper Ridge – for the OGS CO_2#1 well, and the Potsdam Formation for the Northern Appalachian Basin basis well. The East Bend #1 was perforated in the lower Mount Simon, where there was high permeability. The OGS CO_2#1 well is open-hole below the Rose Run to Maryville The Northern Appalachian Basin basis well is a characterization well drilled up to the upper portion of the Potsdam. The well in the model injects in these perforations/open-hole layers.

All models were considered to be reservoirs fully saturated with formation brine. A maximum bottom-hole pressure (BHP) constraint was specified for the injector well, essentially allowing the dynamic simulator to vary the CO_2 injection rate with the near-wellbore pressure. This BHP was set as per assumed regulatory restrictions preventing injection beyond 0.733 psi/ft at the top of the injection zone. In the case of the OGS well, however, this exceeded the minimum horizontal stress gradient. The max BHP constraint for each of the East Bend #1, OGS CO_2#1 and the Northern Appalachian Basin basis well was thus set to 2500 psi, 4500 psi, and 5000 psi, respectively. The injection (and hence the total simulation time) is for a total period of 30 years. The simulation was not carried out beyond this period as the pore-pressure increases only during the injection.

Each edge of the fluid-flow model may be modelled either as a “no-flow” boundary to represent a fault, or as a constant pressure boundary maintained by other wells in that location. The use of large pore-volume modifiers on gridblocks at the edge of the model may also be used to imply “infinite-acting” conditions or large swathes of uncaptured rock volume in that direction. Thus, a variety of scenarios (ranging from completely compartmentalized to semi-confined to completely open) may be modeled by using some combination of these conditions for each of the four boundaries of the model. Considering however, that (1) a very large area of the subsurface is being modelled, (2) data are extrapolated based on only one well in the vicinity, and (3) conservativeness is desired in predicting the pressure and stress-field response to injection in the caprock and the reservoir, the continuity of the properties extracted from the well was assumed to be limited to 25,000 acres (~100 km2) – or the extent of the fluid-flow model – and each site has thus been modelled as an extensive compartment isolated by four “no-flow” boundaries.

The Peng-Robinson Equation-of-State model was used in CMG-GEM to calculate the fluid properties of brine and CO_2. Henry’s correlation is used to determine the solubility of CO_2 in the brine. The thermal expansion co-efficient of the rock is ignored in isothermal simulations.

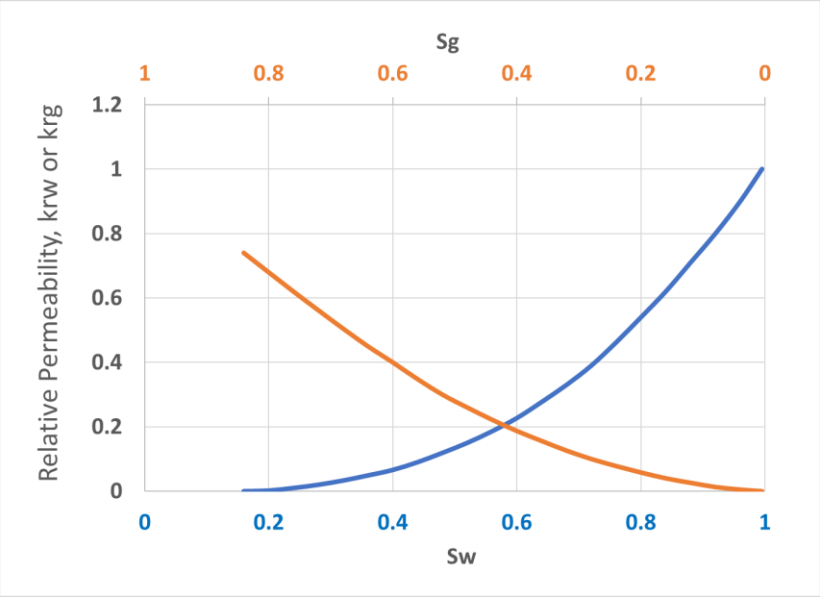

Figure 6-53: The relative permeability curves used for water and gas in the fluid-flow grid for site models in this work.

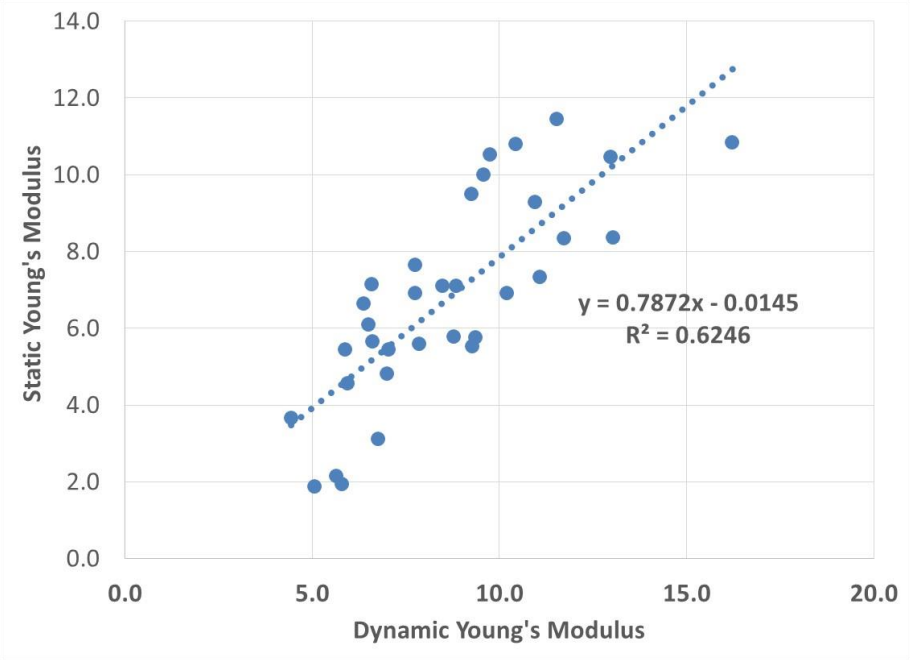

Figure 6-54: The correlation between the dynamic and static Young's modulus extracted based on measurements performed on cores extracted from various wells drilled throughout Ohio. This correlation was applied to correct the log-based static Young's modulus estimate in the OGS CO_2 #1 well.

6.3.2.4 General Analysis Methodology

The relevant analysis that was performed to meet each objective is listed in Table 6-8.

Table 6-8: Table of objectives of the modelling work and, the relevant analysis is described. These analyses are performed on the output of a single simulation with the base-case scenario inputs, for each well.

Objective	Analysis
Evaluate Caprock/Intermediate/Injection zones' geomechanical integrity: Tensile Failure	The minimum effective stress in all layers after injection must be at least ~250 psi.
Evaluate Caprock/Intermediate/Injection zones' geomechanical integrity: Shear Failure	Mohr circle comparison (see Figure 6-50) before and after injection against a failure envelope with an appropriately chosen rock cohesion and a range of coefficient of friction angles.
Evaluate areal uplift at the surface	Plot of the computed values of total cumulative vertical displacement of the surface layer at varying distances from the injector well, with time.
Demonstrate the isolation of stress-strain perturbations within the subsurface	Vertical profile of the minimum effective stress before and after injection. Cross-section of the change in effective stress in the formations after injection. Cross-section of volumetric strain in the formations after injection.
Demonstrate CO_2 plume migration and the effectiveness of caprock	Cross-sections of the pressures and gas saturation distribution after injection. Plot of CO_2 volumes in the Reservoir and Intermediate layers with time.
Quantify the effective CO_2 storage capacity of the well	Total volume of cumulative CO_2 injected with time.

The analysis of each site will be presented in subsequent sections in the following manner. First, the site-specific model inputs to the coupled fluid-flow and geomechanics simulation will be listed. Second, the results of the simulation run will be displayed via the following graphs (in order): change in pressure and cumulative CO_2 stored in each formation versus years of injection, cross-section of the model showing CO_2 saturation, cross-section of the model showing pressures, cross-section of the model showing reduction in the minimum effective horizontal stress, cross-section of the model showing the volumetric strain, a vertical profile of the minimum horizontal effective stress, and a two-paned image with an aerial view of the uplift at the surface at the top and a plot of the uplift at the surface at various distance and the total stored CO_2 versus years of injection in the bottom pane. Third, the integrity analysis is presented via two figures: a plot showing the effective stresses in each direction and the cumulative CO_2 volumes versus years of injection, and a plot showing the Mohr's circles using Figure 6-50, with three lines representing different gradients for the failure envelope (see Figure 6-48). Detailed descriptions of all figures have been provided.

6.3.2.5 Sensitivity Analysis Methodology

We note that there is significant uncertainty in the model's geomechanical parameters, stemming from the fact that a large lateral extent of the subsurface has been modelled, generally using log-based data extrapolated from only one well in the vicinity and/or a literature search. As discussed in Section 6.3.2, acknowledging these limitations in the available data necessitated conservative assumptions when constructing the simulation model. Consequently, the predictions of simulation model (e.g.: amount of increase in average reservoir pressure, magnitude of effective stress reduction, effective storage capacity, etc.) may be assumed to be an estimate of only the "worst-case" scenario.

A sensitivity analysis considering the uncertainties/effects of individual geomechanical parameters (as opposed to geologic parameters) on the desired performance measures (see Table 6-8), was thus required in order to quantify a range of potential outcomes at each site upon injection. To that end, our approach was to model progressively more optimistic scenarios – treating the initial model as a baseline representing the most conservative scenario – based on varying combinations of the most uncertain inputs. These inputs are: the minimum and maximum horizontal stress gradients, Young's modulus, Biot's coefficient, and the presence of boundaries.

Minimum and maximum horizontal stress gradients are generally associated with a greater level of uncertainty than the vertical stress gradient. This is a critical consideration given that these principal stresses control the size of the Mohr's circle (see Figure 6-44), which represents the normal and shear stresses experienced within the rock. A larger Mohr's circle would bring the rock closer to the shear failure envelope (see Figure 6-50), while a smaller Mohr's circle would have the opposite effect. Thus for instance, lowering the maximum horizontal stress and increasing the minimum horizontal stress would have the greatest impact on rocks in the strike-slip faulting regime ($\sigma_{H,max} > \sigma_v > \sigma_{h,min}$). A stiffer rock with a higher (static) Young's modulus leads to lower vertical displacement for the same stress change, resulting lower areal uplift at the surface. While the Poisson's ratio is also an important factor in this respect, there were much lower levels of uncertainty observed in this parameter, for the sites studied in this project. Note also that the Young's modulus also affects the magnitude of stress changes that occur in the rock. The Biot's coefficient controls the magnitude of the stress perturbation directly caused by a rise in pore-pressure (see Equation 6.3). Therefore, for the same pressure increase (in the absence of poro-elastic effects), a smaller value of the Biot's coefficient will lead to a lower magnitude of effective stress reduction. Modelling each site as 25,000-acre compartment isolated by four "no-flow" boundaries serves the desired purpose of exaggerating the pressure response and proportionally, the stress-strain field perturbation upon injection. The rapid rise in average reservoir pressure, also tends to throttle the injection rate leading to lower estimates of effective storage capacity. On the other hand, if the compartment is much larger (e.g.: the injected formation is more continuous with little evidence of faulting), injection will lead to a more subdued response in the pressure and the stress-strain field. The use of large pore-volume modifiers on gridblocks at the edge of the model may also be used to imply "infinite-acting" conditions or, equivalently, large swathes of uncaptured rock volume in that direction.

Table 6-9 describes the five sensitivity scenarios simulated and the changes in the corresponding combinations of parameters associated with each scenario (as compared to the base case). Numbered 1 to 5 from the most conservative to the least conservative (most optimistic), this system also enables investigating the effect of individual parameters by comparing successively numbered scenarios. For instance, comparing the results of scenarios 4 and 5 would be useful for evaluating

the effect of compartment size, while a comparison of simulation results 3 and 4 would reveal the impact of the Biot's coefficient. Note that a model is built to represent each scenario, and that parameter values have been changed on a per-layer basis in each model. These changes are also implemented only in the caprock, intermediate and injection zone layers, and not in the overburden layers. The simulation results from each model was analyzed using the framework described in Table 6-8. As the most important scenario, the analysis of the base case ("worst-case" or the most conservative scenario) will be emphasized and discussed in great individual detail. The sensitivity analysis on the other hand, will be discussed in a more succinct manner to avoid redundancy given the nature of the system employed.

Table 6-9: Describes the combination of parameters leading to progressively more optimistic scenarios modelled as part of the simulation study. Each parameter is changed with respect to its value from the base case.

Scenario #	Boundary Conditions	Biot's coefficient	Young's modulus	Max. Horizontal Stress Gradient	Min. Horizontal Stress Gradient
1. Base Case *(Most Conservative)*	4 "no-flow" boundaries	1 (max.)	Low	High	Low
2.	4 "no-flow" boundaries	1 (max.)	Low	Decreased	Increased
3.	4 "no-flow" boundaries	1 (max.)	Increased	Decreased	Increased
4.	4 "no-flow" boundaries	Decreased	Increased	Decreased	Increased
5. *(Most Optimistic)*	"Infinite-acting" conditions	Decreased	Increased	Decreased	Increased

6.3.3 Arches Study Site

6.3.3.1 Model Summary

Table 6-10 presents key site-specific inputs to the model. Data points that have been chosen upon consulting available literature are identified. All others have been obtained only from well-log analysis. Formations in blue are in the injection zone, green are in the intermediate zone and red are in the caprock zone. Layers within each formation may be of varying thickness. The permeability values listed represent the average across the number of layers present. Although not listed below, around 200 ft of basement rock has also been modelled in the geomechanical grid. In the absence of characterization data, it has been assumed to have the same properties as the Mount Simon and a minuscule permeability of 0.001.

Table 6-10: Key site-specific data inputs for coupled fluid-flow – geomechanics simulation for the East Bend #1 well.

Formation	Average Depth / ft	Thickness / ft	No. of Layers	Average Porosity	Average Permeability / md	σ_v gradient / psi/ft	σ_H gradient / psi/ft	σ_h gradient / psi/ft	Static Young's modulus[d] / psi	Poisson's ratio	Average Initial Pressure / psi
Lower Mount Simon	3484	116	3	11.1%	61 [a]	1.08	1.2 [b]	0.7 [b,c]	4.05E+06	0.28	1604
Upper Mount Simon	3303	189	4	7.7%	12	1.08	1.2	0.7	4.99E+06	0.26	1517
Lower Eau Claire	3137	233	2	7.2%	0.03	1.08	1.2	0.95 [c]	3.98E+06	0.30	1449
Upper Eau Claire	2898	212	3	6.4%	0.0005	1.08	1.2	0.95	3.98E+06	0.30	1332
Davis	2744	96	2	7.5%	0.0001	1.08	1.2	0.95	3.73E+06	0.31	1265

a. Average permeability obtained from transient analysis on injection fall-off tests (Battelle, 2010).
b. Stress measurements based on three hydraulic fracture tests and 2 hydraulic tests on pre-existing fractures (Cornet & Battelle, 2014).
c. Minifrac test in the Eau Claire, Injection and step rate tests in the Mount Simon conducted in Illinois (Bauer, Carney, & Finley, 2016).
d. 70% of the Log-based dynamic Young's modulus.

6.3.3.2 Simulation Results

Figure 6-55 shows the average reservoir pressure increase and the volumes stored in each formation after 30 years of injection. Most of this volume is stored in the Mount Simon (26.5 million tons), with around 2 million tons of CO_2 migrating into the Eau Claire. This results in the average reservoir pressure of the Mount Simon and Eau Claire formations rising by around 750 and 450 psi, respectively. No CO_2 penetrates the Davis or the caprock, and there is negligible pressurization of the caprock. For both the Eau Claire and the Mount Simon, the average reservoir pressure rises in tandem and consistently during the period of injection, and the slope of the total cumulative CO_2 stored plot (which suggests the rate of injection) flattens after around 12 years, suggesting that boundary effects are first felt after this time. Migration of CO_2 into the Eau Claire is prominent after around 4 years of injection, and the total cumulative accumulation of CO_2 within this intermediate zone is significant (more than 0.5 million tons) only after 10 years of injection. Throughout the injection period, no significant retardation of the slope of the total cumulative CO_2 stored curve and pressure increase curve is observed, suggesting that further injection beyond 30 years may be possible. This is because the average reservoir pressure in the Mount Simon has not risen to close to the specified bottom-hole pressure constraint – which would throttle the injection rate.

Figure 6-56 to Figure 6-60 present more simulation results via cross-sections through the fluid-flow grid. The relevant formations have been identified. Figure 6-56 shows that CO_2 injected into the Mount Simon forms a plume with a maximum radius of approximately 5000 ft. around the wellbore. Some of the CO_2 migrates into the lower-most region of the Eau Claire within 50ft of the Mount Simon (see caption of Figure 6-55). None of the CO_2 penetrates the Davis caprock.

Figure 6-57 presents the distribution of pressures in the three formations after injection, and reveals that the lower Eau Claire experiences greater pore-pressures (~2300 psi) than the upper Eau Claire (~1600 psi). Despite not being the target of the injection, the lower Eau Claire attains as much pressure as the main injection zone or the Mount Simon (~2400 psi), due to the upward migration of CO_2. Figure 6-58 shows that the entire vertical section of from the Mount Simon including the lower Eau Claire, experiences a nearly uniform pressure increase (between 800 - 850 psi). The increase in pore pressure is much more moderate in the upper Eau Claire (~200 psi). Pressure increase at the furthest extents of the model (17000 ft.) in these formations is also significant (more than 100 psi). While the pressure impulse from injection is always generally expected to extend beyond the CO_2-plume, the relatively high permeability of the Mount Simon – especially in the lower layers – results in it reaching the (imposed) boundaries of the formation, and pressurization occurs over a large regional extent, as opposed to being localized around the wellbore. Injectivity is not an issue in this well and further injection will be possible until the entire Mount Simon uniformly reaches a pressure of 2500 psi. We note however, that the model extent has been limited by design – as part of the conservative approach to modelling – which exaggerates the pressurization and consequently, the effective stress-perturbations experienced within all formations.

Figure 6-59 shows that the horizontal effective stress reduction is greatest in the formations penetrated by the plume, i.e., the Mount Simon and lower Eau Claire, with negligible impact on the Davis. The reduction of this effective stress is much greater in the lower Eau Claire (~350 psi) than that the upper Eau Claire (~100 psi), which is also reflective of the corresponding pore-pressure increases described earlier. The quantity of (horizontal) effective stress reduction in the Mount Simon (~300 psi) is also similar to that in the lower Eau Claire. The discrepancy between the pore-pressure increase and effective stress reduction in these zones – considering a value of unity for the

Biot's coefficient – suggests that there are significant poro-elastic effects. The increase in total (external) stress in these formations in response to the injection, has a dampening effect on the perturbation of the effective stress (see Equation 6.3).

Figure 6-60 shows that the volumetric expansion is greatest in the formations penetrated by the plume, i.e., the Mount Simon and the Eau Claire, with comparatively negligible impact on the Davis. The lower Eau Claire is impacted far more than the upper Eau Claire.

Figure 6-61 shows that the stress perturbations induced as a result of injection have been generally contained beneath the caprock, or the Davis. Note that the vertical profile extends below the injection zone, reflecting the fact that the part of the basement rock has also been included in the geomechanical grid. This enables obtaining a more realistic estimate for the vertical uplift at the surface.

Figure 6-62 shows two panes that capture the uplift-related impacts of injection. The top pane of displays the total vertical displacement on the surface layer of the geomechanical grid. These data are presented graphically in the bottom pane, which shows that 26.5 million MT of CO_2 injection into the East Bend #1 well causes a maximum of 27 mm of uplift at the surface within a radius of around 3000 ft. around the well, after 30 years of injection. This vertical uplift at the surface decreases radially outward from the injector well, with the widest tract of land experiencing around 23 mm of vertical displacement. Although the predicted amount of uplift at the surface is still considered acceptable (less than 30 mm), the influence of conservative modelling assumptions is worth noting. The combination of the limited extent of the model and high injectivity leads to large pore-pressure increases, which in turn translate to large stress-field perturbations. Secondly, the elastic modulus values assigned to the Mount Simon and Eau Claire are conservative (low), tending to amplify the level of deformation experienced in the subsurface, and consequently communicated through the overburden to the surface. It is likely that the level of vertical uplift experienced at the surface may be lower in practice.

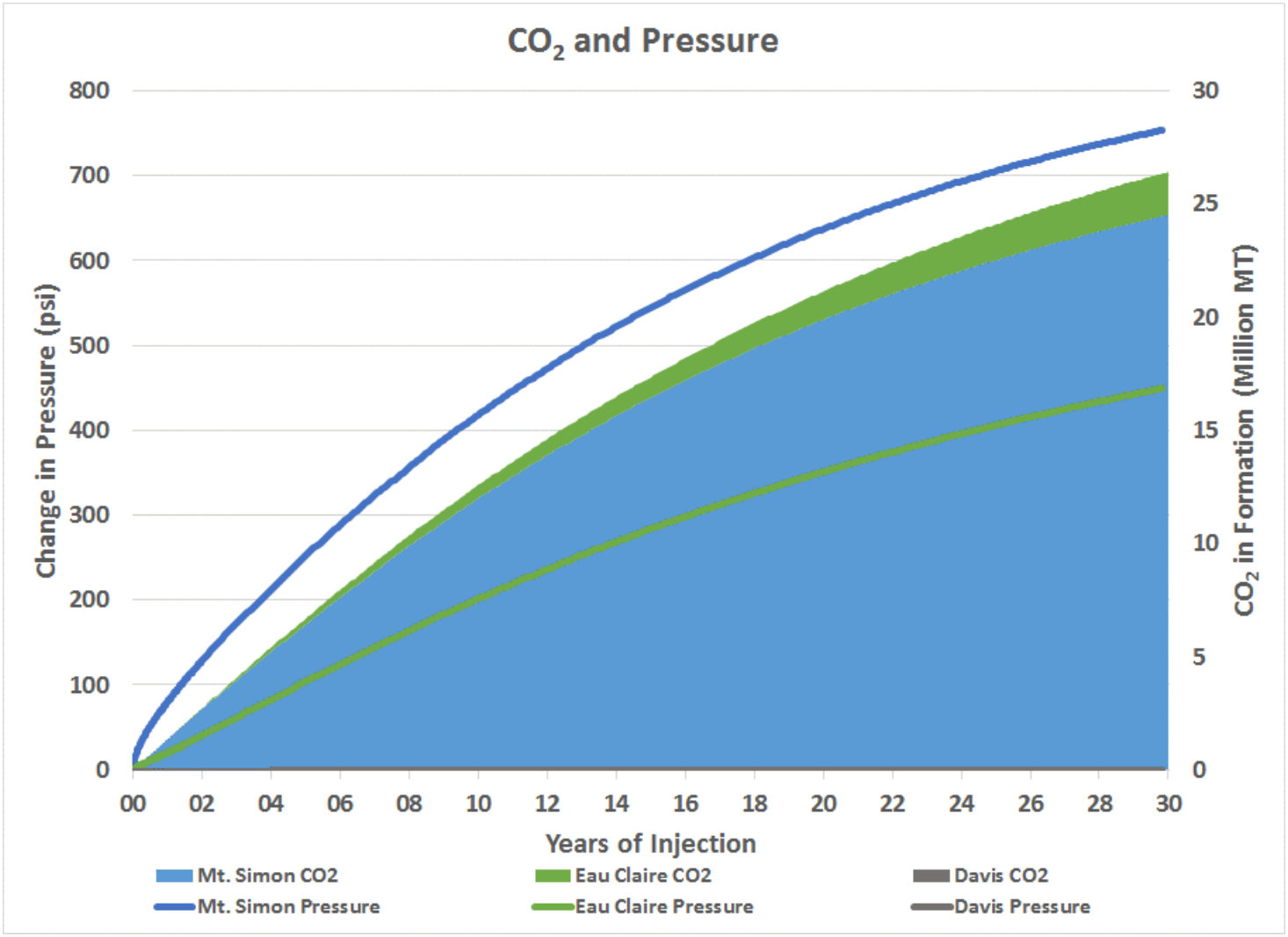

Figure 6-55: 30 years of injection into the East Bend #1 well results in approximately 26.5 million MT of CO_2 storage.

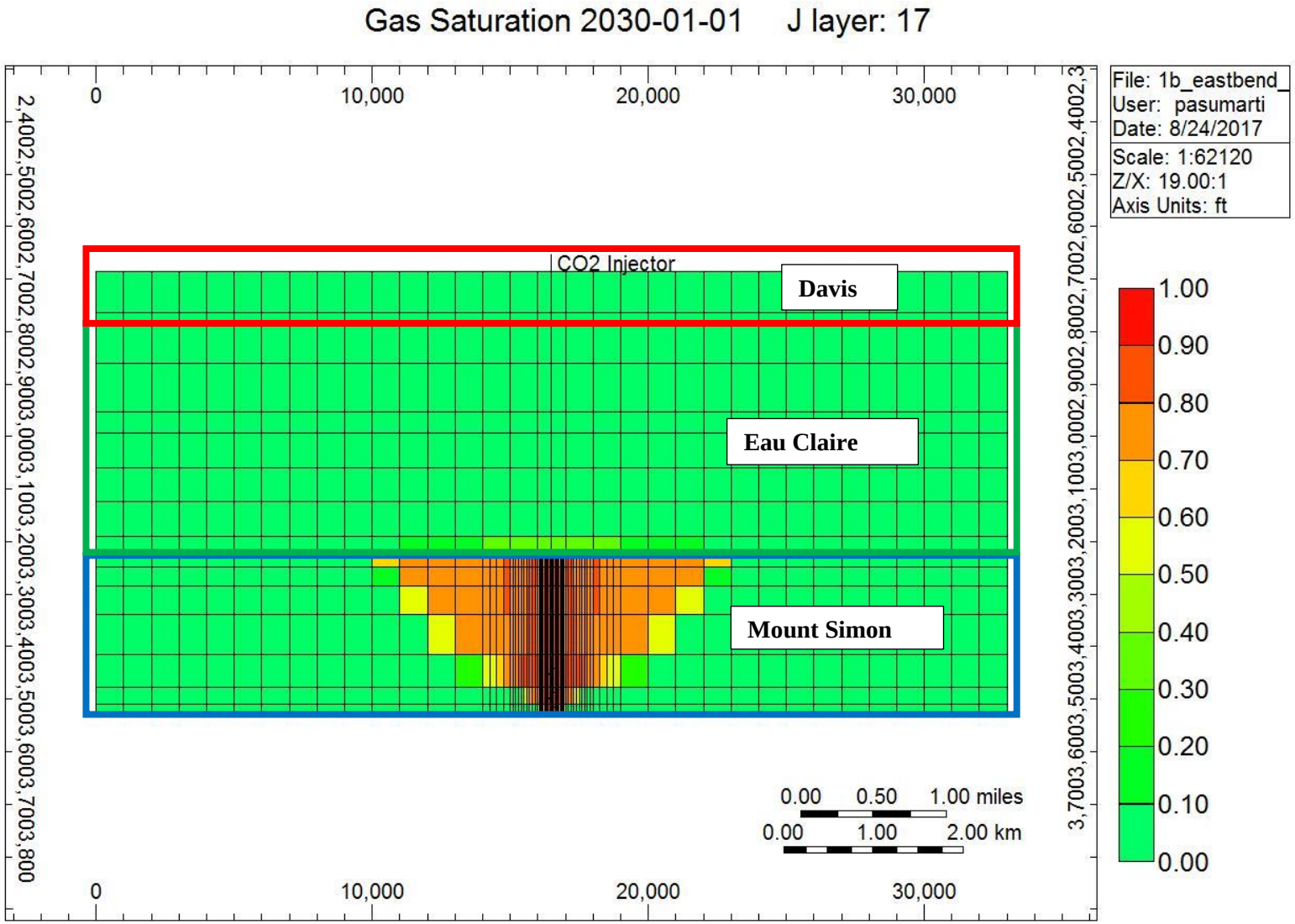

Figure 6-56: The CO_2 saturation distribution attained in the subsurface after 30 years of injection into the East Bend #1 well, is shown via a cross-section through the middle of the fluid-flow grid.

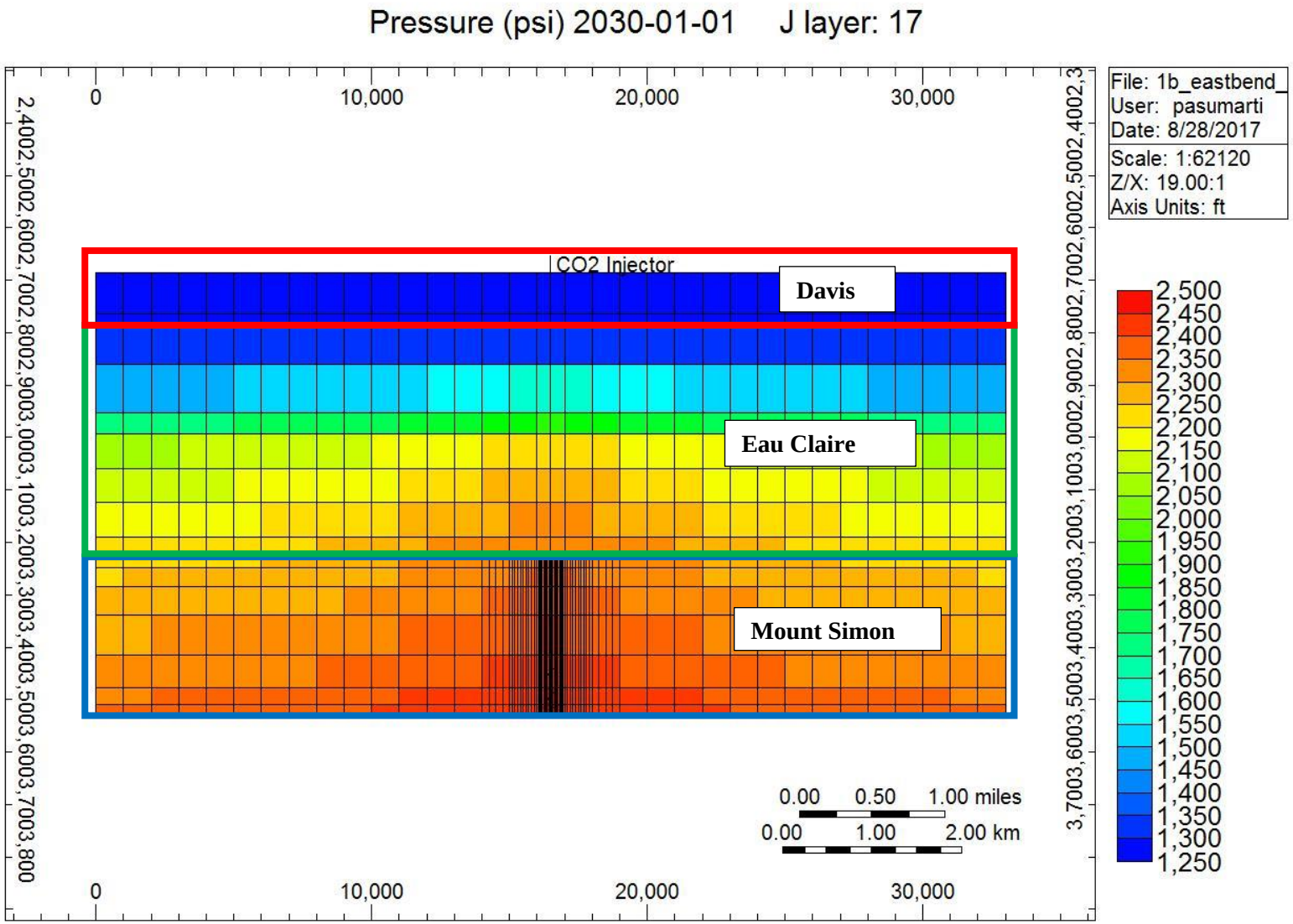

Figure 6-57: The pressures attained in the subsurface after 30 years of injection into the East Bend #1 well, is shown via a cross-section through the middle of the fluid-flow grid.

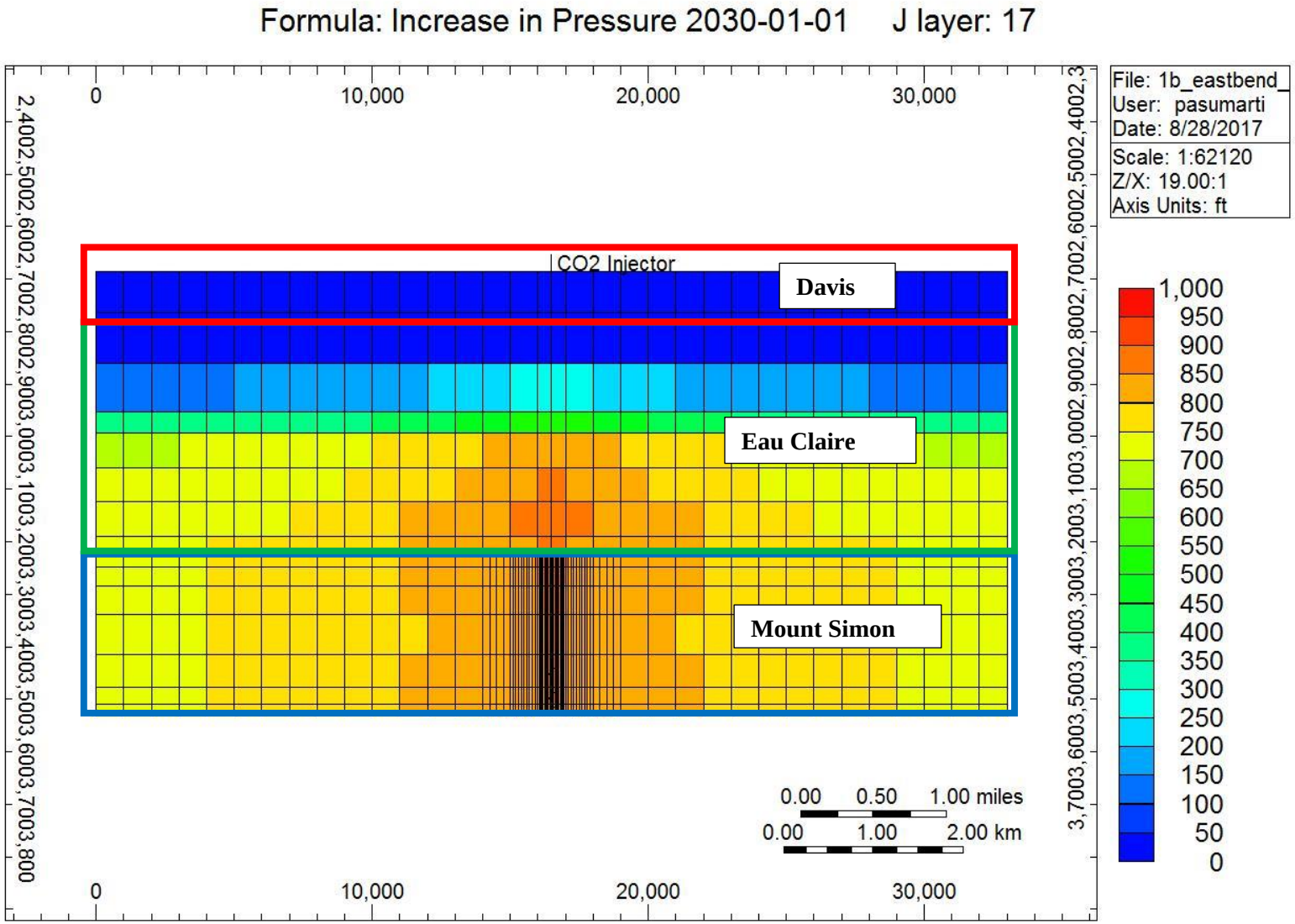

Figure 6-58: The amount of pressure increase in the subsurface after 30 years of injection into the East Bend #1 well, is shown via a cross-section through the middle of the fluid-flow grid.

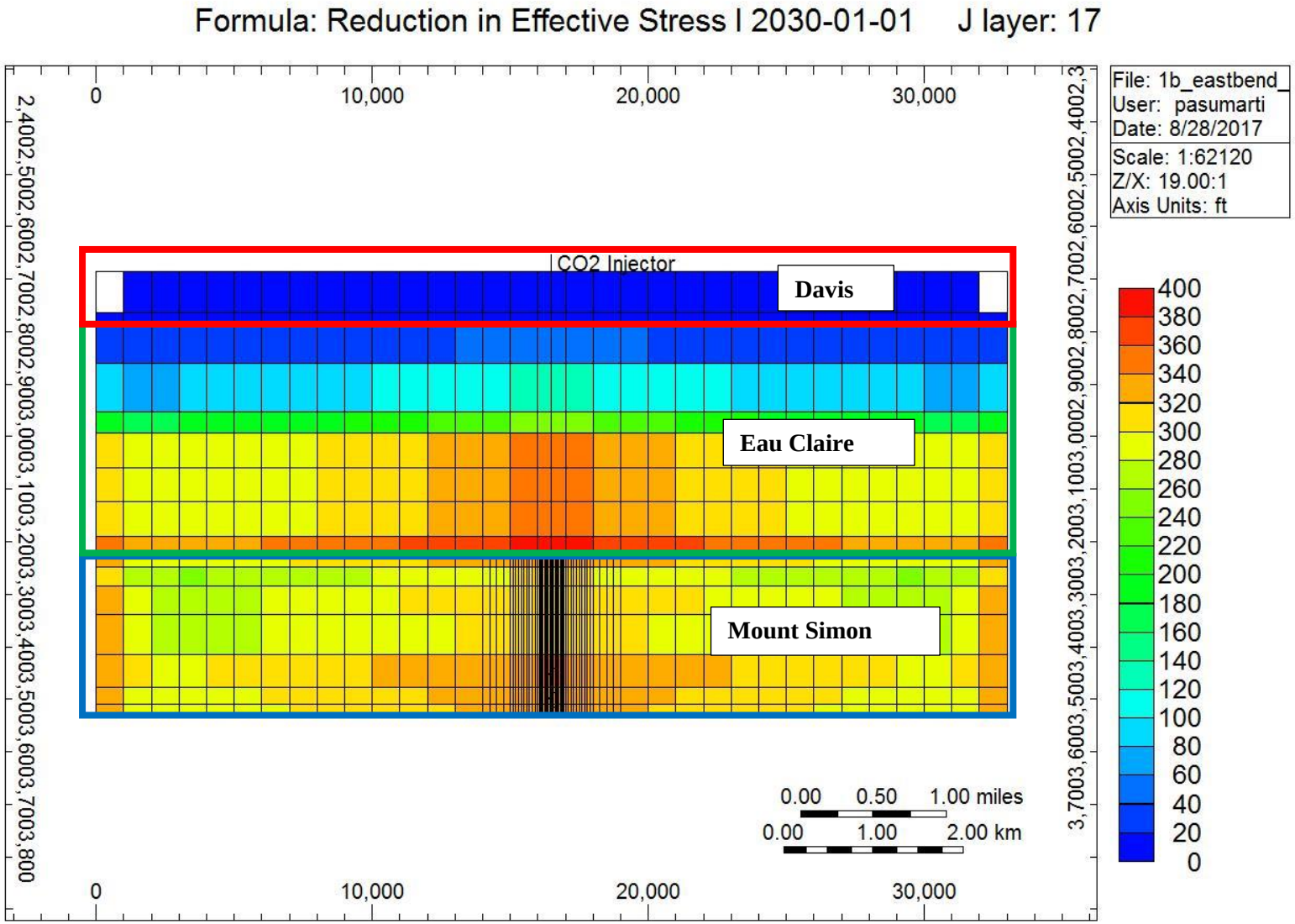

Figure 6-59: The reduction in the minimum horizontal effective stress occurring in the subsurface after 30 years of injection into the East Bend #1 well, is shown via a cross-section through the middle of the fluid-flow grid.

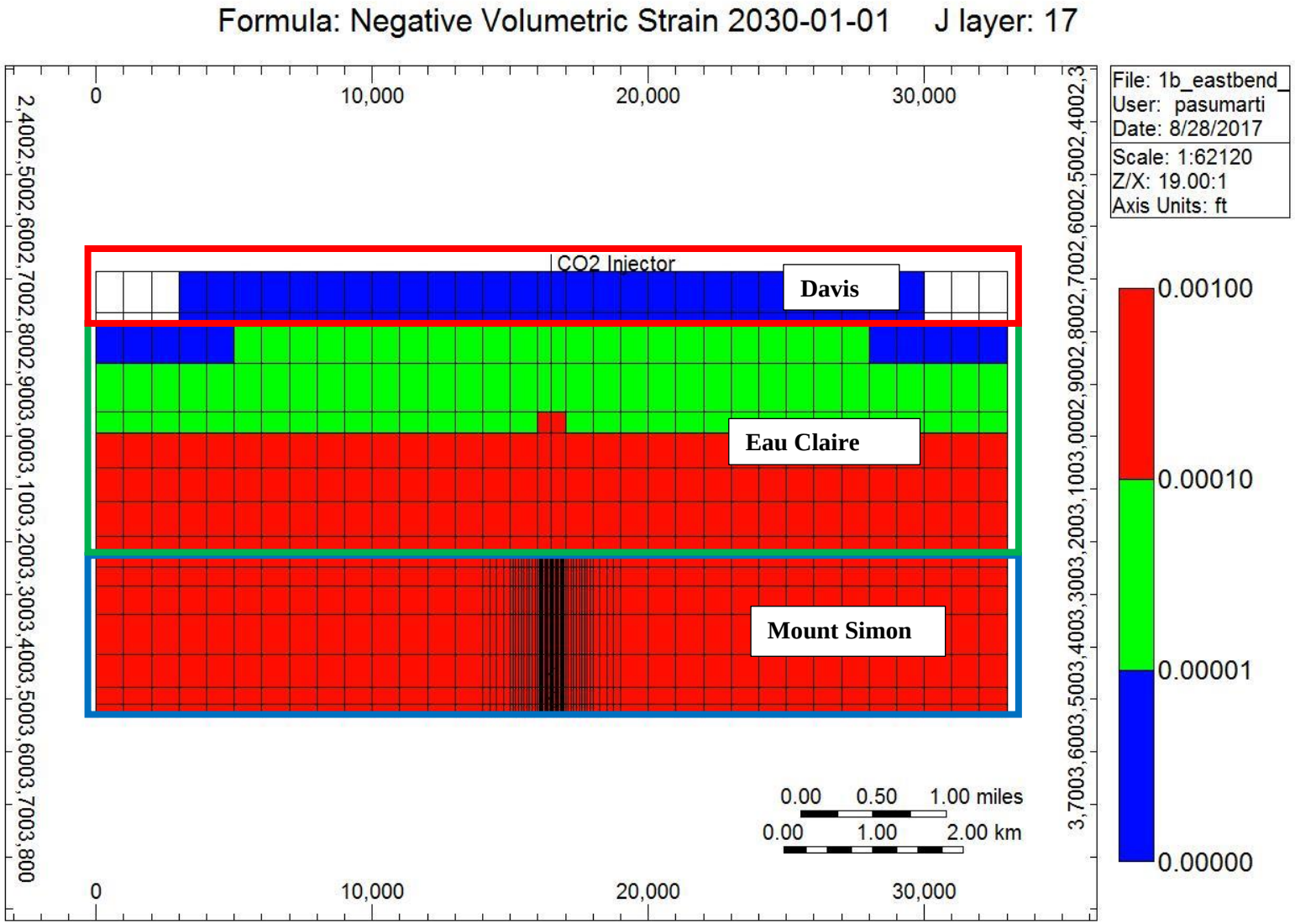

Figure 6-60: The fraction of bulk volume expansion (positive value) within the subsurface after 30 years of injection into the East Bend #1 well, is shown via a cross-section through the middle of the fluid-flow grid.

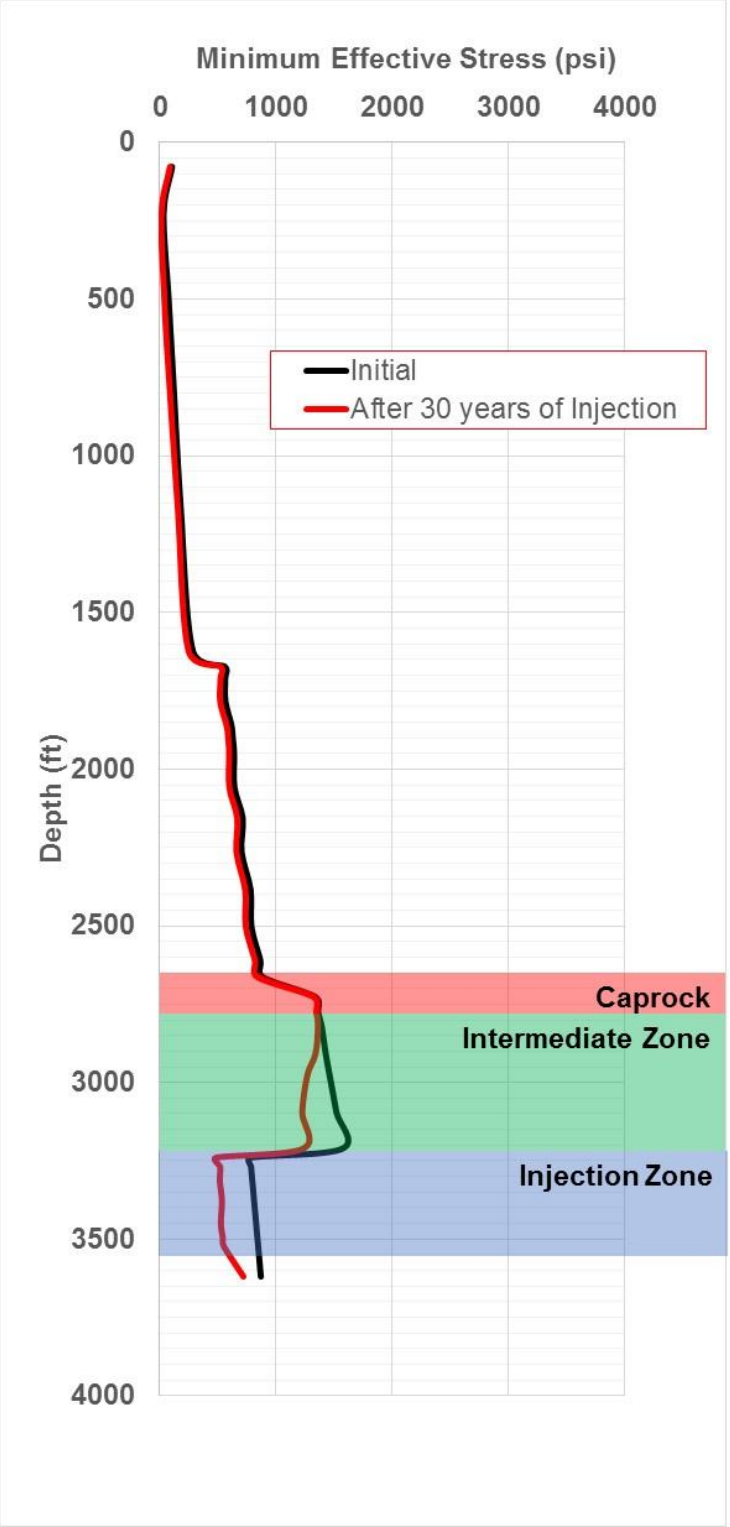

Figure 6-61: A vertical profile (from the surface to the injection zone) of the minimum horizontal effective stress is shown before and after injection into the East Bend #1 well, with the relevant zones highlighted.

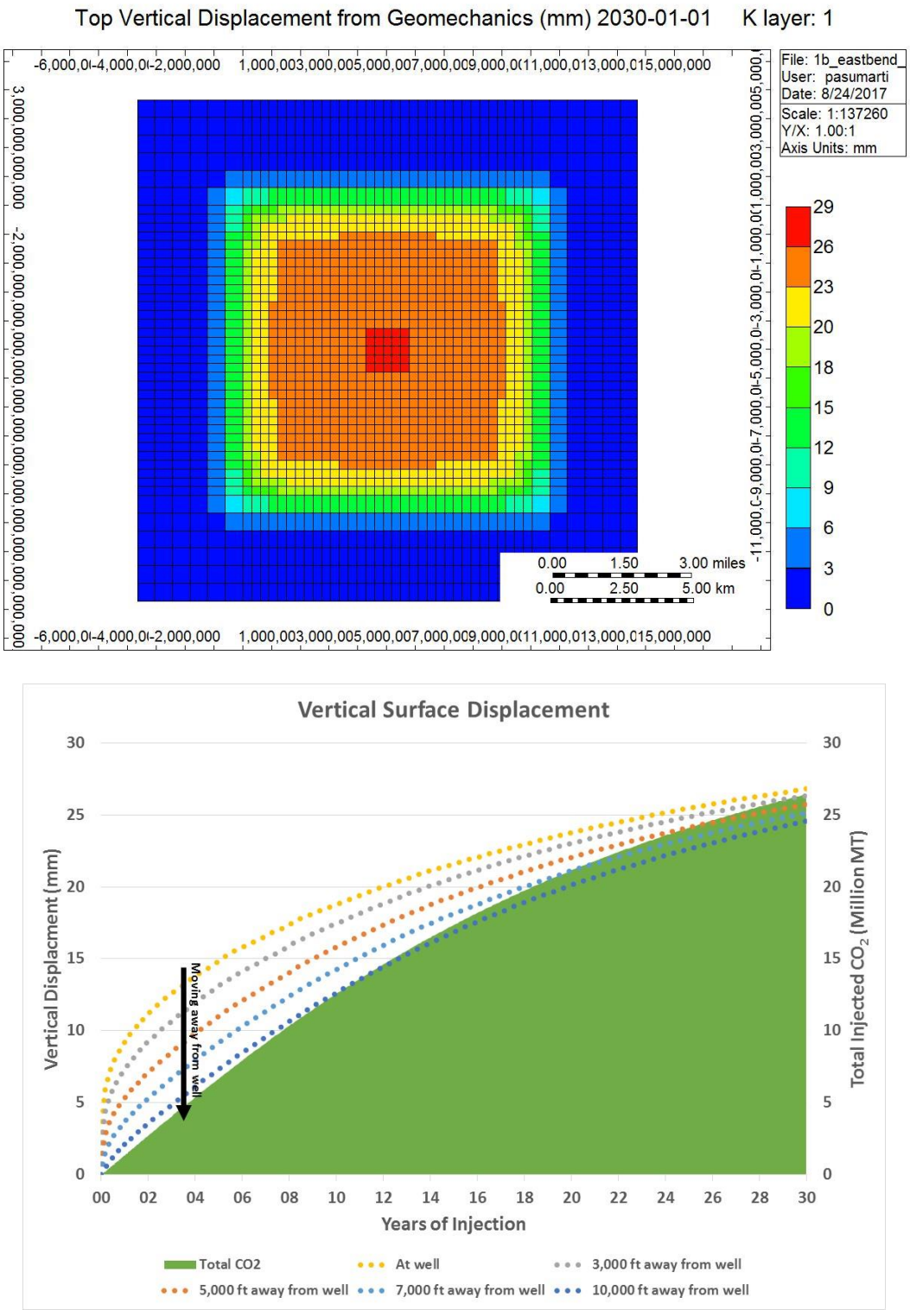

Figure 6-62: A two-paneled graphic summarizing the effects of injection into the East Bend #1 well on areal uplift at the surface is shown.

6.3.3.3 Caprock Integrity Analysis

Figure 6-63 shows that there has been no migration of CO_2 (in either dissolved or supercritical state) into the Davis caprock, and that any impact on the three principal stresses due to injection is minimal (less than 25 psi).

Figure 6-64 shows the three Mohr's circles that have been drawn representing stresses on all planes through the Davis. Although there is no pore pressure increase in the caprock, the external (total) stress has decreased, leading to a very slight – almost indiscernible – reduction in the effectives stresses in the rock and shifting the Mohr's circles to the left. The three black lines represent the linearized Mohr-Coulomb failure envelope lines with varying coefficients of friction. The steepest line represents a value of 1 (least conservative), the middle line 0.8 (moderate), and the gentlest line 0.6 (most conservative). The Davis formation is not known to be heavily fractured, and a value of 1000 psi likely represents a very conservative (low) estimate of cohesion. No tensile failure or shear failure has occurred in the simulated scenario, as the minimum effective stress is well above 250 psi (around 1400 psi) and that largest Mohr's circle is a considerable distance from any of the shear failure envelopes lines.

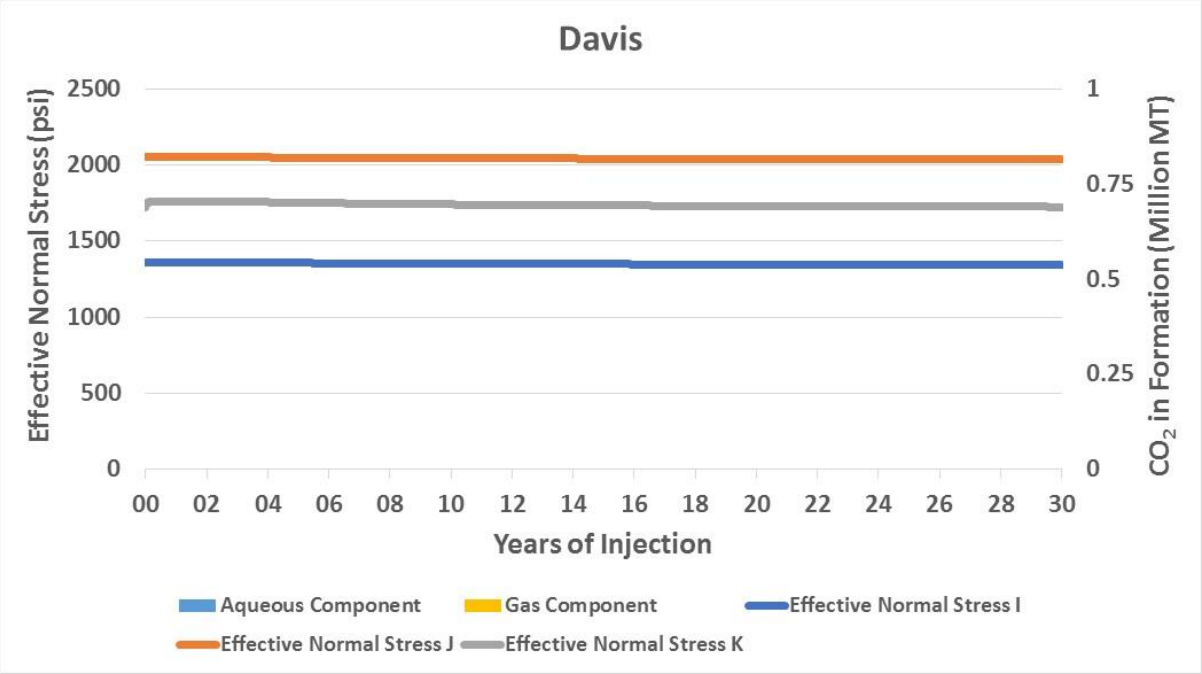

Figure 6-63: Shows that there has been no migration of CO_2 into the Davis caprock, and that any impact on the principal stresses due to injection are minimal.

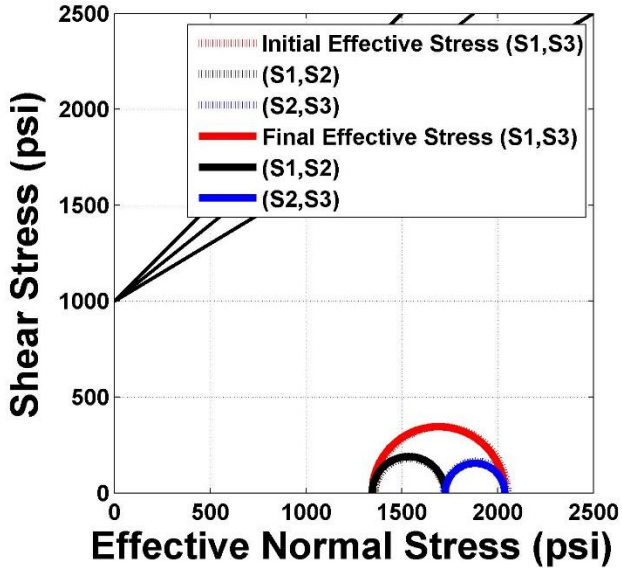

Figure 6-64: Mohr's Circles are drawn to represent the stresses in the Davis caprock, before and after injection.

6.3.3.4 Reservoir and Intermediate Zone Integrity Analysis

The bottom graphic in Figure 6-65 shows that after 30 years of injection resulting in about 24.5 million MT of CO_2 stored in the Mount Simon (injection zone), the effective stress in the vertical direction is more greatly impacted (reduction of around 830 psi) than both the effective stresses in the horizontal direction (reduction of around 310 psi). This phenomenon is due to the poro-elastic effects of injection, where the total (external) stresses rise mainly in the horizontal direction rather than the vertical direction (see Equation 6.3). Only a small volume of the injected CO_2 dissolves into the brine, and most of the CO_2 is contained within the plume.

The top graphic in Figure 6-65 shows that a small quantity of CO_2 of around 2 million MT, has migrated into the lower Eau Claire (intermediate zone). Again, due to the poro-elastic effects of injection, the effective vertical stress has been impacted to a greater extent (reduction of around 840 psi) than both the effective horizontal stresses (reduction of around 380 psi). In fact, after around 20 years of injection, this phenomenon causes a regime change. The faulting regime has changed from being strike-slip ($\sigma_{H,max} > \sigma_v > \sigma_{h,min}$) to reverse ($\sigma_{H,max} > \sigma_{h,min} > \sigma_v$). The minimum stress was originally in the horizontal direction. Due to the poro-elastic effects of injection however, the minimum stress is now in the vertical direction for the lower Eau Claire.

The three Mohr's circles in Figure 6-66 represent stresses on all planes for each formation. As expected during injection, the Mohr's circles have shifted left and enlarged (shrunk) because of poro-elastic effects and the increase in pore pressure. The three black lines represent the linearized Mohr-Coulomb failure envelope lines with varying coefficients of friction. The steepest line represents a value of 1 (least conservative), the middle line 0.8 (moderate), and the gentlest line 0.6 (most conservative). The Mount Simon formation is not known to be heavily fractured, and a value of

1000 psi likely represents a very conservative estimate of cohesion. There is, however, some evidence of sparsely scattered fractures in the Eau Claire, and a cohesion value of 1000 psi represents a more moderate scenario. No tensile failure or shear failure has occurred in either formation as the minimum effective stress is well above 250 psi (around 500 psi in the Mount Simon and 1150 psi in the Eau Claire) and that largest Mohr's circle is a considerable distance from any of the shear failure envelopes lines.

Due to the large pore pressure increases observed, the Mohr's circles of both formations have moved considerably to the left upon injection. The largest Mohr's circle (red) has become enlarged in Eau Claire. Given the regime change to a reverse faulting environment (vertical stress is now the minimum stress) and the fact that effective stress in the vertical direction is impacted more than the horizontal stresses (due to poro-elasticity), further injection will likely shift and enlarge the Mohr's circles of the Eau Claire to a greater degree than in the Mount Simon. However, considering the distance of the failure envelope from the Mohr's circles, it is likely that tensile failure will occur before shear failure (in either formation). Any tensile fractures thus created in the Eau Claire would be horizontal fractures opening against the vertical stress. Note however, given that no shear or tensile failure occurs in spite of the extremely conservative nature of the model – the boundary conditions imposed serve to amplify the pressure increases and effective stress reductions observed – suggests that even such tensile failure would be a highly unlikely scenario in practice.

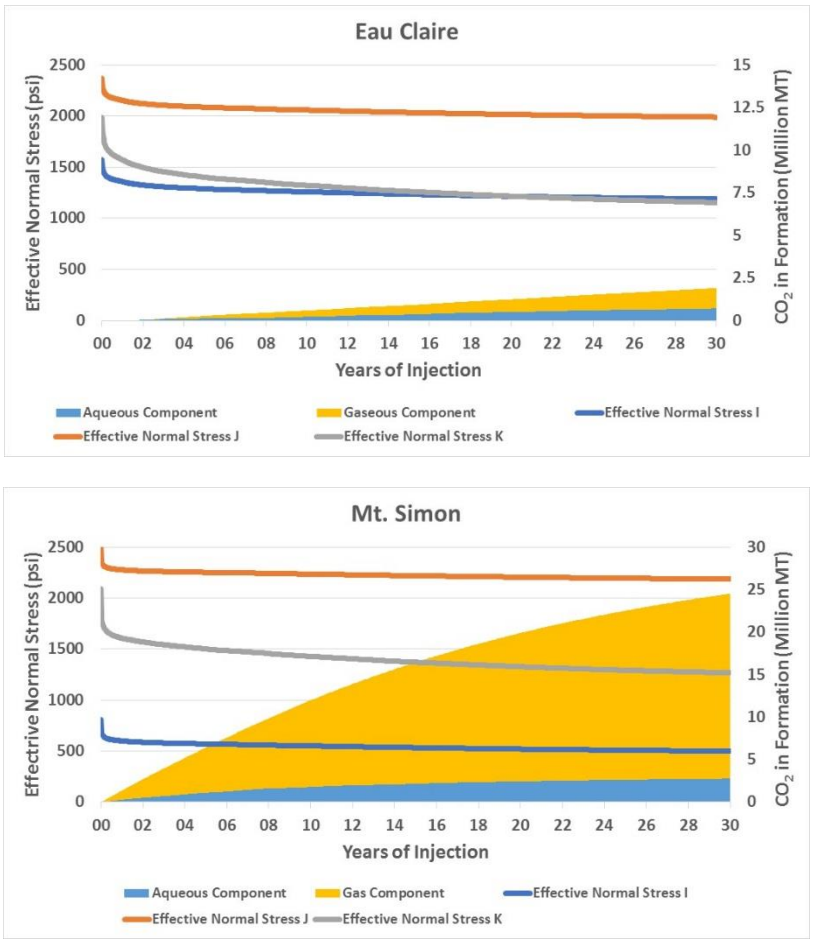

Figure 6-65 (Vertical Panel on the Left): Plots presenting the volume of CO_2 trapped in each formation as well as the impact of CO_2 injection on the principal effective stresses in the Mount Simon (bottom) and Eau Claire (right) are shown.

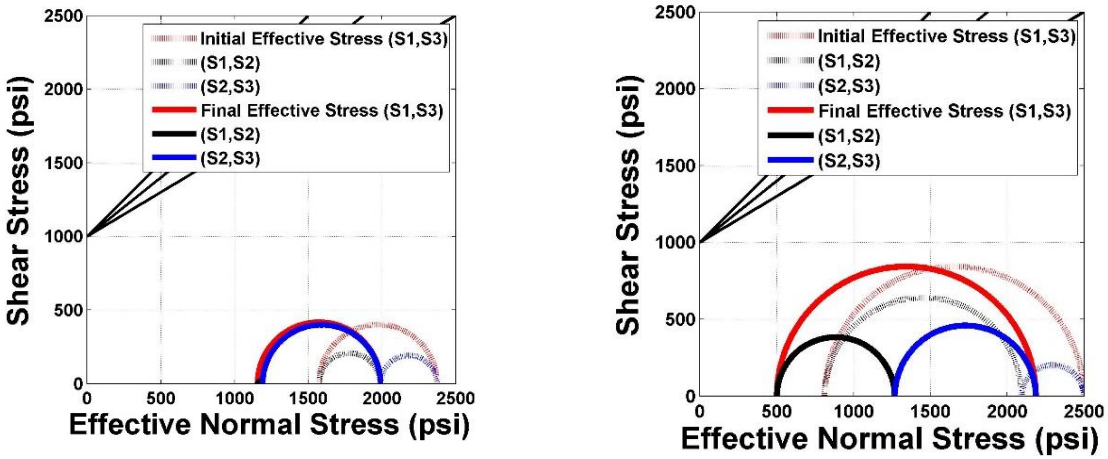

Figure 6-66 (Vertical Panel on the Right): Mohr's Circles drawn to represent the stresses in the Mount Simon (left) and the Eau Claire (right) before and after injection are shown.

6.3.3.4 Sensitivity Analysis: Input Values

Tables 6-11 to 6-13 present the values of key geomechancial parameters, as altered from the base case or Scenario 1. The altered parameters values used in this sensitivity study were still considered to be realistic, and were chosen to remain within the limits of uncertainty observed in the data, while also being geologically consistent (e.g. preserving the faulting regime of the formation). For Scenario 2, the minimum horizontal stress gradient has been increased while the maximum horizontal stress has been reduced, having the effect of shrinking the Mohr's circles (shear and normal stresses) in the formations. For Scenario 3, the static Young's modulus has been increased by around 20%, tending to reduce the amount of vertical uplift observed at the surface. For Scenario 4, the Biot's coefficient has been decreased to 0.8, which has the effect of reducing the amount of perturbation of the stress-strain field caused by pore-pressure rise. For Scenario 5, in addition to using the using the same values as Scenario 4, the pore-volumes of the grid-blocks at all four boundaries have been increased through the use of pore-volume modifiers, reflecting the continuity of the formation beyond an area of 25,000 Acres around the well.

Table 6-11: Values of key geomechanical parameters for Scenario 2 (East Bend #1 well). Values for the horizontal stresses in the base case (Scenario 1) are included in parentheses for reference.

Formation	σ_H gradient / psi/ft	σ_h gradient / psi/ft
Lower Mount Simon	1.1 (1.2)	0.75 (0.7)
Upper Mount Simon	1.1 (1.2)	0.75 (0.7)
Lower Eau Claire	1.1 (1.2)	1 (0.95)
Upper Eau Claire	1.1 (1.2)	1 (0.95)
Davis	1.1 (1.2)	1 (0.95)

Table 6-12: Values of key geomechanical parameters for Scenario 3 (the East Bend #1 well). Values for the Young's modulus in the base case (Scenario 1) are included in parentheses for reference.

Formation	σ_H gradient / psi/ft	σ_h gradient / psi/ft	Static Young's modulus / psi
Lower Mount Simon	1.1 (1.2)	0.75 (0.7)	4.86E+06 (4.05E+06)
Upper Mount Simon	1.1 (1.2)	0.75 (0.7)	5.98E+06 (4.99E+06)
Lower Eau Claire	1.1 (1.2)	1 (0.95)	4.78E+06 (3.98E+06)
Upper Eau Claire	1.1 (1.2)	1 (0.95)	4.78E+06 (3.98E+06)
Davis	1.1 (1.2)	1 (0.95)	4.48E+06 (3.73E+06)

Table 6-13: Values of key geomechanical parameters for Scenario 3 (the East Bend #1 well). Values of the Biot's coefficient in the base case (Scenario 1) are included in parentheses for reference.

Formation	Biot's coefficient / psi/ft	σ_H gradient / psi/ft	σ_h gradient / psi/ft	Static Young's modulus / psi
Lower Mount Simon	0.8 (1)	1.1 (1.2)	0.75 (0.7)	4.86E+06 (4.05E+06)
Upper Mount Simon	0.8 (1)	1.1 (1.2)	0.75 (0.7)	5.98E+06 (4.99E+06)
Lower Eau Claire	0.8 (1)	1.1 (1.2)	1 (0.95)	4.78E+06 (3.98E+06)
Upper Eau Claire	0.8 (1)	1.1 (1.2)	1 (0.95)	4.78E+06 (3.98E+06)
Davis	0.8 (1)	1.1 (1.2)	1 (0.95)	4.48E+06 (3.73E+06)

6.3.3.5 Sensitivity Analysis: Results

Tables 6-14 to 6-16 present key outputs based on the coupled fluid-flow and reservoir geomechanics simulations of the five sensitivity scenarios. Tables 6-14 and 6-15 summarize results for the Mount Simon and Eau Claire respectively. The risks of rock failure are assessed by examining the Mohr's circles depicting the shear and normal stresses in the formation after injection, for distance from the failure envelope (shear failure), and from the origin (tensile failure risk when the minimum effective stress is less than 250 psi). Given that stresses are affected more in the vertical direction than the horizontal, a stress-regime change may occur if the reduction of stresses in the vertical direction is drastic enough. Instead of the average reservoir pressure, the maximum increase in pore-pressure is listed (close to the wellbore). The magnitude of the reduction in effective stress is listed for all three directions. A comparison of these quantities against the maximum pore-pressure increase suggests the level of poro-elastic effects in the formation. Table 6-16 summarizes more regional-scale outputs. Stresses in the geomechanical grid (rocks from the basement to the surface) were examined to confirm that stress changes occurred below the Davis formation (see Figure 6-61). The widest radius of the CO_2 plume, and the furthest extent to which the pore-pressures had risen by more than 300 psi was noted. The areal uplift experienced at the surface at increasingly further distances from the wellbore are listed (see Figure 6-62). The quantity of CO_2 storage achieved at the site is broken down into that stored in the injection zone and that migrating upward into the intermediate zone.

The stress-gradient changes imposed in Scenario 2 did not result in any significant effects. Note the minimal discrepancy between the increase in pore-pressures and the vertical effective stress reduction, suggesting minimal poro-elastic effects in this direction. A comparison of Scenario 2 and 3 however suggests that a 20% increase in the stiffness of the rocks, has the effect of reducing the areal uplift at the surface by around 15% (from around 25 mm to 21 mm). This also results in only marginally greater pressurization in the injected and intermediate zones (~30 psi). However, it is sufficient to throttle the injection rate enough to reduce the effective storage capacity by around 10%

(from 26.5 million tons to 23.9). A comparison of Scenario 3 and 4 reveals that the impact of reducing the Biot's coefficient by 20% (from 1 to 0.8) translates one-to-one onto the effective stresses (also reduced by 20% as expected according to Equation 6.3), and onto the areal uplift experienced at the surface (from around 21 mm to 17 mm).

Scenario 5 however suggests that the formation extent is the most important factor influencing the level of pressurization and consequently the magnitude of stress-field perturbations. This is unsurprising given the high permeability values of the Mount Simon that translate into the pressure pulse reaching the boundaries quicker. In the most optimistic scenario of the Mount Simon extending well beyond 25,000 Acres around the well without encountering any major faults or sharp permeability changes, more than twice as much CO_2 may be stored (from 24 million tons to 51) with around 30% lesser pressurization (850 psi to around 590 psi) and as much as 40% lesser effective stress reduction (from 685 psi to 415 psi). A much greater formation extent strongly impacts the vertical displacement at the surface. Where the deformation occurred nearly uniformly in the spatially-limited model (~5% reduction away from the wellbore from 17.9 mm to 16.9 mm), in Scenario 5 however, not only was the amount of areal uplift much lower (from 17.9 mm to 9.4 mm over a radius of 3000 ft. from the well), it was also more localized (~50% reduction away from the wellbore from 9.4 mm to 4.7 mm). Note also, that a stress-regime change in the Eau Claire does not occur in this scenario. Within the bandwidth of uncertainty considered in this analysis (outside of the most optimistic scenario), the effective storage capacity achieved by this well may vary between 24 to 26.5 million tons, causing between 18 to 26 mm of uplift at the surface.

6.3.3.6 Summary and Recommendations

Table 6-17 summarizes the main conclusions and recommendations for the East Bend #1 well. In general, the simulations did not indicate tensile failure or shear failure/activation of existing fractures. The models suggested 17-26 mm of uplift over a broad area. Simulations were sensitive to model boundary conditions, but a 30-year effective capacity of this well may be higher than 26.5 million MT (up to 51 million MT). A leak-off test and core studies to constrain the stress-magnitudes in the Eau Claire would reduce uncertainty in the model.

Table 6-14: Key outputs from the simulations of each sensitivity scenario, for the injection zone (Mount Simon) are listed.

Scenario #	Injection Zone						
	Shear failure?	**Tensile failure?**	**Stress-regime change?**	**Maximum pore-pressure increas (psi)**	**Magnitude of effective stress reduction in I direction (psi)**	**Magnitude of effective stress reduction in J direction (psi)**	**Magnitude of effective stress reduction in K direction (psi)**
1. Base Case	No.	No.	No.	850	335	335	830
2.	No.	No.	No.	850	335	335	830
3.	No.	No.	No.	860	345	345	850
4.	No.	No.	No.	850	280	280	675
5. Most Optimistic	No.	No.	No.	590	190	190	430

Table 6-15: Key outputs from the simulations of each sensitivity scenario, for the intermediate zone (Eau Claire) are listed.

Scenario #	Intermediate Zone						
	Shear failure?	**Tensile failure?**	**Stress-regime change?**	**Maximum pore-pressure increase (psi)**	**Magnitude of effective stress reduction in I direction (psi)**	**Magnitude of effective stress reduction in J direction (psi)**	**Magnitude of effective stress reduction in K direction (psi)**
1. Base Case	No.	No.	Yes	860	385	385	830
2.	No.	No.	Yes	860	385	385	830
3.	No.	No.	Yes	875	400	400	860
4.	No.	No.	Yes	875	315	315	685
5. Most Optimistic	No.	No.	No.	590	206	206	415

Table 6-16: Key regional-scale outputs from the simulations of each sensitivity scenario are listed.

Scenario #	Spatial Extent of Impact			Areal Uplift at Surface				Effective Storage Capacity		
	Stress-strain perturbations isolated below caprock?	**Maximum plume extent ft**	**Pore-pressure increase (>300 psi) extent ft**	**3000 ft mm**	**5000 ft mm**	**7000 ft mm**	**10,000 ft mm**	**Injection Zone**	**Intermediate Zone**	**Total**
1. Base Case	Yes	5000	16,500 (entire model)	26.3	25.7	25.1	24.6	24.5	2.0	**26.5**
2.	Yes	5000	16,500 (entire model)	26.3	25.7	25.1	24.6	24.5	2.0	**26.5**
3.	Yes	5000	16,500 (entire model)	22.5	22	21.6	21.2	22.1	1.7	**23.9**
4.	Yes	5000	16,500 (entire model)	17.9	17.6	17.2	16.9	22.3	1.7	**24.0**
5. Most Optimistic	Yes	8000	8000	9.4	8.3	6.9	4.7	48.4	2.6	**51.0**

Table 6-17: Summary of the main conclusions of the simulation study for the East Bend #1 well and relevant recommendations.

Objective	Conclusions
Evaluate Caprock's geomechanical integrity: Tensile Failure	The minimum effective stress is nearly unchanged at around 1400 psi. **No tensile failure in the Davis Formation.**
Evaluate Caprock's geomechanical integrity: Shear Failure	Negligible movement of the Mohr's Circles. **No shear failure or fracture activation in the Davis Formation.**
Evaluate injection & intermediate zones' geomechanical integrity: Tensile Failure	The minimum effective stress in the Mount Simon is around 500 psi. The minimum effective stress in the Eau Claire is around 1150 psi. **No tensile failure in the Mount Simon or Eau Claire.**
Evaluate injection and intermediate zones' geomechanical integrity: Shear Failure	Mount Simon: Large pore-pressure increase between 800 to 850 psi. Largest Mohr's Circle shifted considerably left, but did not enlarge. **No shear failure or fracture activation in the Mount Simon.** Eau Claire: Pore-pressure and stress-changes are significant mainly in the lower Eau Claire. Large pore-pressure increase between 800 to 850 psi. Faulting regime change from strike-slip to reverse. Largest Mohr's Circle shifted considerably left, and became slightly larger. **No shear failure or fracture activation in the Eau Claire.**
Evaluate areal uplift at the surface	**Between 17-26 mm of areal uplift at the surface may be expected over an area of 25,000 Acres.**
Demonstrate the isolation of stress-strain perturbations within the subsurface	Reduction of effective stresses and volumetric strains are significant only up to the lower Eau Claire. **No significant perturbation in the stress-strain field, in any layer above the caprock.**
Demonstrate CO_2 plume migration and the effectiveness of caprock.	CO_2 plume extends to around 5000 ft from the injector, and only penetrates as far upward as the lower Eau Claire. 1 million MT of CO_2 migrated into the lower Eau Claire **No CO_2 or pressure increase detected in the Davis Formation.**
Quantify the effective CO_2 storage capacity of the well	Simulation results are reflective of conservative boundary conditions. Around 22 - 24.5 million MT of CO_2 stored in the Mount Simon. Around 2 million MT of CO_2 migrated outside of the injection zone into the lower Eau Claire. No risks of geomechanical failure in reservoir, intermediate zone or caprock during injection. **Conservative estimate of the effective CO_2 capacity after 30 years of injection: 24 - 26.5 million MT**
Recommendations	For the Mount Simon, a closed site model with a lateral extent of 17,000ft. likely represents a highly conservative scenario leading to rapid pore-pressure increase. Despite this assumption however, no geomechanical risks were observed. Limited well-site characterization data of the Mount Simon and Eau Claire forces conservative assumptions when modelling geomechanical risks. **In practice, the 30-year effective capacity of this well is likely to be much higher than 26.5 million MT (up to 51 million MT). A leak-off test and core studies to constrain the stress-magnitudes in the Eau Claire would reduce uncertainty in the model.**

6.3.4 E-Central Appalachian Basin Site

6.3.4.1 Model Summary

A summary of key inputs to the model is shown in Table 6-18. Note that with the exception of stress gradients, all other data have been obtained primarily from well-log analysis. Formations in blue are in the injection zone, green are in the intermediate zone and red are in the caprock zone. Layers within each formation may be of varying thickness. The permeability values listed represent the average across the number of layers present. Although not listed below, around 200 ft of basement rock has also been modelled in the geomechanical grid. It has been assumed to have the same properties as the Lower Maryville in the absence of characterization data.

Table 6-18: Key site-specific data inputs for coupled fluid-flow – geomechanics simulation for the OGS CO_2 #1 well.

Formation	Average Depth (ft)	Thickness (ft)	No. of Layers	Average Porosity	Average Permeability (md)	σ_v gradient (psi/ft)	σ_H gradient (psi/ft)	σ_h gradient (psi/ft)	Static Young's modulus[b] (psi)	Poisson's ratio	Average Initial Pressure (psi)
L. Maryville	8424	195	2	1.3%	0.002	1.15	1	0.65	1.11E+07	0.27	3875
U. Maryville	8115	334	4	1.3%	7.0	1.15	1	0.65	1.15E+07	0.29	3727
Nolichucky	7948	95	1	1.0%	3.3	1.15	1.3	0.74	1.16E+07	0.28	3656
L. Copper Ridge	7782	205	5	4.0%	1.8	1.15	1.45	0.8	1.08E+07	0.29	3578
Copper Ridge B	7664	63	1	3.0%	0.01	1.15	1.45	0.8	1.05E+07	0.27	3525
U. Copper Ridge	7570	119	2	2.3%	0.31	1.15	1.45	0.8	1.09E+07	0.26	3481
Rose Run	7446	137	5	4.0%	0.29	1.15	0.9	0.6	8.49E+06	0.24	3425
Beekmantown	7297	146	4	5.3%	2.1	1.15	1.6	0.8	9.18E+06	0.27	3356
Wells Creek	7209	43	1	5.5%	0.01	1.15	1.4	0.8	7.74E+06	0.28	3316
Lower Chazy	7174	27	1	1.4%	0.009	1.15	1.4	0.8	7.40E+06	0.30	3300
Gull River	7135	51	1	0.4%	0.06	1.15	1.4	0.8	8.55E+06	0.30	3282
Upper Chazy	7073	73	1	0.8%	0.001	1.15	1.4	0.8	7.37E+06	0.31	3254
Black River	6846	405	3	1.0%	1.1	1.15	1.65	0.8	7.83E+06	0.30	3149

a. Comprehensive regional study combining mini-frac test data, core analysis, log-analysis and stress-polygon diagram analysis (Battelle, 2017).
b. Log-based dynamic Young's modulus corrected using the correlation shown in Figure 4-12.

6.3.4.2 Simulation Results

Figure 6-67 shows the pressure increase and the volumes stored in each formation after 30 years of injection. Almost all of the injected volume (10.25 million tons) stays within the target formations (Upper Maryville to Upper Copper Ridge), with only around 0.25 million tons of CO_2 migrating into the intermediate layers. The reservoir pressure in the injection zones and the intermediate layers rises very moderately, to only between 60 and 90 psi. The slope of the cumulative stored CO_2 plot suggests the rate of injection. The constant rate of injection, moderate pressure increases and minimal upward migration of the CO_2 plume suggests that boundary effects are not very significant and that there is scope for further injection of CO_2 in this well.

Figure 6-68 to Figure 6-72 present more simulation results via cross-sections through the fluid-flow grid. The relevant formations are highlighted. Figure 6-68 shows that CO_2 injected into the formations between Maryville and the Upper Copper Ridge forms a plume of a maximum radius of approximately 5000 ft around the wellbore. Most of the CO_2 plume (and storage) occurs in the Lower Copper Ridge. There is a small but significant amount of CO_2 migration into the intermediate zone. None penetrates the caprock.

Figure 6-69 shows that the pressure front (gridblocks of the same color) appears conical reflecting the fact that pressures increase with depth, and that the pressure perturbations decay with radial distance from the plume. Figure 6-70 shows that the pressure perturbation extends much further than the plume front (see Figure 6-68) although it does not reach the boundaries of the model (pressure increase at model extent is less than 100 psi). Figure 6-69 and Figure 6-70 show that the formations in the injection zone are is not uniformly pressured throughout and are still in a somewhat transient state. The pressure is not uniform across the injection zone as observed for the Mount Simon, due to the much lower permeability of the injection zone (maximum of 61 md in Mount Simon vs a maximum of 7 md in the Maryville) and the greater vertical heterogeneity distorting the lateral advance of the pressure front. The pressurization as a result is far more localized (as opposed to regional) in extent. The highest pressures are observed around the wellbore region in Maryville of around 4500 psi. The pore-pressure has increased between 750 psi (in the immediate vicinity of the well) to around 450 psi within a 5000 ft. radius around the wellbore in the injection zone and – because of CO_2 migration – in the intermediate zone as well. The pore-pressure in the caprock does not increase significantly (less than 100 psi).

Figure 6-71 shows that the reduction in the minimum effective stress (I-direction) is greatest around the vicinity of the plume. The effective stress reduction is greatest inside the CO_2 plume. There is a reduction of around 300 psi within a radius of around 3000 ft. around the wellbore in both the injection and – because of CO_2 migration – intermediate zones. This impact, however, may be considered to be only fairly modest. This stress-perturbation is not as significant (at least 250 psi) beyond this distance, and does not extend as far into the individual formations as the pressure front (see Figure 6-70). This stress perturbation appears to take on a cylindrical front decaying radially outward from the well, reflective of the transient nature of the pore-pressure impulse in the reservoir. The discrepancy between the pore-pressure increases and the reduction in effective stress is just as large as that observed for the East Bend site, suggesting that poro-elastic effects, are just as strong in these formations. Mirroring the negligible impact on its pore-pressures, the caprock experiences only a very marginal impact on its stress-field (less than 50 psi).

Figure 6-72 shows that the volumetric expansion is greatest is greatest inside the CO_2 plume, and reflects the localized effect of the pore-pressure impulse around the wellbore, and within the injection and intermediate zones. The volumetric strain within the caprock is an order of magnitude (around 1e-6) smaller than that experienced within the injection zone (3.5e-5) and intermediate zone (5e-5).

Figure 6-73 shows that the stress-perturbations induced as a result of injection have been generally contained beneath the caprock layers. Note that the vertical profile extends below the injection zone, reflecting the fact that the part of the basement rock has also been included in the geomechanical grid. This enables obtaining a more realistic estimate for the vertical uplift at the surface.

Figure 6-74 shows two panes that capture the uplift-related impacts of injection. The top pane of displays the total vertical displacement on the surface layer of the geomechanical grid. The data are presented graphically in the bottom image, which shows that the 10.25 million MT of CO_2 injection into the OGS CO_2 #1 well causes a maximum of 5 mm of uplift at the surface within a radius of around 3000 ft. around the well, after 30 years of injection. This vertical uplift at the surface decreases radially outward from the injector well, with the widest tract of land experiencing around 2.5 mm of vertical displacement. Note that the vertical uplift predicted for this well is much smaller than that observed for the East Bend #1 well. This may be attributable to a combination of factors including: the East Bend site has a smaller overburden (around 2800 ft. vs 7000 ft.), the Mount Simon has a smaller Young's modulus than the formations encountered in the OGS CO_2 #1 well (around 4.5e+6 psi vs 1.08e+7 psi), and that the East Bend site experiences a greater level of pore-pressure increase (around 850 psi vs 450 psi).

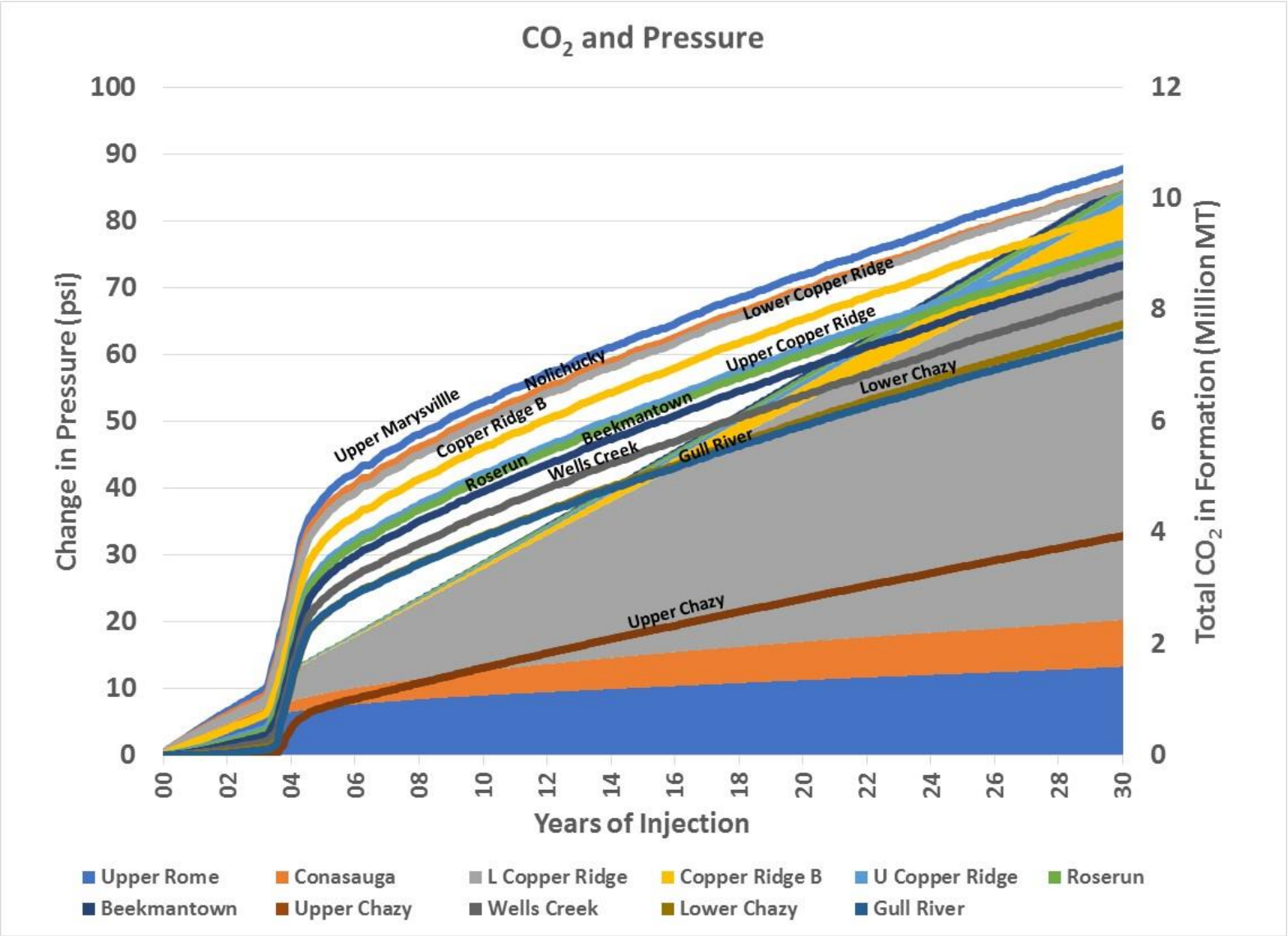

Figure 6-67: 30 years of injection into the OGS CO_2 #1 well results in approximately 10 million MT of CO_2 storage.

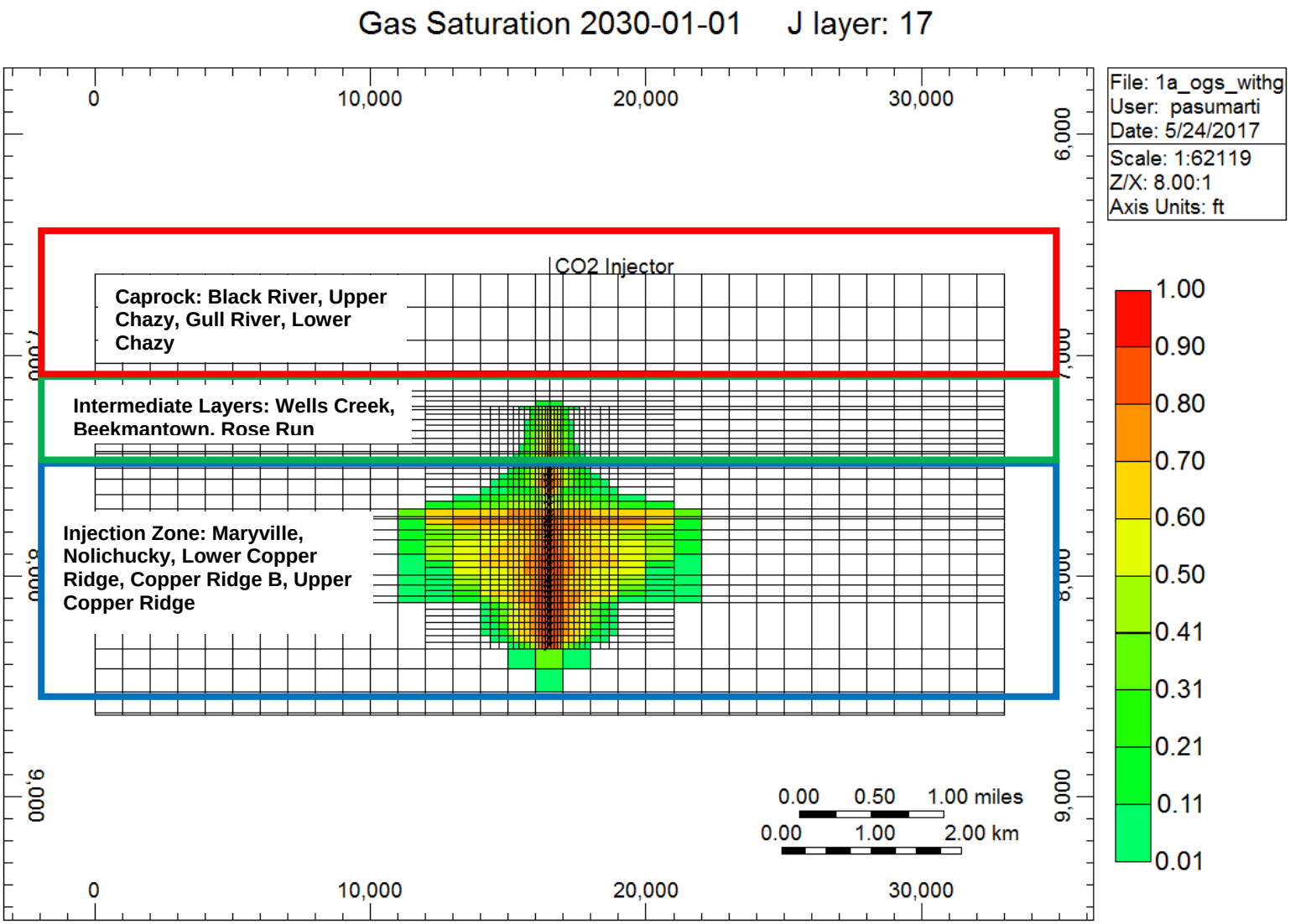

Figure 6-68: The CO_2 saturation distribution in the subsurface after 30 years of injection into the OGS CO_2 #1 well, is shown via a cross-section through the middle of the fluid-flow grid.

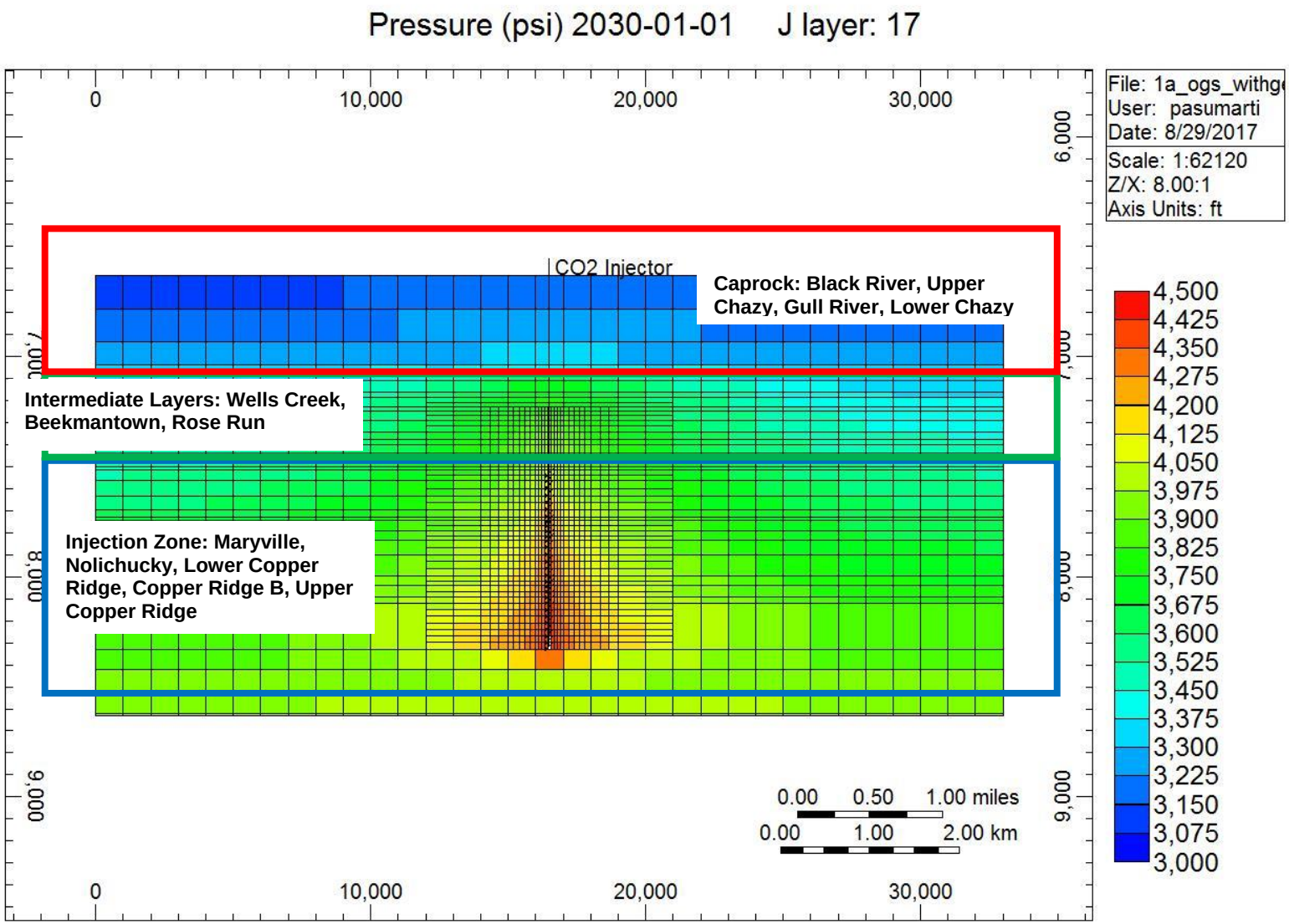

Figure 6-69: The pressures attained in the subsurface after 30 years of injection into the OGS CO_2 #1 well, is shown via a cross-section through the middle of the fluid-flow grid.

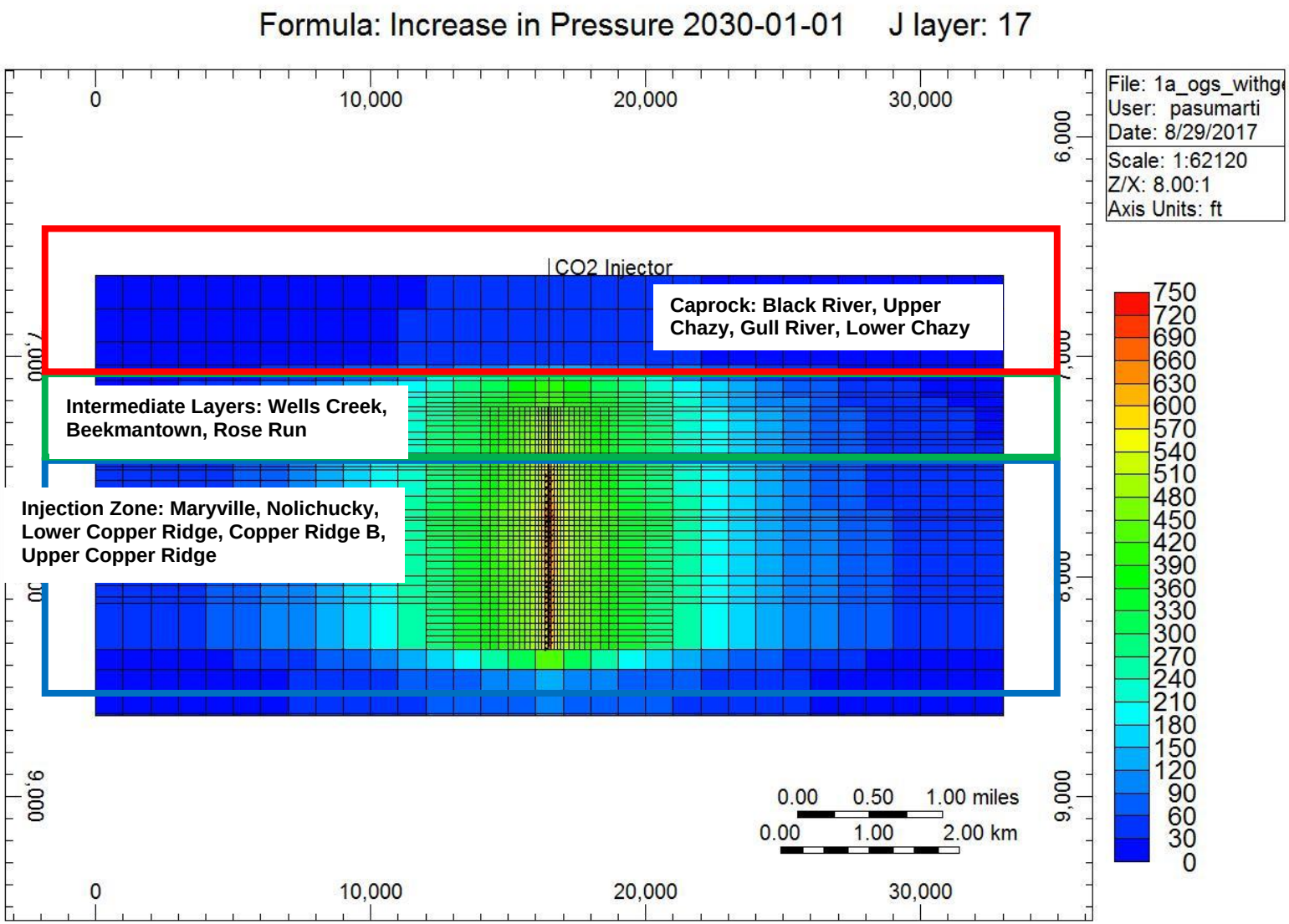

Figure 6-70: The amount of pressure increase attained in the subsurface after 30 years of injection into the OGS CO_2 #1 well, is shown via a cross-section through the middle of the fluid-flow grid.

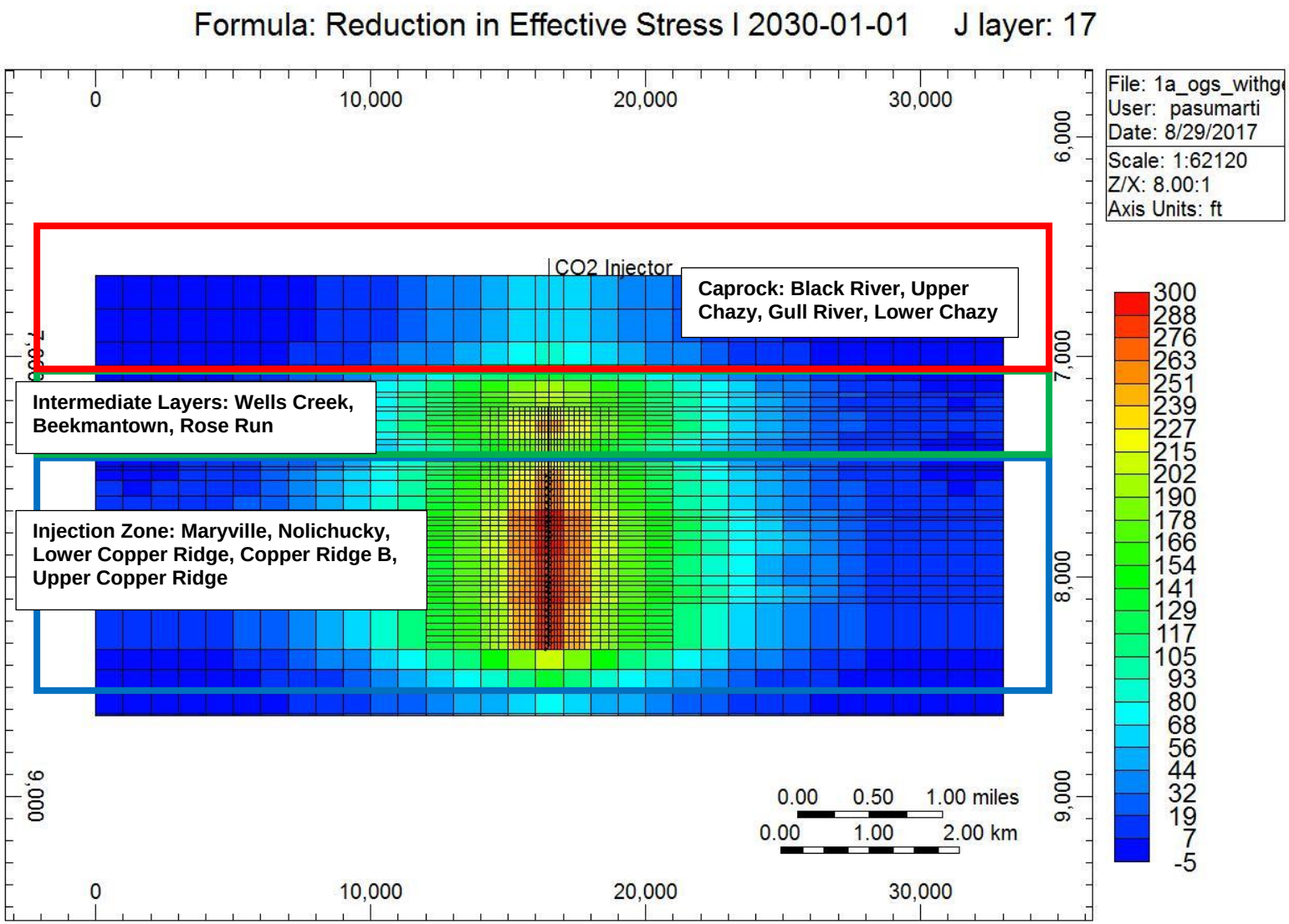

Figure 6-71: The reduction in the minimum horizontal effective stress occurring in the subsurface after 30 years of injection into the OGS CO_2 #1 well, is shown via a cross-section through the middle of the fluid-flow grid.

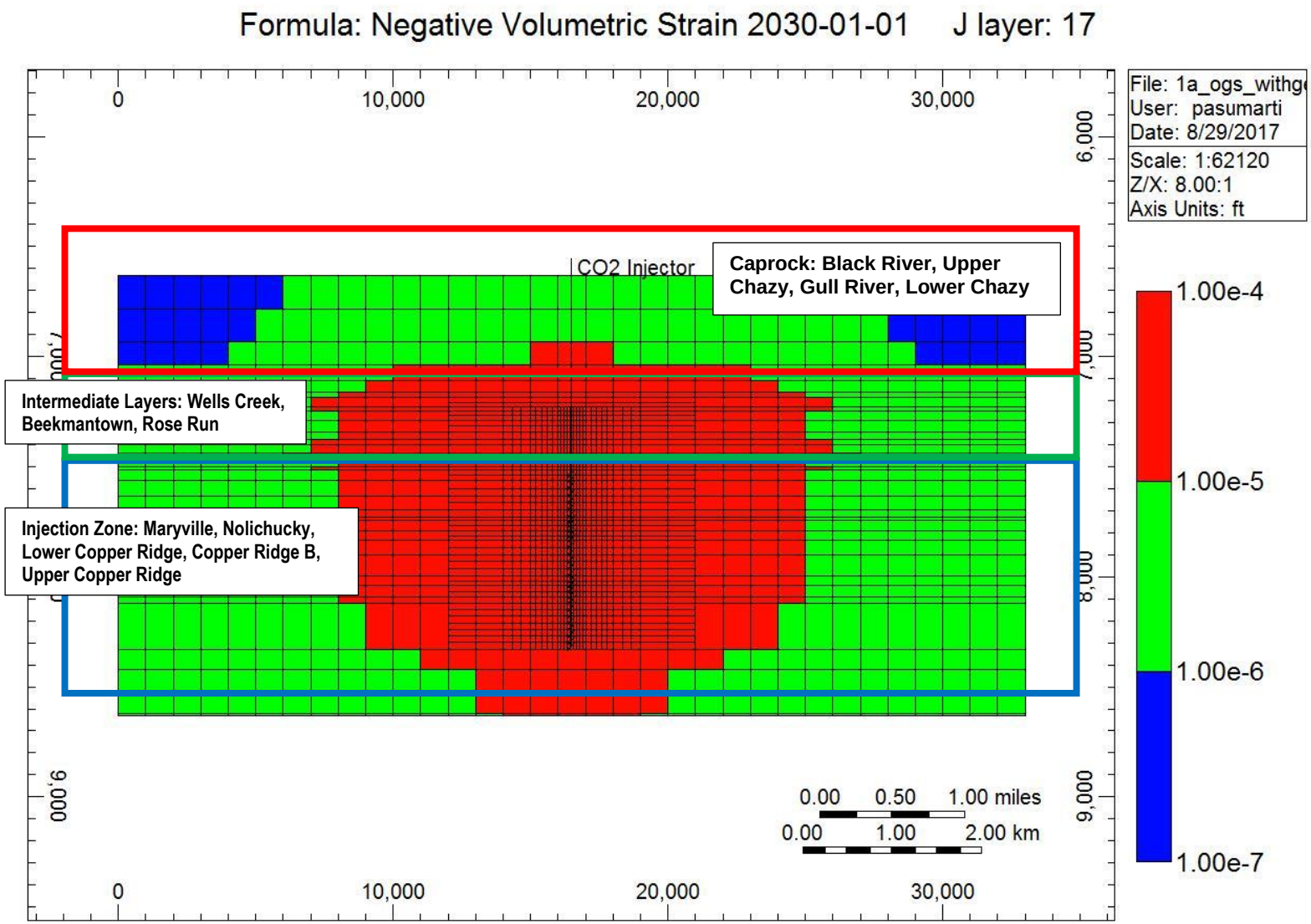

Figure 6-72: The fraction of bulk volume expansion (positive value) within the subsurface after 30 years of injection into the OGS CO_2 #1 well, is shown via a cross-section through the middle of the fluid-flow grid.

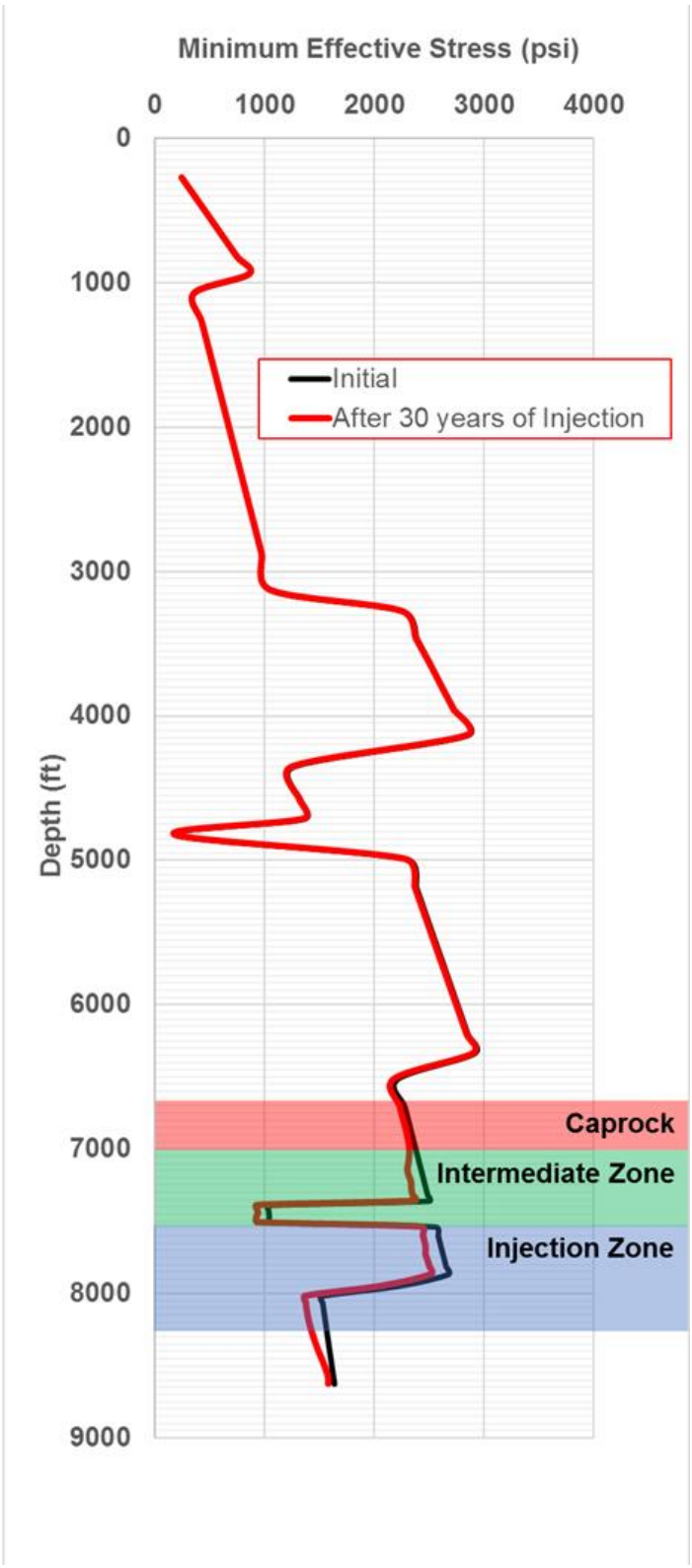

Figure 6-73: A vertical profile (from the surface to the injection zone) of the minimum horizontal effective stress is shown before and after injection, into the OGS CO_2 #1 well, with the relevant zones highlighted.

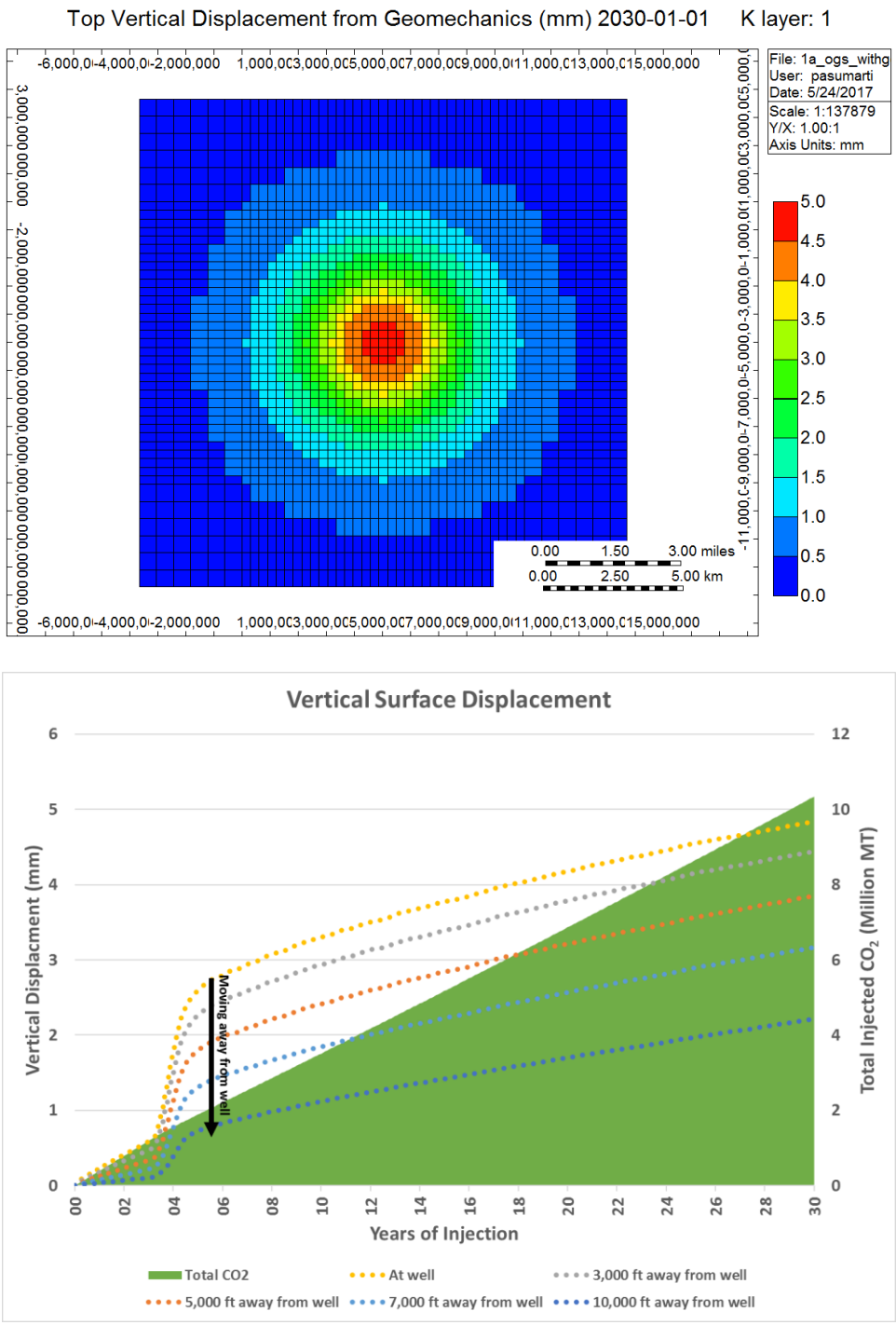

Figure 6-74: A two-paneled graphic summarizing the effects of injection into the OGS CO_2 #1 well on areal uplift at the surface is shown.

6.3.4.3 Caprock Integrity Analysis

Figure 6-75 shows that after 30 years of injection there is no CO_2 migration into caprock, and that there is only a small reduction in effective stresses (around 50 psi), mainly in the lower layers of the caprock (Lower Chazy and Gull River). Although there is only minimal to no pore pressure increase in the caprock, the external (total) stress has decreased very slightly, leading to the reduction in effective stresses in the lower two layers.

Figure 6-76 shows the three Mohr's circles representing stresses on all planes, before and after injection. The three black lines represent the linearized Mohr-Coulomb failure envelope lines with varying coefficients of friction. The steepest line represents a value of 1 (least conservative), the middle line 0.8 (moderate), and the gentlest line 0.6 (most conservative). None of these formations are known to be heavily fractured, and a value of 1000 psi likely represents a very conservative (low) estimate of cohesion. The Black River, however, appears to have some very sparsely scattered fractures, and a cohesion value of 1000 psi represents a more moderate scenario. No tensile failure or shear failure has occurred in any layer of the caprock, as the minimum effective stress is well above 250 psi (lowest around 2100 psi in the Lower Chazy) and that largest Mohr's circle (of all layers) is a considerable distance from any of the shear failure envelopes lines.

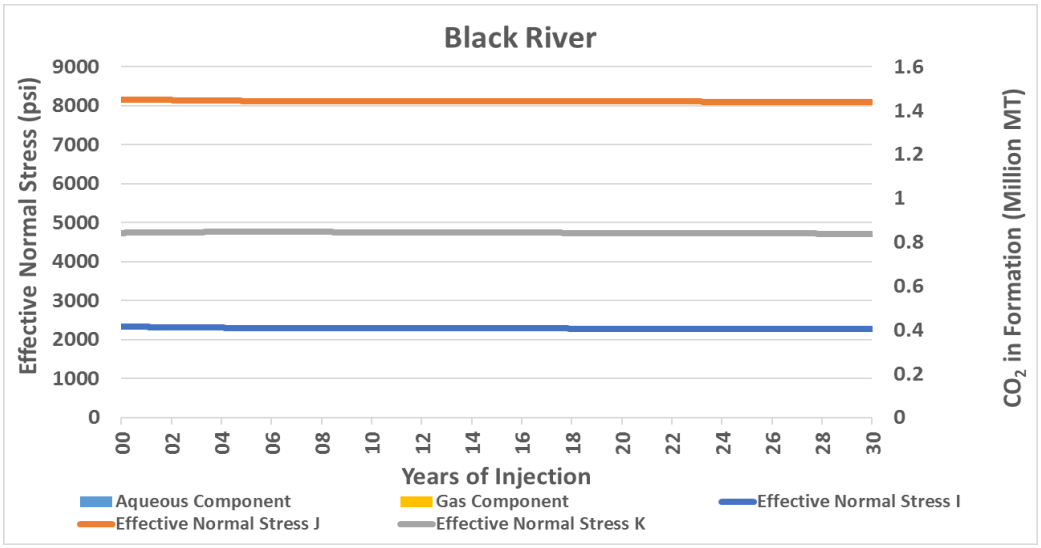

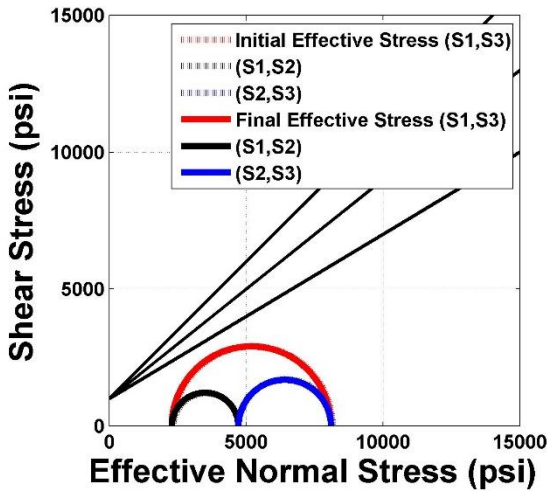

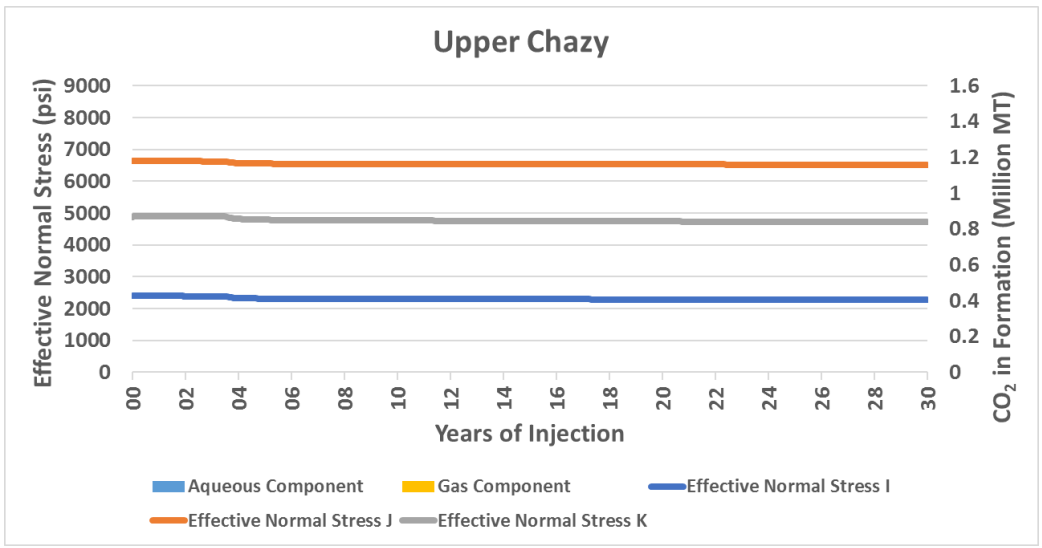

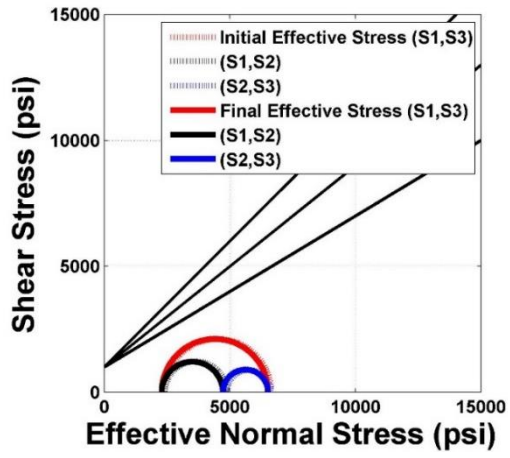

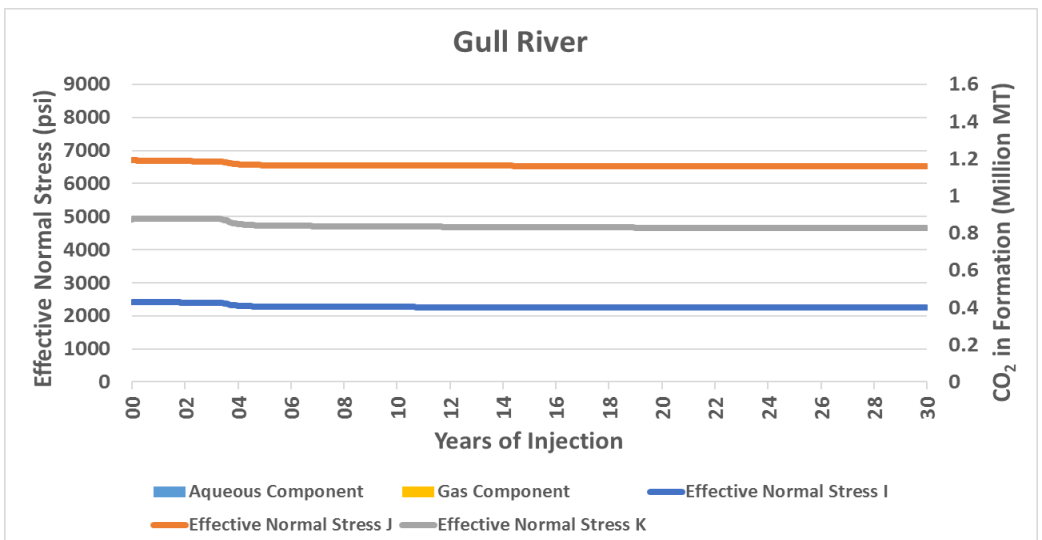

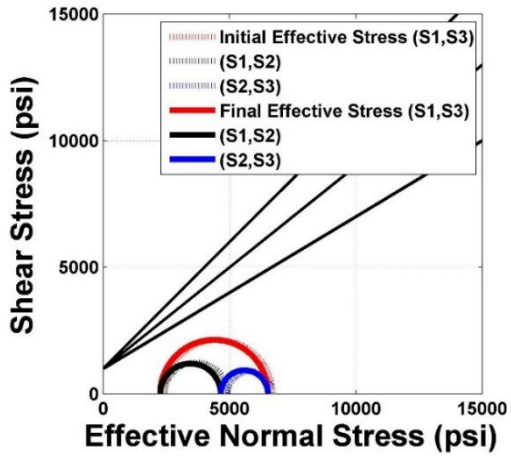

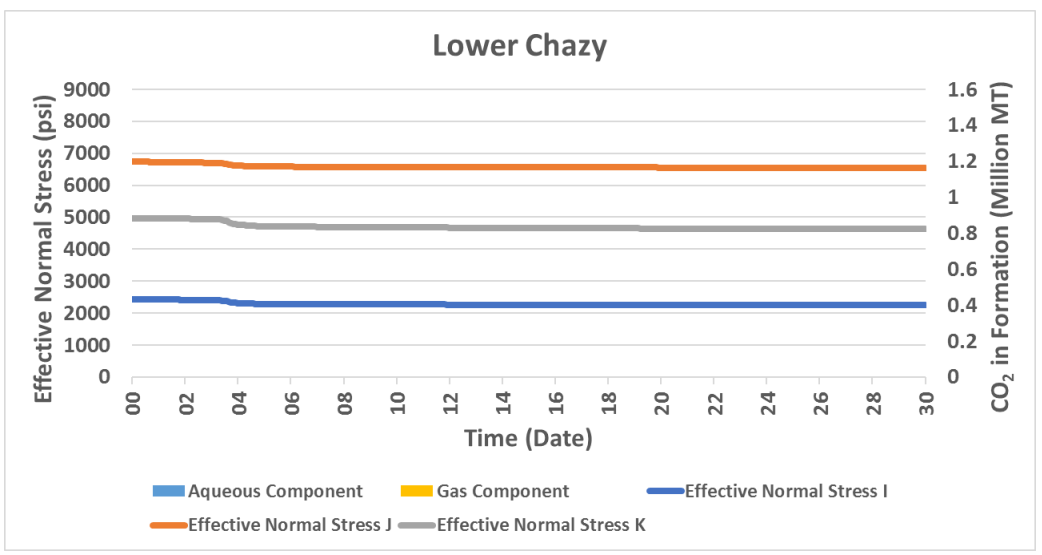

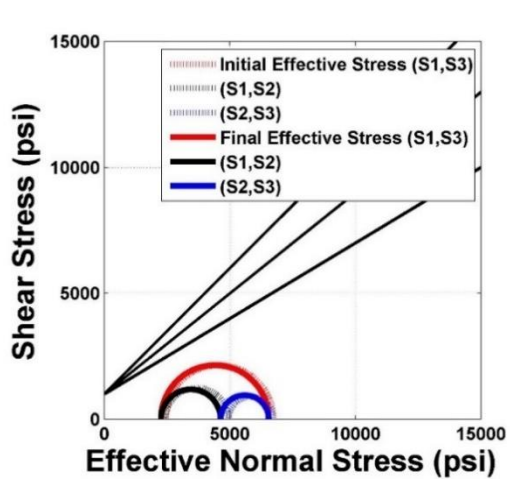

Figure 6-75 (Vertical Panel on the Left): Plots presenting the volume of CO_2 trapped in each formation as well as the impact of CO_2 injection on the principal effective stresses in the caprock layers are shown. Layers have been labelled in the order they occur in the subsurface.

Figure 6-76 (Vertical Panel on the Right): Mohr's Circles drawn to represent the stresses in the caprock layers are shown.

6.3.4.4 Reservoir Integrity Analysis

Figure 6-77 shows that after 30 years of injection resulting in about 10 million MT of CO_2 stored, there are small perturbations in the stress field (between 100 to 300 psi) and that the reduction is more pronounced in the vertical direction (up to 300 psi in the Upper Maryville). This phenomenon is due to the poro-elastic effects of injection, where the external (total) stresses rise mainly in the horizontal direction rather than the vertical direction (see Equation 1). Only a small volume of the injected CO_2 dissolves into the brine, and most of the CO_2 is contained within the plume.

Figure 6-78 shows Mohr's circles drawn to represent the stresses in each layer of the injection zone, before and after injection. The three Mohr's circles representing the stresses on all planes have been drawn. Given that the reduction in effective stress was small, the Mohr's circles have neither shifted too far to the left nor enlarged (shrunk) due to poro-elastic effects. There have been no regime changes in any formation such as those observed in the East Bend #1 well. The three black lines represent the linearized Mohr-Coulomb failure envelope lines with varying coefficients of friction. The steepest line represents a value of 1 (least conservative), the middle line 0.8 (moderate), and the gentlest line 0.6 (most conservative). None of the formations are known to be heavily fractured, and a value of 1000 psi likely represents a very conservative estimate of cohesion. There is, however, some evidence of sparsely scattered fractures in the Lower Copper Ridge, and a cohesion value of 1000 psi represents a more moderate scenario. No tensile failure or shear failure has occurred in both formations, as the minimum effective stress is well above 250 psi (lowest around 1000 psi in the Maryville) and that largest Mohr's circle (of all layers) is not tangent to any of the shear failure envelopes lines.

Given that the effective stress in the vertical direction is impacted more than the horizontal stresses, vertical stress is the maximum stress in the Upper Maryville (normal faulting regime) and an intermediate stress in the other formations (strike-slip faulting regime), further injection is not likely to enlarge and push the Mohr's circles closer toward shear failure in any formation – the largest (red) Mohr's circle will tend to shrink in the case of the Upper Maryville – although with extremely high injection, shear failure would likely to happen sooner than tensile failure. Considering however, the conservativeness of the model, and the dissipative effect of injecting over such a large interval on pore-pressures (800 ft.) – and consequently effective stresses – a large volume of CO_2 can likely be stored before this becomes a tangible risk.

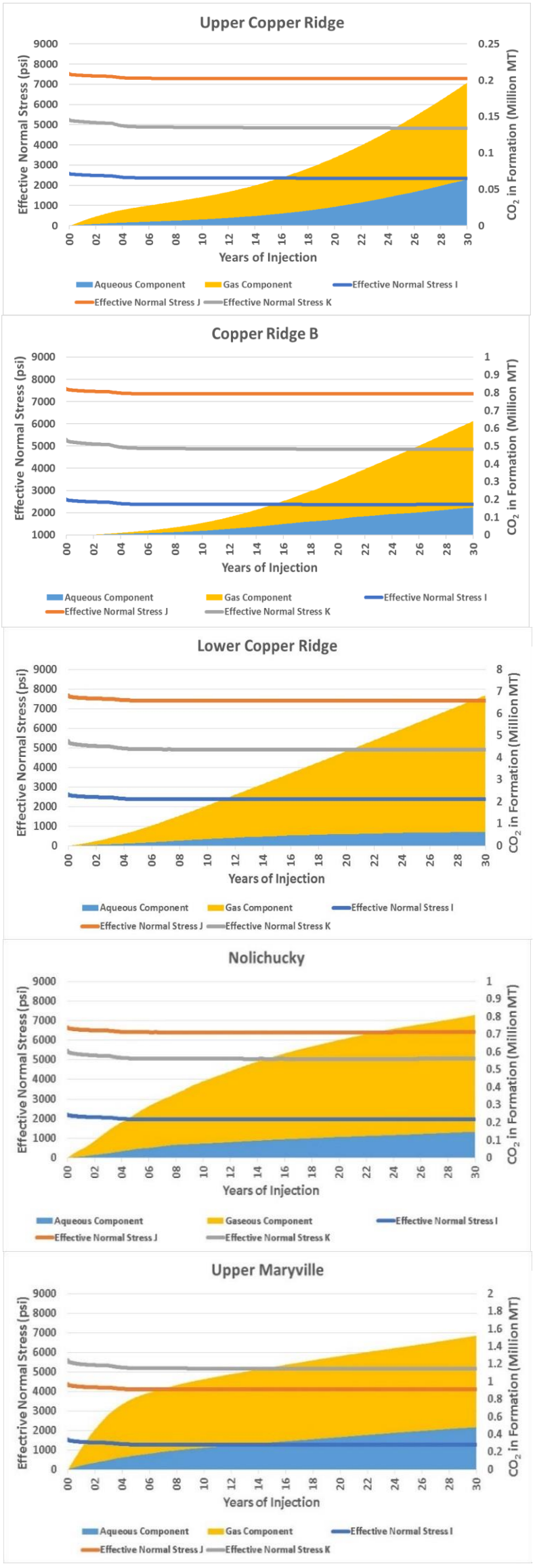

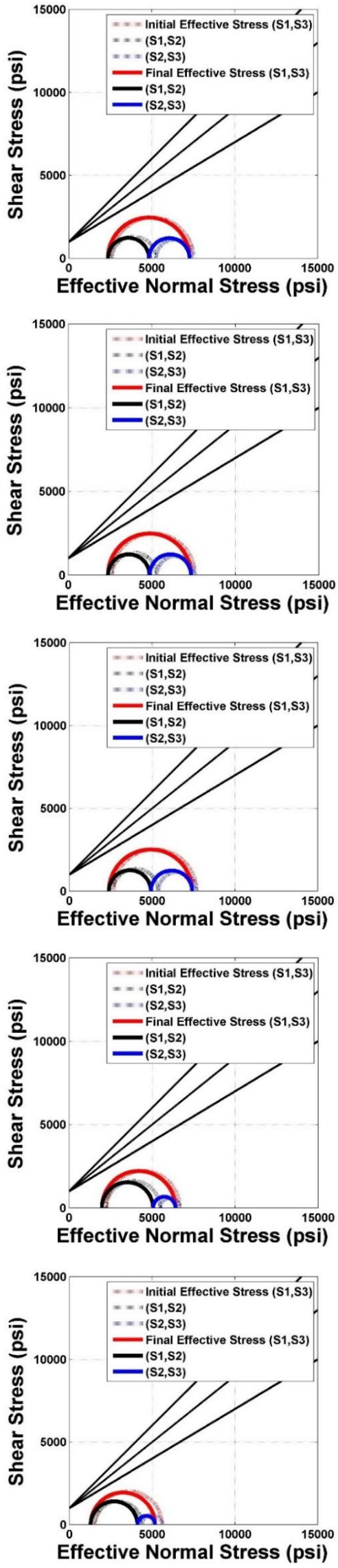

Figure 6-77 (Vertical Panel on the Left): Plots presenting the volume of CO_2 trapped in each formation as well as the impact of CO_2 injection on the principle effective stresses in the injection zone layers are shown. Layers have been labelled in the order they occur in the subsurface.

Figure 6-78 (Vertical Panel on the Right): Plots presenting the volume of CO_2 trapped in each formation as well as the impact of CO_2 injection on the principle effective stresses in the injection zone layers are shown.

6.3.4.5 Intermediate Zone Integrity Analysis

Figure 6-79 shows that after 30 years of injection resulting in about 10 million MT of CO_2 stored, a small quantity has migrated into the intermediate layers. With the exception of the Wells Creek, only a small volume of the injected CO_2 dissolves into the brine, and most of the CO_2 is contained within the plume. There are small perturbations in the stress field (between 100 to 200 psi) and that the reduction is more pronounced in the vertical direction (up to 200 psi in the Rose Run). This is due to the poro-elastic effects of injection, where the external (total) stresses rise mainly in the horizontal direction rather than the vertical direction (see Equation 6.3).

Figure 6-80 shows Mohr's circles drawn to represent the stresses in each layer of the intermediate zone, before and after injection. The three Mohr's circles representing the stresses on all planes have been drawn. The three black lines represent the linearized Mohr-Coulomb failure envelope lines with varying coefficients of friction. The steepest line represents a value of 1 (least conservative), the middle line 0.8 (moderate), and the gentlest line 0.6 (most conservative). None of the formations are known to be heavily fractured, and a value of 1000 psi likely represents a very conservative estimate of cohesion. There is, however, some evidence sparsely scattered fractures in the Rose Run, and a cohesion value of 1000 psi represents a more moderate scenario. No tensile failure or shear failure has occurred in both formations as the minimum effective stress is well above 250 psi (lowest around 1000 psi in the Rose Run) and that largest Mohr's circle (of all layers) is not tangent to any of the shear failure envelopes lines.

Given that effective stress in the vertical direction is impacted more than the horizontal stresses (due to poro-elasticity), vertical stress is the maximum stress in the Rose Run and an intermediate stress in the other formations, further injection is not likely to enlarge and push the Mohr's circles closer toward shear failure in any formation – the largest (red) Mohr's circle will tend to shrink in the case of the Rose Run – although with extremely high injection, shear failure would likely to happen sooner than tensile failure. Considering however, the conservativeness of the model, and the dissipative effect of injecting over such a large interval (800 ft.) on pore pressures – and consequently effective stresses – a large volume of CO_2 can be stored before this becomes a tangible risk.

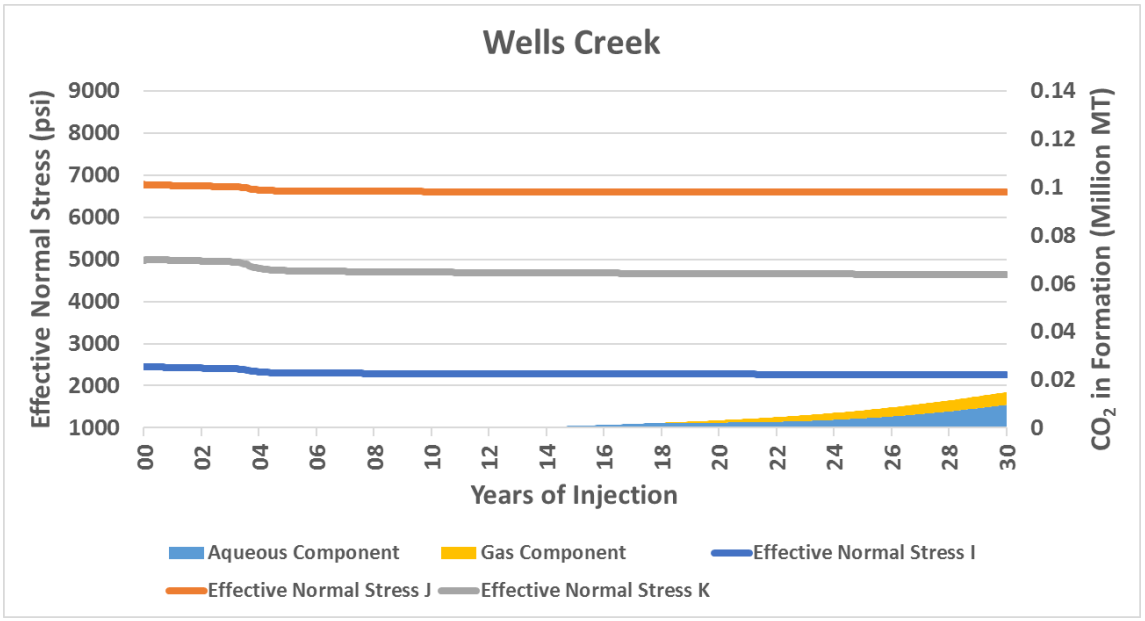

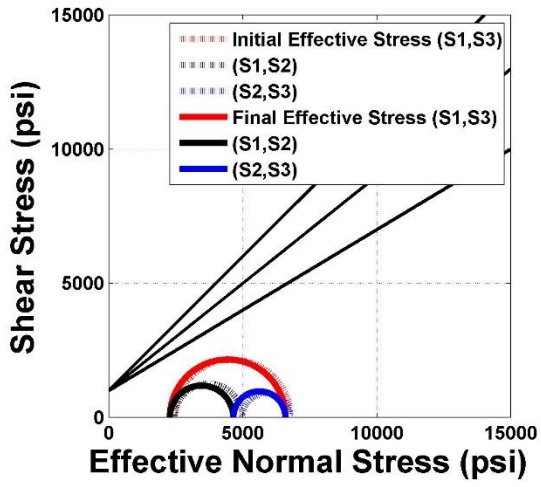

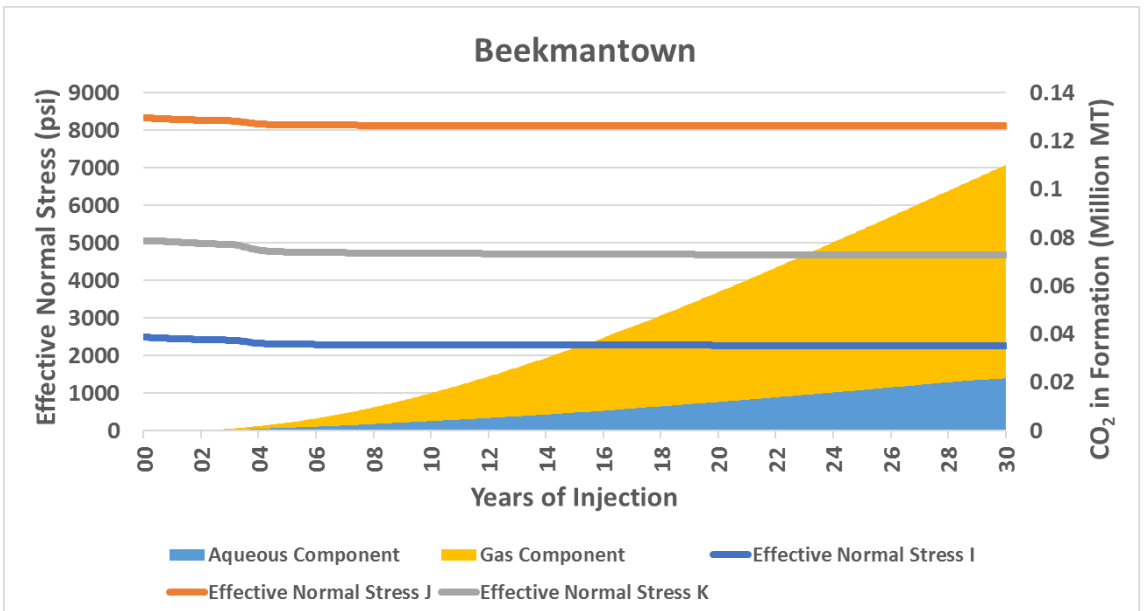

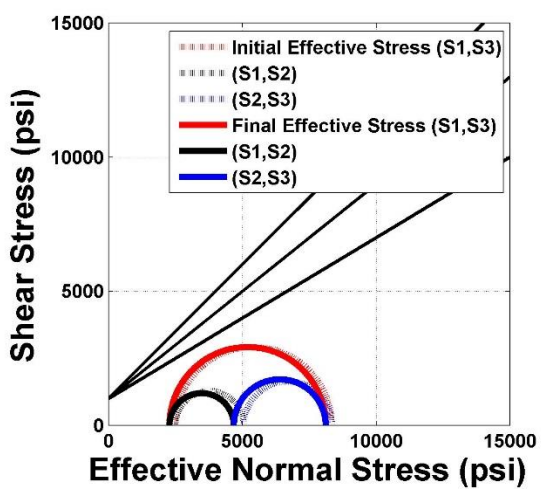

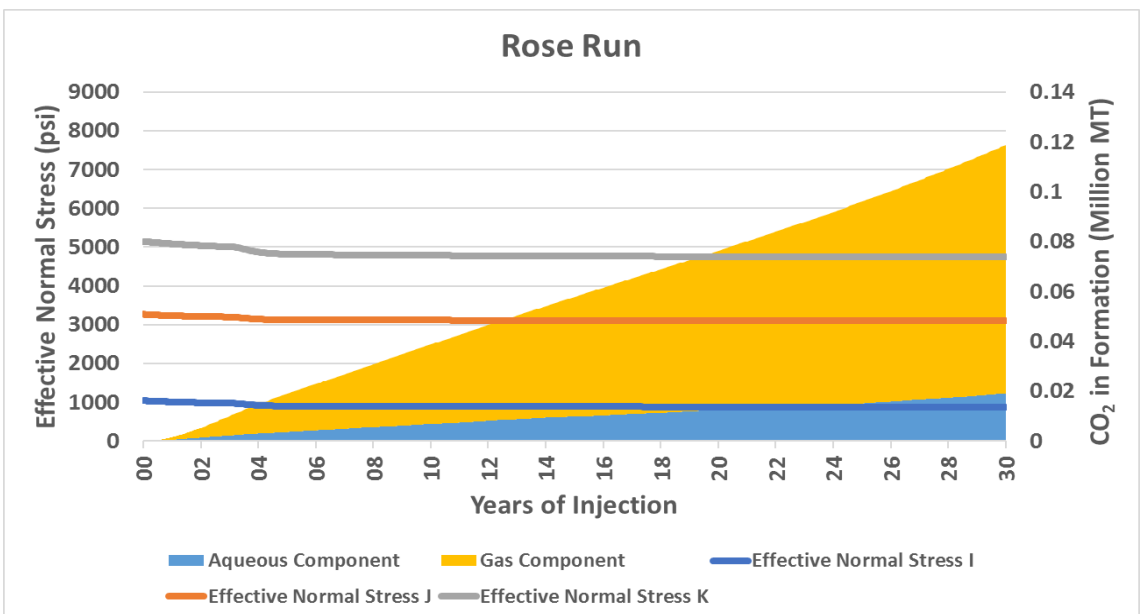

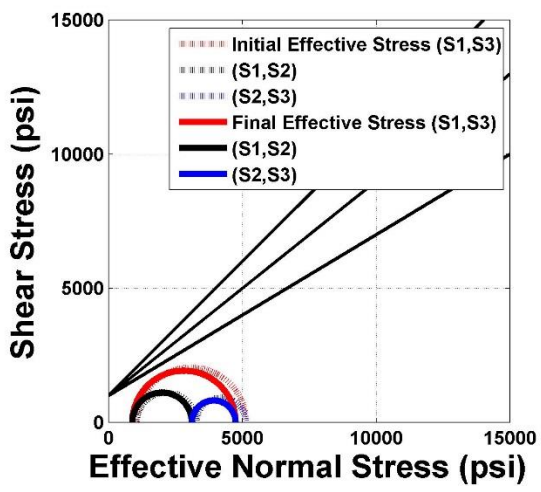

Figure 6-79 (Vertical Panel on the Left): Plots presenting the volume of CO_2 trapped in each formation as well as the impact of CO_2 injection on the principle effective stresses in the intermediate zone layers are shown. Layers have been labelled in the order they occur in the subsurface.

Figure 6-80 (Vertical Panel on the Right): Plots presenting the volume of CO_2 trapped in each formation as well as the impact of CO_2 injection on the principle effective stresses in the intermediate zone layers are shown.

6.3.4.6 Sensitivity Analysis: Input Values

Tables 6-19 to 6-21 present the values of key geomechancial parameters, as altered from the base case or Scenario 1. The altered parameters values used in this sensitivity study were still considered to be realistic, and were chosen to remain within the limits of uncertainty observed in the data, while also being geologically consistent (e.g. preserving the faulting regime of the formation). For Scenario 2, the minimum horizontal stress gradient has been increased while the maximum horizontal stress has been reduced, having the effect of shrinking the Mohr's circles (shear and normal stresses) in the formations. For Scenario 3, the static Young's modulus has been increased by around 20%, tending to reduce the amount of vertical uplift observed at the surface. For Scenario 4, the Biot's coefficient has been decreased to 0.8, which has the effect of reducing the amount of perturbation of the stress-strain field caused by pore-pressure rise. For Scenario 5, in addition to using the using the same values as Scenario 4, the pore-volumes of the grid-blocks at all four boundaries have been increased through the use of pore-volume modifiers, reflecting the continuity of the formation beyond an area of 25,000 Acres around the well.

Table 6-19: Values of key geomechanical parameters for Scenario 2 (OGS CO_2 #1 well). Values for the horizontal stresses in the base case (Scenario 1) are included in parentheses for reference.

Formation	**σ_H gradient / psi/ft**	**σ_h gradient / psi/ft**
L. Maryville	0.95 (1)	0.7 (0.65)
U. Maryville	0.95 (1)	0.7 (0.65)
Nolichucky	1.2 (1.3)	0.8 (0.74)
L. Copper Ridge	1.35 (1.45)	0.85 (0.8)
Copper Ridge B	1.35 (1.45)	0.85 (0.8)
U. Copper Ridge	1.35 (1.45)	0.85 (0.8)
Rose Run	0.85 (0.9)	0.65 (0.6)
Beekmantown	1.5(1.6)	0.9 (0.8)
Wells Creek	1.3 (1.4)	0.9 (0.8)
Lower Chazy	1.3 (1.4)	0.9 (0.8)
Gull River	1.3 (1.4)	0.9 (0.8)
Upper Chazy	1.3 (1.4)	0.9 (0.8)
Black River	1.55 (1.65)	0.9 (0.8)

Table 6-20: Values of key geomechanical parameters for Scenario 3 (OGS CO_2 #1 well). Values for the Young's modulus in the base case (Scenario 1) are included in parentheses for reference.

Formation	σ_H gradient / psi/ft	σ_h gradient / psi/ft	Static Young's modulus / psi
L. Maryville	0.95 (1)	0.7 (0.65)	1.34E+07 (1.11E+07)
U. Maryville	0.95 (1)	0.7 (0.65)	1.38E+07 (1.15E+07)
Nolichucky	1.2 (1.3)	0.8 (0.74)	1.40E+07 (1.16E+07)
L. Copper Ridge	1.35 (1.45)	0.85 (0.8)	1.30E+07 (1.08E+07)
Copper Ridge B	1.35 (1.45)	0.85 (0.8)	1.26E+07 (1.05E+07)
U. Copper Ridge	1.35 (1.45)	0.85 (0.8)	1.31E+07 (1.09E+07)
Rose Run	0.85 (0.9)	0.65 (0.6)	1.02E+07 (8.49E+06)
Beekmantown	1.5(1.6)	0.9 (0.8)	1.10E+07 (9.18E+06)
Wells Creek	1.3 (1.4)	0.9 (0.8)	9.29E+06 (7.74E+06)
Lower Chazy	1.3 (1.4)	0.9 (0.8)	8.88E+06 (7.40E+06)
Gull River	1.3 (1.4)	0.9 (0.8)	1.03E+07 (8.55E+06)
Upper Chazy	1.3 (1.4)	0.9 (0.8)	8.84E+06 (7.37E+06)
Black River	1.55 (1.65)	0.9 (0.8)	9.40E+06 (7.83E+06)

Table 6-21: Values of key geomechanical parameters for Scenario 3 (OGS CO_2 #1 well). Values of the Biot's coefficient in the base case (Scenario 1) are included in parentheses for reference.

Formation	Biot's coefficient	σ_H gradient / psi/ft	σ_h gradient / psi/ft	Static Young's modulus / psi
L. Maryville	0.8 (1)	0.95 (1)	0.7 (0.65)	1.34E+07 (1.11E+07)
U. Maryville	0.8 (1)	0.95 (1)	0.7 (0.65)	1.38E+07 (1.15E+07)
Nolichucky	0.8 (1)	1.2 (1.3)	0.8 (0.74)	1.40E+07 (1.16E+07)
L. Copper Ridge	0.8 (1)	1.35 (1.45)	0.85 (0.8)	1.30E+07 (1.08E+07)
Copper Ridge B	0.8 (1)	1.35 (1.45)	0.85 (0.8)	1.26E+07 (1.05E+07)
U. Copper Ridge	0.8 (1)	1.35 (1.45)	0.85 (0.8)	1.31E+07 (1.09E+07)
Rose Run	0.8 (1)	0.85 (0.9)	0.65 (0.6)	1.02E+07 (8.49E+06)
Beekmantown	0.8 (1)	1.5(1.6)	0.9 (0.8)	1.10E+07 (9.18E+06)
Wells Creek	0.8 (1)	1.3 (1.4)	0.9 (0.8)	9.29E+06 (7.74E+06)
Lower Chazy	0.8 (1)	1.3 (1.4)	0.9 (0.8)	8.88E+06 (7.40E+06)
Gull River	0.8 (1)	1.3 (1.4)	0.9 (0.8)	1.03E+07 (8.55E+06)
Upper Chazy	0.8 (1)	1.3 (1.4)	0.9 (0.8)	8.84E+06 (7.37E+06)
Black River	0.8 (1)	1.55 (1.65)	0.9 (0.8)	9.40E+06 (7.83E+06)

6.3.4.7 Sensitivity Analysis: Results

Tables 6-22 to 6-24 present key outputs based on the coupled fluid-flow and reservoir geomechanics simulations of the five sensitivity scenarios. Tables 6-22 and 6-23 summarize results for the reservoir and caprock respectively. The risks of rock failure are assessed by examining the Mohr's circles depicting the shear and normal stresses in the formation after injection, for distance from the failure envelope (shear failure), and from the origin (tensile failure risk when the minimum effective stress is less than 250 psi). Given that stresses are affected more in the vertical direction than the horizontal, a stress-regime change may occur if the reduction of stresses in the vertical direction is drastic enough. Instead of the average reservoir pressure, the maximum increase in pore-pressure is listed (close to the wellbore). The magnitude of the reduction in effective stress is listed for all three directions. A comparison of these quantities against the maximum pore-pressure increase suggests the level of poro-elastic effects in the formation. Table 6-22 summarizes more regional-scale outputs. Stresses in the geomechanical grid (rocks from the basement to the surface) were examined to confirm that stress changes occurred below the Davis formation (see Figure 6-61). The widest radius of the CO_2 plume, and the furthest extent to which the pore-pressures had risen by more than 300 psi was noted. The areal uplift experienced at the surface at increasingly further distances from the wellbore are listed (see Figure 6-62).

The stress-gradient changes imposed in Scenario 2 did not result in any significant effects, although the formations were more than 7000 ft deep (the change in in-situ stresses of the rock would be greater than for the East Bend well). Note however the discrepancy between the increase in pore-pressures and the vertical effective stress reduction, suggesting significant poro-elastic effects in this direction (unlike in the Arches site). A comparison of Scenario 2 and 3 suggests that a 20% increase in the stiffness of the rocks, only has the effect of reducing the areal uplift at the surface by around 5% or less (from 4.4 mm to 4.2 mm – almost negligible difference). Unlike in the East Bend well, the uncertainty in the Young's modulus does not have any significant effect on the pressurization in the injected and intermediate zones. A comparison of Scenario 3 and 4 reveals that the impact of reducing the Biot's coefficient by 20% (from 1 to 0.8) translates one-to-one onto the effective stresses (also reduced by 20% as expected according to Equation 6.3), and onto the areal uplift experienced at the surface (from 4.2 mm to 3.4 mm). Unlike in the East Bend well, Scenario 5 does not suggest that the formation extent is an important factor influencing the level of pressurization and consequently the magnitude of stress-field perturbations (although the amount of areal uplift at the surface is marginally lower). This is likely due to the (generally) low permeability and porosity values of the formations encountered in the injection zone, which ensure that the reservoir remains in a somewhat transient state (the pressure pulse does not reach the boundary). For the bandwidth of sensitivities considered, this study yielded that the uncertainty in geomechanical parameters does not translate to a significant range in the geomechanical impacts of injection or effective storage capacity for this well. Around 10.25 million tons of effective storage capacity may be achieved by this well, causing around 4 mm of uplift at the surface.

6.3.4.8 Summary and Recommendations

Table 6-25 presents a summary of the Ohio CO2 #1 well. There was no tensile failure or shear failure predicted in the injection zone or the caprock interval. The simulations suggested that the stacked, multi-reservoir storage zone had a 30-year effective capacity likely to be higher than 10.25 million MT.

Table 6-22: Key outputs from the simulations of each sensitivity scenario, for the injection zone (Maryville to Upper Copper Ridge) are listed.

Scenario #	Injection Zone						
	Shear failure?	**Tensile failure?**	**Stress-regime change?**	**Maximum pore-pressure increase (psi)**	**Magnitude of effective stress reduction in I direction (psi)**	**Magnitude of effective stress reduction in J direction (psi)**	**Magnitude of effective stress reduction in K direction (psi)**
1. Base Case	No.	No.	No.	Deep: 700 *(U. Maryville)* Middle: 715 *(Nolichucky)* Shallow: 730 *(L. Copper Ridge)*	Deep: 275 *(U. Maryville)* Middle: 285 *(Nolichucky)* Shallow: 300 *(L. Copper Ridge)*	Deep: 275 *(U. Maryville)* Middle: 285 *(Nolichucky)* Shallow: 300 *(L. Copper Ridge)*	Deep: 400 *(U. Maryville)* Middle: 450 *(Nolichucky)* Shallow: 470 *(L. Copper Ridge)*
2.	No.	No.	No.	Deep: 700 *(U. Maryville)* Middle: 715 *(Nolichucky)* Shallow: 730 *(L. Copper Ridge)*	Deep: 275 *(U. Maryville)* Middle: 285 *(Nolichucky)* Shallow: 300 *(L. Copper Ridge)*	Deep: 275 *(U. Maryville)* Middle: 285 *(Nolichucky)* Shallow: 300 *(L. Copper Ridge)*	Deep: 400 *(U. Maryville)* Middle: 450 *(Nolichucky)* Shallow: 470 *(L. Copper Ridge)*
3.	No.	No.	No.	Deep: 705 *(U. Maryville)* Middle: 720 *(Nolichucky)* Shallow: 730 *(L. Copper Ridge)*	Deep: 290 *(U. Maryville)* Middle: 300 *(Nolichucky)* Shallow: 305 *(L. Copper Ridge)*	Deep: 290 *(U. Maryville)* Middle: 300 *(Nolichucky)* Shallow: 305 *(L. Copper Ridge)*	Deep: 415 *(U. Maryville)* Middle: 470 *(Nolichucky)* Shallow: 480 *(L. Copper Ridge)*
4.	No.	No.	No.	Deep: 705 *(U. Maryville)* Middle: 720 *(Nolichucky)* Shallow: 730 *(L. Copper Ridge)*	Deep: 235 *(U. Maryville)* Middle: 240 *(Nolichucky)* Shallow: 245 *(L. Copper Ridge)*	Deep: 235 *(U. Maryville)* Middle: 240 *(Nolichucky)* Shallow: 245 *(L. Copper Ridge)*	Deep: 330 *(U. Maryville)* Middle: 375 *(Nolichucky)* Shallow: 385 *(L. Copper Ridge)*
5. Most Optimistic	No.	No.	No.	Deep: 700 *(U. Maryville)* Middle: 715 *(Nolichucky)* Shallow: 730 *(L. Copper Ridge)*	Deep: 230 *(U. Maryville)* Middle: 240 *(Nolichucky)* Shallow: 245 *(L. Copper Ridge)*	Deep: 230 *(U. Maryville)* Middle: 240 *(Nolichucky)* Shallow: 245 *(L. Copper Ridge)*	Deep: 325 *(U. Maryville)* Middle: 370 *(Nolichucky)* Shallow: 380 *(L. Copper Ridge)*

Table 6-23: Key outputs from the simulations of each sensitivity scenario, for the intermediate zone (Rose Run to Wells Creek) are listed.

Scenario #	Intermediate Zone						
	Shear failure?	**Tensile failure?**	**Stress-regime change?**	**Maximum pore-pressure increase (psi)**	**Magnitude of effective stress reduction in I direction (psi)**	**Magnitude of effective stress reduction in J direction (psi)**	**Magnitude of effective stress reduction in K direction (psi)**
1. Base Case	No.	No.	No.	Deep: 615 *(Rose Run)* Middle: 535 *(Beekmantown)* Shallow: 430 *(Wells Creek)*	Deep: 215 *(Rose Run)* Middle: 225 *(Beekmantown)* Shallow: 200 *(Wells Creek)*	Deep: 215 *(Rose Run)* Middle: 225 *(Beekmantown)* Shallow: 200 *(Wells Creek)*	Deep: 420 *(Rose Run)* Middle: 395 *(Beekmantown)* Shallow: 340 *(Wells Creek)*
2.	No.	No.	No.	Deep: 615 *(Rose Run)* Middle: 535 *(Beekmantown)* Shallow: 430 *(Wells Creek)*	Deep: 215 *(Rose Run)* Middle: 225 *(Beekmantown)* Shallow: 200 *(Wells Creek)*	Deep: 215 (Rose Run) Middle: 225 *(Beekmantown)* Shallow: 200 *(Wells Creek)*	Deep: 420 *(Rose Run)* Middle: 395 *(Beekmantown)* Shallow: 340 *(Wells Creek)*
3.	No.	No.	No.	Deep: 620 *(Rose Run)* Middle: 540 *(Beekmantown)* Shallow: 435 *(Wells Creek)*	Deep: 215 (Rose Run) Middle: 225 *(Beekmantown)* Shallow: 200 *(Wells Creek)*	Deep: 215 (Rose Run) Middle: 225 *(Beekmantown)* Shallow: 200 *(Wells Creek)*	Deep: 435 *(Rose Run)* Middle: 410 *(Beekmantown)* Shallow: 355 *(Wells Creek)*
4.	No.	No.	No.	Deep: 620 *(Rose Run)* Middle: 540 *(Beekmantown)* Shallow: 435 *(Wells Creek)*	Deep: 170 *(Rose Run)* Middle: 180 *(Beekmantown)* Shallow: 160 *(Wells Creek)*	Deep: 170 *(Rose Run)* Middle: 180 *(Beekmantown)* Shallow: 160 *(Wells Creek)*	Deep: 345 *(Rose Run)* Middle: 325 *(Beekmantown)* Shallow: 280 *(Wells Creek)*
5. Most Optimistic	No.	No.	No.	Deep: 615 *(Rose Run)* Middle: 535 *(Beekmantown)* Shallow: 430 *(Wells Creek)*	Deep: 170 *(Rose Run)* Middle: 180 *(Beekmantown)* Shallow: 155 *(Wells Creek)*	Deep: 170 *(Rose Run)* Middle: 180 *(Beekmantown)* Shallow: 155 *(Wells Creek)*	Deep: 340 *(Rose Run)* Middle: 320 *(Beekmantown)* Shallow: 275 *(Wells Creek)*

Table 6-24: Key regional-scale outputs from the simulations of each sensitivity scenario are listed.

Scenario #	Spatial Extent of Impact			Areal Uplift at Surface (mm)				Effective Storage Capacity (million metric tons)		
	Stress-strain perturbations isolated below caprock?	Maximum plume extent (ft)	Pore-pressure increase (>300 psi) extent (ft)	3000 ft	5000 ft	7000 ft	10,000 ft	Injection Zone	Intermediate Zone	Total
1. Base Case	Yes	5500	4500	4.4	3.9	3.2	2.2	10	0.25	**10.25**
2.	Yes	5500	4500	4.4	3.9	3.2	2.2	10	0.25	**10.25**
3.	Yes	5500	4500	4.2	3.7	3.0	2.2	10	0.25	**10.25**
4.	Yes	5500	4500	3.4	2.9	2.4	1.8	10	0.25	**10.25**
5. Most Optimistic	Yes	5500	3500	3.1	2.7	2.2	1.5	10	0.25	**10.25**

Table 6-25: Summary of the main conclusions of the simulation study for the East Central Appalachian Basin well and relevant recommendations.

Objective	Conclusion
Evaluate Caprock's geomechanical integrity: Tensile Failure	The minimum effective stress in all the layers of the caprock zone is nearly unchanged at around 2300 psi. **No tensile failure in the caprock zone: Lower Chazy, Gull River, Upper Chazy, Black River**
Evaluate Caprock's geomechanical integrity: Shear Failure	Negligible movement of the Mohr's Circles for in all the layers of the caprock zone. **No shear failure or fracture activation in the caprock zone: Lower Chazy, Gull River, Upper Chazy, Black River**
Evaluate injection and intermediate zones' geomechanical integrity: Tensile Failure	The lowest minimum effective stress encountered in the injection zone is around 1000 psi. The lowest minimum effective stress encountered in the intermediate zone is around 1000 psi. **No tensile failure in any of the formations in the injection zone: Maryville, Nolichucky, Copper Ridge** **No tensile failure in any of the formations in the intermediate zone: Rose Run, Beekmantown, Wells Creek**
Evaluate injection and intermediate zones' geomechanical integrity: Shear Failure	Injection zone: Largest observed pore-pressure increase was in the Upper Maryville, of only around 90 psi. Minor movement of the Mohr's Circles, and even shrinkage of the Mohr's Circle observed (Upper Maryville). **No shear failure or fracture activation in injection zone: Maryville, Nolichucky, Copper Ridge.** Intermediate zone: Largest pore-pressure increase was in the Rose Run, of only 75 psi. Minor movement of the Mohr's Circles, and even shrinkage of the Mohr's Circle observed (Rose Run). **No shear failure or fracture activation in the intermediate zone: Rose Run, Beekmantown, Wells Creek**
Evaluate areal uplift at the surface	**Between 2.5 to 5 mm of areal uplift at the surface may be expected over an area of 25,000 acres.**
Demonstrate the isolation of stress-strain perturbations within the subsurface	Reduction of effective stresses and volumetric strains are significant only up to Gull River. **No significant perturbation in the stress-strain field, in any layer above the caprock.**
Demonstrate CO_2 plume migration and the effectiveness of caprock.	CO_2 plume extends to around 5000 ft from the injector, and penetrates as far upward as Beekmantown in the intermediate zone. Only 0.25 million MT of CO_2 migrated into the Intermediate zone. **No CO_2 or pressure increase in in the caprock zone: Lower Chazy, Gull River, Upper Chazy, Black River**
Quantify the effective CO_2 storage capacity of the well	No boundary effects detected from simulation results. Around 10 million MT of CO_2 stored in the injection zone Around 0.25 million MT of CO_2 migrated outside of the injection zone. No risks of geomechanical failure in injection, intermediate or caprock zones during injection. **Conservative estimate of CO_2 capacity after 30 years of injection: 10.25 million MT**
Recommendations	The dissipative effect of injecting over a 800 ft. interval, leads to very small increases in pore-pressure. **1. Neither a higher bottom-hole pressure constraint nor further injection beyond 30 years is likely to pose any additional geomechanical risks.** **2. In practice, the 30-year effective capacity of this well is likely to be higher than 10.25 million MT.** **3. This well is an ideal candidate for stacked, multi-reservoir storage of commercial-scale volumes of CO_2.**

6.3.5 NE Appalachian Basin Site

6.3.5.1 Model Summary

Table 6-26 presents the key inputs to the model. All data have been obtained from well-log analysis. Porosity and permeability data, however, have been obtained from an the basis well. The permeability in the injection zone is extremely low (0.0033 md), and as a result extremely low injectivity is expected. The formations in blue is in the injection zone while those in red are in the caprock zone.

Table 6-26: Key site-specific data inputs for coupled fluid-flow – geomechanics simulation for the Northern Appalachian Basin well.

Formation	Average Depth (ft)	Thickness (ft)	No. of Layers	Average Porosity	Average Permeability (md)	Average Initial Pressure (psi)
Potsdam	7241	200	1	2.7%	0.0033	3331
Gallaway_D	7167	69	2	1.1%	0.0009	3297
Gallaway_C	7064	146	2	0.3%	0.0011	3251
Gallaway_B	6915	136	3	3.6%	0.001	3181
Gallaway A	6719	303	2	1.1%	0.0017	2989
Little Falls	6385	274	3	2.1%	0.0147	2933
Tribe Hill	6224	101	3	4.9%	0.04	2863
Trenton	5799	653	4	1.0%	0.02	2662
Utica	5106	848	4	8.1%	0.0002	2350

Formation	σ_v gradient (psi/ft)	σ_H gradient (psi/ft)	σ_h gradient (psi/ft)	Static Young's modulus[a] (psi)	Poisson's ratio	
Potsdam	1.08	0.88	0.6	8.41E+06	0.21	
Gallaway_D	1.08	0.94	0.7	9.16E+06	0.23	
Gallaway_C	1.08	1.09	0.8	9.89E+06	0.26	
Gallaway_B	1.08	1.00	0.7	8.35E+06	0.25	
Gallaway A	1.08	1.03	0.7	8.96E+06	0.25	
Little Falls	1.08	0.99	0.7	7.87E+06	0.25	
Tribe Hill	1.08	1.02	0.8	6.06E+06	0.28	
Trenton	1.08	1.06	0.8	6.86E+06	0.30	
Utica	1.08	1.06	0.9	4.28E+06	0.29	

a. 70% of the Log-based dynamic Young's modulus estimate.

6.3.5.2 Simulation Results

Figure 6-81 shows how the low permeability (0.0033 md) of the Potsdam formation prevents any meaningful injection. The injectivity is so meagre that only an average of 250 MT/year can be injected, and only around 8500 MT of CO_2 was stored in 30 years, which is insufficient for exploring the use of this well for commercial-scale storage purposes (several million tons). With such low volumes of injection, there are negligible geomechanical impacts, and further analysis of the simulation results for the integrity of the injection, intermediate and caprock zones and uplift at the surface is not necessary. Simulations thus suggest the Northern Appalachian Basin well is not suitable for a commercial-scale CO_2 storage operation due to the extremely low permeability of the injection zone.

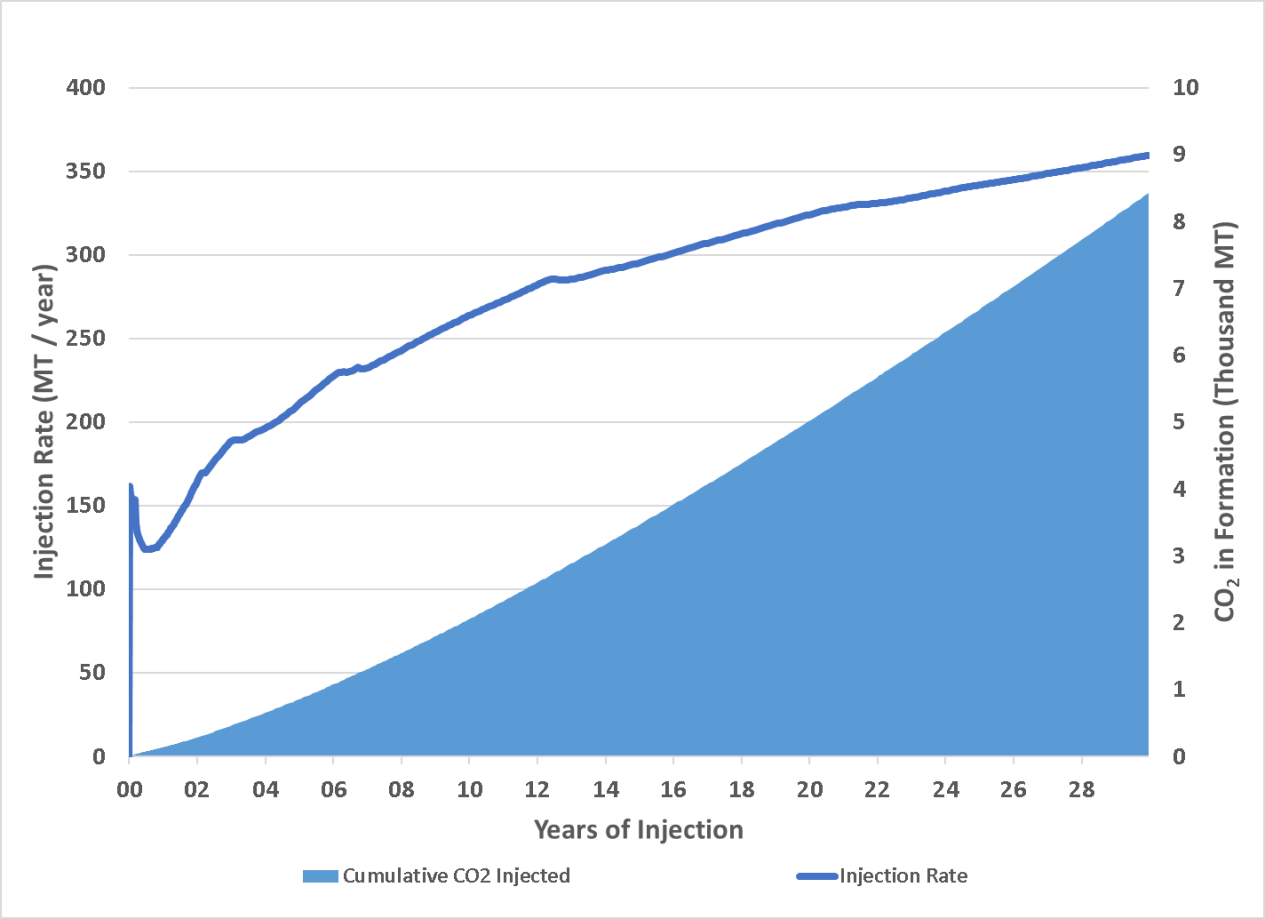

Figure 6-81: Plot of the annualized injection rate of the Northern Appalachian Basin basis well and the Cumulative CO_2 injected into the Potsdam formation after 30 years.

6.3.5.3 Fractured Modelling Approach

Before dismissing this location as unsuitable for commercial scale CO_2-injection – our simulations showed that the Potsdam formation was unable to store even as little as a hundred thousand tons of CO_2 over 30 years – it is worthwhile to examine if the higher effective permeability of the Rose Run (due to the presence of natural fractures) has any impact on improving this site's suitability for CO_2 storage. Note that data constraints are even more extreme in this well; while image logs indicate many high-angle natural fractures within certain isolated sub-layers of the Rose Run, very limited analysis (published literature on well-tests or laboratory measurements) has previously be done on the nature (fracture permeability, porosity, cohesion, etc.) and extent (localized around wellbore vs regionally pervasive) of these natural fractures. **As such, the work described in this and the next sub-sections serves as a preliminary investigation, with the single objective of establishing whether the fracturing in the Rose Run can be harnessed as a store of CO.**

To that end, a slightly different approach to the one applied to the previous two sites was employed. First, a dual-permeability model was used for the Rose Run, Little Falls and Tribes Hill formations, reflecting the close vertical spacing of the fractures encountered in the well. In addition, the image logs were used to further vertically sub-divide each of these formations into fractured and "un-fractured" or intact layers. Second, while the reservoir grid was constructed to the injection zone (Rose Run), intermediate zone (Little Falls and Tribes Hill) and the caprock (lower 400 ft of the Trenton) overlying the basement rock (upper 200 ft of the Gallaway A) as per normal, the geomechanical grid did not include the overburden (rock layers up to the surface) in order to reduce run-times (lower number of gridblocks) for the coupled fluid-flow and reservoir geomechanics simulations. Models were still however, constructed over the 25,000 acre lateral extent. In the same vein, injection of CO_2 was modelled only up to 5 years instead of 30, mainly since the intent was only to investigate if a significant improvement in the injection capacity of the well was possible, but also in light of long simulation run-times (more than 24 hours). Lastly, in lieu of a sensitivity analysis, two scenarios reflecting the major source of uncertainty pertaining to the objective of these simulations were modelled: one where natural fractures occur over the entire lateral extent of the model (Scenario 1), and the second where the rock is fractured only up to a limited area around the well (Scenario 2).

6.3.5.4 Fractured Model Summary

Table 6-27 presents key site-specific inputs to the model. All data has been obtained only from well-log analysis. Formations in blue are in the injection zone, green are in the intermediate zone and red are in the caprock zone. Layers within each formation may be of varying thickness. The permeability values listed represent the average across the number of layers present. Although not listed below, around 200 ft of Gallaway A (see Table 6-26) has been modelled as the basement rock. Table 6-28 presents the fractures modelled in individual layers. Since there was no evidence of fracture sets, all fractures were modelled as equally spaced vertical fractures occurring only in the I direction, as per the Warren and Root Model (1963). The spacing in the I direction is a function of the strike and dip angles of the vertical fractures detected in the image logs. Figure 6-82 shows how the scenario with fractures occurring only at a limited area around the well (Scenario 2) was modelled. CO_2 was injected into the formation with a bottom-hole pressure constraint set at 3500 psi, below regulatory restrictions.

Table 6-27: Key data inputs for coupled fluid-flow – geomechanics simulation for the fractured formations of the Northern Appalachian Basin well.

Formation	Average Depth (ft)	Thickness (ft)	No. of Layers	Average Matrix Porosity	Average Matrix Permeability (mD)	Average Initial Pressure (psi)
Rose Run	6453	187	16	1.3%	0.002	3331
Little Falls	6316	87	4	2.8%	0.015	3297
Tribes Hill	6222	100	5	4.3%	0.04	3251
Trenton	5962	400	20	0.3%	0.02	3181
Formation	**σ_v gradient (psi/ft)**	**σ_H gradient[a] (psi/ft)**	**σ_h gradient[a] (psi/ft)**	**Static Young's modulus[a] (psi)**	**Poisson's ratio**	**Average Initial Pressure (psi)**
Rose Run	1.08	0.95	0.65	8.41E+06	0.21	3331
Little Falls	1.08	1.2	0.8	9.16E+06	0.23	3297
Tribes Hill	1.08	1.2	0.8	9.89E+06	0.26	3251
Trenton	1.08	1.65	0.8	8.35E+06	0.25	3181

a. Gradient values may be different from those presented in Table 4-6, to incorporate data extrapolated from that found in a separate comprehensive study of a well at a different site, but one that was drilled through the Rose Run. (Battelle, 2017)

Table 6-28: Fracture properties for sections of the Tribes Hill, Little Falls and the Rose Run.

Formation	Thickness / ft	Fracture count	Equivalent I-direction fracture spacing / ft	Fracture porosity / %	Fracture permeability / md
Tribes Hill 1	19.3	4	0.4	10%	270
Tribes Hill 2	32.6				
Tribes Hill 3	26.1	21	0.4	10%	270
Tribes Hill 4	15.0				
Tribes Hill 5	7.3	3	0.4	10%	270
Little Falls 1	16.6				
Little Falls 2	6.0	3	0.6	10%	270
Little Falls 3	10.2				
Little Falls 4	54.0	1			
Rose Run 1	22.3				
Rose Run 2	22.8	9	0.5	10%	270
Rose Run 3	9.7				
Rose Run 4	9.0	6	0.3	10%	270
Rose Run 5	9.9				
Rose Run 6	10.6	3	0.4	10%	270
Rose Run 7	27.6				
Rose Run 8	4.1	3	0.4	10%	270
Rose Run 9	9.2				
Rose Run 10	14.0	15	0.2	10%	270
Rose Run 11	4.1				
Rose Run 12	2.7	2	0.2	10%	270
Rose Run 13	12.4				
Rose Run 14	4.1	3	0.3	10%	270
Rose Run 15	14.3				

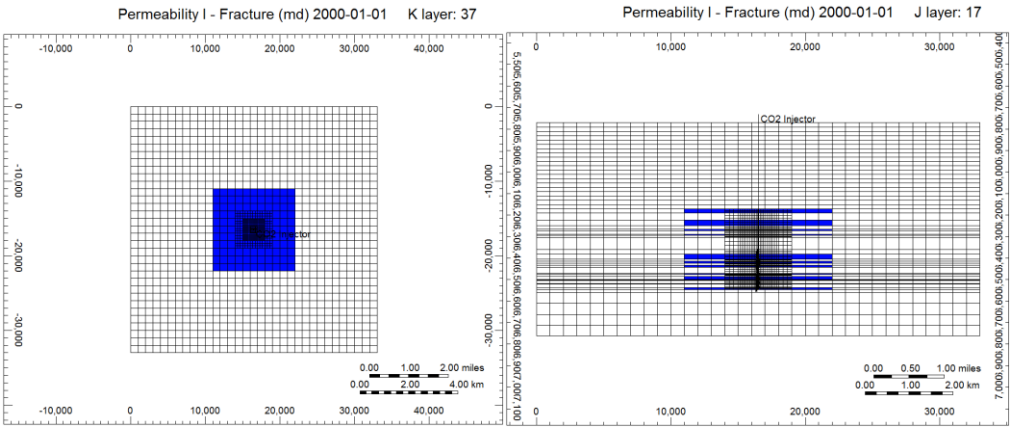

Figure 6-82: Shows an areal cross-section (left) and a vertical cross-section (vertical) of the scenario where the rock is fractured only in a limited area around the well (Scenario 2).

6.3.5.5 Preliminary Fractured Model Simulation Results and Recommendations

Figures 6-83 to Figure 6-87 present the results of simulating the injection of CO_2 into the Rose Run, for a period of 5 years. Figure 6-83 presents the main finding of this feasibility study: the natural fractures have the capacity to store commercial-scale volumes of CO_2. In the optimistic scenario (Scenario 1) where the entire Rose Run is fractured, nearly 10 million tons are stored. Even in the more limited scenario (see Figure 6-82), around 3 million tons of storage is achieved. By virtue of storing more CO_2, the amount of pressurization of the Rose Run is greater in the scenario with regional-scale fractures (175 psi) than the localized-fractures scenario (100 psi). Figure 6-84 represents the stresses in the Rose Run before and after injection, for Scenario 1. Using a moderate value of 1000 psi for fracture cohesion, and considering the distance of the Mohr's circles from the shear failure envelope and the origin, neither shear failure nor tensile failure has occurred. Note that the Mohr's circles after 5 years appear to have shrunk (as well shifted to the left), indicating poro-elastic effects. Figure 6-85 shows the spatial distribution CO_2 in the Rose Run after 5 years of injection, for Scenario 2. The CO_2 is found mainly in the sub-layers that are fractured. Figures 6-86 and Figures 6-87 show the spatial distribution of the increase in pore-pressure and the associated (magnitude of) reduction in the minimum horizontal stress respectively, for Scenario 1. Figure 6-86 shows that the pore-pressure increase decays radially outward from the well from around 500 psi in the immediate vicinity of the well to around 300 psi around 10,000 ft from the well. This however corresponds to a reduction of only 200 psi of reduction in the minimum horizontal stress in the immediate vicinity of the well and about 60 psi around 10,000 ft from the well. The discrepancy between the two sets of values re-affirms the finding suggested by Figure 6-84 of significant poro-elasticity.

These promising results – multiple millions of tons of CO_2 injected, accompanied by only a mild increase in pressure and strong poro-elastic effects that prevent shear/tensile failure – suggest that the natural fractures in the Rose Run can have a potentially transformative effect on the viability of this site for CO_2 storage purposes (compared to Figure 6-81). This encouraging finding merits deeper investigation as a follow-up such as: core/well-testing to quantify the nature (porosity, permeability, dimensions, etc.) and lateral extent of the natural fractures in all three of the Rose Run, Little Falls and Tribes Hill formations, other forms of testing to constrain estimates of geomechanical parameters, and a more detailed coupled fluid-flow and reservoir geomechanics simulation study for a more quantitative assessment of effective storage capacity.

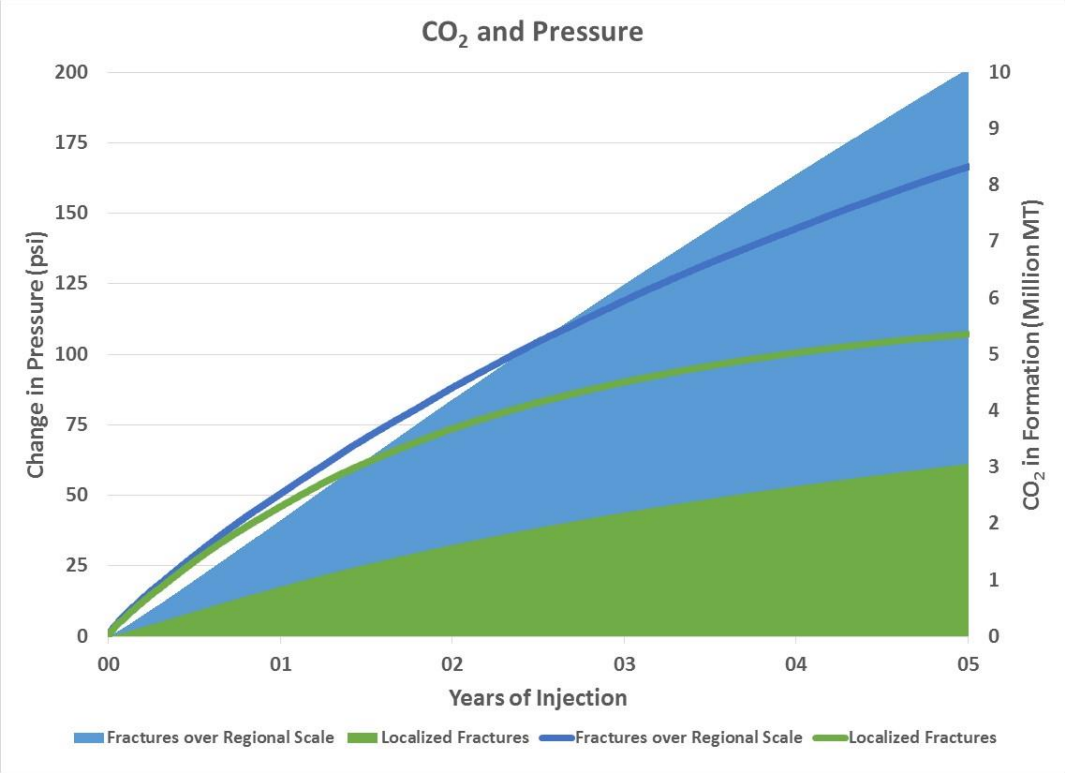

Figure 6-83: Shows the amount of CO_2 stored and the accompanying increase in the average reservoir pressure of the Rose Run, in both the scenarios.

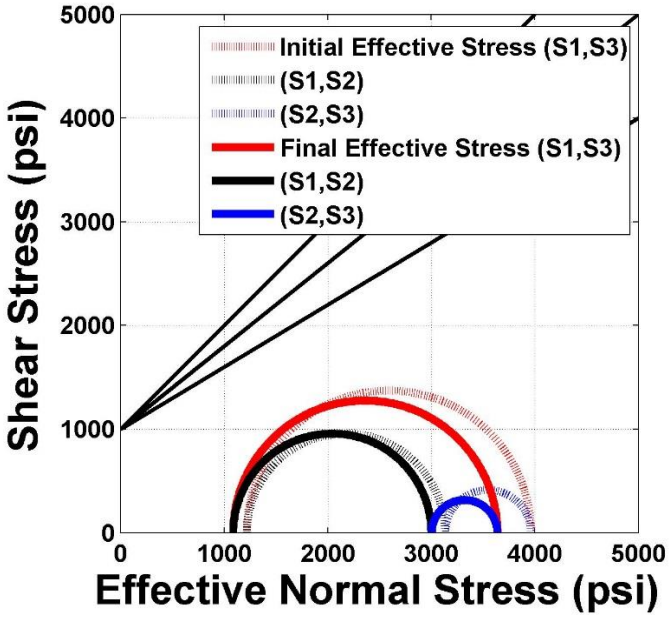

Figure 6-84: Mohr's Circles are drawn to represent the stresses in the Rose Run caprock, before and after 5 years injection. These are the stresses from the model with regional-scale fracturing.

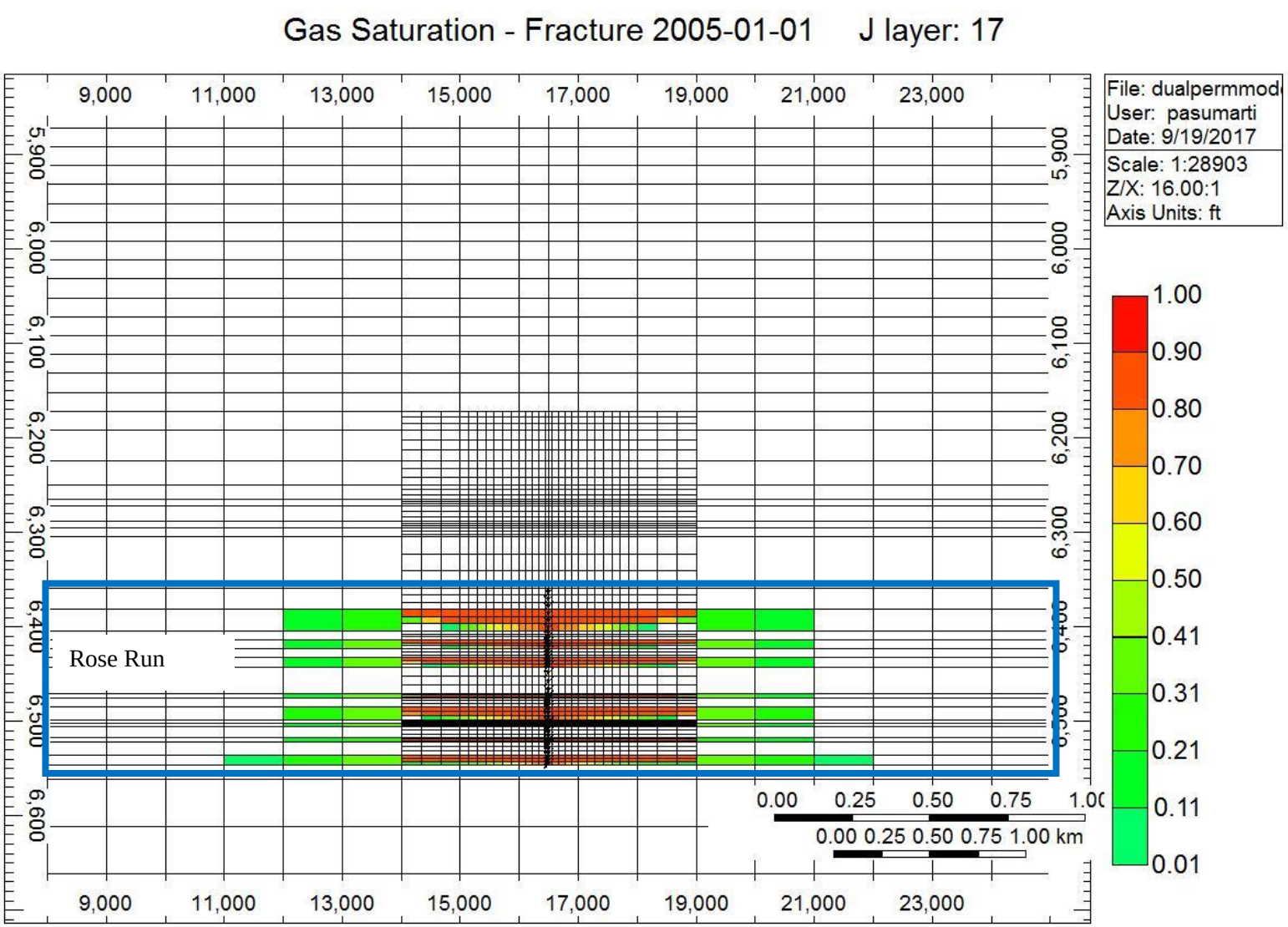

Figure 6-85: Shows a vertical cross-section through Rose Run of the gas saturation. This is the scenario where the fractures in the model are limited to an area around the well. The injected CO_2 has penetrated laterally only within the sub-layers with fractures in them.

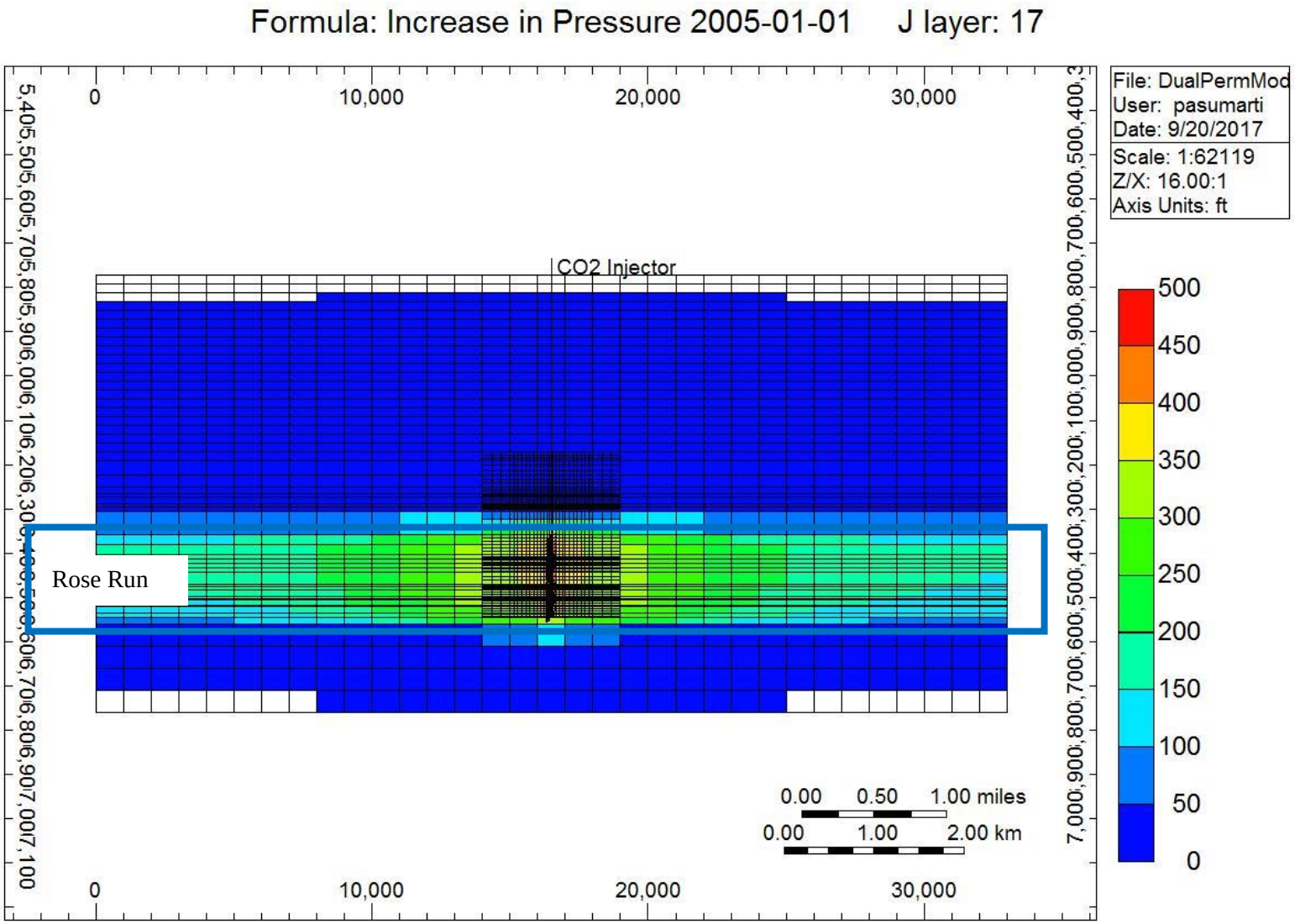

Figure 6-86: The amount of pressure increase attained in the subsurface after 5 years of injection into the Rose Run, is shown via a cross-section through the middle of the fluid-flow grid.

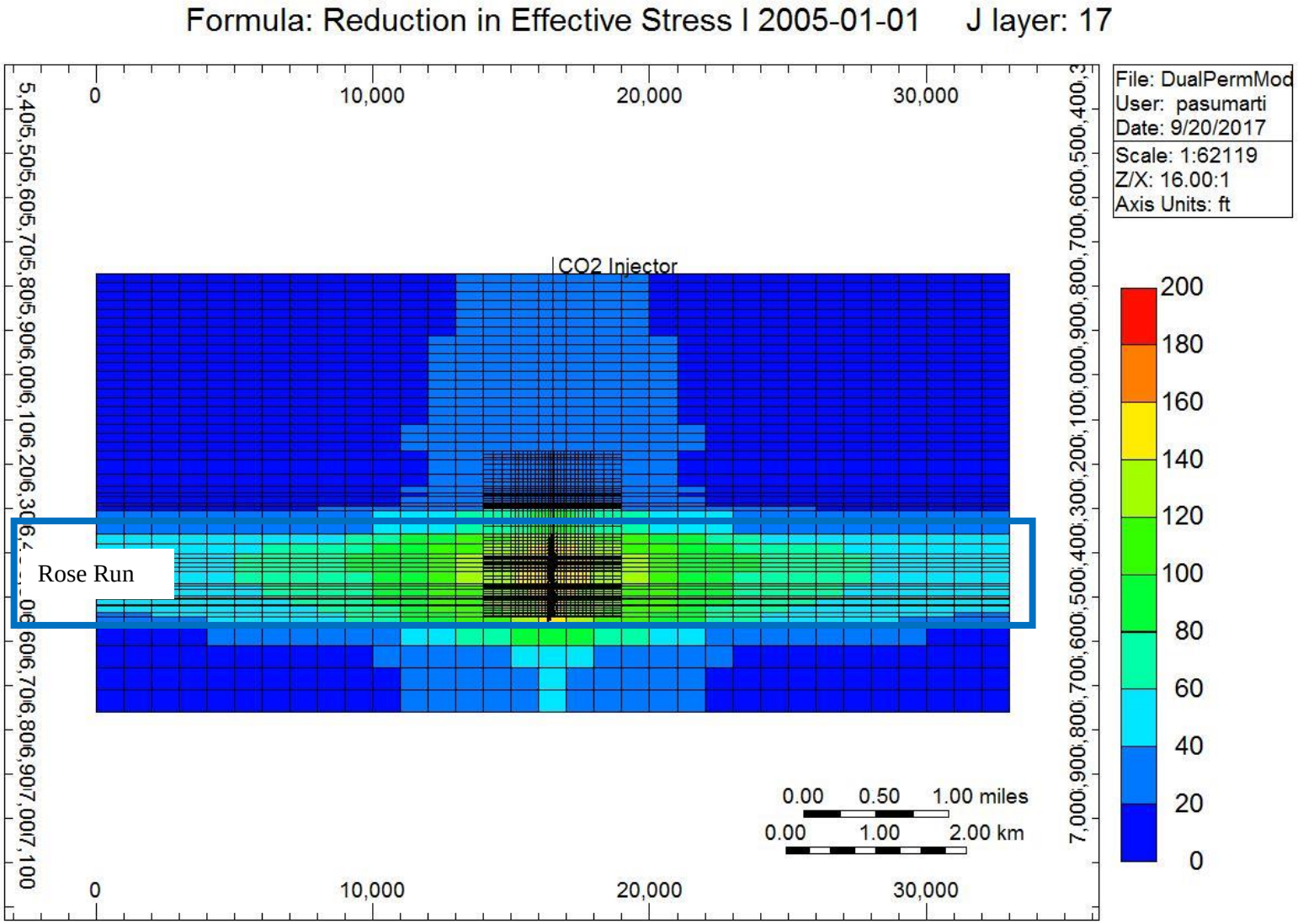

Figure 6-87: The reduction in the minimum horizontal effective stress occurring in the subsurface after 5 years of injection into the Rose Run, is shown via a cross-section through the middle of the fluid-flow grid.

7.0 CO_2 Storage/Shale Gas Risk Factor Assessment

The objective of this task was to evaluate the interaction of CO_2 storage and shale gas development for the region. The task involved mapping CO_2 storage zones and shale gas plays. Based on this information, risk factors were classified according to the potential impact of shale gas development on CO_2 storage zones. Shale gas development with hydraulic fracturing has resulted in over 13,000 new wells in the Utica shale and Marcellus shale in the Appalachian Basin. These layers are also part of the series of shale and carbonate rocks, overlying CO_2 storage intervals such as the Knox Group, Mount Simon, and other zones. Penetration of the hydraulic fractures into the immediate containment zones could impact CO_2 storage security.

Traditional vertical oil and gas wells in this region were often subjected to hydraulic fracturing to increase production, but the treated zone was generally limited to the area near the borehole. Hydrocarbon production from shale gas rock formations requires drilling horizontal wells and large-volume hydraulic fracturing of the rock matrix surrounding the well path. Unconventional shale gas wells are up to 15,000 ft long with 20 to 75 fracture stages, and they affect a large lateral area in the subsurface. As of early 2016, more than 13,000 unconventional shale gas wells had been drilled in the Midwest United States. Consequently, it is important to assess where these hydraulically fractured volumes may intersect promising CO_2 storage zones.

7.1 Geologic Framework and CO_2 Storage Zones

A geologic framework model was developed to show the relationship between CO_2 storage zones, caprock layers, large CO_2 sources, and shale gas wells. This geologic model (Figure 7-1) was based on maps for major deep saline formations, caprocks, and hydrocarbon intervals. The model illustrates the major structures, formation thickness, and depths of the geologic layers. It includes key structural surface maps for the Precambrian surface, Cambrian age rocks, Utica shale, above Utica (Upper Ordovician-Lower Devonian), Marcellus shale, Devonian shale, and post-Devonian rocks. The framework model illustrates the regional structures along with the thickness of the key units and ground surface. As shown, the shale gas plays are fairly thin layers in relation to the entire sedimentary column. The geologic model was used to show the 3D trajectory of shale gas wells.

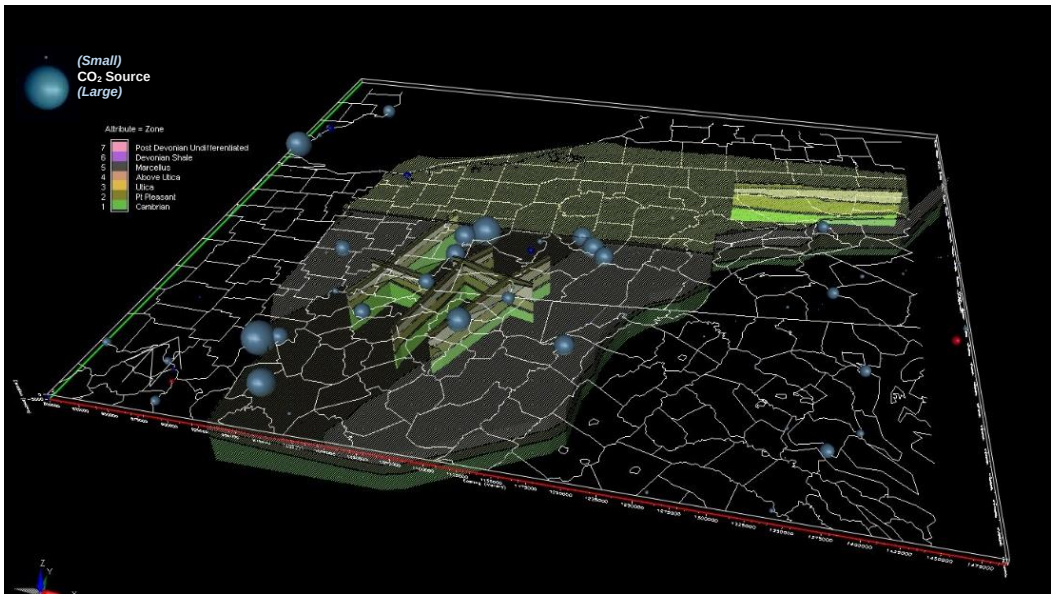

Figure 7-1: Earthvision geologic model for shale gas plays in the Midwest United States.

7.2 Shale Gas Plays in the Midwest United States

Organic rich shales are considered source rock for much of the hydrocarbon present in the Midwest United States, but the rock formations did not have the reservoir quality for conventional production methods. Horizontal drilling and large-volume hydraulic fracturing technologies allowed operators to effectively produce from these intervals. As of early 2016, more than 13,000 horizontal shale gas wells had been drilled in the region, mostly in the Marcellus and Utica-Point Pleasant formations. Operators have expanded horizontal drilling to other organic shales (Geneseo, Rhinestreet, Burkett) and other formations (Berea, Clinton-Medina). Consequently, the impact of unconventional hydrocarbon production will likely extend into additional rock formations.

The Devonian age Marcellus Formation is an organic shale present in the lower portion of the thick Devonian shale interval. The formation is present throughout most of the Appalachian Basin, but the thickest portions are in north-central Pennsylvania, southwestern Pennsylvania, and northern West Virginia. In these areas, the Marcellus is approximately 6,000 ft to 8,000 ft deep and forms a northeast-southwest oriented fairway where most wells are located. The Marcellus Formation produces mainly dry gas. October 2016 Marcellus production was approximately 18 billion cubic feet (Bcf) per day natural gas and 38,000 barrels per day (bbl/day) oil. Resource estimates for the Marcellus range from 42 to 144 trillion cubic feet (Tcf) gas per USGS (2011) to 229 to 489 Tcf gas in other assessments (Zagorski et al., 2012). For comparison, total historical gas production in the Midwest United States up to the early 2000s was on the order of 50 Tcf.

The Utica-Point Pleasant play includes a series of Upper Ordovician strata in the Appalachian Basin. As noted in the *Geologic Play Book for Utica Shale Appalachian Basin Exploration* (Patchen and Carter, 2015): “The most productive hydrocarbon source rocks tend to be the Point Pleasant Formation and the upper and Logana members of the Lexington/Trenton Formation.”

These units are located stratigraphically below the proper Utica shale formation. The units generally consist of interbedded limestones and black shales. Most operators attempt to land horizontal wells at the base of the overall Utica-Logana interval to fracture across the entire sequence. The main

production fairway for this field is present in eastern Ohio, stretching from Trumbull County to Washington County where the play is approximately 7,000 ft to 9,000 ft deep. There is more oil and natural gas liquids production in the western portion of the fairway, with dry gas production located toward the eastern portion of the fairway. October 2016 Utica-Point Pleasant production was approximately 3.6 Bcf per day natural gas and 69,000 bbl/day oil. Resource estimates for the Utica-Point Pleasant range from 75 to 398 million barrels (MMbbl) oil and 21 to 61 Tcf gas per USGS (2011) to 1,960 MMbbl oil and 782.2 Tcf gas in the Utica Shale Play Book Study (Patchen and Carter, 2015).

7.2.1 Horizontal Well Mapping

To depict the total extent of unconventional shale gas wells in the subsurface, the well trajectories were added to the 3D geologic model. Well paths were based on well top-hole and bottom-hole locations from state oil and gas databases. The precise well pathway was not plotted since this information is not always readily available for wells. Therefore, wells appear as straight line paths from wellhead to bottom-hole location, even though most wells follow a more complicated pathway. However, the approach is suitable for regional analysis.

Data for horizontal shale gas wells in Ohio were obtained from the Ohio Department of Natural Resources (ODNR) Division of Oil & Gas Resources database (ODNR, 2017). Data for horizontal oil and gas wells in West Virginia were obtained from the West Virginia Geological and Economic Survey data files for West Virginia Horizontal Wells (WVGES, 2017). Data for Pennsylvania horizontal wells were obtained from the West Virginia GIS Technical Center Unconventional Resources Atlas (WVGISTC/NETL, 2017). Data for New York wells were obtained from the New York State Department of Environmental Conservation Oil & Gas Searchable Database (NYSDEC, 2017). All data were collected circa December 2016, and additional wells have been drilled since this research.

Figure 7-2 shows Marcellus shale drilled as of Fall 2015. The map illustrates where unconventional well density is highest in portions of northern West Virginia, southwest Pennsylvania, and northeast Pennsylvania. The map also shows the approximate subsurface path of the wells. It should be noted that approximately 20% of the Marcellus wells have been drilled but not completed for production via hydraulic fracturing.

Figure 7-3 shows the location and well paths for Utica-Point Pleasant wells as of fall 2015. Unconventional Utica-Point Pleasant wells are concentrated in portions of east-central Ohio. Approximately 20% of the Utica-Point Pleasant wells have not been completed via hydraulic fracturing for production. In general, Utica-Point Pleasant drilling is more limited in overall areal extent than the Marcellus.

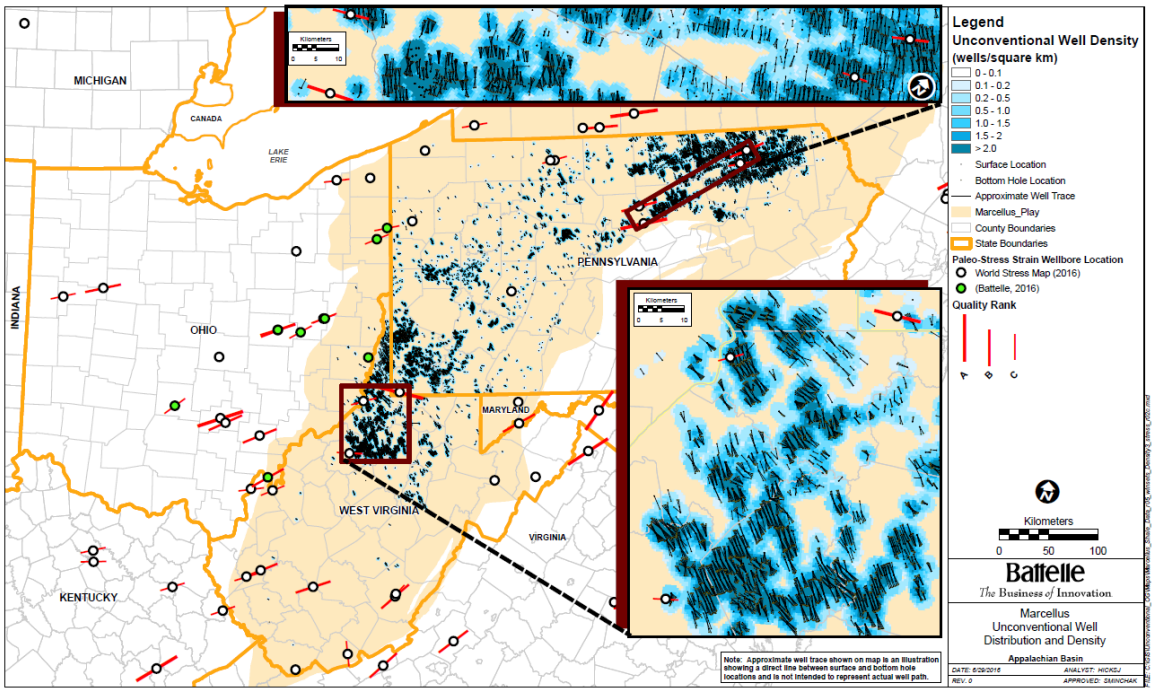

Figure 7-2: Marcellus unconventional well distribution and density as of fall 2015.

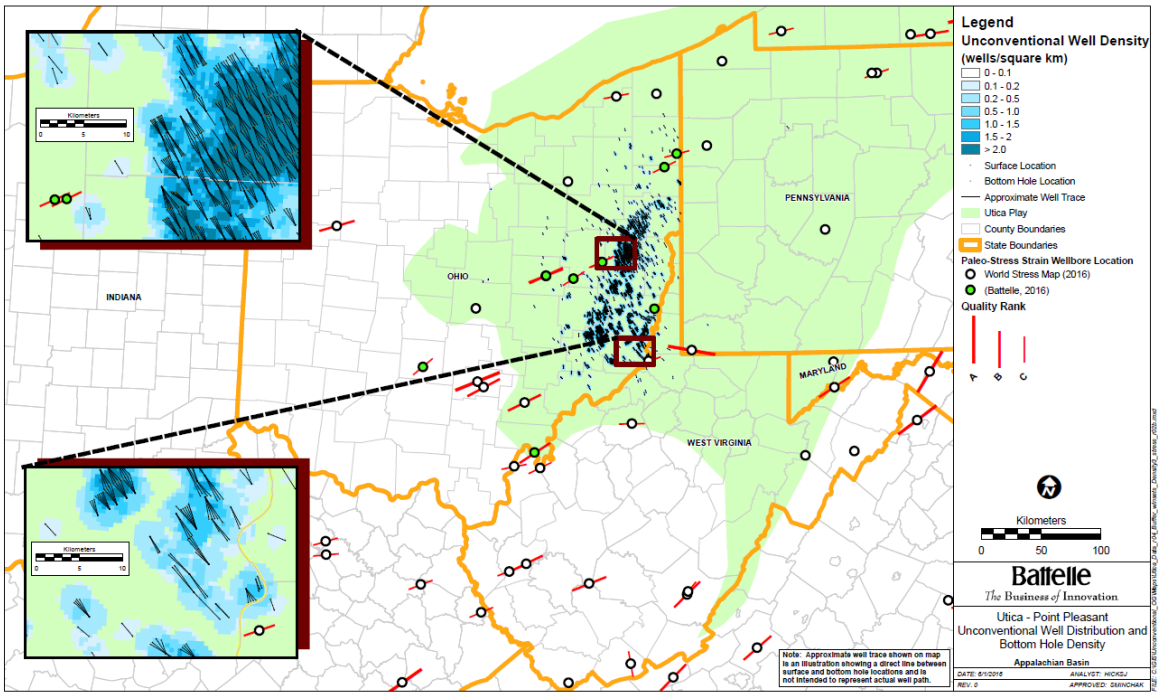

Figure 7-3: Utica-Point Pleasant unconventional well distribution and density as of fall 2015.

Figure 7-4 summarizes wells' horizontal length based on review of reported top-hole and bottom-hole locations for Marcellus and Utica horizontal shale gas wells. As listed, a total of 10,719 Marcellus wells with available bottom-hole data were collected. Marcellus wells had an average horizontal length of 5,668 ft and maximum listed length of 14,995 ft. A total of 2,114 Utica-Point Pleasant wells with available bottom-hole data were identified. Utica-Point Pleasant wells had an average horizontal length of 7,258 ft and maximum length of 14,280 ft.

Marcellus Statistics

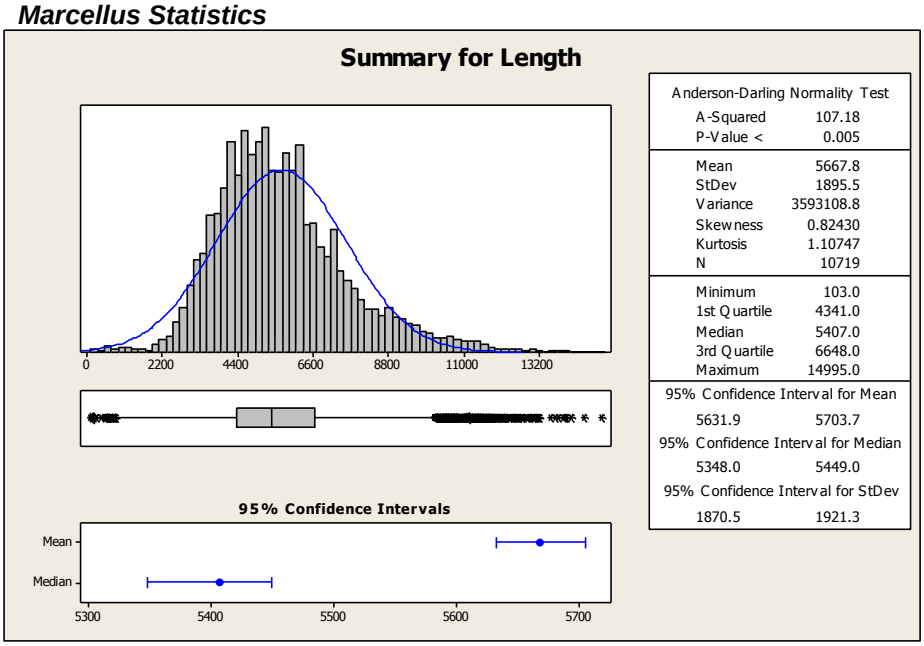

Utica-Point Pleasant Statistics

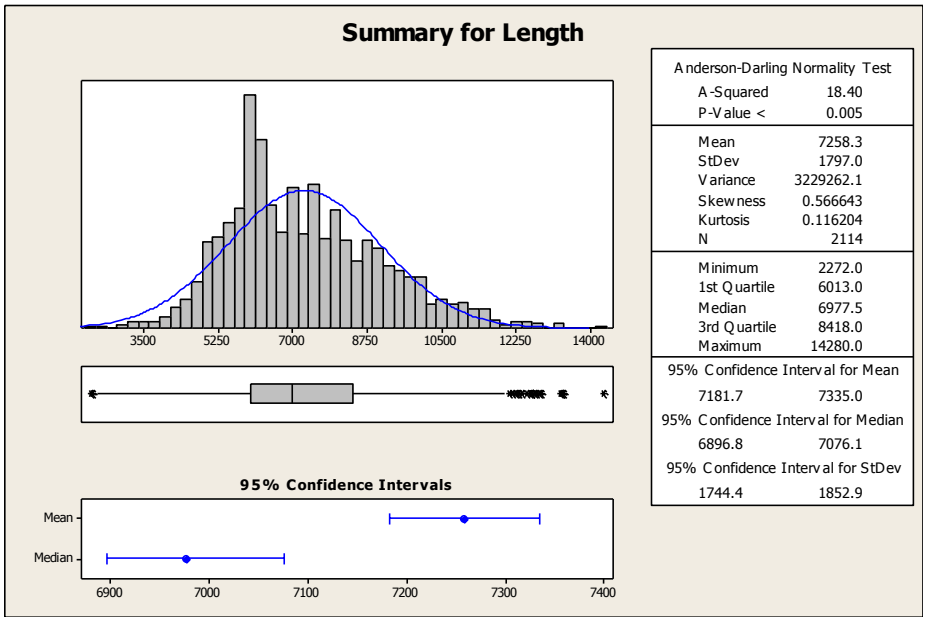

Figure 7-4: Well length statistics for Marcellus and Utica-Point Pleasant horizontal wells compiled for this project.

7.2.2 Horizontal Well Stimulated Reservoir Volume Mapping

Many oil and gas companies, service companies, and researchers have investigated the fracture patterns created by large-volume hydraulic fracturing in horizontal wells (Blanton, 1986; Maxwell et al., 2002; Detournay, 2004; Gu and Siebrits, 2008; Jeffrey et al., 2009; Xu et al., 2009; Chuprakov et al., 2010; Fisher, 2010; Warpinski, 2010; Ciezobka, 2011; Hammack et al., 2014; Abbas et al., 2014; Weng, 2015). That effort has proven to be a challenge because the fractures are located deep underground where direct observation is not possible. Many operators have deployed microseismic monitoring to track seismic effects during hydraulic fracturing jobs. In addition, reservoir simulators and well treatment programs have been used to provide numerical prediction of the stimulated reservoir volume (SRV) based on treatment materials and rock properties. However, the SRV is difficult to determine. Each well and fracture stage may exhibit a different fracture pattern due to geologic variations, treatment fluids, stage pattern, pressure/rate, proppant, and many other factors.

To accomplish the well mapping across the 13,000+ horizontal wells in the Appalachian Basin, it was assumed that all wells have a similar lateral and vertical extent for their SRV. Based on research by Hammack et al. (2014) on Marcellus shale horizontal wells, the SRV extended in a radial pattern approximately 1,000 ft laterally from the well. Data from Fisher (2010) on the vertical height of SRV for Marcellus wells averaged approximately 500 ft. Consequently, fracture width was set at 1,000 ft on both sides of the horizontal well and fracture height was specified as 500 ft (Figure 7-5).

With many horizontal shale gas wells having 20 to 75 treatment stages, the conceptual model for the SRV is a sort of fracture-tunnel running along the length of the horizontal well (Figure 7-6). In practice, fracture jobs will all have somewhat different geometry based on many factors such as treatment volume, treatment materials, treatment pressure schedule, well orientation, geomechanical properties of the rocks, and many other influences. However, it was not possible to evaluate over 200,000 stages of treatment, so a general SRV was applied. In addition, each fracture stage is not likely interconnected, because this would result in “losing” the fracture job (called “frac hits”) where fracture pressure migrates into a previous fracture stage and bypasses the target treatment zone.

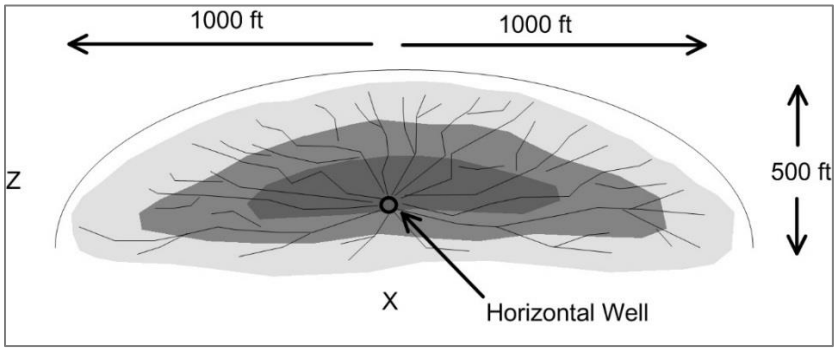

Figure 7-5: Conceptual diagram of SRV for typical Marcellus/ Utica-Point Pleasant hydraulic fracture treatment stage.

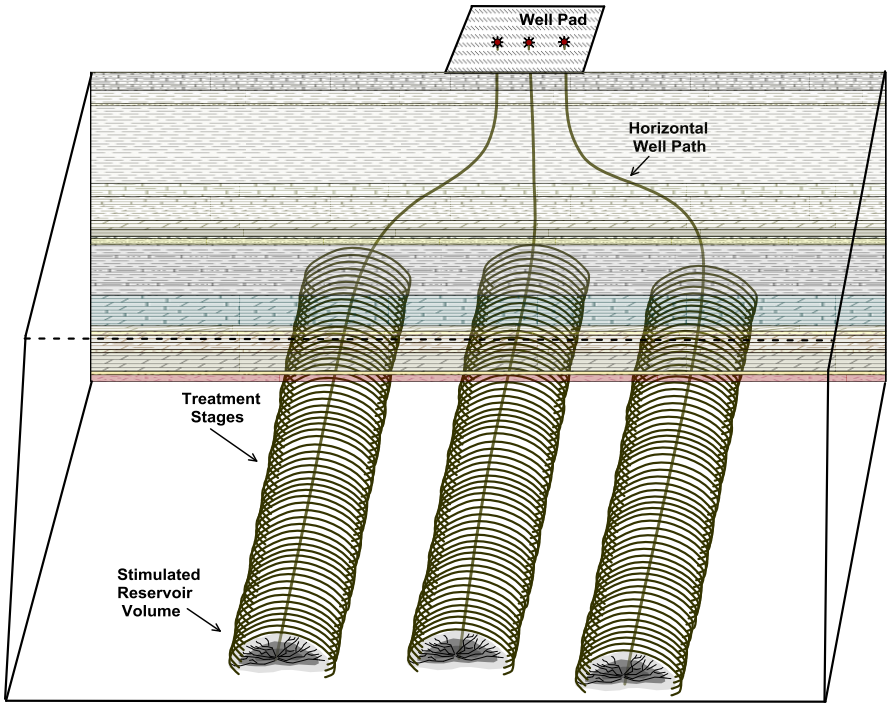

Figure 7-6: Conceptual diagram of multiple treatment stages along three horizontal wells.

To depict the subsurface footprint of the horizontal wells, the well paths were added to the 3D geologic model. Each well was depicted as a 1,000-ft-wide and 500-ft-high SRV from top-hole to bottom-hole location. The visualization shows the collective extent of the wells in relation to other geologic units. Figure 7-7 shows the regional extent of the horizontal wells. As shown, there are fields of Marcellus wells concentrated in northeastern and southwestern Pennsylvania. Marcellus wells are also present in northern West Virginia. Utica-Point Pleasant wells are concentrated in east-central Ohio.

Figures 7-8 through 7-14 show closer 3D model views of horizontal wells drilled at selected locations in the region. All maps illustrate how operators generally drill wells in the direction of minimum horizontal stress (S_{hmin}) to ensure maximum SRV.

- Figure 7-8: view of horizontal wells along the Ohio River Valley.
- Figure 7-9: zoomed-in east-west view of Marcellus wells in northeastern Pennsylvania, where there is a large area of development in the formation.
- Figure 7-10: east-west view of wells in southwestern Pennsylvania, illustrating the well geometries on a local scale.
- Figure 7-11: long, north-south view of wells through northern West Virginia and southwestern Pennsylvania adjacent to the Ohio River Valley.
- Figure 7-12: north-south transect in eastern Ohio with Utica-Point Pleasant wells.
- Figure 7-13: view of multi-layered shale gas wells, where both the Marcellus and Utica-Point Pleasant have been developed off the same well pad.
- Figure 7-14: tract along the Ohio River where the Marcellus and Utica-Point Pleasant overlap.

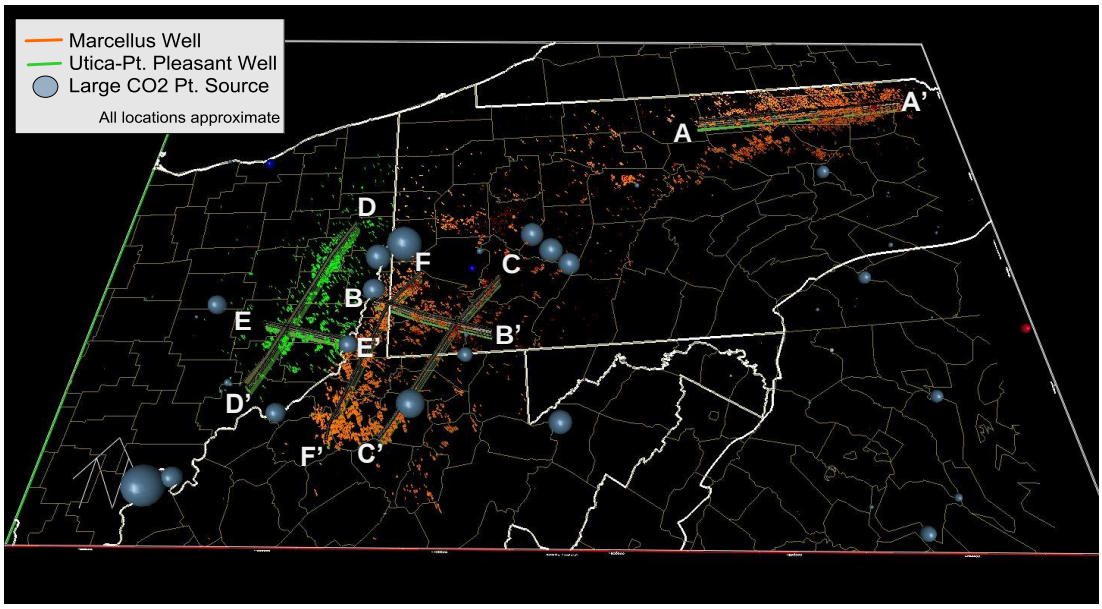

Figure 7-7: 3D model illustrating horizontal wells in the Appalachian Basin.

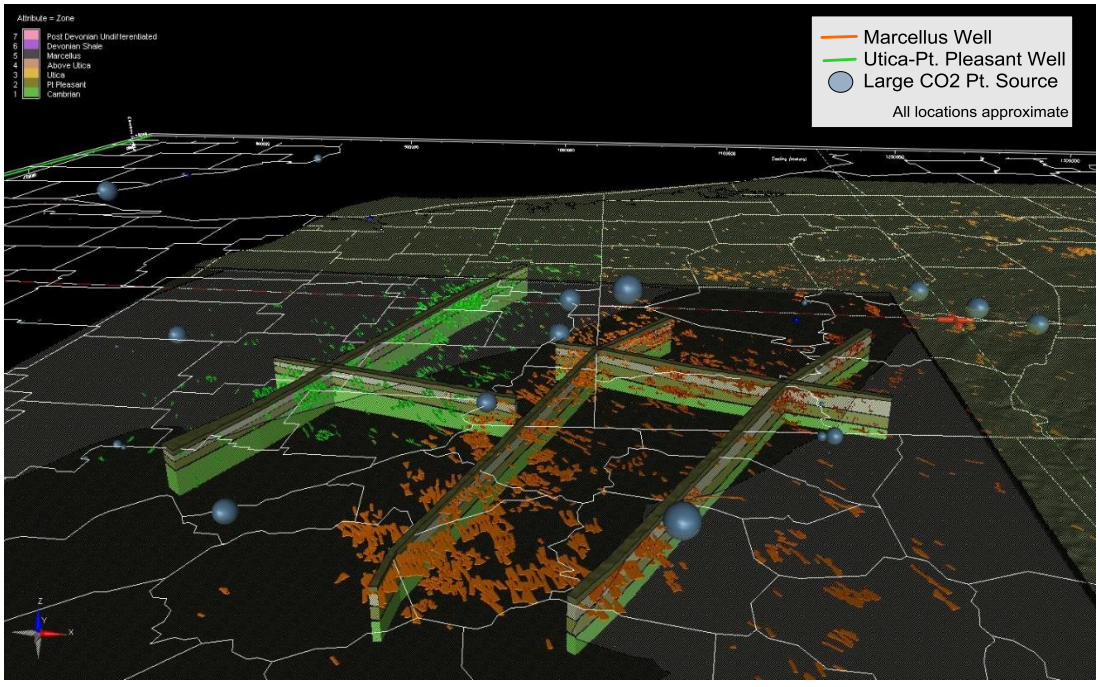

Figure 7-8: 3D model illustrating horizontal wells along the Ohio River Valley.

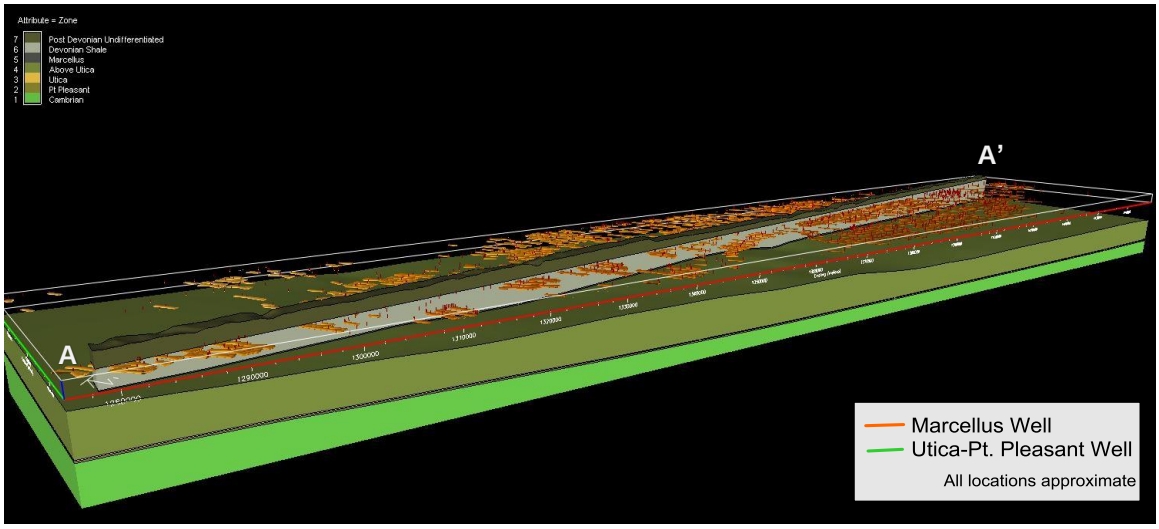

Figure 7-9: 3D model illustrating Marcellus horizontal wells in northeast Pennsylvania.

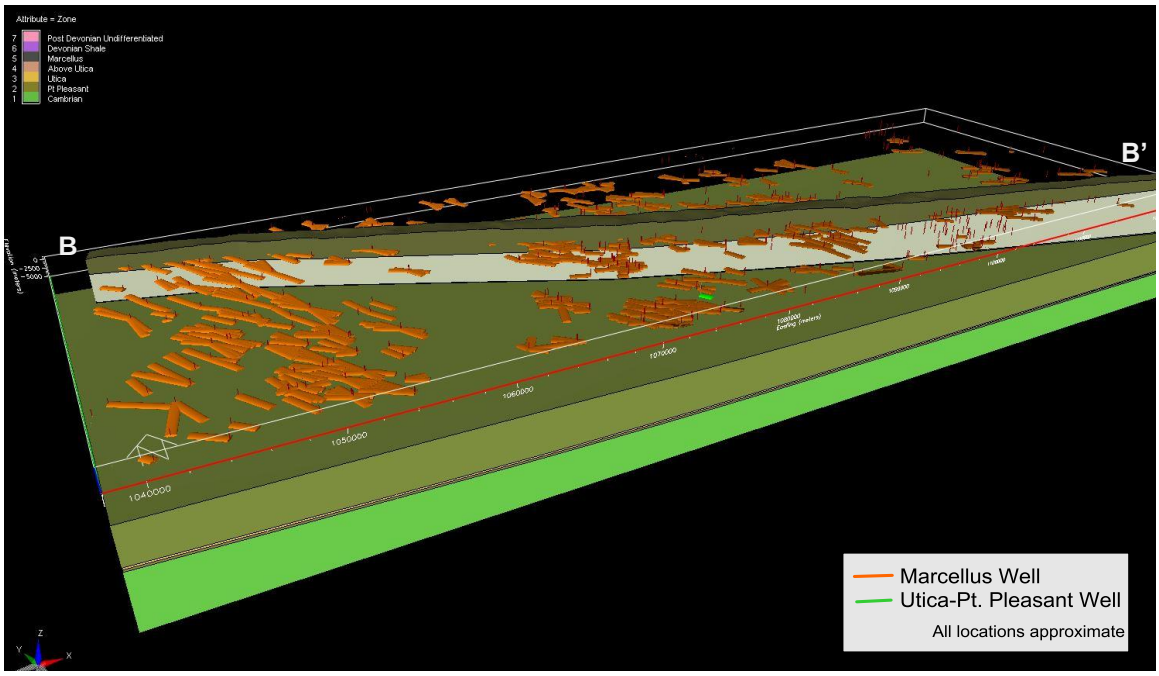

Figure 7-10: 3D model illustrating Marcellus horizontal wells in southwest Pennsylvania.

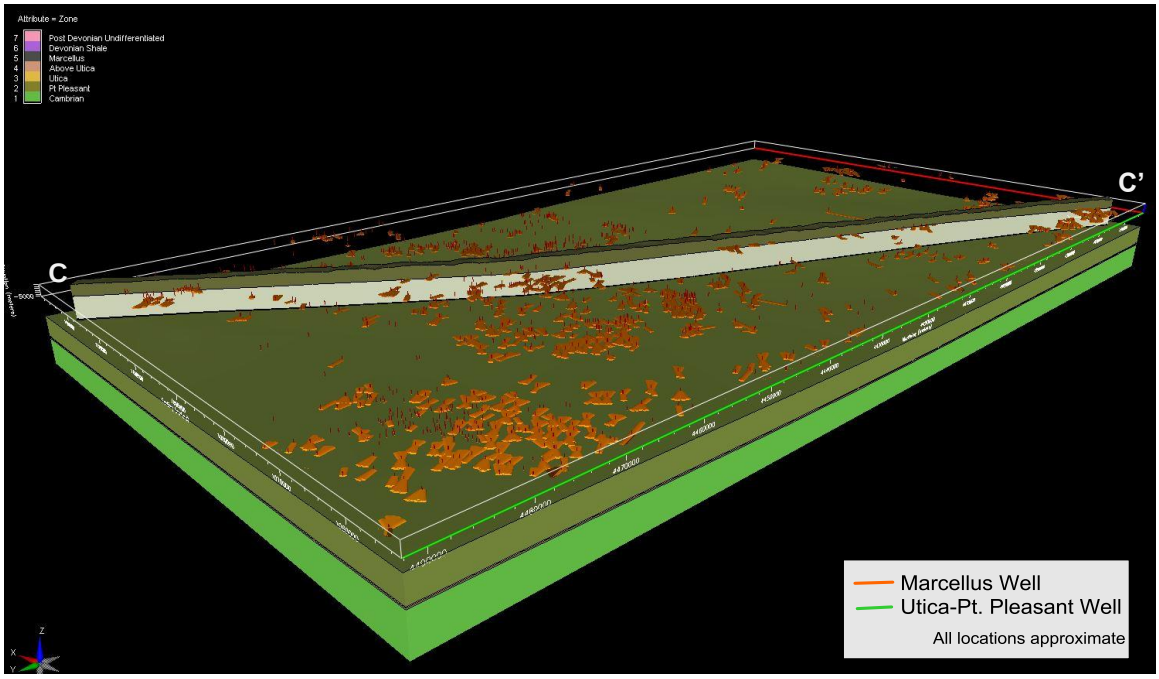

Figure 7-11: 3D model illustrating Marcellus horizontal wells in northern West Virginia and southwestern Pennsylvania.

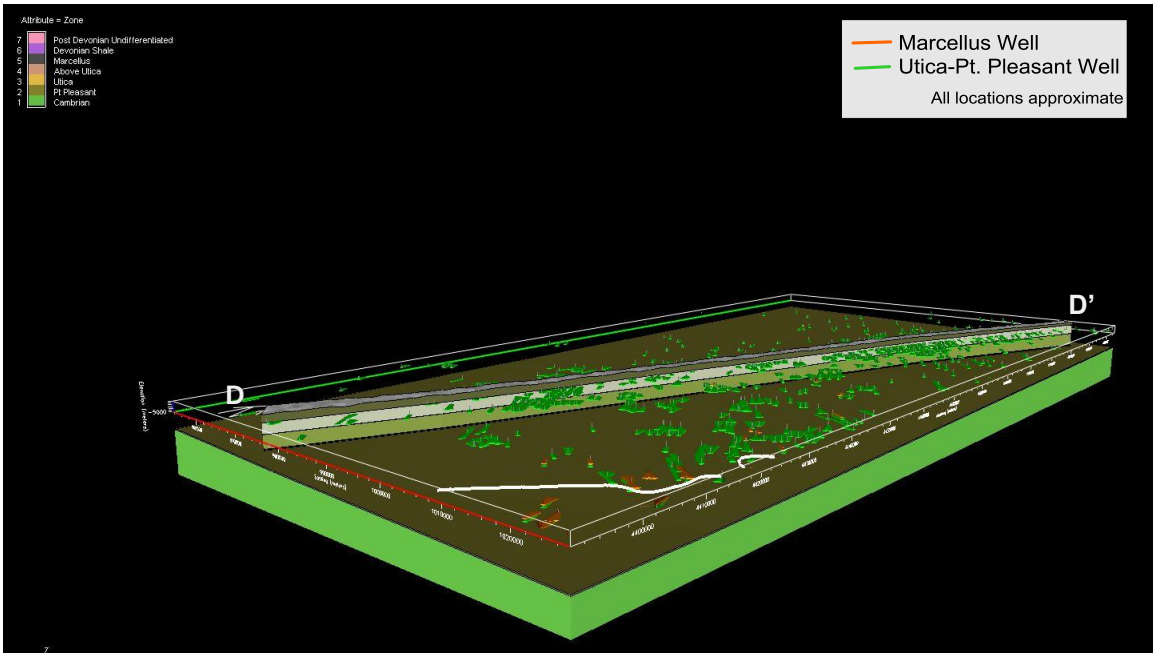

Figure 7-12: 3D model illustrating Utica-Point Pleasant wells in eastern Ohio.

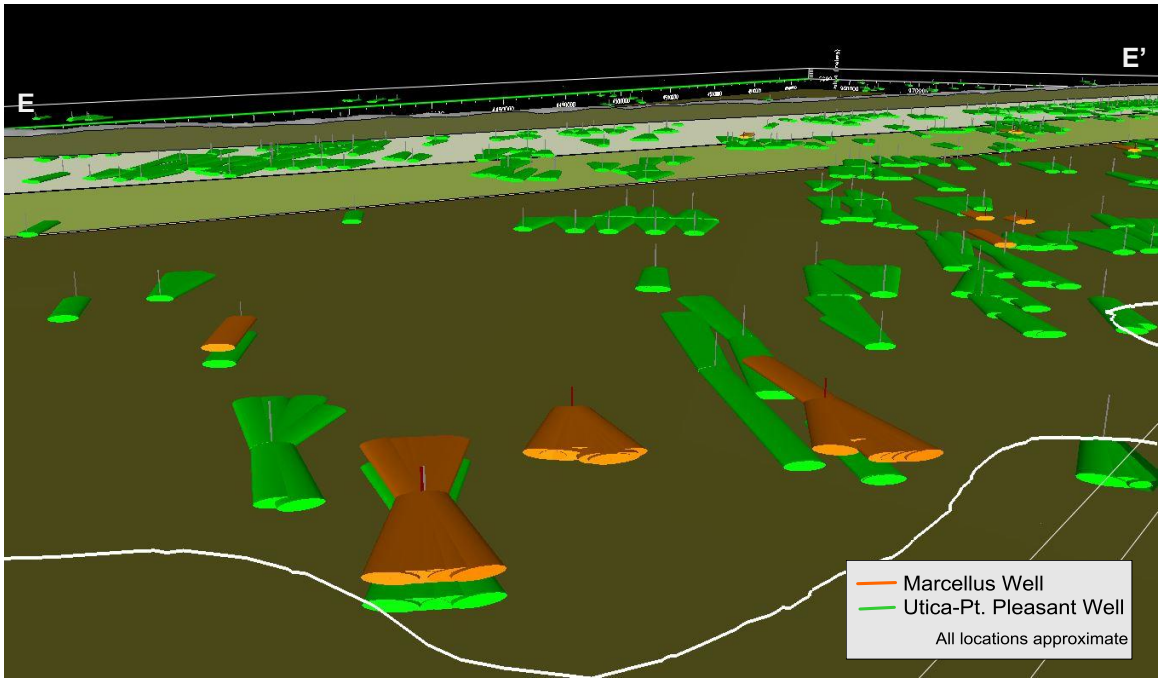

Figure 7-13: 3D model illustrating multi-layered Marcellus and Utica-Point Pleasant horizontal wells.

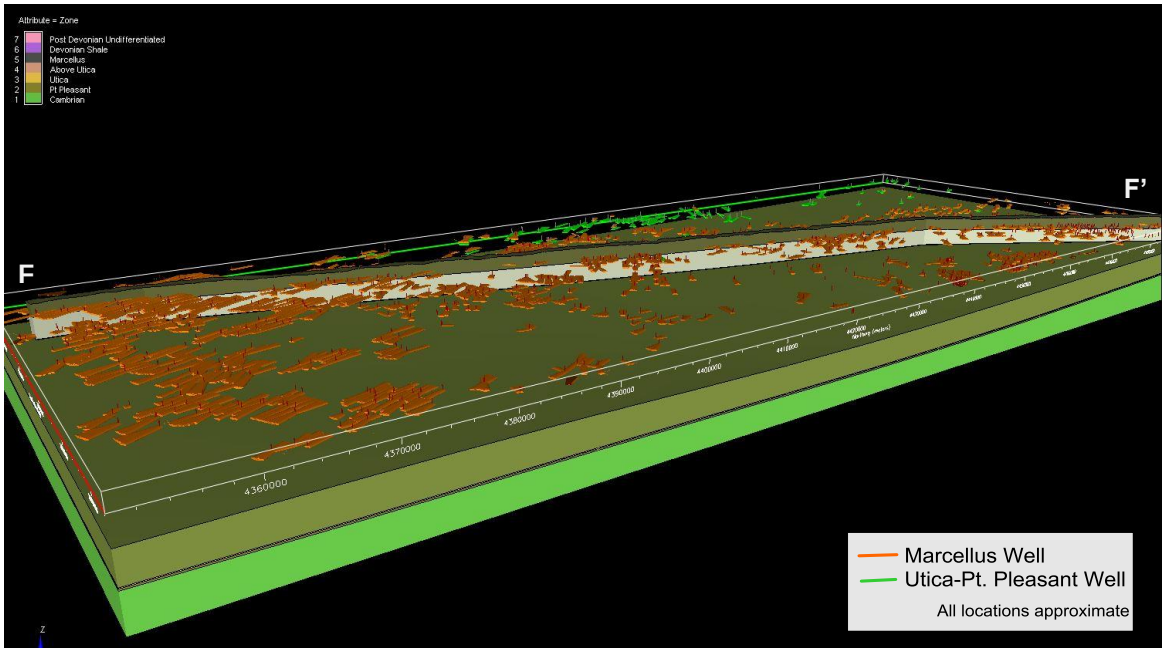

Figure 7-14: 3D model illustrating Marcellus and Utica-Point Pleasant horizontal wells along the Ohio River Valley.

7.3 Classification of Risk Factors Related to CO_2 Storage and Shale Gas Development

CO_2 storage in deep rock formations near shale gas development may involve risk factors related to the hydraulic fractures and stress changes near the horizontal wells. These changes may affect a large zone in the subsurface compared to conventional wells. Fractures created by shale gas wells could extend into caprock zones, creating migration pathways for CO_2. Stress changes near highly fractured intervals could affect the subsurface geomechanical conditions, leading to instability under certain scenarios. Therefore, classification of risk factors related to CO_2 storage and unconventional shale gas development provides guidance for evaluating interactions of these technologies.

7.3.1 Caprock Integrity

One concern for CO_2 storage applications near areas of shale gas development is hydraulic fractures extending into caprocks. These fractures may provide migration pathways for upward and lateral CO_2 migration. Several researchers have investigated the vertical extent of hydraulic fractures in relation to near-surface groundwater resources (Hammack et al., 2014). In general, these studies have concluded that fractures created by shale gas wells are isolated in the deep rock zones, with no effect on groundwater resources. Many other researchers have examined the effect of CO_2 saturation on caprock properties and the potential for CO_2 injection to cause fractures in caprocks. However, few studies have compared the extent of unconventional shale gas wells' hydraulic fractures in relation to CO_2 storage zones.

To outline the relationship of hydraulic fractured zones and CO_2 storage intervals, geologic columns were developed for typical Marcellus and Utica-Point Pleasant wells. The Marcellus well was based on wells in northern West Virginia, where the Marcellus is present at depths of approximately 7,000 ft to 8,000 ft below ground surface. As shown in Figure 7-15, the Marcellus shale gas wells affect a limited interval at the base of a thick Devonian age shale. Figure 7-16 illustrates how Marcellus wells overlie the Oriskany sandstone, which is a potential CO_2 storage zone. However, the Onondaga and Huntersville formations separate the Oriskany from the Marcellus. In general, the Onondaga limestone and Huntersville chert are competent rock formations, or "fracture barriers," that are not likely to be fractured. In addition, hydraulic fractures are most likely to propagate upward and outward according to the subsurface stress distribution.

Figure 7-17 shows a geologic column for a typical Utica-Point Pleasant well. The well was based on typical geology for Utica-Point Pleasant wells in east-central Ohio. As shown, the Utica-Point Pleasant has thick confining layers above and below the targeted shale gas interval. The Kope and Queenston shales have combined thickness over 1,000 ft above the typical Utica-Point Pleasant stimulated interval. The Trenton-Black River-Well Creek interval is located beneath the Utica-Point Pleasant, with combined thickness over 800 ft. Overall, the Utica-Point Pleasant is separated from any major CO_2 storage zones or caprocks.

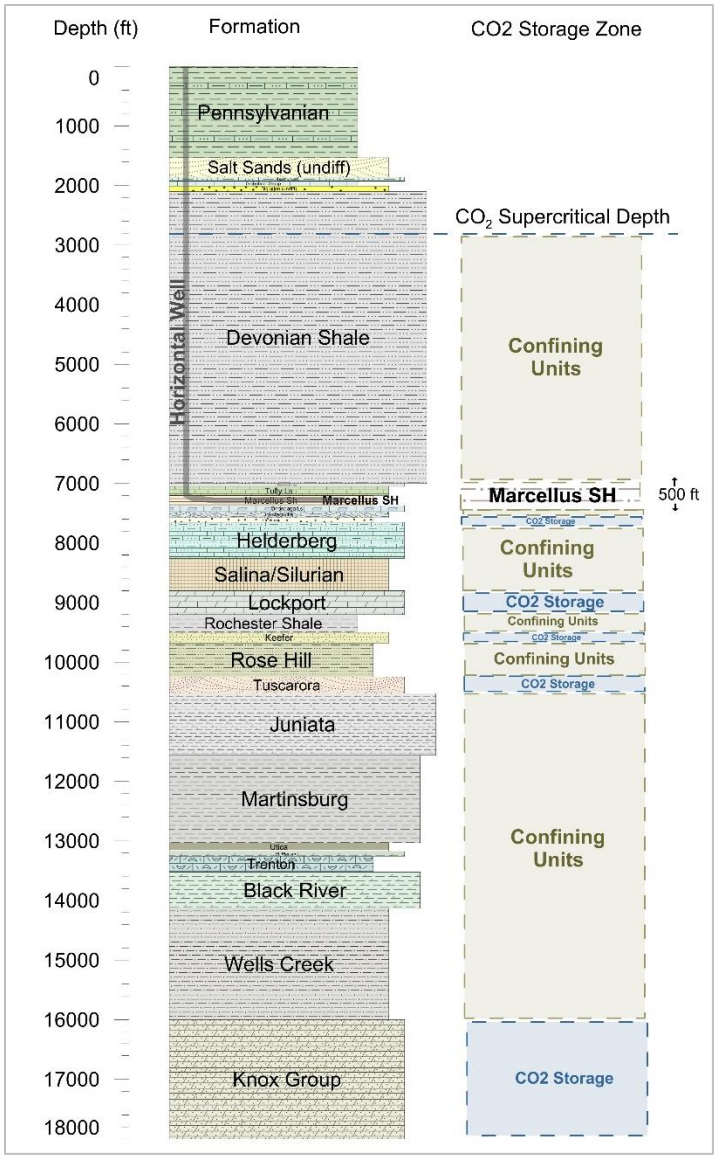

Figure 7-15: Geologic column for a typical Marcellus well illustrating the vertical arrangement of CO_2 storage and confining units.

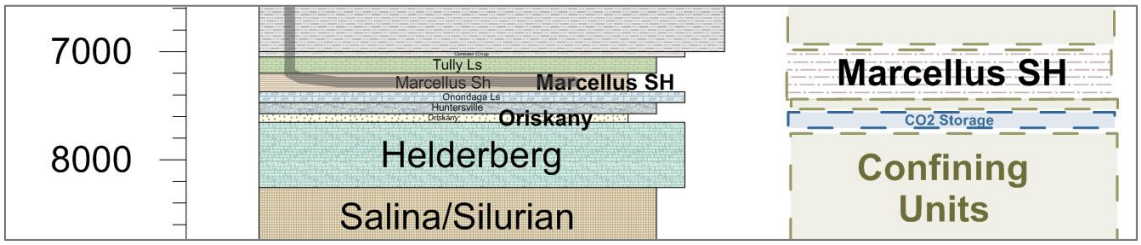

Figure 7-16: Detailed geologic column illustrating the vertical relationship between the Oriskany sandstone and Marcellus shale.

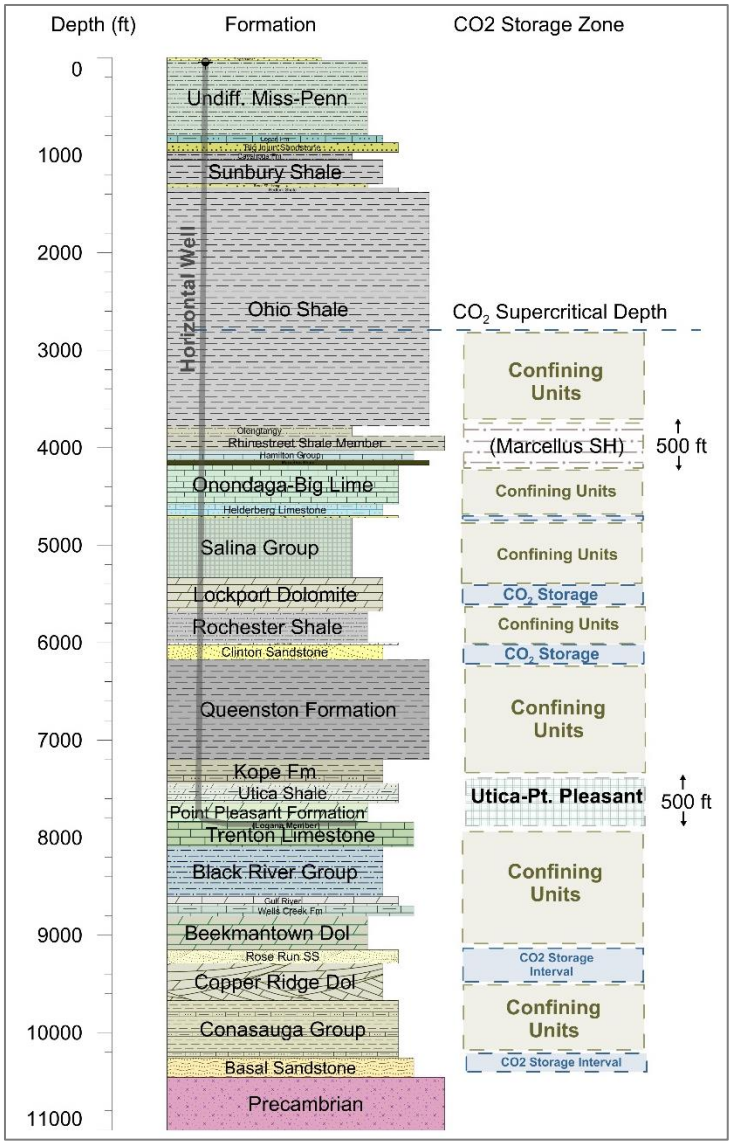

Figure 7-17: Geologic column for a typical Utica-Point Pleasant well illustrating the vertical arrangement of CO_2 storage and confining units.

While shale gas zones are not considered a primary option for CO_2 storage due to their inherent low permeability, some researchers have examined using shales for CO_2 storage (Levine et al., 2016; Schaef and McGrail, 2016; Ripepi et al., 2016; Kang et al., 2011). Much of this research considers injecting CO_2 into depleted unconventional wells, taking advantage of shale treatment zones. Other work examines the potential for enhanced gas recovery, where injected CO_2 may desorb natural gas from organic shale. Research on organic shale gas isotherms indicates that there is large capacity for organic shale layers to adsorb CO_2 (Nuttall et al., 2005; Godec et al., 2016). In general, the research concludes that CO_2 sorption potential is proportional to total organic carbon. Adsorption isotherm tests suggest that organic shales also preferably adsorb CO_2 compared to methane desorbed (at ratios of 2:1 or greater CO_2 to methane).

Total organic carbon in Devonian black shales in the Appalachian Basin averages approximately 7%, and total thickness is more than 1,000 ft in much of the basin. Consequently, the Devonian shale has the potential to adsorb a large amount of CO_2. Research from the MRCSP based on shale gas isotherms suggests there may be potential for 40 billion metric tons of CO_2 storage in Devonian shales in the Appalachian Basin (Wickstrom et al., 2005).

If CO_2 migrated into the Devonian shale interval via a hydraulically fractured Marcellus zone, isotherm experimental data suggest it would likely be adsorbed onto organic material in the shales. As Wickstrom et al. (2005) also noted, the organic Devonian shale section has the capacity to adsorb an enormous amount of CO_2. Adsorbed CO_2 would be effectively trapped compared to supercritical-phase CO_2, which can migrate along fractures and permeable pathways via buoyant flow if it is not structurally contained. In addition, since there is a thick section of additional Devonian shale above the Marcellus, this zone provides additional low-permeability caprock. Consequently, fractured zones in the Marcellus shale may not be a meaningful risk factor for CO_2 storage in relation to CO_2 migration through caprocks. In terms of CO_2 storage, these Devonian shales would be most pertinent to the underlying Oriskany sandstone.

Similarly, the Utica-Point Pleasant interval is part of a thick Ordovician shale sequence, which includes the overlying Utica shale, Kope Formation, and Queenston shale. Together, these shale formations form a thick series of shales, but the Ordovician shales are not considered as highly organic as the Devonian black shales. The formations are considered caprocks in terms of potential for CO_2 migration. However, there are no major CO_2 storage intervals directly below the Utica-Point Pleasant. Thus, the Utica-Point Pleasant and overlying Ordovician shales have lower risk for CO_2 migration.

7.3.2 Stress Changes

Another risk factor related to shale gas development is the alteration in subsurface stress conditions. Hydraulic fracturing in horizontal wells, followed by gas production, could alter the stress regime across large areas within the subsurface. Stress changes in the subsurface have the potential to result in processes like fracture activation, induced seismicity, hydraulic fractures, and surface uplift. Conversely, changes in the stress regime may moderate these processes by stabilizing stress conditions. Oil and gas production has resulted in widespread depleted oil and gas zones, which may have lowered the stress envelope in terms of fault or fracture failure.

During the hydraulic fracturing process, injection pressures are elevated above the formation fracture breakdown pressure to initiate fractures. Then a mixture of fluid and proppant is injected, usually well above the fracture breakdown pressure, to produce a network of hydraulic fractures around the well stage. During injection of the fracture fluid, pressures may be transmitted ‘out of zone’ via pre-existing fractures and/or faults. Conceptually, the increase in pressure may result in a net negative stress change, moving a fracture or fault toward failure. There have been isolated instances of unconventional hydraulic fracturing resulting in induced seismicity (Warpinski and Fisher, 2012; NRC, 2013; Friberg et al., 2014; Baturan et al., 2015; Walsh and Zoback, 2016). However, the vast majority of hydraulic fractured shale gas wells produce only microseismic activity (Fisher, 2010).

Conversely, gas production after initial hydraulic fracture treatment would conceptually deplete pore pressure, which may stabilize the stress regime. There are only isolated occurrences of induced

seismicity related to primary production of oil and gas, and these incidents are often related to water floods or enhanced oil recovery. Considering the amount of conventional oil and gas production throughout the world, this finding provides historical evidence that primary production does not move critically stressed areas to failure. There are many instances of large-scale hydrocarbon production causing subsidence (Pratt and Johnson, 1926; Holzer and Bluntzer, 1984; Vanhasselt, 1992; Bowersox and Shore, 1990; Fielding et al., 1998). These cases of subsidence are usually associated with shallow (<3,000-ft-deep), poorly lithified rock layers which undergo elastic deformation due to pore pressure depletion. Often, these fields have large volumes of produced water associated with hydrocarbon production.

In terms of CO_2 storage applications, there is potential for "stress interference" from multiple proximate wells in the subsurface. For example, a field of unconventional shale gas wells may create changes in stress magnitude near a CO_2 injection well, which itself has affected the stress regime. If these stress changes extend into each other, they may combine to intensify the overall stress changes. Many unconventional wells exhibit this "stress shadowing" effect, where one fracture stage affects the adjacent stages. However, these fracture stages are relatively closely spaced (<1,000 ft), subject to short-term, high-intensity stimulation. Stress shadowing is generally more of a lateral process contained within the reservoir. Most shale gas reservoirs have a competent caprock formation that inhibits vertical fracture propagation above the reservoir. As discussed in Section 7.2, most CO_2 storage zones in the Midwest United States are fairly isolated vertically from the major shale gas plays. However, many areas in the region have multi-layered oil and gas fields and/or natural gas storage. In fact, many unconventional shale gas wells have been drilled near (Figure 7-18) or even through (Figure 7-19) active natural gas storage fields. These gas storage operators ensure that the wells are properly cemented through the gas storage zones. They may also sample and analyze gas from the new shale gas wells to see if it reflects storage gas.

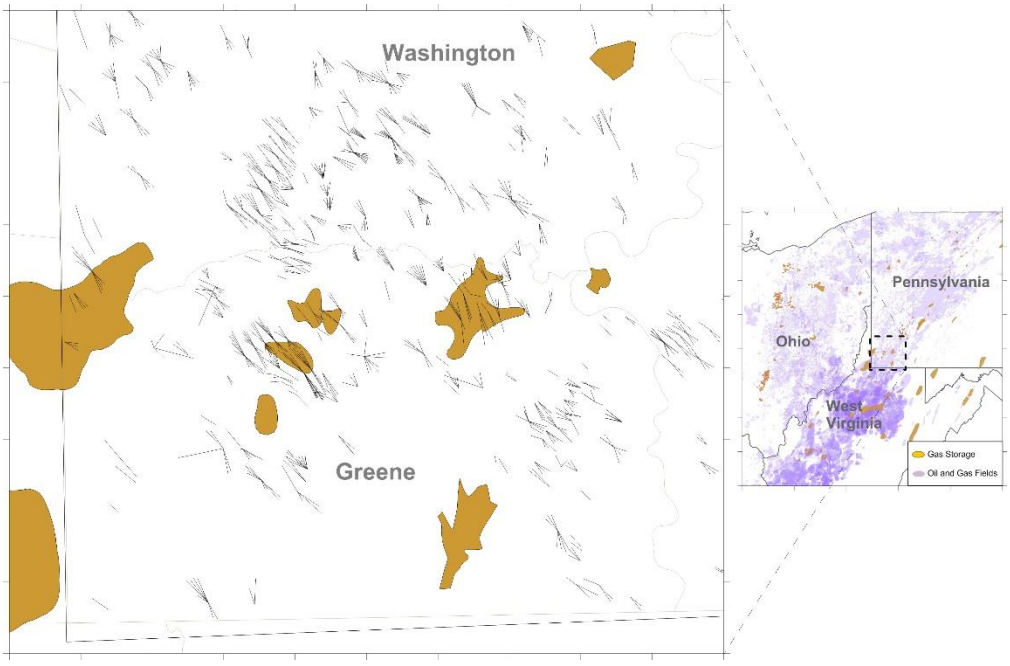

Figure 7-18: Paths of Marcellus shale horizontal wells in southwest Pennsylvania in relation to gas storage fields.

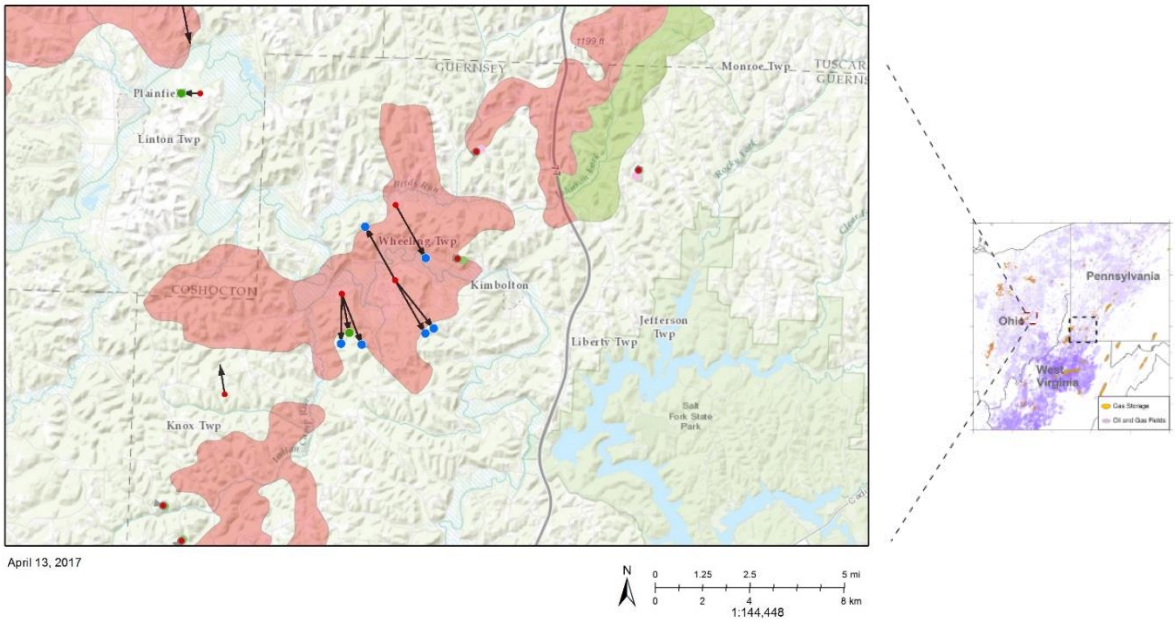

Source: ODNR, 2017.

Figure 7-19: Paths of several Utica-Point Pleasant horizontal wells that penetrate through the Guernsey gas storage field in the Oriskany sandstone.

To better understand how stress conditions may affect shale gas zones and intermediate layers above CO_2 storage formations, stress profiles from geomechanical simulations were analyzed for three project study areas: Arches Province, East-Central Appalachian Basin, and northern Appalachian Basin. In theory, where CO_2 storage fields and shale gas development intersect, subsurface pressures and stress changes may combine to result in elevated stress conditions that could lead to increased potential for development/activation of fracture systems. During hydraulic fracturing processes, pore pressures are temporarily increased above minimum horizontal stress magnitudes to fracture the rock formation. However, this fracturing process typically lasts only a few hours for an individual stage and a few days or weeks during the well stimulation process. After the well is fractured, the pore pressures would decrease during hydrocarbon production. There may be potential to activate or extend the hydraulic fractures if pressure and stress changes from a CO_2 storage application extend into the shale gas play. These induced fracture systems may provide pathways for CO_2 migration. However, given that shale gas zones are vertically separated from most CO_2 storage zones, stress changes would need to vertically migrate past several caprock zones to result in stress interactions.

The conceptual diagram in Figure 7-20 illustrates the vertical relationship between CO_2 storage zones and the Marcellus unconventional shale gas play. As shown, the Marcellus play is typically produced at a depth of 7,000 ft to 8,000 ft. CO_2 storage zones near the Marcellus would likely include the Oriskany, Lockport, Keefer, or Tuscarora sandstone formations. The CO_2 storage process would result in elevated pore pressures in these formations, but they are vertically separated from the Marcellus by over 1,000 ft of caprock/intermediate rocks. The Oriskany sandstone is another CO_2 storage zone located only a few hundred feet below the Marcellus in most of the Appalachian Basin. As such, there may be more potential for interaction between the Oriskany and Marcellus. The Oriskany has variable thickness of 0 ft to 150 ft, with best reservoir quality in southwestern Pennsylvania and West Virginia. These areas also have extensive Marcellus development. Oriskany CO_2 storage applications in these areas would need to consider interactions with unconventional Marcellus shale gas wells.

The conceptual diagram in Figure 7-21 illustrates the vertical relationship between CO_2 storage zones and the Utica-Point Pleasant unconventional play. The Utica-Point Pleasant is also typically developed at depths of 7,000 ft to 8,000 ft. The Utica-Point Pleasant is separated from deeper CO_2 storage intervals like the Rose Run sandstone, Copper Ridge dolomite, and basal sandstone by more than 1,000 ft of caprock layers in the Beekmantown, Wells Creek, and Trenton-Black River Formations. The Queenston shale separates the Utica-Point Pleasant from the overlying “Clinton”-Tuscarora and Lockport dolomite potential CO_2 storage units. In general, there appears to be little potential for geomechanical interaction between Utica-Point Pleasant unconventional shale hydrocarbon development and CO_2 storage applications.

Stress profiles with depth illustrate how the subsurface stress changes caused by CO_2 injection would interact with overlying layers. The minimum horizontal stress profile with depth was exported from geomechanical simulations completed under Task 6 of this project. These geomechanical simulations were completed to assess the stress changes that may occur due to CO_2 injection for three sites in the region: the Arches site in Northern Kentucky, the East-Central Appalachian Basin site in eastern Ohio, and the Northern Appalachian Basin site in southwestern New York. Baseline simulation results were analyzed at the injection well location after 30 years of CO_2 injection. These profiles reflect the stress change induced via injection. Figure 7-22 shows a simulated stress profile for the Arches study area geomechanical simulation. As shown, the stress changes are contained within the Mount Simon sandstone storage formation and the lower portions of the Eau Claire Formation. No unconventional shale gas formations are present in this area, but the analysis illustrates the stress profile for CO_2 storage applications.

Figure 7-23 shows a simulated stress profile for the East-Central Appalachian Basin study area geomechanical simulation. The stress profile shows how subsurface stress effects are contained within the storage interval and the lower caprock, based on geomechanical simulations. In the study area, the Utica-Point Pleasant is present at an approximate depth range of 6,100 ft to 6,400 ft, where there is minimal change in stress conditions.

Results from the Northern Appalachian Basin study area simulation suggested low potential for CO_2 injection, and it was difficult to analyze these results. However, this area appears to contain many caprock layers which would effectively contain stress perturbations caused by CO_2 storage.

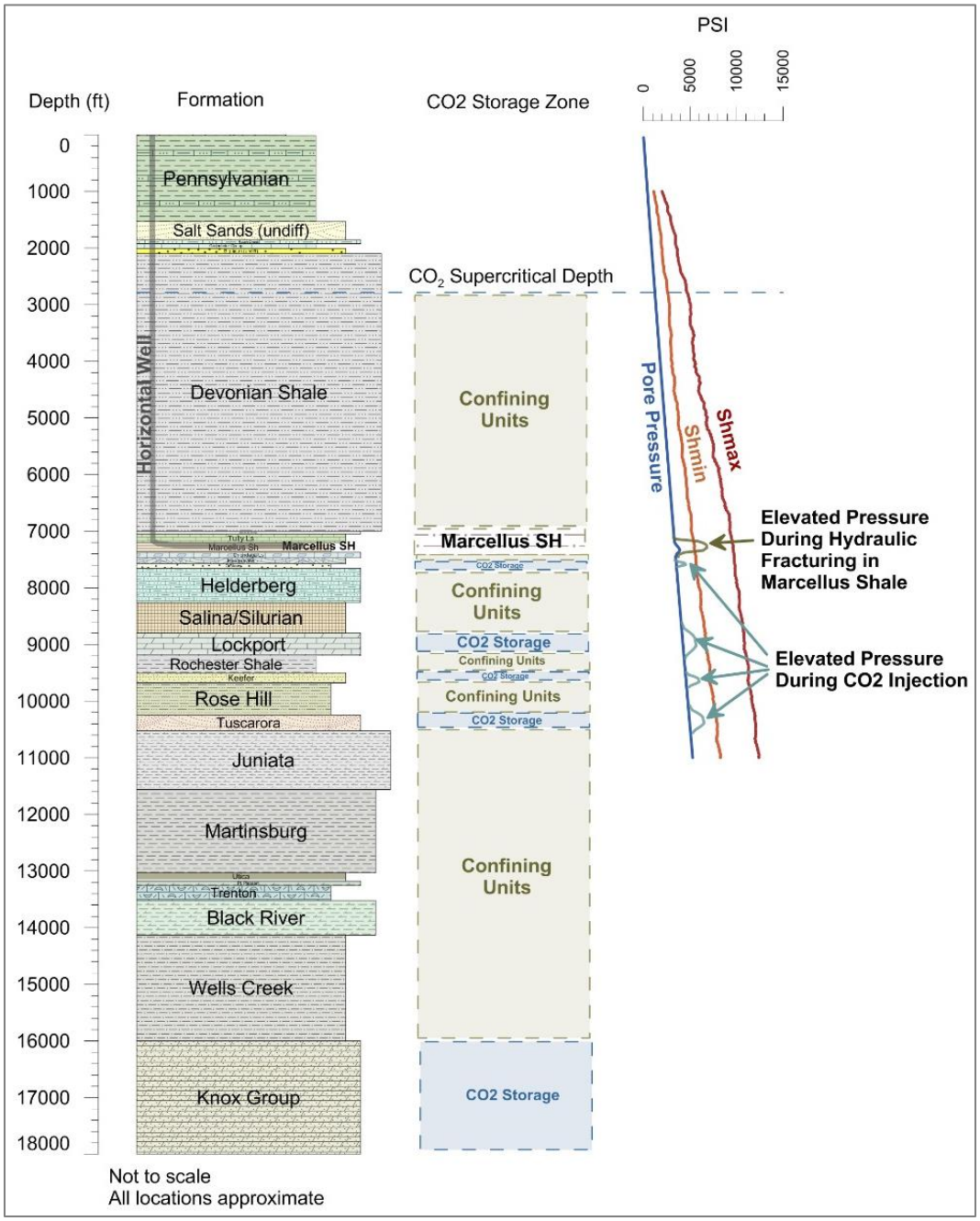

Figure 7-20: Conceptual diagram illustrating potential interaction between CO_2 storage intervals and the Marcellus shale play.

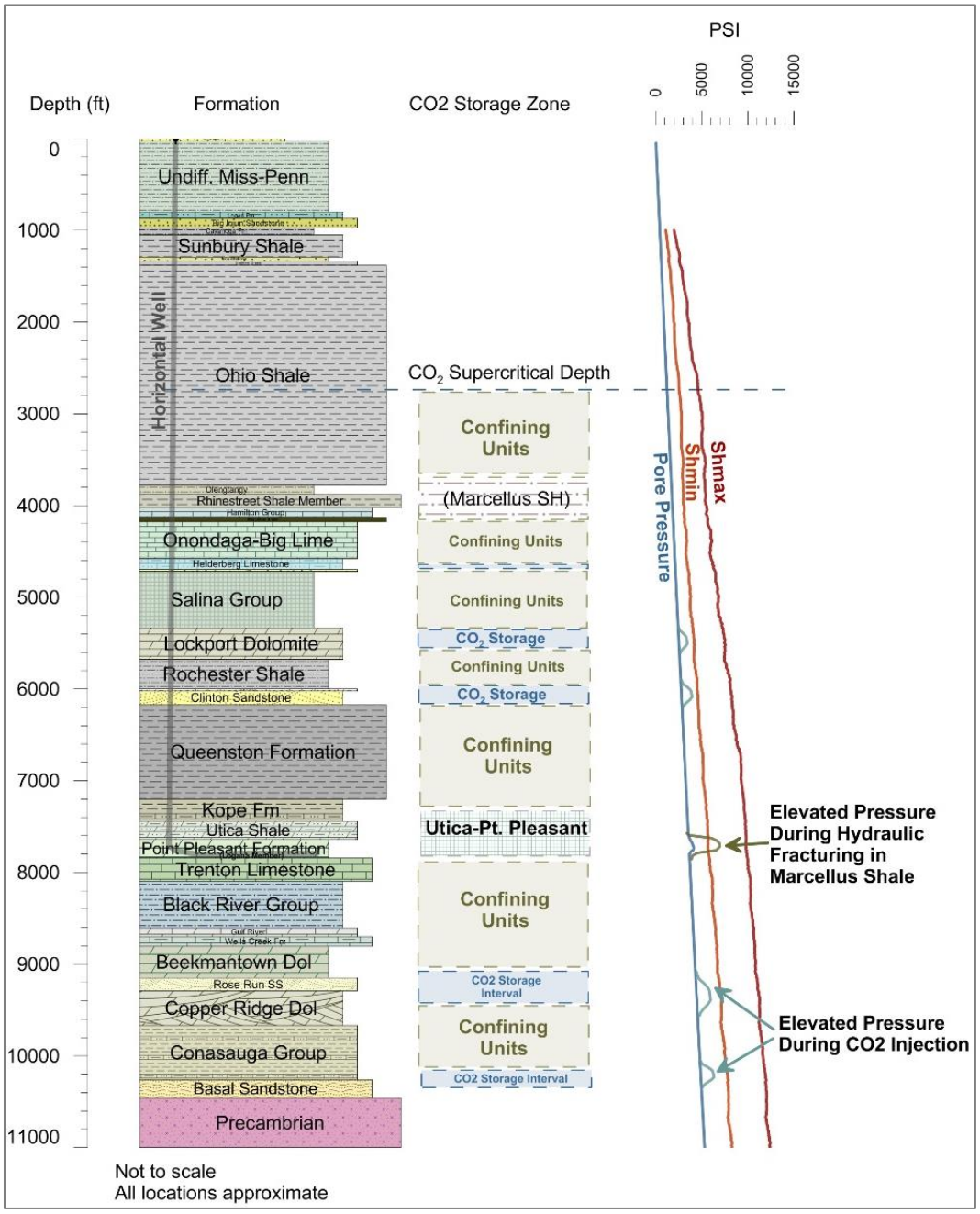

Figure 7-21: Conceptual diagram illustrating potential interaction between CO_2 storage intervals and the Utica-Point Pleasant shale play.

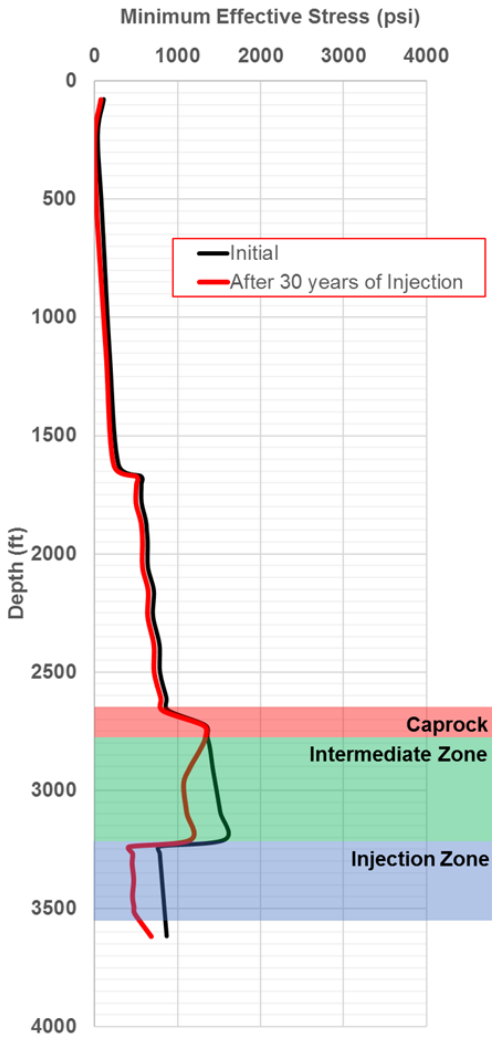

Figure 7-22. Minimum horizontal stress profile for the CO_2 injection geomechanical simulation in the Arches study area.

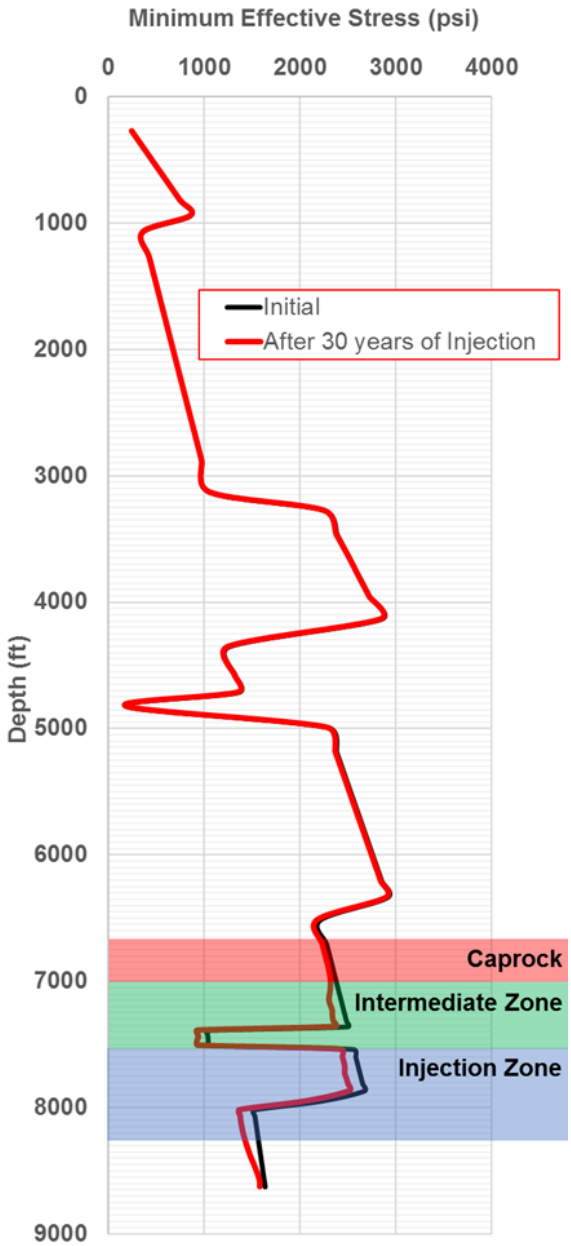

Figure 7-23. Minimum horizontal stress profile for the CO_2 injection geomechanical simulation in the East-Central Appalachian Basin study area.

7.3.3 Geomechanical Effects on Legacy Oil and Gas Wells

Geomechanical effects of hydraulically fractured horizontal wells could intercept legacy oil and gas wells, which may provide a pathway for upward migration of gas. The legacy oil and gas wells may include active/producing wells, plugged and abandoned wells, and unknown wells. During the fracturing process, fracture pressure may be transmitted to a legacy borehole if the legacy well is intercepted by the SRV. In practice, there are few, if any, instances of hydraulic fractures communicating with existing vertical wells. More commonly, operators experience “frac hits” where fractures between two offset horizontal fracture stages interconnect. This type of intercommunication is contained within the reservoir and presents little risk for gas migration.

In terms of CO_2 storage applications, legacy oil and gas wells would present the highest risk if they were located directly in the CO_2 storage plume or pressure field. Brownlow et al. (2017) examined the spatial relationship of hydraulic fracturing near abandoned and converted oil and gas wells in Texas. The research concluded that the risk of hydraulic fractures intercepting legacy oil and gas wells primarily depends upon the depth of the abandoned wells and SRV depth. As discussed in Section 7.2, most CO_2 storage formations in the Midwest United States are vertically isolated from shale gas zones. In addition, most legacy oil and gas wells are significantly shallower than Marcellus and Utica-Point Pleasant shale gas wells, which are mostly 6,000 ft to 9,000 ft deep. To affect CO_2 storage security via legacy oil and gas wells:

1. The unconventional well’s SRV must intercept legacy oil and gas wells in a spatial and vertical standpoint.
2. The unconventional oil and gas fracturing process must extend into the legacy oil and gas wells at a high enough magnitude to compromise the borehole integrity.
3. The CO_2 storage zone must also intersect the affected legacy oil and gas wells.

Given these requirements, there are generally few areas where these three conditions may occur. While unconventional shale plays cover large areas of the Midwest, the plays are limited to discrete vertical intervals. Figure 7-24 shows the Marcellus shale play, unconventional Marcellus horizontal well paths, and legacy oil and gas wells over 2,800 ft deep. There are many older oil and gas wells in the Marcellus play, mostly in southwest Pennsylvania. However, these are mostly shallow legacy oil and gas wells that do not penetrate the Marcellus or immediate overlying layers. Figure 7-25 shows well density for legacy oil and gas wells that are located within 500 ft of a horizontal well path. The main areas with legacy oil and gas wells near Marcellus development are located in northern West Virginia.

Similarly, Figure 7-26 shows the Utica-Point Pleasant play, unconventional Utica horizontal well paths, and legacy oil and gas wells. There are few oil and gas wells in the central Utica play, and this is a fairly unproductive area in terms of hydrocarbons in the Appalachian Basin. Figure 7-27 shows well density for legacy oil and gas wells located within 500 ft of a Utica-Point Pleasant well path. There are few areas where deeper oil and gas wells exist near Utica development. In general, it appears that geomechanical effects on legacy oil and gas wells from combined shale gas and CO_2 storage operations in the subsurface would be limited to isolated areas.

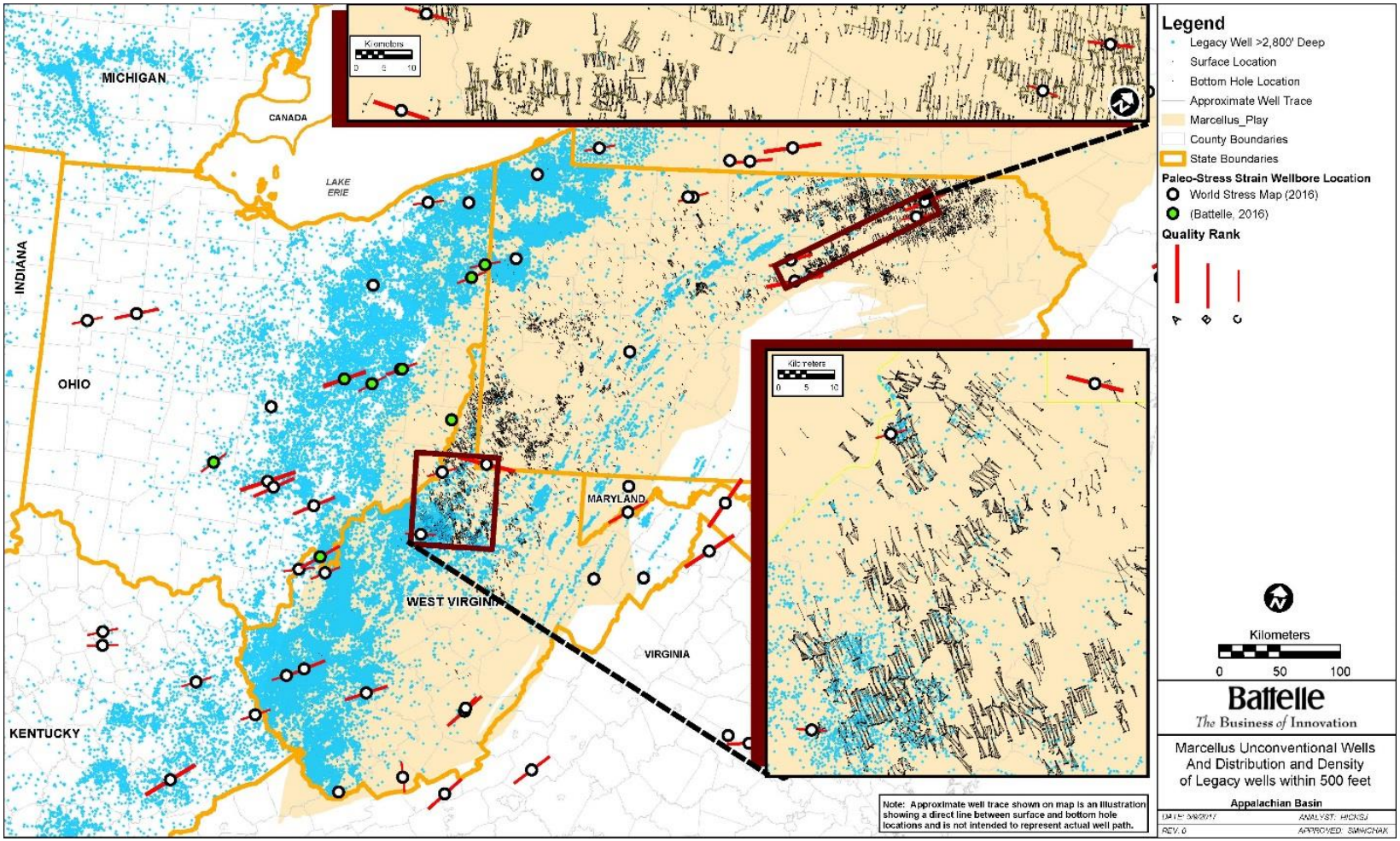

Figure 7-24: Map of Marcellus shale play, unconventional wells, and legacy oil and gas wells more than 2,800 ft deep.

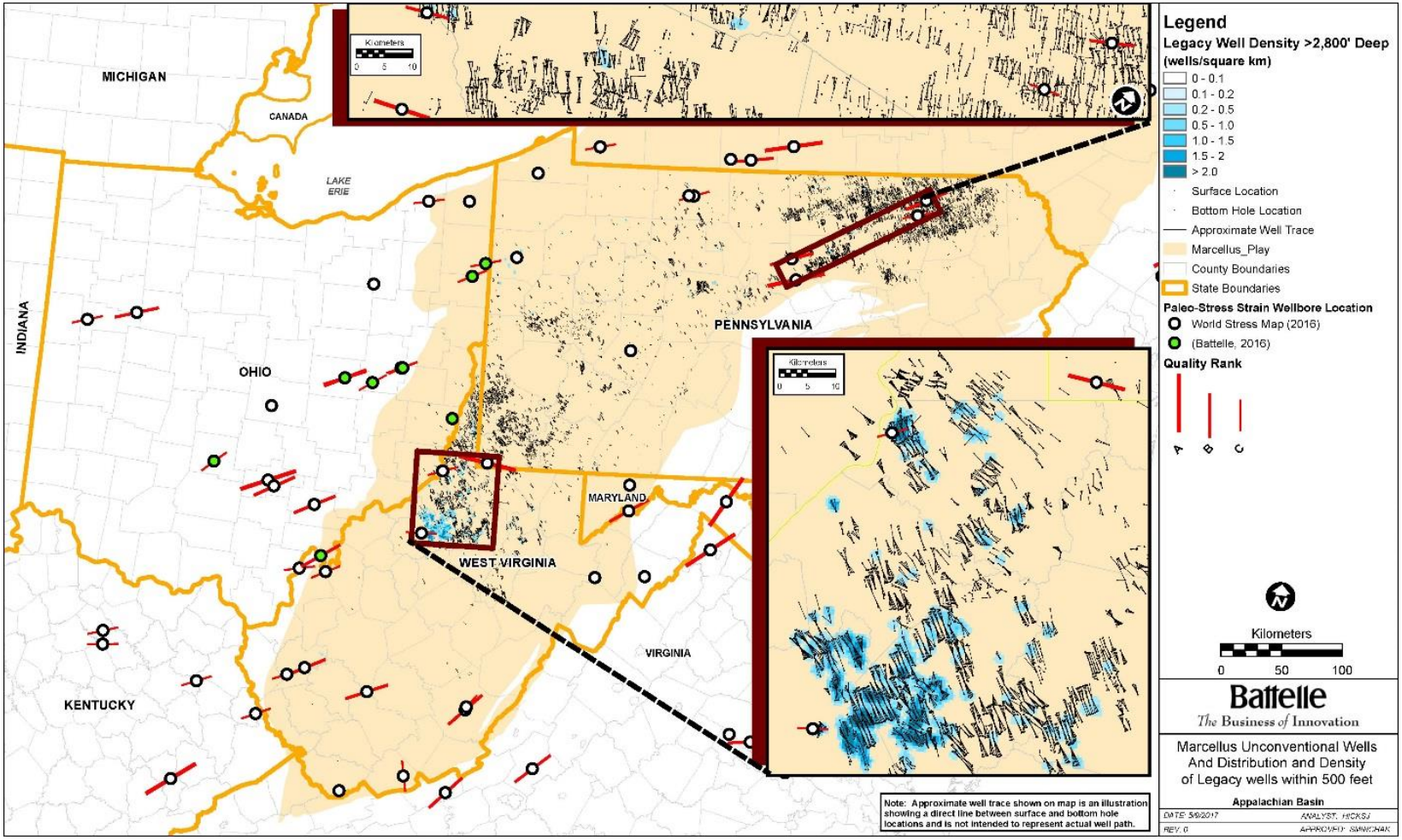

Figure 7-25: Map of legacy oil and gas well density near unconventional Marcellus wells.

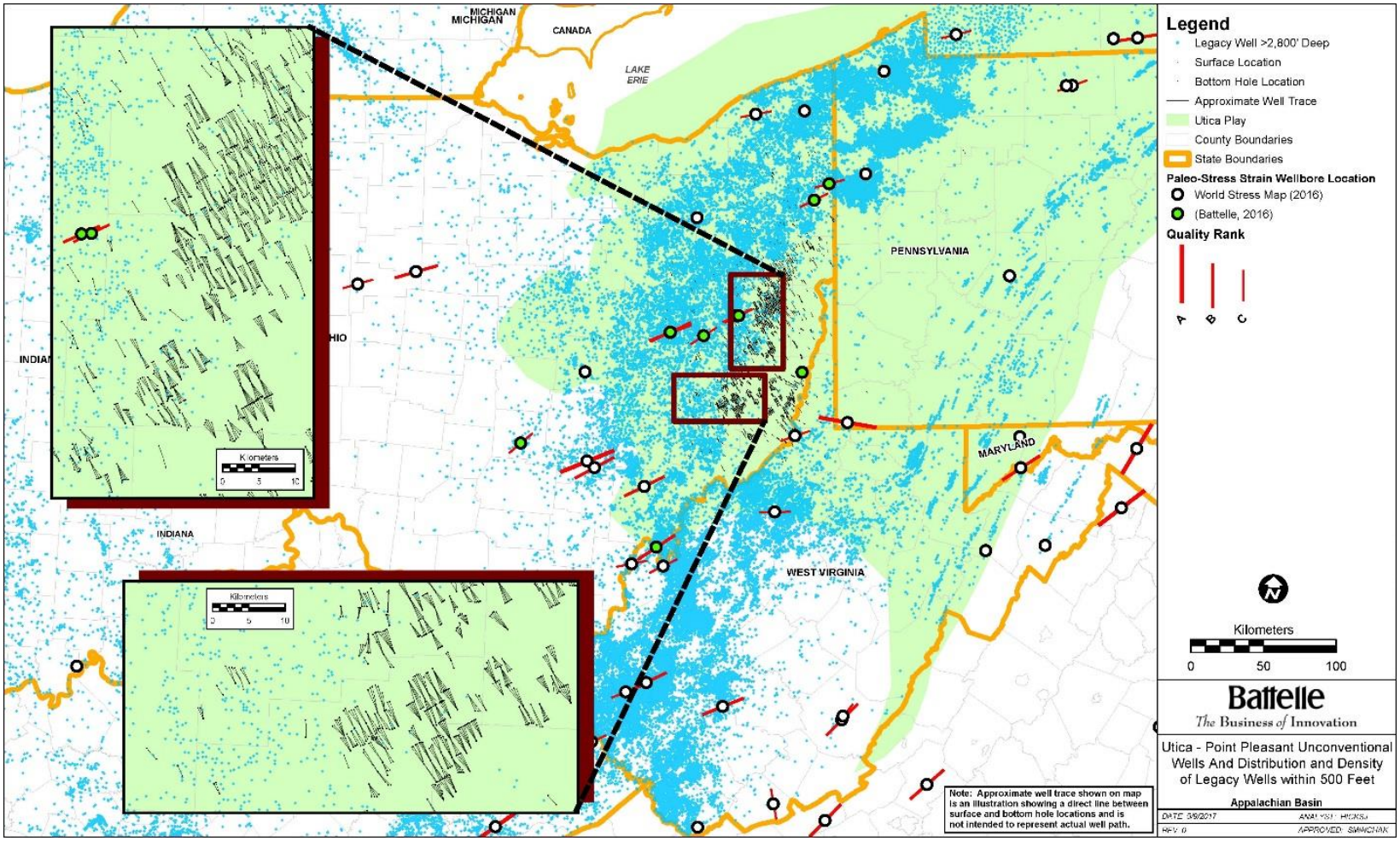

Figure 7-26: Map of Utica-Point Pleasant shale play, unconventional wells, and legacy oil and gas wells more than 2,800 ft deep.

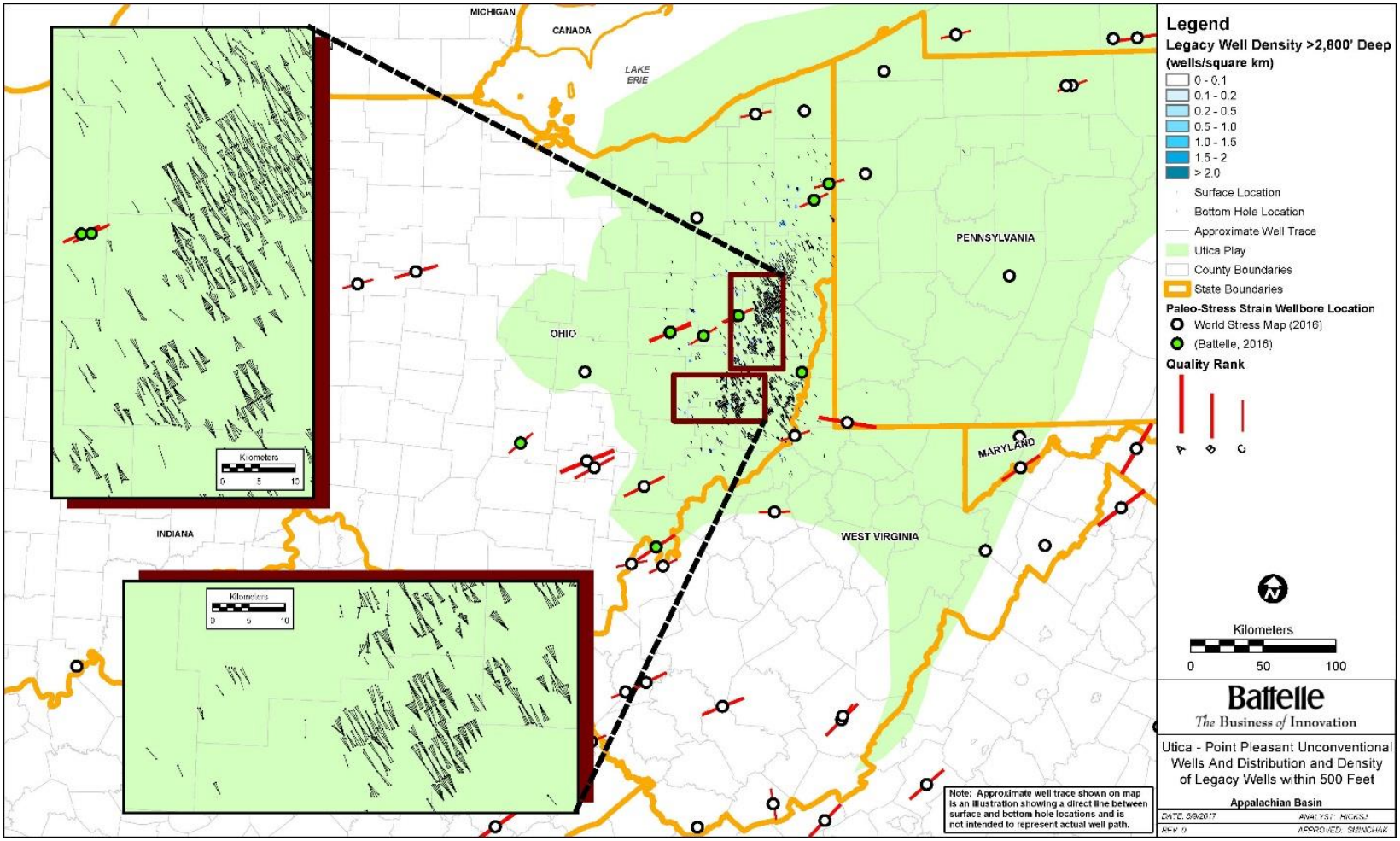

Figure 7-27: Map of legacy oil and gas well density near unconventional Utica-Point Pleasant wells.

8.0 Technology Transfer

Technology transfer activities included a series of presentations, DOE-NETL program review meetings, and technical papers. A project overview presentation was made at a FOA1037 kickoff meeting at the DOE-NETL Pittsburgh office by Joel R. Sminchak and Neeraj Gupta on November 12, 2014. The presentation described the project methods, expected outcomes, and initial technical work. In addition, project updates were presented at the DOE-NETL annual program review meetings. Synergistic activities included discussions with other researchers in the FOA 1037 program, DOE-NETL National Risk Assessment Partnership team, MRCSP, and OCDO project on advanced characterization of geologic reservoirs and caprocks in the upper Ohio River Valley (OCDO Grant D-13-22).

8.1 Presentations

The following presentations were given at technical meetings to communicate project results to the research community, industry, and regulators:

Project Results: Geomechanical Framework for Secure CO_2 Storage in Fractured Reservoirs and Caprocks for Sedimentary Basins in the Midwest U.S. (Presentation), J.R. Sminchak, U.S. DOE Carbon Storage R&D Project Review Meeting, Pittsburgh, Pennsylvania, August 2, 2017.

Assessing the effective CO_2 storage capacity of a reservoir using a geomechanical framework: A case study of a site in the Arches Province of the Midwest U.S., Ashwin Pasumarti, Samin Raziperchikolaee, Joel Sminchak, Shuvajit Bhattacharya, Neeraj Gupta. Abstract submitted to SPE Carbon Management Technology Conference, July 20, 2017, Houston, Texas.

Geomechanical Factors for Assessing the Effects of Subsurface Injection in the Midwestern U.S., J.R. Sminchak, Ground Water Protection Council 2017 UIC Conference, February 23, 2017, Austin, Texas.

Geomechanical Assessment of Sub-Knox Formations for Safe CO_2 Injection Study in the Midwest U.S., Shuvajit Bhattacharya, Joint 52nd Northeastern/North-Central Annual 2017 Geological Society of America Meeting, March 19-21, Pittsburgh, Pennsylvania.

Project Update: Geomechanical Framework for Secure CO_2 Storage in Fractured Reservoirs and Caprocks for Sedimentary Basins in the Midwest U.S. (Presentation), J.R. Sminchak, U.S. DOE Carbon Storage R&D Project Review Meeting, Pittsburgh, Pennsylvania, August 16-18, 2016.

Evaluating the influence of Mineralogical Components of CO_2 Storage Zones on Mechanical Characterization in northern Appalachian Basin (Poster), Joel Sminchak, Ola Babarinde, Neeraj Gupta, Samin Raziperchikolaee and Mark Kelley, Carbon Capture, Utilization, and Storage Conference, Tysons, Virginia, June 14-16, 2016.

Subsurface Geomechanics, Fracture Breakdown Pressures, and 'Fracture-Tunnels' in the Midwest U.S., J.R. Sminchak, James E. Hicks, and Glenn E. Larsen, Eastern Section AAPG Meeting 2016, September 20-22, 2016, Lexington, Kentucky.

Integrated Analysis of Geomechanical Factors for Geologic CO_2 Storage in the Midwestern United States, Joel R. Sminchak, Ola Babarinde, and Neeraj Gupta, 13th International Conference on Greenhouse Gas Control Technologies (GHGT-13), Lausanne, Switzerland, November 14-18, 2016.

Project Update: Geomechanical Framework for Secure CO_2 Storage in Fractured Reservoirs and Caprocks for Sedimentary Basins in the Midwest U.S. (Presentation), J.R. Sminchak, U.S. DOE Carbon Storage R&D Project Review Meeting, Pittsburgh, Pennsylvania, August 18-20, 2015.

Geomechanical Assessment of Fractured Cambrian-Ordovician Reservoirs for Carbon Storage (Poster), Ola Babarinde, U.S. DOE Carbon Storage R&D Project Review Meeting, Pittsburgh, Pennsylvania, August 18-20, 2015.

Structural and Geomechanical Analysis of Fractured Cambrian-Ordovician Reservoirs in the Northern Appalachian Basin, Ola Babarinde, Eastern Section AAPG Meeting, September 20-22, 2015, Indianapolis, Indiana.

8.2 Technical Papers

Technical papers generated through this research are listed below. In addition, the project team is working on developing additional technical articles for future publication.

Assessing the effective CO_2 storage capacity of a reservoir using a geomechanical framework: A case study of a site in the Arches Province of the Midwest U.S., Ashwin Pasumarti, Samin Raziperchikolaee, Joel Sminchak, Shuvajit Bhattacharya, Neeraj Gupta. SPE Paper #CMTC-486410, SPE Carbon Management Technology Conference, July 20, 2017, Houston, Texas, 17 p.

Integrated Analysis of Geomechanical Factors for Geologic CO_2 Storage in the Midwestern United States. J.R. Sminchak, Ola Babarinde, and Neeraj Gupta. Energy Procedia, Volume 114, July 2017, Pages 3267-3272, ISSN 1876-6102. http://dx.doi.org/10.1016/j.egypro.2017.03.1458.

Natural Fractures within Knox Reservoirs in the Appalachian Basin: Characterization and Impact on Fluid Injectivity by Poromechanics Solutions, S. Raziperchikolaee, O. Babarinde, J. Sminchak, and N. Gupta, 2016. AAPG Bulletin (Accepted with Minor Revision).

9.0 Conclusions

The geological setting, geotechnical parameters, geomechanical conditions, coupled fluid flow-geomechanical simulations, site characterization guidance, and potential interactions of CO_2 storage with shale gas development were examined to determine the subsurface geomechanical effects of large-scale CO_2 storage applications in the Midwest U.S. This research focused on integrating field data from across the region along with three field study areas. While the geomechanical properties of the deep rock layers vary across the region, the Ordovician-Cambrian age rocks are highly lithified with few indications of extensive natural fracture zones. As such, the rock formations provide a suitable framework for CO_2 storage applications. Coupled fluid flow-geomechanical simulations suggest that subsurface geomechanical effects would not be a significant constraint on CO_2 storage applications. However, stress and pressure changes may affect existing faults and/or conductive fractures. Major conclusions of the technical tasks are summarized as follows.

Basin-Scale Paleo Stress Strain Analysis- Geologic structures and features reflect regional tectonic and structural evolution of broad sedimentary basin and arch structures in the Midwest U.S. Wellbore breakouts, drilling induced fractures, and natural fractures in 14 geophysical image logs showed a consistent northeast stress orientation with depth. Paleo-stress orientation and magnitude analysis indicate that the stress field is a factor controlling the orientation of fractures in the region. Analysis suggested that none of the natural fractures were stressed in their original state but at elevated pressure, Mohr's circle analysis suggested increasing likelihood of fractures failing. Image logs had a low fracture intensity, with mostly less than 20 natural fractures per 100 ft vertical log interval. Rock core geomechanical test data compiled from a variety of rock samples in the region showed a compressional velocity average of 17,302 ft/s, shear velocity average of 9,791 ft/s, Dynamic Young's modulus average of 8.69 1E+6 psi, Dynamic Poisson's ratio average of 0.25, Static Young's modulus average of 6.23 1E+6 psi, and Static Poisson's ratio average of 0.26. The properties reflect the age, depth, and fabric of the deep rock layers.

Site Data Analysis and Log Integration- Study areas in the Arches Province, East-Central Appalachian Basin, and Northern Appalachian Basin were identified where deep wells had a modern set of geophysical logs and geomechanical rock core testing to provide control on geomechanical conditions in the subsurface. The sites illustrate variability of geomechanical factors for CO_2 storage in the region. Processing and interpretation of more than 9,700 ft of image log digital files from the sites was completed to provide a systematic review of any natural fractures, wellbore breakouts, faults, bedding planes, and drilling induced fractures. Results indicated sparse natural fractures and faults, mostly less than 10 fractures per 100 ft of vertical interval. The maximum horizontal stress indicated by drilling induced fractures and borehole breakouts averaged approximately N65E orientation, which matches closely with the world stress map data. Image log analysis suggested that the southwestern part of the Appalachian Basin was more fractured than the northeastern part, and the Arches study area appeared to contain very few fractures. Stress magnitudes were constrained by examining over 20,000 data points on fracture breakdown pressures and measured shut-in pressures from wells in the region.

For each study area, geomechanical parameters were derived from geophysical logs to provide input for coupled fluid flow geomechanical simulations of CO_2 injection. The Arches and East-Central Appalachian Basin well sites indicated high caprock moduli values in comparison to the reservoir rocks, meaning that strong caprocks are present along the Cincinnati arch and East-Central

Appalachian Basin. The Northern Appalachian Basin basis well indicated high moduli values throughout the well with the highest values in the Galway dolomites. Most of the reservoir rocks displayed high moduli values showing few weak zones and a low potential for hydraulic fracturing.

Coupled Fluid-Flow Geomechanical CO_2 Storage Simulations - Geo-cellular models were developed for the Arches, East Central Appalachian Basin, and Northern Appalachian Basin local study areas to depict site-specific variations in subsurface geology and geomechanical parameters. Geophysical logs and rock-core tests were used to derive site-specific geomechanical parameters and subsurface conditions. The three sites had distinct combinations of geological and geomechanical properties. The Arches study area was a relatively shallow site, consisting of the Eau Claire shale overlying the Mount Simon sandstone as a target for CO_2 injection. The East-Central Appalachian study area included several deeper Ordovician-Cambrian age rock formations that were targets evaluated for storage. The Northern Appalachian study area is more influenced by the Appalachian Mountains and associated geologic structures. This site had an indication of moderate fracture matrix in the Galway-Rose Run formation. The information from the geological models was translated to inputs for the numerical modelling of the CO_2 injection process.

Coupled fluid-flow and geomechanics simulations were completed for each site to evaluate site-specific geomechanical constraints on industrial-scale CO_2 storage feasibility. Simulation results were processed to assess the integrity of the caprock, intermediate and reservoir zones, as well as quantifying the areal uplift at the surface. The simulation results were also examined to ensure that the stress-stress perturbations were isolated to be within the subsurface, and that there was only limited upward migration of the CO_2. At the Arches study site, simulations suggested the capacity to inject 24-51 million metric tons CO_2 into the Mount Simon Sandstone over 30 years in a single well. The simulation showed no tensile or shear failure in any of the layers in the caprock, intermediate or reservoir zone, despite highly conservative assumptions in the model. Stress-strain perturbations were generally isolated beneath the caprock. Surface uplift was estimated at 26 mm or less in the simulations. The East Central Appalachian Basin simulations showed no tensile or shear failure in any of the layers in the caprock, intermediate or reservoir zone, and stress-strain perturbations were isolated beneath the caprock. Up to 5 mm of uplift may be expected at the surface, which was lower than that predicted for the Arches site, owing to the lower level of pore-pressure increase, the much higher Young's modulus values, and the deeper location of the injection zone. Simulations suggest the 30-year effective capacity of this well is at least 10.25 million metric tons of CO_2. This well is an appealing candidate for stacked, multi-reservoir storage of commercial-scale volumes of CO_2. The Northern Appalachian basin site simulation results showed that commercial-scale injection was not feasible due to extremely low injectivity, mainly due to the low permeability of the deep rock layers. However, dual permeability fracture matrix simulations suggest much higher injection rates of more than 500,000 metric tons per year. These simulations have a high degree of uncertainty on the fracture matrix parameters, because they are based on single well geophysical image logs that make it difficult to determine the extent of the fractured zone.

Injection testing and core studies at the well site are recommended to constrain the estimates for geomechanical parameters (minimum and maximum horizontal stress gradients, Young's Modulus, Poisson's Ratio, rock cohesion), especially in the Galway-Rose Run Sandstone formation. Increased confidence in these critical inputs to the coupled fluid flow reservoir-geomechanics simulations would improve the accuracy of the model predictions. Together, these three study areas provide a realistic portrayal of the range of geomechanical impacts of CO_2 storage in the Midwest U.S. Acquiring site-

specific geomechanical parameters is essential for a wholistic evaluation of CO_2 injection sites. Simulation results generated in this research benefit the establishment of CO_2 storage applications.

Development of Methodology for Geomechanical Site Characterization – A wide variety of geophysical logging, rock core testing, well testing, and site monitoring options are available for geomechanical site characterization in support of CO_2 storage projects. The technologies have advantages, limitations, and cost considerations. However, combinations of technologies can be used to design site-specific programs to ensure safe, effective operations of the storage site. Hydraulic fracturing of the injection zone and/or caprock, fracture activation, induced seismic activity, wellbore damage, and surface uplift/deformation are key geomechanical processes that may affect a CO_2 storage project. Geophysical well logging, rock core testing, well testing, and site monitoring methods can be used to provide either indirect and/or direct parameters that may be used to analyze the geomechanical effects of CO_2 storage. The CO_2 storage system specifications, geological setting, and subsurface conditions will dictate the methods most appropriate for a project. Sites with few geomechanical issues may require a low level of site characterization and monitoring that could be integrated with other activities.

CO_2 Storage/Shale Gas Risk Factor Assessment - Mapping of unconventional hydrocarbon plays, 12,833 horizontal Marcellus/Utica-Point Pleasant wells, and CO_2 storage formations suggested that there is minor potential for interactions between shale gas development and CO_2 storage applications in the Midwest U.S. Unconventional shale gas wells have average lateral lengths of 5,000 to 7,250 feet and 20 to 75 fracture stages, affecting a much greater area in the subsurface than conventional vertical oil and gas wells. While the Marcellus shale and the Utica-Point Pleasant shale cover vast lateral areas, unlike conventional oil and gas pools that have more restricted boundaries, both plays have fairways where there is concentrated well density because of favorable conditions for hydrocarbon production. The Marcellus shale and the Utica Point-Pleasant shale are vertically separated from most key CO_2 storage rock formations by several caprock layers and/or intermediate layers with a combined thickness of >1,000 feet in most areas. In terms of CO_2 storage, the Oriskany sandstone is located only a few hundred feet below the Marcellus shale in much of the Appalachian Basin. As such, there may be more potential for interaction between Oriskany CO_2 storage and Marcellus shale operations, mostly in southwestern Pennsylvania and West Virginia. Organic shale sequences in the Midwest may have a very large capacity to adsorb CO_2, and they may provide additional caprock security for CO_2 storage. Geomechanical simulation results indicate that stress changes from CO_2 storage applications are unlikely to extend into developed shale gas intervals where they might activate previously hydraulically fractured zones. Overall, the interaction of shale gas development and CO_2 storage applications in the Midwest U.S. requires consideration, but no critical technical issues were identified that may prevent CO_2 storage near shale gas fields. The subsurface footprint of shale gas development in the Midwest has expanded rapidly since the mid-2000s and continues to grow, so there may be perception issues for any CO_2 storage projects near areas with a dense concentration of unconventional shale gas wells.

10.0 References

Aadnoy, B. S., 1990. Inversion technique to determine the in-situ stress field from fracturing data. Journal of Petroleum Science and Engineering: 4, 127–141.

Aamodt, L. and M. Kuriyagawa, 1981, Measurement of instantaneous shut-in pressure in crystalline rock, Los Alamos National Lab., NM (USA).

Abbas, S., Gordeliy, E., Peirce, A., Lecampion, B., Chuprakov, D.A., and Prioul, R. 2014. Limited height growth and reduced opening of hydraulic fractures dkue to fracture offsets: an XFEM application. In: Paper SPE 168622, SPE Hydraulic Fracturing Technology Conference, The Woodlands, Texas, USA, 4–6 February.

Al-Awadi et al. 2009. Dolomite: Perspectives on a Perplexing Mineral. Schlumberger Oilfield Review 21, 3, 33-45.

Anderson, E.M., 1905. Dynamics of faulting: Transactions Edinburg Geological society, 8:387-402.

Anderson, WH. 1991. Mineralization and hydrocarbon emplacement in the Cambrian-Ordovician Mascot Dolomite of the Knox Group in southcentral Kentucky. Kentucky Geological Survey Report of Investigation 4, 31 p.

Archer, PL. 1979. Illinois Basin Report, Pennsylvania Geology and Coal and Coalbed Methane Resources of the Illinois Basin, Illinois, Indiana and Kentucky. TRW Energy Systems Group, Contract No. DE-AC21-78MC08089.

Bammi, S., J.J. Walsh, T. Kinoshita, T. Endo, and E. Velez, 2015, Measuring Completion Quality and Natural Fracture Indicators in Horizontal Wells using a New Slim Dipole Sonic Memory Tool Conveyed through the Drillstring and Bit, presented at SEG Annual Meeting New Orleans.

Barree, R.D. and J.L. Miskimins, 2015. Calculation and Implications of Breakdown Pressures in Directional Wellbore Stimulation. SPE Hydraulic Fracturing Technology Conference, Woodlands, Texas, February 2015. SPE-173356-MS. 21 p.

Barton, C., Moos, D., and Tezuka, K. 2009. Geomechanical wellbore imaging: Implications for reservoir fracture permeability. AAPG Bulletin, v. 93, no. 11, p. 1551-1569.

Battelle. 2010. CO_2 Injection Test in the Cambrian-Age Mount Simon Formation, Duke Energy East Bend Generating Station, Boone County, Kentucky. Conducted by the Midwest Regional Carbon Sequestration Partnership (MRCSP). Morgantown, WV: U.S. Department of Energy, National Energy Technology Laboratory, DOE-NETL Cooperative Agreement DE-FC26-05NT42589.

Battelle. 2011, Mountaineer CCs II Project: Phase 1 geological characterization: Final Report prepared for American Electric Power Company, Contract No. 345081X215, 189 p.

Battelle. 2013. Conducting research to better define the sequestration options in eastern Ohio and the Appalachian Basin: Final Report. Ohio Coal Development Office (OCDO) Grant/Agreement CDO/D-10-7a, 131 p.

Battelle. 2014. Defining CO_2 Storage Options in the Upper Ohio River Valley – Advanced Characterization of Geologic Reservoirs and Caprocks, Task 1: Compile and Analyze Data Interim Topical Report. OCDO Grant/Agreement OOE-CDO-D-13-22.

Battelle. 2016. Basin Scale Paleo Stress-Strain Report– Geomechanical Framework for Secure CO_2 STORAGE IN Fractured Reservoirs and Caprocks for Sedimentary Basins in the Midwest United States. DOE Grant/Agreement CDO/D-14-16.

Battelle. 2017. CO_2 Storage Resources and Containment Assessment in Cambrian and Ordovician Formations of Eastern Ohio – Caprock Integrity Assessment Topical Report: Ohio Coal Development Office, Grant/Agreement OOE-CDO-D-13-22.

Baturan, D., Greig, W., and Spriggs, N. 2015. Challenges and Strategies for Monitoring Induced Seismic Activity. AAPG Annual Convention & Exhibition, Denver, Colorado, May 31-June 3, 2015. Article #70193.

Baranoski, M.T., 2002, Structure contour map on the Precambrian unconformity surface in Ohio and related basement features: Ohio Division of Geological Survey Map PG-23, scale 1:500,000, (18 p. text).

Bemer, E., O. Vincke, and P. Longuemare, 2004, Geomechanical Log Deduced from Porosity and Mineralogical Content, Oil & Gas Science and Technology, Rev. IFP, 59(4), 405-426.

Blanton, T.L. 1986. Propagation of hydraulically and dynamically induced fractures in naturally fractured reservoirs. In: Paper SPE 15261, SPE Unconventional Gas Technology Symposium, Louisville, Kentucky, USA, 18–21 May.

Boswell, Ray, 1995, Play UDs: Upper Devonian black shales: in: Roen, John B., and Brian J. Walker, eds., The atlas of major Appalachian gas plays, West Virginia Geological and Economic Survey, Volume V-25, p. 93-99.

Bowen, B.B., R.I. Ochoa, N.D. Wilkens, J. Brophy, T.R. Lovell, N. Fischietto, C.R. Medina, and J.A. Rupp. 2010. “Depositional and Diagenetic Variability within the Cambrian Mount Simon Sandstone: Implications for Carbon Dioxide Sequestration,” Environmental Geosciences, 18(2): 69 - 89.

Bowersox, J.R. 2013. Evaluation of Phase 2 CO_2 Injection Testing in the Deep Saline Gunter Sandstone Reservoir (Cambrian-Ordovician Knos Group), Marvin Blan No. 1 Well, Hancock County, Kentucky. Kentucky Geological Survey Contract Report 52, 96 p.

Bowersox, J.R., and Shore, R.A. 1990. Reservoir compaction of the Belridge diatomite and surface subsidence, South Belridge Field, Kern County, California, AAPG Bulletin, 74 (5):616.

Bogdonov, A. 1947. The intensity of cleavage as related to the thickness of beds. Soviet Geology, v. 16, p. 102-104.

Brownlow, J.W., Yelderman, J.C., and James, S.C. 2017. Spatial Risk Analysis of Hydraulic Fracturing near Abandoned and Converted Oil and Gas Wells. Groundwater, v. 55, no. 2, p. 268-281.

Burgmann, R., P.A. Rosen, and E.J. Fielding, 2000, Synthetic aperture radar interferometry to measure Earth’s surface topography and its deformation. Annu Rev Earth Planet Sci 28:169-209.

Chiaramonte, L. 2009. Geomechanical Characterization and Reservoir Simulation of a Carbon Dioxide Sequestration Project in a Mature Oil Field, Teapot Dome, WY. Ph.D. Dissertation, Stanford University.

Chuprakov, D.S., Akulich, A.V., Siebrits, E., Thiercelin, M. 2010. Hydraulic fracture propagation in a naturally fractured reservoir. In: SPE 128715, SPE Oil and Gas India Conference and Exhibition, Mumbai, India, 20–22 January.

Ciezobka, J. 2011. Marcellus Shale Gas Project: Topical Report Stimulation and Completion. RPSEA, Project 9122-04. 25 August 2011. 15 p.

Cipolla, CL, Williams, MJ, Weng, X, Mack, M, and Maxwell, S. 2010. Hydraulic Fracture Monitoring to Reservoir Simulation: Maximizing Value. Second EAGE Middle East Tight Gas Reservoirs Workshop. December 2010.

Colman, J.L., and Cahan, S.M. 2012. Preliminary catalog of the sedimentary basins of the United States. USGS Open-File Report 2012-111.

Colton, G.W., 1970, The Appalachian Basin; its depositional sequences and their geologic relationship, in Fisher, G.W., Pettijohn, F.J., Reed, J.C. Jr, and Weaver, K.N. eds, Studies of Appalachian geology: central and southern, Interscience Publishers, New York, pp, 5-47.

Copley, D., Gill, B., and Authier, J. 1983. The Akron Dolomite (Bass Islands) Oil Trend in Western New York. Annual Conference- Ontario Petroleum Institute, v. 22, p. 7.1-7.18.

Cornet, F., 2004, Results from the In-Situ Stress Characterization Program, Phase 1: Geomechanical Tests Conducted in the FutureGen Stratigraphic Well (FGA# 1), Internal Report.

Cornet, F., M. Doan, and F. Fontbonne, 2003, Electrical imaging and hydraulic testing for a complete stress determination: International Journal of Rock Mechanics and Mining Sciences, v. 40, p. 1225-1241.

Demicco, RV. 1983. Wavy and lenticular-bedded carbonate ribbon rocks of the Upper Cambrian Conococheague limestone, central Appalachians: J Sediment Petrol 53:1121-1132.

Demicco, RV. 1985. Platform and off-platform carbonates of the Upper Cambrian of western Maryland, U.S.A.: Sedimentology: 32:1-22.

Detournay, E. 2004. Propagation regimes of fluid-driven fractures in impermeable rocks. Int. J. Geomech. 4: 1–11.

Dietz, RS. 1972. Geosynclines, mountains, and continent building: Scientific American 226(3):30-38.

Dixon, T.H., 1991, An introduction to the Global Positioning System and its geological applications. Rev. Geophys. 29 (2), 249-276.

Drahovzal, JA, Harris, DC, Wickstrom, LH, Walker, D, Baranoski, MT, Keith, BD, and Furer, LC. 1992. The East Continent Rift Basin: A new discovery: Kentucky Geological Survey, Ser.11, Special Publication 18, 25 p.

Driese, SG, Byers, CW, and Dott, RH, Jr. 1981. Tidal deposition of the basal Upper Cambrian Mt. Simon Formation in Wisconsin: J Sediment Petrol 51:367-381.

Endo, T., K. Tezuka, T. Fukushima, A. Brie, H. Mikada and M. Miyairi, M., 1998, Fracture Evaluation from Inversion of Stoneley Transmission and Reflections, Proceedings of the 4th Well Logging Symposium of Japan, 389-394.

Engelder, T. 1993. Stress regimes in the lithosphere: Princeton University Press, 457 p.

Engelder, T., 2004, Tectonic implications drawn from differences in the surface morphology on two joint sets in the Appalachian Valley and Ridge, Virginia: Geology, v. 32,p. 413–416, doi:10.1130/G20216.1.

Engelder, T., and A. Whitaker, 2006, Early jointing in coal and black shale: Evidence for an Appalachian-wide stress field as a prelude to the Alleghanian orogeny: Geology, v. 34, p. 581–584, doi:10.1130/G22367.1.Ettensohn. 2008.Enterline, 1991.

Engelder, T., Lash, G.G., Uzcategui, R.S., 2009. Joint sets that enhance production from middle and upper Devonian gas shales of the Appalachian basin: Environmental Geoscience 93(7):857-889

Enterline, DS. 1991. Depositional environments of the Cambro-Ordovician Rose Run formation in N.E. Ohio and equivalent, Gatesburg Formation in N.W. Pennsylvania: University of Akron, M.S. thesis, 163 p.

Ettensohn, F.R. 2008. Chapter 4: The Appalachian foreland basin in the eastern United States, in Miall, A., ed., The Sedimentary basins of the United States and Canada: Sedimentary Basins of the World, Amsterdam, Elsevier, p. 105–179.

Fielding, E.J., Blom, R.G., and Goldstein, R. 1998. Rapid subsidence over oil fields measured by SAR interferometry. Geophysical Research Letters, 25 (17): 3215-3218.

Fisher, G. 2010. Data Confirm Safety of Well Fracturing. American Oil and Gas Reporter, July 2010.

Flugel, E. 2004. Microfacies of Carbonate Rocks: Analysis, Interpretation and Application. 1st Edition. Springer, Verlag Berlin Heidelberg.

Franquet, J. A., & Rodriguez, E. F. (2012, January 1). Orthotropic Horizontal Stress Characterization From Logging And Core Derived Acoustic Anisotropies. American Rock Mechanics Association.

Friberg, P., Besana-Ostman, G., and Dricker, I. 2014. Characterization of an earthquake sequence triggered by hydraulic fracturing in Harrison County Ohio. Seismological Research Letters, 85, 6.

Gale, J. Self-organization of natural mode-I fracture apertures into power-law distributions. ARMA, Houston 2004.

Gercek, H. 2007. Poisson's ratio values for rocks. Int. Journal of Rock Mechanics and Mining Sciences. Vol. 44, (2007) 1-13.

Gerst, J., L. Cumming, J. Miller, G. Larsen, N. Gupta, and A. Modroo, 2014, Using baseline data to strengthen geological characterization of a Niagaran Pinnacle Reef: Energy Procedia, v. 63, pp. 3923-3934.

Gillespie, P., Howard, C., Walsh, J., and Watterson, J. 1993. Measurement and characterization of of spatial distributions of fractures: Tectnophysics, v. 226, p. 113-141.

Ginsburg, RN. 1982. Actualistic depositional models for the Great American Bank (Cambro-Ordovician) (abs.): International Association of Sedimentologists, 11th International Congress on Sedimentology, Abstracts, Hamilton, Ontario, p. 114.

Glumac, B., and Walker, KE. 2002. Effects of grand-cycle cessation on the diagenesis of Upper Cambrian carbonate deposits in the Southern Appalachians, U.S.A.: J Sediment Res 72:570-586.

Glumac, B., and Walker, K.E., 2000, Carbonate deposition and sequence stratigraphy of the terminal Cambrian grand cycle in the southern Appalachians, U.S.A.: Journal of Sedimentary Research, v.70, p. 952-963.

Godec, M., Koperna, G., Petrusak, R., and Oudinot, A. 2016. Potential for enhanced gas recovery and CO_2 storage in the Marcellus Shale in Eastern United States. International Journal of Coal Geology, 118: 95-104.

Gooding, PJ. 1992. Unconformity at the top of the Knox Group (Cambrian and Ordovician) in the subsurface of south central Kentucky, Kentucky Geological Survey, Thesis Series 4, 40 p.

Gu, H., and Siebrits, E. 2008. Effect of formation modulus contrast on hydraulic fracture height containment. SPE Prod. Oper. (May), 173–176.

Gupta, N., M. Kelley, R. Osborne, M. Moody, J. Gerst, S. Mishra, E. Howat, C. Sullivan, G. Spitnogle, I. Bhattacharya, and M. Hammond, 2013, Development of conceptual design for commercial-scale geologic storage and monitoring system at the American Electric Power Mountaineer Plant: Energy Procedia, v. 37, pp. 6156-6169.

Gwinn, V F., 1964, Thin skinned tectonics in the plateau and northwestern Valley and Ridge Provinces of the central Appalachians. Geological Society of America Bulletin, v. 75, pp. 863-900.

Haddox, CA, and Dott, RH, Jr. 1990. Cambrian shoreline deposits in Northern Michigan: J Sediment Petrol 60:697-716.

Haimson, B.C. and F.H. Cornet. 2003. ISRM suggested methods for rock stress estimation—part 3: hydraulic fracturing (HF) and/or hydraulic testing of pre-existing fractures (HTPF) (in International Journal of Rock Mechanics and Mining Sciences 40 (7): 1011-1020.

Hammack, R., Harbert, W., Sharma, S., Stewart, B., Capo, R., Wall, A., Wells, A., Diehl, R., Blaushild, D., Sams, J., and Veloski, G. 2014. An Evaluation of Fracture Growth and Gas/Fluid Migration as Horizontal Marcellus Shale Gas Wells are Hydraulically Fractured in Greene County, Pennsylvania. NETL-TRS-3-2014.

Hansen, M. C., 1997. The Geology of Ohio – The Ordovician. *Ohio Geology,* Fall 1997.

Hansen, M. C., 1998a. The Geology of Ohio – The Silurian. *Ohio Geology,* Spring 1998.

Hansen, M. C., 1998b. The Geology of Ohio – The Cambrian. Ohio Department of Natural Resources (ODNR), Division of Geologic Survey, GeoFacts No. 20, 2 pp.

Harris, DC, Hickman, JB, Baranoski, MT, Drahovzal, JA, Avery, KL, and Nuttall, BC. 2004. Rome Trough Consortium final report and data distribution: Kentucky Geological Survey, ser. 12, Open File Report 04-06, 1 CDROM.

Harris, J.M., R.C. Nolen-Hoeksema, R.T. Langan, M. Van Schaack, S.K. Lazaratos, and J.W. Rector, 1995, High-resolution crosswell imaging of a west Texas carbonate reservoir: Part 1—Project summary and interpretation. Geophysics 60:667–681

Harris, J.M. and R. T. Langan. "Crosswell Seismic Fills the Gap." Geophysical Corner (1991). Available at: http://www.searchanddiscovery.com/documents/geophysical/harris_langan/

Heffer, K. and Breven, T. 1990. Scaling relationships and natural fractures: Data, theory, and applications. Society of Petroleum Engineers, Europec 90, The Hague, October 22-24, SPE Paper 20981, p. 367-376.

Heidbach, O, Tingay, M, Barth, A, Reinecker, J, Kurfeß, D, and Müller, B. The World Stress Map based on the database release 2008, equatorial scale 1:46,000,000: Commission for the Geological Map of the World, Paris, doi:10.1594/GFZ.WSM.Map2009, 2009. http://dc-app3-14.gfz-potsdam.de/pub/poster/poster.html. Accessed 09/18/2015.

Holzer, T.L., and R.L. Bluntzer. 1984. Land subsidence near oil and gas-fields, Houston, Texas. Ground Water, 22 (4): 450-459.

Howell, PD, and van der Pluijm, BA. 1999. Structural sequences and styles of subsidence in the Michigan basin: Geol Soc Am Bull 111:974-991.

Huck, Scott W. 2013. Controls on natural fractures in the upper Lexington limestone and point pleasant formation: central ohio. Graduate Thesis, Bowling Green State Univesity, August 2013, 135 p.

Hurd, O, and Zoback, M. 2012. Intraplate earthquakes, regional stress and fault mechanics in the Central and Eastern U.S. and Southeastern Canada: Tectonophysics 581:182–192.

Jadoon, IAK, Bhatti, KM, Siddiqui, FI, Jadoon, SK, Gilani, SRH, and Afzal, M. 2007. Subsurface Fracture Analysis in Carbonate Reservoirs: Kohat/potwar Plateau, North Pakistan.

Janssens, A. 1973. Stratigraphy of Cambrian and Lower Ordovician rocks in Ohio: Ohio Division of Geological Survey, Bulletin 64, 197 p.

Jeffrey, R.G., Bunger, A., Lecampion, B., Zhang, X., Chen, Z., As, A., Allison, D.P., de Beer, W., Dudley, J.W., Siebrits, E., Thiercelin, M., Mainguy, M. 2009. Measuring hydraulic fracture growth in naturally fractured rock. In Paper SPE 124919, SPE Annual Technical Conference and Exhibition, New Orleans, Louisiana, 4–7 October.

Kang, S.M., Fathi, E., Ambrose, J., Akkutlu, I.Y., Sigal, R.F. 2011. Carbon Dioxide Storage Capacity of Organic-rich Shales. SPE Journal (Society of Petroleum Engineers) 2011, 16 (04): 14 p. Paper: SPE 134583-PA.

Kelley, M. et al. 2011. CO_2 Injection Test in the Cambrian-Age Mt. Simon Formation Duke Energy East Bend Generating Station, Boone, County, Kentucky. Report prepared by the Midwest Regional Carbon Sequestration Partnership under DOE-NETL Agreement DE-FC26-05NT42589. 157 p.

Kriegshauser, B., O.N. Fanini, R.A. Mollison, L. Yu, T. Wang, and X.M. Ming, 2005, Method of Using Electrical and Acoustic Anisotropy Measurements for Fracture Identification, US Patent 6925031 B2.

Lash, G. G., and T. Engelder, 2009, Tracking the burial and tectonic history of Devonian shale of the Appalachian Basin by analysis of joint intersection style: Geological Society of America Bulletin, v. 121, p. 265–277, doi:10.1130/B26287.1.

Leetaru, H. E., & McBride, J. H. 2009. Reservoir uncertainty, Precambrian topography, and carbon sequestration in the Mt. Simon Sandstone, Illinois Basin. Environmental Geosciences, 16(4), 235-243.

Levine, J.S., Fukai, I., Soeder, D., Bromhal, G., Dilmore, R., Guthrie, G., Rodosta, T., Sanguinito, S., Fraily, S., Gorecki, C., Peck, W., and Goodman, A. 2016. U.S. DOE NETL methodology for estimating the prospective CO_2 storage resource of shales at the national and regional scale. International Journal of Greenhouse Gas Control, August 2016, 51: 81-94.

Ljunggren, C., Y. Chang, T. Janson, and R. Christiansson, 2003, An overview of rock stress measurement methods: International Journal of Rock Mechanics and Mining Sciences, v. 40, p. 975-989.

Lucier, A., M. Zoback, N. Gupta, and T.S. Ramakrishnan, 2006, Geomechanical Aspects of CO_2 Sequestration in a Deep Saline Reservoir in the Ohio River Valley Region, Environmental Geosciences, 13(2), 85-103.

Luthi, S.M., and P. Souhaite. 1990. Fracture apertures from electrical borehole scans. Geophysics, v. 55, no. 7, p. 821-833.

Mandl, G. (2005). Rock joints. Berlin: Springer.

Marchefka, A, and Glumac, B. 2002. Stratigraphy of the Big Spring Station Member of the Conococheague Limestone, southcentral Pennsylvania [abs.]: Abstracts with Programs, Geological Society of America 34:15.

Marrett, R., Ortega, O., and Kelsey, C. 1999. Extent of power-law scaling for natural fractures in rock. Geology, v. 27, no. 9. p. 799-802.

Maxwell, S.C., 2010, “Microseismic: Growth Born from Success,” The Leading Edge, Vol. 29, pp. 338-343. doi:10.1190/1.3353732

Maxwell, S.C., Urbancic, T.I., Steinsberger, N.P., Zinno, R. 2002. Microseismic imaging of hydraulic fracture complexity in the Barnett shale. In: Paper SPE 77440, SPE Annual Technical Conference and Exhibition, San Antonio, Texas, 29 September – 2 October.

Mayerhofer, MJ, Lolon, EP, Warpinski, NR, Cipolla, CL, Walser, D, and Rightmire, CM. 2010. What is stimulated reservoir volume? SPE Production and Operations, 25(1):89.

McNeil, C., I. Bhattacharya, T. Lohner, J.H. Holley, M. Kennedy, S. Mawalkar, N. Gupta, S. Mishra, R. Osborne, and M. Kelley, 2014, Lessons learned from the post-injection site care program at the American Electric Power Mountaineer Product Validation Facility: Energy Procedia, v. 63, pp. 6141-6155.

Medina, C. R., and J.A. Rupp. 2010. Reservoir Characterization and Lithostratigraphic Division of the Mount Simon Sandstone: Implications for Estimations of Geologic Sequestration Storage Capacity. AAPG Eastern Section, Annual Meeting, 9/26/10-9/28/10, Kalamazoo, Michigan.

Midwest Geological Sequestration Consortium (MGSC). 2005. "An Assessment of Geological Carbon Sequestration Options in the Illinois Basin," U.S. DOE Contract: DE-FC26-03NT41994, The Board of Trustees of the Univ. of Illinois, Illinois State Geological Survey, Final Report December 31.Miall, AD. 1984. Principles of Sedimentary Basin Analysis: Springer-Verlag, New York, 490 p.

Milici, RC. 1980. Relationship of regional structure to oil and gas producing areas in the Appalachian basin. U.S. Geological Survey Miscellaneous Investigations Series Map I–917–F, 5 sheets, scale 1:2,500,000.

Montanez, IP. 1994. Late diagenetic dolomitization of Lower Ordovician, Upper Knox carbonates: a record of the hydrodynamic evolution of the southern Appalachian Basin: Am Assoc Petr Geol Bull 78:1210-1239.

Montgomery, SL. 1984. Michigan Basin: exploring the deep frontier. Petroleum Frontiers.

MRCSP (Midwest Regional Carbon Sequestration Partnership). 2005. Characterization of Geologic Sequestration Opportunities in the MRCSP Region: Phase I Task Report Period of Performance: October 2003–September 2005, Open File Report 2005-1. Prepared under DOE Cooperative Agreement No. DE-PS26-05NT42255, 152 p. 211-229.

Mussman, WJ, and Read, JF. 1986. Sedimentology and development of a passive- to convergent-margin unconformity: Middle Ordovician Knox unconformity, Virginia Appalachians: Geol Soc America Bull 97:282-295.

Mussman, WJ, Montanez, IP, and Read, JF. 1988. Ordovician Knox paleokarst unconformity, Appalachians, in James, NP, and Choquette, PW, eds., Paleokarst. Spring-Verlag, New York, p.

Nakamura, K, Jacob, KH, and Davies, JN. 1977. Volcanoes as possible indicators of tectonic stress orientation – Aleutians and Alaska. Pure Appl Geophys 115:87–112.

Nelson, E.J., S.T. Chipperfield, R.R. Hillis et al. 2007. The relationship between closure pressures from fluid injection tests and the minimum principal stress in strong rocks (in International Journal of Rock Mechanics and Mining Sciences 44 (5): 787-801.

Nelson, WJ. 1990. Structural styles of the Illinois basin: Interior Cratonic Basins, AAPG, p. 209-243.

NRC (National Research Council). 2013. Induced Seismicity Potential in Energy Technologies: Washington, D.C., The National Academies Press, 262 p., doi: 10.17226/13355.

Nuttall, B., Drahovzal, J., Eble, C., and Bustin, R. 2005. Analysis of the Devonian Black Shale in Kentucky for Potential Carbon Dioxide Sequestration and Enhanced Natural Gas Production. Final report prepared for U.S. DOE-NETL contract DE-FC26-02NT41442.

NYSDEC (New York State Department of Environmental Conservation). 2017. Wells Data Search. Oil & Gas Searchable Database. http://www.dec.ny.gov/cfmx/extapps/GasOil/search/wells/index.cfm

Nygaard, R. 2010. Geomechanical Analysis- Wabamun Area CO_2 Sequestration Project. Report prepared for Energy and Environmental System Group, Institute for Sustainable Energy, Environment, and Economy. 14 p.

New York State Energy Research and Development Authority (NYSERDA). 2011. Carbon Sequestration Feasibility Study in the Chautauqua County, New York Area. https://www.nyserda.ny.gov/-/media/Files/Publications/Research/Environmental/Carbon-Sequestration-Feasibility-Study.pdf

Ochoa, R. 2011. Porosity characterization and diagenetic facies analysis of the Cambrian Mount Simon Sandstone: Implications for a regional CO2 sequestration reservoir. MS Dissertation, Purdue University.

ODNR (Ohio Department of Natural Resources). 2017. Ohio Oil & Gas Well Database. ODNR Division of Oil & Gas Resources. http://oilandgas.ohiodnr.gov/well-information/oil-gas-well-database

ODNR (Ohio Department of Natural Resources). 2015. Division of Oil and Gas Resources. The Risk Based Data Management System (RBDMS) Database. http://oilandgas.ohiodnr.gov/industry/rbdms. Accessed 09/18/2015.

Ortega, O. J., Marrett, R. A., & Laubach, S. E. (2006). A scale-independent approach to fracture intensity and average spacing measurement. AAPG Bulletin, 90(2), 193-208.Pashin and Hinkle, 1997

Patchen, D.G., and Carter, K.M. (eds). 2015. *Geologic Play Book for Utica Shale Appalachian Basin Exploration.* Utica Shale Appalachian Basin Exploration Consortium.

Plumb, R. and Hickman, S. 1985. Stress-induced borehole elongation: A comparison between the four-arm dipmeter and the borehole televiewer in the Auburn Geothermal Well. Journal of Geophysical Research, vol. 90, issue B7, p. 5513-5521.

Pratt, W.E., and Johnson, D.W. 1926. Local subsidence of the Goose Creek oil field, J. Geol., 34 (7): 577-590.

Read, JF. 1989. Controls on evolution of Cambrian-Ordovician passive margins, U.S. Appalachians: In Crevello, PS (ed.), Controls on Carbonate Platform and Basin Development: Society of Economic Mineralogists and Paleontologists Special Publication 44, p. 147-162.

Richardson, GB 1941. Geologic Structure and Occurrence of Gas in Part of Southwestern New York – Part 2. Subsurface Structure in Part of Southwestern New York and Mode of Occurrence of Gas in the Medina Group. United States Department of the Interior Geological Survey Bulletin 899-B, pp 69-79.

Riley, R.A., and Baranoski, M.T., 2006, Regional Cross Sections Illustrating the Middle and Upper Ordovician Stratigraphic Framework in the Appalachian Basin: AAPG Eastern Section annual Meeting Poster, Buffalo, NY, October 8-11. Downloaded from OGS website: http://geosurvey.ohiodnr.gov/publications-maps-data/free-downloads/poster-presentations

Riley, RA, Harper, JA, Baranoski, MT, Laughrey, CD, and Carlton, RW. 1993. Measuring and predicting reservoir heterogeneity in complex deposystems: The Late Cambrian Rose Run sandstone of eastern Ohio and western Pennsylvania. Appalachian Oil and Natural Gas Research Consortium, West Virginia University, Morgantown, West Virginia, U.S. Department of Energy, Contract No. DE-AC22-90BC14657, 257 p.

Ripepi, N., Karmis, M., and Gilliland, E. 2016. Central Appalachian Basin Unconventional (Coal/Organic Shale) Reservoir Small-Scale CO_2 Injection Test. U.S. DOE NETL Carbon Storage and Oil & Natural Gas Technologies Review Meeting, August 16-18, 2016, Pittsburgh, PA.

Roen, JB, and Walker, BJ (eds). 1996. The Atlas of Major Appalachian Gas Plays. U.S. Department of Energy, Gas Research Institute, and West Virginia Geological and Economic Survey.

Rogers, W B., and Rogers, H.D., 1843, On the physical structure of the Appalachian chain, is exemplifying the laws which have regulated the elevation of great mountain chains, generally, Association of American Geologists and Naturalists Reports, Boston, pp. 474-531

Rutqvist, J. and O. Stephansson, 1996, A cyclic hydraulic jacking test to determine the in situ stress normal to a fracture: International journal of rock mechanics and mining sciences & geomechanics abstracts, p. 695-711.

Ryder, R.T., 1992a, Stratigraphic framework of Cambrian and Ordovician rocks in the Central Appalachian basin from Morrow County, Ohio, to Pendleton County, West Virginia: U.S. Geological Survey Bulletin 1839-G, 25 p., 1 pl.

Ryder, RT. 1992b. Stratigraphic framework of Cambrian and Ordovician rocks in the Central Appalachian basin from Lake County, Ohio, to Juniata County, Pennsylvania: U.S. Geological Survey Miscellaneous Investigations Series, Map I-2200.

Ryder, RT. 1996. Fracture Patterns and Their Origin in the Upper Devonian Antrim Shale Gas Reservoir of the Michigan Basin: A Review: U. S. Geological Survey Open-File Report 96-23. http://pubs.usgs.gov/of/1996/of96-023/. Accessed 09/18/2015.

Ryder, RT, Harris, AG, and Repetski, JE. 1992. Stratigraphic framework of Cambrian and Ordovician rocks in the Central Appalachian basin from Medina County, Ohio, through southwestern and south-central Pennsylvania, to Hampshire County, West Virginia: U.S. Geological Survey, Bulletin 1839-K, 32 p.

Ryder, RT, Repetski, JE, and Harris, AG. 1997. Stratigraphic framework of Cambrian and Ordovician rocks in the Central Appalachian basin from Campbell County, Kentucky, to Tazewell County, Virginia: U.S. Geological Survey, Miscellaneous Investigations Series, Map I-2350.

Ryder, RT, Trippi, MH, Swezey, CS, Crangle, RD, Hope, RS, Rowan, EL, and Lentz, EE. 2012. Geologic Cross Section C-C' Through the Appalachian basin from Erie County, North-Central Ohio, to the Valley and Ridge province, Bedford County, South-Central Pennsylvania: United States Geological Survey, Scientific Investigations Map 3172.

Schaef, H.T., and McGrail, B.P. 2016. CO_2 Utilization in Unconventional Reservoirs. U.S. DOE NETL Carbon Storage and Oil & Natural Gas Technologies Review Meeting, August 16-18, 2016, Pittsburgh, PA.

Schuchert, C., 1923, Sites and nature of North American geosynchnes. Geological Society of America Bulletin, v. 34, pp. 151-230.

Shahinpour, A., 2013, Borehole Image Log Analysis for Sedimentary Environment and Clay Volume Interpretation, MS Thesis, Norwegian University of Science and Technology, 84 p.

Shrake, DL, Wolfe, PJ, Richard, BH, Swinford, EM, Wickstrom, LH, Potter, PE, and Sitler, G.W. 1990. Lithologic and geophysical description of a continuously cored hole in Warren County, Ohio, including description of the Middle Run Formation (Precambrian?) and a seismic profile across the core site: Ohio Division of Geological Survey Information Circular 56.

Shumaker, R. 1996. A Structural History of the Appalachian Basin, in The Atlas of Major Appalachian Gas Plays. U.S. Department of Energy, Gas Research Institute, and West Virginia Geological and Economic Survey.

Solano-Acosta, Wilfrido, Stephen Greb, John Rupp, James Drahovzal, Lawrence Wickstrom and Joel Sminchak. 2006. *Preliminary Assessment of Potential CO_2 Storage Reservoirs and Caprocks at the Cincinnati Arch Site*.

Sminchak, J.R. 2015. Geologic and Hydrologic Aspects of Brine Disposal Intervals in the Appalachian Basin. *Environmental Geosciences*, Vol 22, Num. 4.

Sminchak, J. and N. Gupta, 2003. Aspects of induced seismic activity and deep-well sequestration of carbon dioxide. Geosciences 10(2):81-89.

Swezey, C. 5., 2002, Regional stratigraphic and petroleum systems of the Appalachian basin, North America, U.S. Geological Survey, Geologic Investigations Series Map 1-2768.

Tang, XM, and Cheng, A. 2004. Quantitative Borehole Acoustic Methods: Elsevier, 261 p.

Thomas, W.A. 2006. Tectonic inheritance at a continental margin: GSA Today, v. 16, no. 2, p 4-11. Pennsylvania Geological Survey, 4th ser., Special Publication 1, 888 p.

Thomas, W.A., and Astini, R. 199 Simple-shear confugate rift margins of the Argentine Precordillera and Ouachita embayment of Laurentia: Geological Society of America Bulletin, v. 111, p 1069-1079.

Townend, J, and Zoback, MD. 2000. How faulting keeps the crust strong. Geology 28:399–402.

Tran, D., Settari, A., and Nghiem, L. 2004. New Iterative Coupling Between a Reservoir Simulator and a Geomechanics Module. SPE-88989-PA. SPE Journal, vol. 9, no. 3.

USGS (U.S. Geological Survey). 2011. Assessment of Undiscovered Oil and Gas Resources of the Devonian Marcellus Shale of the Appalachian Basin Province, 2011. Fact Sheet 2011-3092.

Vanhasselt, J.P. 1992. Reservoir compaction and surface subsidence resulting from oil and gas-production: a review of theoretical and experimental research approaches. Geologie En Mijnbouw, 71 (2): 107-118.

Veltman, W., Velez, E., Lujan, V. 2012. A fresh look for natural fractures using advanced borehole acoustics techniques. AAPG Annual Convention and Exhibition, Long Beach, California, April 22-25, 2012.

Verdon, J.P., M.J. Kendall, A.L. Stork, R.A. Chawick, D.J. White, and R.C. Bissell, 2013. Comparison of geomechanical deformation induced by megaton-scale CO_2 storage at Sleipner, Weyburn, and In Salah: Proceedings of the National Academy of Science USA, Vol. 110, no. 30 pp. E 2762-E2771.

Walsh, R., and Zoback, M. 2016. Probabilistic assessment of potential fault slip related to injection-induced earthquakes: Application to north-central Oklahoma, USA. Geology 44(12), p 991-994.

Warpinski, N. 2010. Measurements and Observations of Fracture Height Growth.

Warpinski, N., and Fisher, K. 2012. Hydraulic-Fracture-Height Growth: Real Data; SPE Production and Operations; February 2012; p 19.

Weng, X. 2015. Modeling of complex hydraulic fractures in naturally fractured formation. Journal of Unconventional Oil and Gas Resources, 9 (March 2015), p. 114-135.

Wickstrom, L., Riley, R., Spane, F., McDonald, J., Slucher, E., Baranoski, M., Zody, S., Wells, J, and Howat, E. 2011. Geologic Assessment of the Ohio Geological Survey CO2 No. 1 Well in Tuscarawas County and Surrounding Vicinity. Prepared for the Ohio Coal Development Office and U.S. DOE National Energy Technology Laboratory. 658 p.

Wickstrom, L. H., Venteris, E. R., Harper, J. A., and 26 other authors, 2005, Characterization of geologic sequestration opportunities in the MRCSP region: Final report under DOE cooperative agreement no. DE-PS26-05NT42255, 152 p.

Wickstrom, L.H., E.R. Venteris, J.A. Harper, J. McDonald, E.R. Slucher, K.M. Carter, S.F. Greb, J.G. Wells, W.B. Harrison, III, B.C. Nuttall, R.A. Riley, J.A. Drahovzal, J.A. Rupp, K.L. Avary, S,

Lanham, D.A. Barnes, N. Gupta, M.A. Baranoski, P. Radhakkrishnan, M.P. Solis, G.R. Baum, D. Powers, M.E. Hohn, M.P. Parris, K. McCoy, G.M. Grammer, S. Pool, C. Luckhardt, and P. Kish. 2006. “Characterization of Geologic Sequestration Opportunities in the MRCSP Region: Phase I Task Report (October 2003-September 2005).” DOE Cooperative Agreement No. DE-PS26-05NT42255.

Wickstrom, L.H., Gray, J.D., and Stieglitz, R.D., 1992, Stratigraphy, structure, and production history of the Trenton Limestone (Ordovician) and adjacent strata in northwestern Ohio: Ohio Department of Natural Resources, Division of Geological Survey Report of Investigations 143, 78 p. Willis, B., 1893, The mechanisms of Appalachian structure, U.S. Geological Survey 13th Annual Report, pt. 2, pp. 211-281.

Wilson, T., Smith, V., and Brown, A. 2014. Developing a model discrete fracture network, drilling and EOR strategy in an unconventional naturally fractured reservoir using integrated field, image log, and 3D seismic data. AAPG Bulletin, 03 November 2014.

Witherspoon, P.A., Wang, J., Iwai, K., and Gale, J. 1979. Validity of Cubic Law for Fluid Flow in a Deformable Rock Fracture.

Wright, C.A., E.J. Davis, G. Wang, and L. Weijers, 1999, Downhole tiltmeter fracture mapping: A new tool for direct measurement of hydraulic fracture growth. American Rock Mechanics Association.

WVGES (West Virginia Geological and Economic Survey). 2017. Data Files for West Virginia Horizontal Wells. http://www.wvgs.wvnet.edu/www/datastat/devshales.htm#DataHoriz

WVGISTC/NETL (West Virginia GIS Technical Center/National Energy Technology Laboratory). 2017. UCR Atlas: Unconventional Hydrocarbon Resources. http://www.unconventionalenergyresources.com/viewer/index.html#

Xu, W., Calvez, J.L., and Thiercelin, M. 2009. Characterization of hydraulically-induced fracture network using treatment and microseismic data in a tight-gas formation: A geomechanical approach. In: Paper SPE 125237, SPE Tight Gas Completions Conference, San Antonio, Texas, USA, 15–17 June.

Zagorski, W., Wrightstone, G., and Bowman, D. 2012. The Appalachian Basin Marcellus Gas Play: Its History of Development, Geologic Controls on Production, and Future Potential as a World-class Reservoir. In J.A. Breyer, ed., Shale reservoirs- Giant resources for the 21st century: AAPG memoir 97, p. 172-200. doi:10.1306/13321465m973491

Zimmerman, R. W., G. Chen, T. Hadgu, and G. S. Bodvarsson. 1993. A numerical dual-porosity model with semi-analytical treatment of fracture/matrix flow. Water Resour. Res., vol. 29, pp. 2127-37, 1993.

Zoback, MD. 2007. Reservoir Geomechanics: Cambridge University Press, 505 p.

Zoback, M.D., C.A. Barton, M. Brudy, et al. 2003. Determination of stress orientation and magnitude in deep wells (in International Journal of Rock Mechanics and Mining Sciences 40 (7): 1049-1076.

Zoback, MD, and Gorelick, SM. 2012. Earthquake triggering and large-scale geologic storage of carbon dioxide. Proceedings of the National Academy of Sciences, 109(26):10164-10168.

Zumberge, J.F., M.B. Heflin, D.C. Jefferson, M.M. Watkins, And F.H. Webb, 1997, Precise point positioning for the efficient and robust analysis of GPS data from large networks. J Geophys. Res. Solid Earth (1978-2012) 102 (B3), 5005-5017.